CONETEC

THE CONE PENETRATION TEST:
BETTER INFORMATION, BETTER DECISIONS

A CPT Design Parameter Manual

First Edition
February 2023

THE CONE PENETRATION TEST:
BETTER INFORMATION
BETTER DECISIONS

A CPT Design Parameter Manual

Produced by:
ConeTec

Authored by:
Paul W. Mayne, PhD, P.E.
Ethan Cargill, P.E., D.GE
James Greig, P.Eng.

With contributions by:
Mark Styler, PhD, P.E.
Iman Entezari, PhD
Jamie Sharp, P.Eng.

First Edition
February 2023
Revision 1.1

Scan to access more
technical resources at conetec.com

Table of Contents

1 Introduction to Cone Penetration Testing 1

1.1 Cone Penetration Testing (CPT) 1

1.1.1 Cone Probe Dimensions 2

1.1.2 Types of Cone Penetrometers 2

1.1.3 Unequal End Area Corrections 3

1.2 CPT Vehicles 4

1.3 CPT Soundings 6

1.4 Pore Pressure Dissipation (PPD) Tests 7

1.5 Stratigraphic Profiling 8

1.6 CPT Soil Identification by Rules of Thumb 9

1.7 Seismic Cone Penetration Testing (SCPTU) 10

1.8 Site Characterization 14

1.9 Objectives 15

2 Soil Unit Weight and Overburden Stresses 16

2.1 Total Soil Unit Weight (γ_t) 16

2.1.1 Unit Weight Estimated from Soil Behavior Type 18

2.1.2 Unit Weight Estimated from CPT Measurements 19

2.1.3 Unit Weight Estimated from V_s 23

2.2 Estimating V_s from CPT profiles 25

2.3 Unit Weight in Man-Made Deposits 28

2.3.1 Fluid Tailings 28

2.3.2 Metal Mine Tailings 28

2.4 Overburden Stress and Porewater Pressure 29

2.4.1 Total Overburden Stress 29

2.4.2 Equilibrium Porewater Pressure 29

2.4.3 Groundwater Table Depth 29

2.4.4 Non-Hydrostatic Water Table 30

2.4.5 Effective Vertical Stress 30

2.5 Horizontal Stress and K_0 31

3 Stratigraphy and Soil Type 35

3.1 Initial Conditions 36

3.2 Soil Behavior Type (SBT) 36
3.2.1 q_t versus R_f 37
3.2.2 Q versus F_r 38
3.2.3 Q_{tn} versus F_r 40
3.2.4 Q versus B_q 42
3.2.5 Q versus $\Delta u/\sigma'_{vo}$ 43
3.2.6 $Q(1-B_q)+1$ versus F_r 44
3.2.7 SBT Index $I_{C,BJ}$ 44
3.2.8 Conflicting SBT profiles 45
3.3 Apparent Fines Content 46
3.3.1 AFC from Material Index, I_c 46
3.3.2 AFC from CPT Index, I_B 47
3.4 Drained versus Undrained Response for CPT 48
4 Soil State and Stress History 51
4.1 Void Ratio 51
4.2 Relative Density of Clean Sands 51
4.2.1 Calibration Chamber Testing 53
4.2.2 Quartz-Silica Sands 54
4.2.3 Carbonate-Calcareous Sands 56
4.3 State Parameter 58
4.4 Overconsolidation Ratio and Yield Stress Ratio 59
4.4.1 Analytical CPT Model for YSR in Clay 61
4.4.2 Simplified Expressions for Intact Insensitive and Inorganic Clays 62
4.4.3 CPTU Screening for Sensitive Clays 63
4.4.4 CPTU Screening for Organic Clays 65
4.4.5 Evaluation of Yield Stress from CPTU in Sensitive Clays 66
4.4.6 Evaluation of Yield Stress from CPTU in Organic clays 67
4.5 Yield Stress of Sands from CPT 68
4.5.1 Case Study: Blessington Sand Site, Ireland 70
4.6 Unified Interpretation of Yield Stress in Soils by CPT 71
4.7 Evaluation of YSR from V_s 74
5 Effective Friction Angle and Drained Strength 76
5.1 Drained Strength of Soils 76

5.1.1 Critical State Friction Angle, ϕ'_{cs} 76
5.1.2 Peak Friction Angle, ϕ'_p 77
5.1.3 Drained Friction Angle of Sands from Cone Resistance 80
5.1.4 Sand Friction Angle with CPT Material Index, I_c 84
5.1.5 Case Study: Silty Sands at Georgia Tech 85
5.2 Effective Friction Angle of Clays from CPTU (NTH Solution) 86
5.2.1 Case Study: Soft Clay at Sandpoint Idaho 87
5.2.2 Approximate NTH Solution for ϕ' in Clays 90
5.2.3 Case Study: Soft Chicago Clay at Northwestern University 90
5.2.4 Case Study: Soft to Firm Clay at Newbury, MA 92
5.2.5 Friction Angle Database in Clays 93
5.3 Friction Angle of OC Intact Clays 96
5.3.1 Case Study: CPTU in OC Clay, Anchorage 96
5.4 Friction Angle of OC Fissured Clays by CPTU 99
5.4.1 Case Study: CPTU in Fissured Beaumont Clay 99
5.5 Summary of NTH Solutions for NC and OC Clays 101
5.6 Effective Cohesion Intercept, c' 102
5.7 Effective Friction Angle(s) of Sensitive Clays 102
5.8 Peak versus Fully-Softened versus Residual Strength 103
6 Undrained Shear Strength 104
6.1 Mode of Shearing and Strength Anisotropy 105
6.2 Undrained Strength from Stress History 106
6.3 Undrained CPT Penetration 112
6.3.1 Case Study: Sandpoint Idaho 118
6.3.2 Case Study: Tiller-Flotten Quick Clay, Norway 118
6.4 Evaluation of s_u from V_s 119
6.5 Relationship for Undrained Strength with Vane Shear Test 119
6.6 Remolded Undrained Strength and Clay Sensitivity 120
6.7 Sample Disturbance of Laboratory Reference Strengths 122
7 Ground Stiffness and Soil Moduli 125
7.1 Consolidation Theory 125
7.2 Elastic Moduli 126
7.2.1 Constrained Modulus from Compressibility Parameters 127

- 7.2.2 Constrained Modulus from CPT 128
- 7.2.3 Small-Strain Shear Modulus 130
- 7.3 Modulus Reduction Curves 130
- 7.4 Stress-Strain-Strength Curves 132
- 7.5 Poisson's Ratio 134
  - 7.5.1 Poisson's Ratio From Lab Tests 134
  - 7.5.2 Poisson's Ratio from Geophysical Tests 135
- 7.6 Backfigured Drained Moduli from Foundation Performance on Sands 135
- 7.7 Undrained Modulus from Rigidity Index 136
  - 7.7.1 Case Study: Sandpoint 139

8 Flow Parameters from Dissipation Testing 140
- 8.1 from Dissipation Tests 141
  - 8.1.1 Dissipation Evaluation from Strain Path Method 143
  - 8.1.2 Dissipation Evaluation from SCE-CSSM Solution 144
  - 8.1.3 Approximate SCE-CSSM Solution 147
  - 8.1.4 Simplified SCE-CSSM Solution for Monotonic Dissipations 147
  - 8.1.5 Case Study: Sandpoint 148
  - 8.1.6 Case Study: Gloucester, Ontario 149
- 8.2 Adjusted Dilatory Dissipation Curves 150
- 8.3 Permeability 152
  - 8.3.1 Soil Permeability Anisotropy 152
  - 8.3.2 Soil Permeability from Dissipation Tests 153
  - 8.3.3 Permeability from Soil Behavior Type 154
- 8.4 Case Study: Bothkennar, UK 155

9 Liquefaction Evaluation by CPT 157
- 9.1 Flow Liquefaction 158
  - 9.1.1 State Parameter 158
  - 9.1.2 CPT Parameters 159
- 9.2 CPT Screening Methods for Flow Liquefaction 160
  - 9.2.1 State Parameter Approach 160
  - 9.2.2 Normalized Cone Resistance Approach 162
  - 9.2.3 Yield Stress Ratio from CPT 163
- 9.3 Case Histories of Flow Liquefaction 166

- 9.3.1 Jamuna Bridge, Bangladesh ... 166
- 9.3.2 Compacted Tailings, Western Canada ... 167
- 9.3.3 Cadia Tailings Failure, Australia ... 169
- 9.3.4 Fundão Tailings Failure, Brazil ... 170
- 9.3.5 Addition of New Surcharge Loadings ... 172
- 9.4 Cyclic Liquefaction Evaluation By CPT ... 173
  - 9.4.1 Seismic Ground Motions ... 173
  - 9.4.2 NCEER Approach ... 176
  - 9.4.3 UCD Method for Cyclic Liquefaction from CPT ... 179
  - 9.4.4 Yield Stress Ratio for Screening of Cyclic Liquefaction ... 182
- 9.5 Case Studies Involving Cyclic Liquefaction ... 183
  - 9.5.1 Case Study: Felipito Bridges, Mexico ... 183
  - 9.5.2 Case Study: Wildlife Site, California ... 185
  - 9.5.3 Case Study: Christchurch, New Zealand ... 185
- 9.6 Post-cyclic Undrained Strength Evaluation ... 186
  - 9.6.1 UIUC Method ... 186
  - 9.6.2 UCD Approach ... 187
  - 9.6.3 Robertson Method ... 189
- 9.7 Ground Deformations from Liquefaction ... 189
  - 9.7.1 Volumetric Strains ... 190
  - 9.7.2 Case Study from Felipito Bridge, Mexico ... 191
  - 9.7.3 Lateral Displacements ... 192
- 9.8 Cyclic Resistance Using Shear Wave Velocity ... 194

10 Advanced Penetration Testing ... 196
- 10.1 Resistivity Piezocone (RCPTU) or Conductivity Cone ... 196
- 10.2 Passive Gamma Piezocone Testing (GCPTU) ... 199
- 10.3 Continuous Interval SCPTU ... 201
- 10.4 Compression Wave Measurements ... 202
- 10.5 Full-Flow Penetrometers ... 205
  - 10.5.1 T-Bar ... 207
  - 10.5.2 Ball Penetrometer ... 209
- 10.6 Variable Rate Penetration Testing ... 212
  - 10.6.1 NTH Solution Applied to VRCPTU ... 216

10.7 Machine Learning and Big Data for CPTu Interpretation 217
  10.7.1 Estimation of Solids and Fines of Tailings 219
  10.7.2 Estimation of Soil Unit Weight 223
  10.7.3 Estimation of Shear Wave Velocity (V_S) 224
11 References 228

Symbol List

Greek Symbols

Symbol	Description	Chapters
α_D	Empirical scaling factor for constrained modulus	7
β	Angle of plastification in the NTH solution	5
γ'	Effective unit weight of soil	2
γ_{dry}	Dry unit weight of soil	2
γ_f	Unit weight of fluid	8
γ_{rock}	Unit weight of rock	2
γ_{sat}	Unit weight of fully saturated soil	2
γ_t	Total soil unit weight	2, 3, 4, 7
γ_{total}	Total soil unit weight	2
γ_w	Unit weight of water	1, 2, 8
γ_{max}	Maximum cyclic shear strain	9
γ_s	Shear strain	6, 7
γ_{ref}	Modulus reduction factor reference strain	7
ε	Strain	5
ε_h	Horizontal strain	7
ε_s	Small strain	7
ε_v	Axial or vertical strain	6, 7
ε_{vol}	Volumetric strain	7, 9
$\varepsilon_{vol\text{-}limit}$	Limiting volumetric strain	9
η	Porosity	4
κ	Electrical conductivity: $\kappa = 1/\rho_b$	10
λ	Slope of critical state line in an e-ln$_e$(p') plot	9
λ_{10}	Slope of critical state line in an e-log$_{10}$(p') plot: assumed equal to C_c	4, 9
Λ	Plastic volumetric strain potential	4
Λ	Plastic volume strain ratio: $\Lambda = (1 - C_s) / C_c$	5, 6, 8, 9
μ_f	Viscosity of fluid	8
ν	Poisson's ratio	7
ν'	Drained Poisson's ratio	7

Symbol	Description	Chapters
ν_u	Poisson's ratio for undrained loading at constant volume	7
ρ_b	Resistivity	10
ρ_t	Mass density of soil	2
σ'	Effective normal stress (typically σ_{vo}')	5
σ_1', σ_2' , σ_3'	Principal effective stresses	4, 5, 7, 9
σ_{atm}	Atmospheric pressure (taken as 101.3 kPa or 100 kPa)	2, 3, 4, 5, 9
σ_h	Horizontal stress	7
σ_{ho}'	Effective horizontal stress	2, 4
σ_{hc}'	Horizontal effective consolidation stress	4
σ_{oct}	Octahedral stress	7
σ_p'	Pre-consolidation stress or yield stress	4, 5, 6, 7, 9
σ_{pc}'	Maximum past vertical effective stress	2
σ_v	Vertical stress	7
σ_{vo}	Total vertical overburden stress	2, 3, 9, 10
σ_{vo}'	Effective vertical overburden stress	2, 3, 4, 5, 6, 7, 8, 9, 10
σ_{vc}'	Vertical effective consolidation stress	4
σ_{ho}	Pressuremeter lift off pressure	2
τ	Shear stress	5, 7
τ_{ave}	Average shear stress	9
τ_d	Drained shear strength	6
τ_{max}	Maximum shear stress	5, 6, 7
$\tau_{residual}$	Residual shear strength	5
ϕ	Friction angle	8
ϕ'	Effective friction angle	2, 5, 6, 9, 10
ϕ_1'	Friction angle at peak strength (q_{max})	4, 5
ϕ_2'	Friction angle at maximum obliquity (M.O.)	4, 5
ϕ_ψ'	Dilatancy angle	5
ϕ_{cs}'	Critical state friction angle	5
ϕ_{crit}'	Critical state friction angle : $\phi_{crit}' = \phi_{cs}'$	5
ϕ_p'	Effective peak friction angle	5
ψ	State parameter	4, 9

Symbols

Symbol	Description	Chapters
^{40}K	Potassium radioisotope	10
^{232}Th	Thorium radioisotope	10
^{238}U	Uranium radioisotope	10
a’	Attraction: $a' = c' \cot(\sigma')$	5
a_c	Probe radius	8
a_{max}	Peak horizontal ground acceleration (PGA)	9
a_{max}/g_a	Normalized peak ground acceleration	9
a_q	Slope parameter: $a_q = (u_2 - \sigma_{vo}) / q_{net}$ or $a_q = (U-1)/Q$	4, 5, 6
a_v	Empirical fitting parameter for CRR from shear wave velocity	9
A_{net}	Net area ratio (tip)	1
atm	Atmospheric pressure (taken as 101.3 kPa or 100 kPa)	1
b_{net}	Calibration chamber derived correction factor for sleeve	1
b_v	Empirical fitting parameter for CRR from shear wave velocity	9
b_x	Factor to limit the volumetric strain (liquefaction displacement)	9
bx	Jamiolkowski D_R compressibility adjustment term	4
B_q	Pore pressure parameter: $B_q = \Delta u/q_{net}$ or $B_q = U/Q$	2, 3, 5, 6, 9, 10
$B_{q\text{-}ref}$	Reference value for pore pressure parameter	10
c	empirical fitting parameter for variable rate CPT testing	10
c’	Effective cohesion intercept	5
c_u	Undrained shear strength	6, 7
c_h	Coefficient of consolidation (horizontal direction)	8
c_v	Coefficient of consolidation (vertical direction)	8, 10
c_{vh}	Coefficient of consolidation – no direction implied	8, 10
C_α	Coefficient of secondary compression	7
C_σ	Liquefaction overburden stress factor coefficient (UCD)	9
C_c	Virgin compression index	4, 5, 6, 7
C_r	Recompression index	6, 7
C_s	Recompression or swelling index	4, 5, 6, 7
C_{FC}	Site specific fines content adjustment factor	3, 9
C_{Ne}	Stress normalization factor (UCD): $C_{Ne} = (\sigma_{atm}/ \sigma_{vo}')^m$	9
CRR	Cyclic resistance ratio	9
$CRR_{7.5,\sigma'v=1atm}$	Cyclic resistance ratio for benchmark earthquake having $M_w = 7.5$ and effective stress of 1 atmosphere	9

Symbol	Description	Chapters
CSR	Cyclic stress ratio: $CSR = \tau_{ave} / \sigma_{vo}'$	9
$CSR_{7.5}$	Cyclic stress ratio at benchmark magnitude $M_w = 7.5$ having a duration of 15s	9
d	Penetrometer/probe diameter	1, 4, 8, 10
d*	Dimensionless modulus number (m_D) exponent	7
D	Chamber test diameter	4
D	Diameter in general	4, 8
D’	Constrained modulus	7, 8
D_{50}	Mean particle size	4, 5, 9
D_R	Relative density	4, 5, 7, 9
e	Void ratio	9
e_o	Initial void ratio	2, 4, 6, 7, 9
e_{cs}	Void ratio at critical state for a constant mean effective stress	9
e_{min}	Minimum void ratio	4
e_{max}	Maximum void ratio	4
e_{CSL}	Void ratio at the critical state line (failure)	4
Δe	Change in void ratio	6
E’	Young’s modulus	7
E_{max}	Initial small strain tangent Young’s modulus	7
E_{sec}	Secant Young’s modulus	7
E_{tan}	Tangent Young’s modulus	7
E_u	Undrained Young’s modulus	7
E_{ur}	Unload-reload Young’s modulus	7
f_s	Sleeve friction	1, 2, 3, 4, 5, 9, 10
f_{st}	Total (corrected) sleeve resistance	1
F	Normalized friction ratio (in percent): $F = 100 \cdot f_s / q_{net}$	9
F_r	Normalized friction ratio (in percent): $F_r = 100 \cdot f_s / q_{net}$	3, 8, 9
FC	Fines content	3, 4, 9
FS	Factor of safety	7, 9
FS_{limit}	Limiting factor of safety	9
FS_{liq}	Factor of safety against liquefaction	9
g	Modulus reduction factor exponent	7
g_a	Acceleration of gravity	2, 7, 9
G	Shear modulus	4, 6, 8
G’	Drained shear modulus	7
G_o	Small-strain shear modulus	7
G_{max}	Small-strain shear modulus: $G_{max} = G_o$	7
G_u	Undrained shear modulus	7
G_s	Specific gravity of solids	2

Symbol	Description	Chapters
h_w	Equivalent head of water	1, 2
H	Height	4
H	Vertical settlement geometry: free face height	9
I_c	CPT soil behavior type material index (generic)	3, 8, 10
$I_{c,BJ}$	CPT soil behavior type material index as defined by Been and Jefferies: $I_{c,BJ} = \sqrt{\{3 - log_{10}[Q \cdot (1 - B_q) + 1]\}^2 + \{1.5 + 1.3 \cdot log_{10}(F_R)\}^2}$	3, 4
$I_{c,RW}$	CPT soil behavior type material index as defined by Robertson and Wride (1998) and modified by Robertson (2009): $I_{c,RW} = \sqrt{\{3.47 - log_{10}(Q_{tn})\}^2 + (\{1.22 + log_{10}(F_R)\})^2}$	2, 3, 4, 5, 8, 9
$I_{cR'09}$	Same formulation as that shown above for $I_{c.RW}$	3
I_c*	CPT material type index as defined by Been and Jefferies: $I_c^* = \sqrt{\{3 - log_{10}[Q \cdot (1 - B_q) + 1]\}^2 + \{1.5 + 1.3 \cdot log_{10}(F)\}^2}$	9
I_{SBT}	Revised CPT material index based on 2010 Robertson and Cabal dimensionless modified SBT chart: $I_{SBT} = \sqrt{\{3.47 - log_{10}({}^{q_t}/_{\sigma_{atm}})\}^2 + (\{1.22 + log_{10}(R_f)\})^2}$	4
$I_{Q\text{-}Bq}$	$I_{Q\text{-}Bq} = Q \cdot 10^{(-1.9\,Bq)}$	3
I_B	Alternate CPT soil behavior type index	3
I_{DR}	Density Index (same as D_R)	4
I_G	Small strain rigidity index	10
I_R	Rigidity index	4, 6, 7, 8
k	Coefficient of permeability	8
k_h	Coefficient of permeability in the horizontal direction	8
k_v	Coefficient of permeability in the vertical direction	8
k’	Empirical fitting parameter for state parameter: $k' = M_c \cdot (3 + 0.85/ \lambda_{10})$	9
K’	Bulk modulus	7
K_o	At-rest lateral stress coefficient	2, 5
$(K_o)_{NC}$	Normally consolidated lateral stress coefficient	2
K_c	Consolidation lateral stress coefficient	7
K_p	Passive stress coefficient	2, 5
K	Intrinsic permeability	8
K_α	Liquefaction slope correction factor	9
K_σ	Liquefaction overburden correction factor	9
K_c	Liquefaction clean sand equivalent adjustment factor	9
L	Liquefaction vertical settlement geometry: Free face distance (location) from CPT	9
LL	Liquid limit	4

Symbol	Description	Chapters
m	Stress normalization factor exponent for UCD parameter C_{Ne}	9
m’	Yield stress (Mayne) exponent: $m' = 1 - \frac{0.28}{1 + (I_c/2.65)^{25}}$	4, 9
m’	Empirical fitting parameter for state parameter: $m' = 11.9 - 13.3 \cdot \lambda_{10}$	9
m_D	Dimensionless (constrained) modulus number	7
m_q	Slope of cone resistance vs depth: $m_q = \Delta q_t / \Delta z$	2
m_x	Factor to limit the volumetric strain	9
$m_{\Delta u}$	Slope of pore pressure vs depth: $m_{\Delta u} = \Delta u_2 / \Delta z$	2
M	Frictional envelope in Cambridge University type q-p’ space: $M = (6 \cdot \sin\phi_{cs}) / (3 - \sin\phi_{cs})$	4, 8
M’	Constrained modulus	7
M_o	Small-strained constrained modulus	7
M_c	Friction parameter in q-p’ space (M): $M_c = (6 \cdot \sin\phi') / (3 - \sin\phi')$	4, 6, 8, 9
M_{c1}	M_c defined at peak strength (q_{max})	4, 6
M_{c2}	M_c defined at maximum obliquity	4, 6
M_w	Moment magnitude of an earthquake	9
MSF	Magnitude scaling factor	9
MSF_{max}	Maximum magnitude scaling factor	9
n	Number of points in a data set	2, 10
n	Variable stress exponent for Q_{tn}: $n = 0.381 \cdot I_{cRW} + 0.05 \cdot \sigma_{vo}'/ \sigma_{atm} - 0.15 \leq 1.0$	3, 9
N_{ball}	Ball CPT undrained shear strength factor	10
N_{ke}	Undrained shear strength factor for S_u based on q_E	6
N_{kt}	Undrained shear strength factor for S_u based on q_{net}	6, 10
N_m	Cone resistance number	5
N_{mc}	Modified cone resistance number	5
N_q	End bearing factor	5
N_u	Porewater bearing factor	5
$N_{\Delta u}$	Undrained shear strength factor for S_u based on Δu	3, 6
N_{Tbar}	T-bar undrained shear strength factor	10
OCD	Over-consolidation difference or prestress: $OCD = \sigma_p' - \sigma_{vo}'$ or $OCD = \Delta\sigma_p'$	4
OCR	Over-consolidation ratio	2, 3, 4, 5, 6, 7, 8
p_o	Mean total stress	9
p’	Effective mean normal stress	4, 5, 9

Symbol	Description	Chapters
p_o'	Mean effective stress	9
p_f'	Mean effective stress at failure	5
P_o	Lift off pressure	2
P_a	Atmospheric pressure	9
PF	Percent fines	9
PGA	Peak ground acceleration	9
PI	Plasticity index	4, 5
P_L	Probability	5
P_L	Probability of liquefaction	9
q	Deviator stress: $q = \sigma_1 - \sigma_3$	4
q_{ball}	Ball CPT tip resistance	10
q_c	Measured tip resistance	1, 4, 9, 10
q_{c1}	Stress normalized tip resistance (exponent = 0.5): $q_{c1} = (q_c / \sigma_{atm}) \cdot (\sigma_{atm} / \sigma_{vo}')^{0.5}$	4
q_{c1}	Stress normalized tip resistance (UIUC): $q_{c1} = [1.8 \cdot q_c] / [0.8 + (\sigma_{vo}'/\sigma_{atm})]$	9
$q_{c1N\text{-}cs}$	Clean sand equivalent normalized tip resistance (UCD): $q_{c1N\text{-}cs} = q_{c1N} + \Delta q_{c1N}$	9
$q_{c1Ncs\text{-}Sr}$	Normalized cone resistance corrected for FC for residual strength (UCD): $q_{c1Ncs\text{-}Sr} = q_{c1N} + \Delta q_{c1Ncs\text{-}Sr}$	9
Δq_{c1N}	Clean sand equivalent fines content correction (UCD)	9
$\Delta q_{c1Ncs\text{-}Sr}$	Clean sand equivalent fines content correction for residual strength (UCD)	9
q_e	Effective tip resistance: $q_e = q_t - u_2$	4, 6
q_E	Effective tip resistance (same as q_e): $q_E = q_t - u_2$	2, 9
q_{max}	Peak loading in triaxial compression test (maximum deviator stress)	4, 5, 6, 7
q_{net}	Net tip resistance: $q_{net} = q_t - \sigma_{vo}$	2, 3, 4, 5, 6, 7, 9
q_t	Corrected tip resistance: $q_t = q_c + (1 - A_{net}) \cdot u_2$	1, 3, 4, 5, 6, 7, 8, 9, 10
q_{t1}	Stress normalized tip (q_t) resistance (exponent = 0.5): $q_{t1} = (q_t / \sigma_{atm}) \cdot (\sigma_{atm} / \sigma_{vo}')^{0.5}$	4, 5
q_{Tbar}	T-bar tip resistance	10
Q	Normalized tip resistance (generic term)	3, 5
Q	Normalized tip resistance: $Q = q_{net} / \sigma_{vo}'$	9, 10
Q_{c1N}	Normalized cone resistance for clean sands (UCD): $Q_{c1N} = C_{Ne} \cdot q_c / \sigma_{atm}$	9
$Q_{drained}$	Normalized tip resistance in drained testing	10
Q_E	Normalized effective cone resistance: $Q_E = (q_t - u_2) / \sigma_{vo}'$ or $Q_E = Q \cdot (1 - B_q) + 1$	9
Q_p	Linear normalized tip resistance in terms of mean normal stresses: $Q_p = (q_t - p_o) / p_o'$	9
Q_{ref}	Reference value for normalized Q	10

Symbol	Description	Chapters
Q'	Modified cone resistance number for friction angle of OC clays: $Q' = Q/OCR$ ^	5
Q_t	Normalized tip resistance (linear method by Robertson 1990)	3, 5, 9
Q_{t1}	Renamed linear normalized tip resistance: Q_t is now $Q_{t1} = q_{net}/ \sigma_{vo}'$	3, 5, 9
Q_{tn}	Normalized tip resistance (iterative method by Robertson 2009) : $Q_{tn} = (q_{net}/ \sigma_{atm}) \cdot (\sigma_{atm} / \sigma_{vo}')^n$	5, 8, 9, 10
$Q_{tn,cs}$	Clean sand equivalent of Q_{tn}: $Q_{tn,cs} = (Q_{tn} \cdot K_c)$	9
Q_x	Mineralogical component for ϕ_p'	5
r^2 or R^2	Coefficient of determination	2, 5, 10
r_d	Liquefaction analysis stress reduction coefficient	9
R1, R2	Seismic test radial distance(s) from source	1
R_f	Friction ratio, in percent: $R_f = 100 \cdot f_s / q_t$	1, 2, 3, 10
RF	Modulus reduction factor	7
R_x	Fitting parameter for ϕ_p'	5
s_z	Seismic induced permanent settlements	9
S	Degree of Saturation: $S = V_w/V_s$	2
S	Normalized undrained shear strength ratio = $(s_u/\sigma_v')_{NC}$	6
S	Vertical settlement geometry: Slope angle	9
S_{total}	Total settlement	7
$S_{initial}$	Initial settlement (during undrained loading)	7
$S_{consolidation}$	Drained primary consolidation	7
S_{creep}	Long-term secondary compression	7
S_r	Residual undrained strength (same as $S_{u(LIQ)}$)	9
S_t	Sensitivity: $S_t = S_u / S_{ur}$	6, 10
S_u	Undrained shear strength of soil	3, 4, 6, 7, 8, 10
S_{uc}	Undrained shear strength in triaxial compression	10
$(S_u)_{fv}$	Undrained shear strength from field vane testing	10
$S_{u(liquefied)}$	Residual undrained strength or liquefied undrained strength	9
$S_{u(liq)}$ or $S_u(LIQ)$	Residual undrained strength or liquefied undrained strength	9
S_{ur}	Remolded undrained shear strength	6
S_{uAVE}	Undrained shear strength – average of triaxial compression, simple shear, triaxial extension	10
t	Time	8
t_{50}	Time to reach 50% consolidation (porewater pressure being halfway between initial u and $u=u_o$)	8
t1, t2	Seismic test arrival time (for characteristic feature)	1
T’	Modified time factor for SCE-CSSM	8
T*	Modified time factor	8

Symbol	Description	Chapters
T^*_{50}	Theoretical time factor for 50% consolidation	8
u	Dynamic porewater pressure (generic position)	1
u_i	Initial porewater pressure	8
u_o	Equilibrium porewater pressure (at rest porewater pressure)	1, 3, 8, 9, 10
u_1	Dynamic porewater pressure at u_1 position (tip face)	1
u_2	Dynamic porewater pressure at u_2 position (behind shoulder)	1, 2, 3, 4, 5, 6, 8, 9, 10
u_3	Dynamic porewater pressure at u_3 position (tip face)	1
Δu	Differential or excess porewater pressure: $\Delta u = u_2 - u_o$	1, 3, 5, 7, 9, 10
Δu_2	Differential porewater pressure : $\Delta u_2 = u_2 - u_o$	4, 6, 8
Δu_{oct}	Octahedral component of excess porewater pressure	8
Δu_{shear}	Shear component of excess porewater pressure	8
$\Delta u / \Delta u_i$	Normalized excess porewater pressure ratio	8
U	Degree of consolidation	8
U	Normalized porewater pressure parameter: $U = (u_2 - u_o)/ \sigma_{vo}'$	3, 5, 9
U'	Normalized porewater pressure parameter for OC clays: $U' = U/OCR$ ^	5
v	actual penetration velocity	10
ΔV	Volume change	6, 7, 10
V	Volume of soil sample	2
V	Normalized CPTu penetration velocity	10
V'	Normalized CPTu penetration velocity	10
V_{50}	Empirical fitting parameter for variable rate CPT testing	10
V_o	Initial volume	6
V_p	Compression wave velocity	7, 10
V_r	Strength ratio of vane test to triaxial compression mode testing defined as (S_{uv}/S_{uc})	6
V_s	Volume of solids in sample	2
V_s	Shear wave velocity	4, 5, 7, 9, 10
V_{s1}	Normalized effective stress shear wave velocity: $V_{s1} = V_s / (\sigma_{vo}'/ \sigma_{atm})^{0.25}$	2, 9
V_{s1}^*	Reference normalized shear wave velocity based on specific fines content values used in calculating CRR	9
V_T	Total volume of sample	4
V_v	Volume of voids in sample	2, 4
V_w	Volume of water in sample	2
w_n	Natural (gravimetric) water content	2, 4
W	Weight of soil sample	2

Symbol	Description	Chapters
W_S	Weight of solids in sample	2
W_W	Weight of water in sample	2
x_S	Thickness of shear zone	8
YSR	Yield stress ratio (was OCR): $YSR = \sigma_p' / \sigma_{vo}'$	4, 6, 9
YSR_{CSL}	Yield stress ratio at critical state: $YSR_{CSL} = (2 / \cos \phi')^{1/\wedge}$	9
z	Penetration depth	1, 2, 4, 9, 10
z_w	Groundwater table depth	2, 8

Abbreviations

Abbreviation	Description	Chapters
AASHTO	American Association of State Highway and Transportation Officials	3
AC	Alternating current	10
AFC	Apparent fines content	3
ASF	Age scaling factor	2
ASTM	ASTM International Standards Organization	1, 3, 4
BPT	Ball penetration test	10
cps	counts per second: gamma-ray incidents in GCPTu	10
CAUC	Anisotropically consolidated undrained compression test	4, 5, 6
CCT	Calibration chamber test	4
CD	Contractive-dilative line (boundary)	9
CHT	Crosshole seismic test	2, 7
CIDC	Isotropically consolidated drained compression test	7
CIUC	Isotropically consolidated undrained compression test	4, 5
CiVS	Continuous-interval shear waves	10
CiSCPTU	Continuous-interval seismic piezocone test	10
CK_oUC	K_o consolidated undrained triaxial compression test	5
CK_oUE	K_o consolidated undrained triaxial extension test	6
COV	Coefficient of variation	5
CPT	Cone penetration test	1, 2, 3, 4, 5, 9
CPTu	Cone penetration test with pore pressure measurements	4, 8, 9, 10
CRR	Cyclic resistance ratio	9

Abbreviation	Description	Chapters
CRS	Constant rate of strain oedometer	4
CSL	Critical state line	4, 9
CSR	Cyclic stress ratio	9
CSSM	Critical state soil mechanics	4, 5, 9
DC	Direct current	10
DMT	Flat plate dilatometer test	7, 9, 10
DSS	Direct simple shear	6
DST	Downhole seismic test	1, 2, 7, 10
FC	Fines content	3, 4, 9
FS	Factor of safety	7, 9
GCPTu	Gamma piezocone penetration test	10
GSC	Geologic Survey of Canada	9
HF	Hydraulic fracture	2
IL	Incremental load oedometer	4
ISO	International Standards Organization	1
LD	Liquefaction induced lateral displacements	9
LDI	Liquefaction lateral displacement Index	9
LL	Liquid limit	4
LOC	Lightly over-consolidated	4, 5
ML	Machine learning	2, 10
M.O.	Maximum obliquity	4, 5, 6
MSF	Magnitude scaling factor	9
NC	Normally consolidated	5, 6, 7
NCEER	National Center for Earthquake Engineering Research	9
NORMs	Naturally occurring radioactive minerals	10
NSF	National Science Foundation	9
NTH	Norwegian Institute of Technology (Norges Tekniske Høgskole)	5, 10
OC	Over-consolidated	5, 7
OCD	Over-consolidation difference or prestress	4
OCR	Over-consolidation ratio	2, 3, 4, 5, 6, 7, 8
OL	Organic soil of low plasticity	4
OH	Organic soil of high plasticity	4
OST	Oil sand tailings	10
PEER	Pacific Earthquake Engineering Research Center	2
PF	Percent fines	9
PGA	Peak ground acceleration	9

Abbreviation	Description	Chapters
PI	Plasticity index	4, 5
PMT	Pressuremeter test	2, 6
PSC	Plain strain compression	6
PSE	Plane strain extension	6
P-Wave	Compression waves (geophysics)	1
RCPTu	Resistivity piezocone test	10
RF	Restricted flow oedometer	4
RF	Modulus reduction factor	7
RF	Machine learning: Random Forest algorithm	10
R_p	Overconsolidation ratio in terms of effective mean normal stress	9
S	Normalized strength ratio	6
SASW	Spectral analysis of surface waves	7
SBPMT	Self-boring pressuremeter test	2, 6
SBT	Soil behavior type	3, 4
SBTn	Normalized soil behavior type	3, 4, 8
SCE	Spherical cavity expansion theory	4
SCE-CSSM	Spherical cavity expansion - critical state soil mechanics	8, 9
SCPT	Seismic cone penetration test	10
SCPTu	Seismic piezocone penetration test	1, 2, 9, 10
S.D.	Standard deviation	5
SDMT	Seismic flat plate dilatometer test	7
SEY	Standard error of the Y-estimate	2, 5
SI	System International	1
SPT	Standard penetration test	5, 9
SQD	Sample (specimen) quality designation	6
SS	Simple shear	6
SVM	Machine learning: support vector machine	10
TBT	Tailings behavior type	10
TC	Triaxial compression	6
TE	Triaxial extension	6
TSC	Total stress cell	2
TSF	Tailings storage facility	2
TSP	Strain path method	8
U	Degree of consolidation	8
UC	Unconfined compression	6
UCD	University of California-Davis	9
UIUC	University of Illinois-Urbana-Champaign	9
USCS	Unified soil classification system	3
USDA	United States Department of Agriculture	3
USGS	United States Geologic Survey	9
UU	Unconsolidated undrained	6

Abbreviation	Description	Chapters
V	Normalized CPTu penetration velocity	10
V_{sVH}	Vertically propagating and horizontally polarized shear wave	1, 7
VCL	Virgin compression line	4
VisCPT	Vision cone penetration test	3
VRCPT	Variable rate cone penetration test	10
VRCPTU	Variable rate piezocone penetration test	10
VST	Vane shear test	6, 10
YSR	Yield stress ratio (was known as OCR)	4, 6, 9

1 Introduction to Cone Penetration Testing

1.1 Cone Penetration Testing (CPT)

In the cone penetration test (CPT), an instrumented electronic probe (cone penetrometer) is situated at the front end of a string of steel rods that are hydraulically pushed into the ground at a constant rate of 20 mm/s to measure soil response, geostratigraphy, and engineering parameters. A CPT vehicle, anchored rig, or hydraulic ram set are often used to provide the reaction and pushing force. The penetrometer takes three continuous readings with depth: (1) measured cone tip resistance (q_c), (2) sleeve friction (f_s), and dynamic porewater pressure (u_2), as depicted in ***Figure 1.1***. Cone penetration tests (CPT) and piezocone tests (CPTU) are routinely performed to depths in excess of 30 m; regularly to 60 m; and in special cases to depths over 200 m.

The cone penetrometer can be used to deploy additional sensors into the subsurface. These additional sensors are typically attached as modules immediately behind the cone probe. Some of these modules include resistivity electrodes, seismic sensors, passive gamma ray scintillating crystals, environmental monitoring sensors, or even image-capturing electronics to visually identify the in-situ soils.

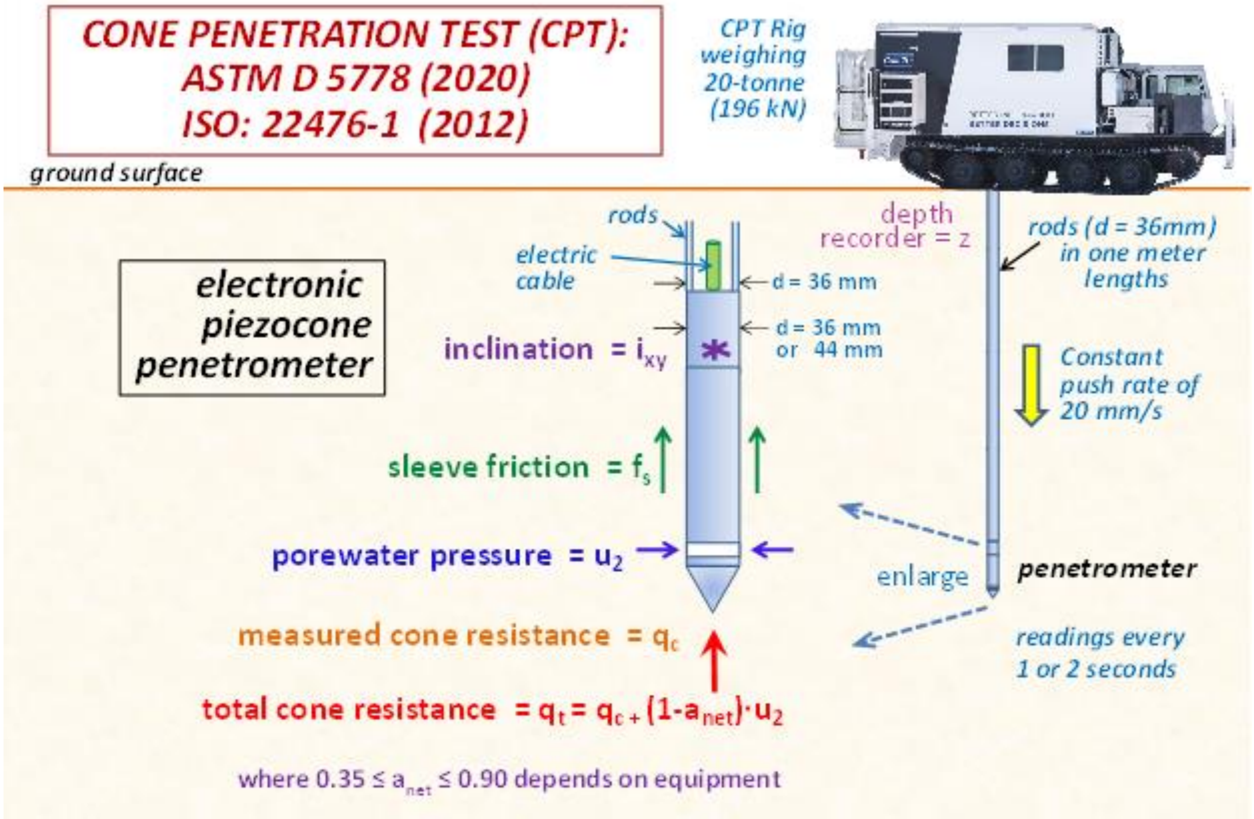

Figure 1.1: Basic setup and conduct of the Cone Penetration Test (CPT) and Piezocone (CPTU)

1.1.1 Cone Probe Dimensions

The internal components of the penetrometer include load cells and transducers to measure axial force, friction, pressure, and inclination. Data are transmitted up to a field computer at the surface through the hollow center of the rods usually by electrical cable, although wireless systems are available including infrared or audio signals. The outer shell of the penetrometer is configured with hardened steel parts to resist abrasion and wear. The tip design is a 60° conical apex and the sleeve is a cylindrical shell. The conventional standard size penetrometer is 35.7 mm in diameter, giving a 10 cm^2 cross-sectional area, although a slightly larger 43.7 mm diameter version has become more prevalent, resulting in a 15 cm^2 cross-sectional area.

Mini-cones as small as 1 cm^2 and 5 cm^2 are available for improved resolution in highly-stratified deposits, varved clay-silts, and shallow soundings, as well as for laboratory research chamber testing. In contrast, large penetrometers up to 40 cm^2 have been manufactured for use in gravelly soils. ***Figure 1.2*** shows a selection of available penetrometers for field use. Moreover, for special small scale lab testing such as centrifuge modeling, a series of micro-penetrometers have been developed that are as small as 10 mm to 1 mm in diameter (0.08 to 0.0008 cm^2).

Figure 1.2: Family of Cone Penetrometers including: (a) standard 10- and 15-cm^2 sizes; (b) standard sizes in comparison with smaller versions

1.1.2 Types of Cone Penetrometers

A selection of common penetrometer designs is shown in ***Figure 1.3***. In the basic penetrometer design, the electronic tip-friction cone suffices for profiling deep deposits of clean sand, soil formations and fills with no groundwater, or geomaterials that do not generate excess porewater pressures. In ground conditions that exhibit a porewater response, such as clays, silts, and sands with fines, penetration porewater pressures (u_m) should also be measured, as detailed by ASTM standard D 5778 (2020) and ISO standard 22476-1 (2012) for the piezocone penetration test (CPTU). As with many site investigations involving natural soil deposits and formations, the use of CPTU is preferred since the soil types are not known in advance.

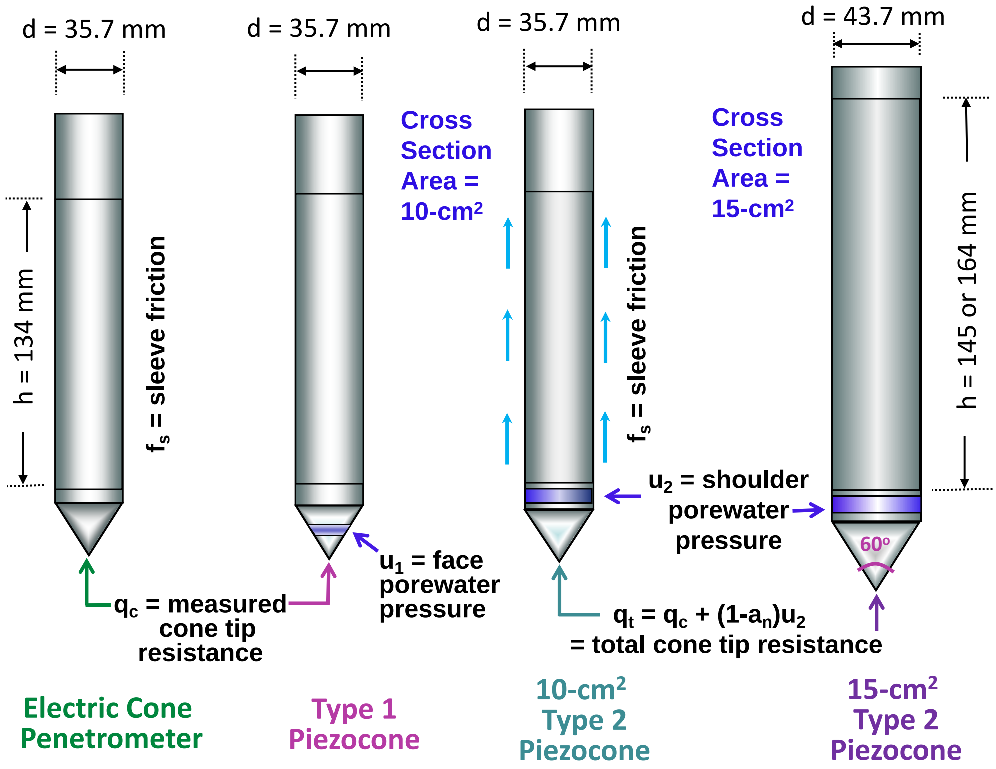

Figure 1.3: Types of Electric Cone and Piezocone Penetrometers

1.1.3 Unequal End Area Corrections

Porewater pressure readings can be taken at the apex or mid-face (designated u_1), shoulder position (just above the cone tip, or u_2), or behind the sleeve (u_3), but the standard required position is the shoulder position (u_2). This is because the effects of pressures at the joint warrants a systematic correction for the point stress, termed the total cone tip resistance (q_t) a.k.a. "corrected cone tip resistance" (Campanella et al. 1982; Lunne et al. 1997; Mayne 2007a):

$$q_t = q_c + (1 - a_{net}) \cdot u_2 \tag{1.1}$$

where a_{net} is the net area ratio of the cone tip, as determined by calibration in a pressurized triaxial cell (Lunne et al. 1997; Mayne 2007). Preferably, $a_{net} \geq 0.80$ in order to minimize the correction magnitude, however, it should be realized that the available commercial systems in use have a range of $0.35 \leq a_{net} \leq 0.85$, with the result that some CPT systems require a large correction that can affect the reliability and uncertainty of measurements.

This is a systematic correction to the total cone tip resistance. It is presented here in the introduction because all subsequent use of the cone tip resistance will be in terms of q_t. Many published studies using the CPT in sands have continued to use the designation q_c since the correction is small because q_c is much greater than u_2. While this correction is small in sands, it is still a systematic correction and therefore more correct to report and use q_t.

The sleeve reading should also be corrected to a total sleeve resistance (i.e., $f_s \rightarrow f_{st}$), but this requires measurements of both u_2 and u_3, thus deemed impractical for production testing (Lunne et al. 1997). In that case, the sleeve should be designed with equal end areas top and bottom, in order to minimize the error. Note that some European manufacturers of CPT equipment have adopted an empirical f_{st} correction procedure by assuming an interrelationship between u_2 and u_3 because their sleeve designs have unequal end areas. However, interrelationships between u_2 and u_3 are soil type-dependent and thus the "corrected" f_{st} values can in be error, thereby misclassifying soil types and leading to other issues in interpretation.

An approximate correction for sleeve friction is given by (Mayne 2007a):

$$f_{st} = f_s - (b_{net})u_2 \tag{1.2}$$

where the b_{net} value is also determined by calibration of the penetrometer in a pressurized triaxial cell. Some European penetrometers have b_{net} values on the order of 0.005 to 0.02, which can be a significant correction in soft to firm clays. With equal areas on top and bottom of the sleeve, a value of b_{net} = 0 is ideal from a pragmatic standpoint.

ConeTec uses penetrometers that are designed and manufactured in-house by Adara Systems Ltd. with values of a_{net} = 0.80 and b_{net} = 0.0, thus optimal for production testing. Therefore, the reported CPTU data are fully corrected.

1.2 CPT Vehicles

A variety of specialized CPT rigs have been designed and built to facilitate the hydraulic pushing of cone penetrometers and other in-situ probes on a routine production basis. For full size capability, a 30-tonne hydraulic capacity system is mounted on a vehicle for field operations. Common types of vehicles include small- to medium- to large- trucks providing dead weight reactions on the order of 10 to 30 tonnes. For difficult access, CPT vehicles also include track-mounted rigs, all-terrain trucks, and portable frames. For light-weight rigs, anchoring systems can be provided to increase the total reaction capacity. A selection of cone rigs is shown in ***Figure 1.4***.

Figure 1.4: Various Truck- and Track-Mounted CPT Vehicles for Production In-Situ Testing

In situations involving overwater soundings, the platforms for CPT hydraulic systems can be barge, ship, jackup platforms, or special pushing frame units lowered overboard that are deployed remotely from the seabed. For mine tailings investigations, special amphibious rigs have been developed to facilitate difficult soft ground access. Also, in areas of remote access or limited headroom, portable hydraulic ram-set systems are available to provide CPT services.

Hollow steel rods are typically 35.7 or 43.7 mm in diameter and usually added in 1-m increments. A pair of hydraulic or mechanical lateral grips grasp the rods during the vertical pushing (and eventual extraction). Routine depths of 30 m for CPT can be achieved in about 1 hour. In exceptional cases, soundings over 200 m have been completed.

While a conventional drill rig can be employed for the purpose of CPTs, they are usually limited to soft ground conditions because of low dead-weight capacity, poor rate control during pushing, and slow rod handling operations due to a direct threaded rod connection with the kelly bar, rather than the mechanical or hydraulic grips used in CPT rigs. Moreover, many CPT soundings by drill rigs have terminated early due to inadequate capacity for reaction.

1.3 CPT Soundings

Results from the channels recorded during a piezocone sounding are plotted with depth, as illustrated from the CPTU in Virginia shown in ***Figure 1.5***. In this case, the leftmost graph shows the profile of the corrected cone tip resistance (q_t) versus depth, the middle graph presents the measured sleeve friction resistance (f_s) versus depth, and the rightmost graph gives the penetration porewater pressures at the shoulder (u_2) versus depth. In the original metric system, units were given in kilograms per square centimeter (kg/cm^2) or bars (1 bar = 1.02 kg/cm^2), whereas in the System International (SI), kiloPascals (kPa) or MegaPascals (MPa) are preferred (1 bar = 100 kPa). In North America, it is still common to use English Imperial units for reporting the measured stresses and pressures (i.e., tons per square foot, or tsf). Also, it can be convenient to provide the results in terms of dimensionless values by dividing the pressures or stresses by atmospheric pressure (σ_{atm}). As a reasonable approximation, unit conversions can be expressed: $1\ \sigma_{atm} \approx 1\ bar = 100\ kPa \approx 1\ tsf \approx 1\ kg/cm^2$. Note: Exact conversions for stress and/or pressure: $1\ \sigma_{atm} = 101.3\ kPa = 1.058\ tsf = 1.033\ kg/cm^2$. Also note: 1 bar = 100 kPa. For units of length: $1\ meter = 3.28\ feet$.

It is also common to report the penetration porewater pressures in terms of equivalent height of water (h_w). In these cases, the equivalent $h_w = u_2/\gamma_w$, where γ_w = unit weight of water (γ_w = $9.81\ kN/m^3$ = $62.4\ pcf$).

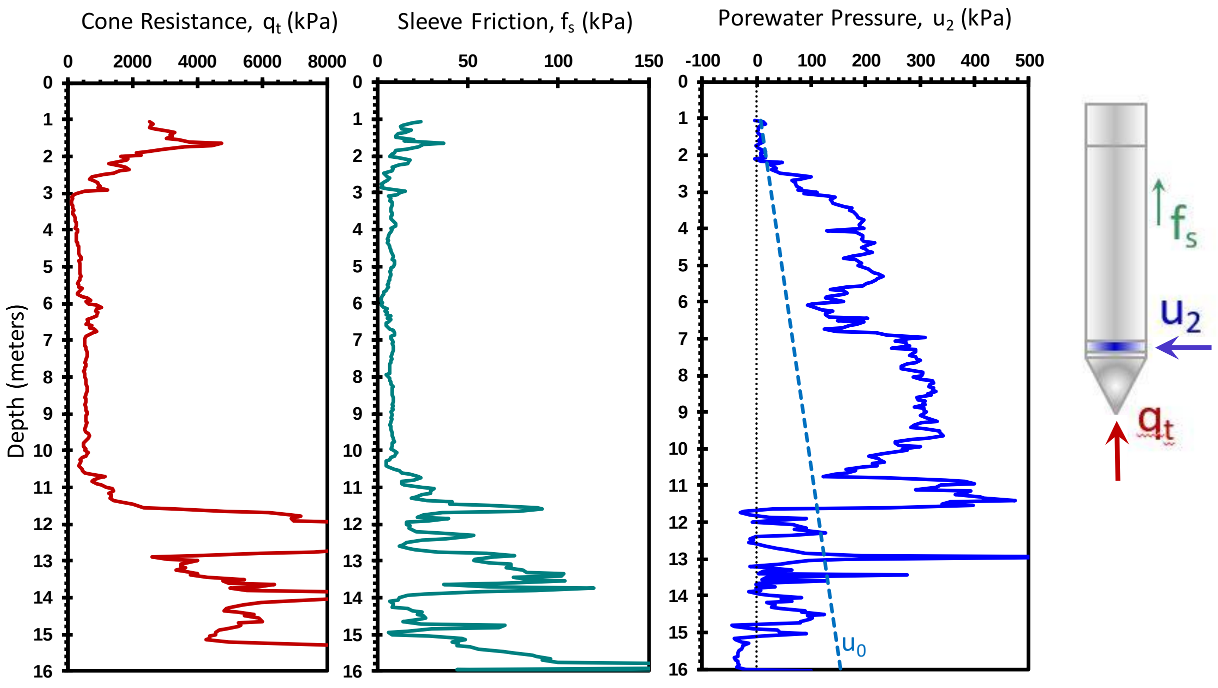

Figure 1.5: Representative piezocone sounding in marine sediments at southeast Virginia

1.4 Pore Pressure Dissipation (PPD) Tests

The measured penetration porewater pressures reflect the prevailing soil drainage conditions surrounding the probe. Usually in loose to firm permeable clean sands, a drained response occurs ($u_2 \approx u_0$), whereas in saturated clay soils having low permeability, an undrained condition arises. The latter results in a temporary elevated response of high excess porewater pressures caused locally by the insertion of the penetrometer. Similar manifestations occur with the installation of driven piling foundations and/or other in-situ probes into saturated fine-grained soils. If the penetration process is halted, the excess porewater pressures (Δu) will decay with time as they seek equilibrium. The monitoring of these readings with time is termed a dissipation test.

In most soft clays and silts, the porewater pressures will decrease monotonically with time, with a maximum value occurring during penetration (u_2), then dropping and eventually reaching an equilibrium porewater pressure (u_0). Since the rate of dissipations slow with time, they are often alternatively plotted on logarithmic time scales or square root time plots to show the full response records (Styler et al. 2019). As such, it is not convenient or practical to wait for 100% dissipation, therefore many dissipation tests are taken only to 50% completion, whereby regular CPT operations are resumed and the penetrometer pushed at 20 mm/s. From a CPTU conducted near the Mississippi River in Memphis, TN, ***Figure 1.6*** shows a measured monotonic dissipation record at a depth of 17.1 m.

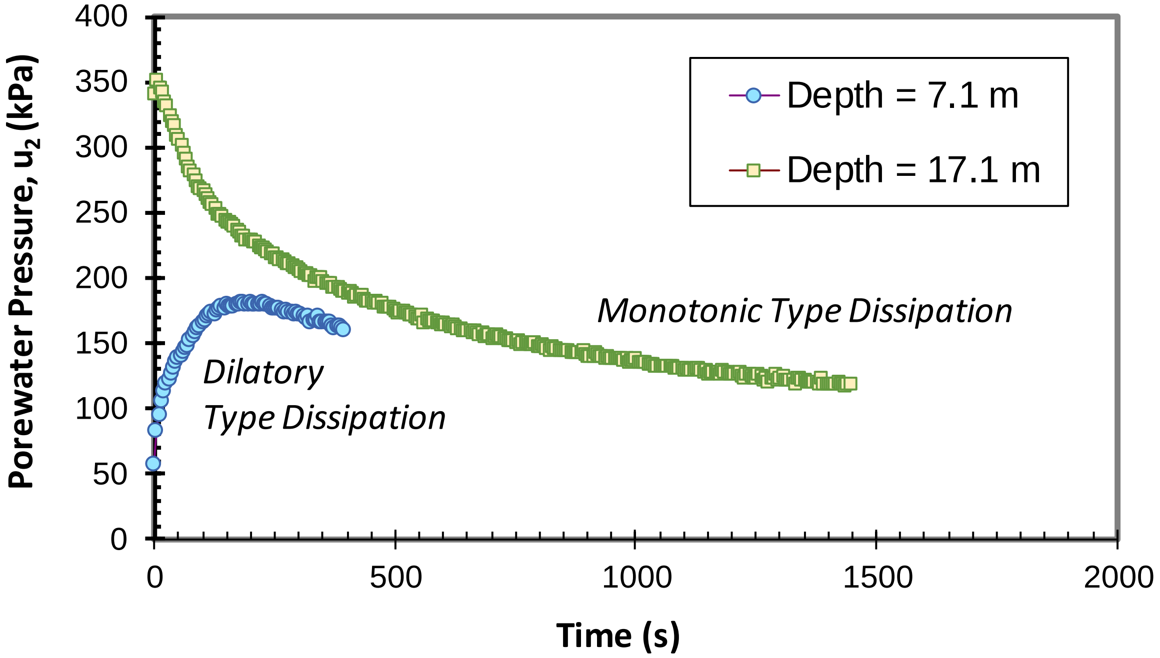

Figure 1.6: Example piezo-dissipation results from Mud Island, Tennessee, including: (a) Monotonic pore pressure response at 17.1 m, and (b) Dilatory behavior at 7.1 m

For the shoulder filter position, dilatory porewater response can also be observed, whereby the pressures initially increase up to a peak value followed subsequently by decay with time. Dilatory behavior is primarily encountered in overconsolidated clays, silts, and dense dilative sandy soils. ***Figure 1.6*** shows an example dilatory dissipation curve at a depth of 7.1 meters.

1.5 Stratigraphic Profiling

Because of its ability to record continuous resistances with depth, the cone penetrometer is unrivaled in its ability to detect changes in subsurface strata and delineate soil layering, as well as also identify weak zones, thin lenses, and anomalous ground conditions. Not only is this evident for one channel of readings, but for all three simultaneous penetrometer recordings obtained using a piezocone

The detail in piezcone profiling can be seen in the CPT records from New Orleans presented in ***Figure 1.7***. The data acquisition system captures readings at approximately 1 to 2 seconds, therefore resolution in the profiling capabilities is generally in the 1 cm to 5 cm range. Moreover, ***Figure 1.7*** shows the reliability and repeatability of CPT soundings from the results of two adjacent soundings. These were made by two separate cone rigs, crews, and penetrometer systems where the tests were made some three months apart. Other than minor differences due to localized sand content and silt lenses and silty sand pockets, both soundings show remarkable agreement in the cone tip resistance (q_t), sleeve friction (f_s), and penetration porewater pressure (u_2) readings with depth.

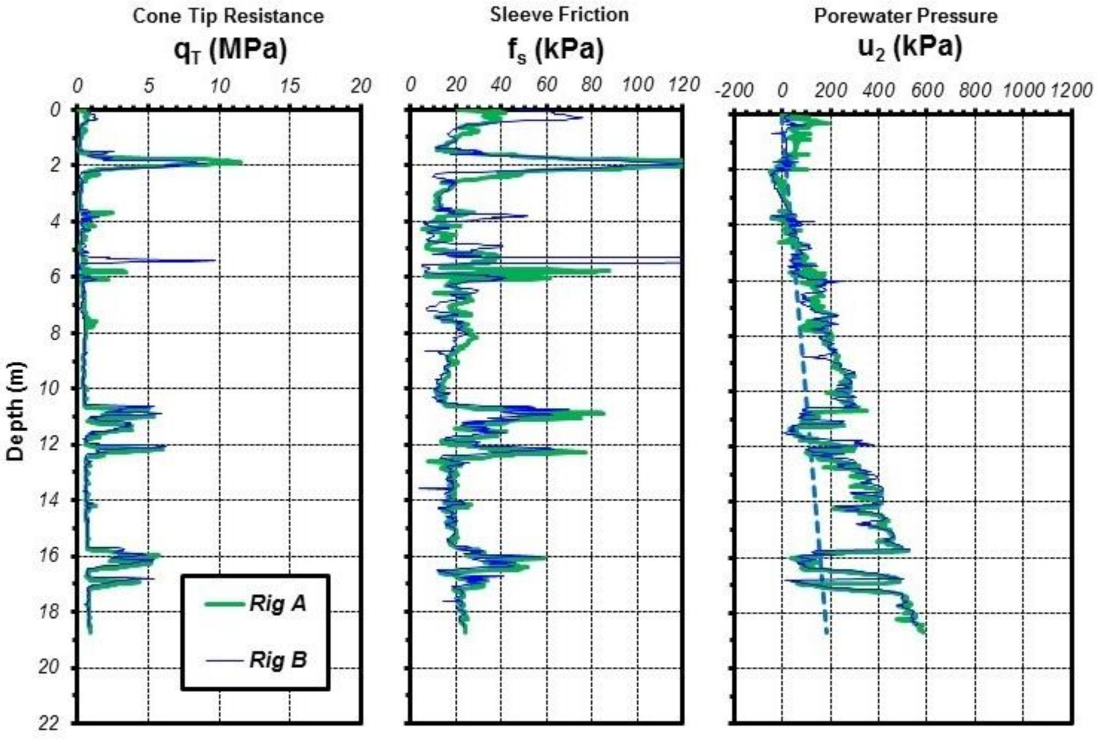

Figure 1.7: Profiling and repeatability of CPTU readings with depth using two separate rigs

1.6 CPT Soil Identification by Rules of Thumb

Some simple rules-of-thumb can be used to identify coarse-grained soils (sands) versus fine-grained soils (clays and silts) by visual examination of the cone readings. For reference, the following benchmark values are established: (a) cone resistance $q_t = 50$ atm; (b) friction ratio $R_f = 100 \cdot f_s/q_t = 1\%$, and (c) $u_2 = u_0$. For illustration, a CPTU example from Biloxi Mississippi is shown in ***Figure 1.8***. For the cone tip resistance presented in Figure 1.8a, a reference value q_t = 50 atm is drawn, whereby measured $q_t >$ 50 atm imply sands and $q_t <$ 50 atm suggests clays. At this site, it can be seen that the upper 7 meters of soils contain alternating layers and lenses of sand and clay. A thick clay layer extends from 7 to 15.5 m that is underlain by a sand layer from 15.5 m to 20 m, below which indicates clay until the sounding termination depth at 25 m.

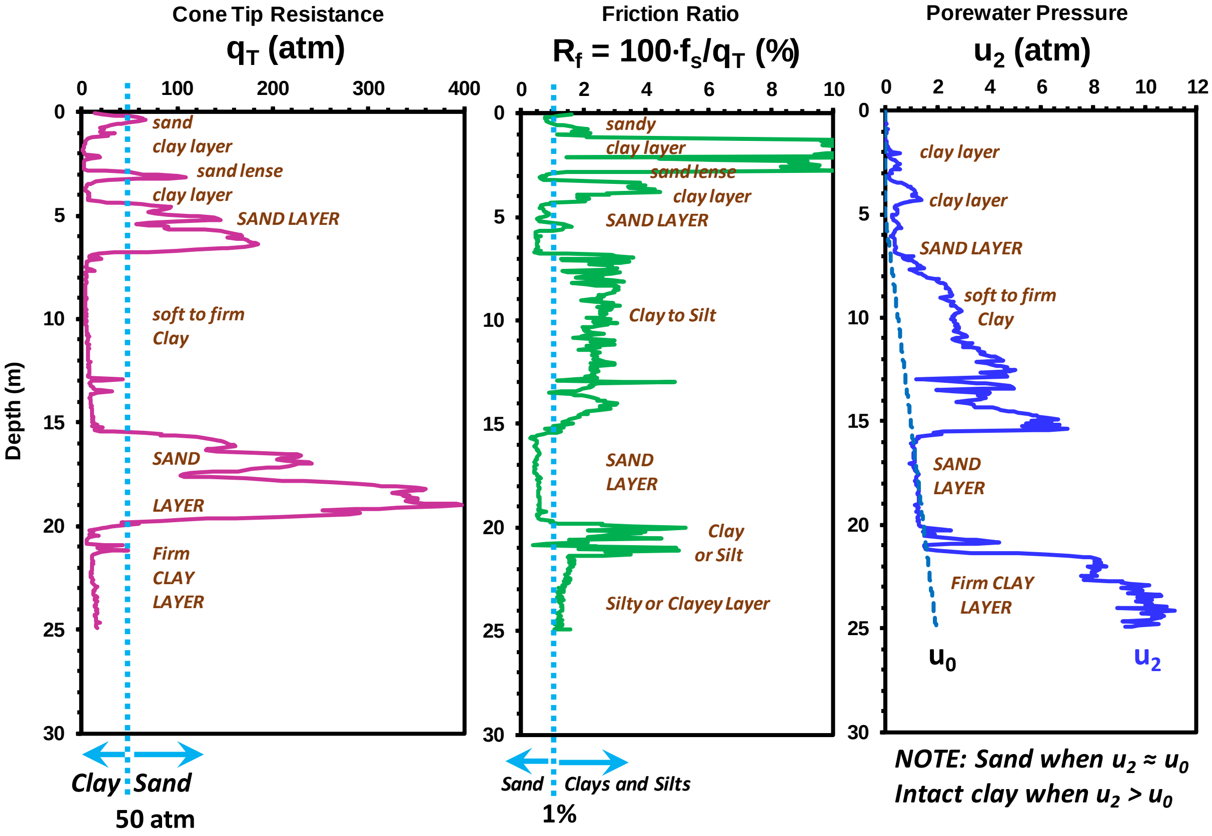

(a) *(b)* *(c)*

Figure 1.8: Piezocone record illustrating visual soil identification method and rules of thumb

For the friction sleeve reading, it is convenient to plot the friction ratio, $R_f = 100 \cdot f_s/q_t$ (%). As such, clean sands are identified by $R_f <$ 1%, whereas fine-grained insensitive silts and clays often exhibit $R_f >$ 1%. Using this criterion, a similar geostratigraphy can be ascertained at the site from the R_f profile. Note, however, for sensitive to quick clays, the friction ratio is small and often approaches zero. Thus, the R_f criterion should not be solely used for soil type evaluation but in combination with the q_t and u_2 readings. Additionally, when the friction ratio exceeds about 8% it is an indication of organic soils. In ***Figure 1.8b***, the rule of thumb suggests an organic clayey layer from depths of about 1 to 3 m.

Lastly, for the porewater pressure channel, it is advantageous to plot the hydrostatic porewater pressure line as a reference:

$$u_0 = h_w \cdot \gamma_w \tag{1.3}$$

where h_w = height of the water (depth less groundwater table) and γ_w = unit weight of water (freshwater: γ_w = 9.81 kN/m^3 = 62.4 pcf). In ***Figure 1.8c***, the groundwater lies 5 m deep and a dashed blue line is shown to represent hydrostatic conditions. Above the groundwater table, the ambient u_0 is often taken equal to zero in clean sands; however, in clays and fine-grained soil materials, u_0 can be negative due to capillarity effects depending upon the degree of saturation, recent rainfall, soil permeability, and other site features.

In clean "hourglass" sands, the measured porewater pressures are often close to hydrostatic ($u_2 \approx u_0$). In ***Figure 1.8***, the sand layers can be identified by this simple rule. However, if the sands are very dense, dilatancy may result in u_2 readings less than u_0. Below the groundwater table, intact clays can be found by examining where $u_2 \gg u_0$. As a general guide, the ratio of u_2/u_0 increases with clay compactness, such that for soft clays $u_2/u_0 \approx 2$; firm clays $u_2/u_0 \approx 4$; stiff clays $u_2/u_0 \approx 8$; and hard clays: $u_2/u_0 \approx> 15$. Referencing ***Figure 1.8c***, the thick clay layer from 7 to 15.5 m can be easily discerned in this manner. The lower clay layer at depths below 20 m is also evident. Of additional mention is the fine detail in soil profiling collected by CPTU, specifically the q_t and u_2 readings at a depth of 20.2 m in ***Figure 1.8*** implicate a thin sandy lense.

Of final note, the magnitude of porewater pressures in stiff fissured overconsolidated soils are often less than hydrostatic ($u_2 < u_0$), in fact, can often be negative and may reach values as low as $u_2 \approx$ -100 kPa (Mayne et al. 1990).

1.7 Seismic Cone Penetration Testing (SCPTU)

Of particular value in routine site exploration is the seismic piezocone test (SCPTU) as it is a hybrid procedure that combines cone penetrometer recordings (ASTM D5778) with geophysical downhole shear wave velocity measurements (ASTM D7400) into one sounding (***Figure 1.9***).

During the penetration portion of the SCPTU, continuous records of q_t, f_s, and u_2 are collected over a 1-m interval, whereby during the temporary halt for the next rod addition, a geophysical downhole test (DST) is performed. This involves an impulse-type surface source generator to create a shear wavelet that is monitored by one or more geophones or accelerometers located within the penetrometer.

For the DST, the shear wave is a vertically-propagating and horizontally-polarized mode ($V_{S,VH}$ type) with the length of the surface source oriented in the same parallel plane as the geophone axis. A single horizontal geophone can be used (pseudo-interval method), or else two geophones at different elevations (true-interval). In addition, biaxial sets of geophones at the same elevation can be used to account for orientation alignments due to rotation or off-parallel setups. Triaxial geophone arrays provide a third (vertical) component that can collect information on compression wave arrivals (P-waves).

The original setup for SCPTU simply employed a sledgehammer and crossbeam for the source (Campanella et al. 1986). Pairs of left- and right-strikes were required at each depth to ascertain the arrival of the shear wave, using either the first arrival, where the two signals diverge, or a procedure termed first crossover, at the point where the two signals cross after the initial main wavelet. A set of paired left- and right-strikes at each one-meter depth are presented in ***Figure 1.10***. Here, the SCPTU was performed to a final test depth of 43 m in Charleston, SC. The left wavelets are shown as red lines and the right wavelets as blue lines. The downhole shear wave velocity is determined for each vertical depth interval from measured arrival times obtained at two successive depths (Campanella 1994):

$$V_S = \frac{R_2 - R_1}{t_2 - t_1} \tag{1.4}$$

where R = hypotenuse distance = $\sqrt{(z^2 + x^2)}$ at each depth, z = depth, t = characteristic time at depth z, and x = perpendicular offset distance from the horizontal source to the axis of the vertical downhole test. Note that the distance x should be kept to less than 1 m so that waves are V_{sVH} type. Moreover, if x > 1 m, it will be necessary to consider the correction of time arrivals for the interval time method analysis (Hallal & Cox 2019; Stolte & Cox 2020).

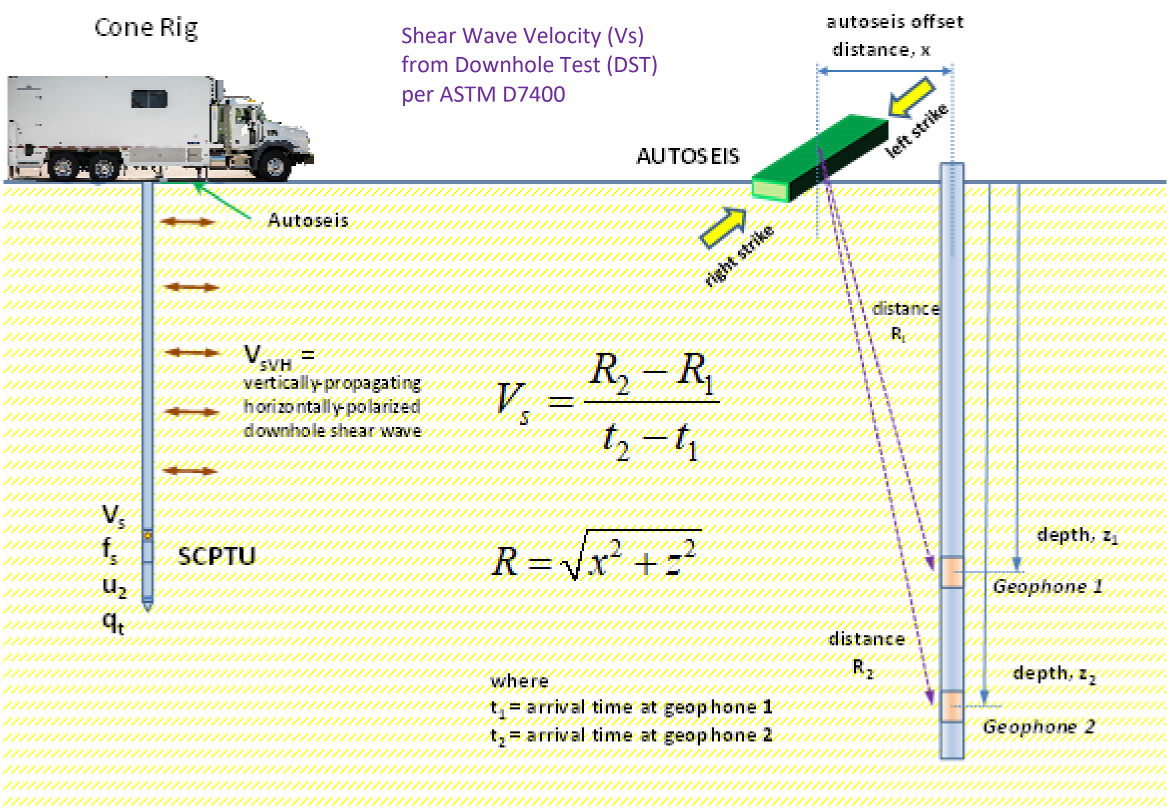

Figure 1.9: Setup and Procedure for Conducting Seismic Piezocone Test (SCPTU) using the Downhole Test (DST) for evaluation of shear wave velocity (V_S)

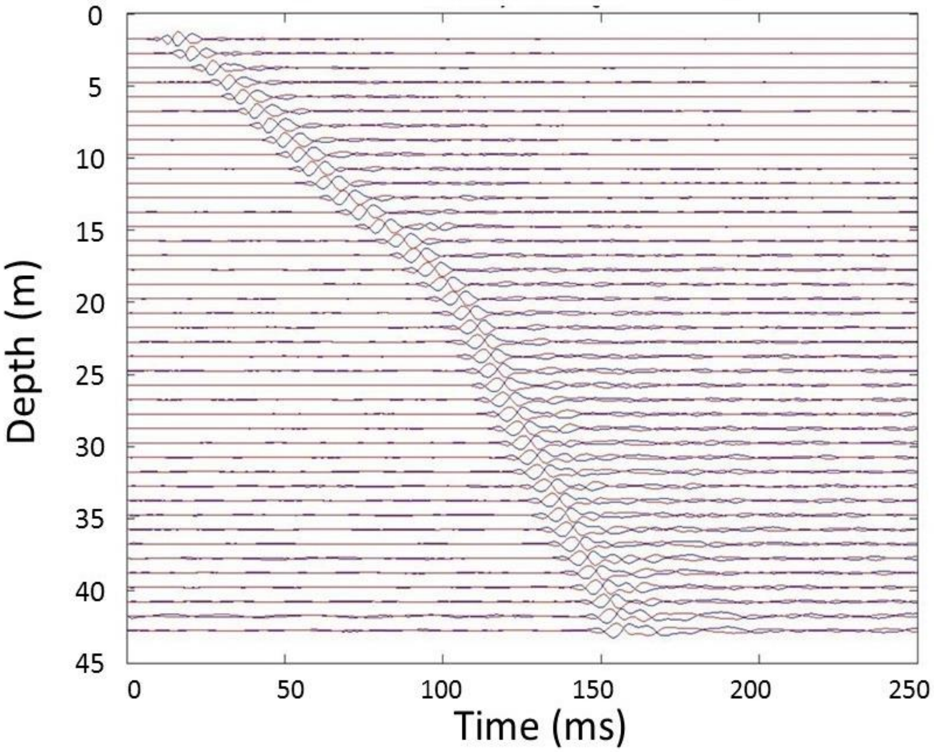

Figure 1.10: Paired Wavelets from Left- and Right-strikes at one-meter Depth Intervals During Downhole Testing by Seismic Cone in Charleston, SC

The interpretation of V_s from downhole testing can be made using: (a) first arrival time of shear waves (when the left and right strikes first diverge), (b) first crossover, (c) cross-correlation, and/or (d) frequency domain methods (Liao & Mayne 2006; Ku et al. 2013a, 2013b). These can be applied to pseudo-interval and true-interval DST methods. In the cross-correlation method, each successive wavelet is matched to the prior event to determine the incremental time difference over the depth interval. The cross-correlation method for post-processing of shear waves can be handled via Excel spreadsheets, Matlab, or special geophysics software packages.

Commercial automatic hydraulic hammers have been in industry use for about 20 years. These devices use an internal hydraulic cylinder to strike two plates in both directions and generate reverse polarity waves. They are fast, efficient, and create reproducible seismic waves.

Improvements in the recorded signals, reliability, and quality of the derived shear wave profiles are attained by use of autoseis units because of their repeatability and consistency (Mayne and McGillivray 2008). Autoseis units have been developed on the basis of electrical, electromechanical, pneumatic, and hydraulic force impact (***Figure 1.11)***. For shallow profiling of shear waves at depths < 30 m (100 feet), a portable electric autoseis unit will suffice. For deeper soundings, a heavy-duty hydraulic autoseis may be preferred. An alternate approach is to use stacking, whereby several successive strikes are averaged to increase the signal to noise ratio and improve the wavelet qualities.

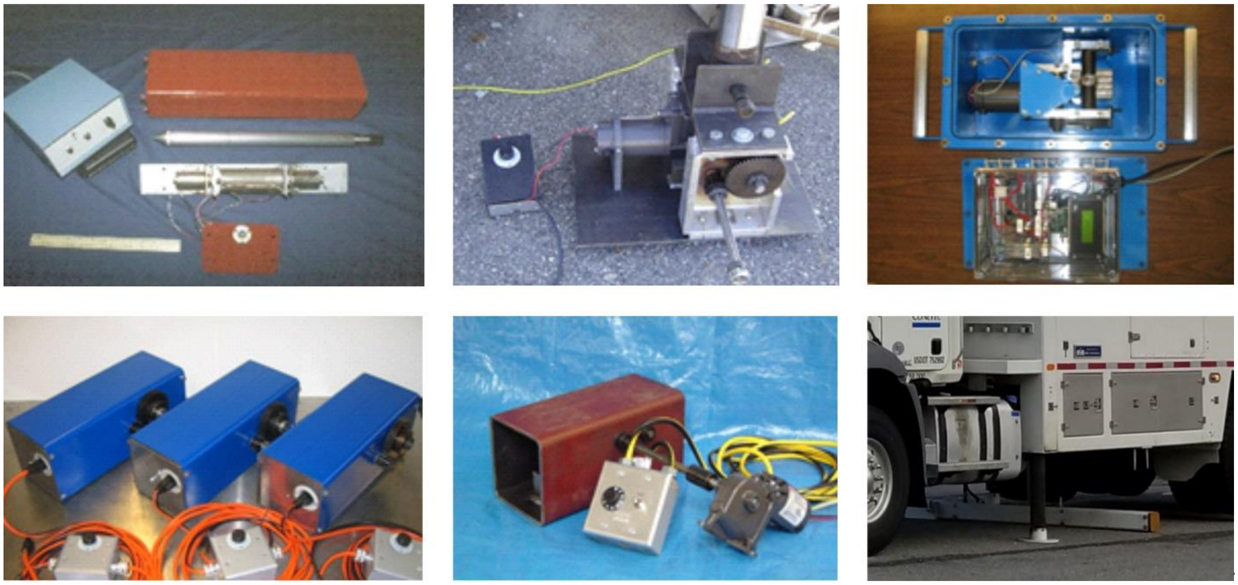

Figure 1.11: Selection of Electric, Electromechanical, and Hydraulic Type Autoseis Generators for use in Downhole Shear Wave Measurements

The combined results of the alternating field procedure of cone penetrometer testing (CPTU) and geophysical downhole testing (DST) at one-meter depth intervals form a hybrid method termed seismic piezocone testing (SCPTU). An illustrative example of a SCPTU sounding from Hartford, CT is presented in ***Figure 1.12*** showing all four readings with depth: q_t, f_s, u_2, and V_s.

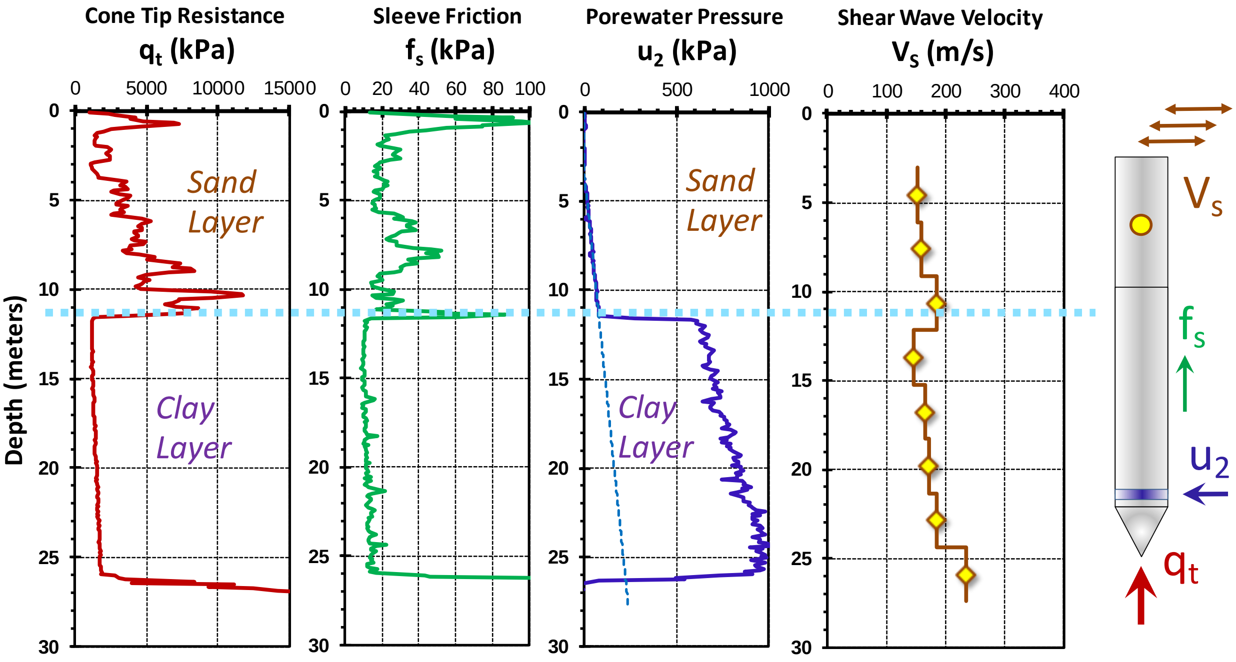

Figure 1.12: Seismic Piezocone Test (SCPTU) from Hartford, Connecticut

An example of SCPTU results taken for the Pitt River Bridge in British Columbia is presented as ***Figure 1.13*** (Tara 2012). These results show the exceptional depths on the order of 96 m (315 feet) that can be achieved using seismic piezocone testing. This offers significant advantages over routine methods that rely on drilling, sampling, casing, and borehole geophysics that are approximately ten times more costly in terms of field time and budget expenses.

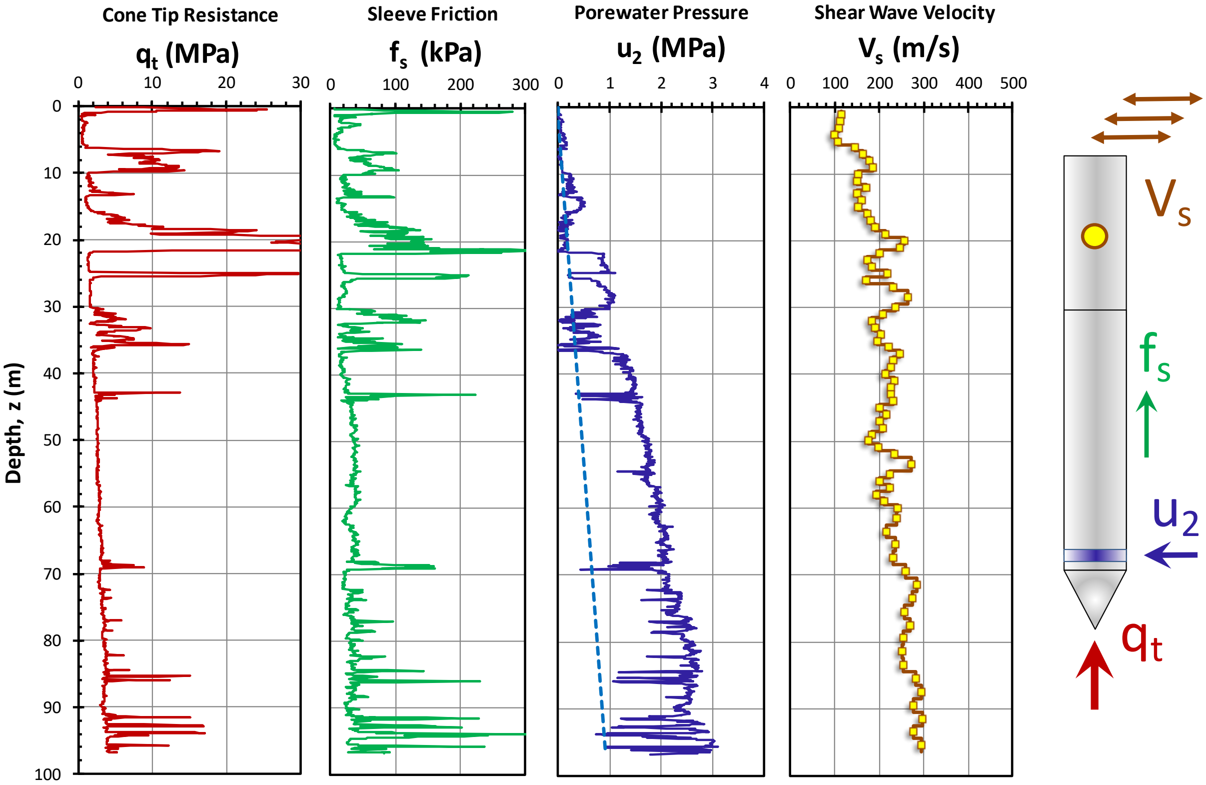

Figure 1.13: Results from 95-m deep SCPTU at Pitt River Bridge, British Columbia

1.8 Site Characterization

Geotechnical site investigations encompass the entire suite of all in-situ tests, sampling, laboratory tests, geophysical measurements, and field observations made on a site. A site investigation is simply a set of measurements or observations in time and space.

Geocharacterization combines the site investigation with geological inference and engineering judgment and interpretation in order to create geotechnical models for engineering analysis and design. These models may include 2D and 3D cross-sections that bridge the divide between the sparse results from the geotechnical site investigation. Detailed site characterization is highly dependent on local experience and judgment.

The most important part of the site characterization is to define the geometry of the problem. This geometry is the spatial location and extent of various soil layers. The continuous depth profiles from cone penetration testing are ideal for delineating the location and thickness of various soil layers.

A common concern is an inadequate site investigation. The site investigation plan details the numbers, locations, and target depths of the field testing and sampling program. The sufficiency of a site investigation clearly depends on the project and geology. A preliminary investigation may only consist of a few soundings and depending upon the complexity of the stratigraphy, soil layering, strata inclination, and degree of homogeneity and/or heterogeneity of the site, the final geotechnical program may need to consider a good number of soundings that are supplemented with drilling, soil borings, sampling, and laboratory testing as well as geophysics in order to provide adequate information for analysis and design.

1.9 Objectives

The objective of this guide is to be a reference for interpreting CPT results. The Reader should be familiar with the basic principles of soil mechanics, such as covered by Holtz et al. (2011).

Chapter 1 has shown how the geostratigraphy of a site can be determined directly with a few simple rules-of-thumb from CPT logs. Only once the geometry of the problem is defined do these soil properties have meaning in the geotechnical analysis and design. Further analysis of the CPT results requires a characterization of unit weights, overburden calculations, equilibrium porewater pressures, and effective stress profile, as covered in ***Chapter 2***. Soil behavior type charts can then be used to infer the soil types based on how they respond to an advancing cone probe, as covered in ***Chapter 3***. The stress history of soils is reflected by its preconsolidation, or yield stress, which affects soil response and many aspects of other dependent geoparameters as outlined in ***Chapter 4***.

The effective friction angle is a fundamental property of the soil and its importance to CPT interpretation is covered in **Chapter 5**. For clays, the undrained shear strength (***Chapter 6***) is a total stress parameter that is needed for bearing capacity of shallow foundations and axial, lateral, and moment capacity of deep foundations, as well as used in slope stability, excavations, and embankment analyses. ***Chapter 7*** details a discussion of ground stiffness, including soil modulus that is highly nonlinear starting from the nondestructive region to intermediate strains to large strains. The analysis of porewater pressure dissipation curves is presented in ***Chapter 8*** to ascertain the in-situ values of flow parameters, including the coefficient of consolidation (c_v) and soil permeability (k).

Of increasing importance to society, the phenomena of soil liquefaction, both *flow (or static) liquefaction* that can occur in earth embankment dams, tailings, and fly ash impoundments and *cyclic liquefaction* caused by earthquakes, as evaluated using CPT, are detailed in ***Chapter 9***.

This guide concludes with a brief description of special advanced cone testing topics (***Chapter 10***). Additional CPT procedures (e.g., variable rate testing; P-wave measurements) and cone modules (e.g., gamma, resistivity) have special applications where they might provide more information and additional soil properties that cannot be obtained with the standard cone penetration test.

2 Soil Unit Weight and Overburden Stresses

The behavior of soils depends upon the effective stresses in the ground. As stated by the first principle of soil mechanics, the effective stress is equal to the total overburden stress minus the porewater pressure. The total overburden is the accumulation of soil unit weight times soil layer thickness and is caused by gravitation forces acting on the soil particles, while the porewater pressure is a buoyancy phenomenon. As such, the unit weight of soils is needed in order to calculate total and effective overburden stresses with depth.

It is routine practice to estimate total vertical stress profiles for interpreting CPT logs. This is accomplished by either assuming, measuring, or estimating total unit weights for the soil layers.

2.1 Total Soil Unit Weight (γ_t)

Soil unit weights (γ_t) are best obtained by securing "undisturbed" samples (e.g., thin-walled Shelby tubes; piston samples; Laval samples) from various depths. The ratio of the weight of the sample over a known volume of soil provide the total unit weight: $\gamma_t = W/V$. The profile of soil unit weight with depth is needed in the calculation of overburden stresses, as well as in the conversion of shear wave velocity to small-strain shear modulus. The unit weight relates to the more fundamental mass density (ρ_t) through ***Equation 2.1***.

$$\gamma_t = \rho_t \cdot g_a \tag{2.1}$$

where g_a = gravitational constant (= 9.8 $m/s^2 = 32.2 ft/s^2$).

Soil identity relationships provide information about the air-water-solids composition of the soil. One primary soil identity expression is:

$$G_s \cdot w_n = S \cdot e_0 \tag{2.2}$$

where G_s is the specific gravity of solids (for "normal" soils: $G_s = 2.70 \pm 0.1$), w_n is the natural (gravimetric) water content ($= W_w/W_s$ which can vary from zero in dry soils to 1000% in highly plastic montmorillonite), W_w = weight of water, W_s = weight of solids, S is the degree of saturation ($= V_w/V_v$ ranges from zero in dry soil to 100% in fully saturated soils), and e_0 is the initial void ratio ($= V_v/V_s$), where V_w = volume of water, V_s = volume of solids, and V_v = volume of voids.

The total unit weight can be calculated in terms of these variables using:

$$\gamma_t = \left(\frac{1+w_n}{1+e_0}\right) \cdot G_s \cdot \gamma_w \tag{2.3}$$

where γ_w is the unit weight of water (γ_w = 9.8 kN/m^3 = 62.4 pcf for freshwater; and $\gamma_w \approx$ 10.0 kN/m^3 = 64.0 pcf for salt water). Depending upon the water content and degree of saturation, two boundary cases are commonly taken in soil mechanics: (a) completely dry soil (with w_n = 0); and (b) fully-saturated soil with S = 1 (and then: $e_0 = G_s \cdot w_n$). This gives:

$$\gamma_{dry} = \left(\frac{G_s \gamma_w}{1+e_0}\right) \tag{2.4}$$

$$\gamma_{sat} = \left(\frac{G_s + e_0}{1+e_0}\right) \cdot \gamma_w \tag{2.5}$$

An extreme case would be a geomaterial with zero porosity (e_0 = 0) corresponding to solid rock:

$$\gamma_{rock} = G_s \cdot \gamma_w \tag{2.6}$$

Thus the hierarchy for assignment of unit weights would be $\gamma_{dry} \leq \gamma_t \leq \gamma_{sat} \leq \gamma_{rock}$.

For soils above the groundwater table, a dry unit weight would apply for no capillarity (i.e., clean sands), while if full capillarity exists (e.g., clays), then a saturated unit weight would be appropriate. If the soil is partially saturated, the total unit weight will depend upon the ambient degree of saturation, likely a value that changes with the weather, humidity, and temperature. For most soils below the water table, it is often assumed that the total unit weight is equal to the saturated unit weight. In some cases, calculations involve the effective unit weight ($\gamma' = \gamma_{sat} - \gamma_w$), also referred to as the buoyant unit weight or submerged unit weight.

As these unit weights are in terms of void ratio, degree of saturation, and specific gravity, the direct relationships between γ_{dry}, γ_{total}, and γ_{sat} from equation (2.3) for a specific gravity of solids G_s = 2.70 are shown in ***Figure 2.1***.

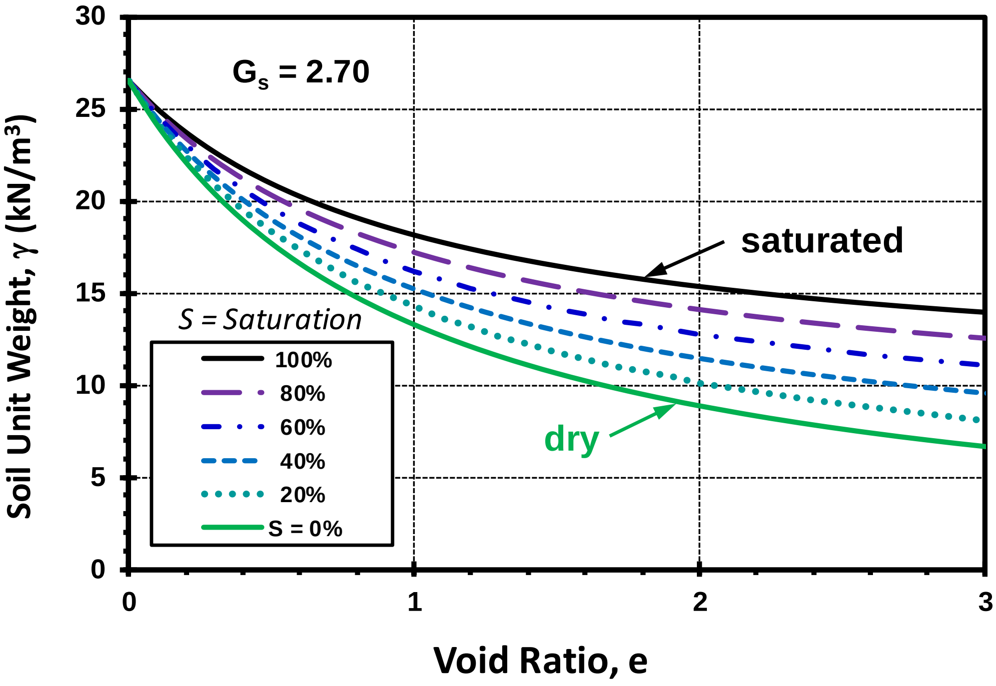

Figure 2.1: Interrelationship between soil unit weight, void ratio, and saturation

For immediate results, direct in-situ methods for ascertaining soil unit weights are available using gamma ray density penetrometers (Sully and Eschesuria 1988). These probes find use on critical and demanding projects. However, the utilization of these probes adds appreciable burdens in terms of time, costs, environmental risks, and/or safety during deployment on regular day-to-day projects. Therefore, it is of interest to have indirect CPTU methods for assessing unit weights of geomaterials from the basic penetrometer readings (q_t, f_s, and u_2) as well as shear wave velocity (V_s).

2.1.1 Unit Weight Estimated from Soil Behavior Type

Total unit weights can be estimated based on soil behavior type classifications or local knowledge of the soil type. ***Table 2.1*** details typical unit weights for different materials tested with the CPT. The unit weights from Lunne et al. (1997) are based on a 12-zone non-normalized soil behavior type chart (Robertson et al. 1986) that is applicable to shallow soils.

Table 2.1: Typical total unit weights for various materials encountered by the CPT (to convert from kN/m^3 to Imperial units, multiply by 6.367 for pcf)

Geomaterial	Total unit weight (kN/m^3)	Reference
(Zone 1) Sensitive Fines	17.5	Lunne et al. (1997)*
(Zone 2) Organics	12.5	"
(Zone 3) Clay	17.5	"
(Zone 4) Silty Clay to Clay	18.0	"
(Zone 5) Clayey Silt to Silty Clay	18.0	"
(Zone 6) Sandy Silt to Clayey Silt	18.0	"
(Zone 7) Silty Sand to Sandy Silt	18.5	"
(Zone 8) Sand to Silty Sand	19.0	"
(Zone 9) Sand	19.5	"
(Zone 10) Gravelly Sand to Sand	20.0	"
(Zone 11) Very Stiff Fine Grained	20.5	"
(Zone 12) Stiff Sand to Clayey Sand	19.0	"
Fluid Tailings	9.8 to 14.0	Styler et al. (2018b)
Iron Tailings	17.8 to 18.9	Hu et al. (2017)
Copper Tailings	15.9 to 18.1	Hu et al. (2017)
Gold Tailings	17.7 to 19.4	Ishihara (1984)
Zinc/Lead Tailings	19.7 to 20.3	Quille and O'Kelly (2010)
Coal Tailings	8.0 to 21.0	Adamczyk (2012)
Coal Combustion Residuals (Ash)	16.3 to 17.3	Walton and Butler (2009)
Compacted Volcanic Ash	15.7	Ishihara (1984)

*Note: 12-zone soil behavior charts presented by Robertson et al. (1986)

2.1.2 Unit Weight Estimated from CPT Measurements

As CPT provides three readings (q_t, f_s, u_2) for each sounding, it would be convenient to use one or more values to estimate γ_t. For instance, in clays, Larsson and Mulabdić (1991) developed charts for estimating unit weights of different fine-grained soil types of Scandinavia in terms of net cone resistance ($q_{net} = q_t - \sigma_{vo}$) and porewater parameter $B_q = (u_2 - u_0)/(q_t - \sigma_{v0})$. For granular soils, Młynarek, et al. (2005) showed a family of dry density curves in terms of q_c and σ'_{v0} based on CPTU data taken in alluvial and fluvioglacial sands of Poland.

Using data from 18 soils, Robertson and Cabal (2010) present a correlation for γ_t in terms of q_t and friction ratio ($R_f(\%) = 100 \cdot f_s/q_t$) shown in ***Figure 2.2*** and given by:

$$\gamma_t = \gamma_w \left(0.27 \log_{10} R_f + 0.36 \log_{10}\left(\frac{q_t}{\sigma_{atm}}\right) + 1.236\right) \tag{2.7}$$

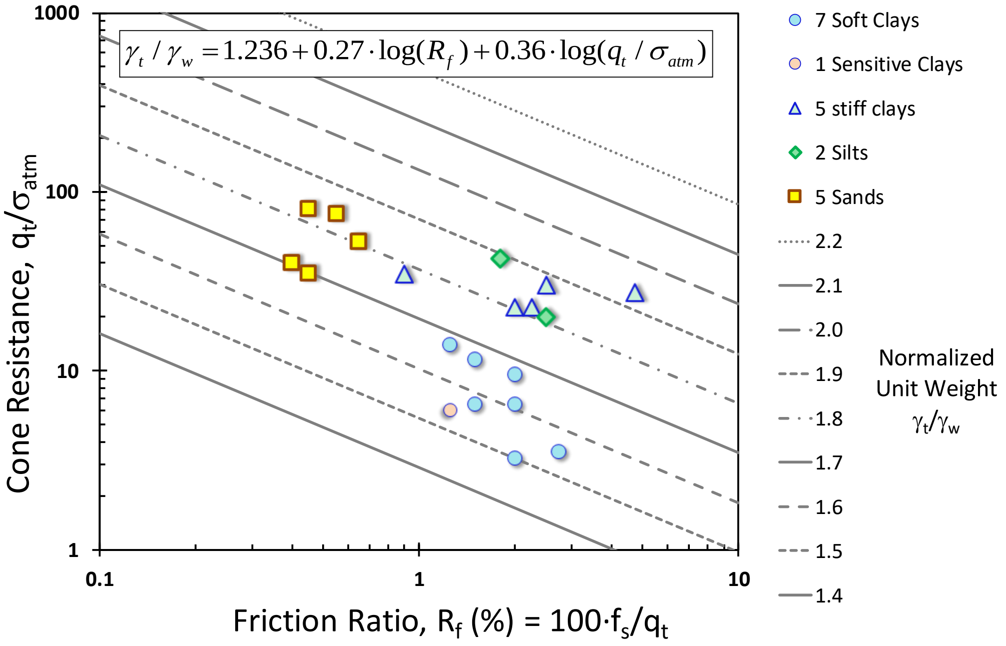

Figure 2.2: Direct unit weight estimation from cone resistance and friction ratio (after Robertson and Cabal 2010)

In a broader study using data from 44 onshore sites comprised of clays, silts, and sands, a set of regression analyses produced the relationship in ***Figure 2.3*** (Mayne et al. 2010):

$$\gamma_t = 1.81\gamma_w \left(\frac{q_t - \sigma_{v0}}{\sigma_{atm}}\right)^{0.017} \left(\frac{\sigma'_{v0}}{\sigma_{atm}}\right)^{0.05} \left(\frac{f_s}{\sigma_{atm}}\right)^{0.073} \left(B_q + 1\right)^{0.16} \tag{2.8}$$

Further research using additional data from offshore sites (Mayne and Peuchen 2012) and onshore locations (Mayne 2014) found that the sleeve friction alone provided a quick estimate of soil unit weight, as presented in ***Figure 2.4*** (N = 83 sites; n = 1009):

$$\gamma_t = \gamma_w \cdot [1.22 + 0.345 \cdot log_{10}(100 \cdot (f_s/\sigma_{atm}) + 0.010)] \tag{2.9}$$

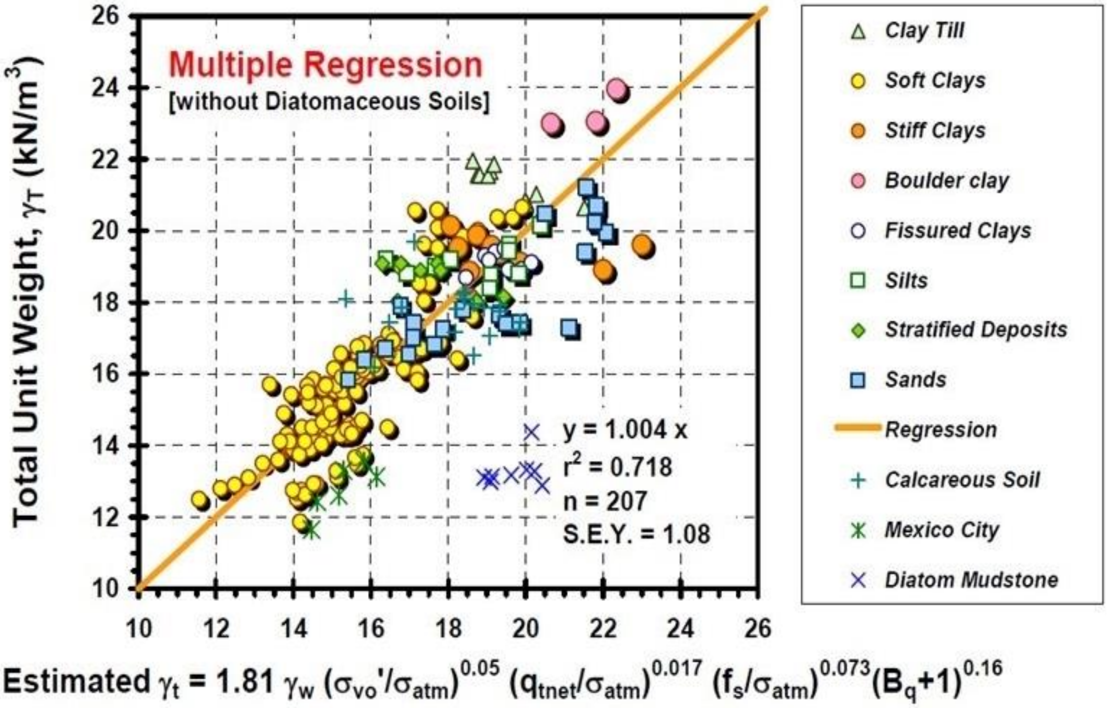

Figure 2.3: Unit weight relationship from multiple regression of CPTU data at 44 sites (after Mayne and Peuchen (2012)). Note: excludes data from diatomaceous and/or organic soils

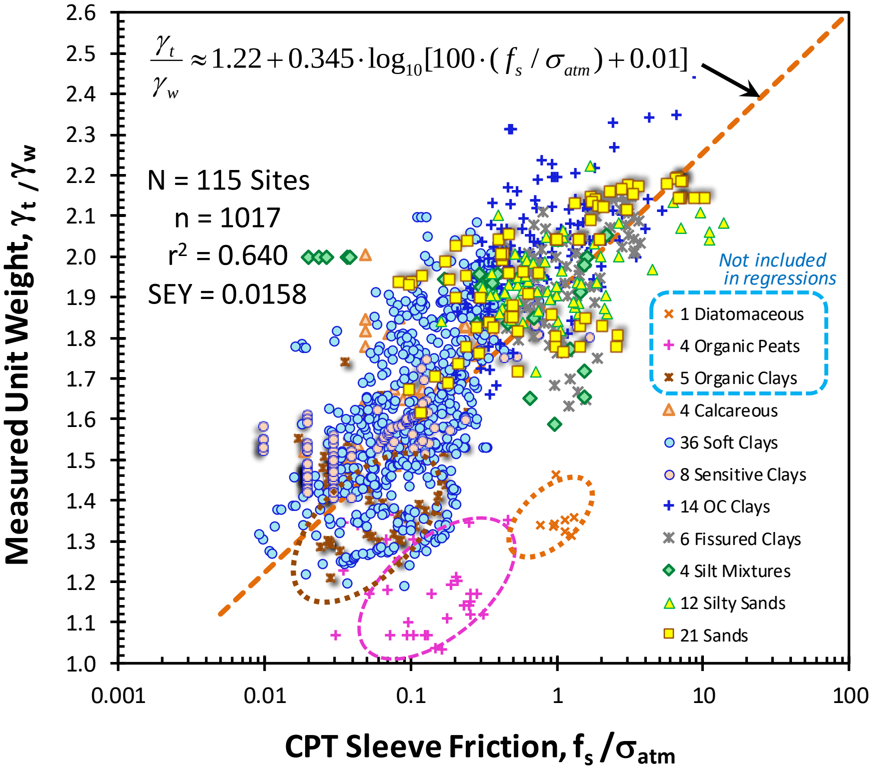

Figure 2.4: Total soil unit weight versus sleeve friction (Rix et al. 2019). Note: not applicable to organic clays, peats, or diatomaceous soils

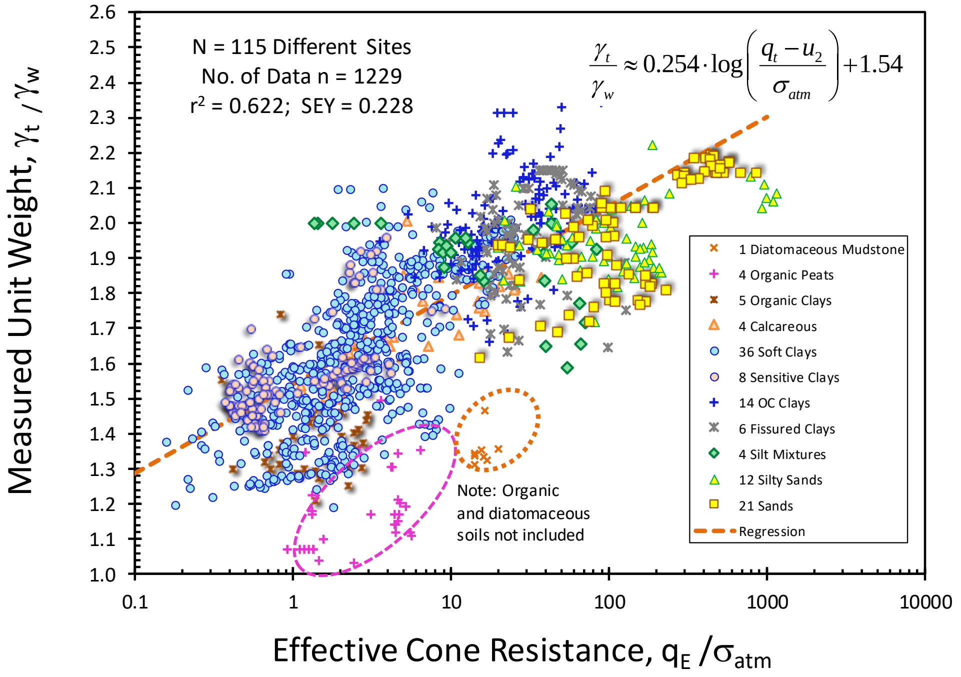

Figure 2.5: Normalized soil unit weight vs effective cone resistance for 115 different sites

In the latest review of available compiled data, a total dataset of n = 1229 from 115 different soils has been used to quantify the soil unit weight from three expressions using the CPTU, including eqn (2.7), (2.9), and a new one shown in ***Figure 2.5*** using effective cone resistance: $q_E = q_t - u_2$. ***Table 2.2*** presents the findings. The highest value of coefficient of determination (r^2) and lowest value of SEY is found from the average of all three methods.

Table 2.2 Expressions for Estimating Soil Unit Weight of Sands, Silts, & Clays from CPTU

Reference	Expression*	Eqn. No.
Robertson & Cabal (2010)	$\frac{\gamma_t}{\gamma_w} \approx +1.776 + 0.27 \cdot \log_{10}(f_s / \sigma_{atm}) + 0.09 \cdot \log_{10}(q_t / \sigma_{atm})$ r^2 = 0.609; SEY = 0.217	(2.10)**
Mayne (2014)	$\frac{\gamma_t}{\gamma_w} \approx +1.22 + 0.345 \cdot \log_{10}[100 \cdot (f_s / \sigma_{atm}) + 0.01]$ r^2 = 0.570; SEY = 0.158	(2.11)
This Manual (Figure 2.5)	$\frac{\gamma_t}{\gamma_w} \approx +1.54 + 0.254 \cdot \log_{10}(q_E / \sigma_{atm})$ r^2 = 0.622; SEY = 0.228	(2.12)
Recommended	Average (γ_t/γ_w) from all 3 eqns r^2 = 0.631; SEY = 0.148	(2.13)

*Note: Not applicable to organic soils, diatomaceous earth, or cemented geomaterials

**Note: Equation (2.10) provides same values of unit weight as (2.7) by separation of R_f terms.

Of further mention, Machine Learning (ML) has also been used to estimate the soil unit weight from CPT readings. Entezari, et al. (2021) applied ML on the aforementioned large database of soils ($n = 1229$) and obtained an $r^2 = 0.86$ in the measured vs. predicted statistical analyses.

For soft clays, approximate estimates of soil unit weight can be obtained from the slope of cone resistance (q_t) versus depth (z), defined as the parameter $m_q = \Delta q_t/\Delta z$ (Mayne et al. 2011, 2012). For 34 soft clays (19 offshore and 15 onshore), the following trend was found:

$$(\gamma_t / \gamma_w) \approx 1 + 0.125 \cdot (m_q / \gamma_w) \tag{2.14}$$

where m_q and γ_w are in the same units (e.g., kN/m^3). Soft clays can be identified when the ratio $(m_q/\gamma_w) < 8$. When the ratio $(m_q/\gamma_w) > 8$, then the presence of stiff to hard clays, including calcareous and/or fissured clays may be assumed and a different procedure is recommended in estimating the soil unit weight (Mayne 2014).

For soft clays, a similar approach can be adopted by defining the parameter: $m_{\Delta u} = \Delta u_2/\Delta z$, which can be utilized to identify unit weight trends for three categories of soft clay type: (a) regular or normal soft clays; (b) organic soft clays, including peats; and (c) sensitive soft clays, as presented in ***Figure 2.6***.

Soft regular clays: $(\gamma_t/\gamma_w) = 1.0 + 0.322 \cdot (m_{\Delta u}/\gamma_w)$ (2.15)

Soft organic clays: $(\gamma_t/\gamma_w) = 1.0 + 0.286 \cdot (m_{\Delta u}/\gamma_w)$ (2.16)

Soft sensitive clays: $(\gamma_t/\gamma_w) = 1.0 + 0.213 \cdot (m_{\Delta u}/\gamma_w)$ (2.17)

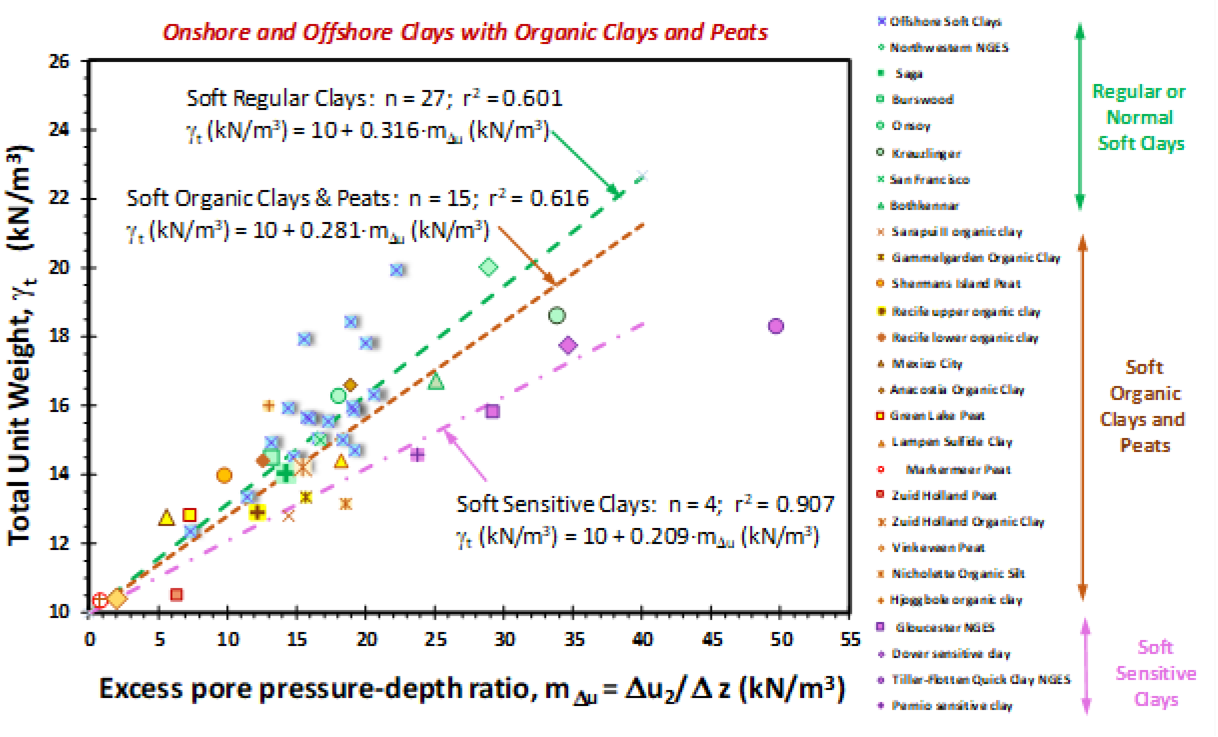

Figure 2.6: Unit weight trends with slope parameter $m_{\Delta u}$ for soft clays, including regular soft clays, organic soft clays & peats, and sensitive soft clays with slope parameter $m_{\Delta u}$

2.1.3 Unit Weight Estimated from V_s

When SCPTU results are available, the unit weight can be estimated from the shear wave velocity (V_s in m/s) and depth (z in meters):

$$\gamma_t\left(\frac{kN}{m^3}\right) = 8.31\log_{10} V_S\left(\frac{m}{s}\right) - 1.61\log_{10} z\,(m) \tag{2.18}$$

This relationship is shown in ***Figure 2.7*** and applies to a wide range (n = 1018) of particulate geomaterials (sands, silts, and clays) that are not cemented or bonded. The expression is not applicable to saprolites, rocks, cemented calcareous or carbonate soils, or special geomaterials such as diatomaceous earth.

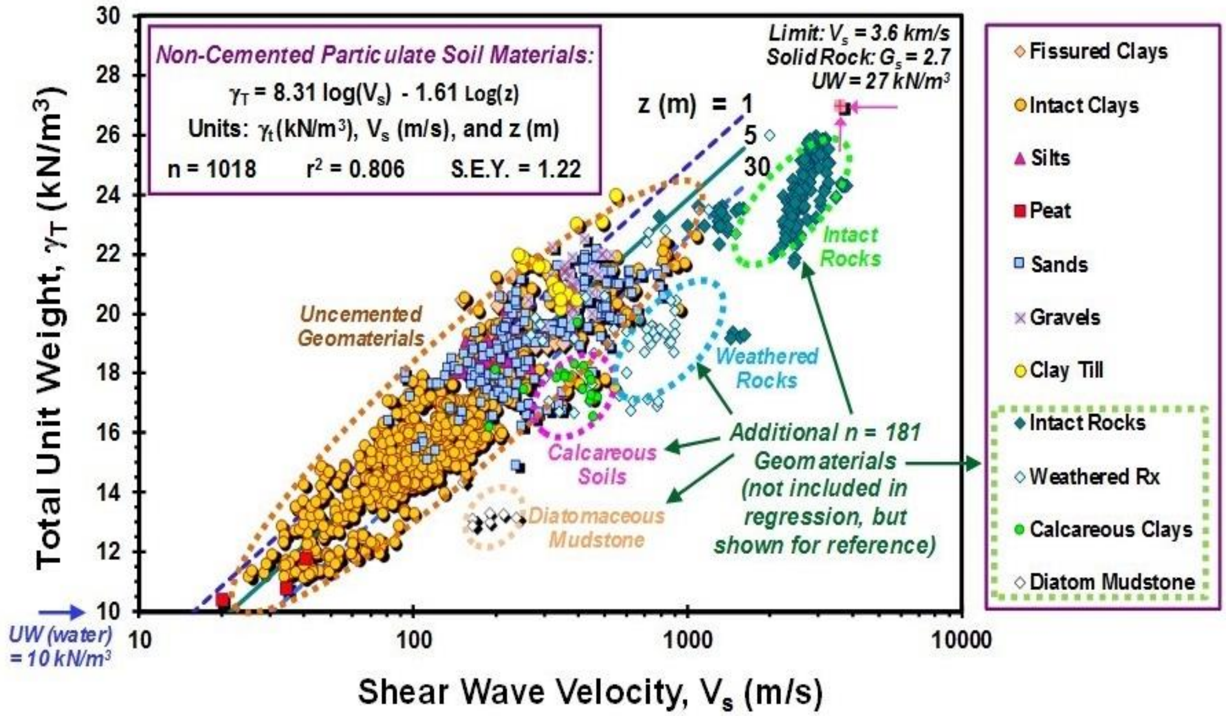

Figure 2.7: Relationship for unit weight in terms of shear wave velocity and depth for uncemented geomaterials (modified after Mayne 2001)

A more fundamental trend for unit weight is derived in terms of V_s (m/s) and σ'_{v0} (in kPa) since the latter term also includes the effect of groundwater conditions. This relationship is shown in ***Figure 2.8*** and the regression for γ_t is expressed:

$$\gamma_t(kN/m^3) = 4.17 \ln V_{s1} - 4.03 \tag{2.19}$$

where $V_{s1} = V_s/(\sigma'_{v0}/\sigma_{atm})^{0.25}$ is the effective stress-normalized shear wave velocity. Since an assessment of unit weight is required in order to calculate σ'_{v0}, then an iterative procedure between the profiles of V_{s1} and γ_t will be needed.

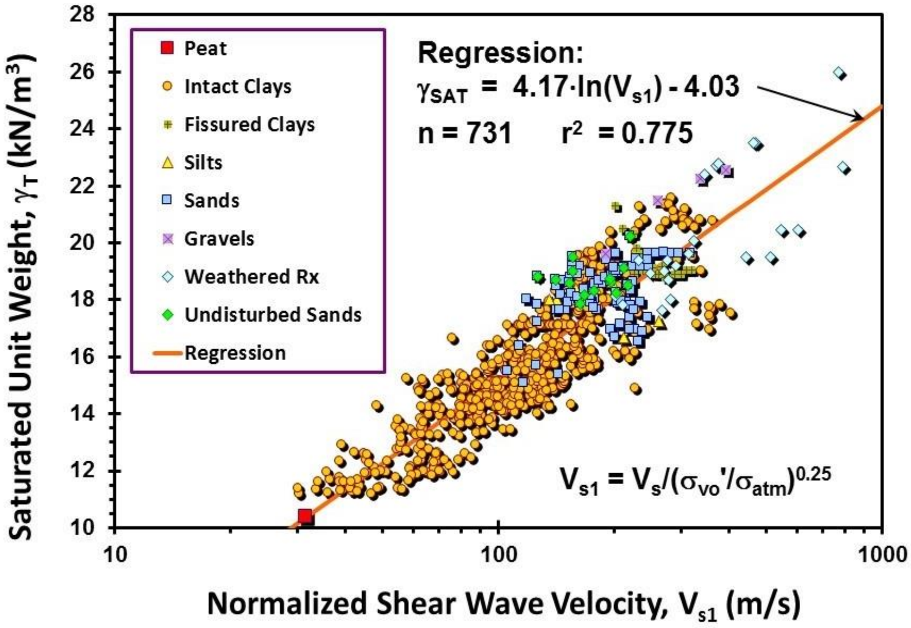

Figure 2.8: Soil unit weight with stress-normalized shear wave velocity (Mayne 2007b)

2.2 Estimating V_s from CPT profiles

If shear wave velocity measurements are not available, it is possible to estimate the V_s profile from the CPT data, although this will incur additional uncertainties. Many initial correlations were developed for a particular soil type and often for a specific geologic setting. For instance, Baldi et al. (1989) found a relationship for clean sands in Italy shown in ***Figure 2.9*** and given by:

$$V_s(\frac{m}{s}) = 277(q_t\ (MPa))^{0.13}(\sigma'_{v0}\ (MPa))^{0.27} \tag{2.20}$$

For granular soils, a more recent relationship developed from SCPTU data at 105 sand sites in eastern Canada has been found (Perret et al. 2016). Here, sandy soils with $I_{C,RW} < 2.6$ and $B_q < 0.1$ are applicable and the shear wave velocity can be estimated from:

$$V_s(\frac{m}{s}) = 124.7\left(\frac{q_t}{\sigma_{atm}}\right)^{0.135}\left(\frac{f_s}{\sigma_{atm}}\right)^{0.014}\left(\frac{\sigma_{v0}'}{\sigma_{atm}}\right)^{0.169} \tag{2.21}$$

On the other hand, for clays, Mayne and Rix (1995) compiled data from 31 different clay sites and found an overall trend shown by ***Figure 2.10*** that can be expressed:

$$V_s(\frac{m}{s}) = 31.4\left(\frac{q_t}{\sigma_{atm}}\right)^{0.627} \tag{2.22a}$$

$$V_s(\tfrac{m}{s}) = 1.75\cdot[q_t(kPa)]^{0.627} \tag{2.22b}$$

If the void ratio (e_0) of the clay is known (or alternatively, the water content), then a stronger regression equation that relates V_s to qt and e_0 for intact clays (Mayne & Rix 1995):

$$V_s(\tfrac{m}{s}) = 9.44\cdot(100\cdot q_t/\sigma_{atm})^{0.435}\cdot(e_0)^{-0.532} \tag{2.23}$$

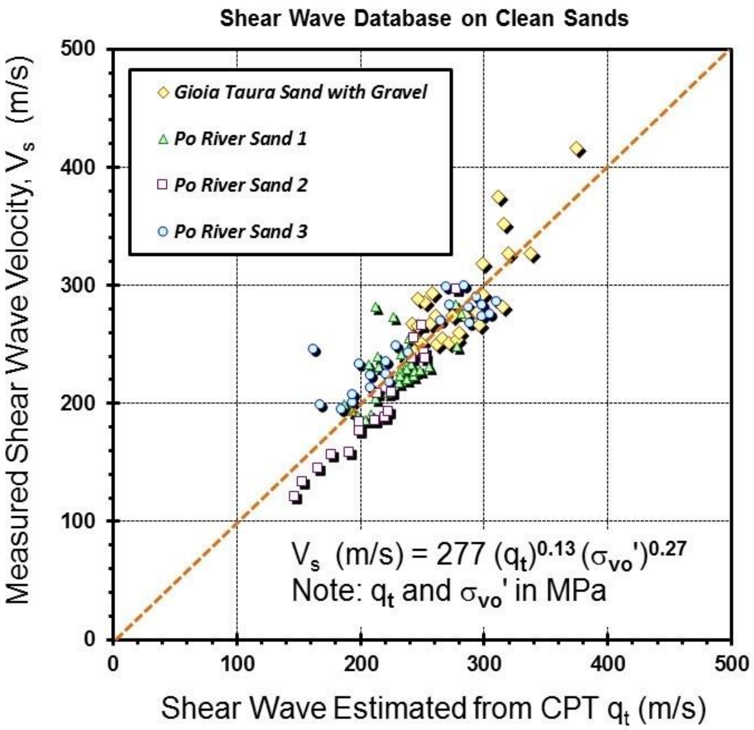

Figure 2.9: Empirical relationship for V_s in clean sands from CPT (after Baldi et al. 1989)

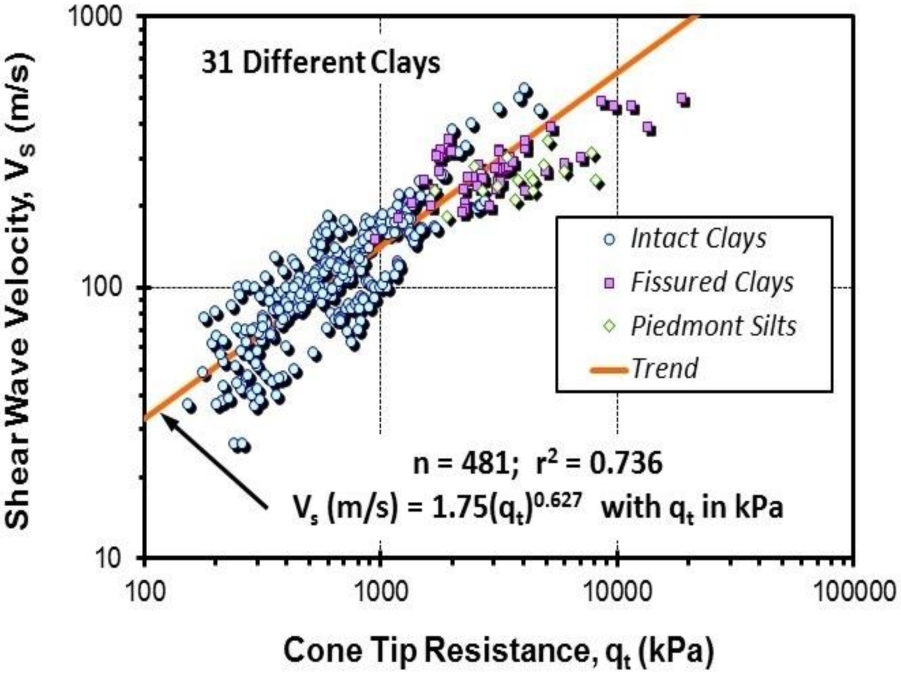

Figure 2.10: Empirical relationship for V_S in clays from CPT (after Mayne and Rix 1995)

L'Heureux & Long (2017) provide a review of 22 V_s correlative trends with CPT for clays. For the sensitive clays of Norway, they found the following statistical expression ($n = 101$; $r^2 = 0.89$):

$$V_s(m/s) = 71.7 \cdot (q_{net})^{0.09} \cdot (\sigma_{vo}{}' / w_n)^{0.33} \tag{2.24}$$

where q_{net} and $\sigma_{vo}{}'$ are in kPa and w_n = water content (%).

For a variety of different soil types (clays, silts, sands, and mixed soils), Hegazy and Mayne (1995) expressed the shear wave velocity in terms of the cone tip resistance (q_t in kPa) and friction ratio ($R_f = 100 \cdot f_s/q_t$ in percent):

$$V_s(m/s) = (10.1 \cdot \log_{10} q_t - 11.4)^{1.67} \left(R_f\right)^{0.3} \tag{2.25}$$

Note that this method does not apply to calcareous soils, diatomaceous mudstone, muskeg, or peats.

The effect of time (or age) has been shown to influence CPT correlations. A study of shear wave velocity data in South Carolina found the following relationship for CPTs in a variety of different soil types (Andrus et al. 2007):

$$V_s(m/s) = 2.62(q_t)^{0.395} \left(I_{C,RW}\right)^{0.912} (z)^{0124} (ASF) \tag{2.26}$$

where q_t is in kPa, $I_{C,RW}$ = CPT material index, depth z (m), and ASF is an age scaling factor for the formation (SF = 0.92 for Holocene deposits and 1.12 for Pleistocene soils). The CPT material index I_c is used to determine soil type and discussed in more detail in Section 3. It ranges from about 1 to 2 in clean sands, 2 to 3 in silts, and generally is about 3 or greater in clays.

In a separate study, Robertson (2009b) recommended the evaluation of V_s from CPT net cone resistance and CPT material index:

$$V_s(m/s) = \left(10^{1.68+0.5\left(I_{C,RW}\right)} \left(\frac{q_t - \sigma_{v0}}{\sigma_{atm}}\right)\right)^{0.5} \tag{2.27}$$

A recent review of shear wave velocity correlations conducted by the Pacific Earthquake Engineering Research (PEER) Center recommended to use the average value from the three aforementioned methods, specifically eqns (2.25), (2.26), and (2.27), as documented by Wair et al. (2012).

2.3 Unit Weight in Man-Made Deposits

2.3.1 Fluid Tailings

CPT soundings are frequently used to characterize tailings storage facilities (TSF). These facilities contain tailings in fluid-states with suspended soil particles, recent sedimentary deposits undergoing self-weight consolidation, and soil-like tailings with behavior controlled by the effective stress. Styler et al. (2018) presented the interpretation of CPT results in oil sand tailings facilities showing typical measurements obtained in recycled water, fluid tailings, beach tailings, and into natural ground. In fluid tailings, the cone tip resistance will increase with the measured pore pressure. The effective tip resistance, $q_t - u_2$, will be close to zero. The friction sleeve measurements will also be nearly zero.

The measured pore pressures will equal the total stress in fluid tailings. The weight of the suspended soil particles is carried by the pore fluid; which increases the unit weight of the pore fluid. Piezometer readings have been used in laboratory tests on sedimentation (Sills 1998) to calculate the total stress and in-situ void ratios. These readings were also used in 10 m high standpipe tests on oil sand tailings (Jeeravipoolvarn et al. 2009). Since the CPT u_2 measurements equal total stress, the slope of u_2 versus depth equals the total unit weight of fluid tailings.

Pore pressure dissipation tests can be performed in fluid tailings. These show that the u_2 channel does not dissipate to a hydraulic profile of 9.8 kN/m^3 from the pond-surface. The u_2 channel does not dissipate at all because there are no excess pore pressures from shear or cavity expansion to accommodate the cone probe.

Therefore, the total unit weight, γ_t, is simply the slope of the measured pore water pressure versus depth in fluid tailings with negligible effective stress.

2.3.2 Metal Mine Tailings

Most natural soils have specific gravities that range from $G_s \approx 2.6$ to 2.8. The total unit weights calculated with G_s are fairly insensitive to specific gravity in natural soils.

Metal mine tailings can have heavier specific gravities, values above $G_s > 3$. Consequently, unit weights estimated from SBT zones may be underestimated by over 20% for these deposits. Unit weights from V_s or CPT measurements may still be applicable, but should be confirmed by other means.

2.4 Overburden Stress and Porewater Pressure

2.4.1 Total Overburden Stress

The total vertical (overburden) stress profile is σ_{v0} which is the accumulation of unit weight times layer thickness with depth, equal to the integral:

$$\sigma_{vo} = \int \gamma_t dz \tag{2.28}$$

For practical calculations using a spreadsheet, σ_{vo} is often approximated by:

$$\sigma_{vo} = \sum_{i=1}^{n}(\gamma_{ti} \cdot \Delta z_i) \tag{2.29}$$

2.4.2 Equilibrium Porewater Pressure

Geotechnical soil behavior depends on effective stress. Effective stress is the total stress minus porewater pressure. A porewater pressure profile is required to calculate effective stress. The first principle of soil mechanics states that:

$$\sigma' = \sigma - u \tag{2.30}$$

The equilibrium pore pressure profile can be hydrostatic if there is no ground water flow. If there is ground water flow, due to ongoing soil consolidation or because of hydraulic gradients across the site, then a non-hydrostatic pore pressure profile will need to be characterized.

The depth to the ground water table can be measured in open soil borings, however, this may be affected by the drilling process. Also, borehole closure may be required in certain states or provinces for reasons of safety and/or protection of groundwater aquifers. In other cases, open boreholes can cave due to instability, thus affecting the measure of water levels.

For projects having groundwater as an important role in construction and performance, the installation of observation wells and/or piezometers may be prudent. Piezometers can be installed by conventional drilling and grouting methods, although the newer push-in piezometers are becoming more frequent and popular because of their expedient and economic installation.

For test elevations beneath the groundwater table, the equilbrium porewater pressure can also be ascertained by the use of dissipation testing. In these cases, a full dissipation to 100% degree of consolidation may be warranted to determine the equilibrium value. Additional details on dissipation testing are discussed later in Section 8. A hydrostatic pore pressure profile can be characterized by a single pore pressure dissipation (PPD) performed below the ground water table. A non-hydrostatic pore pressure profile requires multiple PPD tests run to equilibrium over the full depth of the CPT sounding.

2.4.3 Groundwater Table Depth

In unconfined aquifers, the equilibrium pore pressure profile is simply:

$$u_0 = h_w \cdot \gamma_w \tag{2.31}$$

where h_w is the height to the ground water table (GWT). That is, $h_w = z - z_w$, where z = current depth and z_w is the GWT depth. Above the GWT, it is common to take $u_0 = 0$, however in cases of capillarity, negative porewater pressures may occur.

If the soil rate of dissipation exceeds the rate of pore pressure generation, then the measured u_2 profile will equal the equilibrium pore pressure profile during penetration. This is seen in free draining soils such as sands and gravels.

2.4.4 Non-Hydrostatic Water Table

Artesian conditions and drawdown are also common cases where non-hydrostatic water tables are found. Ground water flow, due to soil consolidation or variable hydraulic gradients across a site, results in non-hydrostatic equilibrium pore pressure profiles. An accurate equilibrium pore pressure profile is necessary to calculate effective stress and properly interpret soil properties from the CPTU measurements.

Several case studies can be referred to for non-hydrostatic groundwater conditions. For instance, Johns and Murray (2018) demonstrated the consequences of an incorrect equilibrium pore pressure profile for CPTs performed in a mine tailings dike. Tanaka and Sakagami (1989) report on a CPTU soundings performed in underconsolidated soft clays caused by a recently constructed man-made island, or reclaimed land, within a bay area. A pore pressure profile less than hydrostatic was found at the Tiller-Flotten national test site in Norway due to drawdown with drainage to the east of the site (L'Heureux et al. 2019).

2.4.5 Effective Vertical Stress

The effective vertical stress is simply the total vertical stress minus the equilibrium porewater pressure:

$$\sigma_{vo}' = \sigma_{vo} - u_0 \tag{2.32}$$

For normal cases of hydrostatic equilibrium in flat ground in natural soils, the common cases for calculating u_0 are as follows with z = depth and z_w = depth of the groundwater table (GWT):

Above GWT and dry soil (no capillarity): $u_0 = 0$ (2.33a)

Below GWT and saturated soil: $u_0 = \gamma_w \cdot (z - z_w)$ (2.33b)

Above GWT and full capillarity: $u_0 = \gamma_w \cdot (z - z_w)$ (2.33c)

It is critical to have an accurate evaluation of effective vertical stress in order to interpret soil properties from CPT soundings. An underestimated effective stress will result in over-estimated soil densities and OCRs. This could also result in a misclassification of the soil behavior type.

Conversely, an overestimated effective stress will have the opposite effects on the interpreted results.

In practice, the interpretation of σ_{v0}, u_0, and σ'_{v0} is routine and straight forward. However, mistakes can be made if programs and spreadsheet formulas are used without checking the results. These mistakes could originate from CPTs performed in materials with atypical unit weights. They could occur if there is a drill-out through a surface layer and an incorrect unit weight is used for the overburden. They can occur if a hydrostatic porewater pressure profile is assumed when in fact the site has groundwater flow, drawdown, or artesian conditions.

2.5 Horizontal Stress and K_0

The lateral earth stress coefficient, K, is the ratio between horizontal effective stress and vertical effective stress: $K = \sigma_h'/\sigma_v'$. When the vertical and horizontal stresses correspond to the principal stress directions, the lateral earth stress coefficient is known as K_0, the lateral at-rest stress coefficient. Furthermore, K_0 applies to one-dimensional vertical loading under conditions of zero lateral strain (ϵ_h = 0). This relates to field conditions during the formation of marine sediment in the oceans, as well as the imposed conditions during 1-d consolidation tests in the soils laboratory. The at-rest lateral stress coefficient is defined by ***Equation 2.34***:

$$K_0 = \sigma_{ho}'/\sigma_{vo}' \tag{2.34}$$

K_0 is a state parameter of the soil and is related to overconsolidation ratio, OCR. When an unconfined soil is loaded vertically, it will expanded laterally. When this expansion is restricted – by a steel ring in a laboratory apparatus or by adjacent soil elements in the field under the same increase in vertical stress – then effective horizontal stresses develop to maintain zero lateral strain. The value of K_0 in overconsolidated soil is higher than K_0 in normally consolidated soil.

Figure 2.11 is a plot of σ'_{v0} versus σ'_{h0} for a soil element under zero lateral strain. This soil element is consolidated by increasing the vertical stress. Horizontal stresses develop due to the zero-lateral strain boundary condition, resulting in a proportional increase in σ'_{h0} during normal consolidation. This proportional increase in σ'_{h0} is equal to $(K_0)_{NC}$ on the normal consolidation line. The soil element is then unloaded by removing vertical effective stress. The horizontal stresses are not relieved at the same increment as during normal consolidation. As the vertical stress is unloaded, the OCR and K_0 of the soil both increase. At some point, σ'_{v0} will equal σ'_{h0} and K_0 equals 1. Continued unloading of vertical stress will further increase OCR and increase K_0 beyond 1. Over-consolidated soils can have higher σ'_{h0} than σ'_{v0}. Reloading the soil decreases OCR and K_0, but the horizontal stress lags behind the increase in σ'_{v0}. ***Figure 2.11*** shows that K_0 is highly related to OCR, but it also shows that K_0 depends on whether the soil is being unloaded or reloaded. The same soil can have the same OCR, but different K_0.

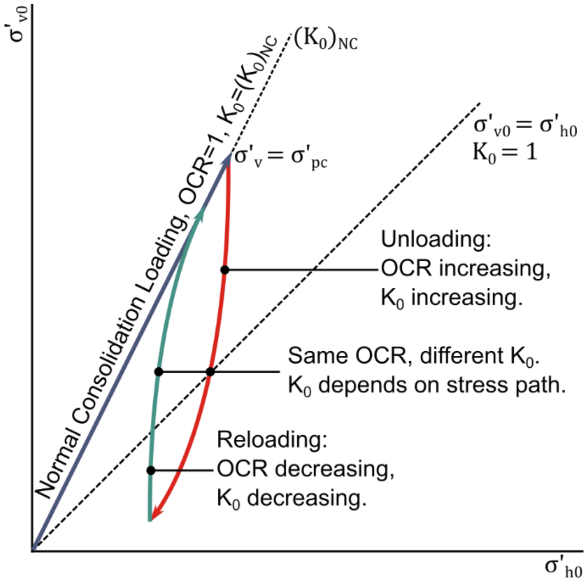

Figure 2.11: Stress path for normal consolidation (blue), unloading (red), and reloading (green) in σ'_v and σ'_h space (modified from Sully 1991)

In field programs, the value of K_0 can be assessed directly using in-situ tests, including: (a) lift-off pressure (P_0 = σ_{h0}) from self-boring pressuremeter tests (SBPMT); (b) the final equilibrium stress (σ_{h0} from push-in spade cells, also known as Glötzl cells or total stress cells (TSC)); (c) the closure pressure from hydraulic fracture (HF) tests; and (d) paired sets of directional and polarized shear wave velocities, such as crosshole (CHT) and downhole (DST) geophysics surveys (Ku and Mayne 2015). Indirect measures of in-situ K_0 can be made by use of the flat dilatometer test (DMT) and Iowa stepped blade (ISB). Several laboratory approaches have also been devised to ascertain the magnitude of K_0, including triaxial stress-path testing with local strain measurements, instrumented consolidometers with lateral stress sensors, and suction measurements on high-quality specimens.

Towards a pragmatic solution, laboratory data from 171 different soils (clays, silts, sands, and gravels) that were subjected to either triaxial and/or instrumented consolidometer tests were compiled to investigate trends (Mayne and Kulhawy 1982). Laboratory data for K_0 measurements on 43 clays are summarized in ***Figure 2.12***. Similar findings are available for virgin loading and unloading of silts and sands in laboratory K_0 tests.

For loading-unloading of uncemented sands and non-structured clays of low to medium sensitivity, the following power law expression was offered:

$$K_0 = (1 - \sin\phi) \cdot OCR^{\sin\phi} \tag{2.35}$$

where ϕ' = effective friction angle and OCR = overconsolidation ratio. For highly-structured soils, higher values of K_0 can be realized where the exponent term is related to the clay sensitivity (Hamouche et al. 1995).

Confirmation of equation (2.35) is also found in ***Figure 2.13*** that shows field K_0 data from total stress cell (TSC) measurements and self-boring pressuremeter tests (SBPMT) in clays.

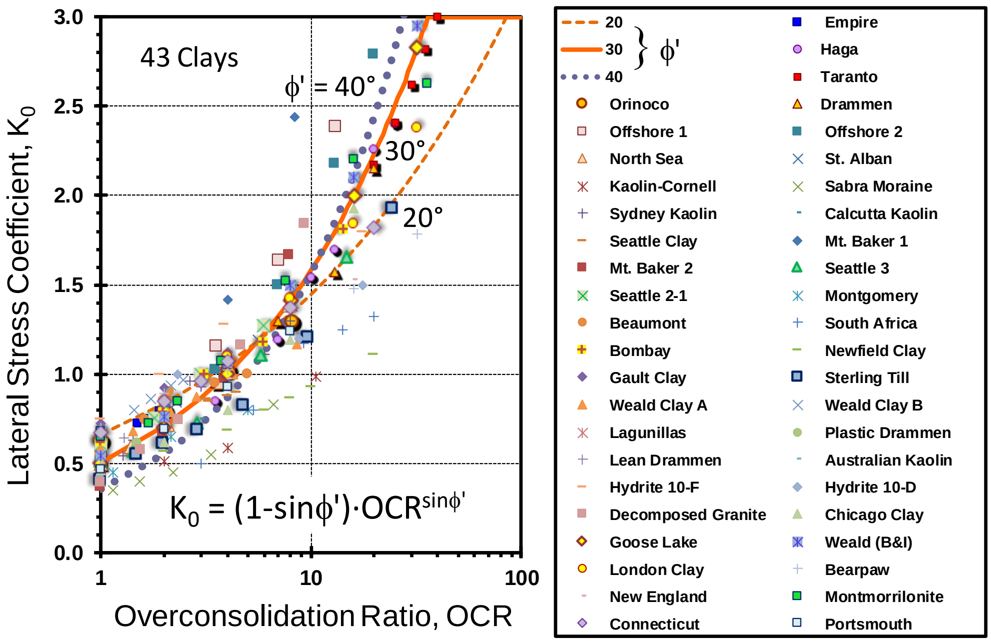

Figure 2.12: Summary of laboratory K_0 data on 43 clays showing effects of OCR during virgin loading and unloading

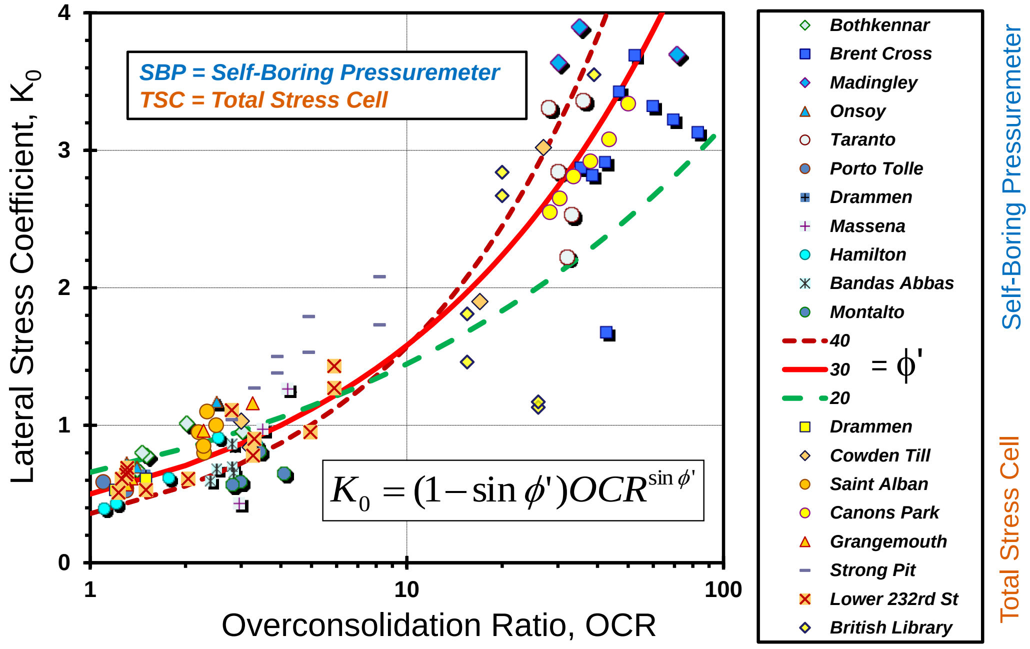

Figure 2.13: Lateral stress coefficient K_0 from in-situ field measurements by TSC and SBPMT versus OCR for 19 clays (Mayne 2020)

For clean unaged and uncemented quartz and silica sands, available data are compiled in ***Figure 2.14***. These results include K_0 data from large calibration chamber tests, small laboratory triaxial and oedometer test series, as well as field pressuremeter tests (PMT) from Po River Sand (Italy), Stockholm (Sweden), Holmen (Norway), and Thanet Sand (UK).

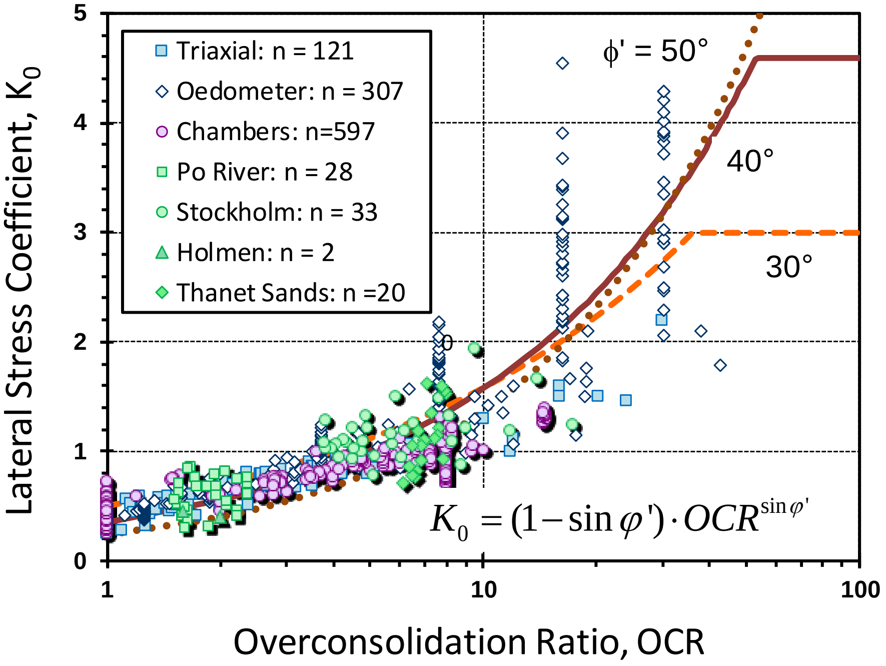

Figure 2.14: Lateral stress coefficient K_0 versus OCR from field and lab tests on sands with OCR$_{limit}$ applied

For ***Equation 2.35***, a maximum value for K_0 during unloading can be established by the passive stress coefficient (K_P), which is given for the simple Rankine case by:

$$K_P = \frac{1+\sin\phi}{1-\sin\phi} = \tan^2(45° + \phi/2) \tag{2.36}$$

The K_P limit is shown in ***Figure 2.14*** for the K_0 versus OCR relationships for sands. As such, a limiting OCR can be calculated:

$$OCR_{limit} = \left(\frac{1+\sin\phi}{(1-\sin\phi)^2}\right)^{1/\sin\phi} \tag{2.37}$$

The OCR represents the stress history of the soil. It is a state variable. Notably, CPT measurements can be used to evaluate OCR, as covered in ***Section 4.4***. For the more complex case of virgin loading, unloading, and reloading of soil, Schmidt (1983) found:

$$K_0 \quad = \quad \frac{1-\sin\phi'}{(OCR_{max}-1)}\cdot[OCR_{max} - OCR + (OCR-1)\cdot OCR_{max}{}^{\sin\phi'}] \tag{2.38}$$

where OCR$_{max}$ = maximum experienced value of OCR during the unloading phase.

3 Stratigraphy and Soil Type

Natural soils and rocks are complex geomaterials having diverse compositions, mineralogies, and varied geologic origins that have been subjected to long exposure to various environmental, seasonal, climatic, and thermal conditions over many thousands to millions of years. Soils are formed by many different processes, many of them from the action of water forming sediment (marine, lacustrine, fluvial, alluvial, deltaic, estuarine), but also produced by wind (dune, aeolian, loess), ice (glacial), and by in-place disintegration and deterioration of the underlying parent bedrock that creates particles (residuum, saprolite, laterites, andosols). Their variety is extensive and limitless (***Figure 3.1***).

Composition of soil particles can include basic minerals (quartz, feldspar, mica, kaolin, etc.) or bio-geo origins (calcareous, carbonates, peats). Their behavior is complicated by aspects involving stress history, anisotropy, drainage, and nonlinear stress-strain-strength response under loading, with additional facets such as strain rate, ageing, cementation, fissuring, and other difficult-to-quantify nuances.

Figure 3.1: Immense variety and wide diversity of geomaterials in the environment

3.1 Initial Conditions

A rather large number of geotechnical parameters have been defined by the profession in an effort to represent soil conditions and behavior. In the grouping of Initial Conditions shown by ***Figure 3.2***, there are two major categories of parameters that reflect: (1) *Indices* which help quantify the compositional makeup and components of the soil particles; and (2) *State parameters* that relate to the packing arrangement and current state of stress of the assemblage of particles. Certainly, a realization of the soil index parameters (first group) requires sampling, laboratory testing, and knowledge of the local geology and terrain formation. With regard to field testing, the identification of soil indices can be aided in part by use of the Vision Cone Penetration Test (VisCPT), as detailed by Hryciw et al. (1998) and Hryciw and Shin (2004).

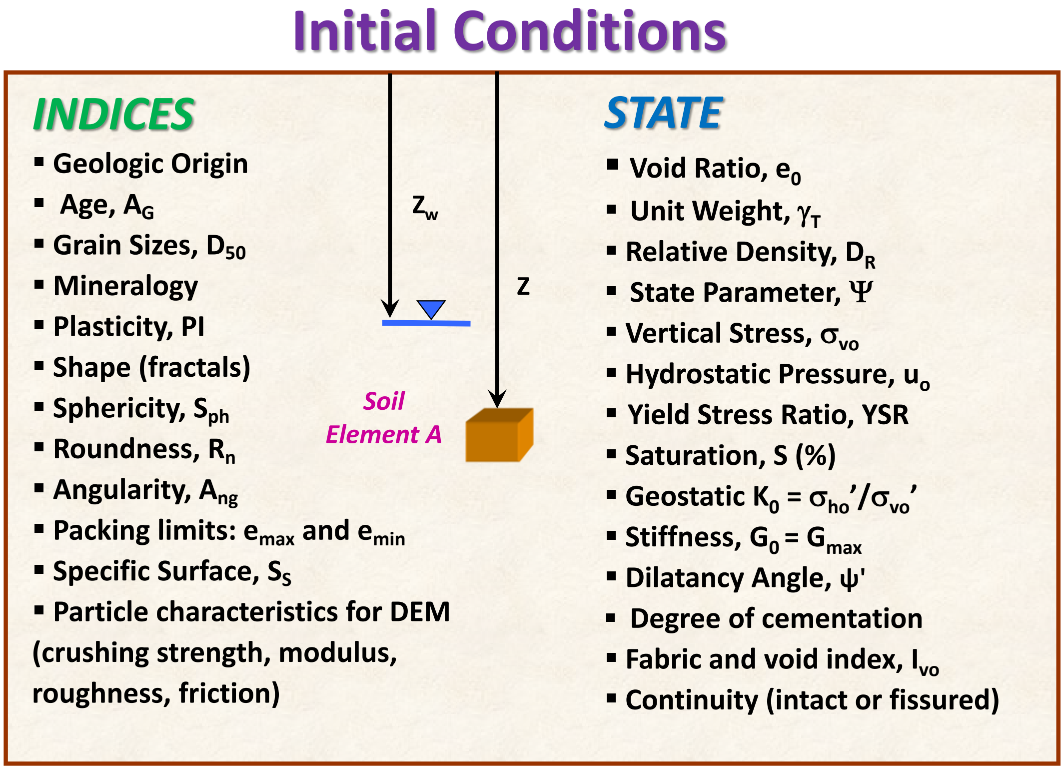

Initial Conditions

INDICES

- Geologic Origin
- Age, A_G
- Grain Sizes, D_{50}
- Mineralogy
- Plasticity, PI
- Shape (fractals)
- Sphericity, S_{ph}
- Roundness, R_n
- Angularity, A_{ng}
- Packing limits: e_{max} and e_{min}
- Specific Surface, S_S
- Particle characteristics for DEM (crushing strength, modulus, roughness, friction)

STATE

- Void Ratio, e_0
- Unit Weight, γ_T
- Relative Density, D_R
- State Parameter, Ψ
- Vertical Stress, σ_{vo}
- Hydrostatic Pressure, u_o
- Yield Stress Ratio, YSR
- Saturation, S (%)
- Geostatic $K_0 = \sigma_{ho}'/\sigma_{vo}'$
- Stiffness, $G_0 = G_{max}$
- Dilatancy Angle, ψ'
- Degree of cementation
- Fabric and void index, I_{vo}
- Continuity (intact or fissured)

Figure 3.2: List of soil parameters to quantify initial soil conditions: (a) particle indices; and (b) in-situ state (modified after Mayne et al. 2009)

3.2 Soil Behavior Type (SBT)

The CPT was first developed as a profiling tool to identify the thickness of soft surface deposits of clays and organic “veen” soils (Barentsen 1936). The conical shaped probe was pushed by hand through the bottom of a borehole until refusal on an underlying stronger layer. The low cone tip resistance above this stronger layer was used to infer the soil type. Therefore, the very first application of cone penetration testing was to profile soil layers based on their observed cone behavior. This is an efficient and economical alternative to characterizing soil types by collecting soil samples and measuring their intrinsic properties in a laboratory.

Soil classification in the laboratory is most often done using sets of nested sieves for coarse particles (sands and gravels) and hydrometric analyses for finer soil particles (silts and clays). Several systems are used in North America including the: (a) Unified Soil Classification System (USCS) as documented by ASTM D-2487 and D-2488; (b) United States Dept. of Agriculture (USDA) that uses a triangular plot of percentages of sand, silt, and clay; (c) American Association of State Highway and Transportation Officials (AASHTO) related to interstate roadways; and other systems. Details on the USCS and AASHTO are given by Rix et al. (2019).

The CPT soil behavior type and laboratory soil classification can be in disagreement. A non-plastic rock flour may behave like a silt, but the particle size may classify as a clay or a sand. A clayey-gravel mixture may behave like a clay if the gravel particles are suspended in the clay matrix, but it may classify in the laboratory as a gravel. If the soil is not being excavated as a borrow material, then in practice it may be more relevant to know how the soil behaves in-situ rather than the actual laboratory classification.

To facilitate the identification of soil types indirectly by CPT, a good number of empirical soil behavior type (SBT) charts have been developed (e.g., Douglas and Olson 1981; Kulhawy and Mayne 1990; Lunne et al. 1997; Fellenius and Eslami 2000; Robertson 2009b; Schneider et al. 2008; 2012). In this section, several of the more popular methods for assessing soil type from CPT are reviewed.

3.2.1 q_t versus R_f

The friction sleeve was added to the cone probe by Begemann (1953) to create a tool for pile foundation design. Begemann (1965) observed that the soil type could be inferred from the ratio of friction resistance to cone tip resistance, termed friction ratio (%): $R_f = 100 \cdot f_s/q_t$. Ratios above 3% were inferred to be clayey soils. Ratios below 1% were inferred to be sandy soils.

Robertson et al. (1986) presented a 12-zone SBT system that compares the cone tip resistance (q_t) and friction ratio (R_f), as seen in **Figure 3.3**. This chart was based on preceding CPT research by other practitioners and experience gained using the CPT in known natural soil deposits. The primary advantage of this chart is that it can be used with almost raw CPT data, the only calculation required being the corrected cone tip resistance q_t. The shortcomings of this chart are exposed in deep CPTs greater than 20 m. As such, the net tip resistance, $q_{net} = q_t - \sigma_{v0}$, is a more valid parameter for SBT classifications as well as for bearing capacity analyses. Deep soundings see an increase in effective stress with depth; which increases the tip resistance. The shortcomings were addressed in a normalized SBTn chart proposed by Robertson (1990, 1991) which is discussed later in this section.

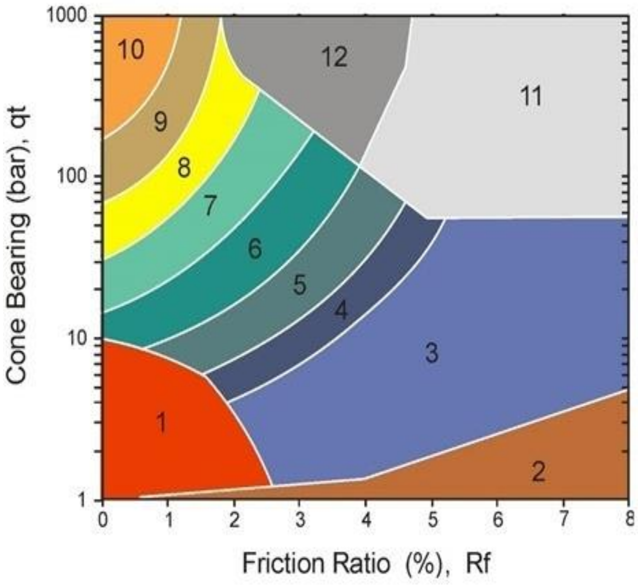

Zone	γ_t kN/m³	Soil Type
1	17.5	Sensitive Fines
2	12.5	Organic Material
3	17.5	Clay
4	18.0	Silty Clay to Clay
5	18.0	Clayey Silty to Silty Clay
6	18.0	Sandy Silt to Clayey Silt
7	18.5	Silty Sand to Sandy Silt
8	19.0	Sand to Silty Sand
9	19.5	Sand
10	20.0	Gravelly Sand to Sand
11	20.5	Very Stiff Fine Grained*
12	19.0	Sand to Clayey Sand *

NOTE: * Overconsolidated or cemented

Figure 3.3: CPT soil behavioral charts for 12 classification zones using cone resistance (q_t) and friction ratio ($Rf = 100 \cdot f_s/q_t$) from Robertson et al. (1986)

3.2.2 Q versus F_r

In order to account for depth effects and overburden stress on the readings, stress-normalized CPT parameters have been defined as follows (Lunne et al. 1997):

$$Q = \frac{q_t - \sigma_{v0}}{\sigma'_{v0}} \tag{3.1}$$

$$F_r(\%) = \frac{100 f_s}{q_t - \sigma_{v0}} \tag{3.2}$$

Note that Q is also now designated as Q_t and Q_{t1}, depending upon research institution or agency. These variables were used to develop a 9-zone SBT chart (Robertson 1990), as presented in ***Figure 3.4***. In this system, basic “vanilla” clay is zone 3 while “hourglass” sands are found in zone 6.

While the definition of Q in (3.1) works well in soft clays, the results of CPT in sands shows that q_{net} is more aligned with the square root of σ_{vo}', especially as the sounding increases with depth. This resulted in an upgrade of Q to Q_{tn} where the effective stress has a variable exponent: $Q_{tn} = q_{net}/(\sigma_{vo}')^n$ (in units of bars) with "n" ranging from 1 (clays) to 0.75 (silts) and 0.5 (sands). In dimensionless terms, $Q_{tn} = (q_{net}/\sigma_{atm})/(\sigma_{vo}'/\sigma_{atm})^n$ for any units (Robertson 2009b).

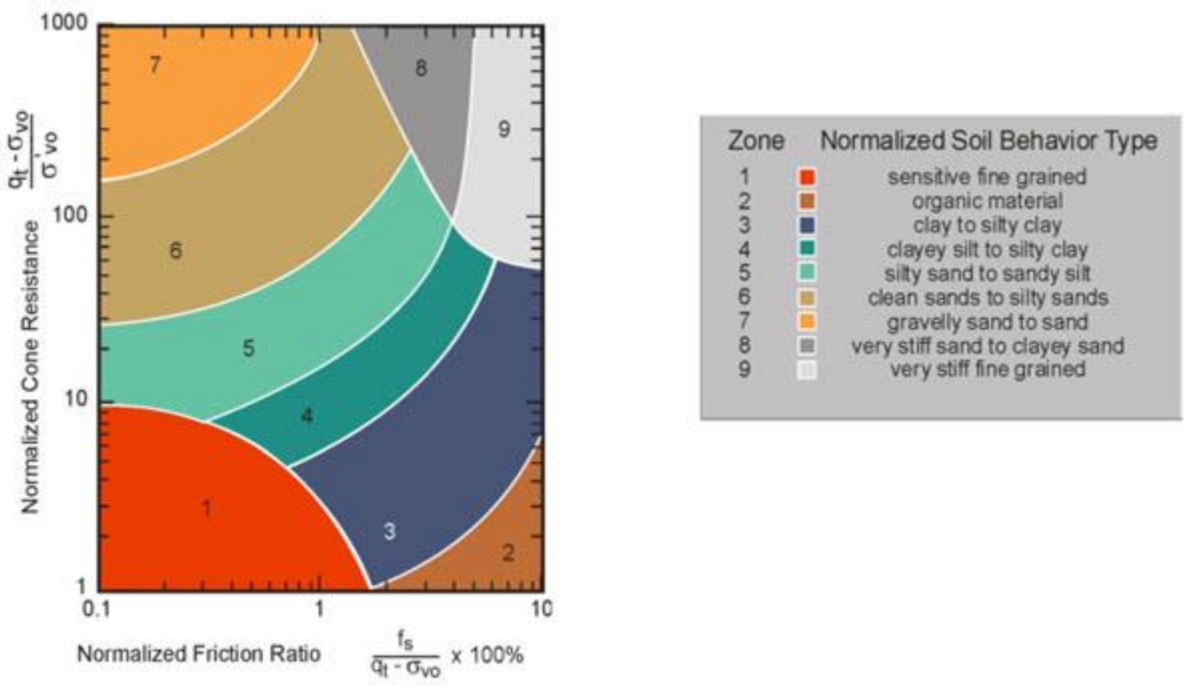

Figure 3.4: CPT soil behavioral type classification charts with 9-zones and normalized Q_{t1} versus F_r (after Robertson 1990, 1991; Lunne et al. 1997; Robertson 2009b)

Using the normalized Q and F parameters, Schneider et al. (2012) developed a 4-zone SBT chart as shown in ***Figure 3.5***. The soil boundaries in this chart were developed analytically and evaluated with field data. The soil boundaries are hyperbolic and intersect the Q_{t1} and F_r axes at theoretically calculated values based on the soil friction angle, rigidity index, and an equivalent normally-consolidated penetration resistance.

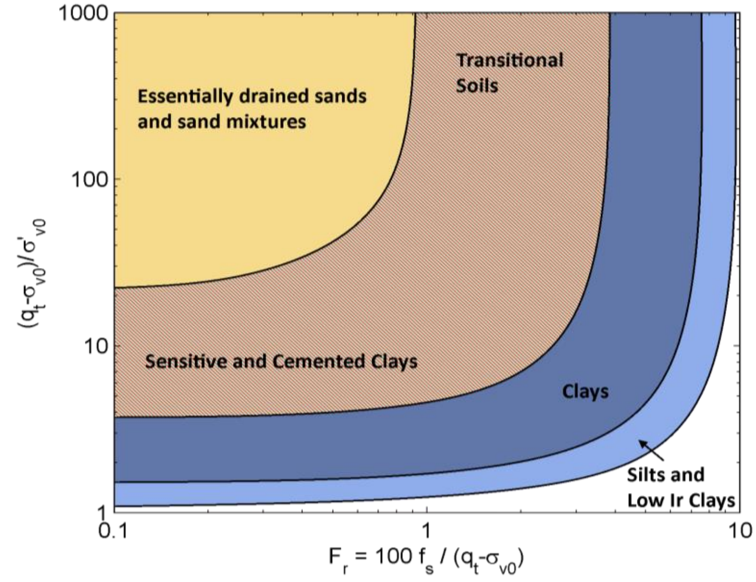

Figure 3.5: SBT chart with hyperbolic boundaries developed by Schneider et al. (2012)

3.2.3 Q_{tn} versus F_r

As noted in the last section, the stress normalization for the net cone tip resistance was upgraded to:

$$Q_{tn} = (q_{net} / \sigma_{atm}) / (\sigma_{vo}' / \sigma_{atm})^n \tag{3.3}$$

or if units of bars are used, it is simply: $Q_{tn} = q_{net}/(\sigma_{vo}')^n$. As seen in ***Figure 3.6***, the CPT material index, I_{cRW}, can be defined as the radius of a circle centered at (Q_{tn} = 2951; F_r = 0.06%):

$$I_c = \sqrt{(3.47 - \log Q_{tn})^2 + (1.22 + \log F_r)^2} \tag{3.4}$$

where the exponent n is initially chosen as 1.0 and then found from (Robertson 2009):

$$n = 0.381 \cdot I_c + 0.05 \cdot (\sigma_{vo}'/\sigma_{atm}) - 0.15 \leq 1.0 \tag{3.5}$$

and therefore requires iteration. Usually only two or three iterations are required. So, for soil zones 2 through 7, only the CPT Index I_{cRW} is needed to identify these soil classifications. A value of I_{cRW} = 2.6 serves as the demarcation for separating drained behavior (I_{cRW} < 2.6) from undrained behavior (I_{cRW} > 2.6).

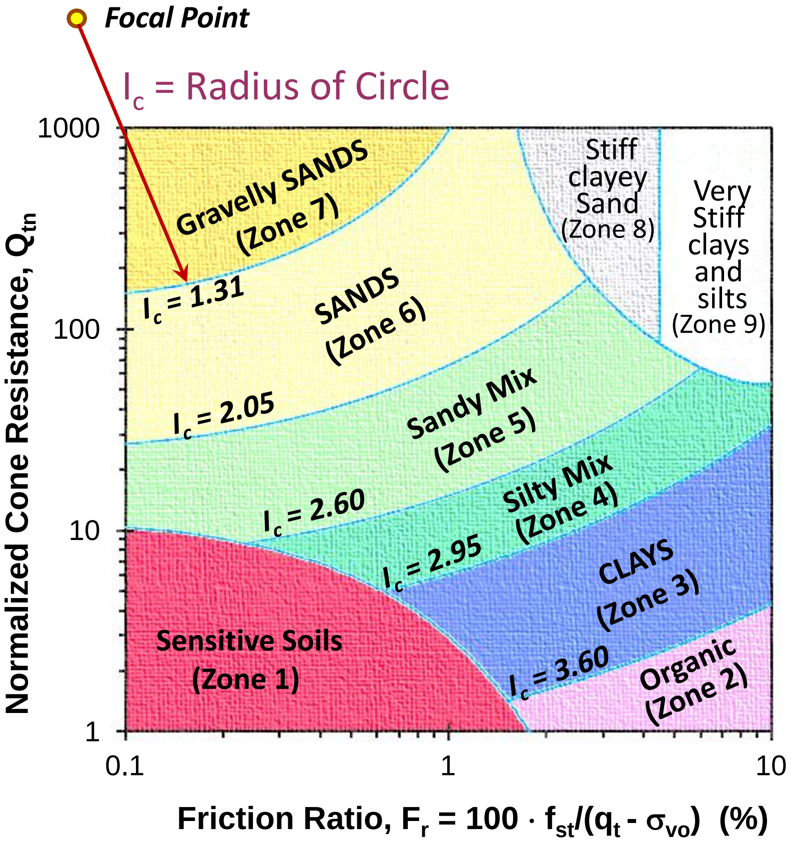

Figure 3.6: CPT classification index $I_{C,RW}$ *applied to* $Q_{tn} - F_R$ *chart for 9-soil behavioral types*

An illustrative example from a piezocone sounding conducted in Biloxi, MS is presented in ***Figure 3.7*** with six side-by-side plots with depth: (a) cone resistance, (b) sleeve friction, (c) friction ratio, (d) dynamic porewater pressure, (e) derived SBTn from the 9-zone chart scaled to the specific zone number and colorized soil behavior type, and (f) text wording of soil type.

These automated SBTn classifications should be compared with the soil types per "rules of thumb" for the same sounding that was presented earlier as Figure 1.8. Generally good matches are found with the various sand and clay layers at this site. The colorization of different soil types provides a quick and valuable visualization of the primary soil types so that the user can appreciate the geostratigraphy quickly and efficiently.

Note that an "undefined" zone may also occur in the soil profile from SBT charts. On occasion, the F_r may fall below 0.1% or above 10%, or a reading with Q_{tn} does not lie in the range of 1 to 1000 from Figure 3.6. Thus, in such cases, an "undefined" classification may result. Also, shallow drillout may produce an "undefined" soil type since no CPT data were collected.

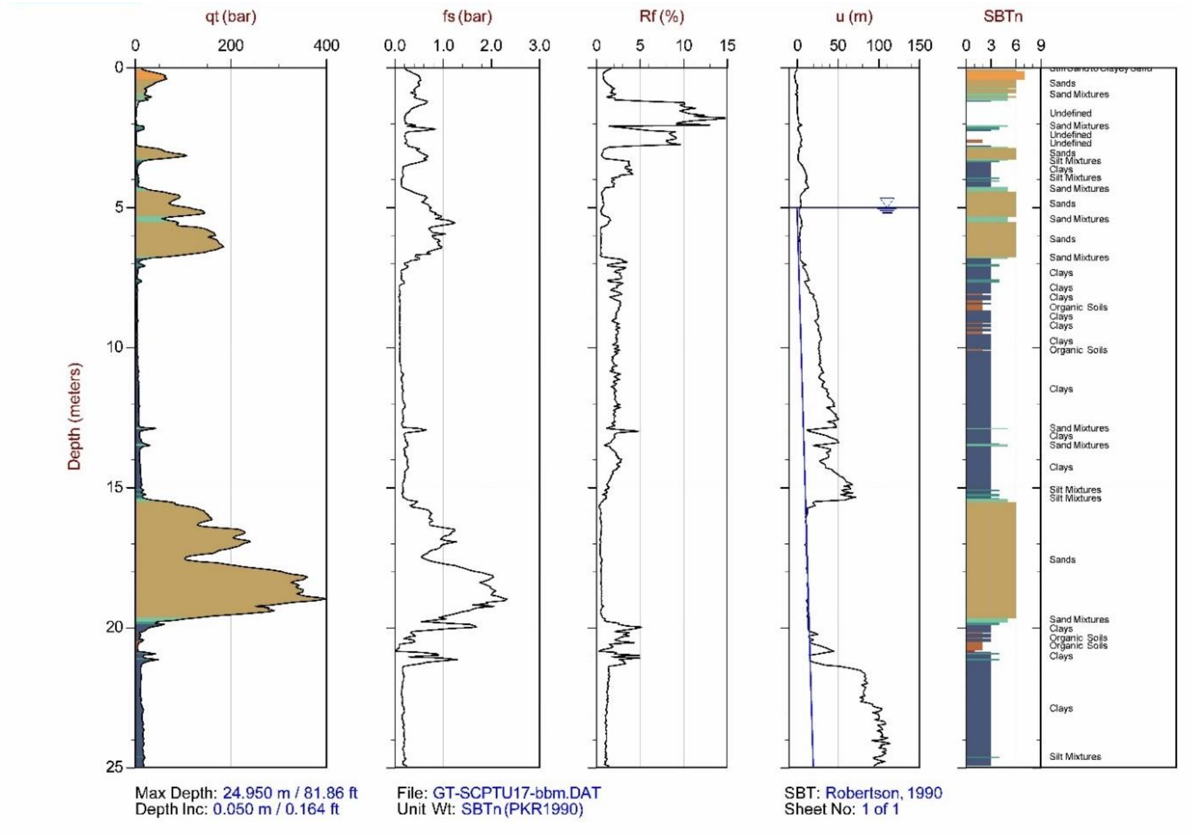

Figure 3.7: Representative piezocone output using colorized and normalized SBTn from CPTU sounding from Biloxi, MS

Robertson (2016) extended the chart in ***Figure 3.6*** by combining the work from Schneider et al. (2012) with a dilative-contractive boundary proposed by Robertson (2010b). A version of this updated chart is shown in ***Figure 3.8*** and includes the hyperbolic lines separating sand-like from clay-like behavior with a zone for transitional soils.

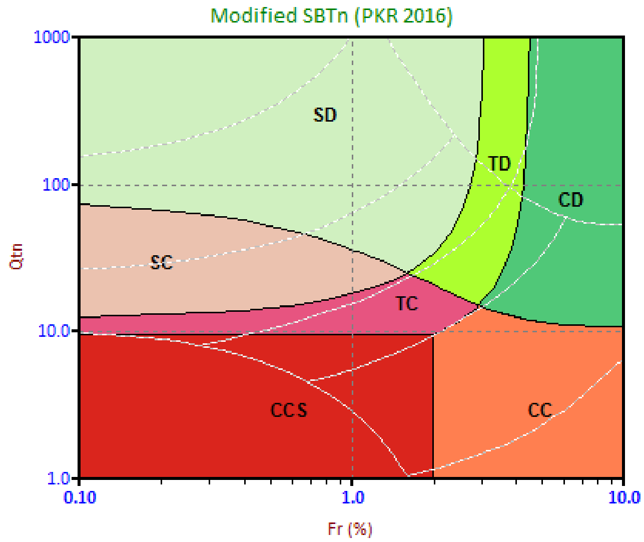

Zone	Soil Type
CCS	Contractive Sensitive Clay
CC	Clay-like, Contractive
TC	Transitional, Contractive
SC	Sand-like, Contractive
CD	Clay-like, Dilative
TD	Transitional, Dilative
SD	Sand-like, Dilative

Figure 3.8: SBT chart proposed by Robertson (2016) based on inferred drainage behavior and contractive (loose) versus dilative (dense) soil states

3.2.4 Q versus B_q

Robertson (1990) developed a companion SBT chart to the Q-F_r chart in Figure 3.4 using the pore pressure parameter B_q defined in ***Equation 3.6:***

$$B_q = \frac{u_2 - u_0}{q_t - \sigma_{v0}} \tag{3.6}$$

The Q_{t1} versus B_q chart is shown in ***Figure 3.9*** and includes the same SBTn zones as in the Q-F_r chart. Soils that behave like sands and gravels have high tip resistances and B_q values near zero due to the rapid dissipation of any generated pore pressure. Soils that behave like clays have low tip resistances and can have large amounts of either positive or negative pore pressures.

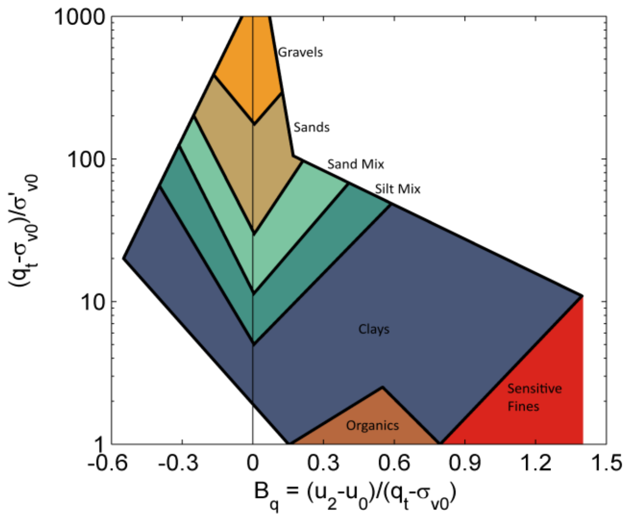

Figure 3.9: Q_{t1} versus B_q SBT chart for 9-zone SBTn classification (after Robertson 1991)

3.2.5 Q versus $\Delta u/\sigma'_{vo}$

Schneider et al. (2008) developed a chart to improve the identification of drained, partially drained, and undrained CPT behavior in soils. This chart is shown in ***Figure 3.10*** and is presented in terms of Q versus an alternate normalized porewater pressure parameter U = $(u_2 - u_0)/\sigma'_{v0}$ instead of the more common B_q. They showed that B_q is not particularly able to distinguish between increasing OCR and increasing coefficients of consolidation. Note that the porewater pressure parameters U and B_q are interrelated via:

$$U = \Delta u_2/\sigma_{vo}' = B_q \cdot Q \tag{3.7}$$

As noted earlier in Section 3.2.2, the term Q is also expressed as Q = Q_t = Q_{t1}.

It will be shown later in Section 6.3 that the excess porewater pressure $\Delta u = (u_2 - u_0)$ is proportional to the undrained strength of the soil, s_u, through an empirical $N_{\Delta u}$ factor. Therefore, $(u_2 - u_0)/\sigma'_{v0}$ is proportional to the undrained strength ratio of the soil (s_u/σ'_{v0}). In this chart an increase in OCR, which increases the undrained strength ratio, increases both Q_{t1} and $\Delta u/\sigma'_{v0}$. An increase in the soils coefficient of consolidation also increases Q_{t1}, but decreases $\Delta u/\sigma'_{v0}$ as excess pore water pressures are dissipated.

$$max\left[-0.5\ln\frac{Q}{20}, -1\right] \leq \frac{\Delta u_2}{\sigma'_{vo}} \leq min\left[0.5\ln\frac{Q}{20}, 1\right]$$

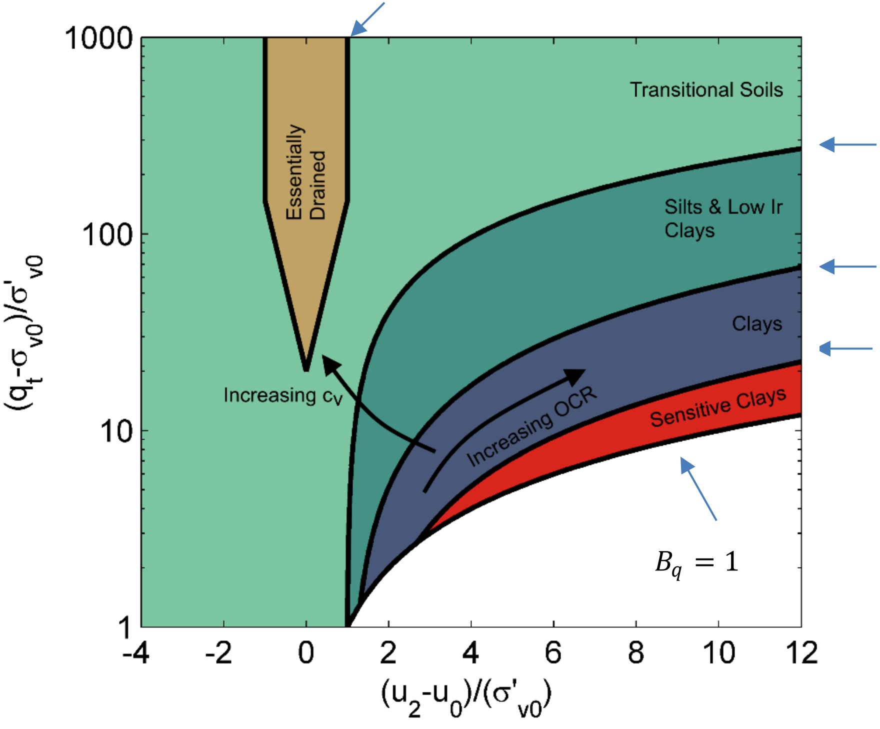

$$\frac{\Delta u_2}{\sigma'_{vo}} = \frac{Q^{1.25}}{100} + 0.99$$

$$\frac{\Delta u_2}{\sigma'_{vo}} = \frac{Q^{0.95}}{5} + 1.05$$

$$\frac{\Delta u_2}{\sigma'_{vo}} = \frac{Q^{0.91}}{1.5} + 1.1$$

Figure 3.10: Q_{t1} versus $\Delta u/\sigma'_{v0}$ SBT chart for separating partial drainage and OCR soil behaviors (after Schneider et al. 2008)

3.2.6 Q(1-B$_q$)+1 versus F$_r$

Jefferies and Been (2006, 2015) use the combined parameter $Q_{t1} \cdot (1 - B_q) + 1$ plotted versus normalized friction ratio, F_R (%) to evaluate soil type, as presented in ***Figure 3.11***. Note that the combined parameter can be reduced to simply the effective cone resistance $(q_t - u_2)$ divided by the effective overburden stress: $Q_{t1} \cdot (1 - B_q) + 1 = (q_t - u_2)/\sigma'_{v0}$.

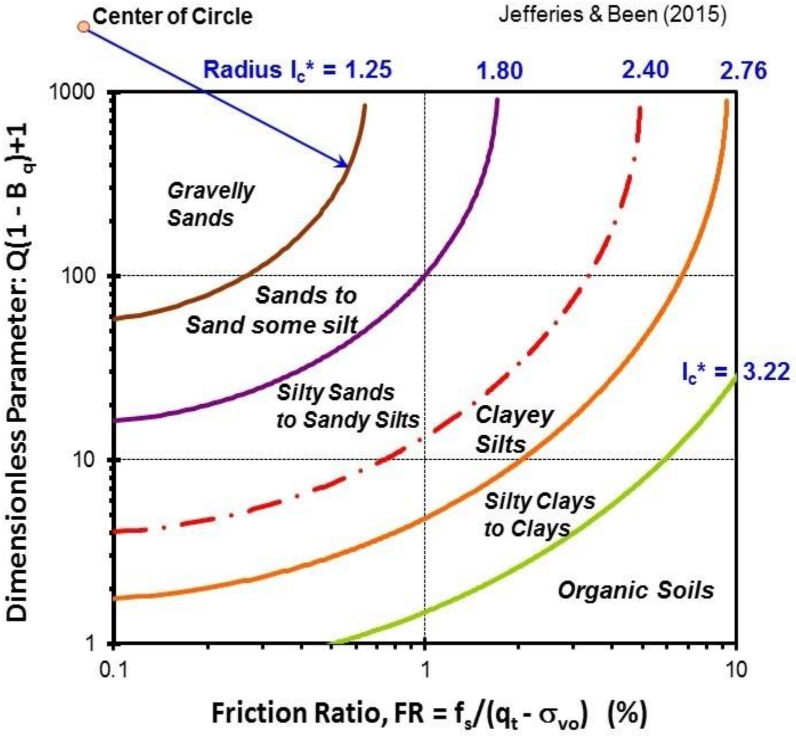

Figure 3.11: Soil behavioral type from $Q_{t1} \cdot (1 - B_q) + 1$ versus normalized friction sleeve (F_R) and CPT material index, $I_{C,BJ}$ (after Jefferies and Been 2006, 2015)

3.2.7 SBT Index I$_{C,BJ}$

The first use of a CPT material index was made by Jefferies & Davies (1991), where it was quite similar to that presented as equation (3.8). The index reduces the three normalized CPT readings to a single number. Jefferies & Been (2006, 2015) defined ***Equation 3.8*** based on their 6-region SBT chart shown in ***Figure 3.11***. The numbers produced by these indices can be used in empirical CPT relationships that depend on soil-type. They are also easily implemented in spreadsheets; where identifying a zone number can be a more difficult.

$$I_{C,BJ} = \sqrt{\left(3 - \log_{10}\left(Q_{t1}\left(1 - B_q\right) + 1\right)\right)^2 + (1.5 + 1.3\log_{10}(F_R))^2} \tag{3.8}$$

In essence, $I_{C,BJ}$ is the radius from an imaginary centerpoint and defines the zonal boundaries between different soil types. For example, referencing ***Figure 3.11***, if $I_{C,BJ} < 1.25$, the interpreted soil classification falls within "gravelly sands". Corresponding soil behavioral types, zone numbers, and associated ranges of material index for $I_{C,BJ}$ are given in ***Table 3.1***.

Table 3.1: Soil Behavioral Type and Zone Number as defined by CPT Material Index (I_C) for Two CPT Classification Systems

Soil classification	**SBT Zone**	$I_{C,BJ}{}^{(a)}$	$I_{C,RW}{}^{(b)}$
Stiff fine-grained soils	9	n/a	$F_R \geq 4.5\%^{I}$
Stiff clayey sands	8	n/a	$1.5 < F_R < 4.5\% \, I$
Sands with gravels	7	$I_{C,BJ} < 1.25$	$I_{C,RW} < 1.31$
Sands: clean to silty	6	$1.25 \leq I_{C,BJ} < 1.80$	$1.31 \leq I_{C,RW} < 2.05$
Sandy mixtures	5	$1.80 \leq I_{C,BJ} < 2.40$	$2.05 \leq I_{C,RW} < 2.60$
Silty mixtures	4	$2.40 \leq I_{C,BJ} < 2.76$	$2.60 \leq I_{C,RW} < 2.95$
Clays	3	$2.76 \leq I_{C,BJ} < 3.22$	$2.95 \leq I_{C,RW} < 3.60$
Organic soils	2	$I_{C,BJ} \geq 3.22$	$I_{C,RW} \geq 3.60$
Sensitive soils	1	n/a	$Q_{tn} < 12\exp(-1.4F_R)$

(a) $I_{C,BJ}$ per ***Equation 3.8*** after Jefferies and Been (2015) and Figure 3.11.

(b) $I_{C,RW}$ per ***Equation 3.4*** after Robertson and Wride (1998) and Robertson (2009b), and using ***Figure 3.6***.

(c) Stiff soils Zones 8 and 9 identified when $Q_{tn} \geq \frac{1}{0.006(F_R-0.9)-0.0004(F_R-0.9)^2-0.002}$

3.2.8 Conflicting SBT profiles

Various SBT charts have been presented. These charts all compare two CPT derived variables to infer the soil behavior type. In many cases these various charts will be in agreement. When the charts disagree, the applicable answer to the geotechnical design may depend on the geotechnical application. A problem involving consolidation or undrained strength may be better characterized by a SBT chart that incorporates the pore pressure measurement, such as ***Figure 3.10***. A problem involving friction, cyclic liquefaction, or drained strengths may be better characterized by a SBT chart that compares the tip and sleeve friction - such as those provided in *Subsection 3.2.1.*

In some cases, the charts may disagree between each other and with laboratory results near layer boundaries. The tip resistance responds to a larger soil zone than the friction sleeve and pore pressure. The ratios of these different measurements may incorrectly identify very thin layers at the boundary between two larger consistent soil types.

3.3 Apparent Fines Content

The fines content (FC) of soils is usually determined on a representative sample by washing particles through a US No. 200 sieve (75 micron = 0.075 mm) size and determining the percentage by weight that passes. As soil samples are not normally taken during CPT, an estimate of the Apparent Fines Content (AFC) may be desired, especially for soil liquefaction analyses.

3.3.1 AFC from Material Index, I_c

Robertson and Wride (1998) created an empirical relationship to estimate an apparent fines content (AFC) from $I_{C,RW}$. Their proposed relationship is given in ***Equation 3.9***.

$$I_{C,RW} < 1.26\text{:}\ \ AFC = 0\% \tag{3.9a}$$

$$1.26\ \leq I_{C,RW} \leq 3.5\text{:}\, AFC\ (\%) = 1.75\left(I_{C,RW}\right)^{3.25} - 3.7 \tag{3.9b}$$

$$I_{C,RW} > 3.5\text{:}\, AFC = 100\% \tag{3.9c}$$

The apparent fines content calculated from ***Equation 3.9*** reflects how soil compressibility and draining conditions affect the CPT penetration resistance. The measured fines content may include hard quartz particles, soft clays, or some intermediate materials.

In a more recent study that included additional data, Boulanger & Idriss (2014) presented the trend shown in ***Figure 3.12***. This also shows the aforementioned relationship by Robertson & Wride (1998).

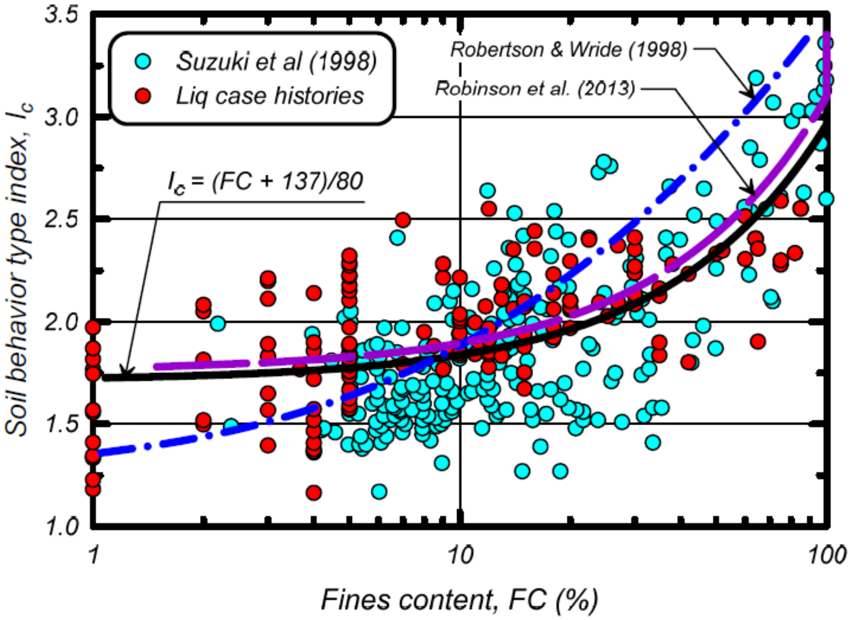

Figure 3.12: Data and trendlines for apparent fines content and CPT material index, I_c (from Boulanger & Idriss 2014)

For estimating AFC, Boulanger & Idriss (2014) recommended:

$$\text{AFC} = 80\cdot(I_c + C_{FC}) - 137 \quad \text{for } 0\% \leq \text{AFC} \leq 100\% \tag{3.10}$$

where C_{FC} = a fitting parameter that can be adjusted to site-specific laboratory data with range: $-0.29 \leq C_{FC} \leq +0.29$. A value $C_{FC} = 0$ is recommended when no lab data are available.

In fact, at least 17 relationships for estimating AFC from I_c have been proposed. Agaiby & Mayne (2020) reviewed these in light of a database of 53 different soil types and found that the apparent fines content could be estimated from I_c using the expression ($r^2 = 0.822$; SEY = 14.34):

$$\text{AFC } (\%) = 1.3\,(I_{cRW})^{3.77} \tag{3.11}$$

They also checked this relationship with five compiled databases (n = 552) and found good agreement, although it lowered the r^2 to 0.761 (SEY = 14.40).

3.3.2 AFC from CPT Index, I_B

The hyperbolic lines shown in Figure 3.8 for Q vs F_r can be expressed in terms of an alternative CPT index, I_B, defined as (Robertson 2016):

$$I_B = 100 \cdot (Q_{tn} + 10)/(Q_{tn}F_R + 70) \tag{3.12}$$

Agaiby & Mayne (2020) related the AFC to index I_B:

$$\text{AFC} = (293/I_B)^{1.65} \tag{3.13}$$

Using data (purple diamonds) from 137 seismic sites compiled by Boulanger & Idriss (2014), ***Figure 3.13*** shows the empirical relationship between AFC and I_B. Also shown superimposed are data from 93 sands, silts, and clays reported in Agaiby & Mayne (2019)

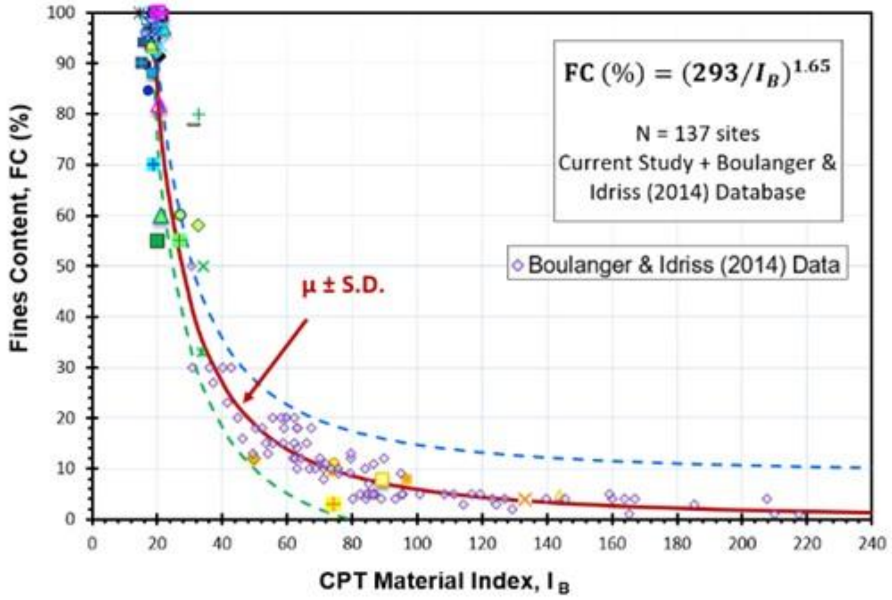

Figure 3.13: Observed trend of apparent fines content (AFC) and CPT Index, I_B

3.4 Drained versus Undrained Response for CPT

In concept, the drained response of soils occurs when no excess porewater pressures are developed during loading, thus $\Delta u = 0$, whilst undrained behavior is associated with constant volume, or $\Delta V/V_0 = 0$. In the laboratory, the response can be controlled artificially by the applied rate of loading and the selection of values that permit or do not permit the free flow of water.

For the standard CPT conducted at a rate of 20 mm/s, the assessment of "drained" versus "undrained" behavior of soil is not always clear. Robertson (2009) suggests that the threshold boundary of drained-undrained response occurs at a value of CPT index, $I_{cR'09} = 2.60$. Following Figure 3.6, the notion of undrained soil behavior can be taken approximately when $I_{cR'09} > 2.60$, as shown by Figure 3.14. Consequently, for values of $I_{cR'09} < 2.60$, the soil response may be considered as drained, or partially drained. However, there can be some uncertainty in the threshold value of $I_c = 2.60$ using the Q_{tn}-F_r chart, depending upon other main characteristics of the soil formation, such as permeability, microstructure, and fabric.

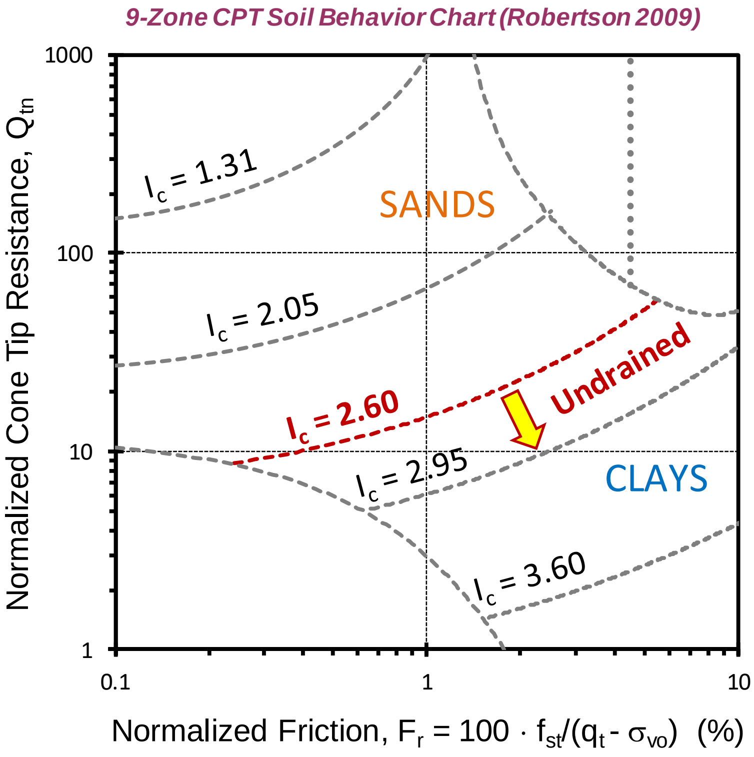

Figure 3.14. Definition of drained-undrained threshold in Q_{tn}-F_r plot according to Robertson (2009)

Alternate means of defining the drained-undrained threshold may be realized from the Q-B_q chart, presented previously as Figure 3.9 (Robertson 1991). Here another CPT material index for defining soil zones has been recommended by Torrez-Cruz (2015). For values of $B_q > 0$, this index is given by:

$$I_{Q\text{-}Bq} = Q \quad 10^{(-1.9\ Bq)} \tag{3.14}$$

Figure 3.15 shows that undrained soil response occurs when the value of $I_{Q\text{-}Bq} < 4$.

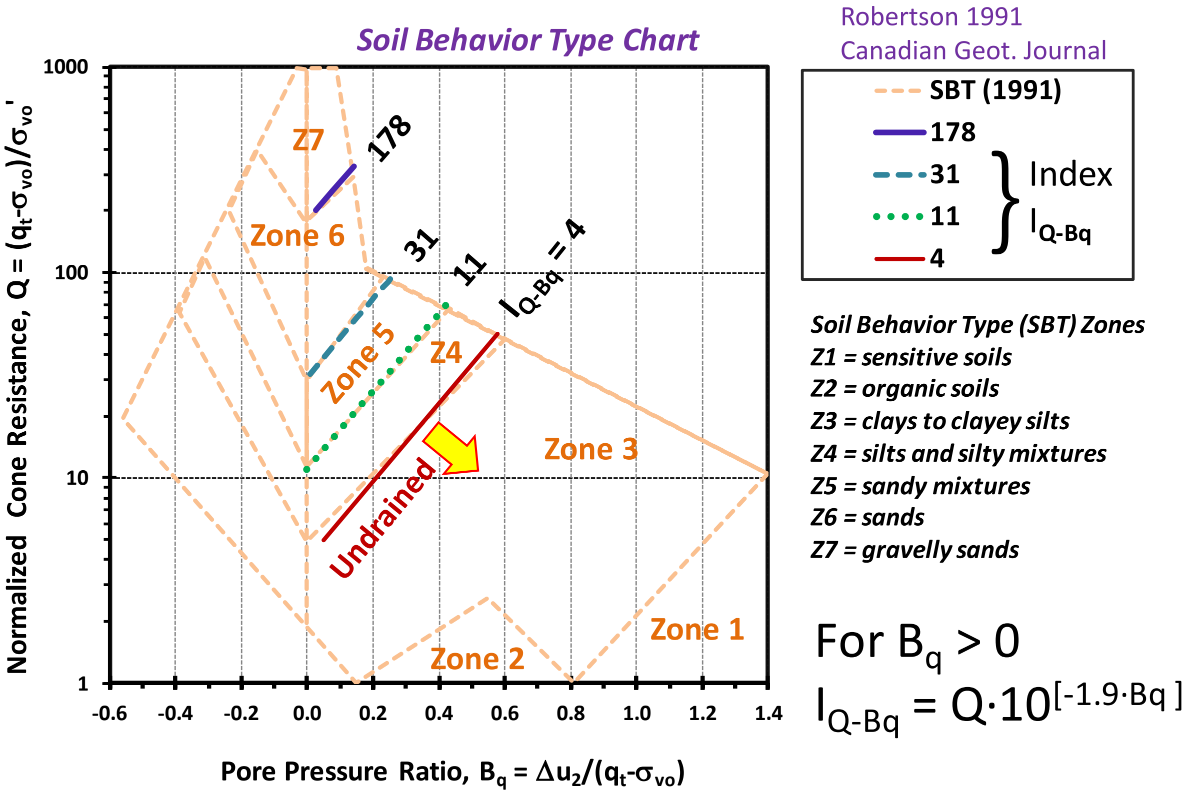

Figure 3.15 Alternate definition of drained-undrained threshold in Q -B_q plot using CPT index from Torrez-Cruz (2015)

Similarly, the soil behavior chart of Q-U devised by Schneider et al. (2008) and presented earlier as Figure 3.10 can be used to defined undrained soil response. Recalling that the value of $U = \Delta u_2/\sigma_{vo}'$ or $U = B_q \cdot Q$, Figure 3.16 illustrates that undrained soil behavior can be defined when:

$$U > 1.05 + 0.2 \cdot Q^{0.95} \tag{3.15}$$

For data that fall outside of this region, the soil response may be considered either fully drained, or partially drained, or "transitional".

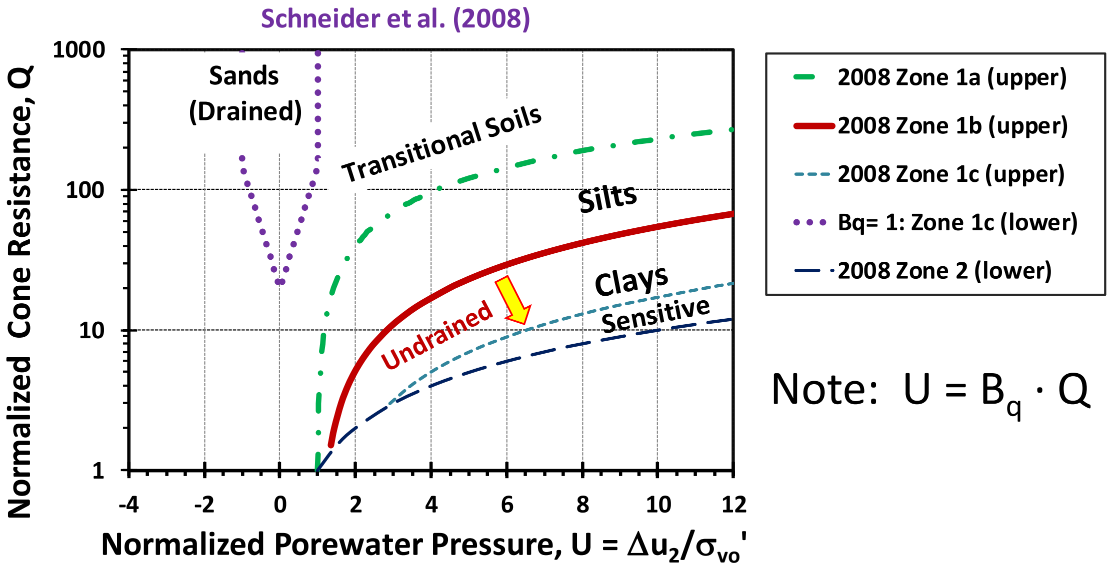

Note: $U = B_q \cdot Q$

Figure 3.16 Alternate definition of drained-undrained threshold in Q -U plot using CPT soil behavior zones defined by Schneider et al. (2008)

4 Soil State and Stress History

CPT measurements primarily depend on the soil stresses, soil type, and soil state. The soil stresses include the overburden stress, porewater pressure, and vertical and horizontal effective stresses. The soil type includes all of the inherent soil variables - such as particle sizes, compressibility, specific gravity, intrinsic friction angles, and other parameters. The soil state is the packing of the particles, including porosity, relative density, fabric, and stress history. The stress history reflects past loading of the soil in terms of effective stress and includes mechanical loading (erosion, glaciation, excavation), as well as apparent preconsolidation due to ageing, desiccation, groundwater, and other geological and environmental factors.

4.1 Void Ratio

The void ratio (e_0) is a classic soil state variable that is used in the soil mechanics laboratory. As void ratio relates to porosity (n), water content (w_n), unit weight (γ_t), relative density (D_R), and state parameter (ψ), there has been significant efforts to use cone penetration tests to help assess in-situ void ratios.

In the laboratory, the in-place void ratio (e_0) is found as the ratio of the volume of the voids (V_v) to the volume of soil solids (V_s):

$$e_0 = \frac{V_v}{V_s} \tag{4.1}$$

Note that ranges of void ratio can vary from e_0 = 0 as a limit in solid rock without voids up to $e_0 > 10+$ in highly compressible plastic clays, such as the infamous Mexico City clay. Since the total volume (V_T) is the sum of the two ($V_T = V_s + V_v$), the void ratio represents the same information as porosity (n), which is a parameter more commonly found in the fields of rock mechanics, powder industry, and materials science and engineering. The porosity is defined as the ratio of volume of voids to the total volume:

$$n = \frac{V_v}{V_T} = \frac{e_0}{1+e_0} \tag{4.2}$$

The full range of porosity is from 0 to 100%, or expressed as a decimal: $0 \leq n \leq 1$.

4.2 Relative Density of Clean Sands

The degree of packing of clean sands is often expressed in terms of relative density (D_R), also called the density index (I_{DR}). This is done under the empirical observations that different sands at the same relative density will exhibit similar behavior. There is no underlying theory supporting the comparison of relative densities between different sand types. If the maximum possible void ratio (loosest state) is designated e_{max} and the densest state represented by e_{min}, then the current void ratio (e_0) gives the relative density (expressed as a percentage in North America, but commonly as a decimal in Europe and Asia):

$$D_R(\%) = I_{DR} = 100\left(\frac{e_{max}-e_0}{e_{max}-e_{min}}\right) \tag{4.3}$$

ASTM provides separate test procedures for direct measurement of e_0, e_{max}, and e_{min}, which is not practical for quality control testing of sands, such as large controlled fill placement for embankments, earth retaining structures, hydraulically-filled ground, and mine tailings. Moreover, a recent study of 6 sands using 4 different standards to determine these index parameters showed differences in values of relative density (Lunne et al. 2019). As such, compaction control in the field is often verified using nuclear density gages or penetration tests, such as SPT or CPT.

In North America, the use of relative density is restricted to sands with fines content not greater than 15%, whereas in Asia, much higher fines contents are allowed. Of interest, several correlations between the relative density index parameters and particle grain characteristics have been studied by Cubrinovski and Ishihara (2002) and Cho, Dodds, and Santamarina (2006). For instance, there exists a general trend between e_{min} and e_{max}, as evidenced from several sand databases compiled in ***Figure 4.1*** which suggests, on average:

$$e_{min} = 0.571(e_{max}) \tag{4.4}$$

The parameters e_{min} and e_{max} are also related to the particle roundness, angularity, uniformity coefficient (UC), and other indices of the sand (Youd 1973; Mayne et al. 2002; Cho et al. 2006).

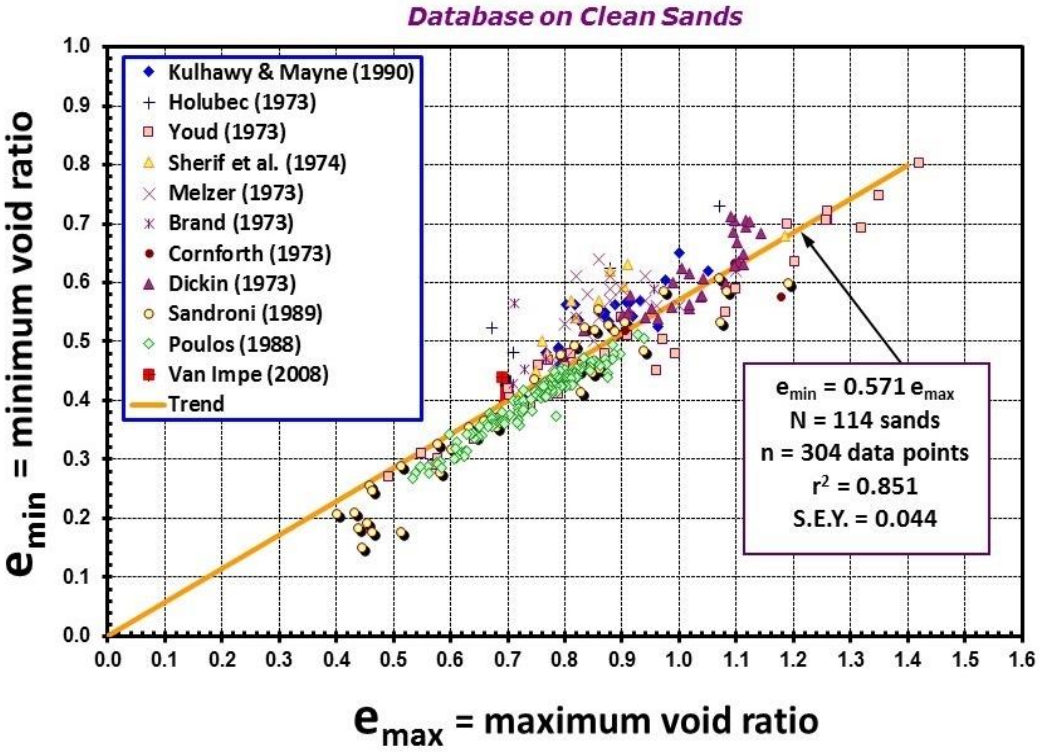

Figure 4.1: Observed trend between minimum and maximum void ratios for clean sands

4.2.1 Calibration Chamber Testing

Natural sands are particularly difficult and expensive to sample in an undisturbed state without risk of altering their in-place void ratio or density. Consequently, early geotechnical studies mostly relied on reconstituted sands for derivation of behavioral aspects. With regard to the use of penetration tests for evaluating the in-situ relative density, a number of research institutions produced CPT data from calibration chamber tests (CCT). These chambers range in size from 0.6 to 2.5 m in diameter (D) and height (H), with typical measurements given by D ≈ 1 m and H ≈ 1 m. ***Figure 4.2*** depicts the general setup and approach to CCT.

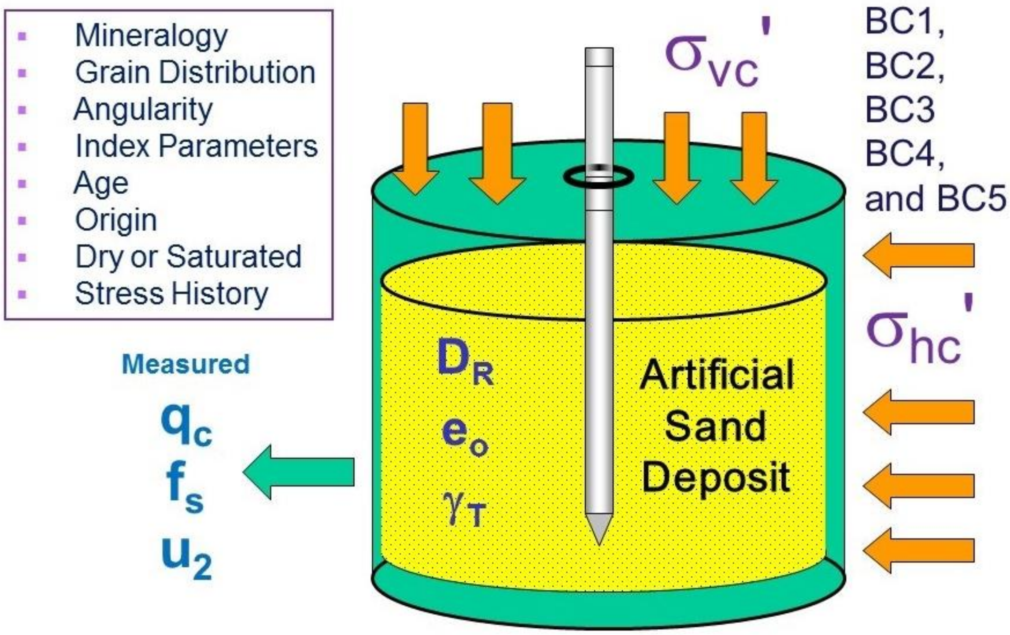

Figure 4.2: Schematic of calibration chamber setup for CPT testing of sands

In essence, the CCT is a very large triaxial sand specimen with a special sealed entry port at the center to allow insertion of a penetrometer while the chamber is pressurized. A large sample of uniform sand (approximately 1 to 5 tons) is artificially-prepared to a known void ratio (and relative density) with variable applied vertical and lateral stresses, as well as induced degrees of preconsolidation ($1 \leq \text{OCR} \leq 15$). The chambers have rigid steel shells on the outside, however, the inner walls are made of flexible rubber membranes that are pressurized to create the effective stress states surrounding the large soil specimens. All aspects of the sand are quantified beforehand (e.g., D_{50}, fines content, mineralogy, dry/saturated, etc.).

Different methods of sample preparation have been used, including: pluviation, moist tamping, slurry, compaction, sedimentation, and vibration. Then, after the sand is placed to a desired initial state (e_0 and D_R), a consolidation stress is applied (σ'_{v0}, σ'_{h0}, and OCR). Finally, a CPT is conducted and the measured q_t, f_s, and/or u_2 are recorded. Each CCT takes approximately one week for preparation, while the CPT is completed in about 15 seconds. Several CCT test series are required in order to develop relationships between the CPT readings and pre-push D_R and stress state (σ'_{v0}, σ'_{h0}, and OCR).

Several early findings of CPT in CCT of select quartzitic sands have been reported; i.e. Schmertmann (1978), Baldi et al. (1981), and Robertson and Campanella (1983). These studies showed that correlations of D_R with clean quartz sands depended on the measured cone tip resistance ($q_t = q_c$) and effective vertical overburden stress (σ'_{v0}), with additional effects caused by more hard-to-quantify factors such as sand compressibility, particle fracture, K_0 horizontal stresses, and grain crushing. The relative size of the cone penetrometer and chamber size also influence the measured resistances.

4.2.2 Quartz-Silica Sands

Notably, CPT calibration chamber test results require a correction factor due to boundary effects and yielding of the flexible walls during testing. Since the chambers are not infinitely wide (as in natural sand deposits), the measured q_c values are lower than the true values corresponding to far-field conditions. The aforementioned correlations therefore overestimate the actual D_R in the field.

A well-known published correlation based on 5 series of uncorrected CCT on clean quartzitic and silica sands (Jamiolkowski et al. 1985) was aware of this important finding, however their recommendation involved a correction factor applied to the field measured q_c before entering their laboratory correlation for D_R in terms of stress-normalized cone resistance: $q_{c1} = (q_c/\sigma_{atm})/(\sigma'_{v0}/\sigma_{atm})^{0.5}$. Many users are apparently unaware of this correction factor and used the lab curves directly, thereby overestimating the relative density on their projects.

The correction for flexible-walled chambers depends upon the type of boundary conditions (BC1, BC2, BC3, or BC4) and relative sizes of the penetrometer and chamber. The correction factor used by Kulhawy & Mayne (1990) for clean sands for the BC1 boundary conditions (general stress state: σ_{vc}' and σ_{hc}') was developed as a function of the penetrometer diameter (d), chamber diameter (D), and relative density of the sand. The correction factor was developed based on statistical analyses of 6 sands that had been tested by different size cones and/or different size chambers at various D_R. Houlsby & Yu (1990) derived correction factors based on large strain cavity expansion analyses that were checked with CCT data obtained at Oxford University. Salgado et al. (1998) used numerical finite element simulations to develop correction curves for CPTs in CCT.

A decade and a half later, Jamiolkowski et al. (2001) returned to their original database, corrected the lab q_c values to equivalent field values, and then produced a direct $D_R - q_{t1}$ relationship (see ***Figure 4.3***). Note that in clean sands, essentially the measured cone resistance is the total cone resistance ($q_c = q_t$) because the measured porewater pressures are close to hydrostatic and the unequal end area correction is very small compared to typical measured tip resistances in sands.

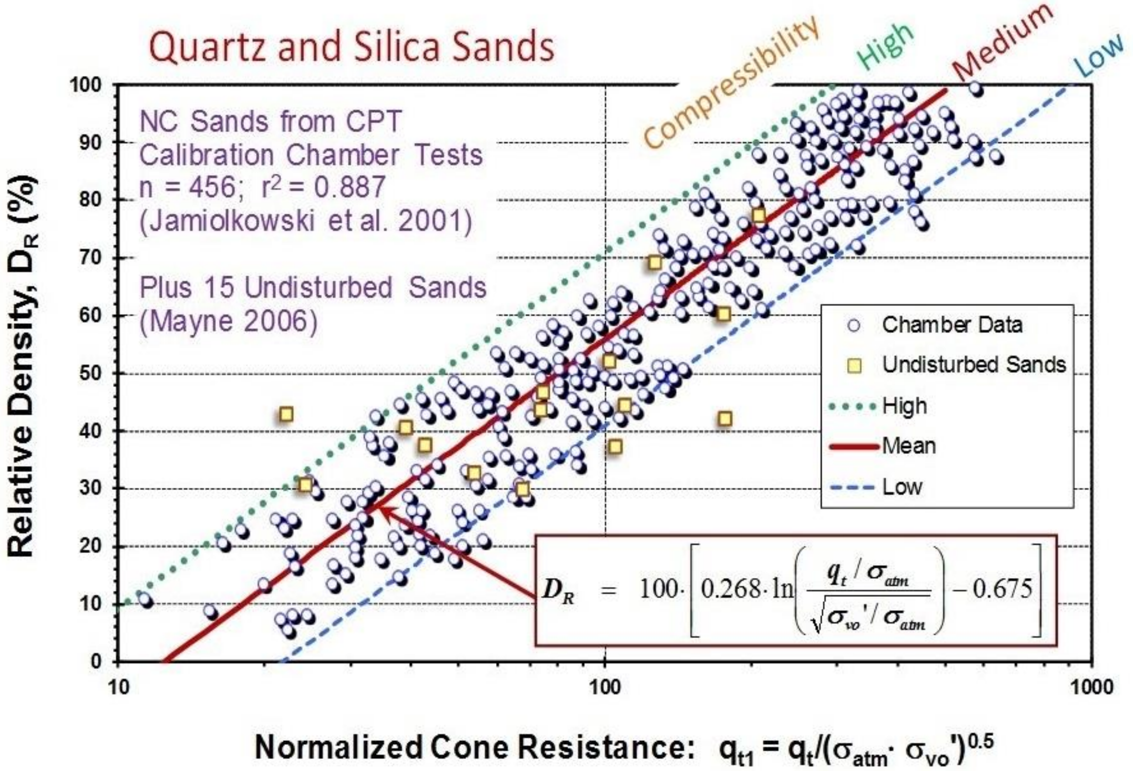

Figure 4.3: Relative density from stress-normalized cone tip resistance in clean NC sands where CPT calibration chamber test data have been corrected for limited D/d ratios (modified after Jamiolkowski, LoPresti, and Manassero 2001)

The derived relationship for relative density in terms of stress-normalized cone tip resistance can be expressed:

$$D_R(\%) = 100(0.268\ln(q_{t1}) - b_x) \tag{4.5}$$

where the term b_x = 0.675 applies to the mean correlation for normally-consolidated (NC) clean sands. Jamiolkowski et al. (2001) show three lines corresponding to different sand compressibilities: high (b_x = 0.525), medium (b_x = 0.675), and low (b_x = 0.825). Their guidance suggests that sands of high compressibility include mica sands, calcareous sands, and carbonate sands. Siliceous sands (approximately equal parts of quartz and feldspar) comprise the medium compressibility range. Sands of low compressibility include those of quartz, such as Ottawa sand. For practical use in sands of unknown mineralogy, the recommended general expression is:

$$D_R(\%) = 100(0.268\ln(q_{t1}) - 0.675) \tag{4.6}$$

Also shown in ***Figure 4.3*** are data from undisturbed samples of 15 sands compiled by Mayne (2006).

Because a complete understanding of boundary effects in CCT is not yet fully realized, the corrections can only be considered approximate at best (Maki et al. 2013). In the statistical approach, the correction factor depends upon the relative sizes of the chamber diameter (D) and penetrometer diameter (d), such that:

$$\frac{q_{t,field}}{q_{t,chamber}} = \left(\frac{D/d-1}{70}\right)^{0.005D_R} \tag{4.7}$$

Data from 705 CCTs on 26 different sands that were corrected for boundary effects produced the overall mean relationship for NC and OC sands (Kulhawy and Mayne 1990, 1991):

$$D_R(\%) = 100\sqrt{\frac{q_{t1}}{305(OCR)^{0.2}}} \tag{4.8}$$

A comparison of the two D_R expressions for NC sands are seen to be in excellent agreement in ***Figure 4.4*** for range of relative densities from 0% to 80% where thereafter, the square root algorithm of ***Equation 4.8*** gives slightly higher D_R values than the log function of ***Equation 4.6***.

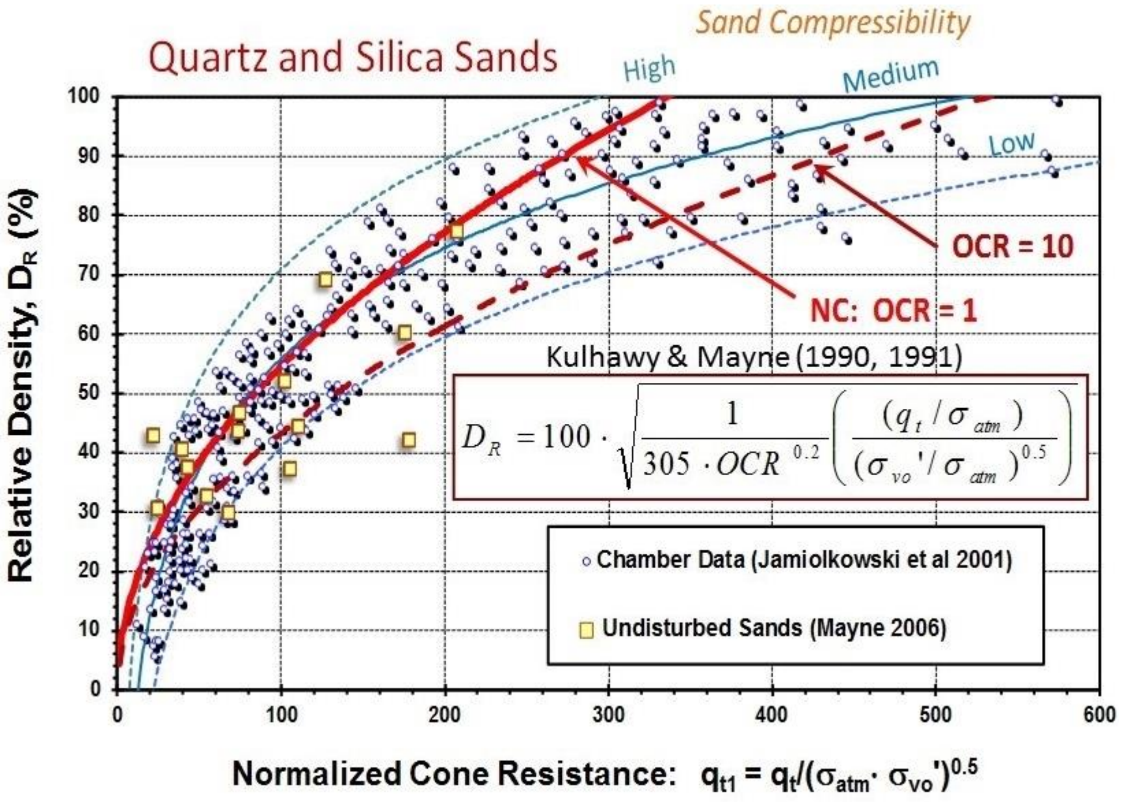

Figure 4.4: Relative density relationships from stress-normalized cone tip resistance in clean NC and OC sands (after Mayne 2014)

4.2.3 Carbonate-Calcareous Sands

Calibration chamber tests have also been used with prepared deposits of calcareous-carbonate sands. ***Table 4.1*** provides a summary of index parameters on 6 carbonate sands that were tested in CPT chambers, including: Quiou Sand (Fioravante et al. 1998); Dogs Bay (Nutt and Houlsby 1991), Ewa (Morioka and Nicholson 2000), Kingfish (Parkin 1991), Kenya (Jamiolkowski and Pepe 2001), and Jeju Sand (Lee et al. 2010). ***Figure 4.5*** presents the trend of q_{t1} versus D_R from the available six series of chamber tests on carbonate sands. The trends for carbonate sands appear to be rather independent of calcite content in the range 42% $< CaCO_3 <$ 98% and indicate simply that:

$$D_R(\%) = 0.87(q_{t1}) \tag{4.9}$$

Table 4.1: Properties of carbonate-calcareous sands tested by CPT in chamber tests

Sand Name	**Quiou**	**Dogs Bay**	**Ewa**	**Kingfish**	**Kenya**	**Jeju**	**Remarks / Notes**
Location	***France***	***Ireland***	***Hawaii***	***Australia***	***Africa***	***S.Korea***	
D_{50} (mm)	0.58	0.25	0.80	0.30	0.13	0.41	Mean grain size
FC (%)	3.00	0.10	1.00	7.00	0	1.00	Fines ($<$ 75 μm)
CU	4.52	2.66	5.60	3.05	1.86	1.61	D_{60}/D_{10}
G_S	2.72	2.75	2.70	2.71	2.785	2.79	Specific Gravity
e_{max}	1.28	1.83	1.30	1.53	1.778	1.44	Maximum void ratio
e_{min}	0.83	0.98	0.66	1.07	1.283	1.03	Minimum void ratio
$CaCO_3$ (%)	77	87 to 92	98	"high"	97	42.60	Calcium Carbonate

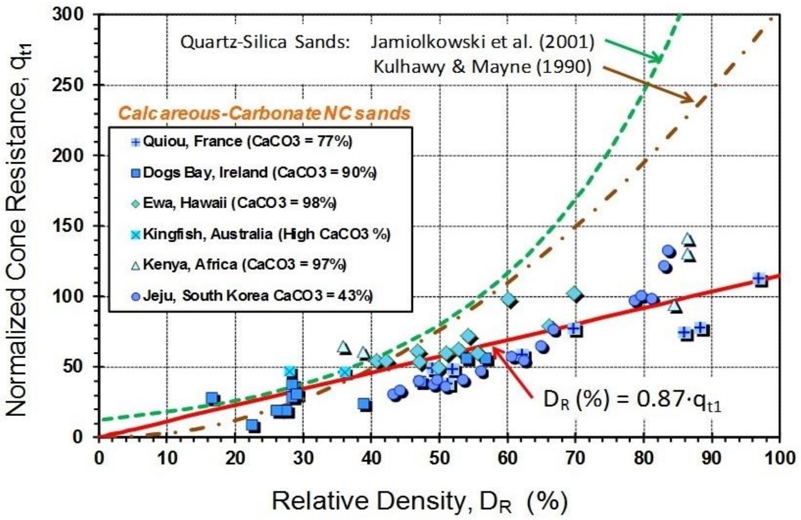

Figure 4.5: Relative density from stress-normalized cone tip resistance in carbonate sands

The two trends for quartz-silica sands are also shown in ***Figure 4.5***. When $D_R <$ 30%, the measured cone tip resistances are similar for all data sets, suggesting that loose sands behave somewhat comparably during full-displacement type penetration despite their mineralogical differences. However, for $D_R > 30\%$, the trends for quartz-silica sands show significant increases in cone resistance, since the hard particles must be forced aside during penetration. On the other hand, the trends for calcareous-carbonate sands remain similar when $D_R > 30\%$ implying grain breakage, fracturing, and crushing as the particles are pushed closer together as they approach their minimum packing arrangement (i.e., e_{min}). Thus, it can be concluded that CPTs in carbonate sands are not particularly sensitive to the in-situ relative density.

An alternative approach to addressing CPTs in carbonate sands involves the use of a shell correction factor (SCF) which "corrects" the cone resistance of the carbonate sand to a value equivalent to that for a "normal" quartz or silica sand, i.e. SCF = q_c (silica)/q_c (calcareous). Suggested SCF trends with D_R are given by Wehr (2005), Mayne (2014), and Mengé et al. (2016).

4.3 State Parameter

The state parameter is a variable defined in critical-state-soil-mechanics (CSSM) to characterize the state of the soil. In CSSM, soil behavior depends on the state parameter. The state parameter, ψ, is the difference in void ratio between the initial value (e_0) and the value at failure (e_{CSL}) under the same effective stress, as shown in ***Figure 4.6*** and expressed by:

$$\psi = e_0 - e_{CSL} \tag{4.10}$$

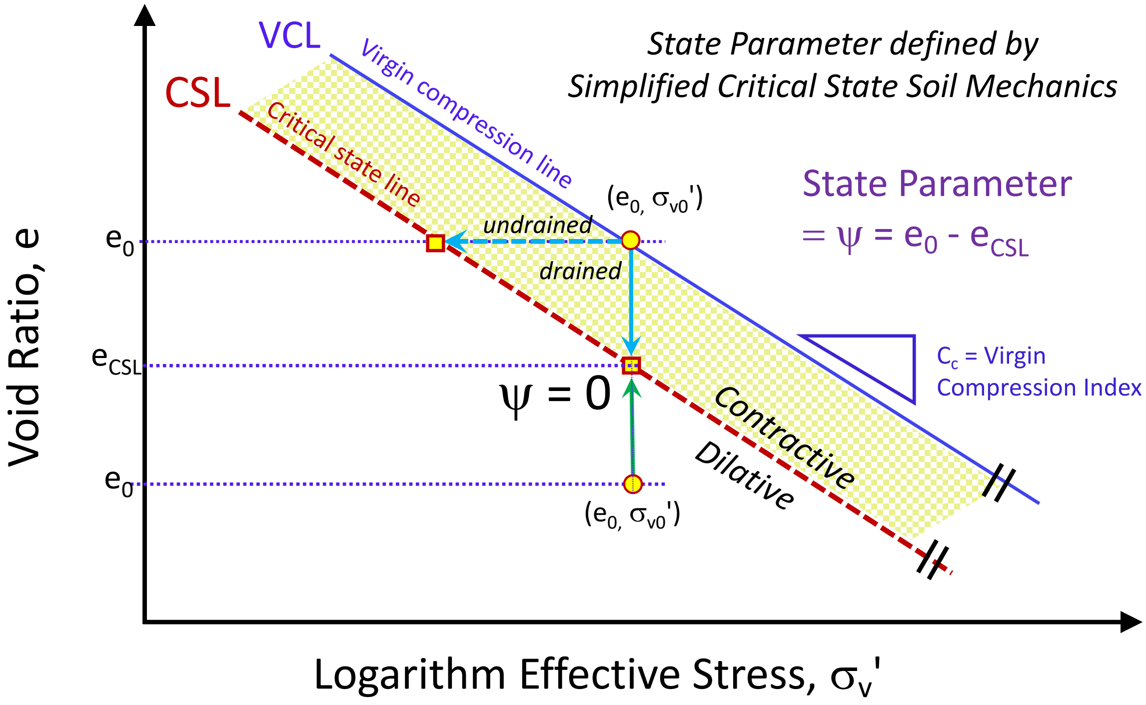

Figure 4.6: Definition of State Parameter in Simplified Critical State Soil Mechanics

This value at failure defines a critical-state-line (CSL) in void ratio versus log mean effective stress space. The state parameter is negative if the soil is dense of critical (called "dilative" or "dilatant") and is positive if the soil is loose of critical (called "contractive"). Soils at different initial void ratios and different initial effective stress states can have identical state parameters.

The CPT method to estimate ψ originated in the analysis of calibration chamber test results presented in Been et al. (1987a; 1987b; 1988, 1989), and Been & Jefferies (1993). This method is discussed later in Chapter 9 as well as alternative approaches.

Under the simplified CSSM assumption that the CSL and NCL are parallel in $e - \log_{10}(p')$ space and defined by the slope λ_{10}, where P' = ⅓(σ_1'+σ_2'+σ_3') = mean effective stress. As such, then λ_{10} equals the compression index, C_c.

4.4 Overconsolidation Ratio and Yield Stress Ratio

In traditional soil mechanics concepts concerning one-dimensional consolidation, the soil state is represented by the overconsolidation ratio: OCR = σ_p'/σ_{vo}', where σ_p' = preconsolidation stress. The effective preconsolidation stress or yield stress of soils is best determined through a series of one-dimensional consolidation tests performed on undisturbed samples taken at different elevations in soil formation. Additional knowledge of the local engineering geology and terrain helps to put the stress history profile in perspective (Locat et al. 2003). ***Figure 4.7*** shows an example consolidation test conducted on a specimen of silty clay taken from a depth of 21.5 feet at a highway embankment site in Evergreen, North Carolina (w_n = 70.8%, LL = 44%, PI = 19%). Results are plotted in terms of void ratio (e) versus log of effective vertical stress (σ'_v), with a calculated in-situ effective overburden stress of σ'_{v0} = 0.43 tsf.

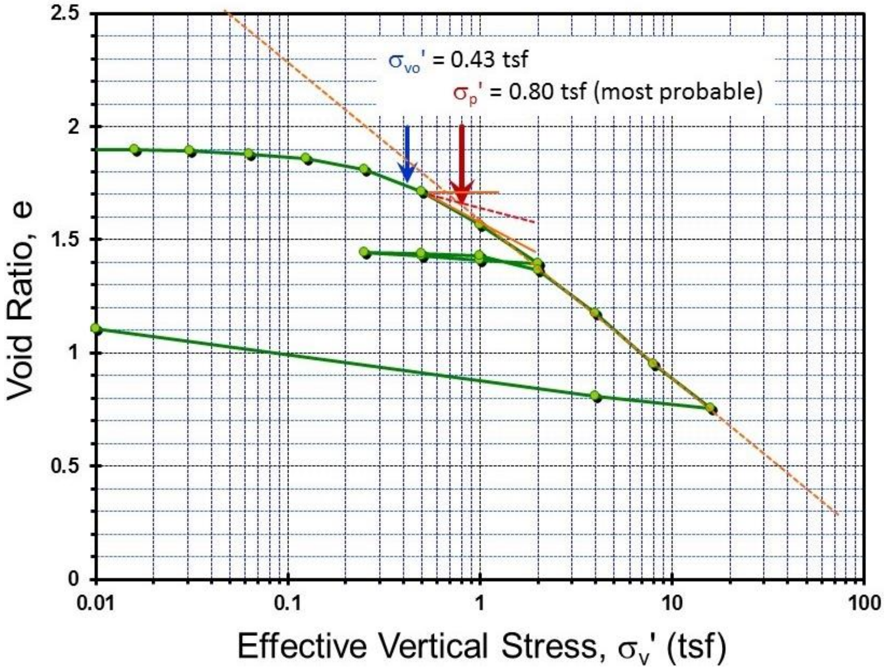

Figure 4.7: Results from one-dimensional consolidation tests on clay from Evergreen, NC

Using the classical construction technique from Casagrande (1936), a most probable magnitude of effective yield stress σ'_p = 0.80 tsf is determined. Following the orange dashed line, a minimum estimate of 0.65 tsf and maximum estimate of 0.90 tsf are also extracted. Beyond this procedure, some 30 different methods have been developed for the evaluation of σ'_p from consolidation test data (Ku and Mayne 2013).

While oedometer and consolidometer tests will remain the benchmark for determining stress history profiles, there are often cases when "undisturbed" samples are difficult to procure because of the silty to sandy nature of the the ground, effects of sample disturbance, and stress relief, as well as the expense and necessary time required for laboratory testing. Therefore, it has become of great interest and motivation in seeking CPT-based methods to evaluate stress history profiles of soils. These can be used to complement the laboratory program and fill in gaps between sampling depths and locations.

The yield stress (σ_p') can also be shown relative to the state parameter ψ in simplified critical state soil mechanics, as seen by ***Figure 4.8***.

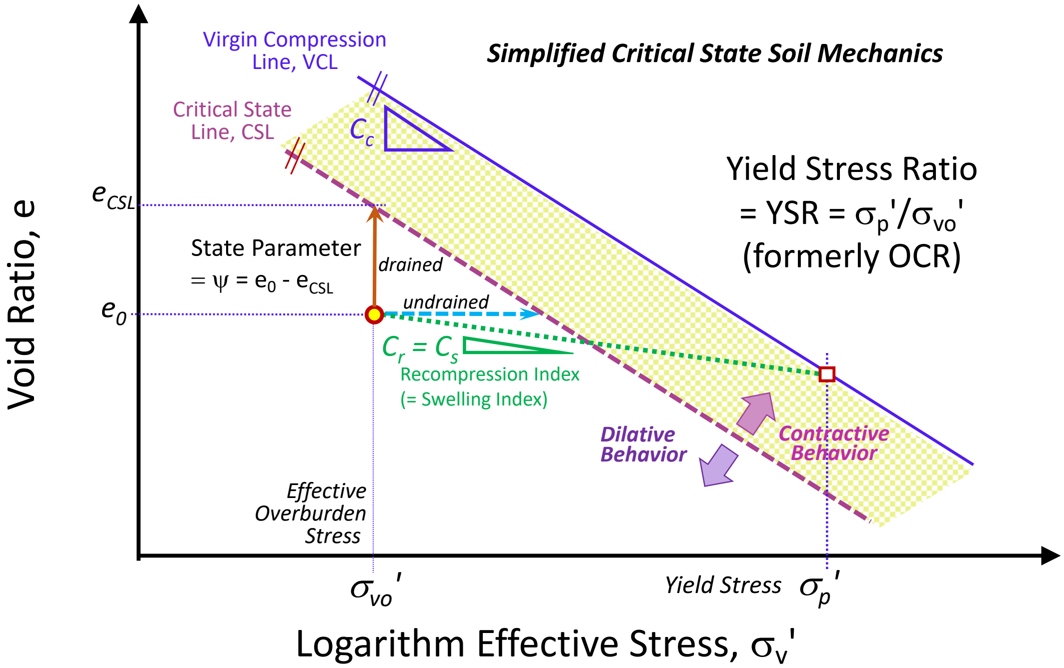

Figure 4.8: Yield stress idealization in traditional e-log(σv') graph for soil consolidation

The preconsolidation stress can be presented in dimensionless terms using a normalized form called the overconsolidation ratio (OCR), or equivalent yield stress ratio (YSR), which is defined by:

$$OCR = \frac{\sigma'_p}{\sigma'_{v0}} = YSR \tag{4.11}$$

The term YSR is becoming more prevalent because the traditional OCR is associated to mechanic unloading effects (i.e., erosion, glaciation, excavation), while other geologic and environmental changes can also cause an apparent preconsolidation, including: desiccation, compaction, cyclic loading, repeated wetting-drying, seasonal thermal changes, diagenesis, and other effects (Leroueil & Hight 2003; Jardine et al. 2004).

Another convenient parameter for representation of soil stress history is the over consolidation difference, OCD = (σ'_p - σ'_{v0}), or YSD, also called prestress ($\Delta\sigma'_p$), as detailed by Locat et al. (2003). The advantage of the OCD (or YSD) is that it is constant with depth for soil deposits that have become preconsolidated by erosion, glaciation, and/or excavation, where in contrast, the magnitude of OCR decreases with depth (Mayne 2007b). For those cases, the two parameters are interrelated via:

$$OCD = \sigma'_{v0} \cdot (OCR - 1) = YSD \tag{4.12}$$

4.4.1 Analytical CPT Model for YSR in Clay

A hybrid analytical model for piezocone penetration in clays was developed by combining Spherical Cavity Expansion (SCE) theory and Critical State Soil Mechanics (CSSM), as detailed by Mayne (1991) and Chen and Mayne (1994). The formulation provided separate evaluations for the OCR in terms of the net cone resistance ($q_{net} = q_t - \sigma_{v0}$) and/or the measured excess porewater pressure ($\Delta u = u_2 - u_0$):

$$OCR = 2 \cdot \left(\frac{(q_t - \sigma_{v0})/\sigma'_{v0}}{\left(\frac{2}{3}\right) M(\ln(I_r)+1) + \frac{\pi}{2} + 1} \right)^{\frac{1}{\Lambda}} \tag{4.13}$$

$$OCR = 2 \cdot \left(\frac{((u_2 - u_0)/\sigma'_{v0}) - 1}{\left(\frac{2}{3}\right) M(\ln(I_r)) - 1} \right)^{\frac{1}{\Lambda}} \tag{4.14}$$

where M = 6 $\cdot \sin\phi_{cs}/(3 - \sin\phi_{cs})$ and is the frictional envelope in Cambridge University type q-p' space, q = deviator stress, p' = mean effective stress, I_r = G/s_u = the undrained rigidity index, G is the shear modulus, s_u is the undrained shear strength, and Λ = the plastic volumetric strain potential. The value of $\Lambda \approx$ 0.8 for many insensitive clays and increases to about $\Lambda \approx 1$ for sensitive and quick clays (Mayne 1988; Ladd 1991; Ladd and DeGroot 2003). The magnitude of Λ also depends upon shear mode (Kulhawy and Mayne 1990). From CSSM, the theoretical value of Λ = 1 – C_S/C_C with C_S = recompression or swelling index, and C_C = virgin compression index.

By combining ***Equations 4.13*** and ***4.14***, a third estimate of OCR can be formulated in terms of effective cone resistance ($q_e = q_t - u_2$) that removes the reliance on rigidity index (I_r):

$$OCR = 2 \cdot \left(\left(\frac{1}{1.95M+1} \right) \left(\frac{q_t - u_2}{\sigma'_{v0}} \right) \right)^{\frac{1}{\Lambda}} \tag{4.15}$$

For soft to firm clays, the shear-component of porewater pressures is small (< 20%) of the total measured porewater pressures, thus ***Equation 4.14*** can be reduced without much error to:

$$OCR \approx 2 \cdot \left(\frac{((u_2 - u_0)/\sigma'_{v0})}{\left(\frac{2}{3}\right) M(\ln(I_r))} \right)^{\frac{1}{\Lambda}} \tag{4.16}$$

The above equations can be simplified from their power law formulations to form linear equations for evaluating effective yield stress in intact clays. For the three respective CPTU expressions given by ***Equations 4.13***, ***4.16***, and ***4.15*** with an adopted value Λ = 1, we obtain:

$$\sigma'_p = \frac{q_t - \sigma_{v0}}{M\left(1 + \left(\frac{1}{3}\right)\ln(I_r)\right)} \tag{4.17}$$

$$\sigma'_p \approx \frac{u_2 - u_0}{M\left(\frac{1}{3}\right)\ln(I_r)} \tag{4.18}$$

$$\sigma'_p = \frac{q_t - u_2}{0.975(M) + 0.5} \tag{4.19}$$

4.4.2 Simplified Expressions for Intact Insensitive and Inorganic Clays

For intact inorganic clays of low sensitivity, these expressions can be further simplified for practical use by adopting characteristic values of M_c = 1.2 (ϕ' = 30°) and I_r = 100 (Mayne 2001, 2005):

$$\sigma'_p = 0.33(q_t - \sigma_{v0}) \tag{4.20}$$

$$\sigma'_p = 0.54(u_2 - u_0) \tag{4.21}$$

$$\sigma'_p = 0.60(q_t - u_2) \tag{4.22}$$

These relationships have been studied for a wide variety of clays, including statistical studies involving 206 different sites (Chen and Mayne 1996). Additional data from 22 sites in Canada confirmed a general validity in that region (Demers and Leroueil 2002), as well as validation by extensive testing for the Pisa tower site in Italy (Jamiolkowski and Pepe 2001).

Figure 4.9 shows the general trend for effective yield stress with net cone resistance given by showing reasonableness in intact soft to firm to stiff to hard clays. Fissured clays are seen to lie above the relationship in a special grouping of data. It is thought here that one-dimensional tests (i.e. constrained compression) of fissured clays will result in closure of existing cracks, fissures, and discontinuities, whereas the corresponding same clays tested in-situ by piezocone will in fact open the discontinuities and cracks due to the full-displacement requirement of testing. Thus, a disconnect between one-dimensional and three-dimensional response for this grouping of fissured geomaterials.

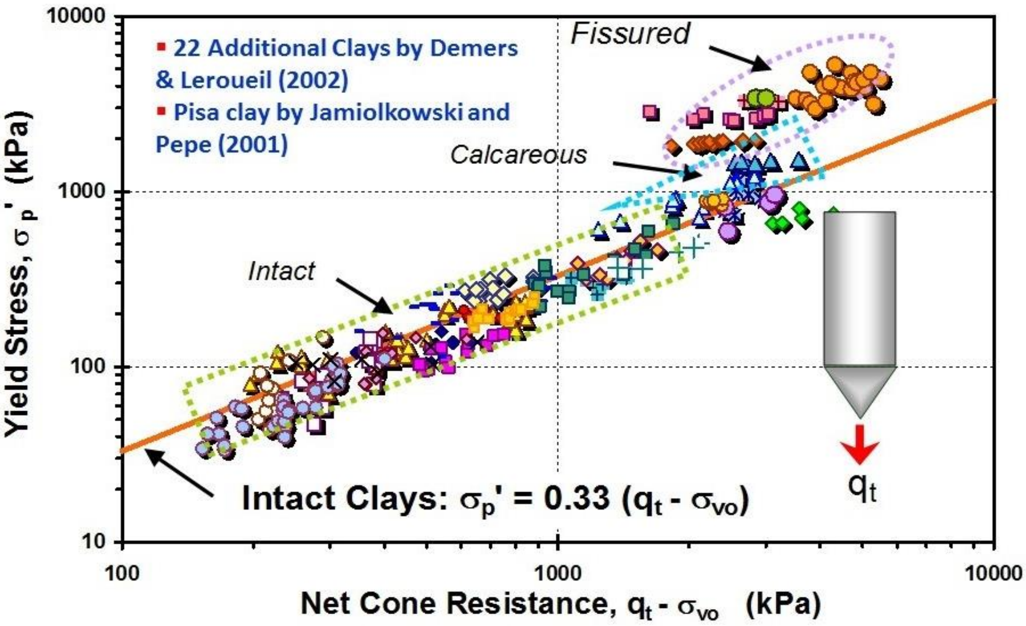

Figure 4.9: Evaluation of preconsolidation stress from cone resistance in intact clays with low organic content and low sensitivity

For intact clays, it is useful to utilize all three equations, as redundancy can be helpful in geotechnical site characterization. If the three methods show consensus, then this helps to validate a "well-behaved" or "vanilla" clay and encourages the use of these relationships. An illustrative application of all three solutions given by ***Equation 4.20***, ***Equation 4.21***, and ***Equation 4.22*** is given in ***Figure 4.10*** for soft clay at the national test site in Bothkennar, UK (Hight et al. 2003). Two soundings are shown with one early series completed in 1992 and the other in 2005 (Powell & Lunne 2005b). The profiles of σ'_p and YSR from the three CPTU-estimates compare well with the rather large set of consolidation test results at this site. Three types of consolidation tests were completed: (a) incremental load (IL) oedometer; (b) restricted flow (RF) consolidometer; and (c) constant-rate-of strain (CRS). The soft Bothkennar clay is lightly-overconsolidated (LOC) with 1.3 < YSRs < 1.8 at depths greater than 4 m.

Thus for "regular" natural clays that are inorganic and relatively insensitive, the following relationships should apply:

$$\sigma_p' \approx 0.33 \cdot q_{net} \approx 0.54 \cdot \Delta u_2 \approx 0.60 \cdot q_E \qquad (4.23)$$

4.4.3 CPTU Screening for Sensitive Clays

If the three methods show disparities, then a closer examination and scrutiny of the lab and/or field data may be warranted, perhaps justification that additional tests and investigation should be conducted. With large amounts of special mineralogy in the soil (i.e., calcite, diatoms, forams, etc.), it may be possible to re-tune these equations for the particular geologic formation attributes (e.g., Mayne 2005).

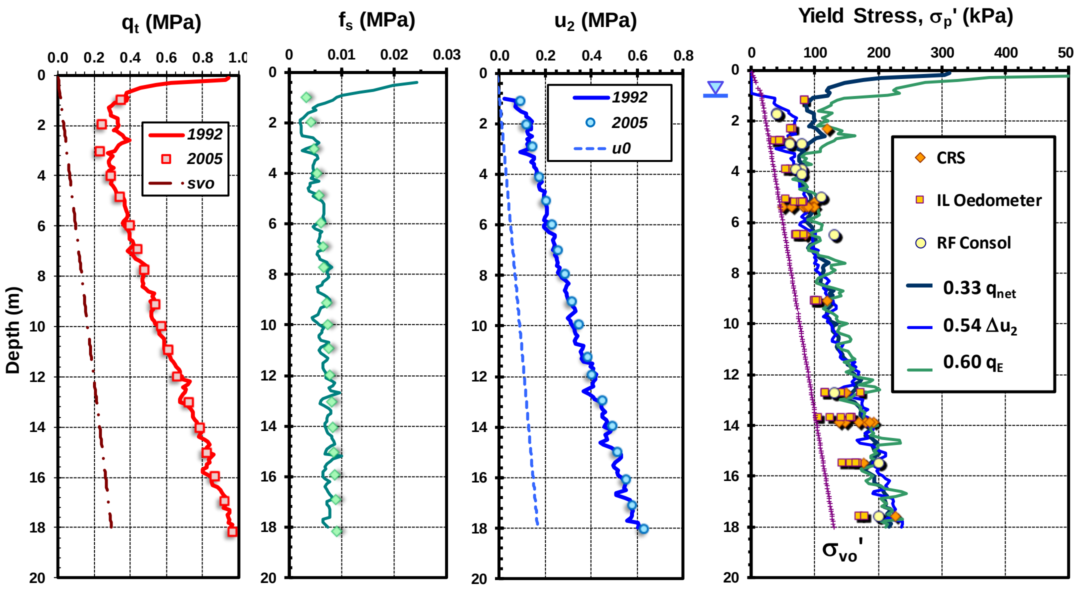

Figure 4.10: Results of CPTU soundings in 1992 and 2005 and yield stresses in regular soft clay at Bothkennar site, UK (lab and field data from Hight et 2003; Powell & Lunne 2005b)

As an alternative or supplement to the SBT charts for the CPTU identification of organic clays and sensitive or structured clays, equations (4.20), (4.21), and (4.22) can be useful. For instance, CPTU results in the soft sensitive Leda clay at the Canadian Test Site 1 in Gloucester, Ontario are presented in ***Figure 4.11***.

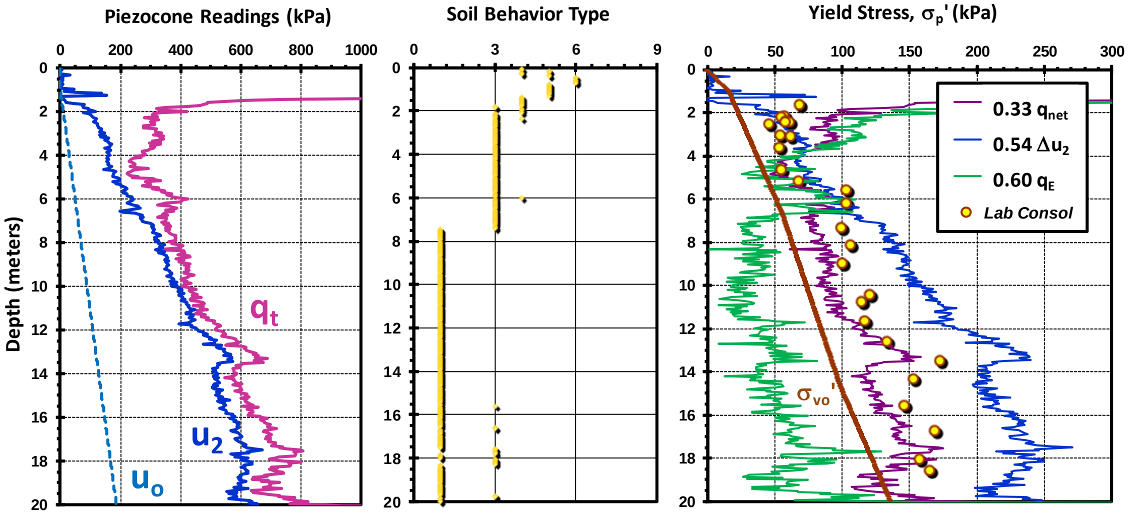

Figure 4.11: Results of CPTU sounding in sensitive soft Champlain Sea clay at Gloucester national test site, Ontario (after Agaiby & Mayne 2018)

In general, it has been found that the signature for sensitive clays is in the following hierarchy (Agaiby & Mayne 2018a; Mayne, Greig, & Agaiby 2018; DiBuö et al. 2019; Mayne & Benoît 2020):

$$0.60 \cdot q_E \quad < \quad 0.33 \cdot q_{net} \quad < \quad 0.54 \cdot \Delta u_2 \tag{4.24}$$

In the Gloucester results, it can be seen that sensitive clays are evident in the depth interval from about 7 to over 20 m. A closer examination of the three post-processed CPTU curves show: (a) crustal layer to 2 m; (b) an implied organic layer from 2 to 3.5 m; (c) slightly sensitive clay from 3.5 to 5.5 m; (d) regular clay layer from 5.5 to 6.8 m; and (e) very sensitive to quick clay below 7 m through the remainder of the sounding beyond 20 m.

4.4.4 CPTU Screening for Organic Clays

Using the set of triplet equations for σ_p', the observed signature of organic soils has been observed to form the following hierarchy (Mayne et al. 2019; 2020):

$$0.54 \cdot \Delta u_2 \quad < \quad 0.33 \cdot q_{net} \quad < \quad 0.60 \cdot q_E \tag{4.25}$$

which surprisingly is the opposite order of that noted previously for sensitive clays.

A representative sounding in soft organic silty clays along the Potomac River in Washington DC are presented in ***Figure 4.12***. The SBTn system puts "organic soils" in Zone 2. However, the SBTn analysis at this site indicates the soils are within zone 3 (clay) and zone 4 (silt mixtures), in contrast to the soil boring logs and lab tests which clearly indicate organic soils (OL and OH) from depths of 1 to 13.5 m. Note that the soft clays in the small region from 13.5 to 15.0 m in Figure 4.12 appear to be "regular" inorganic type soils.

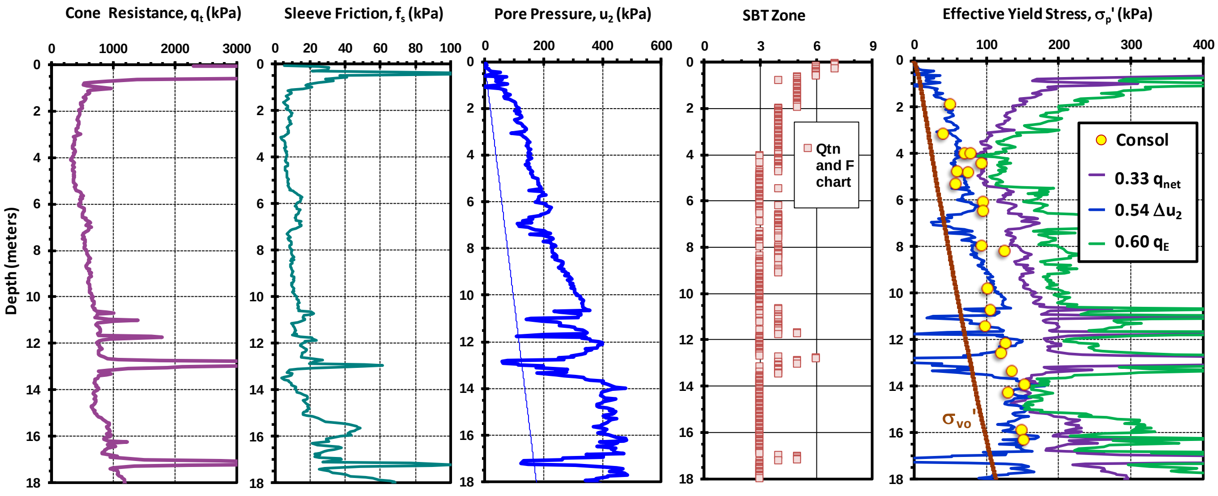

Figure 4.12: Results of CPTU in soft organic clays at Bolling AFB, Washington DC

4.4.5 Evaluation of Yield Stress from CPTU in Sensitive Clays

If the CPTU screening indicates sensitive or structured clay, then a modified SCE-CSSM is available for the evaluation of YSR with depth (Mayne, Greig, and Agaiby 2018). In this case, the former equations 4.13, 4.14, and 4.15 become:

$$YSR = 2 \cdot \left[\frac{Q/M_{c1}}{0.667 \cdot \ln(I_R) + 1.95}\right]^{1/\Lambda} \tag{4.26}$$

$$YSR = 2 \cdot \left[\frac{U^* - 1}{0.667 \cdot M_{c2} \cdot \ln(I_R) - 1}\right]^{1/\Lambda} \tag{4.27}$$

$$YSR = 2 \cdot \left[\frac{Q - \frac{M_{c1}}{M_{c2}} \cdot (U^* - 1)}{1.95 \cdot M_{c1} + \frac{M_{c1}}{M_{c2}}}\right]^{1/\Lambda} \tag{4.28}$$

where $\Lambda \approx 1$ in sensitive clays, $I_R = G/s_u$ = rigidity index, and $M_c = 6 \cdot \sin\phi'/(3 - \sin\phi')$ = frictional parameter in q-p' space. The value of M_c is defined at two points on the effective stress path: (1) M_{c1} at peak strength (i.e., ϕ'_1 at q_{max}) and M_{c2} is the value at maximum obliquity (i.e., ϕ'_2 at large strains), best obtained from either CIUC or CAUC triaxial tests. Note that the condition: $M_{c1} \le M_{c2}$ should be met.

The undrained rigidity index is found from the slope parameter (a_q) by plotting Δu_σ vs. q_{net}. Alternatively, a_q is found as the slope of (U-1) versus Q. Using the CPTU data from sensitive Leda clay at the Gloucester ON site shown in ***Figure 4.11***, the value of the slope parameter is a_q = 0.783, as shown in ***Figure 4.13***. Only data from the sensitive clay portion at depths ranging from 7 to 18 m are used, since the results for depths < 7 m appear to suggest a different clay type. Then, the SCE-CSSM formulation directly provides the assessment of undrained rigidity index:

$$I_R = exp\left[\frac{1.5 + 2.925 \cdot M_{c1} \cdot a_q}{M_{c2} - M_{c1} \cdot a_q}\right] \tag{4.29}$$

For Gloucester, assigned values of ϕ'_1 = 25° and ϕ'_2 = 39° provide corresponding M_{c1} = 0.98 and M_{c2} = 1.59 which are reasonable and comparable to values from laboratory CIUC and CAUC triaxial tests on undisturbed samples made by Bozozuk (1972) and Landon (2007). These values together with a_q provide a calculated I_R = 95. Finally, eqns 4.26, 4.27, and 4.28 can provide three new evaluations of σ_p' and YSR with depth at the Gloucester national test site, as presented in ***Figure 4.14*** (Agaiby & Mayne 2018). Clearly, the three interpreted CPTU curves now all agree with each other and provide values that match the profile determined using laboratory consolidation test data.

For regular clays that are insensitive and inorganic, note that the values of $M_c = M_{c1} = M_{c2}$. Therefore eqn (4.29) reduces to simply:

$$I_R = exp\left[\frac{\frac{1.5}{M_c} + 2.925 \cdot a_q}{1 - a_q}\right] \tag{4.30}$$

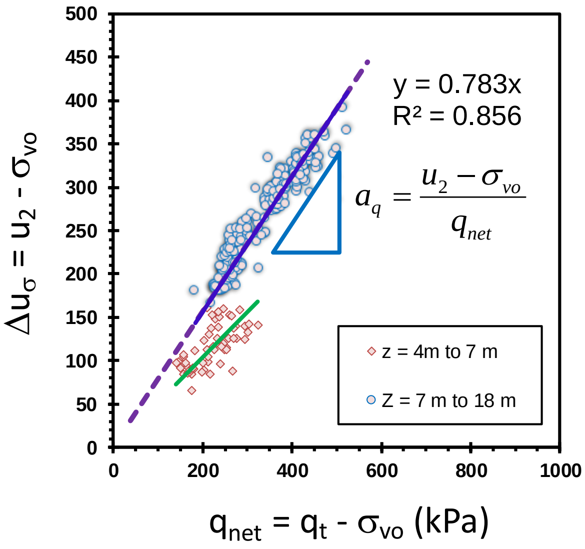

Figure 4.13: Determination of slope parameter a_q from CPTU data in sensitive Leda clay at Gloucester ON test site

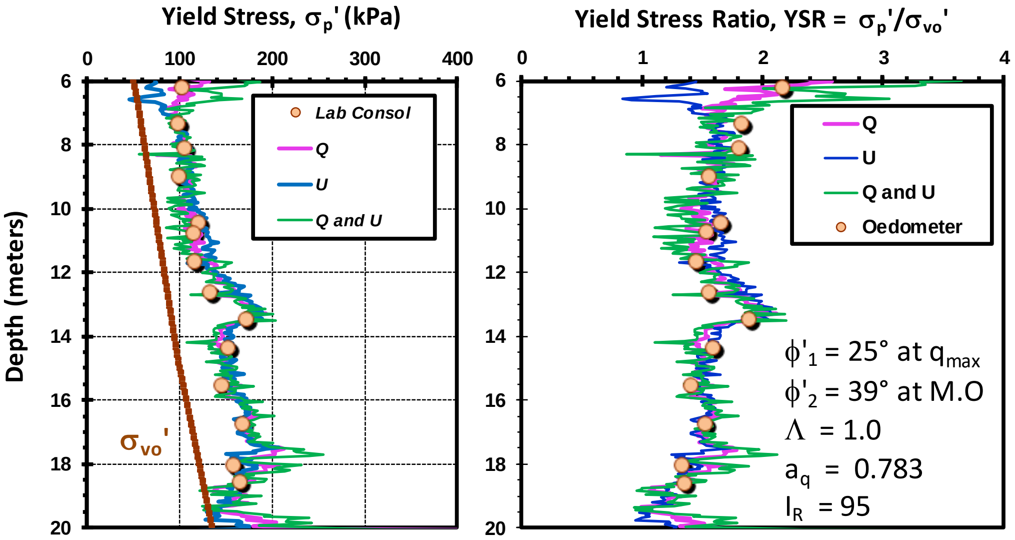

Figure 4.14: Profiles of yield stress and YSR in soft sensitive Leda clay at Gloucester using modified SCE-CSSM solutions

4.4.6 Evaluation of Yield Stress from CPTU in Organic clays

Once the presence of organic soil and organic clay layers have been identified, the effective yield stress can be estimated from (Mayne, Coop, Springman, Huang, & Zornberg 2009):

$$\textbf{\textit{Organic clays:}} \quad \sigma_p' = 0.33\, q_{net}^{\,0.9} \qquad (4.31)$$

For the Bolling AFB data with CPTU in organic clays (prior ***Figure 4.12***), the application of this approach is shown in ***Figure 4.15*** indicating good agreement with the consolidation tests.

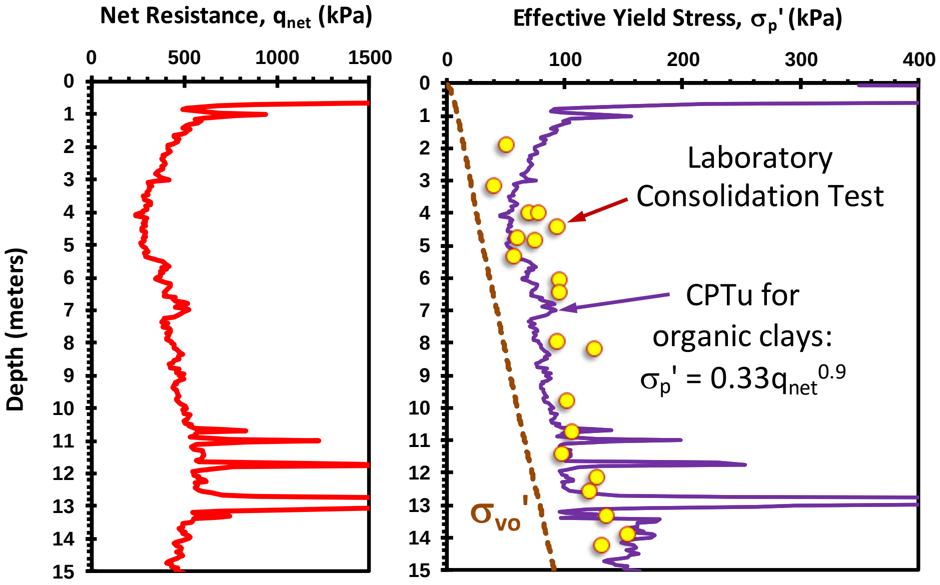

Figure 4.15: Profiles in soft organic clay at Bolling Air Base, Washingon, DC: (a) net cone resistance; (b) yield stress

4.5 Yield Stress of Sands from CPT

A statistical review of over 626 calibration chamber tests on 26 different clean silica and quartz sands determined relationships between the applied stress state, including effective vertical stress (σ'_v), lateral stress ratio ($K_0 = \sigma'_{hc}/\sigma'_{vc}$), and induced OCR, with the measured net cone resistance (q_{net}), as shown by ***Figure 4.16***. The direct expression for evaluating the OCR in clean sands is given by (Mayne 2007a; 2007b; 2017):

$$OCR = \left(\frac{0.192(q_{net}/\sigma_{atm})^{0.22}}{(1-\sin\phi)(\sigma'_{v0}/\sigma_{atm})^{0.31}}\right)^{\frac{1}{\sin\phi-0.27}} \tag{4.32}$$

Taking a characteristic value of friction angle ϕ = 35.5° for clean sands, the above reduces to the linear format:

$$\sigma'_p = 0.08(q_{net})^{0.7}(\sigma_{atm})^{0.7} \tag{4.33}$$

Using SI units, the reference stress σ_{atm} ≈ 1 bar = 100 kPa, therefore further diminishes to the even simpler expression:

$$\sigma'_p(kPa) \approx 0.32(q_{net})^{0.72} \tag{4.34}$$

which bears an uncanny resemblance to the expression for clay given by ***Equation 4.20***. As shown by ***Figure 4.17***, this simplified approach for clean sands compares well with the more rigorous algorithm given by ***Equation 4.32*** for the specified ranges of ϕ, stress levels, and normalized cone resistance. For high stress levels and high ϕ values, the simplified approach will underpredict the yield stresses.

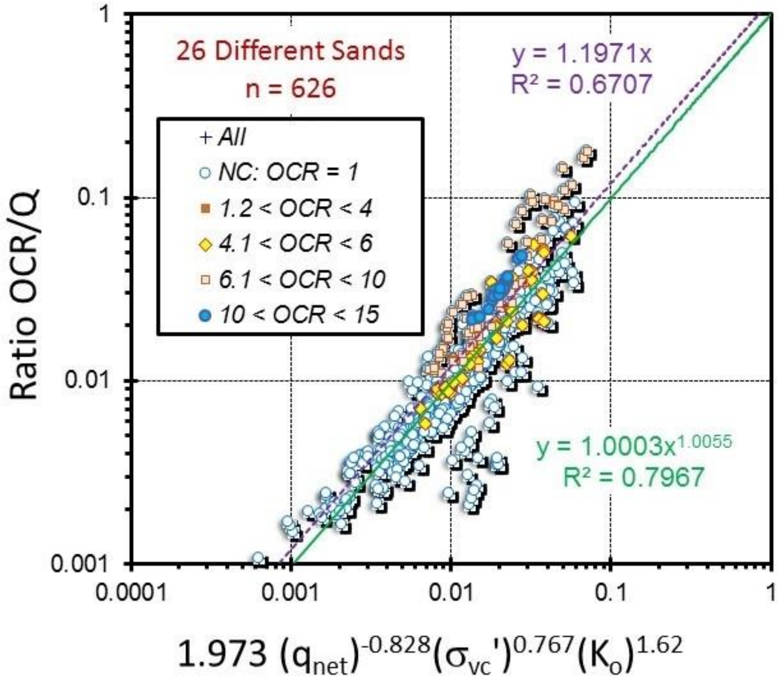

Figure 4.16: Trends from post-processing of CPTs in sand calibration chamber tests; Note: cone resistance and stresses in bars

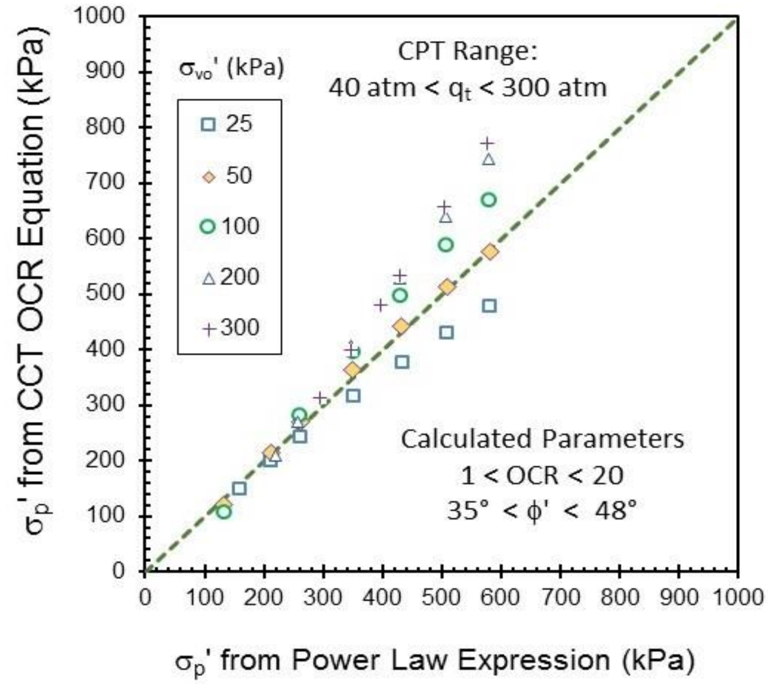

Figure 4.17: Comparison of CCT solution with simplified power law expression for sands

4.5.1 Case Study: Blessington Sand Site, Ireland

The aforementioned approach can be applied to a case study involving dense OC sands in Ireland reported by Doherty et al. (2012) and Igoe & Gavin (2019). The glacially-derived dense fine sands have an in-place relative density around 100% and mean particle size: $0.10 < D_{50}$ (mm) < 0.15 mm. Mineralogies include a predominance of quartz with calcite component, and subsets of feldspar, mica, and kaolinite fractions.

Measured cone tip resistances from 4 CPT soundings at the test site are presented in ***Figure 4.18***. Samples of the sand were procured using sonic drilling methods that were later tested in the laboratory consolidometer to define the yield stress (σ'_p) per Casagrande method. The interpreted profiles of yield stress from the simplified CPT approach are shown in ***Figure 4.18*** along with a comparison to the lab reference values, with good agreement evident.

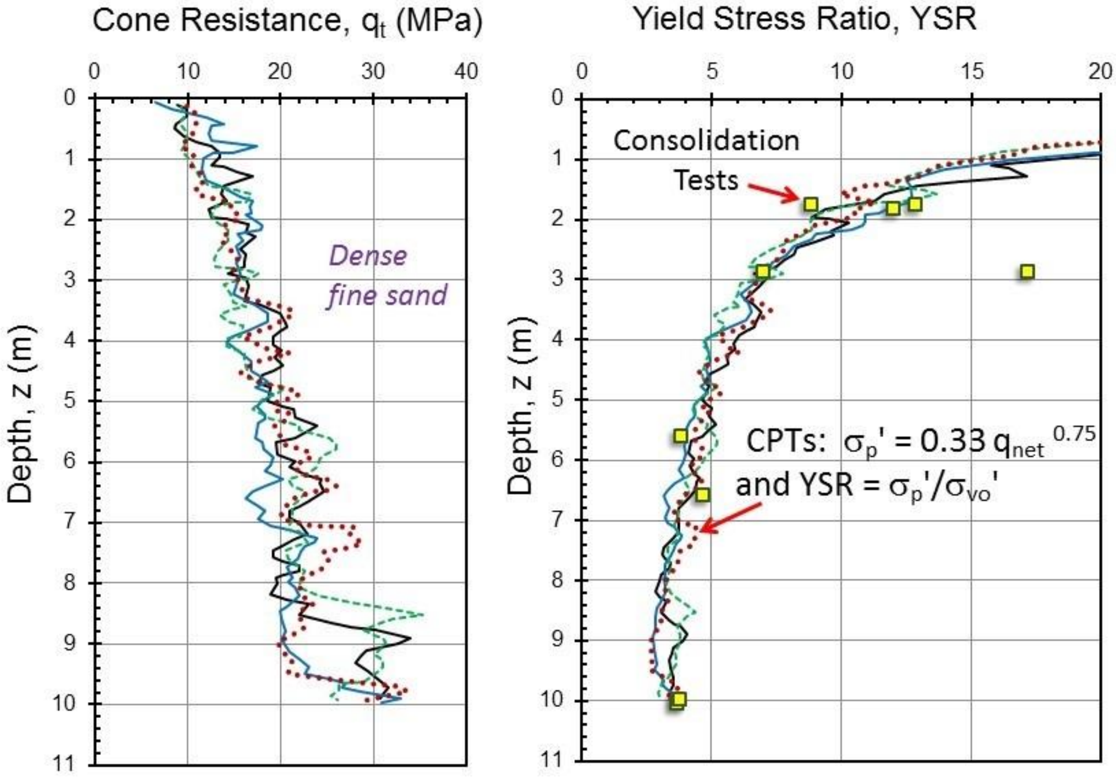

Figure 4.18: Profiles in dense sands at Blessington: (a) cone resistance; (b) yield stress ratio (Note: CPT and consolidation data from Igoe & Gavin 2019)

4.6 Unified Interpretation of Yield Stress in Soils by CPT

For the general case of evaluating effective yield stress in all soil types, ***Figure 4.19*** provides a compilation of data from a variety of natural formations, including sands, silts, clays, and mixed geomaterials. The expressions for clays, ***Equation 4.20***, and sands, ***Equation 4.34***, can be united to provide the general format:

$$\sigma'_p = 0.33(q_{net})^{m'} \cdot \left(\frac{\sigma_{atm}}{100}\right)^{1-m'} \tag{4.35}$$

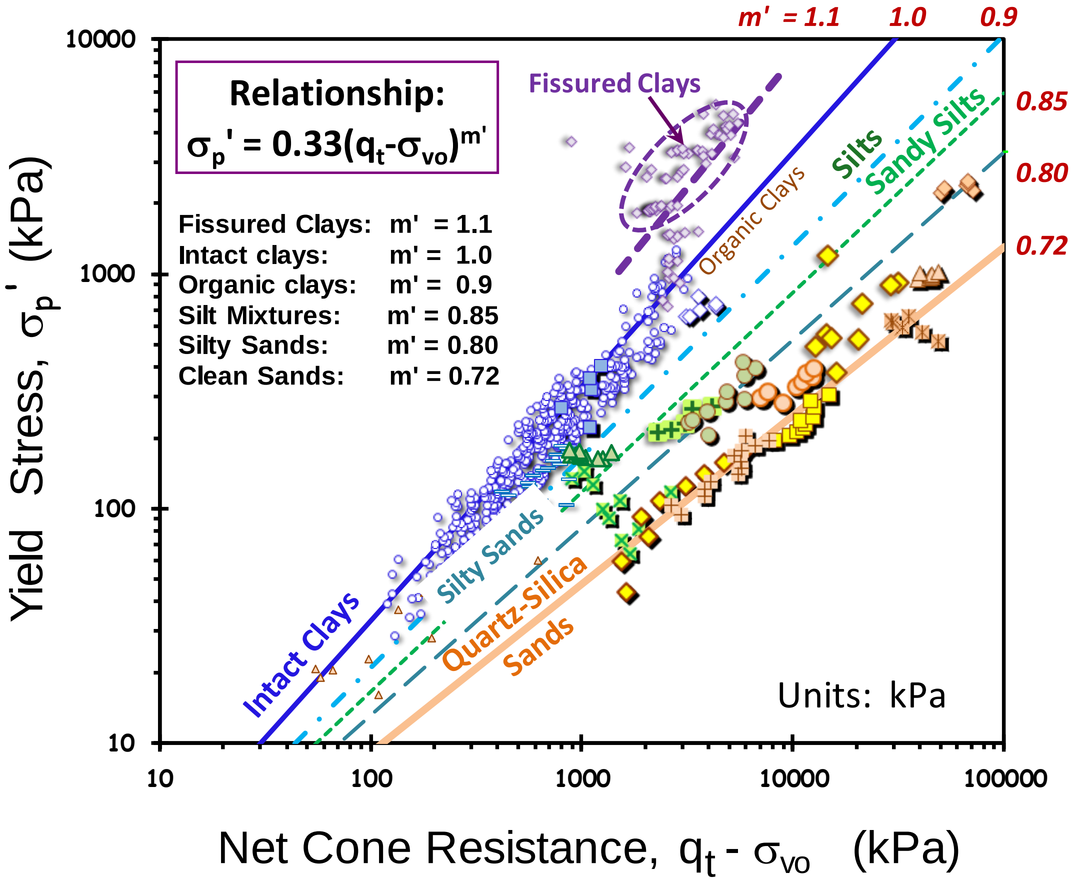

Figure 4.19: General relationship for yield stress in soils from CPT net cone resistance. (modified after Mayne et al. 2009)

where the exponent m' increases with fines content and decreases with mean grain size. Specifically, the value of m' ≈ 0.72 in clean quartz sands, 0.8 in silty sands, 0.85 in silts, 0.90 in organic clays, and m' = 1.0 in intact clays of low sensitivity. It may even take on values of 1.1+ in fissured geomaterials.

If only SI units are used (kPa), the form simply becomes:

$$\sigma_p'(kPa) = 0.33\cdot[q_{net}(kPa)]^{m'} \tag{4.36a}$$

However, for any units:

$$\sigma_p' = 0.33(q_{net})^{m'}\cdot(\sigma_{atm}/100)^{1-m'} \tag{4.36b}$$

The CPT material index $I_{C,RW}$ is logically a means of quantifying the magnitude of exponent m' for general profiling of σ'_p in homogeneous soils, heterogeneous deposits, mixed geomaterials, and stratified formations. ***Figure 4.20*** shows the trend between m' and CPT index (I_c) given by:

$$m' = 1 - \frac{0.28}{1+(I_{C,RW}/2.65)^{25}} \tag{4.37}$$

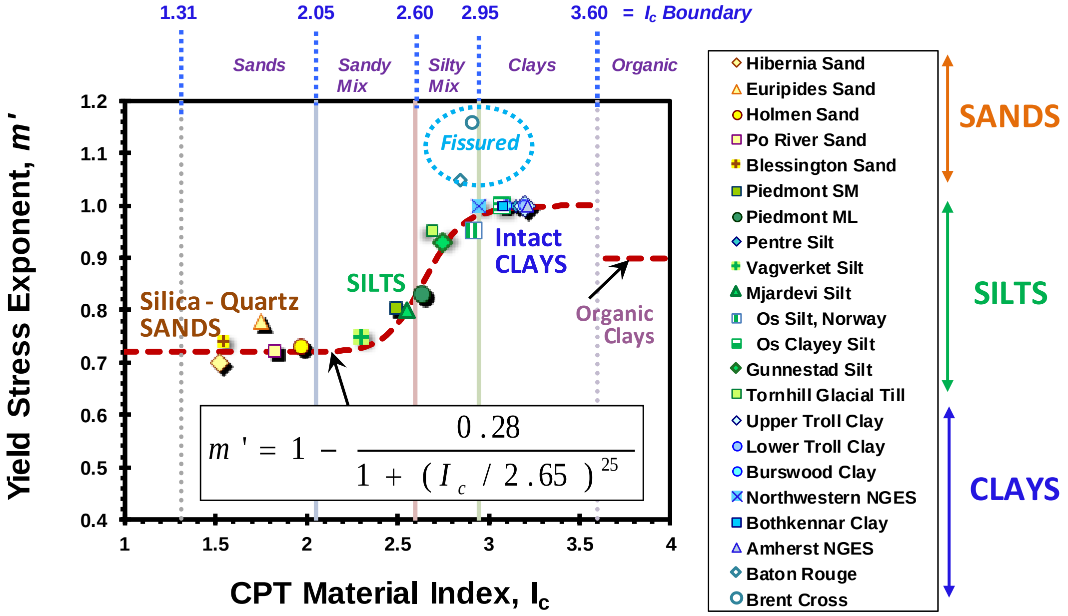

Figure 4.20: Trend for yield stress exponent (m') with CPT material index (I_c)

Where possible, the interpreted σ'_p results should be cross-checked and validated with other information, such as the results from one-dimensional consolidation tests on high-quality undisturbed samples, as well as the geologic stress history. In certain cases, additional results and corroboration may be obtained by running other in-situ tests, such as the flat plate dilatometer test (DMT) and/or vane shear test (VST), as discussed elsewhere (Kulhawy and Mayne 1990; Schnaid 2009).

The exponent m' term has also been related to the fines content (FC), mean grain size (D_{50}), and several definitions of CPT material index, as summarized in ***Table 4.2*** (Agaiby 2018).

Table 4.2. Relationships for CPT Yield Stress Exponent m' with Select Geoparameters (after Agaiby 2018)

Parameter	**Definition**	**Relationship**	**Eqn Number**
D_{50}	Mean grain size (mm)	$m' = 0.72 + \frac{0.28}{1+(16 \cdot D_{50})^5}$	(4.38)
FC	Fines content (% < 0.075 mm)	$m' = 1 - \frac{0.28}{1+(FC/55)^{20}}\ 1$	(4.39)
I_{cRW}	Index per Robertson (2009)[1]	$m' = 1 - \frac{0.28}{1+(I_{cRW}/2.65)^{25}}$	(4.40)
I_{SBT}	Index per Robertson (2010)[2]	$m' = 1 - \frac{0.28}{1+(I_{SBT}/2.4)^{20}}$	(4.41)
I_{cJB}	Index per Jefferies & Been (2015)[3]	$m' = 1 - \frac{0.28}{1+(I_{cJB}/2.5)^{30}}$	(4.42)
I_B	Index per Robertson (2016)[4]	$m' = 0.72 + \frac{0.28}{1+(I_B/32)^8}$	(4.43)
$I_{cR'09}$	Index per Robertson (2022)[1]	$m' = 1 - \frac{0.28}{1+(I_{cR'09}/2.6)^{15}}$	(4.44)

Notes: CPT Indices:

1. $I_{cR'09} = I_{cRW} = \sqrt{(3.47 - \log_{10} Q_{tn})^2 + (1.22 + \log_{10} F_r)^2}$
2. $I_{cSBT} = \sqrt{[3.47 - \log_{10}(q_t/\sigma_{atm})]^2 + [1.22 + \log_{10}(R_f)]^2}$
3. $I_{cJB} = \sqrt{\{3 - \log_{10}[Q \cdot (1-B_q)+1]\}^2 + \{1.5 + 1.3 \cdot \log_{10}(F_r)\}^2}$
4. $I_B = 100 \cdot \frac{(Q_{tn}+10)}{(70 + Q_{tn} \cdot F_r)}$

4.7 Evaluation of YSR from V_s

If SCPTU results are available, then the shear wave velocity can provide a first-order estimate on the yield stress and YSR. ***Figure 4.21*** shows a direct trend between the yield stress and V_s for clays, using an extended database reported by Mayne, Robertson, & Lunne (1998). For intact clays, the general expression is given by:

$$\sigma_p'(atm) \approx \left(\frac{V_s}{100}\right)^{1.5} \qquad (4.45)$$

Alternate equations of similar purpose are given by L'Heureux & Long (2017) and Agaiby & Mayne (2016).

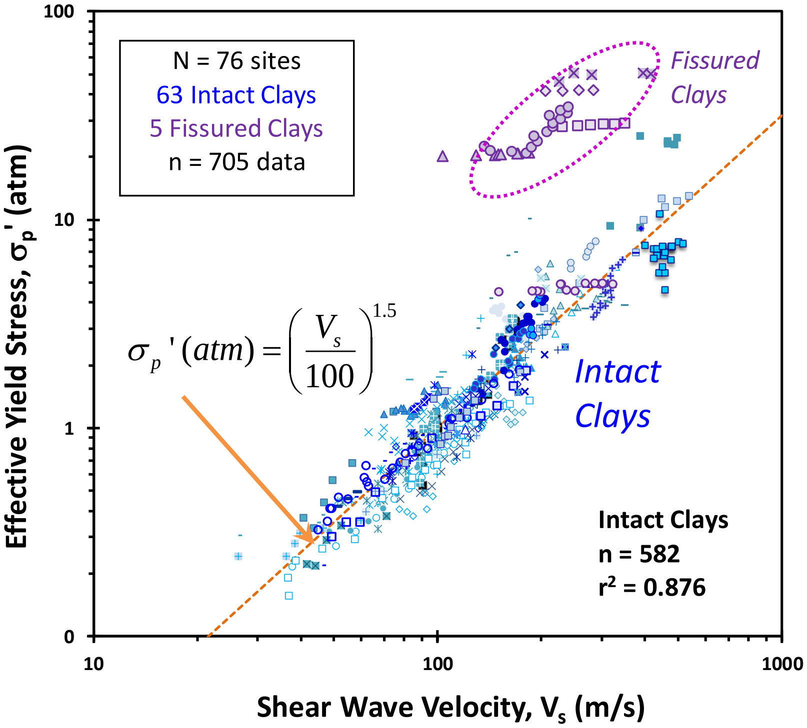

Figure 4.21: Relationship between effective yield stress of clays and shear wave velocity

An illustrative example using eqn (4.45) is presented in ***Figure 4.22*** from a SCPTU conducted along the north shore of Lake Superior for Ministry of Transportation Ontario. Here, the estimated three profiles of yield stress using eqn (4.23) from the piezocone readings compare very well with that from the V_s measurements. Also, the estimated shear wave velocity from eqn (2.22) nicely matches with the actual downhole measured V_s profile. If the latter had not been the case, the implications would be that the clay is not "regular" or "normal", thus warranting additional testing or study into whether the clay was sensitive, organic, cemented, calcareous, or other more special in its behavior.

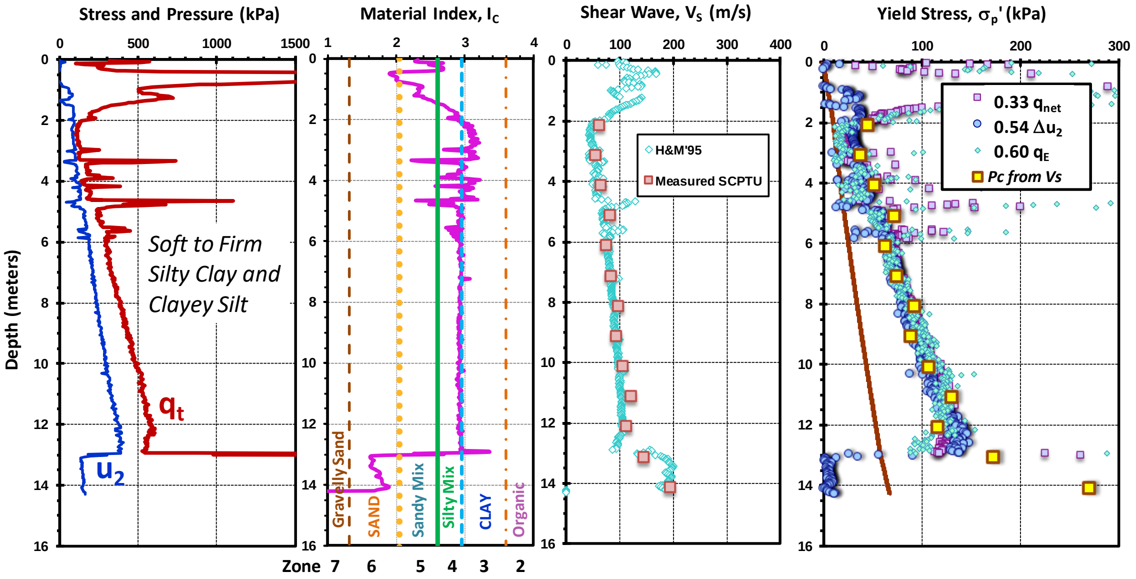

Figure 4.22: SCPTU sounding at Lake Superior showing yield stress profile from V_s data

Similarly, a tentative trend for estimating yield stress can also be found for sands, as presented in ***Figure 4.23***, and expressed:

$$\sigma_p'(atm) \approx \left(\frac{V_s}{158}\right)^{3.43} \tag{4.46}$$

where V_s is in units of m/s.

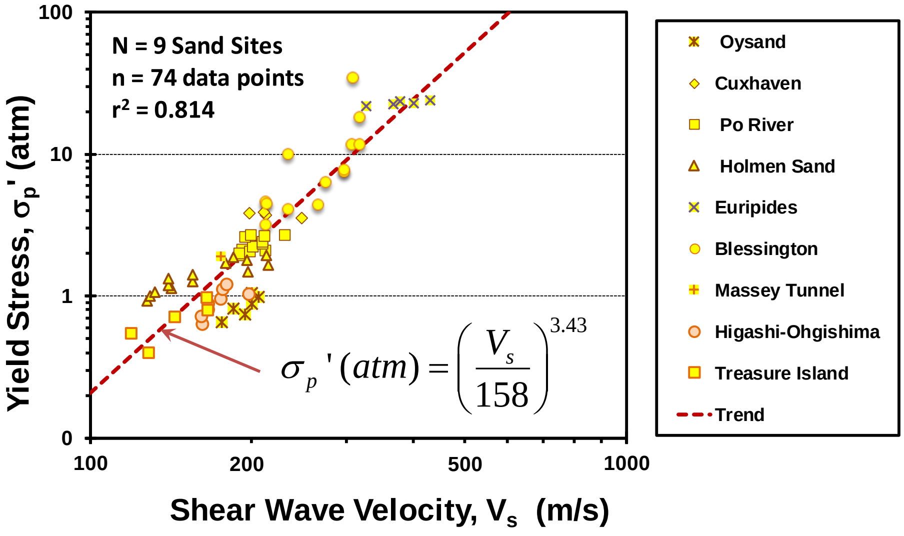

Figure 4.23: Preliminary relationship between effective yield stress of sands and V_s

The estimated yield stress of sand should be verified using other means such as a detailed engineering geologic study and evaluation by other in-situ testing such as CPT and/or DMT.

5 Effective Friction Angle and Drained Strength

The strength of soil is used to calculate the ultimate capacity of foundations, the stability of embankments, retaining walls, and slopes, and the achievable depth of an unbraced trench. It is used in assessing the stability of earth dams and heap leach piles, the resistance to static and cyclic liquefaction, and the trafficability of tailings deposits.

A strength failure usually results in very large deformations until the geometry of the geotechnical structure regains equilibrium. This can be a rotational failure under a foundation, a slump of a slope, or a collapse of an excavation.

The critical strength of a soil is the large strain shear stress that can be supported. This shear stress is the frictional resistance along a plane of soil particles. It depends on the intrinsic friction angle and the effective normal stress at failure through $\tau = \sigma' \cdot \tan\phi_{cs}$. The effective stress at failure depends on the initial state of the soil, the stress path, and drainage conditions during shearing.

A peak strength defined with a peak friction angle may be realized prior to failure. This includes the critical stress plus a dilation component due to the initial state of the soil. An undrained boundary condition may result in a peak undrained shear strength, which depends on the OCR of the soil.

5.1 Drained Strength of Soils

One of the most important soil properties required in analysis and design involving geotechnics is the friction angle (ϕ_{cs}) which is a fundamental property that controls much of its behavioral response to loading and initial stress state. The effective friction angle is a predominant geoparameter that governs the mechanical strength of soils within an important framework called critical state soil mechanics (CSSM). Details on CSSM are given elsewhere (e.g., Schofield and Wroth 1968; Jefferies and Been 2006, 2015; Idriss and Boulanger 2008; Mayne et al. 2009).

The effective stress friction angle of sands (also termed angle of internal friction) represents the strength of the material in stability analyses, footing bearing capacity, pile end-bearing resistance, and side resistance in deep foundations, as well as assessing the coefficient of lateral stress (K_0). In terms of the commonly-adopted Mohr-Coulomb strength criterion, the shear strength (τ_{max}) is expressed:

$$\tau = c' + \sigma' \tan\phi' \tag{5.1}$$

where c’ = effective cohesion intercept (generally c’ = 0 for unbonded geomaterials). In most cases, the normal stress can be taken equal to the effective vertical stress: $\sigma' = \sigma'_{v0}$.

5.1.1 Critical State Friction Angle, ϕ'_{cs}

Characteristic values of ϕ_{cs}' are on the order of 32° for quartz sands, 33° for silty quartz sands with up to 20% fines content, 34° for siliceous sands (76 approx. half quartz-half feldspar), 39° for calcareous sands, and 40° for feldspathic sands (Bolton 1986; Salgado, Bandini, and Karim

2000; Jamiolkowski and Pepe 2001). The friction angle also depends upon mode of testing (i.e., plane strain, triaxial) and direction of loading (compression, extension).

The critical state friction angle (also termed "fully softened" value) depends on the mineralogy, as noted before, and has been found related to the particle roundness. ***Figure 5.1*** shows the trend for ϕ_{cs}' decreasing with roundness for a number of natural and crushed sands (Cho et al. 2006).

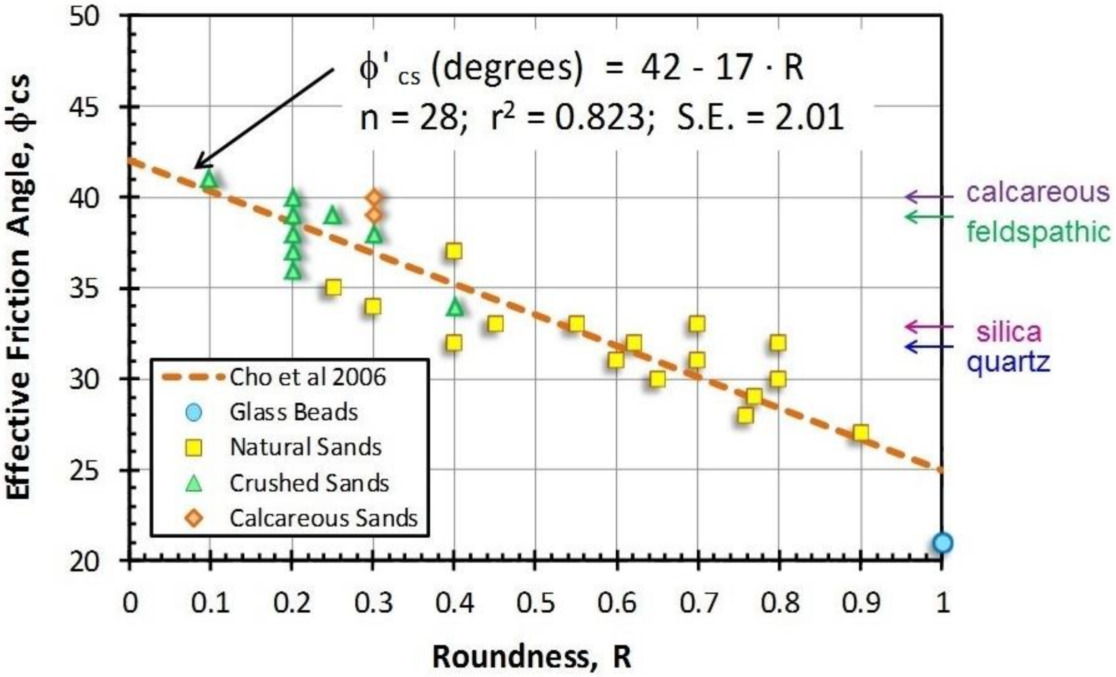

Figure 5.1: Effect of particle roundness on critical-state friction angle of clean sands (modified from Cho et al. 2006)

5.1.2 Peak Friction Angle, ϕ'_p

The peak friction angle (ϕ_p') of sands is composed of two components: (1) a basic frictional value (designated ϕ_{cs}' for critical state) that is due to particle grain shape, compressibility characteristics and mineralogy; and (2) a dilatancy effect (quantified by ϕ'_ψ the dilatancy angle) which reflects the relative packing of particles (e_0 or D_R) and ambient stress level (σ'_{v0} or p'). Together, the two components combine to produce a peak friction angle:

$$\phi'_p \approx \phi'_{cs} + \phi'_\psi \tag{5.2}$$

For illustration, data from a series of triaxial tests on a quartz sand reported by Koerner (1970) are presented in ***Figure 5.2***. As the relative density of the sand increases, so too the measured peak friction angle increases. After attaining the peak ϕ_p', strain softening is observed whereby all sand specimens tend towards their ϕ_{cs}, here approaching 33°. Realistic peak values may range from around 32° to 45° for the triaxial compression mode.

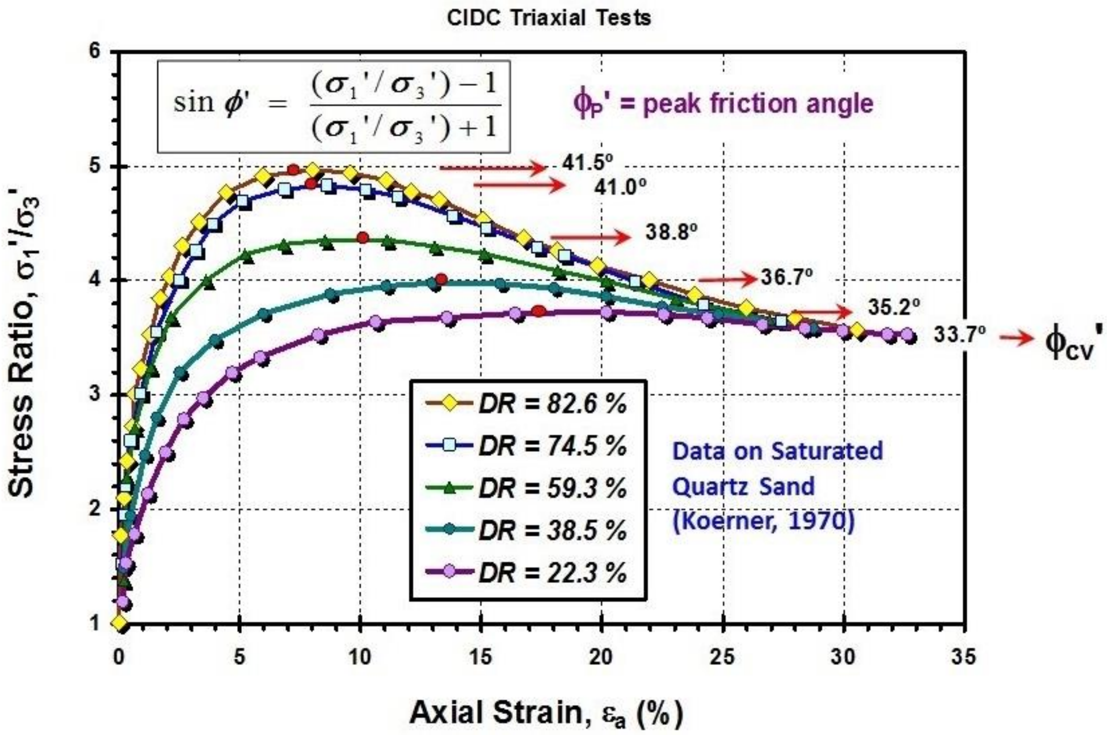

Figure 5.2: Drained triaxial compression tests on quartz sand at different prepared relative densities (data from Koerner 1970)

The effects of dilatancy on peak friction angle must also consider the effective stress state as well. This is best captured in the simplified framework presented by Bolton (1986). This framework is presented in ***Figure 5.3*** where the dilatancy angle, ϕ'_ψ, is expressed in terms of relative density and effective stress level. Data were compiled from triaxial testing of 17 different sands, primarily on reconstituted specimens (Boulanger and Ziotopoulou 2012). The peak friction angle can be expressed in the general format:

$$\phi_p' \approx \phi_{cs}' + 3\left(D_R\left(Q_x - \ln\left(p'_f\right)\right) - R_x\right) \tag{5.3}$$

where Q_x = mineralogical component, R_x = fitting parameter, and p'_f = mean effective stress at failure. For purposes of practicality, the value of p'_f can be taken to be around $2\sigma_{vo}'$ (Kulhawy & Mayne 1990). For quartz sands, recommended values of $Q_x = 10$, $R_x = 1$, and $\phi' \approx 32°$ are given by Bolton (1986). Additional details concerning quartz, silica, glauconitic and calcareous sands, as well as sands with fines content are provided by Jamiolkowski et al. (2001). Note that on the y-axis of Figure 5.3 the term $\phi'_{crit} = \phi_{cs}'$.

A recent review of data from over 500 triaxial tests conducted by the NGI laboratory on primarily clean quartzitic sands from 38 different sites is presented in ***Figure 5.4*** (Andersen and Schjetne 2013). Here, the effects of D_R and effective confining stress are again seen to control the value of peak friction angle and supporting the dilatancy framework for peak friction angle of Bolton (1986).

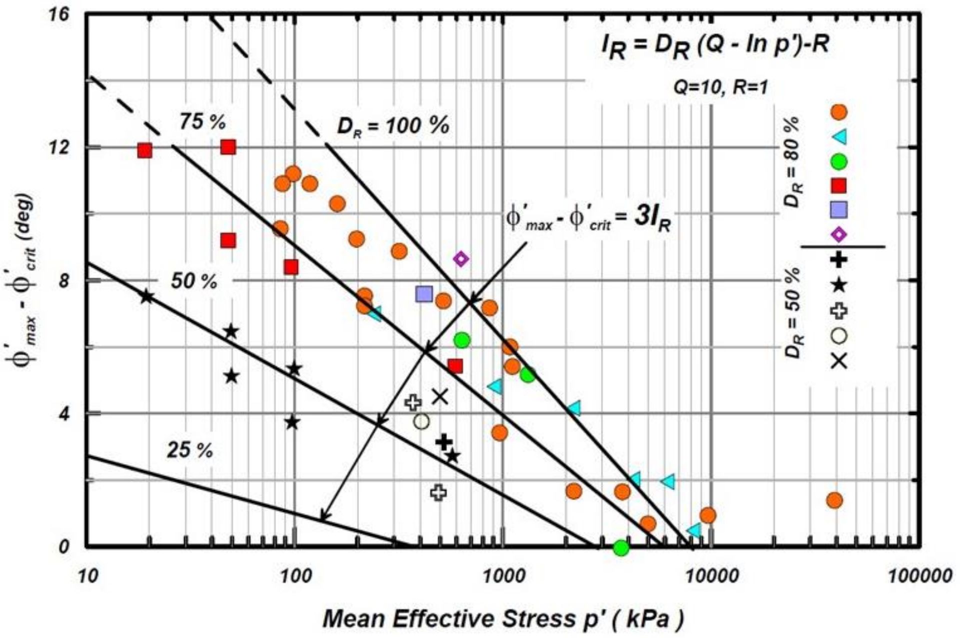

Figure 5.3: Bolton's framework for representing dilatancy effect on peak friction angle of sands (from Boulanger & Ziotopoulou 2012)

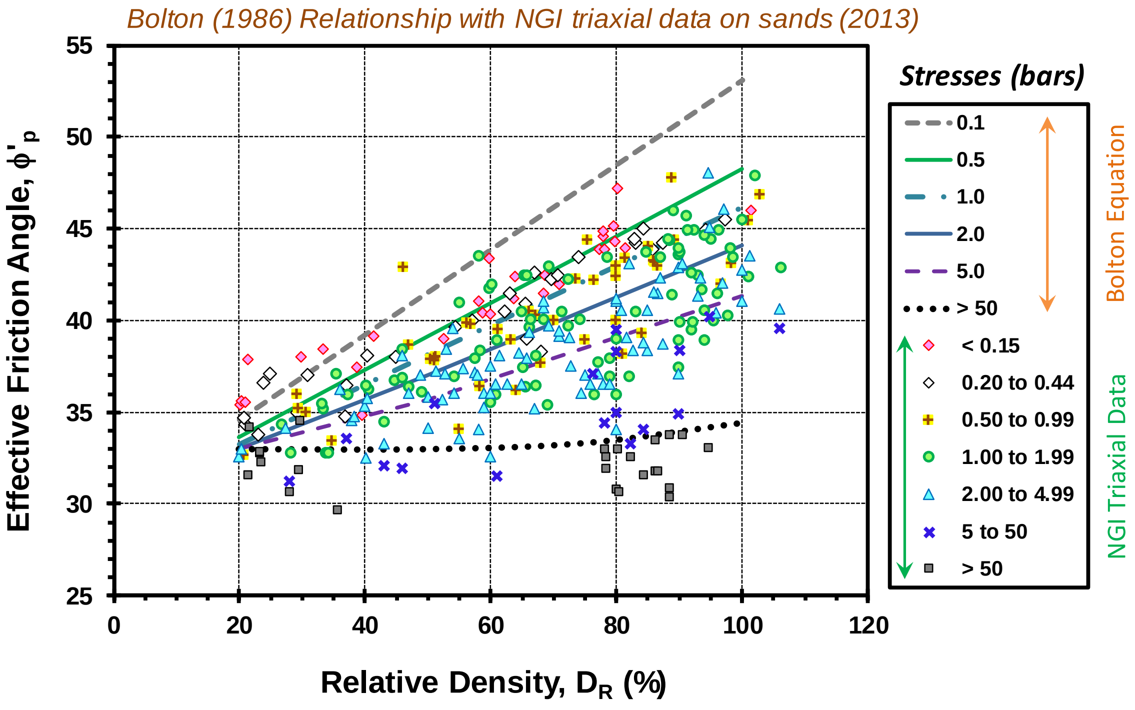

Figure 5.4: Bolton equation with superimposed data from over 500 triaxial tests on clean quartz sands at 38 sites (data from Andersen and Schjetne 2013)

5.1.3 Drained Friction Angle of Sands from Cone Resistance

For the assessment of ϕ_p' of sands from CPT, there are several approaches: (a) use of a dilatancy framework where q_t provides the input D_R for the Bolton expression (b) inverse bearing capacity, such as from cavity expansion or limit plasticity theories (Yu and Mitchell 1998; Mayne 2006; Schnaid 2009); (c) numerical simulation by finite elements, finite differences, and/or discrete elements (e.g., Salgado, Mitchell, and Jamiolkowski 1998; Susila and Hryciw 2003; Lee, Salgado, and Carraro 2004); or (d) direct CPT methods (Lunne et al. 1997; Mayne 2007a; 2007b; Uzielli et al. 2013).

Many early approaches relied on reconstituted samples where small companion triaxial specimens were prepared at similar relative densities and confining stress levels to those of larger calibration chamber tests subjected to CPTs. The procedures for reconstituting specimens are not standardized, however, and include: pluviation, compaction, vibration, sedimentation, moist tamping, and/or slurry methods. Different triaxial results are obtained by the various reconstitution methods. Furthermore, in early studies, CPT data were not yet corrected for boundary conditions from limited size chambers (i.e., D/d ratio).

Towards an improved solution, an elite database was compiled from special expensive undisturbed samples of 13 clean sands, as presented in ***Figure 5.5*** (Mayne 2006). The majority of these sands were initially frozen in-place using one-dimensional freezing technology, then transported to the laboratory for testing. After careful mounting of specimens in triaxial apparatuses with membranes, filter paper, and effective confinement, they were allowed to

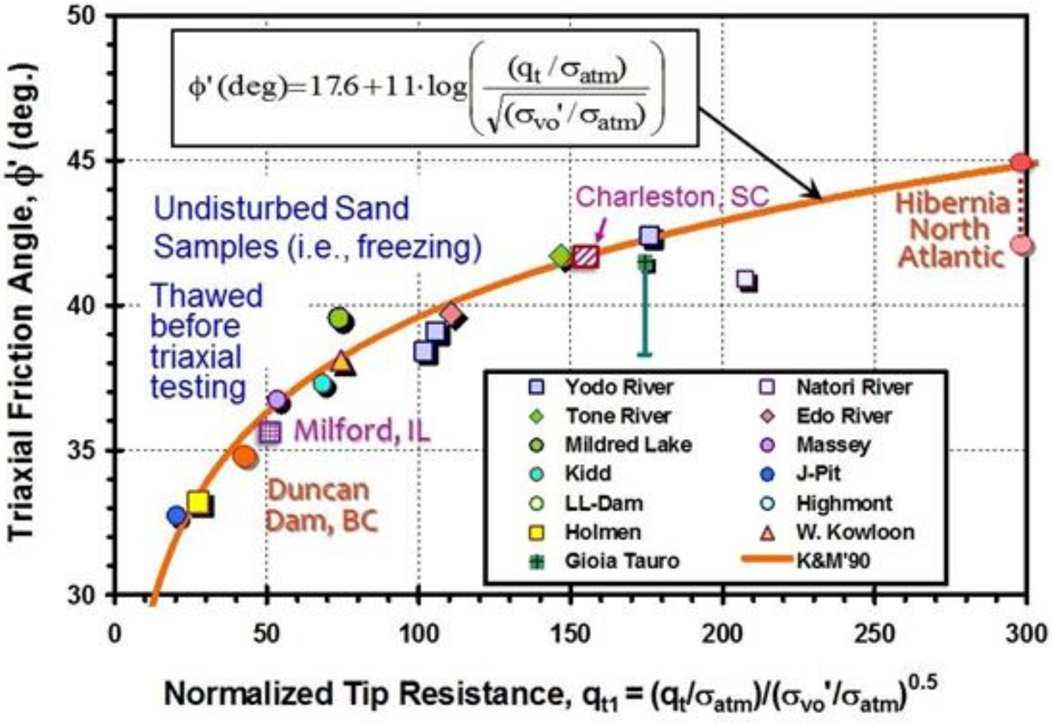

Figure 5.5: Direct CPT assessment of peak ϕ_p from undisturbed clean sands dataset (modified after Mayne 2006)

thaw, and then sheared to failure in compression to derive ϕ_p' corresponding to undisturbed intact sands. The sandy sites were also subjected to SPT, CPT, and V_S measurements, as well as other lab and field testing.

The triaxial data from undisturbed sands can be seen to fit nicely with the expression derived by Kulhawy and Mayne (1990) that was developed on the basis of CPT calibration chamber data that were corrected for boundary effects:

$$\phi_p' = 17.6° + 11.0 \log_{10}(q_{t1}) \tag{5.4}$$

where $q_{t1} = (q_t/\sigma_{atm})/(\sigma'_{v0}/\sigma_{atm})^{0.5}$ = stress-normalized cone tip resistance. Also note that the σ_{atm} terms can be combined so that $q_{t1} = q_t/(\sigma_{atm} \cdot \sigma_{vo}')^{0.5}$. Data from 4 additional natural sands have been added to the original set: (a) Duncan Dam, BC (Plewes et al. 1993); (b) Hibernia Oil Field Thompson and Long (1989; Taylor, Lewis, and Ingersoll 1993); (c) Milford Dam, KS (Stark et al. 2011); and (d) CREC - Charleston, SC (Esposito III and Andrus 2016). The relationship in ***Figure 5.6*** primarily applies to clean quartz to siliceous sands. For sands of high calcareous content, refer to the methodology suggested by Jamiolkowski et al. (2001).

To quantify the reliability of the aforementioned trend, Bayesian statistical and probabilistic analyses were performed (Uzielli et al. 2013), as shown in ***Figure 5.6***. A power law function was employed that gave essentially the same results as with the following deterministic expression:

$$\phi_p' = 25.0°(q_{t1})^{0.10} \tag{5.5}$$

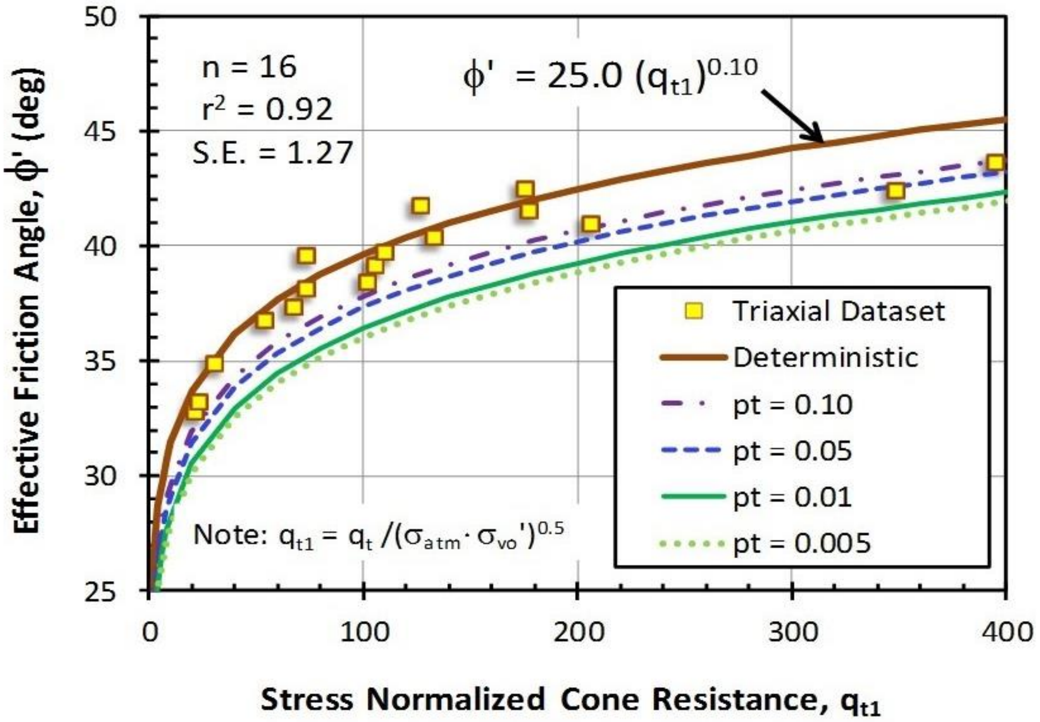

Figure 5.6: Probability curves of non-exceedance in CPT evaluation of peak ϕ' in sands (after Uzielli et al. 2013)

Detailed statistical analysis allowed for parallel design curves to be developed that provided probabilities (P_L) of non-exceedance, with P_L ranging from 0.5% to 10%.

The excellent agreement between the deterministic power law curve given by ***Equation 5.4*** in logarithmic format and the power law given by ***Equation 5.5*** is evident in ***Figure 5.7***. Here, additional data from three sand sites have been included: (a) McDonald's Farm, BC (Robertson and Campanella 1983); (b) Stockholm sand (Dahlberg 1974); and (c) dense OC fine sand at Blessington, Ireland (Doherty et al. 2012).

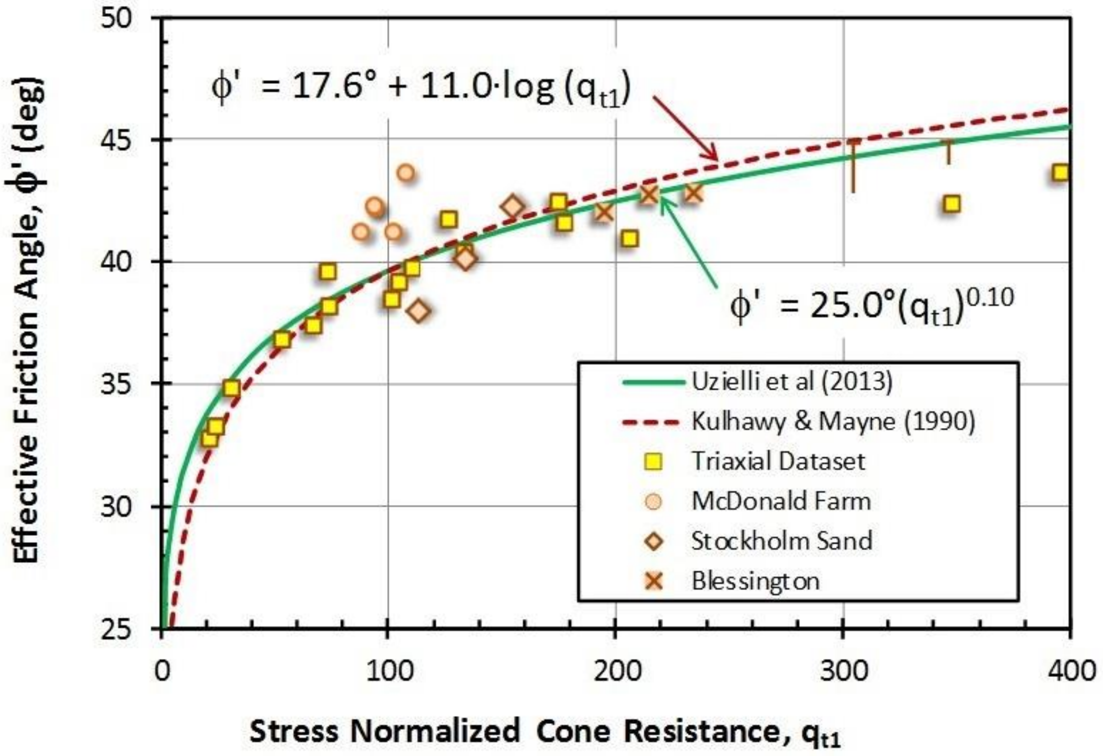

Figure 5.7: Deterministic and probabilistic algorithms for direct CPT evaluation of peak ϕ'

Recent use of ***Equation 5.4*** has employed the updated form for stress-normalized cone resistance, Q_{tn}, in lieu of the simpler q_{t1} (e.g., Robertson and Cabal 2015). Using the most recent set of triaxial tests from undisturbed samples of sands taken by freezing, gel-samplers, and mazier tubes, ***Figure 5.8*** presents data from 27 sands to silty sands with $\phi_p{}'$ as a function of Q_{tn}. For all practical purposes, the substitution works equally as well, resulting in (Uzielli & Mayne 2019):

$$\phi_p{}' = 17.6° + 11.0 \log_{10}(Q_{tn}) \tag{5.6}$$

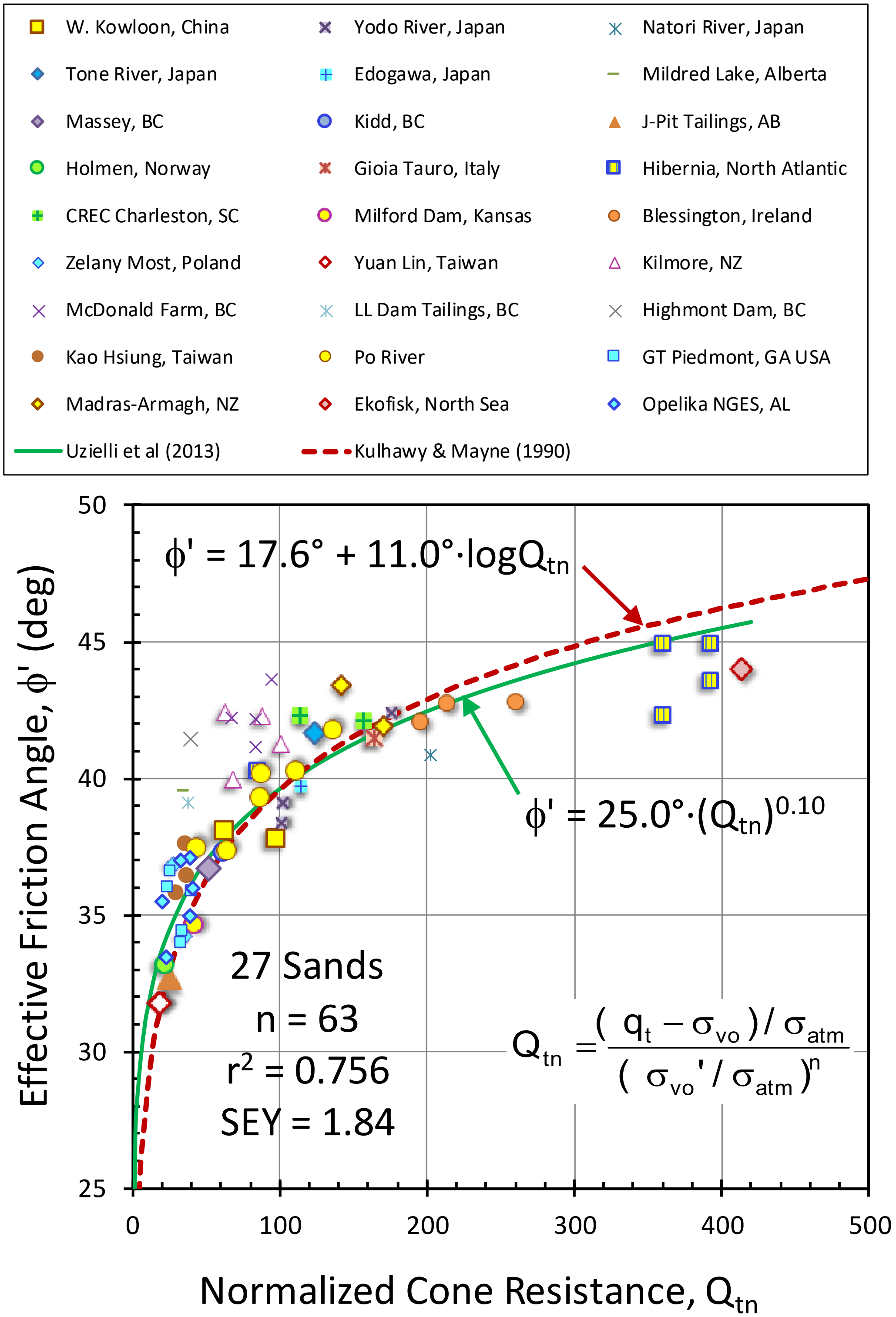

Figure 5.8: Peak friction angle of 27 sands and silty sands versus stress-normalized cone resistance, Q_{tn} (data from Uzielli & Mayne 2019)

The clustering of data above the line in the range of $50 < Q_{tn} < 100$ is believed to be due to the site-specific effects of sand mineralogy and particle angularity-roundness, as discussed earlier for ***Figure 5.1***. Since the original equation was developed primarily for quartzitic and 84 alicaceous sands (Kulhawy and Mayne 1990), the evaluation will be on the low side and underpredict ϕ_p' in angular sands and soils with different mineralogies, such as feldspathic sands, crushed sands, and those with a calcite component.

5.1.4 Sand Friction Angle with CPT Material Index, I_c

The effective friction angle of sands and silty sands is observed to decrease with the CPT material index, as shown in ***Figure 5.9***, resulting in the trend:

$$\phi_p' = 53° - 6.9 \cdot I_{cRW} \tag{5.7}$$

As noted earlier in Section 3.2.3, drained soil behavior is associated with $I_{cRW} < 2.6$, therefore eqns (5.6) and (5.7) will apply in this range.

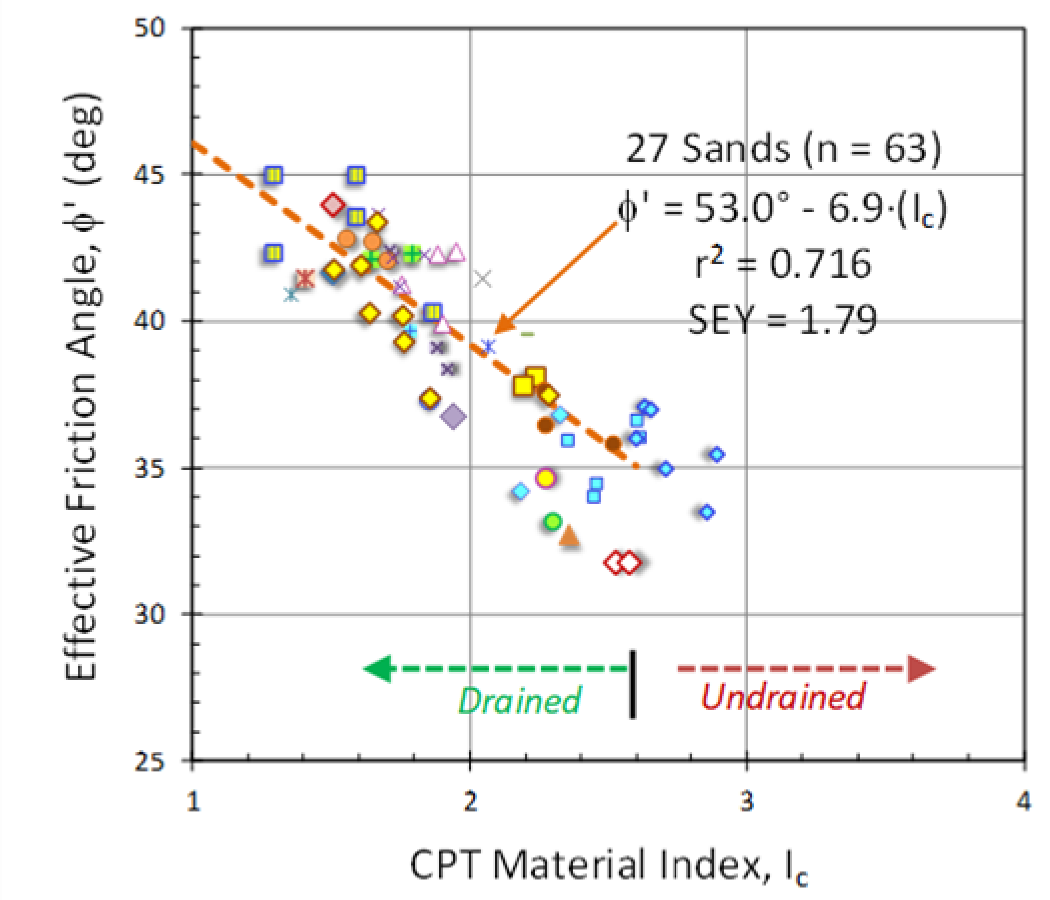

Figure 5.9: Peak ϕ' versus CPT material index for 27 sands and silty sands (data from Uzielli & Mayne 2019)

For silty sands, Lee, Salgado, and Carraro (2004) developed a numerical CPT simulation program for a variety of sands that have silt fractions added to them with corresponding lab measurements. Normalized curves were derived to relate the silty sand parameters to the simulated cone resistances and then fitted to the Bolton expression. Note that these were developed for soils that were reconstituted in the laboratory.

5.1.5 Case Study: Silty Sands at Georgia Tech

A test program on silty sands at the west side of the Georgia Tech campus was established for purposes of drilled shaft loading (Mayne & Harris 1993). Below a 3-m fill layer, the native geomaterials are residual soils derived from the in-place weathering of the parent gneiss and schist bedrock. The site is located within the Appalachian Piedmont geology. Rock was encountered approximately 21 m deep at this site and groundwater was about 16 m below grade. A series of nine boreholes produced 113 samples. The disintegration of rock over time has formed an overburden consisting of silty sands (SM) with an average 67% fine sand, 24% silt, and 7% clay fraction. Mean grain size at the site is about D_{50} = 0.14 mm.

A number of undisturbed Shelby tubes were procured in a boring at this site and transported to two commercial laboratories (Golder and GeoSyntec) for laboratory testing. Results from 13 consolidated triaxial compression tests determined an overall average $\phi_p{}'$ = 35.9° and c' = 0 kPa for this soil, as illustrated by ***Figure 5.10***.

A CPT profile at the site is shown in ***Figure 5.11*** with cone resistance, sleeve friction, and index I_{cRW}. Application of ***Equations 5.6 and 5.7*** to the CPT results in the natural residual silty sands in this case gave very reasonable agreement with the triaxial test values.

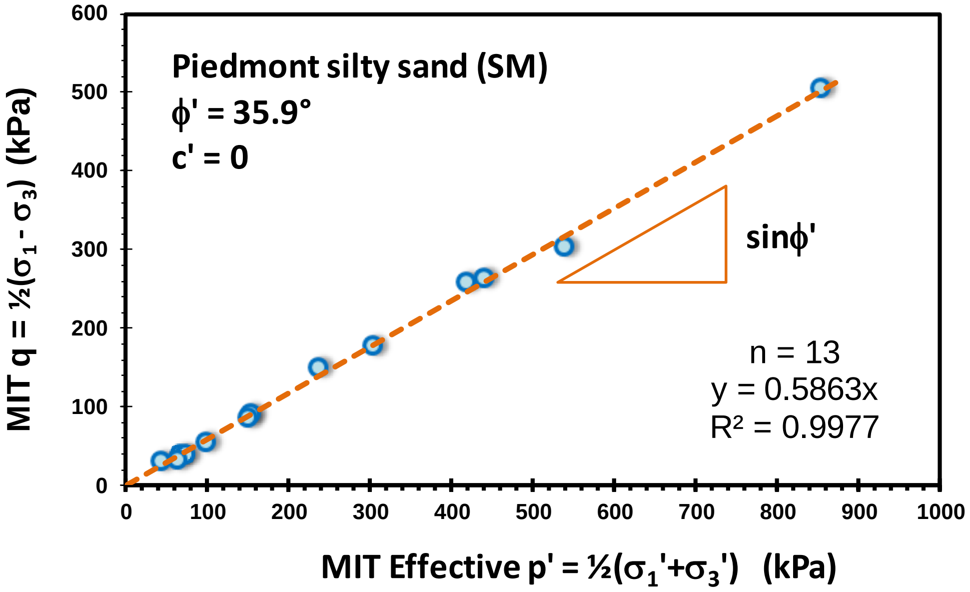

Figure 5.10: Triaxial tests on natural silty sand from GT campus, Atlanta, GA

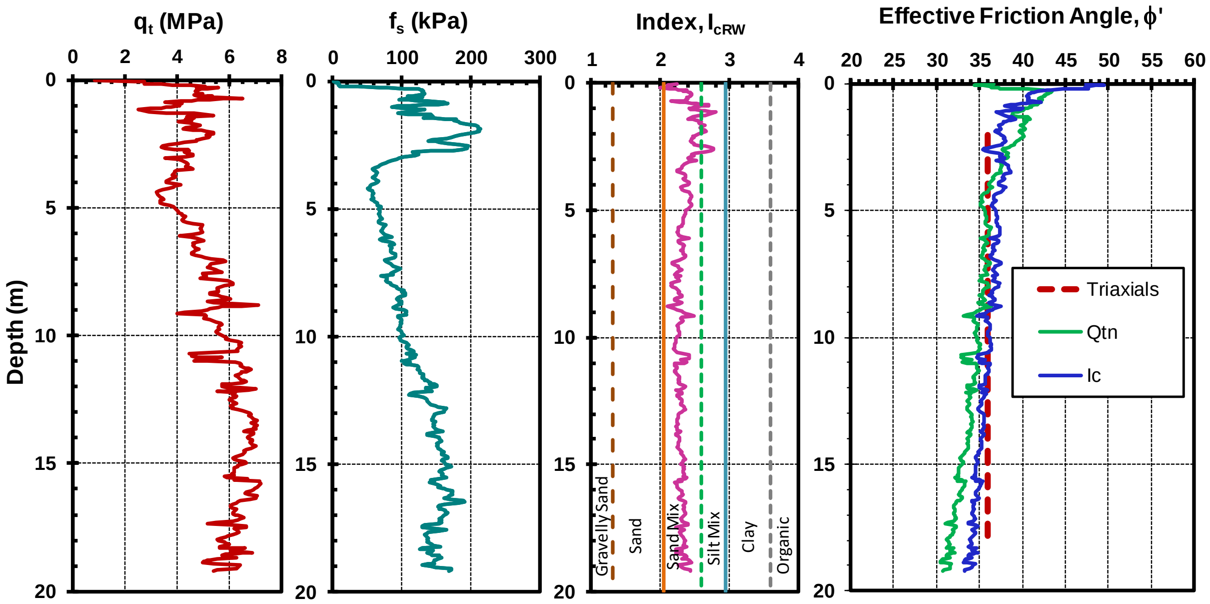

Figure 5.11: Application of CPT for evaluating friction angle of silty sands in Atlanta

5.2 Effective Friction Angle of Clays from CPTU (NTH Solution)

For soft to firm fine-grained silty and clayey soils exhibiting excess porewater pressures during penetration ($B_q > 0.1$), a limit plasticity solution for undrained penetration can be implemented towards the evaluation of ϕ_p'. The theory was developed at the Norwegian Institute of Technology, NTH (Senneset et al. 1988; Senneset et al. 1989). In this approach, a cone resistance number (N_m) is defined by:

$$N_m = \frac{N_q - 1}{1 + N_u \cdot B_q} = \frac{q_t - \sigma_{v0}}{\sigma'_{v0} + a'} \tag{5.8}$$

where $a' = c' \cdot cot\phi'$ = attraction, c' = effective cohesion intercept, N_q = $K_p \exp[(\pi - 2\beta)\tan\phi]$ is the end-bearing factor, $K_p = (1 + \sin\phi')/(1 - \sin\phi')$ is the passive stress coefficient, β = angle of plastification (-30° < β < +30°) which defines the size of the failure zone beneath the tip, $N_u = 6(\tan\phi')(1 + \tan\phi')$ is the porewater bearing factor. The full solution allows for an interpretation of a paired set of c' and ϕ' for all soil types: sands, silts, clays, and mixed soils. For undrained loading, β = 0 (Ouyang & Mayne 2018). A further simplification is taken for the case where c' = 0, therefore the cone resistance number (N_m) becomes equivalent to the normalized cone tip resistance, Q = Q_t = Q_{t1}, or simply: $N_m = Q = (q_t - \sigma_{v0})/\sigma'_{v0}$.

These terms can be combined to produce a single equation :

$$Q = \frac{\tan^2(45° + \phi_p'/2)e^{\pi \tan \phi_p'} - 1}{1 + (6 \tan \phi_p')(1 + \tan \phi_p')B_q} \tag{5.9}$$

resulting in a family of curves (***Figure 5.12***) for various values of porewater pressure ratio, B_q.

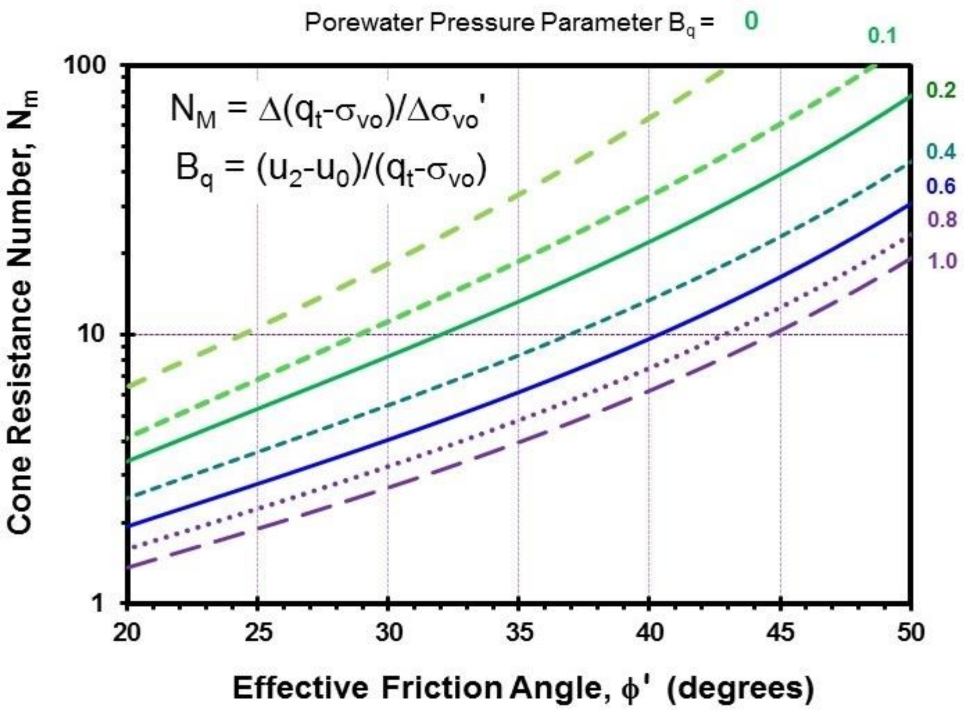

Figure 5.12: NTH Solution for evaluating ϕ_p from CPTU in silts and clays (modified after Senneset et al. 1988; Senneset et al. 1989)

5.2.1 Case Study: Soft Clay at Sandpoint Idaho

To illustrate the use of the NTH method, results from an 80-m deep CPTU conducted for the Idaho DOT State Route 95 in Sandpoint, Idaho are used (***Figure 5.13***). Details on the site conditions can be found in (Fellenius et al. 2004). Primarily, the sounding penetrates through a clayey silt to silty clay deposit with sand layers in the upper 10 m, at depths from 50 to 53 m, and 60 to 66 m. Numerous sand "stringers" and lenses can be seen at other depths. For the post-processing, we are interested in the fine grained clays and silts, thus have chosen some representative points along the profile, as indicated by the open dots.

The procedure for determining the cone resistance number is found as the slope of plotting the net cone tip resistance versus the effective overburden, as illustrated in ***Figure 5.14a***. In this instance, we force the best fit line through the origin (assuming c' = 0) to obtain N_m = Q = 4.2. Similarly, the porewater parameter B_q is determined as the slope of Δu versus net cone resistance (***Figure 5.14b***), giving B_q = 0.75 for the Sandpoint site.

The attained Q and B_q values are entered into the solution chart in ***Figure 5.15***, finding a representative $\phi_p{}'$ = 32.5° for the clayey silt. This compares well with extensive series of laboratory CIUC triaxial tests conducted on undisturbed samples taken at the site (***Figure 5.16***).

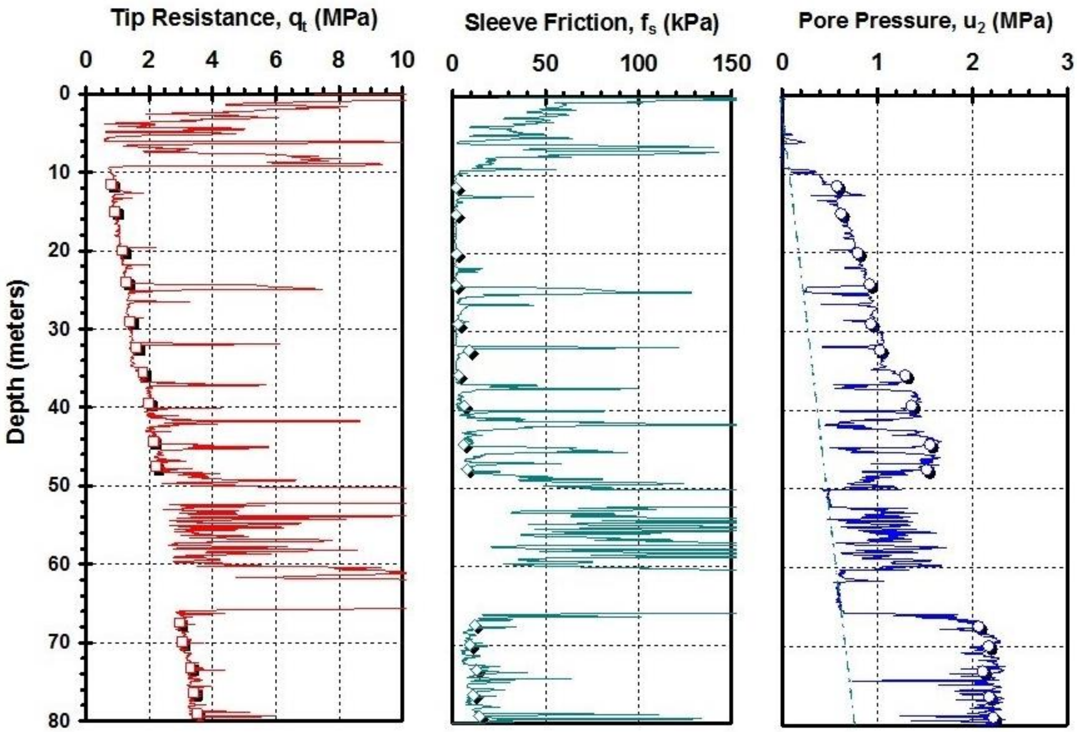

Figure 5.13: Piezocone sounding in soft clayey silt at Sandpoint, Idaho

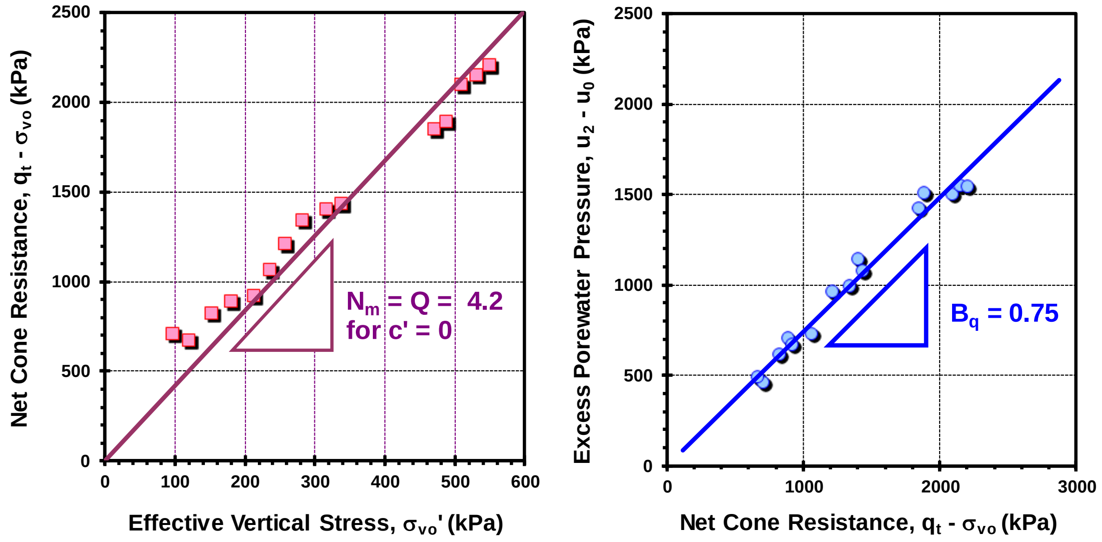

(a) *(b)*

Figure 5.14: NTH post-processing of CPTU data at Sandpoint for determination of (a) cone resistance number, $N_m = Q$ when c' = 0; and (b) porewater pressure parameter, B_q

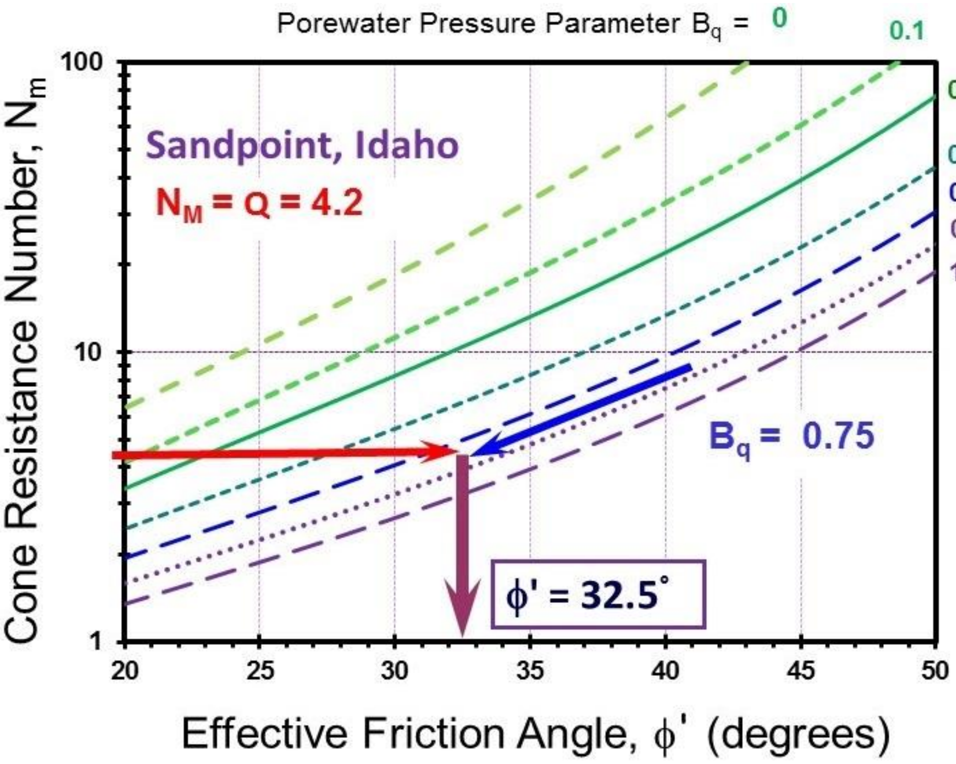

Figure 5.15: Application of Q and B_q values from Sandpoint to NTH Solution for ϕ'

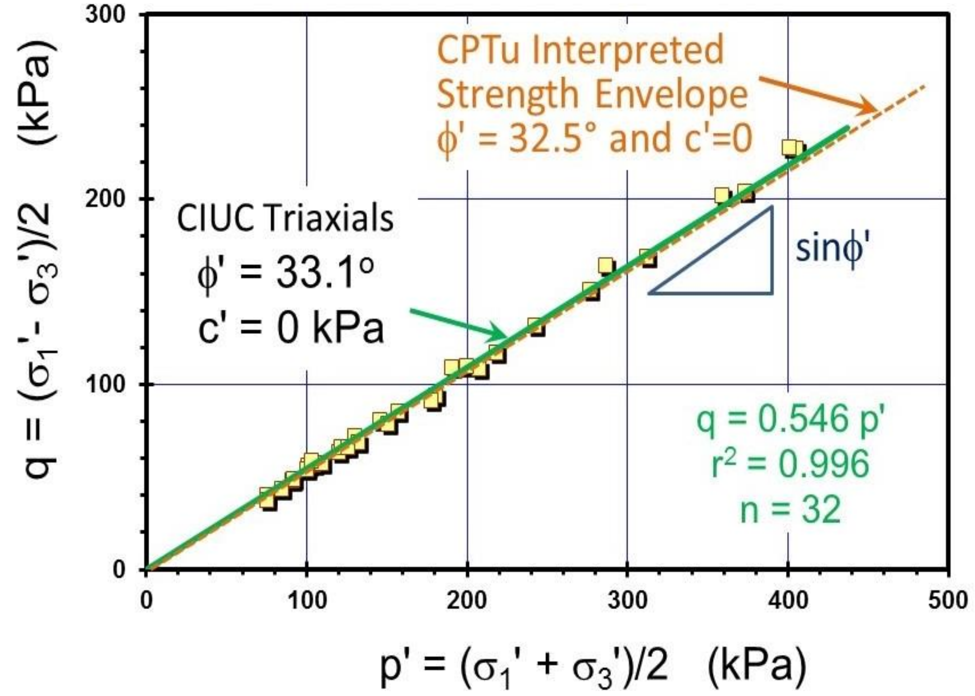

Figure 5.16: Results of triaxial shear tests on clayey silt samples from Sandpoint, Idaho

5.2.2 Approximate NTH Solution for ϕ' in Clays

Since ***Equation 5.8*** necessitates an iterative procedure to evaluate $\phi_p{}'$ from Q and B_q, an approximate NTH algorithm has been devised that allows a line-by-line analysis, easily handled by computer software or spreadsheets (Mayne 2005, 2016):

$$\phi_p{}' = 29.5°B_q^{0.121}\big(0.256 + 0.336B_q + \log(Q)\big) \tag{5.10}$$

that is applicable to soft to firm clays with OCR < 2.5 and for the following ranges of parameters: $20° \leq \phi_p{}' \leq 45°$ and $0.1 \leq B_q \leq 1.0$. ***Figure 5.17*** shows the close match between the theoretical and approximate inversion algorithm over the specified value ranges.

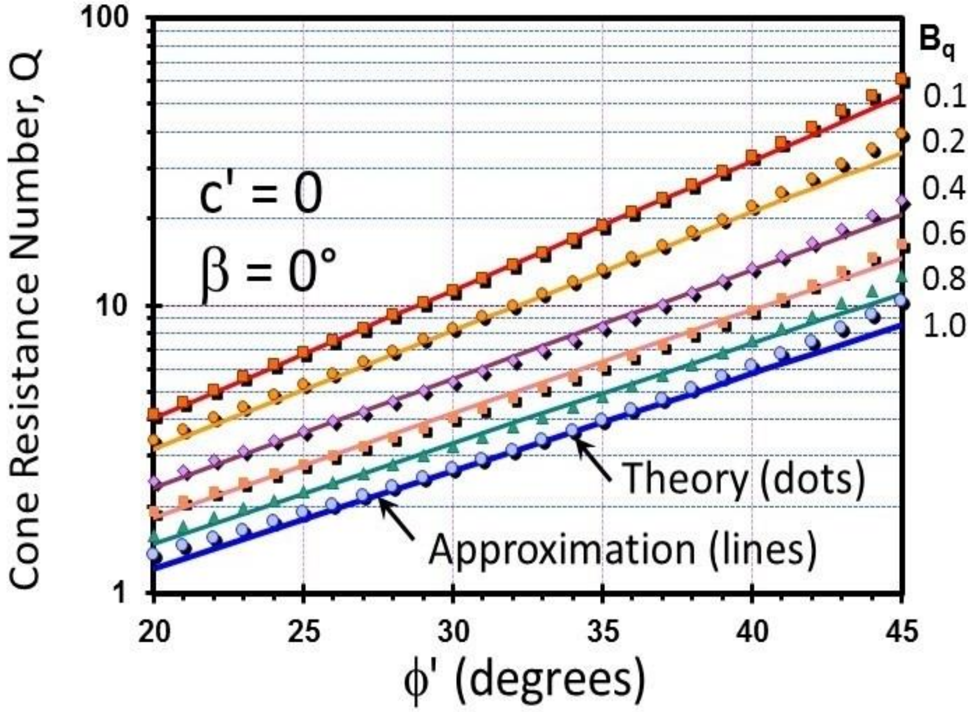

Figure 5.17: Theoretical and approximate NTH solutions for obtaining ϕ from CPTU in clays

5.2.3 Case Study: Soft Chicago Clay at Northwestern University

The national geotechnical experimental site (NGES) at Northwestern University (NWU) in Evanston, Illinois is underlain by a 10 m thick sand layer over 12 m of soft Chicago clay, as well as deeper stiffer layers. A variety of in-situ and laboratory tests have been conducted here to investigate the properties of the clay soils at this site (Finno et al. 2000). ***Figure 5.18*** shows a representative portion of a CPTU sounding in the soft clay layers (Deerfield and Bloggett formations) from 10 to 22 m depths with respective total cone resistance (q_t), sleeve friction (f_s) and porewater pressures (u_2) obtained using the Georgia Tech cone truck (Mayne 2007b). The soft clay under investigation has a mean unit weight of 20 kN/m^3, water content of around 20%, and plasticity index PI= 12%.

Series of CAUC triaxial tests (consolidated anisotropically undrained triaxial compression tests) were conducted on undisturbed samples of these soft clay tills (Chung and Finno 1992). The triaxial results are shown in a MIT q-p' stress space presented as ***Figure 5.19***. An effective stress strength envelope defined by c' = 0 and ϕ_p = 28.3° was determined. ***Figure 5.20*** shows the profiles of Q_{t1} and B_q with depth at the site and application of the approximate NTH solution giving a corresponding ϕ_p = 28.8° that is comparable with the CAUC tests.

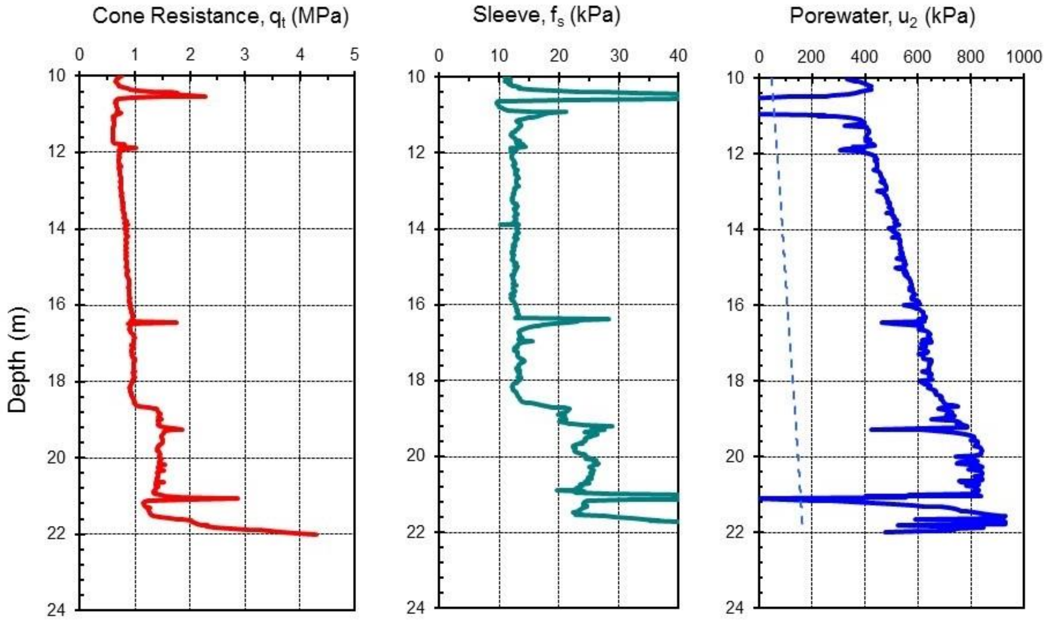

Figure 5.18: Representative CPTU in soft Chicago clay layer at Northwestern University

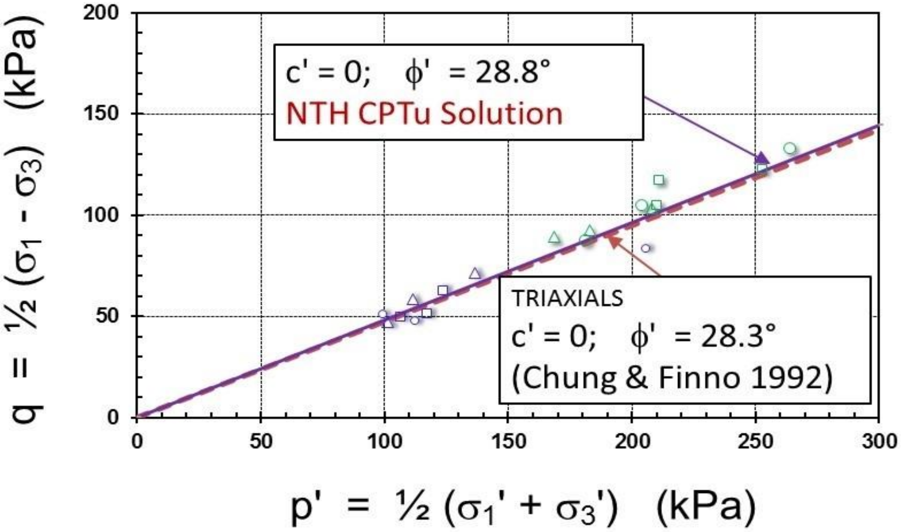

Figure 5.19: Summary of triaxial compression tests on soft Chicago clay from NWU (laboratory results from Chung and Finno 1992)

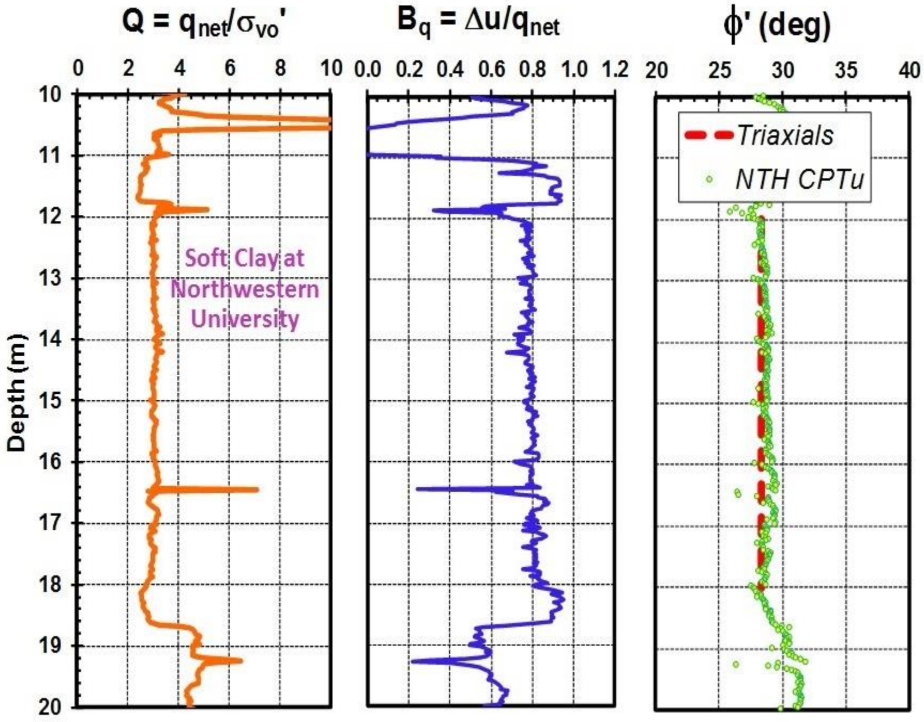

Figure 5.20: Profiles of Q and B_q with derived $\phi_p{}'$ profile in soft Chicago clay at NWU using approximate NTH solution

5.2.4 Case Study: Soft to Firm Clay at Newbury, MA

Boston Blue Clay (BBC) is a glacial marine deposit that exists in the greater Boston area due to deposition from glacial melt water (Landon 2007). At Newbury, Massachusetts, the BBC deposit consists of a 12 m thick clay layer with an overconsolidated crust and low OCRs in soft to firm clay at depth. The BBC at this site has an average water content of 45% and plasticity index PI = 24%. The groundwater table is located 1.7 m below ground level. Summary data from lab and in-situ tests are reported in Landon et al. (2004).

High-quality Sherbrooke block sampling and piston tube sampling were conducted at four depths at the site and trimmed specimens were subjected to laboratory testing to characterize soil parameters (Landon 2007). Beneath the crustal layer, a section of a representative CPTU sounding at the site from depths of 5 to 12 meters is shown in ***Figure 5.21***. The effective peak friction angle from piston and Sherbrooke samples at each of four sampling depths ranges from 35° to 37°, averaging about ϕ_p = 36.5°. The corresponding profile of triaxial ϕ_p is in good agreement with the approximate NTH evaluation using CPTU data.

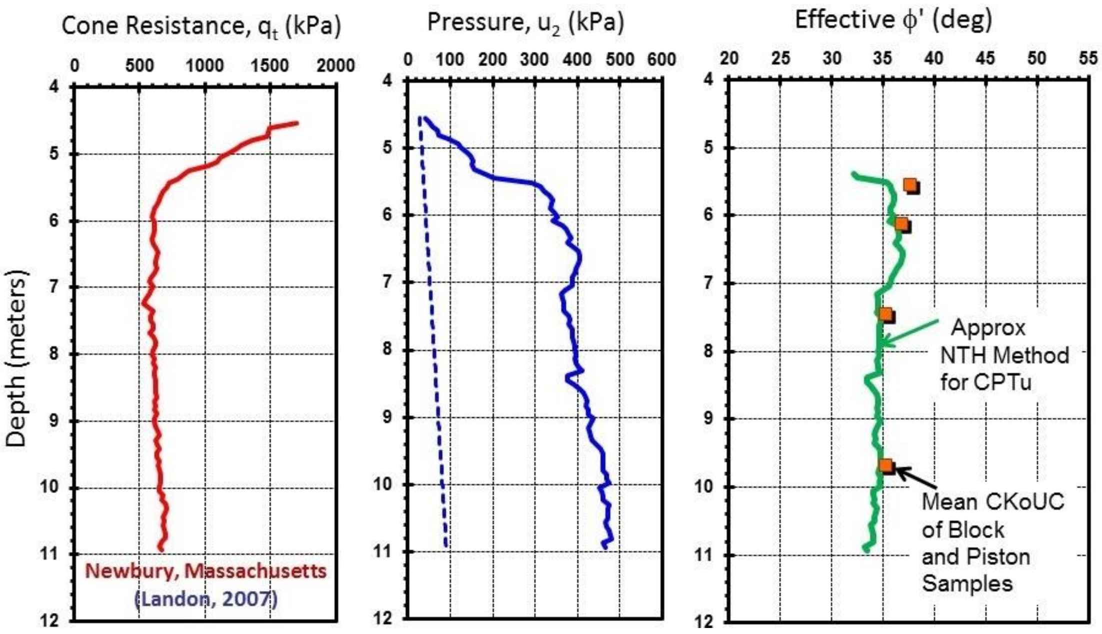

Figure 5.21: Representative CPTU and derived ϕ_p profile for clay at Newbury, MA site (laboratory and field data from Landon 2007)

5.2.5 Friction Angle Database in Clays

Based on a study of 17 clays by Diaz-Rodriguez, Leroueil, and Aleman (1992), the effective stress friction angle of natural clays ranges from 17° to 43°. ***Figure 5.22*** shows a summary plot of the peak friction angle of selected clays with their corresponding yield envelopes that are anchored by their friction angles and yield stress (σ'_p), or preconsolidation stress.

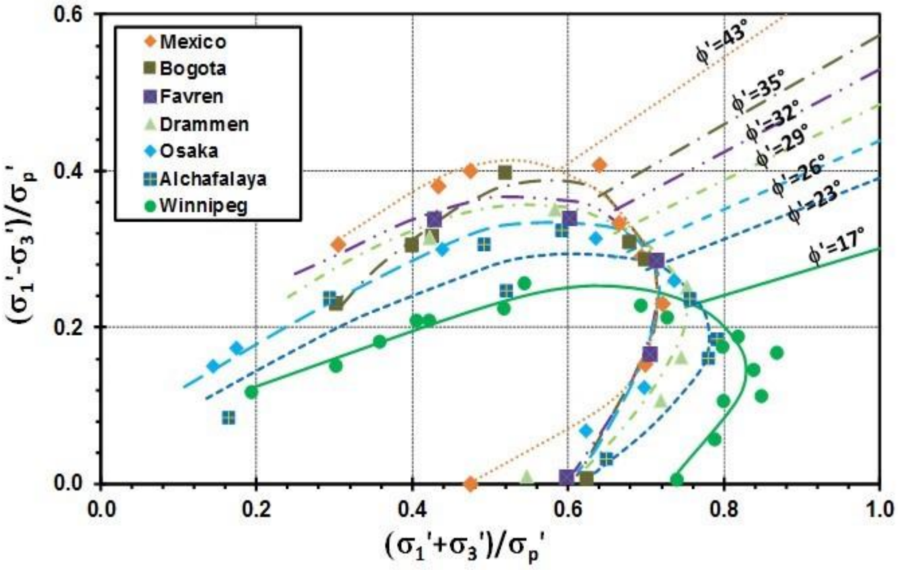

Figure 5.22: Yield surfaces and effective stress envelopes for selected clays (modified after Diaz-Rodriguez, Leroueil, and Aleman 1992)

For purposes of validating the NTH solution, a special database was compiled from 105 clay, silty clay, and clayey silt sites that were subjected to CPTU and laboratory triaxial compression tests (Ouyang and Mayne 2018). The majority of the sites were normally-consolidated (NC) to lightly-overconsolidated (LOC) with $1 < \text{OCRs} < 2.5$. Geologic origins of these soils vary from marine, alluvial, estuarine, glacial, and deltaic to lacustrine. The names of these sites are listed in ***Figure 5.23*** with a unique and individual symbol assigned to each location.

17th St Canal	Adriatic shelf	Agnesburg
Amazon River	Amherst	Anacostia NAS
Ariake	Athlone	Backebol
Ballina	Bangkok	Baton Rouge
Barra da Tijuca	Baytown	BBC Saugus
Belfast	Berthierville	Bogota
Bonneville	Bothkennar	Brent Cross
Broadback	Burswood	Busan
Can Tho	CF-Mining Hardee	Cooper River
Drammen	Eidsvoll	Fucino
Gloucester	Gotaleden	Grande-Baleine
Grandes-Bergeronnes	Gulf of Guinea	Gulf of Guinea1
Gulf of Guinea2b	Hachirogata	Haga
Hamilton AFB	Hilleren	Hong Kong
Houma	Kreuzlingen	Kurihama
Laminaria	La Baie	Les-Cedres
Lianyungang	Louiseville	Lower Pentre
Lower Troll	Luva	Madingley
Madison	Mark Clark Bridge	Marquette Interchange
Maskinonge	Massueville	Matagami
McDonald Farm	Mexico City	Newbury
Nice	Niger Delta	Norrkoping
North Charleston	NWU	Nykirke
offshore west Africa	Onsoy	Os
Osaka Bay	Patterson	Pernio
Pisa	Port-Cartier	Port Huron
Porto Tolle	Queensborough	Recife
Islais Creek	Sandpoint	Santa Cruz
Sarapui	Singapore	St. Alban
St. Hilaire	St. Hyacinthe	St. Jean Vianney
St. Jude	St. Monique	St. Polycarpe
St. Thuribe	Tanjung Bin	Taranto
Teg	Tiller	Tokyo Bay
Torp	Torpa	Upper Troll
Vagverket	Wauwill	Yorktown Formation
- - - 1:1 Line		

Figure 5.23: Summary listing of 105 clays tested both in laboratory triaxial compression and by field piezocone for validation of NTH solution

Plasticity characteristics of these fine-grained soils ranged widely from very lean to highly plastic ($4\% < \text{PI} < 113\%$) with mean PI = 38.9% ± 23.3%. Water contents ranged from 20 to 160% with a mean = 61.6% and S.D. = 31.2%. Triaxial friction angles from triaxial tests ranged from 20.2° to 45.1°, with a mean value $\phi_p{}' = 31.6° \pm 4.5°$. The NTH solution gave a mean value $\phi_p' = 32.2° \pm 4.4°$. Corresponding sensitivities generally were in the range of 2 to 8, indicating low to medium sensitive soils, except a few clays from Canada and Scandinavia that exhibited higher sensitivities.

For these clays, the effective stress friction angle ϕ_p' was obtained from laboratory triaxial tests (CIUC, CK$_0$UC, and/or CAUC) performed on undisturbed samples to establish the benchmark value. The triaxial friction angle can be evaluated on the basis of different criteria, including: (a) maximum deviator stress (q_{max}); (b) maximum obliquity, M.O. = $(\sigma_1'/\sigma_3')_{max}$; (c) value taken at large strains (e.g., ε = 15% axial strain). For the majority of the data, criteria (a) or (b) were used, although for many cases, the actual definition was not provided.

For many insensitive inorganic clays, the above criteria provide comparable values of ϕ'. For instance, CK$_0$UC triaxial tests on soft Atchafalaya clay gave ϕ' = 20.2° for q_{max} and 20.9° for M.O. (Donaghe & Townsend 1978). For soft Chicago clay, ϕ' = 28.3° at M.O. while at large strains, ϕ' = 27.6° (Finno & Chung 1992). These are small differences.

Figure 5.24 presents a summary plot for the measured laboratory triaxial test values of ϕ' versus the CPTU-determined values of ϕ' via the NTH solution. Two sets of statistical measures were made on the data set, including: (a) arithmetic statistics, and (b) regression statistics, as indicated on the figure. The measured laboratory values of ϕ_p' cover the full range from 20.2° to 45.0° and the CPTU-evaluated ϕ_p' from 22.9° to 46.8°. From the arithmetic measures, the ratio of measured/evaluated values ranges from 0.88 to 1.16 with an overall mean of 0.98 and

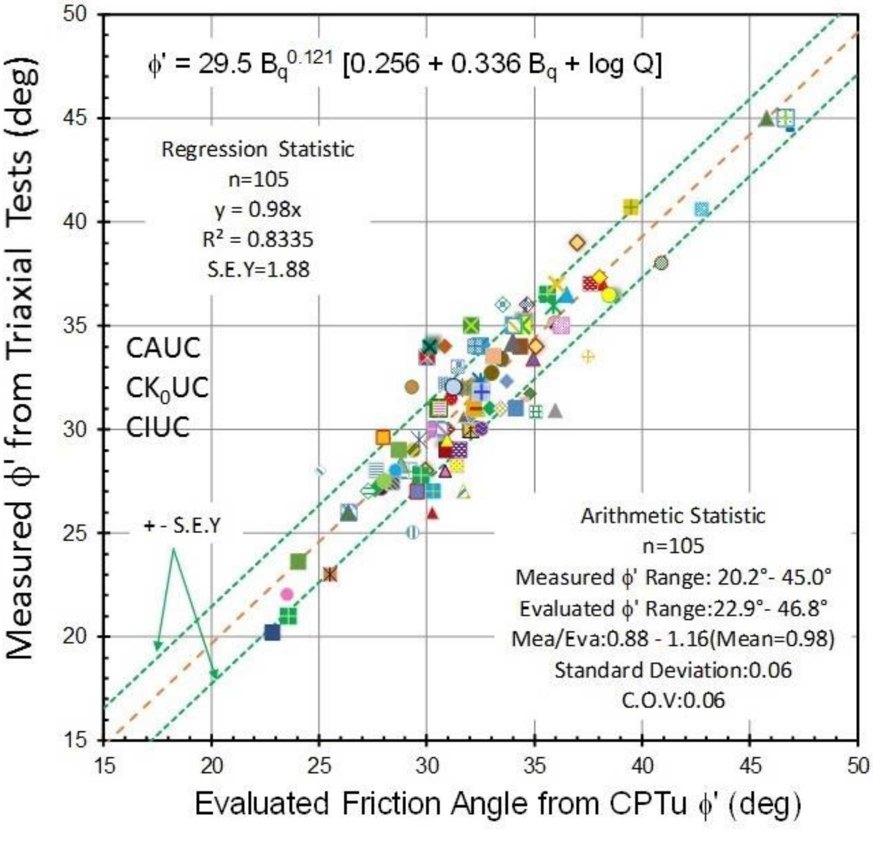

Figure 5.24: Triaxial ϕ' versus CPTU-evaluated value for 105 soft-firm clays with OCRs < 2.5 (Ouyang and Mayne 2018)

standard deviation = 0.06, with corresponding COV (coefficient of variation) = 0.06. From the regression evaluations of lab versus field, the regression slope = 0.98 with a coefficient of determination of r^2 = 0.833 and standard error of the Y-estimate of SEY = 1.88. The above statistics general support that the NTH method gives a reasonable evalution of the effective stress friction angle of clays when referenced to the lab triaxial test as the benchmark value.

5.3 Friction Angle of OC Intact Clays

For CPTU in overconsolidated intact clays, the same methodology applies, however the cone resistance number must be adjusted for stress history effects. For this, the modified cone resistance number (N_{mc}) becomes Q' defined as (Ouyang & Mayne 2019; 2020b):

$$Q' = Q/OCR^{\Lambda} \tag{5.11}$$

where OCR = σ_p'/σ_{vo}' = overconsolidation ratio and Λ = plastic volumetric strain ratio. Typical values of Λ range from 0.5 to 0.7 for artificially prepared samples of clay (i.e., kaolin and kaolinitic-sand mixtures) to around 0.8 ± 0.1 for inorganic and insensitive clays to as high as 1 for structured and sensitive soils.

For OC clays, the normalized porewater pressure parameter U = $\Delta u_2/\sigma_{vo}'$ (Section 3.2.5) is also affected by stress history and can be similarly adjusted:

$$U' = U/OCR^{\Lambda} \tag{5.12}$$

Otherwise, the same NTH solution given by rigorous equation (5.9) or the approximate algorithm (5.10) can be used to evaluate ϕ' using Q' and B_q. Note also that $U' = B_q \cdot Q'$.

5.3.1 Case Study: CPTU in OC Clay, Anchorage

Results of piezocone tests are utilized to illustrate the application of the modified NTH method for evaluating ϕ' in overconsolidated clay at the Port of Anchorage in Alaska. Extensive in-situ and laboratory testing programs have been conducted for the Port of Anchorage Expansion involving use of a SeaCore jack-up platform for conducting soil test borings, laboratory triaxial testing, one-dimensional consolidation, piezocone penetration tests, vane shear, and downhole shear wave velocities to characterize the subsurface profiles (Mayne & Pearce 2005).

Basic mean index parameters on this overconsolidated clay include: natural water content w_n = 20 to 31%, liquid limit LL = 45%, and plasticity index PI = 24%. From the consolidation testing, the mean value of virgin compression index C_c = 0.242 and swelling index C_s = 0.060, giving $\Lambda = 1 - C_s/C_c = 0.75$, which is reasonable for low to medium sensitive clays (Kulhawy & Mayne, 1990). ***Figure 5.25*** shows the profiles of q_t and u_2 from a representative piezocone sounding. Note that depth is measured from the water line and the seafloor begins at 12 m depth. Also a corresponding profile of the overconsolidation ratio (OCR) from the consolidation test data is shown. The OCRs decrease from 9 to 2 with depth in the intervals shown.

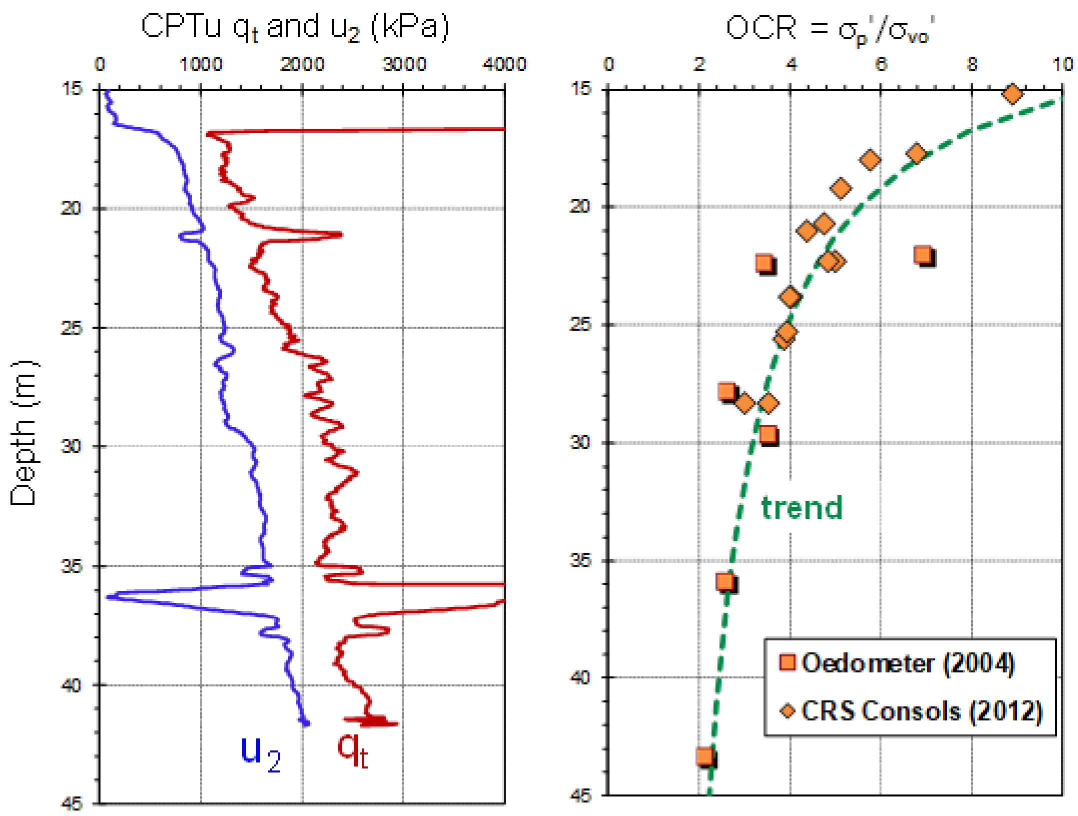

Figure 5.25: Representative profiles at Port of Anchorage, Alaska: (a) CPTU results; (b) overconsolidation ratio from lab consolidation tests (data from Mayne & Pearce 2005)

A series of 19 lab specimens were subjected to isotropically – consolidated type triaxial compression tests with porewater pressure measurements (CIUC). As shown by the effective stress paths in ***Figure 5.26***, the effective stress friction angle ϕ′ can be interpreted as ϕ′ = 28° with c′=0.

Following the procedure for determining both the original cone resistance number N_m = Q and the modified cone resistance N_{mc} = Q′ along with calculation of the normalized porewater pressure B_q, the effective stress friction angle ϕ′ profiles calculated using the CPTU data are presented in ***Figure 5.27***. It can be observed that the original NTH solution generates an unrealistically high friction angle profile (> 42°) whereas the friction angle interpreted using modified NTH solution gives excellent agreement with the corresponding friction angle determined from the laboratory triaxial compression tests at corresponding elevations, more or less centered about ϕ′ ≈ 28°.

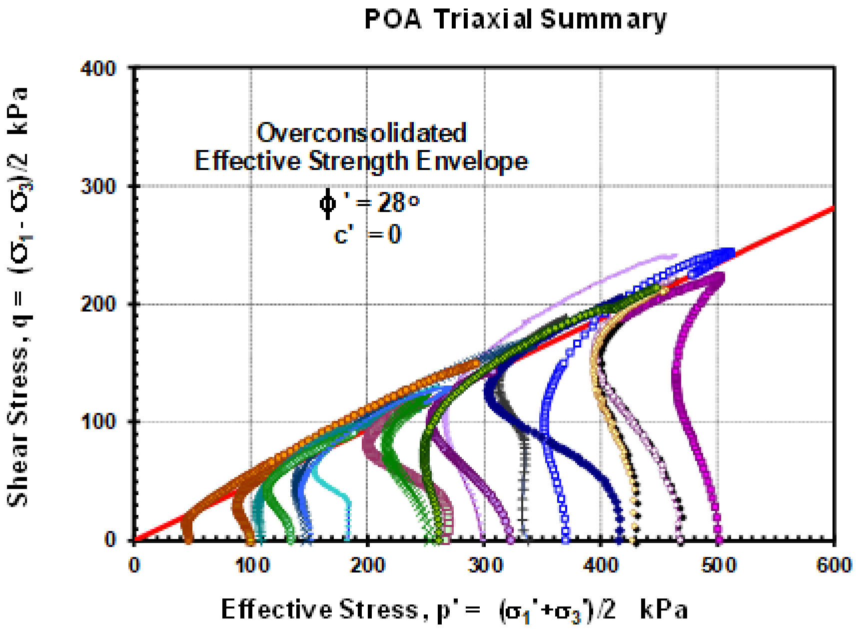

Figure 5.26: Summary of CIUC triaxials on overconsolidated clay at Port of Anchorage (data from Mayne & Pearce 2005)

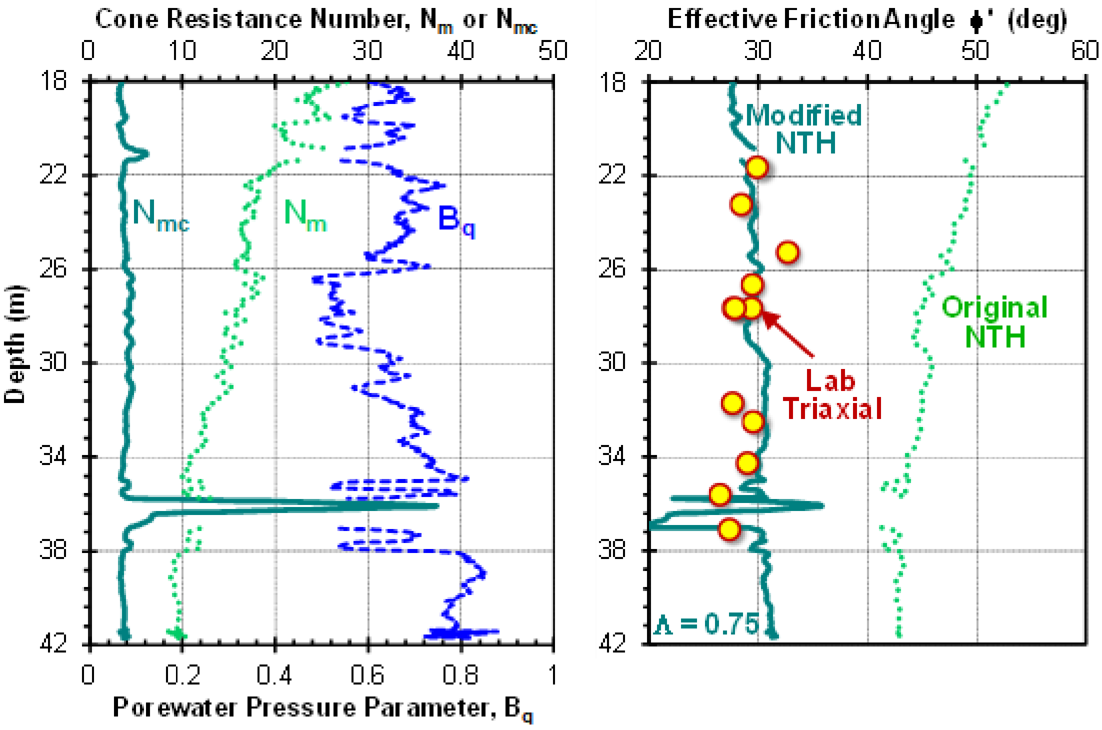

Figure 5.27: Profiles at Anchorage: (a) normalized CPTU parameters; (b) interpreted φ' from triaxial tests and CPTU using modified NTH solution

5.4 Friction Angle of OC Fissured Clays by CPTU

Piezocone tests in fissured overconsolidated clays typically exhibit porewater pressure responses that are close to zero, thus $B_q \approx 0$. Thus, the rigorous equation 5.9 can be used for the case $B_q = 0$ by replacing Q with $Q' = Q/OCR^{\Lambda}$ and solving for ϕ' by iteration. Otherwise, an approximate inversion can be made for the case where $B_q = 0$ which is given by (Ouyang & Mayne 2019):

$$\phi' \approx 8.18 \cdot \ln_e (2.13 \cdot Q') \tag{5.13}$$

5.4.1 Case Study: CPTU in Fissured Beaumont Clay

The well-known Beaumont clay of Texas is a desiccated overconsolidated deltaic clay of Pleistocene age. These soils have shrink-swell problems with shallow foundation performance and rather extensive series of discontinuities and cracks. A representative CPTU sounding at a research tests site in Baytown Texas is shown in ***Figure 5.28*** (Stuedlein 2008). The low u_2 readings are indicative of fissured OC clays.

Series of CIUC triaxial tests on undisturbed samples from the site indicated an effective stress envelope that can be represented by: $\phi' = 24°$ and $c' = 0$, as presented in ***Figure 5.29***. A series of one-dimensional consolidation tests were also conducted, showing the σ_p' profile given in ***Figure 5.30(a)***. If consolidation tests had been unavailable, it can be seen that a quick estimate using the approximate expression $\sigma_p' \approx 0.33 q_{net}$ gives reasonable values for the Baytown site. Using the modified profile of $N_{mc} = Q'$ based on a value $\Lambda = 0.7$, it is evident that (5.13) provides values of ϕ' which are comparable to triaxial compression tests at the Baytown site.

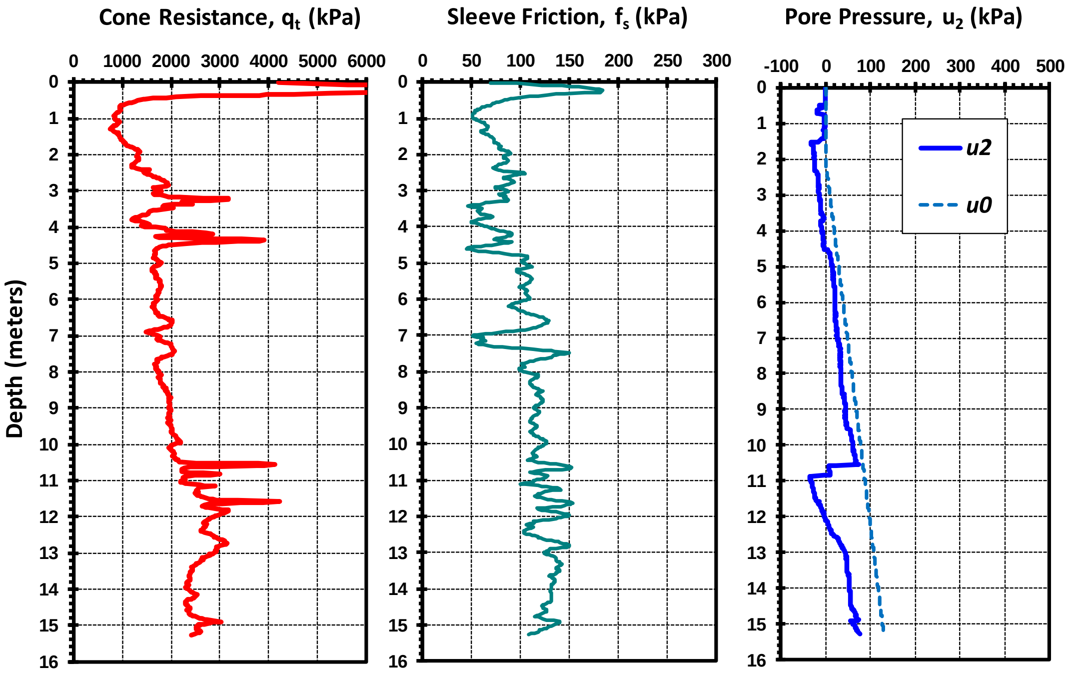

Figure 5.28: Representative CPTU sounding in fissured OC clay at Baytown, Texas

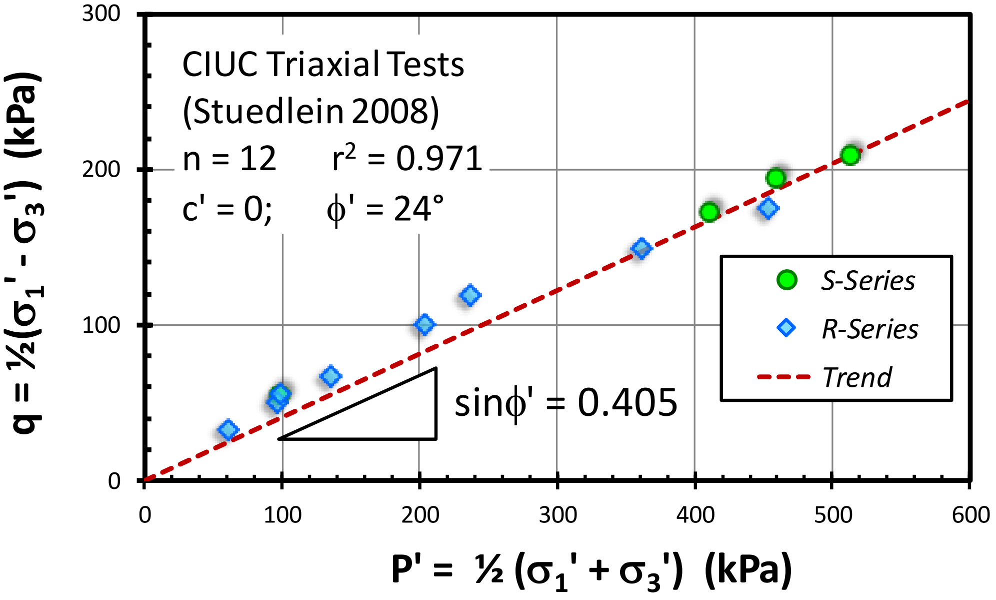

Figure 5.29: Results of CIUC stress paths for fissured OC clay at Baytown

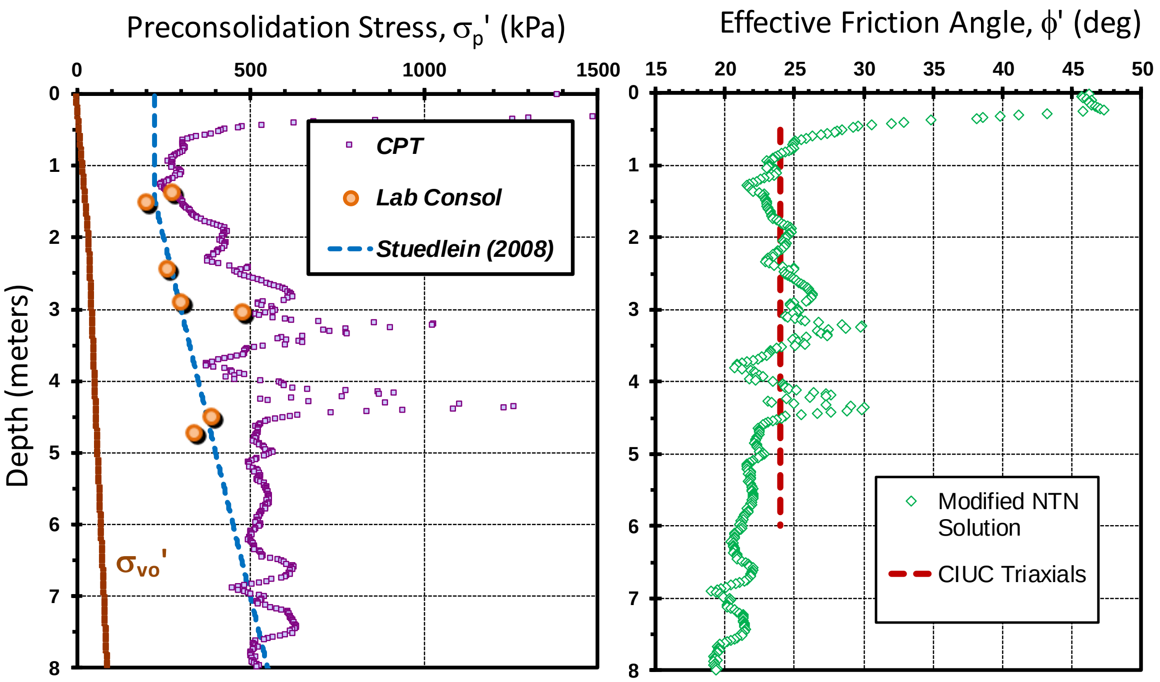

Figure 5.30: Profiles in fissured Beaumont clay at Baytown, TX:
(a) preconsolidation stress; (b) effective friction angle

5.5 Summary of NTH Solutions for NC and OC Clays

In addition to the 105 soft to firm NC to LOC natural clays shown in ***Figures 5.23*** and ***5.24***, the NTH solutions have been applied to piezocone tests in laboratory chamber tests, centrifuge deposits of clay, plus a number of OC intact and fissured clays, as well as VRCPTU, or variable rate piezocone tests (Ouyang & Mayne 2020a). ***Figure 5.31*** shows the full set of some 155 clays that have been tested by both triaxial compression tests in comparison to the original and modified NTH solutions for assessing ϕ' from CPTU. A similar set of arithmetic and regression statistics are shown on the graph, comparable to the discussion in Section 5.2.5.

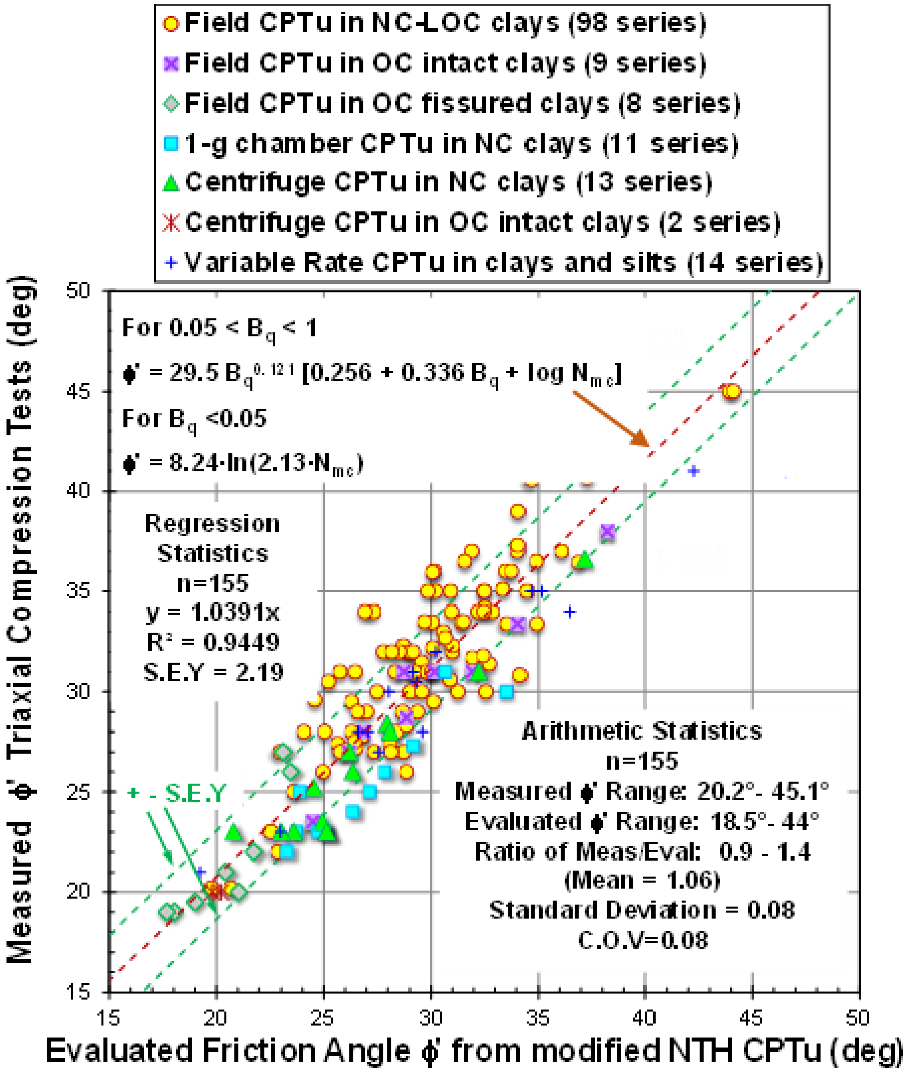

Figure 5.31: Effective friction angle of clays from triaxial compression testing versus value from CPTU using NTH solutions. (modified after Ouyang & Mayne 2020a)

5.6 Effective Cohesion Intercept, c’

Herein, the effective cohesion intercept has been taken as zero (c’ = 0) since the vast majority of soils considered are NC to LOC with low OCRs. Technically, a value of c’ > 0 implies tensile strength which the majority of sands and clays do not have. Notably, c’ = 0 is a common assumption for soft to firm clays with OCRs < 2. Nevertheless, some stability analyses involving natural slopes, excavations, and soil nail walls require an assessment of c’ for limit equilibrium and/or finite element studies. Also, overconsolidated soils may show an apparent cohesion intercept and friction angle.

Guidance on the selection and magnitude of c’ can be found in a few other sources. Mayne & Stewart (1988) review data from CIUC and CAUC triaxial data on 16 different NC to OC clays and conclude that the effective cohesion intercept relates to the effective preconsolidation stress, expressed as the ratio c'/σ_p' (Mayne 2016):

$$c'/\sigma'_p \approx 0.03 \tag{5.14}$$

Additional details concerning c’ values from backfigured stability analyses of 60 case study slope failures are discussed by Mesri & Abdel-Ghaffar (1993) who found that the ratio of effective cohesion intercept to yield stress fell within the following range: $0.003 < c'/\sigma_p' < 0.11$.

Of additional note, a means of extracting c’ directly from the CPTU data is also viable from the NTH solution (Senneset et al. 1989; Sandven 1990; Mayne 2016).

5.7 Effective Friction Angle(s) of Sensitive Clays

In the case of sensitive and quick clays, an analytical model for YSR presented in Chapter 4 utilizes two definitions of ϕ': (1) value at q_{max}, designated ϕ'_1; and (2) value at M.O. = $(\sigma_1'/\sigma_3')_{max}$, designated ϕ'_2. Specifically, the stress-strain-strength behavior of sensitive clays shows a peak deviator stress early, with strains on the order of $\varepsilon \approx 1\%$, while the porewater pressure versus strain curve reaching a maximum value much later on, say $\varepsilon \approx 10\%$ or more. Analogous to the triaxial test, the CPTU can associate the cone resistance (q_t) to ϕ'_1 and the porewater pressure reading (u_2) to the ϕ'_2 value.

To obtain both values of ϕ' from CPTU, the following can be recommended: (a) use of the original NTH solution with Q and B_q provides ϕ'_2; (b) implementation of the modified NTH solution with Q’ and B_q gives the value of ϕ'_1. Case studies that utilize the original and modified NTH solutions for obtaining ϕ'_2 and ϕ'_1, respectively, are given for sensitive clay sites in Canada (Agaiby & Mayne 2018a; Mayne, Greig, & Agaiby 2018), Norway (Mayne et al. 2019), Finland (DiBuö et al. 2019), and the USA (Mayne & Benoît 2020).

In fact, the ratio of ϕ'_1/ϕ'_2 is shown to track with slope parameter a_q = (U-1)/Q that is described earlier in Section 4.4.5 (DiBuö et al. 2019). ***Figure 5.32*** shows a summary of data from 8 regular and 14 sensitive natural clay deposits, as well as 4 artificial kaolinitic clays. The data indicate sensitive clays can be identified when $a_q > 0.5$.

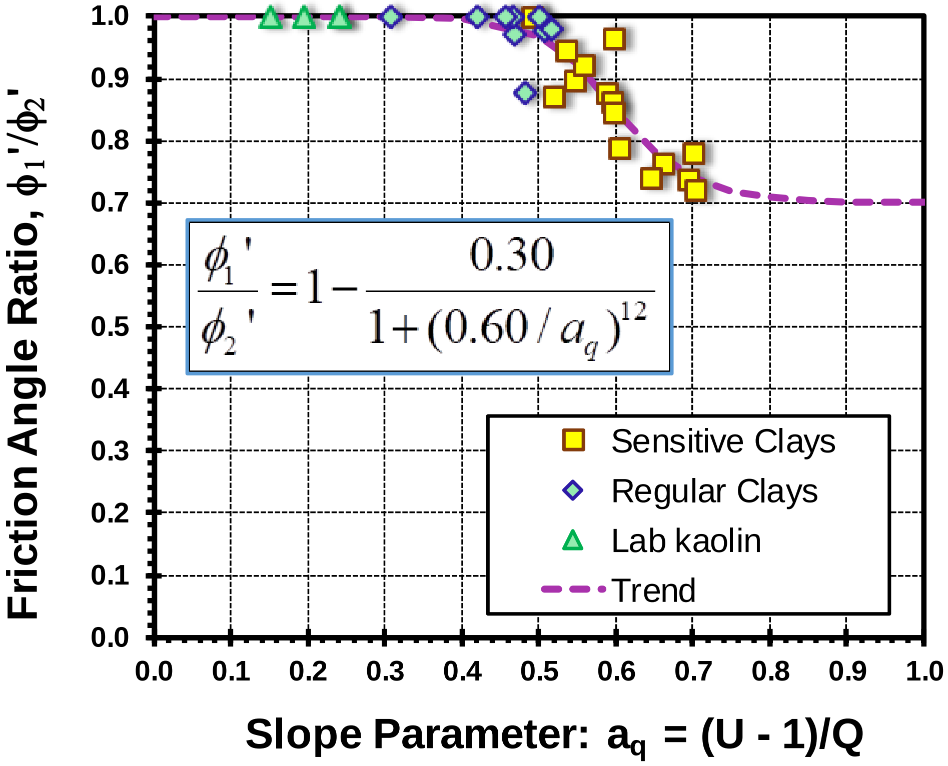

Figure 5.32: Observed trend for ratio ϕ'_1/ϕ'_2 with slope parameter a_q for 26 clays

5.8 Peak versus Fully-Softened versus Residual Strength

The aforementioned discussions on strength reflect test results on soils where the peak strength or softened strength are relevant. The peak strength can be associated to OC clays and the fully-softened strength related to NC clays. In the case of clays involved in landslides and slope instability problems, the residual strength may be appropriate, especially if the clays have slickensides and fissures (Holtz, et al. 2011).

The residual shear strength can be represented by $\tau_{residual}$ given by (Lupini et al. 1981; Holtz, Kovacs, & Sheahan 2011):

$$\tau_{residual} = c'_{residual} + \sigma' \cdot \tan\phi'_{residual} \tag{5.15}$$

Some additional guidance may be found in Stark & Eid (1994, 1997) and Stark & Hussein (2013).

6 Undrained Shear Strength

When loading of soils results in a maintained constant volume of the soil mass ($\Delta V/V_0 = 0$), an undrained shearing mode occurs. This is most often associated with clays because they have low permeability and the rate of loading is usually high, such that water cannot escape the very tiny pores in the clay matrix, at least not immediately. Thus, a time-rate behavior occurs and a consolidation process begins that may take several hours, days, or even years for completion.

In the soils laboratory, the triaxial apparatus is common and the resulting stress-strain-strength response is depicted in ***Figure 6.1***. In terms of deviator stress (σ_1-σ_3) versus axial strain, the undrained shear strength (s_u or c_u) is conventionally defined as one-half the deviator stress at peak. However, other definitions are also found in use, such as maximum obliquity, $(\sigma_1'/\sigma_3')_{max}$ (Abdulhadi, Germaine, and Whittle 2012), as well as large-strains, fully-softened behavior, and sometimes taken at a set specified strain, such as 15%.

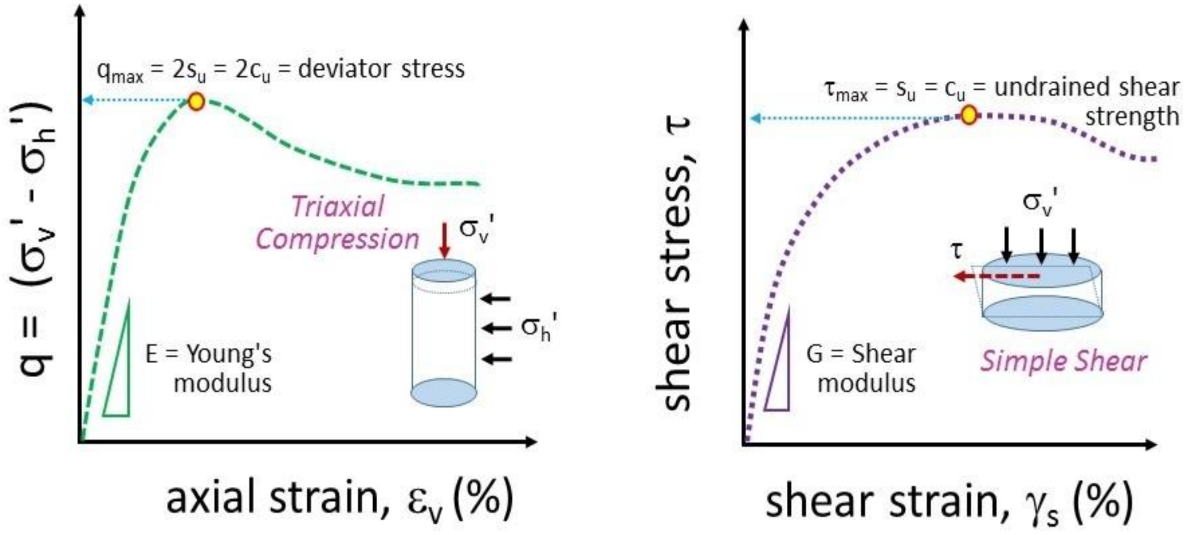

Figure 6.1: Conventional laboratory definition of undrained shear strength at peak stress: (a) triaxial compression; (b) simple shear

Figure 6.1 also shows the corresponding definition of s_u at peak value for the simple shear mode. In this case, direct simple shear (DSS) produces curves of shear stress (τ) versus shear strain (γ_s). The maximum value of shear stress (τ_{max}) is termed the shear strength. If the test is conducted at constant volume, then the measured value is the undrained shear strength ($\tau_{max} = s_u = c_u$).

Note that if volume change is permitted, however, the τ_{max} will represent a different condition. For instance, if no excess porewater pressures occur ($\Delta u = 0$), then the resulting shear strength would be the drained shear strength ($\tau_{max} = \tau_d$). Intermediate shear strengths between fully undrained and fully drained are also possible.

6.1 Mode of Shearing and Strength Anisotropy

The undrained shear strength is not a unique value for a given soil deposit, but depends upon the type of test mode, direction of loading, strain rate, initial stress state, and other factors (Kulhawy and Mayne 1990; Karlsrud et al. 2005). This creates difficulties when trying to assess a representative s_u in clays, as the user will already have selected a bias towards his or her choice of reference test for s_u, such as triaxial or vane shear or unconfined compression.

For any clay, there will actually be a family of s_u profiles. For example, various sets of undrained shear strengths measurements for the well-documented Bothkennar national test site in the UK will be used to illustrate the dilemma. Bothkennar is underlain by up to 30 m of soft clay and has been subjected to all types of in-situ and laboratory tests by a large number of universities, testing firms, and research organizations (Hight et al. 2003). ***Figure 6.2*** shows results from laboratory series of test, including: triaxial compression (CK_0UC), direct simple shear (DSS), and triaxial extension tests (CK_0UE) on undisturbed samples (Hight et al. 2003), as well as in-situ pressuremeter tests (SBPMT) and field vane shear tests (FV). Also shown is the backcalculated su value from a 2.2-m square footing that was load tested to failure at the site and analysed via limit plasticity solutions for bearing capacity. At any given depth, these s_u values range up to a factor of six, depending upon the particular test mode under consideration. The differences are not due to site variability but occur because of the soil behavioral aspects of s_u and its nuances.

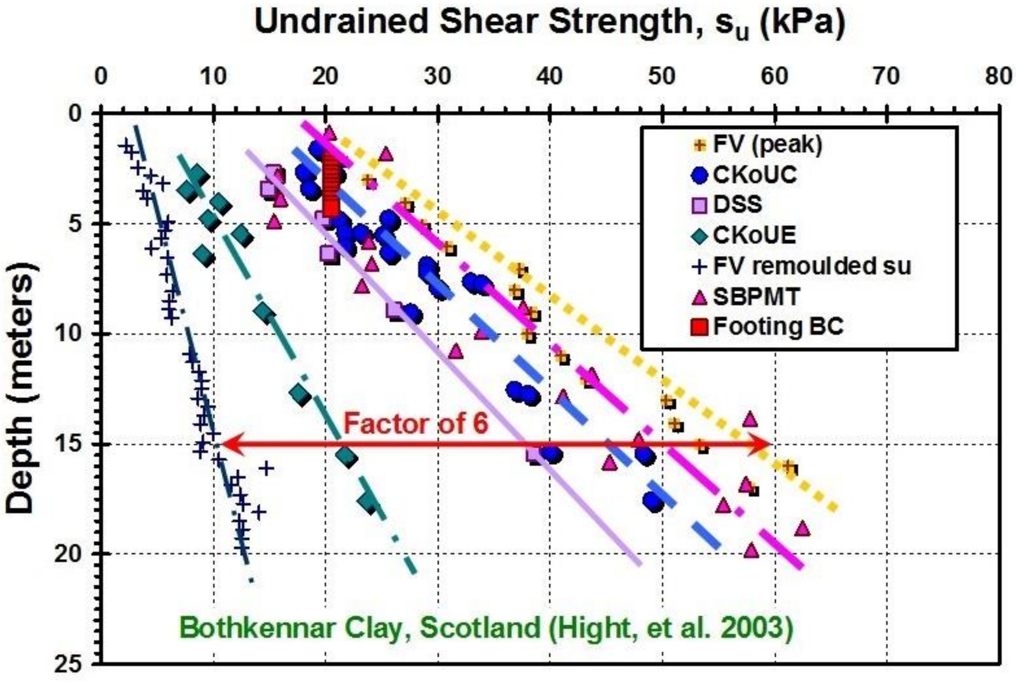

Figure 6.2: Various profiles of undrained shear strengths from different laboratory and field methods in Bothkennar soft clay, UK

Similar wide ranges and variances in s_u profiles can be observed for other clays, such as the well-known Boston Blue Clay (see ***Table 6.1***). Here, the listed values of undrained shear strengths are reported in terms of the normalized strength ratio: S = $(s_u/\sigma'_{v0})_{NC}$ which correspond to normally-consolidated conditions (OCR = 1). ***Table 6.1*** shows results varying from a low value of 0.14 for unconfined compression (UC) testing to a high value of S = 0.42 for pressuremeter tests (PMT) on the same clay. This non-uniqueness of s_u must be addressed if a clear and consistent framework is to be adopted by the geotechnical community in practice.

Table 6.1: Undrained strength ratios (S) for normally-consolidated Boston Blue Clay (data from Ladd et al. 1980; Ladd 1991; Whittle et al. 1994)

Shearing Mode	**S = $(s_u/\sigma'_{v0})_{NC}$**
Self-boring pressuremeter test (SBPMT)	0.42
Plane strain compression (PSC)	0.34
Triaxial compression (CK_0UC)	0.33
Unconsolidated Undrained (UU)	0.275
Field vane shear test (VST)	0.21
Direct simple shear (DSS)	0.20
Plane strain extension (PSE)	0.19
Triaxial extension (CK_0UE)	0.16
Unconfined compression (UC)	0.14

6.2 Undrained Strength from Stress History

One means to evaluating s_u in clays by piezocone involves the utilization of stress history (i.e., OCR or YSR) of the clay deposit to profile a family of undrained strength ratios:

$$\left(\frac{s_u}{\sigma'_{v0}}\right) = S \cdot OCR^m \tag{6.1}$$

where the coefficient S and exponent m can be found using either the MIT SHANSEP (stress history and normalized soil engineering parameters) approach, or CSSM (critical state soil mechanics).

In the SHANSEP approach (Ladd 1991; Ladd and DeGroot 2003), the value of S = $(s_u/\sigma'_{v0})_{NC}$ is experimentally found in the laboratory by extensive testing for large projects, with companion series of plane strain compression (PSC), simple shear (SS), and plane strain extension (PSE) tests on the soils at varied OCRs for embankments and long aligned structures, else series of triaxial compression (TC), simple shear (SS), and triaxial extension (TE) tests for axi-symmetric type loadings (e.g., footings, mats). Otherwise, on small projects, the values of S are estimated from empirical relationships. The exponent m can be determined experimentally and has been generally found to be on the order of 0.8 ± 0.1. The value of S has been slightly related to plasticity index of the clay and ***Figure 6.3*** shows three modes: TC, DSS, and TE.

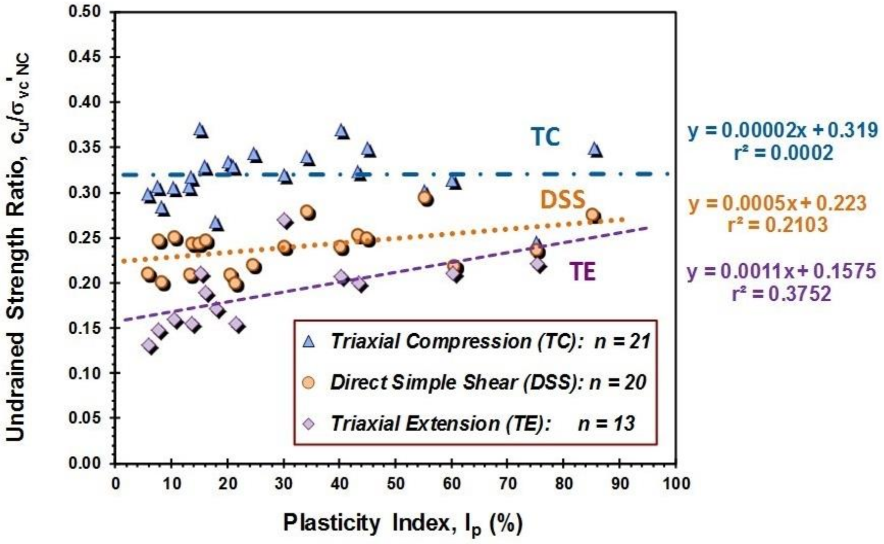

Figure 6.3: Empirical values of S for triaxial compression, simple shear, and triaxial extension (after Jamiolkowski et al. 1985; Ladd 1991)

A more fundamental avenue is afforded through critical-state soil mechanics (CSSM), however, this considers only stress-induced anisotropy effects and does not include the influences of inherent or fabric type anisotropy. In this case, a constitutive soil model provides the hierarchy of the strength modes (i.e., S values), such as presented for the Wroth-Prevost formulation given in ***Figure 6.4***. Note that the equations for "S" modes are given in Kulhawy & Mayne (1990). Thus, a rational evaluation of s_u by piezocone tests in clay is accomplished in a two-step procedure: (a) evaluation of OCR profile using the aforementioned relationships between yield stress σ'_p and (q_t-σ_{v0}), Δu_2, and/or (q_t-u_2); (b) use of ***Equation 6.1*** and selected S values to obtain a complementary suite of s_u profiles.

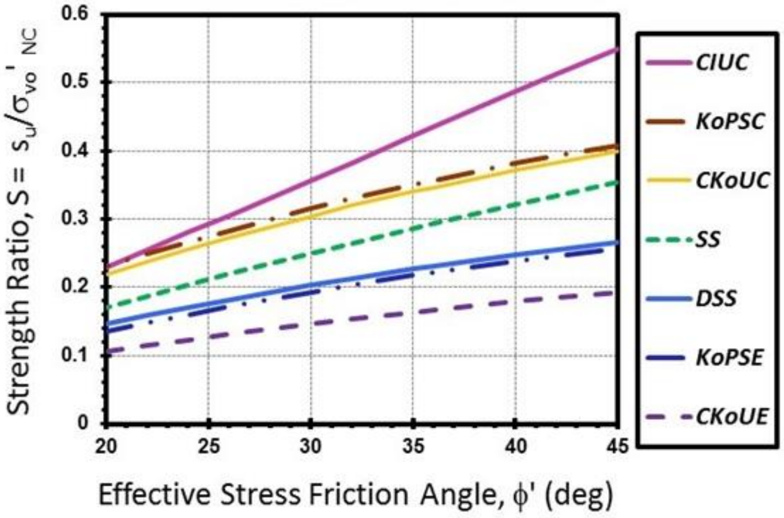

Figure 6.4: Evaluation of normally-consolidated strength ratios (S) of clays for different modes using Wroth-Prevost constitutive soil model (after Kulhawy and Mayne 1990)

In CSSM, the exponent m is derived from theoretical considerations and thus, m = $\Lambda \approx 1 - C_S/C_C$ where C_S = swelling index and C_C = compression index, however, the operational value is assigned more so on the basis of strength data (Mayne 1980):

$$\Lambda = \frac{\Delta \log(s_u / \sigma_{vo}')}{\Delta \log(OCR)} \tag{6.2}$$

Often, Λ is taken to be 0.8 for many inorganic and insensitive "regular" clays (e.g., Kulhawy and Mayne 1990; Karlsrud and Hernandez-Martinez 2013) while $\Lambda \approx 1$ will be appropriate for structured and highly sensitive to quick clays.

The effect of OCR on the normalized undrained strength is essentially similar for all modes, as illustrated by ***Figure 6.5***. Here data from a plastic clay from offshore New Jersey (named AGS for "Atlantic Generating Station") were obtained from laboratory tests using 5 different modes: PSC, TC, DSS, PSE, and TE, with very similar m (i.e., Λ) values, ranging from 0.72 to 0.86, and averaging 0.80 ± 0.06 (Koutsoftas & Ladd 1985).

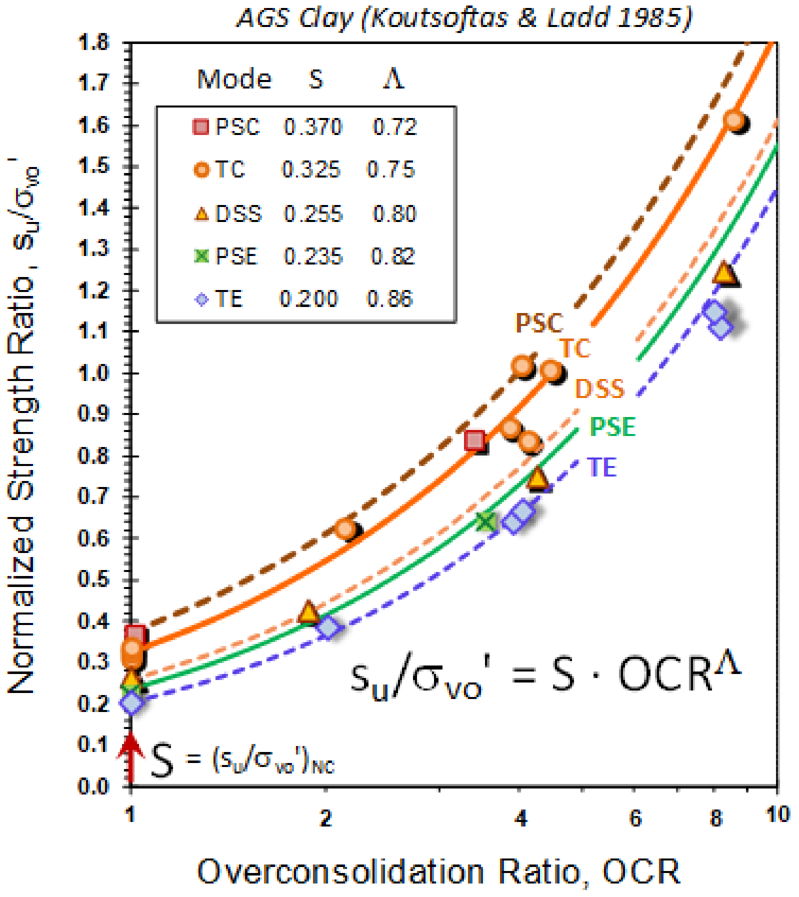

Figure 6.5: Effect of OCR on normalized strength of offshore AGS clay tested under five modes (data from Koutsoftas and Ladd 1985)

In the event that consolidation data or triaxial results are unavailable for a particular clay deposit, ***Table 6.2*** provides a recommended range of exponent values for m = Λ to use for several situations and clay types (Ladd & DeGroot 2003; Ouyang & Mayne 2019).

Table 6.2. Recommended values of exponent term m = Λ for selected clay soils

Soil Type	**Recommended value of Λ**	**Notes and Remarks**
Compacted or Remolded clay; Artificial clay deposits	0.5 to 0.7	Examples include kaolin, Weald clay
Clay deposits from slurry or water sedimentation	0.75	kaolinitic-sand or kaolin-silica mixtures
Natural Clays Regular intact Clays	0.80 ± 0.10	Mode-dependent: triaxial compression (Λ = 0.7), simple shear (Λ = 0.8), triaxial extension (Λ = 0.9)
Natural sensitive and structured clays	0.90 to 1.0	e.g. Champlain Sea clays, Presumpscot clay

The CSSM and SHANSEP procedures allow for a distinct and separate evaluation of each of the various strength modes, therefore helping to sort out the confusion and scatter normally found in s_u plots. The role of the in-situ testing therefore becomes focused on the assessment of the stress history profile, uniquely defined in terms of the effective preconsolidation stress (σ'_p).

If the geotechnical problem has not yet been fully established, then the simple shear (SS) mode is probably a wise value to choose. The SS represents a middle representative value amongst the compression, shear, and extension modes. In the SS, pure shear is applied to the specimens, whereas in several available commercial systems, a direct simple shear (DSS) mode is a close approximation but does not provide the complementary shear stresses on top, bottom, and sides. For OCR=1, the corresponding S_{DSS} = $(s_u/\sigma'_{v0})_{NC[SS]}$ = ½sinϕ (Wroth 1984). Combining terms, the general expression for the undrained shear strength corresponding to the DSS and SS modes for intact clays over a range of overconsolidation ratios is given by (Wroth and Houlsby 1985):

$$\left(\frac{s_u}{\sigma'_{v0}}\right)_{OC[SS]} = \frac{1}{2}(\sin\phi_{cs})OCR^{\Lambda} \tag{6.3}$$

as presented in ***Figure 6.6***. If uncertain about the input parameters, characteristic values may be adopted: ϕ = 28° and Λ = 0.80. This would give (Ladd and DeGroot 2003):

$$\left(\frac{s_u}{\sigma'_{v0}}\right)_{OC[SS]} = 0.22\ OCR^{\Lambda} \tag{6.4}$$

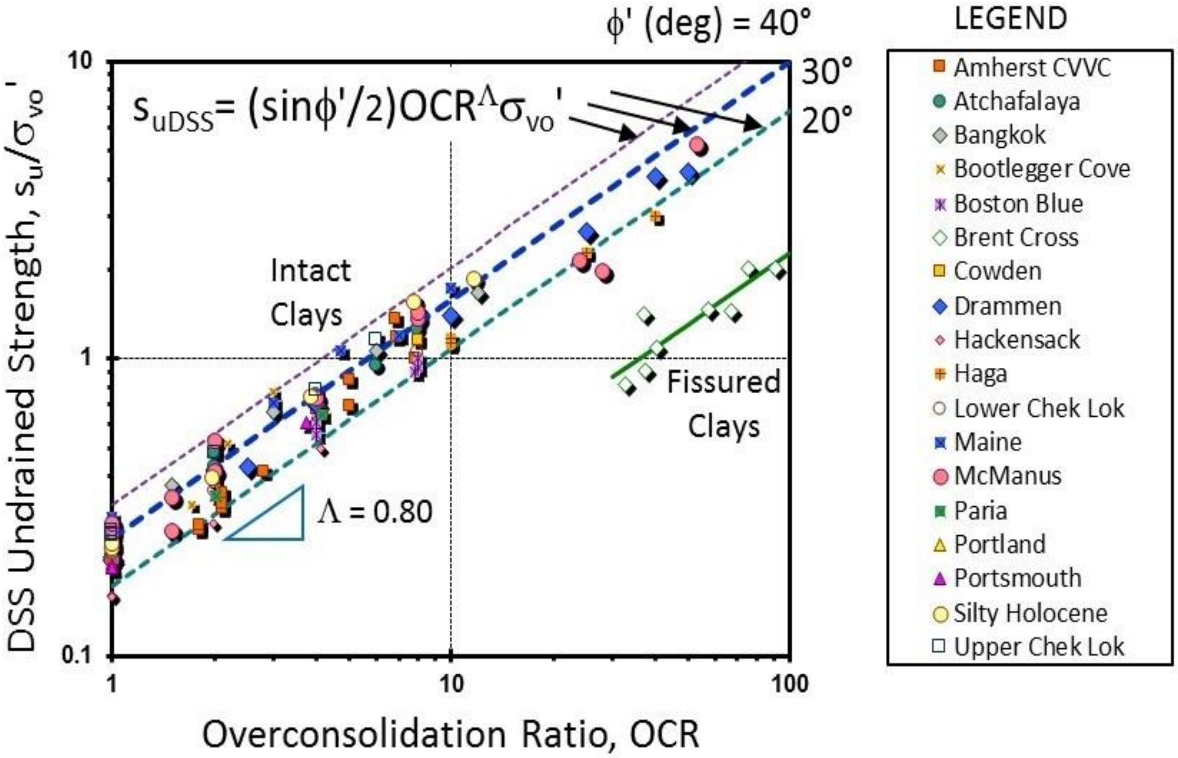

Figure 6.6: Measured and calculated undrained strength ratio with OCR for simple shear mode on normally-consolidated to overconsolidated clays (Mayne 2007a)

In the case of soft lightly-overconsolidated (LOC) to normally-consolidated (NC) clays and clayey silts where OCRs < 2, the expression can deconvolute to the following simple form:

$$s_u \approx 0.22\sigma'_p \tag{6.5}$$

which was surprisingly developed independently by Mesri (1989) by re-analysis of the backcalculated database of case history failures of embankments, footings, and excavations on soft clays that were tested using field vanes.

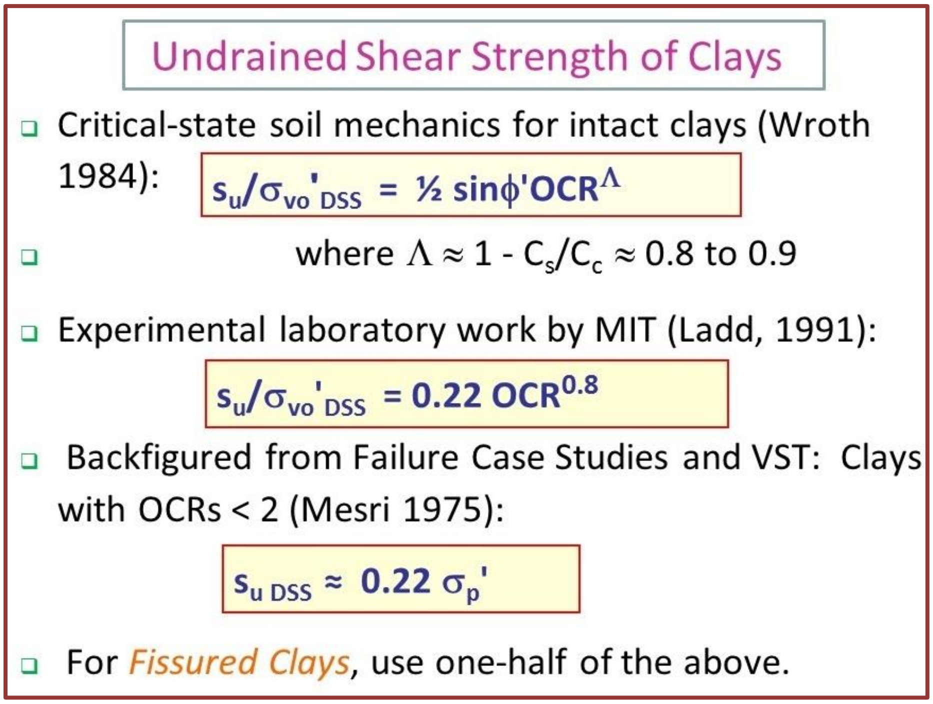

Undrained Shear Strength of Clays

- Critical-state soil mechanics for intact clays (Wroth 1984): $s_u/\sigma_{vo}'_{DSS} = ½ \sin\phi' OCR^{\Lambda}$
- where $\Lambda \approx 1 - C_s/C_c \approx 0.8$ to 0.9
- Experimental laboratory work by MIT (Ladd, 1991): $s_u/\sigma_{vo}'_{DSS} = 0.22\ OCR^{0.8}$
- Backfigured from Failure Case Studies and VST: Clays with OCRs < 2 (Mesri 1975): $s_{u\ DSS} \approx 0.22\ \sigma_p'$
- For *Fissured Clays*, use one-half of the above.

Figure 6.7: Recommended hierarchy of methods using stress history to evaluate s_{uDSS} in clays

In summary, ***Figure 6.7*** shows the hierarchy approach to a consistent interpretation of a representative "average" undrained shear strength for clays and clayey silts, more or less consistent with the simple shear mode (Mayne 2008).

For fissured clays, the calculated undrained strengths should be reduced to one-half of those for intact geomaterials because of the additional planes of weakness offered by the presence of cracks, joints, and discontinuities in the clay matrix.

For the triaxial compression mode, CSSM provides the following evaluation of the undrained shear strength ratio:

$$\frac{s_{uc}}{\sigma_{vo}'} = \left(\frac{M_c}{2}\right)\cdot\left(\frac{OCR}{2}\right)^{\Lambda} \tag{6.6}$$

Figure 6.8 shows a summary of CIUC data on 58 different clays tested over a wide range of OCRs, more or less confirming the validity of CSSM in a general assessment of undrained shear strength. Note that organic soils generally show higher values of ϕ' and s_u/σ_{vo}' than inorganic clays (Edil & Wang 2000). Furthermore, sensitive and structured clays will often show brittle behavior and significant strain softening, if properly sampled, and thus strong consideration and prudent judgment should be utilized when analyzing and designing in these types of geomaterials.

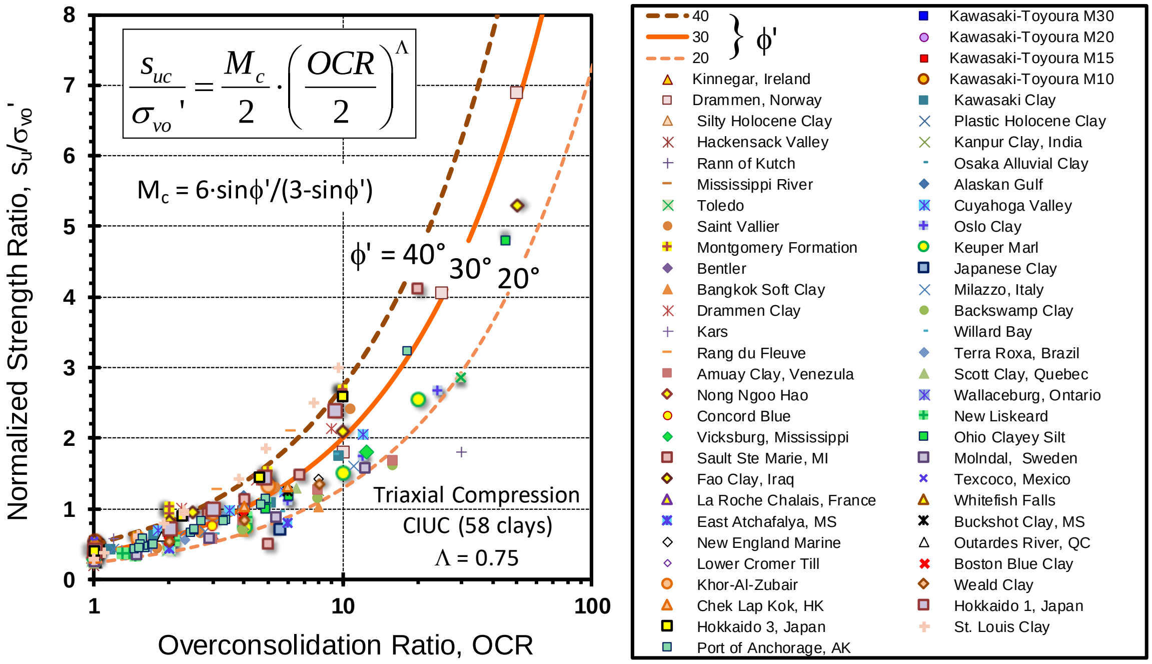

Figure 6.8: Undrained shear strength summary of triaxial compression results on 58 clays

6.3 Undrained CPT Penetration

As the piezocone penetrometer collects at least three readings with depth, the potential exists to utilize three parameters: (a) net cone resistance q_{net}; (b) excess porewater pressure, Δu; and effective cone resistance, q_E; towards the assessment of $peak\ s_u$ in clays, while f_s provides an estimate of the remoulded strength. ***Figure 6.9*** depicts the approach for this purpose.

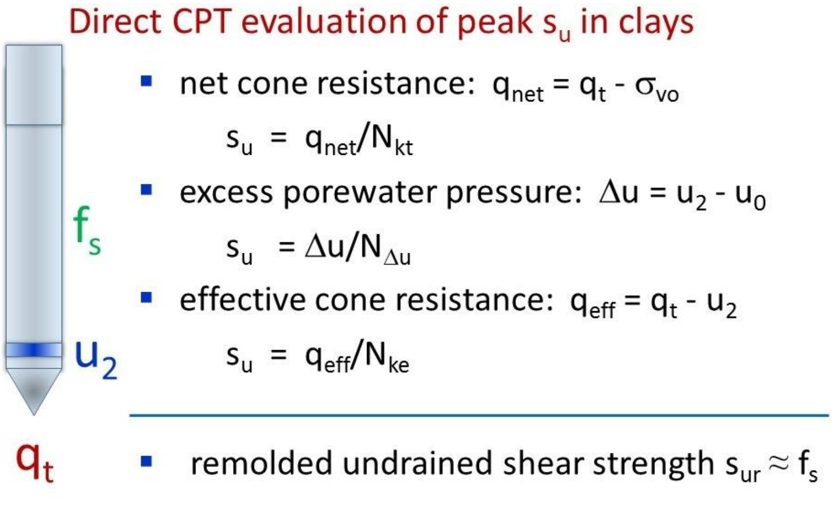

Direct CPT evaluation of peak s_u in clays

- net cone resistance: $q_{net} = q_t - \sigma_{vo}$

  $s_u = q_{net}/N_{kt}$
- excess porewater pressure: $\Delta u = u_2 - u_0$

  $s_u = \Delta u/N_{\Delta u}$
- effective cone resistance: $q_{eff} = q_t - u_2$

  $s_u = q_{eff}/N_{ke}$

- remolded undrained shear strength $s_{ur} \approx f_s$

Figure 6.9: Direct assessment of s_u in clays from piezocone readings

Common practice is to directly evaluate the in-situ undrained shear strength ($s_u = c_u$) from the net cone resistance (q_{net}) which comes from an inverted bearing capacity form:

$$s_u = \frac{q_t - \sigma_{v0}}{N_{kt}} \tag{6.7}$$

where q_t = total (corrected) cone tip resistance (Lunne et al. 1997), σ_{v0} = total vertical overburden stress, and N_{kt} is a bearing factor that depends upon the theory (e.g., limit plasticity, cavity expansion) or numerical simulation method (e.g., strain path method, finite elements), as discussed by Konrad and Law (1987), Yu and Mitchell (1998), Lu et al. (2004), and others. In practice, either an assumed value for N_{kt} is adopted for evaluation of s_u, or else a fitted value is obtained by referencing the results to a benchmark tests, such as field vane (s_{uv}) or laboratory shear test, such as triaxial compression (s_{uc}), simple shear (s_{ud}), or extension (s_{ue}).

Ranges of values for N_{kt} in soft intact clays are generally taken to be between 10 and 20, yet are certainly mode-dependent (Lunne et al. 1997). For CPTU soundings in soft to firm offshore clays, Lunne et al. (2005) recommend a value N_{kt} = 12 for s_{uc}. A study of piezocone data on 3 onshore and 11 offshore clays by Low et al. (2010) found the range: $8.6 \leq N_{kt} \leq 15.3$, with a mean value of N_{kt} = 11.9 for triaxial compression mode. Similarly, a larger study of 51 soft to firm intact clays found a mean value of N_{kt} = 11.8 for s_{uc} corresponding to the CAUC triaxial mode (Mayne et al. 2015). For 17 Norwegian clays, Karlsrud et al. (2005) found that N_{kt} increases with OCR and PI of the clay and is also influenced by sensitivity.

For other shearing modes, other operational values of N_{kt} must be used. For instance, Low et al. (2010) found a mean N_{kt} = 13.6 for the lab average strength (s_{uAVE}) from triaxial compression, simple shear, and triaxial extension (range: $10.6 \leq N_{kt} \leq 17.4$), which is close to a simple shear mode (s_{uSS}). For calibration with the field vane (s_{uv}), they determined N_{kt} averages 13.3 with a range: $10.8 \leq N_{kt} \leq 19.9$.

Several research programs concluded that N_{kt} varies inversely with porewater parameter B_q. The reported trends are summarized in ***Figure 6.10*** and correspond to intact clays. In fissured overconsolidated clays, the characteristic porewater pressure response gives B_q that are zero or negative values. For these geomaterials, N_{kt} factors have been reported in the higher range of 20 to 30, and somewhat dependent upon the degree of fissuring (Powell and Quarterman 1988; Powell and Lunne 2005a).

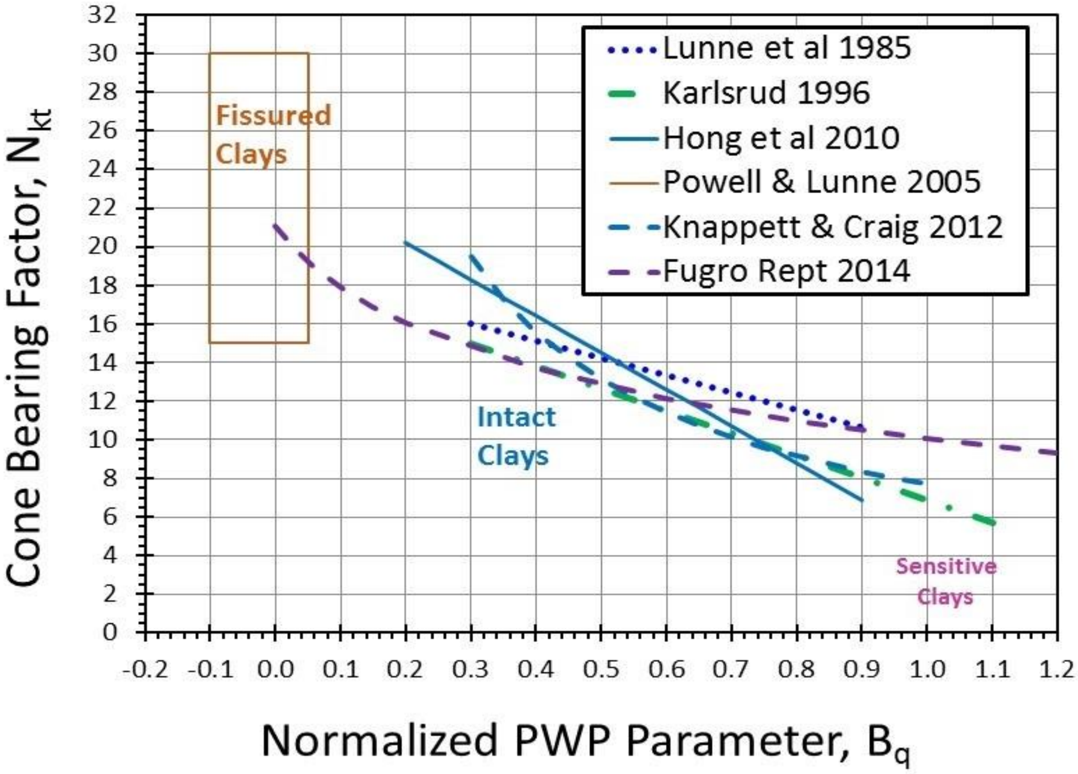

Figure 6.10: Calibrated trends for cone factor N_{kt} with porewater parameter B_q

Using a consistent s_{uc} reference strength from CAUC tests, a summary of q_{net} data from CPTU tests on clays is presented in ***Figure 6.11***, confirming the decrease of N_{kt} with increase in B_q.

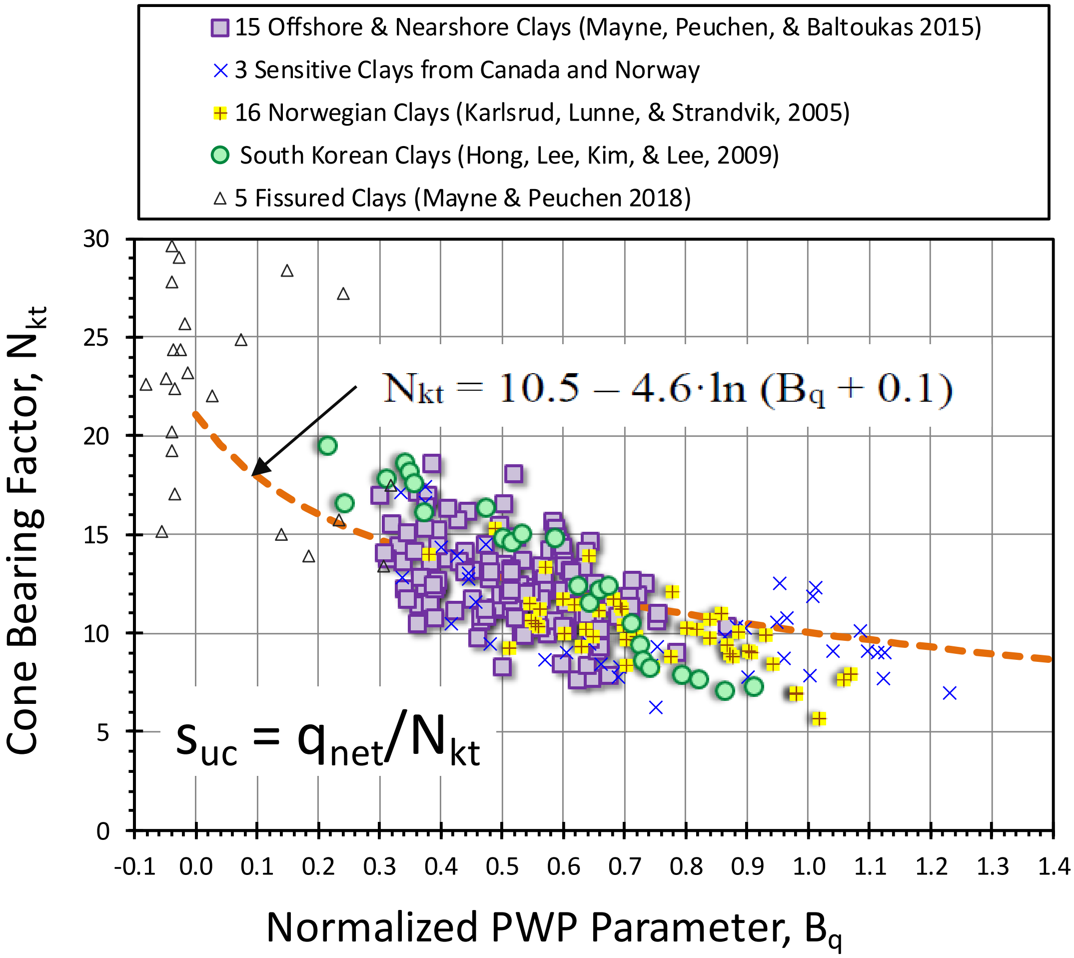

Figure 6.11: Data sets for establishing N_{kt} relationship with porewater parameter B_q

With piezocone data, it is also feasible to independently evaluate a profile of s_u entirely from the excess porewater pressure measurements (Δ u). While this may be best handled by a mid-face element (designated u_1), the shoulder filter element (u_2) reading is usually more common, because u_2 is required in the correction of raw q_c to total resistance q_t. The expression for undrained strength here is given by:

$$s_u = \frac{u_2 - u_0}{N_{\Delta u}} \tag{6.8}$$

where $N_{\Delta u}$ = porewater bearing factor (Tavenas and Leroueil 1987; Lunne et al. 1997). For the triaxial compression mode, Lunne (2012) recommends a value of $N_{\Delta u}$ = 6 for preliminary work or initial estimates until calibrated with laboratory tests on undisturbed samples. From their study on soft offshore deposits, Low et al. (2010) indicated a mean value of $N_{\Delta u}$ = 5.9, while the larger study by Mayne et al. (2015) found a representative $N_{\Delta u}$ = 6.5 for soft to firm clays. Karlsrud et al. (2005) found that $N_{\Delta u}$ decreases with OCR and increases with PI. Hong et al. (2009) also found an increase of $N_{\Delta u}$ with B_q.

Using the CAUC suc reference strengths, a summary of Δu_2 data from CPTU tests on clays is presented in ***Figure 6.12***, confirming the increase of $N_{\Delta u}$ with increasing value of B_q.

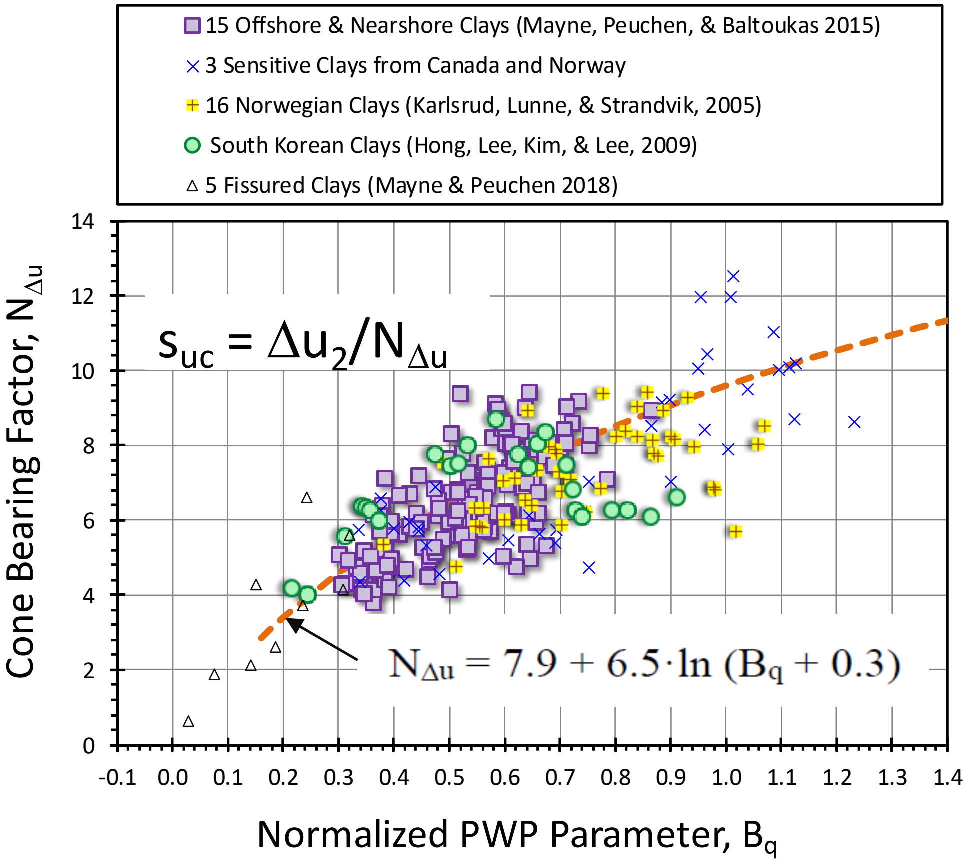

Figure 6.12: Data sets for establishing $N_{\Delta u}$ relationship with porewater parameter B_q. Note: not applicable to CPTU results where $B_q < 0.2$

Furthermore, a third evaluation is possible using the effective cone resistance $(q_t - u_2)$, given by:

$$s_u = \frac{q_t - u_2}{N_{\mathrm{kE}}} \tag{6.9}$$

where N_{kE} = bearing factor averaging about 8.0 in soft-firm NC-LOC clays (Mayne et al. 2015). In the study by Lunne et al. (1985), it was found that N_{kE} decreases with porewater parameter which was also noted by Karlsrud et al. (1996) and Hong et al. (2009).

Using the noted four data sets of CAUC suc reference strengths, a summary of q_E data from CPTU tests on clays is presented in ***Figure 6.13***, confirming the trend of decreasing N_{kE} with increasing porewater pressure parameter B_q.

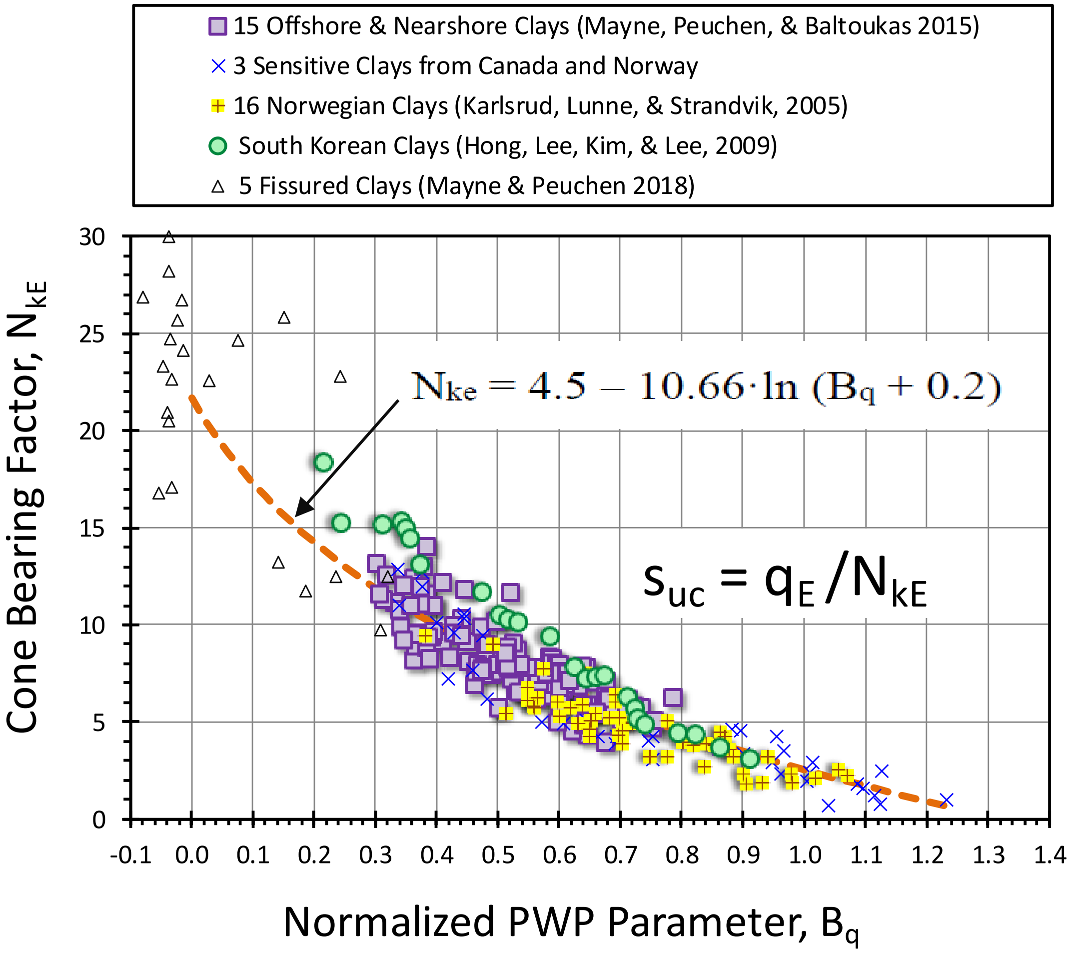

Figure 6.13: Data sets for establishing N_{kE} relationship with porewater parameter B_q

The ability to produce three separate profiles of peak undrained shear strength in the clay formation is actually good, since hopefully the three will support each other. If the individual profiles show consensus, then a higher degree of reliance can be afforded in the design. If the profiles do not agree, then the results may serve as a warning that a higher level of scrutiny needs to be undertaken by the engineer. For instance, perhaps issues with the porous filter becoming partially desaturated, or other possibilities, such as the soil formation itself having unusual aspects and thus falling within the domain of "nontextbook geomaterials" (Schnaid 2005).

6.3.1 Case Study: Sandpoint Idaho

Returning to the CPTU sounding in soft silty clay from Sandpoint Idaho, ***Figure 6.14*** shows the results of a series of triaxial compression tests (CIUC type) that were peformed on undisturbed tube samples. Using the aforementioned characteristic value of B_q = 0.75, estimated values of N_{kt} = 11, $N_{\Delta u}$ = 8, and N_{kE} = 5 were chosen and applied to the q_{net}, Δu_2, and q_E readings, respectively, with the resulting profiles shown in the figure.

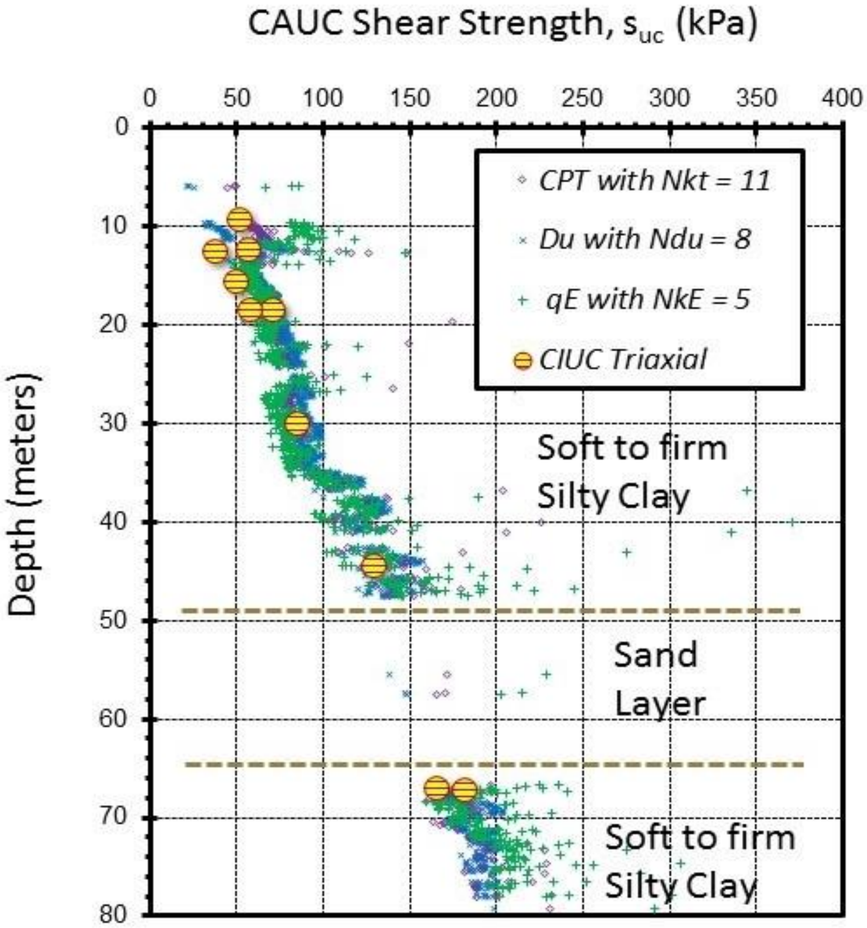

Figure 6.14: Profiles of undrained shear strength from CPTU in soft silty clay using cone bearing factors estimated from B_q at Sandpoint, Idaho

6.3.2 Case Study: Tiller-Flotten Quick Clay, Norway

A second example involves highly sensitive clay at the national test site established in Norway at Tiller-Flotten, near Trondheim (L'Heureux et al. 2019). A representative sounding (TIL18) is shown in ***Figure 6.15*** and the post-processing of the CPTU data with eqns (6.7), (6.8), and (6.9) provide three profiles of suc in the right-hand side. The results are comparable to the CAUC test results on undisturbed samples conducted at the NGI Laboratory.

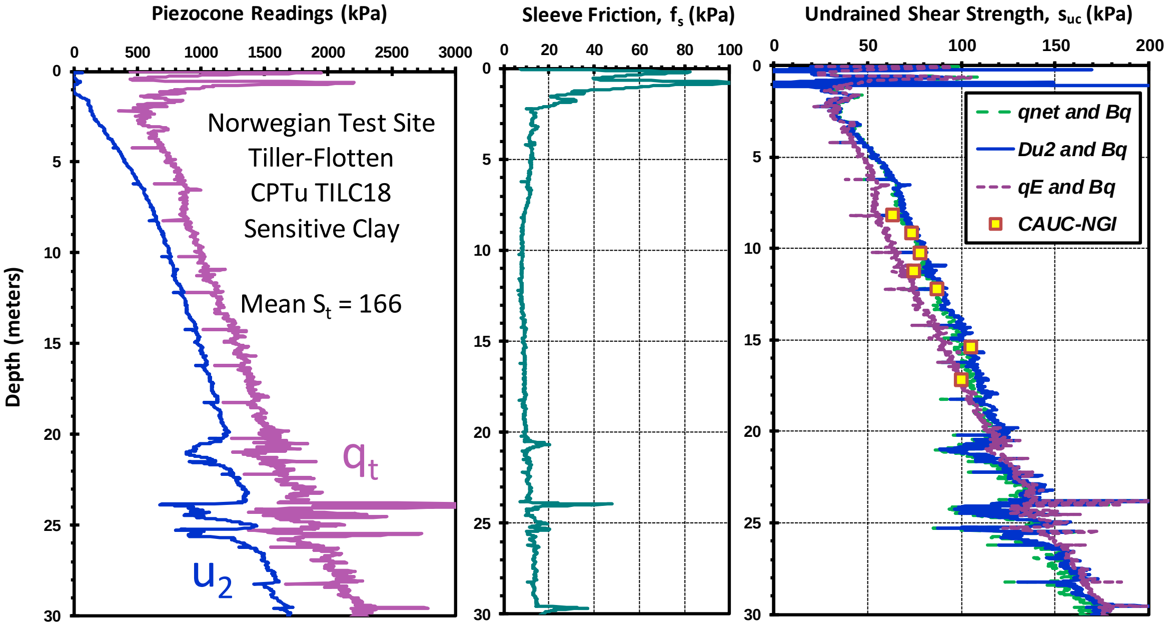

Figure 6.15: Profiles in quick clay at Tiller-Flotten: (a) q_t and u_2; (b) f_s; (c) CAUC s_u

6.4 Evaluation of s_u from V_s

If SCPTU results are available, an independent assessment on undrained shear strength can be afforded through empirical correlations between s_u and shear wave velocity. L'Heureux & Long (2017) provide a review of some 15 relationships for s_u and V_s. In addition, using CAUC triaxial data obtained from 14 Norwegian clays, they develop the following trendline:

$$s_{uc}\text{ (kPa)} = 0.021\cdot[V_s\text{ (m/s)}]^{1.52} \tag{6.10}$$

Similar expressions have been derived by Agaiby et al. (2016) and Agaiby & Mayne (2016).

6.5 Relationship for Undrained Strength with Vane Shear Test

The vane shear test (VST), or field vane (FV), provides a direct in-situ assessment of undrained shear strength, albeit the calculation is based on limit equilibrium analysis. In some instances, it is desirable to compare the results of VST with CPTU. The aforementioned relationships for evaluating undrained strength from the CPTU are specifically for the triaxial compression mode, s_{uc}. Therefore, it is of interest to provide an interrelationship between the vane undrained strength, s_{uv}, with that from triaxials tests. A review by Chandler (1988) found that the strength ratio tracked with clay plasticity index (PI in %):

$$V_r = s_{uv}/s_{uc} \approx 0.55 + 0.008\text{ PI} \tag{6.11}$$

The data used to develop this trend is presented in ***Figure 6.16***.

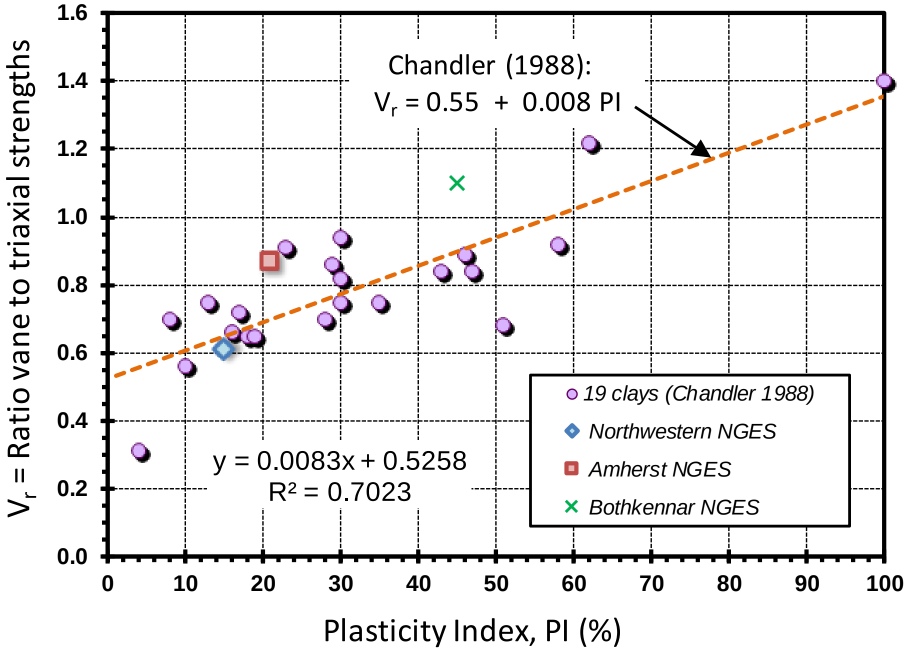

Figure 6.16. Interrelationship of vane and triaxial compression strengths with clay plasticity (modified after Chandler 1988)

6.6 Remolded Undrained Strength and Clay Sensitivity

Studies have long suggested that the measured sleeve friction resistance (f_s) can be considered as a remolded shear strength (s_{ur}) in clays (Gorman, Drnevich, and Hopkins 1975; Lunne et al. 1997; Powell and Lunne 2005a; Robertson 2009b), expressed:

$$s_{ur} \approx f_s \tag{6.12}$$

In ***Figure 6.17***, data have been compiled from a number of sites (N = 15) where reference s_{ur} profiles have been obtained from independent measurements, mostly from field vane tests (FV), however in some cases other reference results were available (e.g., lab fall cone, lab mini-vane, UU). The dataset contains 11 clay deposits of low-medium sensitivity ($S_t < 8$) and 5 clays that have high sensitivity ($S_t > 8$).

It is evident that eqn (6.11) works reasonably in clays that have low sensitivity, however, when needed the most, i.e. sensitive and quick clay deposits, the sleeve friction is not particularly very good at capturing the remolded undrained shear strength. This might be due to the low range of f_s readings < 10 kPa which is near the limit of its resolution in the load cell range, as well as due to porewater pressure effects that act on the sleeve.

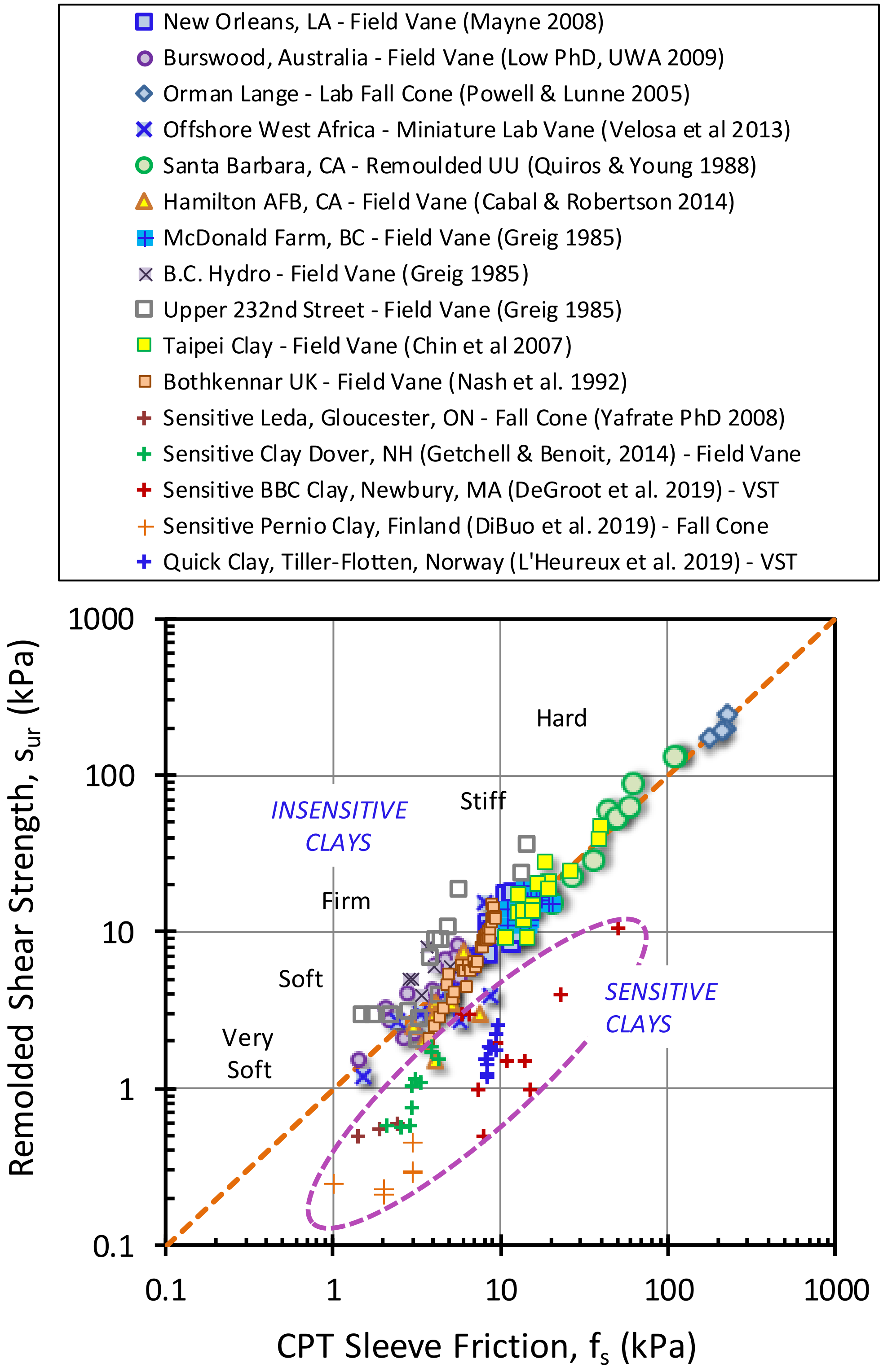

Figure 6.17: Measured remolded shear strengths versus CPT sleeve friction for 16 clays

For clays of low sensitivity, the CPTU can provide an approximate measure of clay sensitivity, S_t, defined as the ratio of peak to remolded shear shear strengths at the same water content:

$$S_t = \frac{s_{u,peak}}{s_{ur}} \tag{6.13}$$

where the peak s_u is evaluated based on the aforementioned procedures, such as eqns (6.7), (6.8), and/or (6.9), and the remolded $s_{ur} = f_s$.

For clays of high sensitivity, the above will not be adequate and will significantly underestimate the clay S_t since the f_s reading poorly captures the remolded undrained strength. Using the crude statistical analyses presented in ***Figure 6.18***, on the average, the f_s reading overestimates s_{ur} by a factor of 5 in sensitive clays.

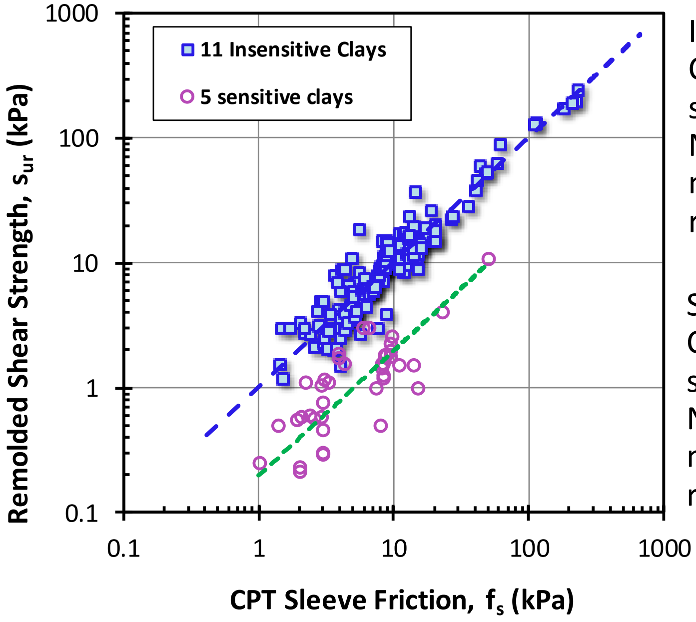

Insensitive Clays:
$s_{ur} = 1.014\ f_s$
N = 11 clays
n = 160 data
$r^2 = 0.973$

Sensitive Clays:
$s_{ur} = 0.198\ f_s$
N = 5 clays
n = 40 data
$r^2 = 0.829$

Figure 6.18: Statistical analyses of remolded strength with sleeve friction for 11 insensitive clays and 5 sensitive clays

6.7 Sample Disturbance of Laboratory Reference Strengths

One issue that frequently arises with CPT interpretation in clays involves a geoengineer who will try and use their lab test results from “undisturbed” samples to adjust the N_{kt} factor for the cone data interpretations. This is often problematic for two reasons: (a) lab-measured s_u values can be significantly altered by sample disturbance effects; and (b) lack of a proper matching for the appropriate strength mode, as discussed already.

An example of the strong influence of sample disturbance on the measured strength and stiffness is given in ***Figure 6.19*** for Ariake clay reported by Tanaka (2000). Here, six different types and qualities of samplers were used to procure undisturbed samples of the soft clay. Each sample was subsequently tested in the laboratory under the unconfined compression mode. It is easily seen that the Sherbrooke sampler provides the highest (and presumably, best representative) value of undrained shear strength (s_u = 38 kPa) whereas the British ELE sampler has the lowest (and correspondingly, most disturbed) value of strength (s_u = 15.5 kPa). The remainder of samplers provide intermediate values between these two extremes. Note also the severe effects on the flattening of the stress-strain curves, thus causing significant differences in derived Young's modulus values. That is, higher quality samples generally provide a higher strength and higher modulus, whereas in contrast, poor quality samples have low strengths and low stiffnesses.

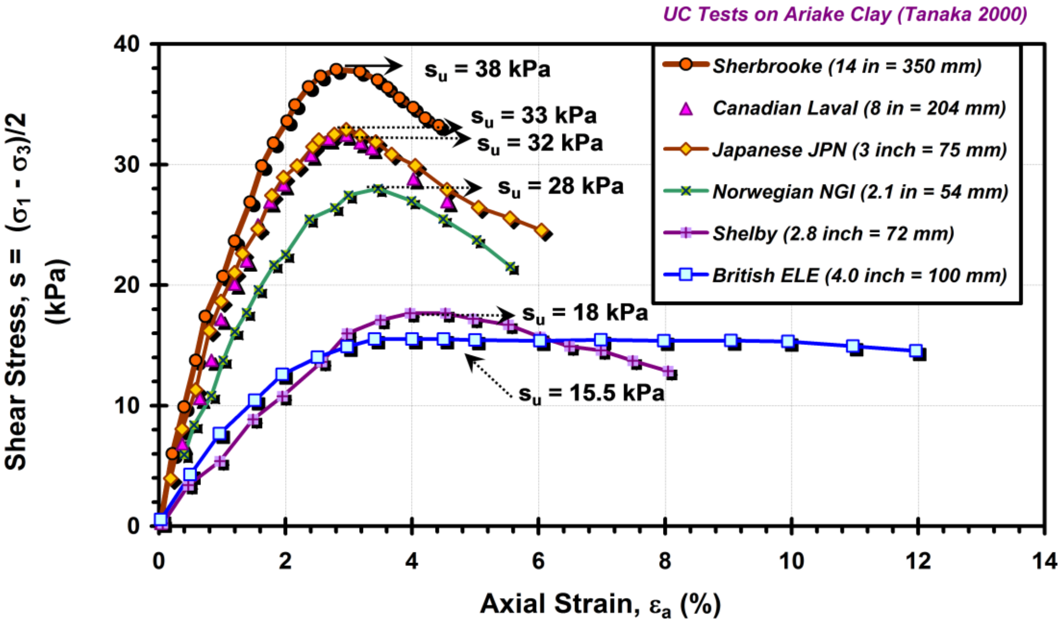

Figure 6.19: Comparison of undrained stress-strain curves for Ariake clay from different quality samples (after Tanaka 2000)

The degree of sample disturbance for each lab specimen can be assessed using one of two methods: (a) specimen quality designation (SQD); or (b) NGI method. After trimming the specimen, both approaches rely on measuring the change in void ratio (Δe) required during reconsolidation to recover to the in-situ effective overburden stress σ_{vo}'. In the SQD method, the vertical strain (ϵ_v) is used to quantify the sample goodness, where: $\epsilon_v = \Delta e/(1+e_0)$. In the NGI method, the ratio of $\Delta e/e_0$ measured during consolidation is utilized. Both methods can be applied to individual specimens from triaxial, consolidation, and direct simple shear tests (Lunne et al. 2006). For example, the sample quality is high if $\Delta e/e_0 < 0.02$ and poor if $\Delta e/e_0 > 0.14$. ***Table 6.3*** details the specific criteria for assessing a grade to each specimen.

Krage et al. (2015) recognized that the recovery of void ratio during sample reconsolidation depends on recompression index of the soil, C_r. Consequently, silt soil samples with lower C_r values could mistakenly be classified as high quality using ***Table 6.3***. They recommended normalizing $\Delta e/e_0$ by C_r in order to apply sample quality criteria to any soils.

Table 6.3: Quantification of sample disturbance on mechanical soil properties based on specimen volume change to reach σ'_{v0} (modified after DeGroot et al. 2005)

SPECIMEN RATING	**SQD = Sample Quality Designation**		**NGI Sample Quality Method**	
	Grade	Strain ε (%), note 1	(Δe/e₀), note 2	(Δe/e₀), note 3
Excellent-Very Good	A	< 1	< 0.04	< 0.03
Good to Fair	B	1 - 2	0.04 - 0.07	0.03 - 0.05
Poor	C	2 - 4	0.07 - 0.14	0.05 - 0.10
Very Poor	D	4 - 8	> 0.14	> 0.10
Forget it	E	> 8	---	----

Notes:

1. Vertical strain during recompression to reach σ_{vo}' where $\varepsilon = \Delta e/(1+e_0)$, Δe = change in void ratio, and e_0 = initial void ratio.
2. For soils with 1 < OCR < 2
3. For soils with 2 < OCR < 4

With regards to the aforementioned issues, some good news here is that the measured ϕ' is apparently little affected by sample disturbance! An example is shown in ***Figure 6.20*** using data from Lierstranda clay in Norway (Lunne et al. 2006). Three different sampler types were used to obtain undisturbed specimens including: (a) high quality block; (b) medium quality 75-mm tube, and (c) low quality 50-mm tube. Each give a different stress-strain curve, pore pressure response, effective stress path, and corresponding peak s_{uc} depending upon the quality of the sample. However, in the effective q-p' stress space plots, it is evident that all specimens converge on the same effective stress friction angle (ϕ = 34.4°). Similar findings are presented by Karlsrud & Hernandez-Martinez (2013) and DeGroot et al. (2019) for other clays.

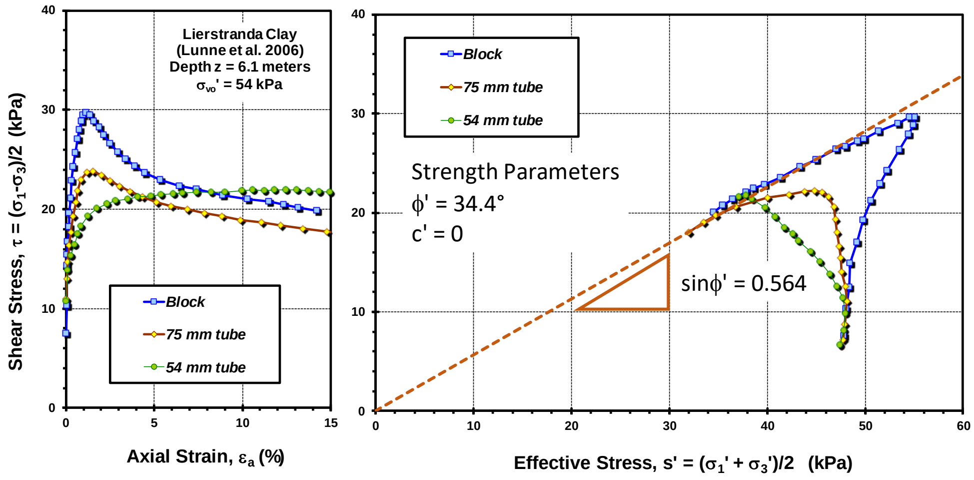

Figure 6.20: Stress-strain curves and effective stress plots for three different quality specimens tested in CAUC triaxial compression (data from Lunne et al. 2006)

7 Ground Stiffness and Soil Moduli

A measure of the soil stiffness is needed for deformation analyses, including foundation settlements, pile displacements, and movement of walls and other civil engineering structures. The stiffness of soils is represented by several types of geoparameters, depending upon the theoretical framework adopted including: (1) one-dimensional consolidation theory and associated compressibility parameters (C_r, C_c, and C_s); (2) elasticity theory in terms of moduli (i.e., E', G', B', D', E_u, G_u); (3) subgrade reaction models (e.g., mat foundations or pavement subgrades; (4) spring models; and (5) other empirical methods. The value of stiffness parameters will vary depending upon the level of applied loading, drainage conditions, loading history (monotonic static, dynamic, or cyclic), initial stress state, and induced strain levels.

7.1 Consolidation Theory

Foundation settlement is a common situation for many geotechnical studies. Many office buildings are built towards tolerable settlements of less than 25 mm (1 inch), while open structures such as parking garages are able to withstand up to 50 mm (2 inches) of vertical movement. Large bridge structures can sustain up to 75 mm (3 inches) movements, yet earthen embankments may undergo displacements of 100 to 1000 mm during initial undrained loading ($s_{initial}$), drained primary consolidation ($s_{consolidation}$), and long-term secondary compression (s_{creep}).

In the traditional approach to calculating displacements of shallow foundations and embankment fills, the full consideration of deformations can be expressed (Holtz et al. 2011):

$$s_{total} = s_{initial} + s_{consolidation} + s_{creep} \tag{7.1}$$

For the calculation of drained primary consolidation and long-term creep components, conventional practice is to utilize the results from one-dimensional consolidation tests, specifically: void ratio versus logarithm of effective stress: e – log σ'_v curves. The derived compressibility parameters include the recompression index (C_r), virgin compression index (C_c), and swelling or rebound index (C_s), as well as evaluation of the preconsolidation or yield stress (σ'_p). For the long-term creep phase, the coefficient of secondary compression (C_α) is also a compressibility parameter.

The initial or immediate displacements are more complex as the situation depends upon whether the ground is fully saturated or partially saturated. Usually, elastic solutions are employed for calculating initial undrained displacements, e.g., Foott & Ladd (1981). The elastic solutions may be required for flood control structures, filling water tanks, and from the rapid installation of prefabricated structures. In most cases, an undrained distortion (or initial displacement) is only of concern when constructing a facility rather quickly over very soft ground conditions, i.e., embankment on soft clay or offshore gravity platform on clay. In fact, most construction advances slowly and immediate settlements are not normally of concern on firm ground. Thus, only the two components of primary consolidation and creep will occur for most projects. Long term creep is problematic only in the case of soft organic clays, peats, muskeg, and sensitive clays. Thus, the main focus of displacements is usually towards the magnitude of drained settlements due to primary consolidation.

In the calculation of settlements due to drained primary consolidation, the effective yield stress (σ_p') plays an important role since applied loading that causes stresses less than σ_p' will often result is small manageable displacements, while loads where stresses > σ_p' can cause large movements that may exceed bearing capacity and stability limits. The evaluation of σ_p' from CPTU was discussed in Section 4. For additional details, please see Holtz et al. (2011).

7.2 Elastic Moduli

The representation of ground stiffness by elastic moduli is common, since these are utilized in simple analytical solutions derived from elasticity theory, as well as serve as input parameters to numerical finite element simulations. In the laboratory, the specific determination of Young's modulus €, shear modulus (G), constrained modulus (D', or also M'), and bulk modulus (K') are found directly from triaxial compression, simple shear, one-dimensional consolidation, and isotropic consolidation testing, as depicted in ***Figure 7.1***.

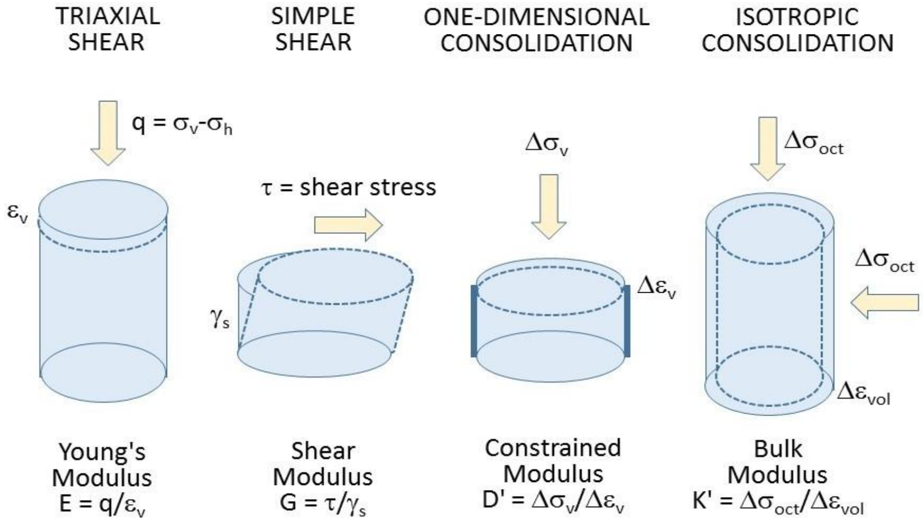

Figure 7.1: Definitions and tests for the four elastic moduli of soils

Elastic continuum theory allows for interrelationships between the elastic moduli in terms of the Poisson's ratio (ν), such that:

$$E = 2G(1+\nu) \tag{7.2}$$

$$D = E\frac{(1-\nu)}{(1+\nu)(1-2\nu)} \tag{7.3}$$

$$K = \frac{E}{3(1-2\nu)} \tag{7.4}$$

The moduli E and G can have both drained values (E’ and G’) as well as undrained values (E_u and G_u), depending upon the specific stress path (i.e., drained when Δu = 0; undrained when ΔV = 0). Note that the constrained modulus (D’) and bulk modulus (K’) take on only a drained value, since strains and void ratios are measured specifically at the end of primary consolidation.

At the drained value of ν' = 0, the theoretical ratio D’/E’ = 1.0, i.e., same value. Moreover, at a practical value $\nu' \approx$ 0.2, the ratio D’/E’ = 1.1. Therefore, the terms constrained modulus and drained Young’s modulus are often used somewhat interchangeably.

In terms of stress-strain curves, there are different definitions for the moduli, particularly Young’s modulus and shear modulus, as depicted in ***Figure 7.2***. These include: (a) initial tangent modulus at small strains, E_{max}: (b) secant modulus, E_{sec}; (c) tangent modulus, E_{tan}; and (d) unload-reload modulus, E_{ur}. These moduli can be specified at established levels of strain (say $E_{0.001}$ at corresponding 0.1% strain), or at certain levels of mobilized stress (say E_{50} at 50% of ultimate strength).

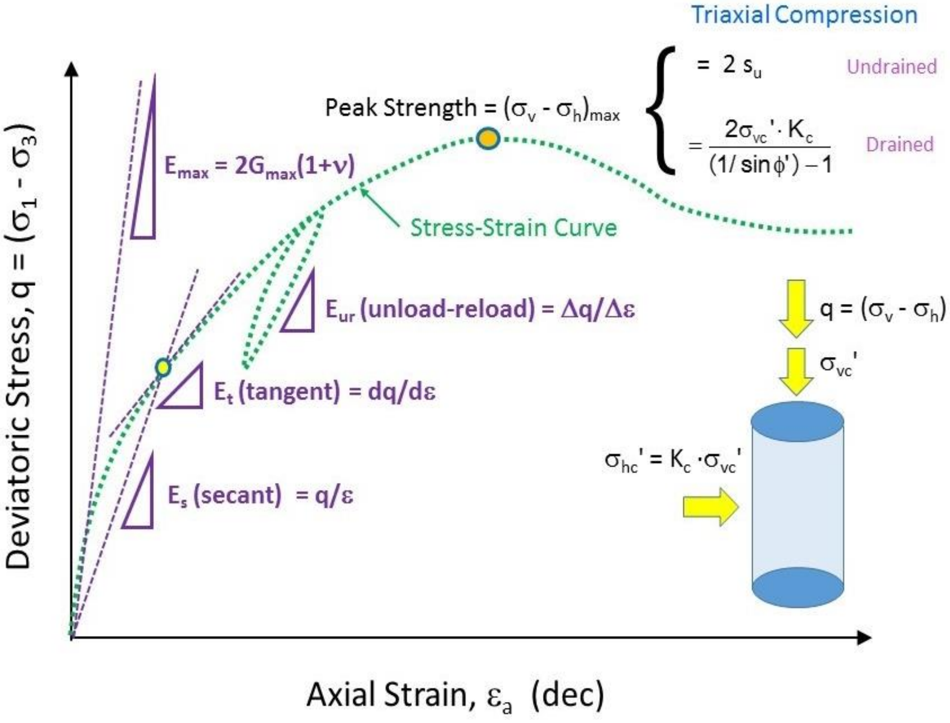

Figure 7.2: Conceptual deviator stress versus axial strain for triaxial compression test showing different definitions of elastic Young’s modulus

7.2.1 Constrained Modulus from Compressibility Parameters

In terms of the compressibility parameters from consolidation testing, the constrained modulus has a tangent definition and can be expressed as functions of the void ratio, effective stress (σ'_{v0}), and compression indices:

$$D = \frac{1+e_0}{C_r}\ln(10)\sigma'_{v0};\ \text{OC Soils} \tag{7.5}$$

$$D = \frac{1+e_0}{C_c}\ln(10)\sigma'_{v0};\ \text{NC Soils} \tag{7.6}$$

7.2.2 Constrained Modulus from CPT

For a quick and direct evaluation of the constrained modulus (and drained Young's modulus) from CPT results, the common approach is expressed in the form:

$$D' = \alpha_D(q_t - \sigma_{v0}) \tag{7.7}$$

where D' corresponds to the current effective stress state (i.e., σ'_{v0}) and α_D is an empirical scaling factor that has been shown to depend upon soil type, confining stress level, relative density, overconsolidation, and other factors (e.g., Kulhawy and Mayne 1990). ***Figure 7.3*** shows that for wide range of soil types: $\alpha_D \approx 5$ is an approximate starting place, excepting soft plastic organic clays and cemented geomaterials. The original database for this compilation relied on laboratory consolidometer data to provide the corresponding D' for clays and silts, while the consolidation phase of calibration chamber tests supplied many of the values of D' for clean quartz sands (Mayne 2007b).

To check the general validity of this trend, three case studies were reviewed: (1) a large footing load test (B = 3 m) on sand at Texas A&M University (Briaud 2007); (2) a long-term drained footing load test on clay (B = 2.2 m) conducted by Imperial College (Lehane and Jardine 2003);

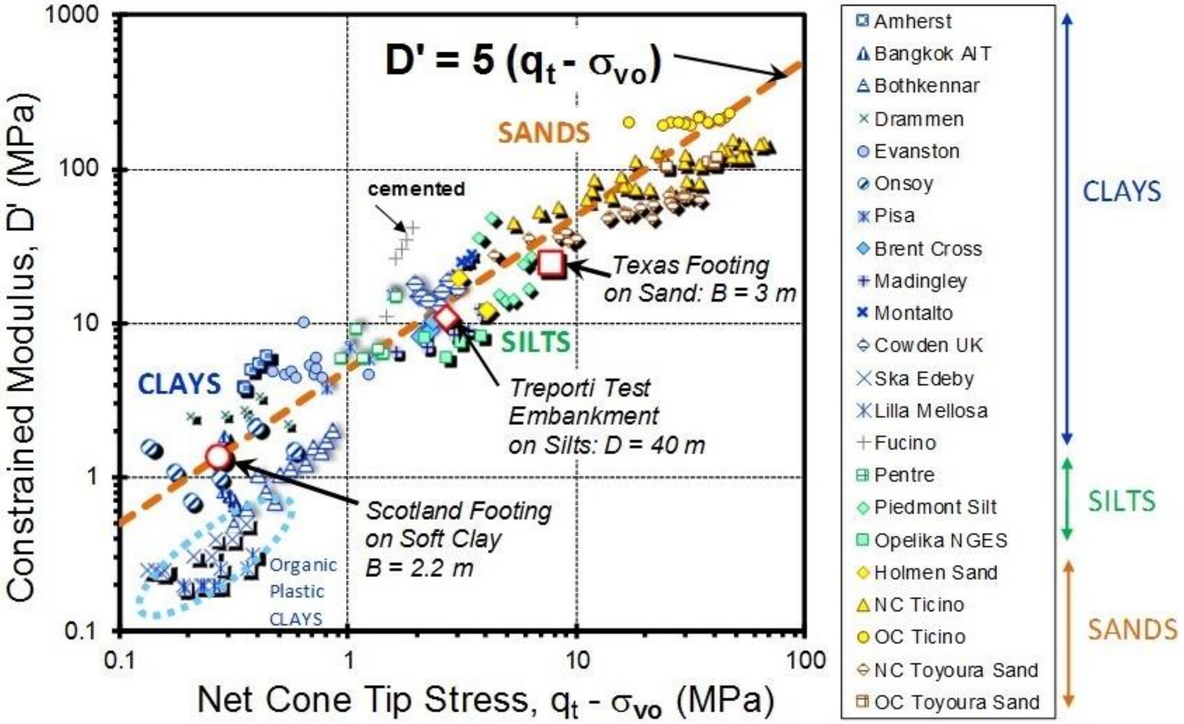

Figure 7.3: First-order trend between drained constrained modulus and net cone tip resistance in various soils (after Mayne 2007)

and (3) the Treporti instrumented test embankment on silty soils near Venice (Marchetti et al. 2004). The net cone resistances were determined as the average values within a depth equal to one foundation width deep beneath the applied loading elevation. The equivalent moduli were back-calculated using elastic continuum theory where the drained response of the Texas footing corresponded to a factor of safety FS = 2 and the drained settlements for the Bothkennar footing were at an applied loading level associated with an undrained FS = 1.6. These case studies are also shown in ***Figure 7.3*** with acceptable agreement.

The flat plate dilatometer test (DMT) provides a modulus termed the dilatometer modulus (E_D) that related directly to the Young's modulus of soil (E) via elastic continuum theory (Marchetti et al. 2004). Robertson (2009b) conducted a comparative study of flat dilatometer tests (DMT) and CPT data taken in the same soils and found a similar relationship ($E \approx 5 \cdot q_{net}$), shown in ***Figure 7.4***. Thus a first-order estimate of the soil modulus can be taken as:

$$D' \approx 5 \cdot q_{net} \tag{7.8}$$

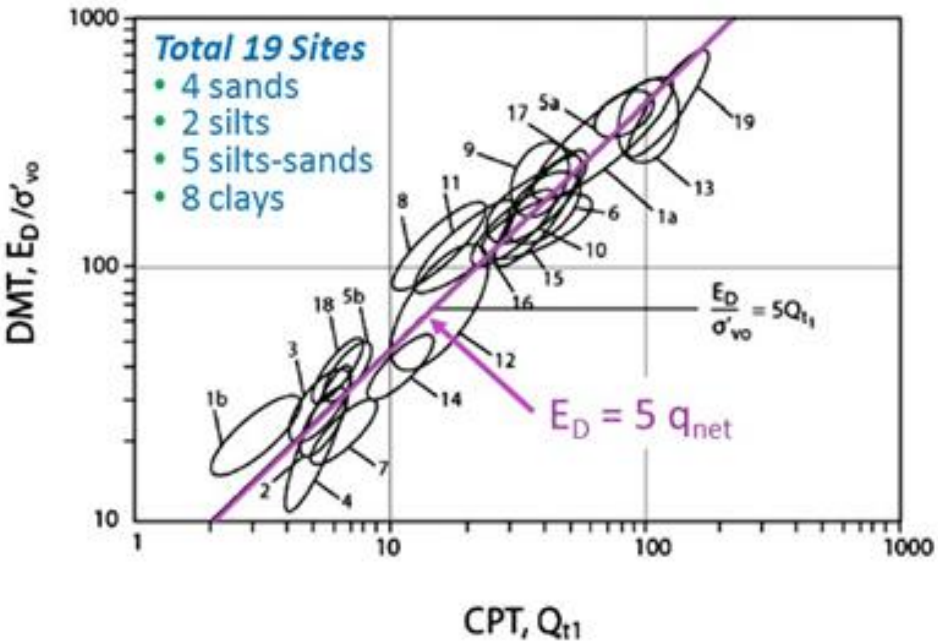

Figure 7.4: Normalized Flat dilatometer modulus versus CPT Q for 19 soils (Robertson 2009b)

Since most undisturbed natural soils are at least lightly-overconsolidated, if not moderately to heavily OC, then the use of a constrained modulus would generally only apply during recompression loading up to the yield stress ($\sigma'_{v0} \leq \sigma'_p$), thereafter a modulus corresponding to NC conditions would need be applied. This can be evaluated through the dimensionless modulus number: $m_D = \Delta D'/(\Delta\sigma'_v)^{d*}$ where d* = exponent that varies from 1 in clays to 0.5 in sands, as discussed by Schmertmann (1986); Senneset et al. (1989); and Kulhawy and Mayne (1990). Of additional note, the modulus number has been empirically correlated to water content (Fellenius 2020).

7.2.3 Small-Strain Shear Modulus

The small-strain shear modulus $G_0 = G_{max}$ is a fundamental stiffness that relates to the initial state of the soil. This stiffness applies to the initial loading for all stress-strain-strength curves, including static, cyclic, and dynamic types of loading, as well as undrained and drained conditions (Burland 1989; Mayne 2001; Leroueil and Hight 2003; Amoroso et al. 2014). The small-strain shear modulus is calculated directly from elasticity theory using the total soil mass density ($\rho_T = \gamma_T/g_a$) and shear wave velocity (V_s), where g_a = 9.8 m/s^2 = gravitational acceleration constant:

$$G_{max} = \rho_T \cdot V_s^2 \tag{7.9}$$

The initial stiffness can be expressed in terms of an equivalent small-strain Young's modulus of soil through elastic theory:

$$E_{max} = 2G_{max}(1 + \nu) \tag{7.10}$$

Preferably, these small-strain moduli should be determined from direct measurements of shear wave velocity, such as in-situ crosshole tests (CHT), downhole tests (DST), and/or surface wave methods (SASW). The seismic piezocone penetration tests (SCPTU) and seismic flat dilatometer test (SDMT) both provide measurements of the DST type, which is an V_{sVH} type (vertically-propagating and horizontally-polarized).

7.3 Modulus Reduction Curves

The value of small-strain shear modulus G_{max} (and corresponding stiffness, E_{max}) applies strictly to the nondestructive range of strains, where $\gamma_s < 10^{-4}$ as a decimal (or $\gamma_s < 10^{-6}\ in\ \%$). For loading levels at strains exceeding a threshold value, the use of modulus reduction curves (RF = G/G_{max}) must be implemented. For cyclic loading and dynamic problems in geotechnical engineering, Vucetic and Dobry (1991) present G/G_{max} curves in terms of soil plasticity and logarithm of shear strain. The appropriate value of secant shear modulus is then obtained from:

$$G = \left(\frac{G}{G_{max}}\right) G_{max} = RF \cdot G_{max} \tag{7.11}$$

A similar procedure can be used for tangent definitions of shear moduli, as discussed by Fahey and Carter (1993).

The ratio (G/G_{max}) is a reduction factor (RF) that is applied to the small-strain modulus, depending on current loading conditions, in order to obtain the relevant G for that situation.

The G/G_{max} curves can be presented in terms of logarithm of shear strain (γ_s), or alternatively in terms of mobilized shear stress (q/q_{max}), as discussed by Fahey (1998). The mobilized shear stress can be considered as the reciprocal of the factor of safety (q/q_{max} = 1/FS). In terms of fitting stress-strain data, G/G_{max} versus mobilized stress level (q/q_{max}) plots are visually biased towards the intermediate- to large-strain regions of the soil response. In contrast, G/G_{max} versus log γ_s curves tend to accentuate the small- to intermediate-strain range.

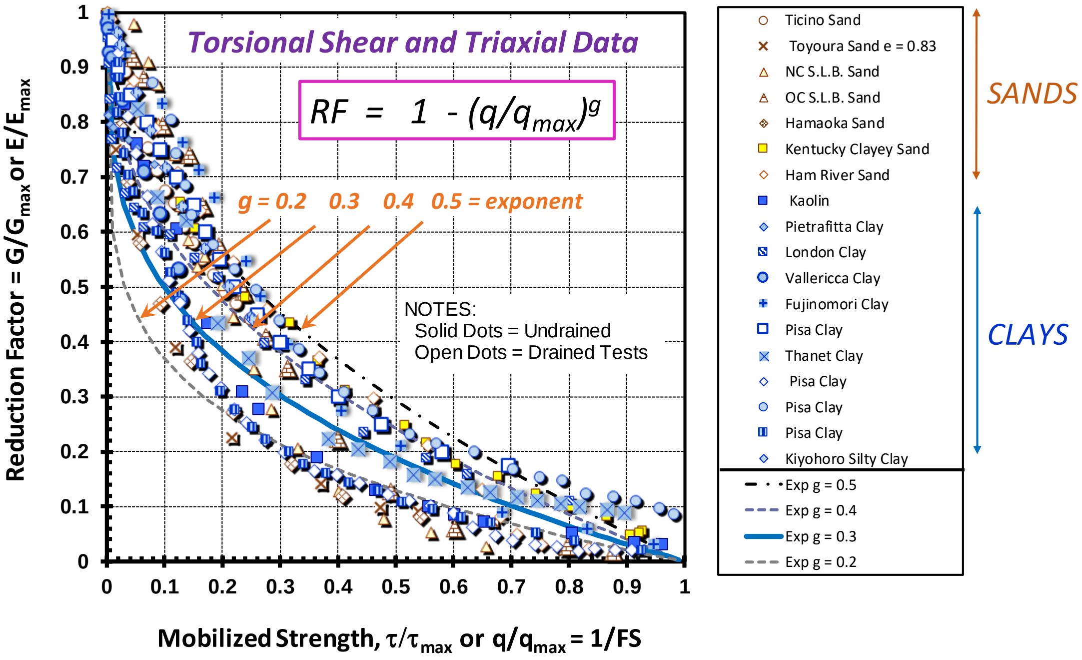

Figure 7.5: Measured modulus reduction curves from monotonic laboratory shear tests on assorted clays and sands under both drained and undrained loading

A selection of modulus reduction curves, represented by the ratio (G/G_{max}), has been collected from monotonic laboratory shear tests performed on an assorted mix of clayey and sandy materials (Mayne 2005; Mayne 2007a,b). The results are presented in ***Figure 7.5***, where $G = \tau/\gamma_s$ = secant shear modulus. These lab tests include static torsional shear and special triaxial tests with internal local strain measurements, so that the initial reference value of E_{max} or G_{max} has been obtained. Where necessary, an assumed constant value of ν has been applied with the conversion: $E = 2G(1+\nu)$ to permit plotting of E/E_{max} versus q/q_{max}, where $q = (\sigma_1 - \sigma_3)$ = deviator stress. Undrained tests are shown by solid dots and drained tests are indicated by open symbols. In general, the clays were tested under undrained loading, and the sands were tested under drained shearing conditions (except Kentucky clayey sand). Pisa clay was tested both drained and undrained. Similar trends for the various curves are noted for both undrained and drained tests on both clays and sands.

A number of different mathematical expressions have been adopted to represent the reduction factor, RF (Mayne 2005). One simple algorithm involves a modified hyperbola where the modulus reduction is given by Fahey and Carter (1993) and Fahey (1998):

$$RF = G/G_{max} = 1 - (q/q_{max})^g \qquad (7.12)$$

with an exponent value of g ≈ 0.3 ± 0.1 for "well-behaved" soils that are uncemented, insensitive, and/or not highly-structured. ***Figure 7.5*** shows several values for exponent g.

7.4 Stress-Strain-Strength Curves

The above approach can be used to generate approximate nonlinear stress-strain-strength curves for all soil types from the results of SCPTU soundings. Specifically for clays under a simple shear mode, the shear stress versus shear strain curves are developed from:

$$\tau = G \cdot \gamma_s \tag{7.13}$$

The τ_{max} value is the undrained shear strength (τ_{max} = s_u) obtained from the CPT resistances and the initial G_{max} is determined from the V_s data. Examples of the evaluated τ versus γ_s responses at various depths for soft Burswood clay are presented in ***Figure 7.6*** in comparison with lab simple shear tests conducted on undisturbed samples (Low et al. 2010).

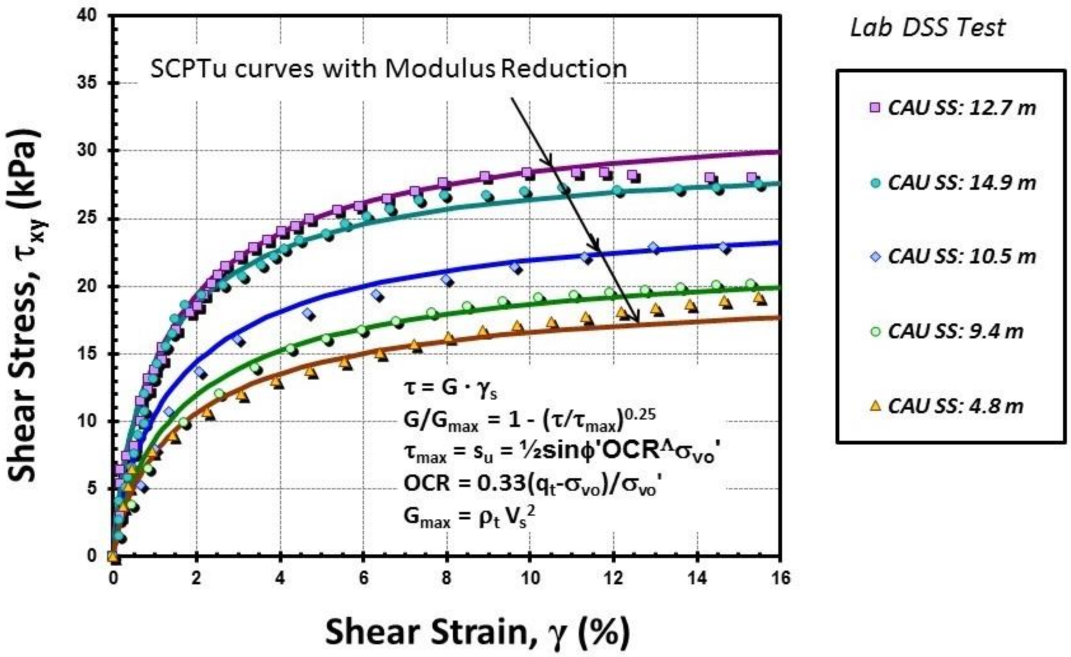

Figure 7.6: Shear stress versus shear strain curves for Burswood clay

A similar set of examples can be shown for triaxial tests on sands. A set of undisturbed samples of sands obtained by special freezing process have been reported for the CREC facility in Charleston, SC (Esposito & Andrus 2016). A series of drained triaxial compression tests (CIDC) were performed on trimmed specimens after thawing, as shown in ***Figure 7.7***. Results from SCPTU tests were available and evaluated to determine the strength (ϕ') from normalized cone resistance and E_{max} from V_s measurements. The maximum deviator stress, or $(\sigma_1 - \sigma_3)_{max}$, from CIDC tests is calculated from the expression in ***Figure 7.2*** for drained tests with K_c = 1 for isotropic consolidation. The modulus reduction factor is the same as ***Equation 7.12***, giving:

$$E = E_{max}\left(1 - \frac{\sigma_1 - \sigma_3}{(\sigma_1 - \sigma_3)_{max}}\right)^{0.3} \tag{7.14}$$

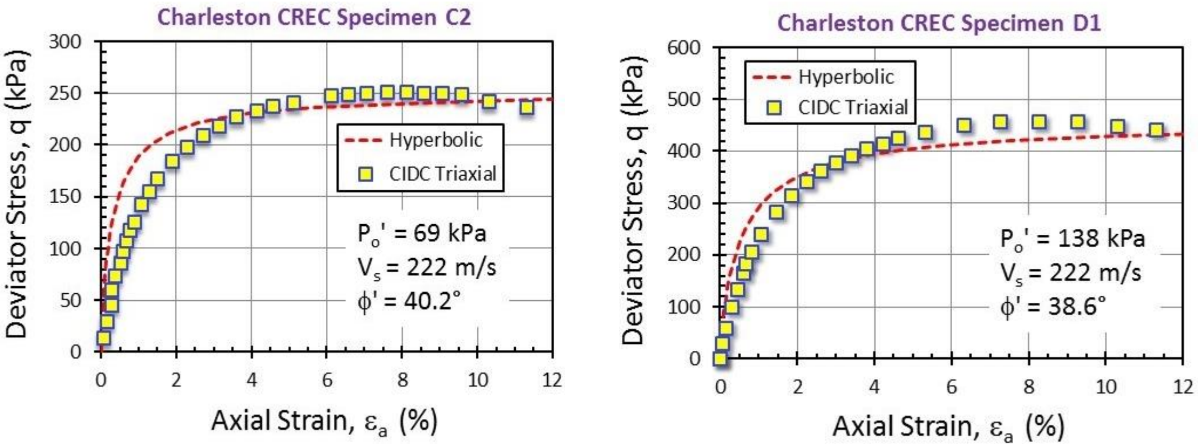

(a) *(b)*

Figure 7.7: Undisturbed triaxial tests and SCPTU-derived stress-strain curves for Charleston SC sands: (a) Specimen C2; (b) Specimen D1

A recent study of laboratory data from 26 clays by Vardanega and Bolton (2013) used a different modified hyperbolic format for the modulus reduction factor (RF). The calibrated expression is shown in ***Figure 7.8***. In this approach, moduli for both static (monotonic) loading and dynamic loading are different because of strain rate effects and can be considered in a unified manner, as given by:

$$\frac{G}{G_{max}} = \frac{1}{1+(\gamma_s/\gamma_{ref})^h} \tag{7.15}$$

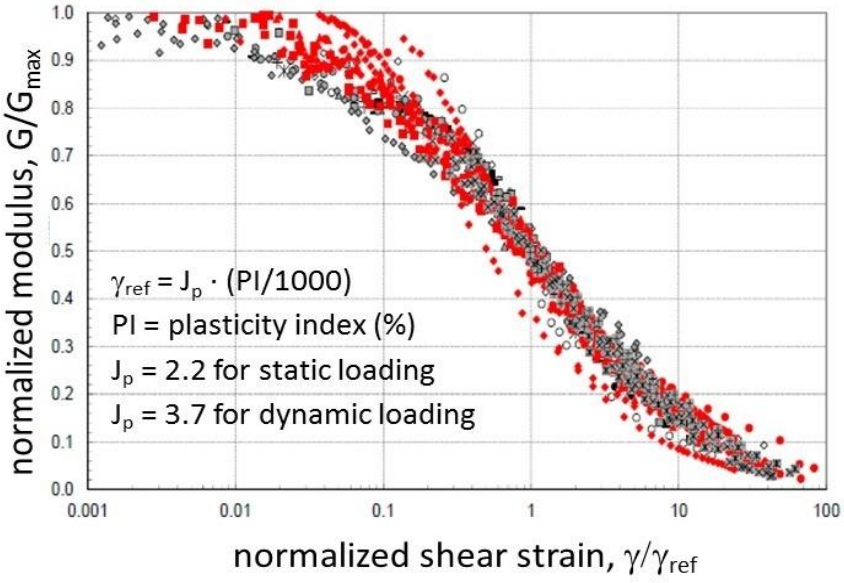

Figure 7.8: Normalized modulus reduction curves for 26 clays reported by Vardanega and Bolton (2013)

where the exponent h = 0.736 (static loading) and h = 0.943 (dynamic loading) and the reference shear strain (γ_{ref}) was found related to the clay plasticity. Specifically, γ_{ref} is determined from:

$$\gamma_{ref} = J_p(0.001 \cdot PI) \tag{7.16}$$

where J_p = 2.2 for static loading and J_p = 3.7 for dynamic loading, and PI (%) = plasticity index. The derived modulus reduction curves for dynamic loading conditions are comparable with the well-known Vucetic-Dobry curves (1991) when adjusted for strain rate effects.

7.5 Poisson's Ratio

Poisson's ratio (ν) is an elastic parameter and defined as the ratio of lateral strain to axial strain:

$$\nu = -\epsilon_h / \epsilon_v . \tag{7.17}$$

The value for Poisson's ratio for undrained loading at constant volume is ν_u = 0.5. For simple isotropic elastic theory, the range of values for drained loading is often taken as: $0 \leq \nu' \leq 0.5$. However, values > 0.5 are possible if dilatancy is considered.

7.5.1 Poisson's Ratio From Lab Tests

For drained loading, local strain measurements made directly on soil specimens with special internal high-resolution instrumentation (e.g., Burland 1989; Lehane and Cosgrove 2000) show that the value of drained ν' is generally lower than those reported from earlier measurements that contained bedding and boundary errors. These on-specimen measurements indicate a range: $0.15 < \nu' < 0.25$ for all types of geomaterials (clays, silts, sands, rocks) at working load levels that correspond to relatively small-strains ($\epsilon_s < 0.1\%$). ***Figure 7.9*** shows a collection of proximeter measurements from several sands and two clays. At higher strains, ν' increases as failure states are approached (Mayne et al. 2009). Thus, a characteristic $\nu' \approx 0.2$ can be adopted for drained loading conditions in the elastic range, generally when FS $\geq$ 2.

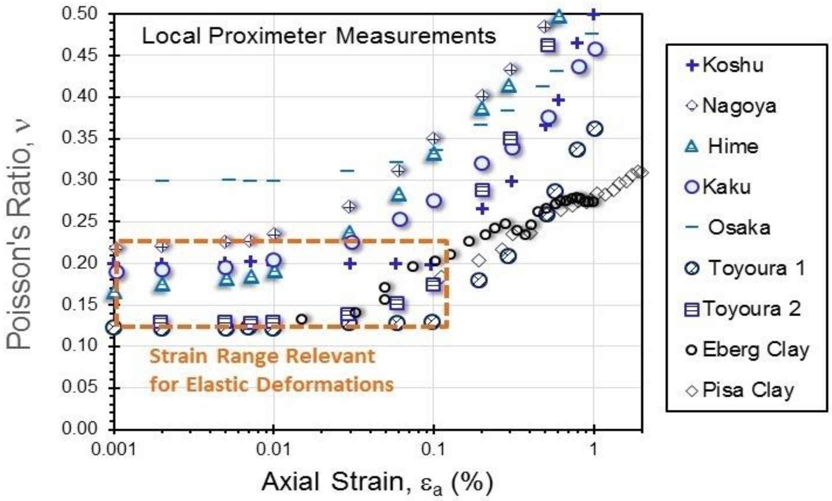

Figure 7.9: Poisson's ratios measured by local strain transducers for 7 sands and 2 clays (modified after Lehane and Cosgrove 2000)

7.5.2 Poisson's Ratio from Geophysical Tests

Poisson’s ratio can also be obtained from shear wave (V_s) and compression wave (V_p) velocities, at least for dry soils and perhaps partially-saturated ground.

The small-strain constrained modulus (M_0) is obtained as:

$$M_0 = \rho_t \cdot V_p{}^2 \tag{7.18}$$

The value of M_0 with small-strain shear modulus (G_0) from eqn (7.9) can then be used to calculate the Poisson’s ratio from isotropic elasticity theory:

$$\nu' = \frac{M_0 - 2 \cdot G_0}{2 \cdot M_0 - 2 \cdot G_0} \tag{7.19}$$

However, it can be noted that once the groundwater table is encountered, the measured V_p data most always reflect the waves travelling through water (a.k.a., Hydro-P), and not the soil skeleton, so that the derived ν values are close to the undrained case, that is: $\nu \approx 0.5$.

7.6 Backfigured Drained Moduli from Foundation Performance on Sands

Schmertmann (1970) is recognized as having introduced CPT into the USA and using the results to help improve calculations of footing settlements on sands. From his work with screw-plate load tests in Florida and mechanical CPT results in fine sands, he recommended:

$$E' = 2 \cdot q_c \tag{7.20}$$

Later efforts using calibration chamber tests on clean sand deposits that were prepared at a range of relative densities and various degrees of overconsolidation found that eqn (7.7) better applied with the a_D factor increasing with OCR and decreasing D_R (Kulhawy & Mayne 1990):

$$\text{NC Sands:} \quad \alpha_D \approx 10^{1.09 - 0.0075 \cdot D_R} \tag{7.21}$$

$$\text{OC Sands:} \quad \alpha_D \approx 10^{1.78 - 0.0122 \cdot D_R} \tag{7.22}$$

Magnitudes of elastic moduli can be backfigured from the field performance of foundations. For shallow foundations on sands, a database of full scale loading tests has been compiled from 67 footings resting on 14 sands where the load versus displacement responses have been evaluated (Mayne and Woeller 2014). These were supplemented with results from measured settlements of bridge and building foundations from 98 structures (Mayne and Dasenbrock 2018). All sands were subjected to CPT soundings and the measured cone resistances were averaged over a depth of approximately 1.5B beneath the foundation bearing elevations.

Figure 7.10 shows the backcalculated equivalent elastic moduli normalized by the cone resistances as a nonlinear function with the normalized displacements (s/B). The overall trend for 130 foundations is represented by:

$$E = 0.5(q_{net})(s/B)^{-0.5} \tag{7.23}$$

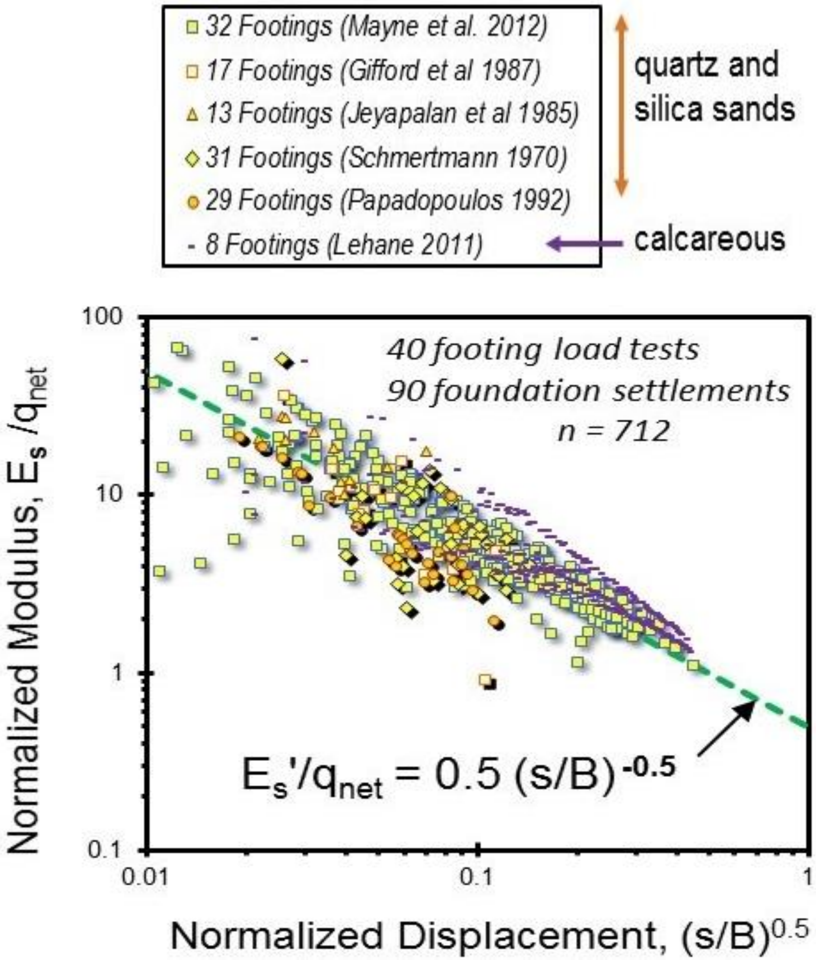

Figure 7.10: Elastic moduli backcalculated for 130 footings on sands

7.7 Undrained Modulus from Rigidity Index

The rigidity index (I_r) is an input parameter to many geotechnical solutions, including those based in cavity expansion, strain path methods, and finite elements. Specifically, I_r is defined as the ratio of shear modulus to shear strength ($I_R = G/\tau_{max}$). For undrained loading, $\tau_{max} = s_u$, and therefore the undrained shear modulus (G_u) can be determined from:

$$G_u = I_R \cdot s_u \tag{7.24}$$

Similarly, the undrained Young's modulus is obtained from the relationship:

$$E_u = 2 \cdot G_u \cdot (1+\nu) = 3 \cdot G_u \tag{7.25}$$

On large or critical projects, the magnitude of I_R can be ascertained from the results of laboratory stress-strain curves on high-quality undisturbed samples. Thus, for undrained conditions, results from simple shear or triaxial tests can be used (Foott & Ladd 1981). ***Figure 7.11*** depicts a shear stress versus shear strain curve and shows that the rigidity index can be considered as the reciprocal of a reference shear strain ($\gamma_{ref} = 1/I_R$).

As per the aforementioned Sections 7.3 and 7.4, it is well-recognized that the modulus of soil is highly nonlinear from the nondestructive range (G_{max}) to intermediate strains (G) to failure at peak strength (G_f). Consequently, there are a number of ways to define a reference value of I_R and associated G. One common value is G_{50} that corresponds to the secant modulus at a factor of safety of FS = 2; that is, a secant shear modulus defined at 50% of its shear strength. Moreover, as many laboratory shear tests intend to reach peak strength at 1% strain in soft to firm clays, the operational rigidity index at failure would be $I_R = 1/\gamma_s = (1/0.01) = 100$, which is often taken as a common default value in practice (e.g., Houlsby & Teh 1988; Teh & Houlsby 1991).

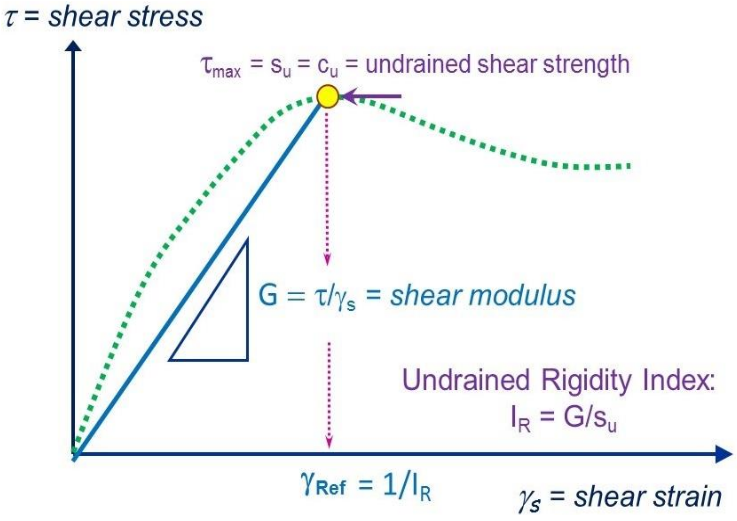

Figure 7.11: Undrained rigidity index from measured τ versus γ_s curve defined at peak

The cone penetrometer is a full-displacement probe. Therefore, since 100% of the soil beneath the axis of the penetrometer is displaced during CPT, it is believed that the operational rigidity index corresponds to that at failure, i.e. $I_R = G_f/s_u$ where G_f is the shear modulus defined at peak strength, as indicated in ***Figure 7.11***.

For estimating a value of I_R from CAUC triaxial tests, empirical trends have been correlated to OCR and plasticity index (PI) of the clay and presented in graphical form by Keaveny and Mitchell (1986). This relationship can be approximated by the expression:

$$I_R \approx \frac{\exp(0.044(137-PI))}{(1+\ln(1+0.038(OCR-1)^{3.2}))^{0.8}} \tag{7.26}$$

By deriving stress-strain curves from SCPTU results, Krage et al. (2014) posed the relationship:

$$I_{R50} = 1.811\frac{G_{max}}{(q_{net})^{0.75}(\sigma'_{v0})^{0.25}} \tag{7.27}$$

where the input terms are all in the same units.

For regular clays that are inorganic and relatively insensitive, the SCE-CSSM solution (Section 4.4.1) provides the operational value of rigidity index (Mayne 2001; Agaiby & Mayne 2018b):

$$I_R = exp\left(\frac{1.5 + 2.925 \cdot M_c \cdot a_x}{M_c \cdot (1 - a_x)}\right) \tag{7.28}$$

where $M_c = (6 \cdot \sin\phi')/(3 - \sin\phi')$ and slope a_x is found by plotting $\Delta u_\sigma = (u_2 - \sigma_{vo})$ versus net cone resistance, $q_{net} = q_t - \sigma_{vo}$; or alternately, slope a_x is determined as the slope of (U-1) versus normalized cone resistance, Q.

A surrogate expression of the solution uses the form:

$$I_R = exp\left[a_y \cdot \left(\frac{1.5}{M_c} + 2.925\right) - 2.925\right] \tag{7.29}$$

where a_y = slope of the plot of net cone resistance, $q_{net} = (q_t - \sigma_{v0})$, versus effective cone resistance, $q_E = (q_t - u_2)$. For inorganic clays of low-medium sensitivity, the variation of I_R with ϕ' and slope a_y is presented in ***Figure 7.12***.

Note that for sensitive and quick clays, Section 4.4.5 provides an expression for undrained rigidity index comparable to that above for a modified SCE-CSSM solution yet requires two values of frictional parameters: M_{c1} (corresponding to ϕ_1' at peak) and M_{c2} (corresponding to ϕ_2' at large strains). For sensitive clays, a chart version of the interrelationship of I_R, slope parameter $a_q = \Delta(U-1)/\Delta Q$, and the two friction angles (ϕ_1' and ϕ_2') is provided by Mayne & Benoît (2020).

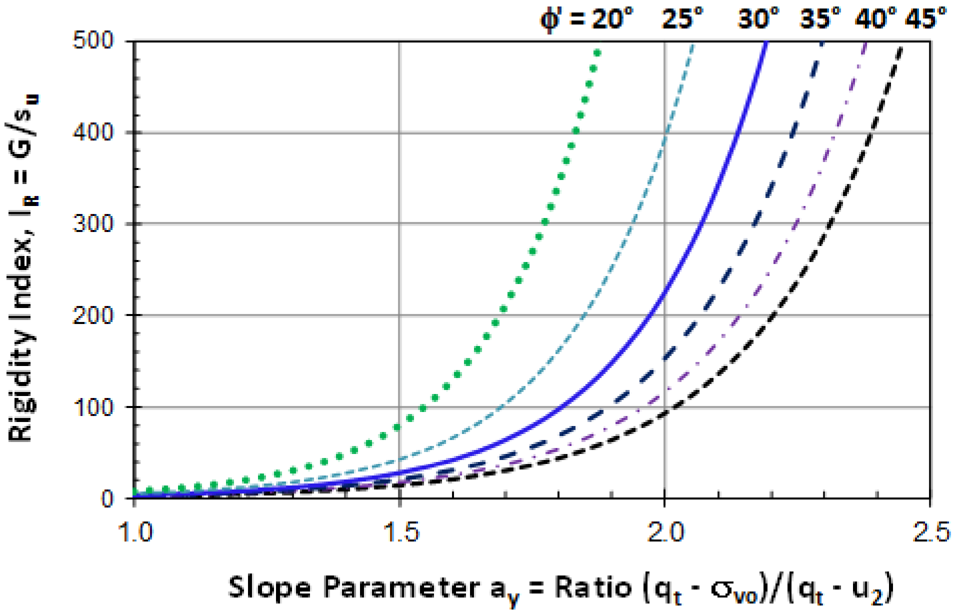

Figure 7.12: Undrained rigidity index (I_R) of clays as a function of effective stress friction angle (ϕ') and slope parameter a_y from SCE-CSSM solution

7.7.1 Case Study: Sandpoint

The results of a CPTU sounding in soft silty clay at Sandpoint, Idaho were shown previously in ***Figure 5.13***. The soils have overall mean index properties: LL = 45.2 $\pm$ 6.3%, PI = 19.9 $\pm$ 4.7%, and w_n = 45.2 $\pm$ 6.4%. Results of DST by SCPTU indicated: V_s (m/s) = 2.35 z (m) + 151.

For a representative OCR = 1.5 and PI = 20%, ***Equation 7.26*** estimated I_R = 170. Using the corresponding G_{max} from the SCPTU profile together with the CPT readings, ***Equation 7.27*** determined an average I_r = 244. For the 2 values of I_R provided by SCE-CSSM, ***Equations 7.28 and 7.29*** provide estimates of I_r = 193 and 184, respectively, as shown by ***Figure 7.13***.

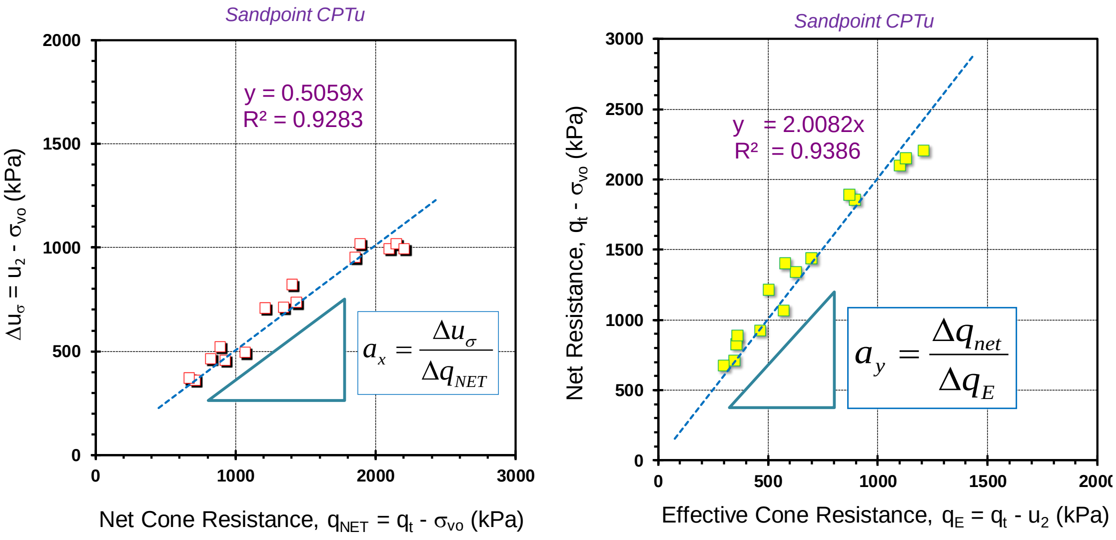

Slope a_x = 0.51
ϕ' (deg) = 33
$\sin\phi'$ = 0.54
M_c = 1.33
Rig.Index, I_R = 193

$$I_R = \exp\left(\frac{1.5 + 2.925 \cdot M_c \cdot a_x}{M_c \cdot (1 - a_x)}\right)$$

Slope a_y = 2.01
ϕ' (deg) = 33
$\sin\phi'$ = 0.54
M_c = 1.33
Rig.Index, I_R = 184

$$I_R = \exp\left[a_y \cdot \left(\frac{1.5}{M_c} + 2.925\right) - 2.925\right]$$

Figure 7.13: Evaluation of the slope parameters a_x and a_y for assessing I_r from SCE-CSSM solution using CPTU data from Sandpoint, Idaho

8 Flow Parameters from Dissipation Testing

Porewater pressures generated during cone penetration in fine-grained soils are transient and caused by insertion of the probe. Once the penetration process is halted, excess pressures will decay with time and readings will eventually reach the equilibrium value (u_0).

Results from porewater pressure measurements taken during a piezocone sounding in soft clay at the Canadian Test Site No. 1 in South Gloucester, Ontario are shown in ***Figure 8.1***. At each rod break, the penetration was stopped and the porewater pressures permitted to dissipate with time. The dissipation traces can be seen as drops in the u_2 readings at one-meter depth intervals.

During undrained penetration, consolidation does not occur since constant volume is maintained. Thus the u_2 penetration reading with depth represents the condition corresponding to a zero degree of consolidation (U = 0%). In due time, the u_2 reading will eventually reach u_0 corresponding to the completion of primary consolidation (U = 100%). For the dissipations at 21 and 22 m depths, full equilibrium was achieved.

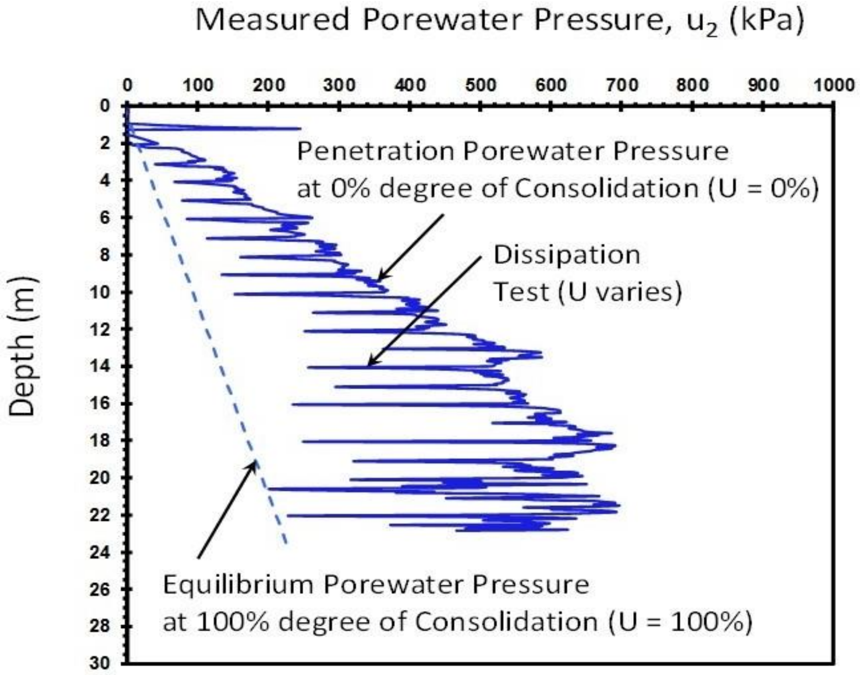

Figure 8.1: Porewater pressure profile from CPTU sounding at South Gloucester, Ontario

By measuring the rate of porewater pressure dissipation, two flow parameters of soil can be assessed: (1) coefficient of permeability (k); and (2) coefficient of consolidation (c_{vh}). This requires plots of the measured u_2 readings versus time, with the latter presented in either arithmetic, logarithmic, or square root plots. ***Figure 8.2*** shows a total of 18 piezo-dissipation records from Gloucester with u_2 plotted versus log time. The dissipations are grouped into three categories, primarily based on their depths to indicate an upper clay, intermediate layer, and lower clay layer.

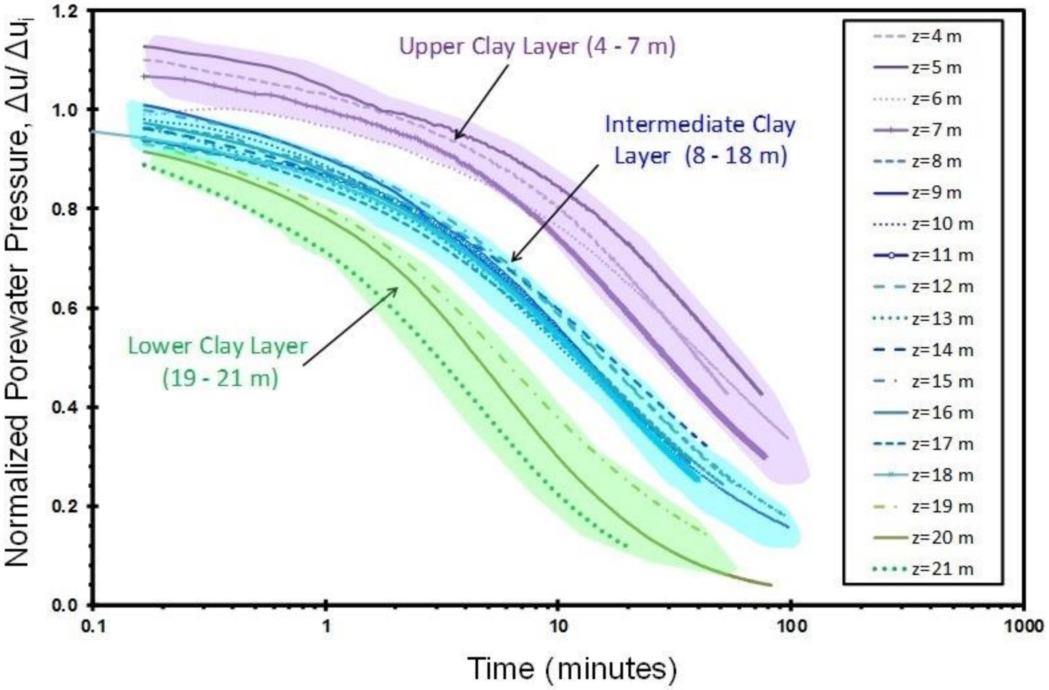

Figure 8.2: Piezo-dissipation records with logarithm time in soft clays at Gloucester site

For convenience, an established time of 50% degree of consolidation, designated t_{50}, is often used in practice to represent a characteristic value from the dissipation data. As noted, the penetration value of the u_2 reading represents 0% degree and the equilibrium value ($u_2 = u_0$) represents 100% degree of consolidation, therefore t_{50} is the time required to reach the porewater pressure value that is half-way between these two values.

Figure 8.3 illustrates the evaluation of t_{50} from a porewater pressure dissipation record in firm clay at a depth z = 4.2 m in Evergreen, NC. This is a monotonic type response, since the porewater pressures are highest during CPT pushing and less at all times following the halting of penetration. First, the u_0 is calculated for the noted groundwater depth of z_w = 0.4 m, assuming unconfined conditions, giving u_0 = 37 kPa. The value of u_2 during penetration is determined as u_2 (t = 0) = 829 kPa. Using the porewater reading corresponding to 50% consolidation(433 kPa) determines the characteristic value t_{50} = 7 minutes for this test.

8.1 from Dissipation Tests

The coefficient of consolidation (c_v) is a flow parameter that governs the rate of porewater pressure dissipation around pile foundations, shallow foundation settlements, and design of vertical wick drains. From one-dimensional consolidation theory, the coefficient of consolidation is given by:

$$c_v = k \cdot D'/\gamma_w \qquad (8.1)$$

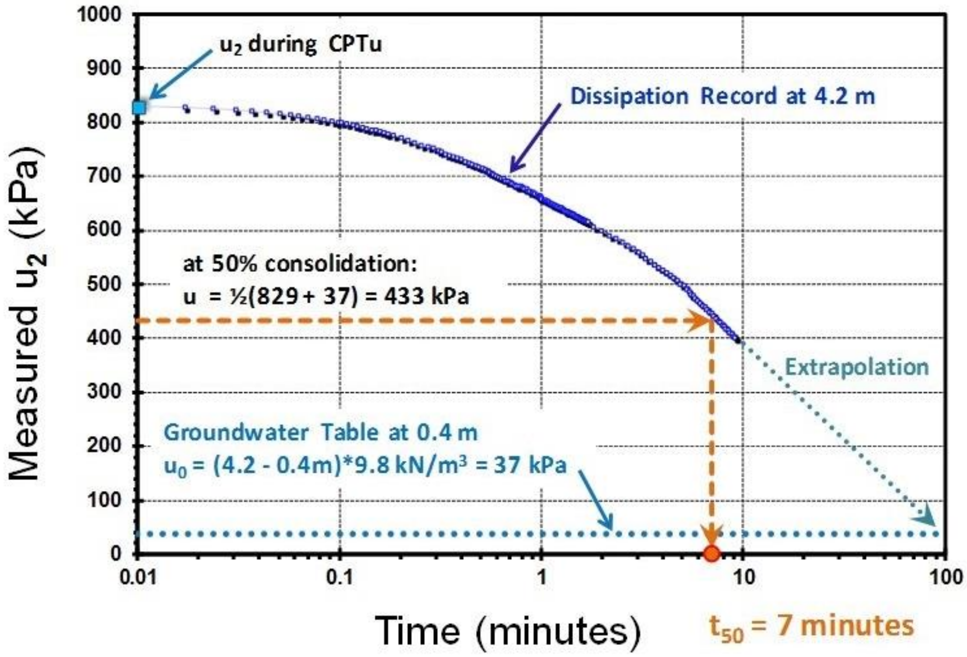

Figure 8.3: Determination of representative time t_{50} from dissipation at Evergreen, NC

where k = coefficient of permeability, D' = constrained modulus, and γ_w = unit weight of water. The evaluation of c_v from lab consolidation tests involves the use of a time factor which depends on the degree of consolidation, as well as the drainage path (Holtz et al. 2011).

In laboratory consolidation tests, the coefficient of consolidation is designated c_v as related to the vertical flow of water through the soil specimen. In contrast, in pile design, wick drains, and piezocone evaluations, the term c_h is used to represent flow in the horizontal direction. Herein, the nomenclature c_{vh} will be used so as to not distinguish any particular direction of flow, since drainage occurs in three dimensions away from the cone tip. Moreover, in many natural marine clay deposits, there is little difference in the permeability anisotropy, i.e., $k_h \approx k_v$ (see later section and ***Table 8.1***).

For the evaluation of c_{vh} from CPTU dissipation tests, there exist multiple interpretative approaches based in theory (cavity expansion, dislocation point), numerical simulations (finite elements, strain path method), and empirical methods. A number of available procedures are discussed by Jamiolkowski et al. (1985) and Burns & Mayne (1998a, 1998b). Herein, two methods will be reviewed:

- Strain Path Method (SPM) for monotonic decay of Δu with time (Houlsby & Teh 1988)
- An analytical Spherical Cavity Expansion-Critical State Soil Mechanics (SCE-CSSM) solution for both monotonic and dilatory porewater pressure response (Burns and Mayne 2002).

8.1.1 Dissipation Evaluation from Strain Path Method

For the strain path method (SPM) solution by Houlsby & Teh (1988), theoretical time factors (T*) for different degrees of monotonic porewater pressure dissipation were evaluated at several key points on a penetrometer (e.g, apex, mid-face, shoulder, upper shaft above sleeve). Using the characteristic dissipation time (t_{50}), the value of c_{vh} is calculated from:

$$c_{vh} = \frac{T*_{50} \cdot (a_c)^2 \cdot \sqrt{I_R}}{t_{50}} \tag{8.2}$$

where the time factors for 50% consolidation are T_{50}^* = 0.118 and 0.245, respectively, for type 1 (midface) and type 2 filter elements (shoulder position), a_c = probe radius (= 1.78 cm for a 10-cm^2 cone and 2.19 for a 15-cm^2 size), and I_R = G/s_u = undrained rigidity index, where G = shear modulus and s_u = undrained shear strength.

The solution for type 2 piezocones at 50% consolidation is depicted graphically in ***Figure 8.4***. If the operational value of rigidity index is unknown, a common default value is taken as I_r = 100. Prior ***Section 7.7*** provides some guidance on the selection of I_R.

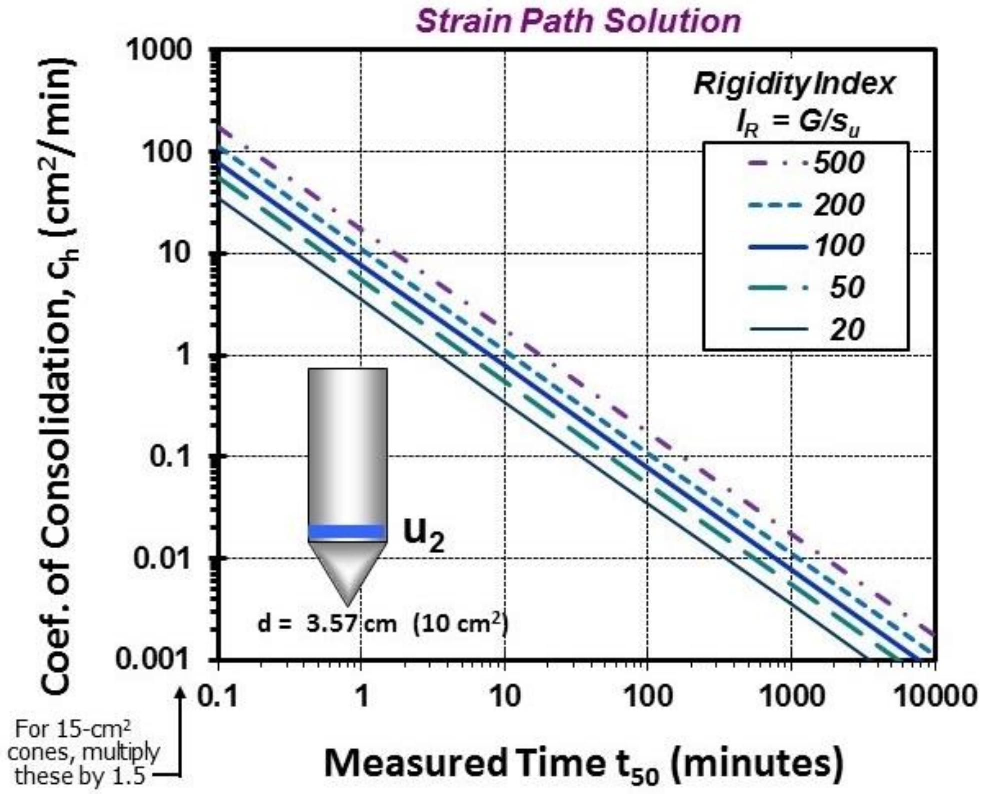

Figure 8.4: Chart solution for evaluating c_{vh} from dissipation tests at 50% consolidation using strain path method (after Houlsby & Teh 1988)

If desired, degrees of consolidation other than 50% can be handled by this method (e.g., 30%, 80%, etc) as detailed by Teh and Houlsby (1991). In fact, a complete matching of the entire measured porewater pressure dissipation curves can be handled by utilizing algorithms that provide all degrees of consolidation (Mayne 2007b; DeJong and Randolph 2012). As such, the normalized excess porewater pressures ($\Delta u/\Delta u_i$) are presented as a function of modified time factor T^* in ***Figure 8.5***.

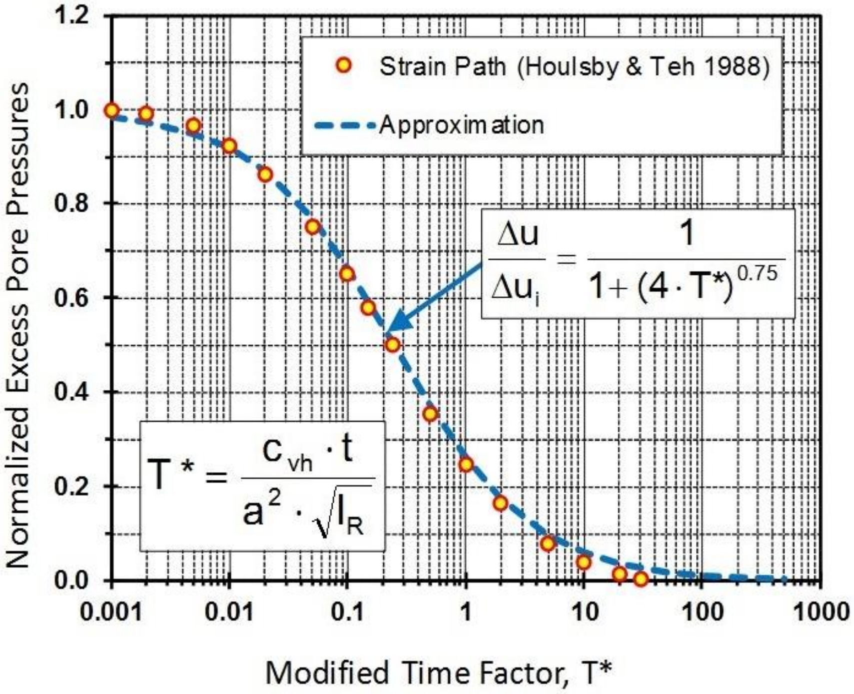

Figure 8.5: Strain path solution for type 2 dissipation at any degree of consolidation (after Teh and Houlsby 1991)

An algorithm that fits approximately the SPM solution over most of the range of values is:

$$\frac{\Delta u}{\Delta u_i} = \frac{1}{1+(4T^*)^{0.75}} \tag{8.3}$$

where the modified time factor (T*) for any degree of consolidation is expressed:

$$T^* = c_{vh}\cdot t/[(a_c)^2\cdot\sqrt{I_R}] \tag{8.4}$$

8.1.2 Dissipation Evaluation from SCE-CSSM Solution

A hybrid analytical solution for piezocone dissipation has been derived from spherical cavity expansion theory and critical state soil mechanics (SCE-CSSM), as presented by Burns and Mayne (1998a, 2002). This approach can handle both monotonic and dilatory porewater dissipation responses. An example fitting of the SCE-CSSM solution is presented in ***Figure 8.6*** for measured dissipations at a depth of 15.6 m in soft silty clay at Sandpoint, Idaho. This shows a monotonic response and iterative procedure to fit the curve.

SCE-CSSM Solution for Piezo-Dissipation

INPUT	VALUE	UNITS	PARAMETER
c_h =	1.2	(mm^2/s)	Coef. of Consolidation
OCR =	1.8	= σ_p'/σ_{vo}'	Overconsolidation Ratio
I_R =	187	= G/c_u	Rigidity Index
ϕ' =	33.5	(degrees)	Effective Friction Angle
Λ =	0.8	= $(1-C_s/C_c)$	Plastic Vol. Strain Poten.
a =	22	(mm)	Probe Radius (mm)
x_t =	2	(mm)	Thickness of shear zone
σ_{vo}' =	116.32	(kPa)	Effective Overburden
u_o =	133.28	(kPa)	Hydrostatic Pressure

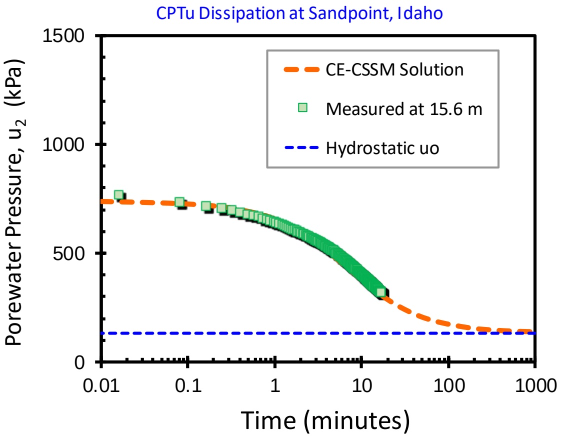

Figure 8.6: Fitting procedure for obtaining c_{vh} from monotonic type dissipation response in soft silty clay at Sandpoint, Idaho

Whereas monotonic decays always decrease with time after penetration stops, dilatory response involves an initial increase of porewater pressures to a peak value, followed by a subsequent decrease with time. An example of a dilatory u_2 dissipation in Chalco Lake clay in Mexico is presented in ***Figure 8.7***. This makes the determination of t_{50} problematic since it is unclear whether to use the initial u_2 value (penetration reading), or the latter peak u_2 reading that occurs during dilatory dissipation. (P.S. It turns out neither is correct).

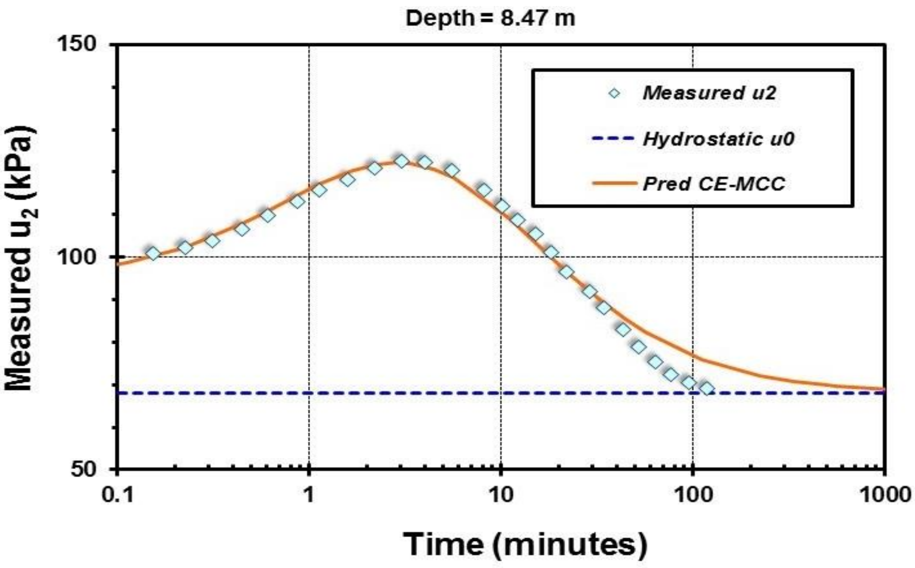

Figure 8.7: Dilatory porewater pressure response and fitted curve for Chalco Lake clay, Mexico (Cruz and Mayne 2006)

Spherical cavity expansion theory states that the large soil mass involved in the dissipation (represented by a ball of diameter D) is related to the size of the intruding penetrometer (diameter d) in the ratio D/d is equal to the cube root of the rigidity index:

$$\frac{D}{d} = \sqrt[3]{I_r} \tag{8.5}$$

Since the rigorous solution involves a second order partial differential solution that depends on several input parameters (ϕ, OCR, I_r, Λ, and c_{vh}), a set of graphical results have been presented (Burns and Mayne 1998a, 1998b). One set of examples is presented in ***Figure 8.8*** for the case (ϕ' = 30°, Λ = 0.8, and I_R = 200) over a range of OCRs from 1 to 100, with normalized excess porewater pressures ($\Delta u/\Delta u_i$) versus a theoretical time factor (T) defined by:

$$T = \frac{c_{vh} \cdot t}{a_c^{\,2}} \tag{8.6}$$

where t = time and a_c = radius of penetrometer.

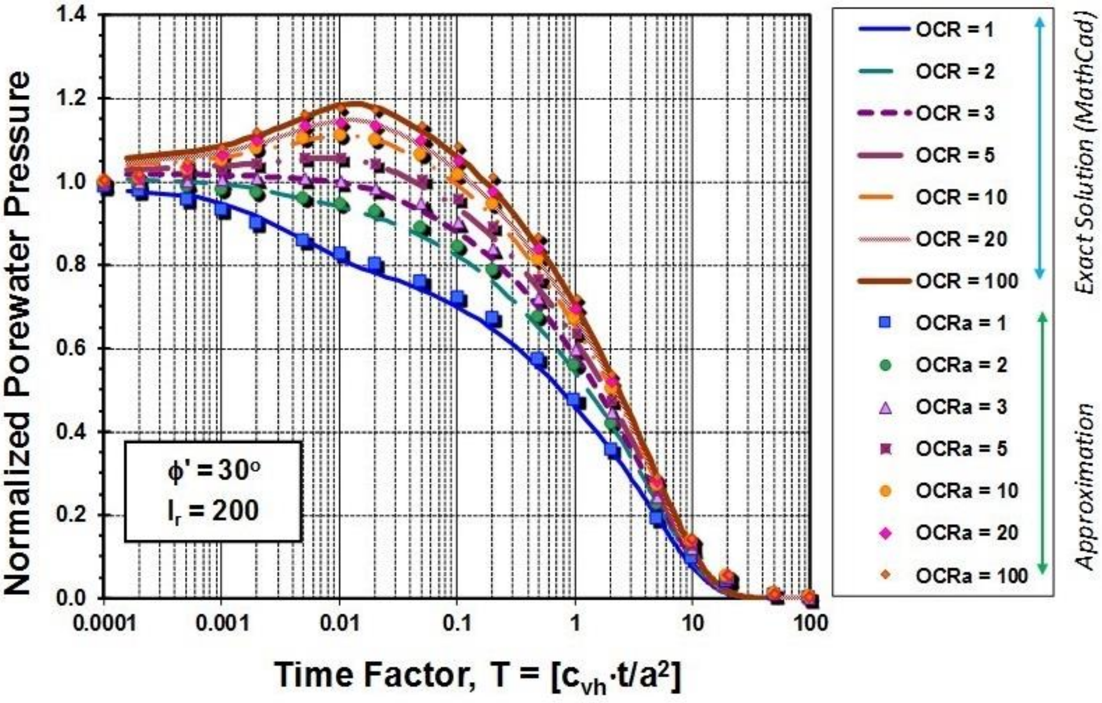

Figure 8.8: Normalized porewater pressures vs. time factor from SCE-CSSM solution (after Burns and Mayne 1998a; 1998b; and Mayne 2001)

8.1.3 Approximate SCE-CSSM Solution

An approximate SCE-CSSM method has been developed for general spreadsheet use (Mayne 2001). As seen by ***Figure 8.7***, the approximate approach compares well with the rigorous solution.

The measured excess porewater pressures are the sum of an octahedral component (SCE) plus a shear-induced component (CSSM). For a type 2 piezocone, the Δu_2 values during penetration can be represented by:

$$\Delta u_2 = (\Delta u_{oct})_i + (\Delta u_{shear})_i \tag{8.7}$$

where the components can be calculated from:

$$(\Delta u_{oct})_i = \left(\frac{2M_c}{3}\right)\left(\frac{OCR}{2}\right)^{\Lambda} \ln(I_r)\sigma'_{v0} \tag{8.8}$$

$$(\Delta u_{shear})_i = \left(1 - \left(\frac{OCR}{2}\right)^{\Lambda}\right)\sigma'_{v0} \tag{8.9}$$

To unify the solutions for a range of I_r values, a modified time factor (T') for the SCE-CSSM model is introduced as:

$$T' = \frac{c_{vh} t}{a_c^2 I_r^{0.75}} \tag{8.10}$$

where t = elapsed time after penetration is halted.

The two porewater pressure components are dissipated at different rates with time:

$$(\Delta u_2)_t = \frac{(\Delta u_{oct})_i}{1+50T'} + \frac{(\Delta u_{shear})_i}{1+(326/x_s)^2 \cdot T'} \tag{8.11}$$

where x_s = thickness of the shear zone in mm (usually 1 mm $< x_s <$ 6 mm). The value of c_{vh} is found by trial-and-error fitting of the analytical curves to the measured dissipation data.

An example fitting is shown in ***Figure 8.9*** for dilatory dissipation data obtained in very hard clay from Taranto, Italy (Pane et al. 1995). Reported lab reference values for this site were in the range of 0.10 to 0.25 mm^2/s which are compatible with the piezocone interpretations.

8.1.4 Simplified SCE-CSSM Solution for Monotonic Dissipations

For clays that show a simple monotonic porewater pressure response, the SCE-CSSM solution resolves to a simpler expression for u_2 dissipations given by:

$$c_{vh} = \frac{T'_{50} \cdot (a_c)^2 \cdot (I_R)^{0.75}}{t_{50}} \tag{8.12}$$

where the modified time factor at 50% consolidation is T'_{50} = 0.028. This solution can also be used for equivalent monotonic dissipations after adjusting the dilatory response curves.

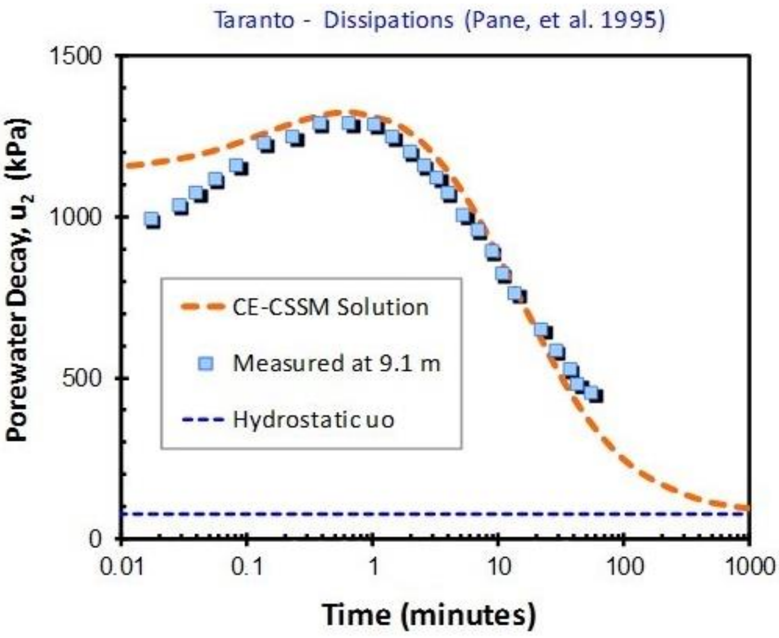

INPUT	VALUE	UNITS	PARAMETER
c_h =	0.1	(mm^2/s)	Coef. of Consolidation
OCR =	15	$= \sigma_p'/\sigma_{vo}'$	Overconsolidation Ratio
I_R =	32	$= G/c_u$	Rigidity Index
ϕ' =	28	(degrees)	Effective Friction Angle
Λ =	0.7	$= (1-C_s/C_c)$	Plastic Vol. Strain Poten.
a =	17.85	(mm)	Probe Radius (mm)
x_t =	6	(mm)	Thickness of shear zone
σ_{vo}' =	101.5	(kPa)	Effective Overburden
u_o =	78	(kPa)	Hydrostatic Pressure

Figure 8.9: Measured and fitted dilatory dissipations from hard Taranto clay at 9.1 m depth using SCE-CSSM solution

8.1.5 Case Study: Sandpoint

Figure 8.10 shows the overall summary profile of c_{vh} in soft clay at Sandpoint, Idaho, as determined from standard laboratory consolidation tests. The measured t_{50} values from several series of CPTU dissipation tests are presented in the left portion of ***Figure 8.10***. From Section 7.7.1, the undrained rigidity index from the SCE-CSSM solution gave 187 which is used to evaluate the c_{vh} from the CPTU dissipation data per equation (8.12). The CPTU c_{vh} values appear slightly higher than the lab reference values. Note carefully that the soil profile at Sandpoint contains many enumerable sandy lenses, as well as several sand layers (reference CPTU in prior Figure 5.13). Since the lab consolidation data represent results only from the soft clay matrix, the piezocone interpretations likely reflect the clay layer plus included sand lenses and sand stringers.

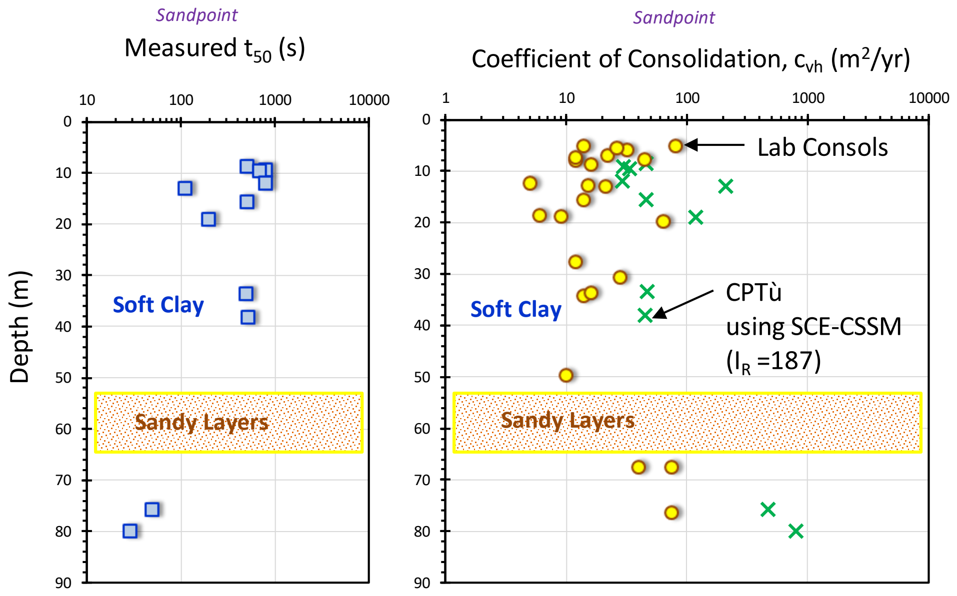

Figure 8.10: Summary of dissipation data and interpreted c_{vh} profile at Sandpoint, Idaho

8.1.6 Case Study: Gloucester, Ontario

A second example is afforded from the series of dissipations shown in prior Figure 8.1 for the Gloucester test site. The reported t_{50} values for the entire profile are given by McQueen et al. (2016). The derived I_R = 96 from the CPTU sounding (Agaiby & Mayne 2016). Using equation (8.12), ***Figure 8.11*** shows a reasonable comparison of c_{vh} values from laboratory and field measurements at the site.

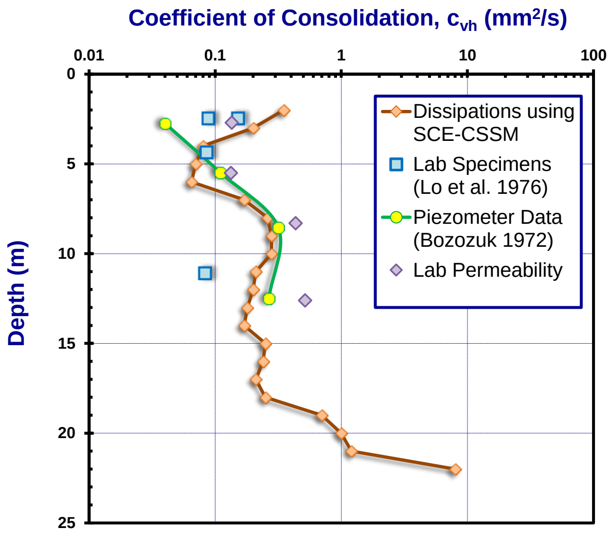

Figure 8.11: Summary comparison of coefficient of consolidation values from laboratory and field tests at Gloucester test site, Ontario

8.2 Adjusted Dilatory Dissipation Curves

For dilatory responses, Sully et al. (1999) recommended several types of empirical adjustments to the measured dissipation records for interpretation. One of these procedures includes the plotting of porewater pressures on a square root time plot to assess a projected initial u_2 reading. This appears to be a reasonable approach to converting measured dilatory dissipations to an equivalent monotonic curve, thus allowing the assessment of t_{50} values (e.g. Schneider & Hotstream 2010; Mahmoodzadeh and Randolph 2014).

From a theoretical viewpoint, dilatory porewater response occurs because the Δu shear-induced components are temporarily negative, but decay rather quickly because they only affect a thin annulus next to the penetrometer. The SCE-CSSM model can therefore be used with a "zero" thickness annulus to find the dissipations solely within the spherical cavity zone. ***Figure 8.12*** shows a calculated family of dilatory dissipations for varying shear thickness zones, suggesting that the square-root of time plot is a valid approach.

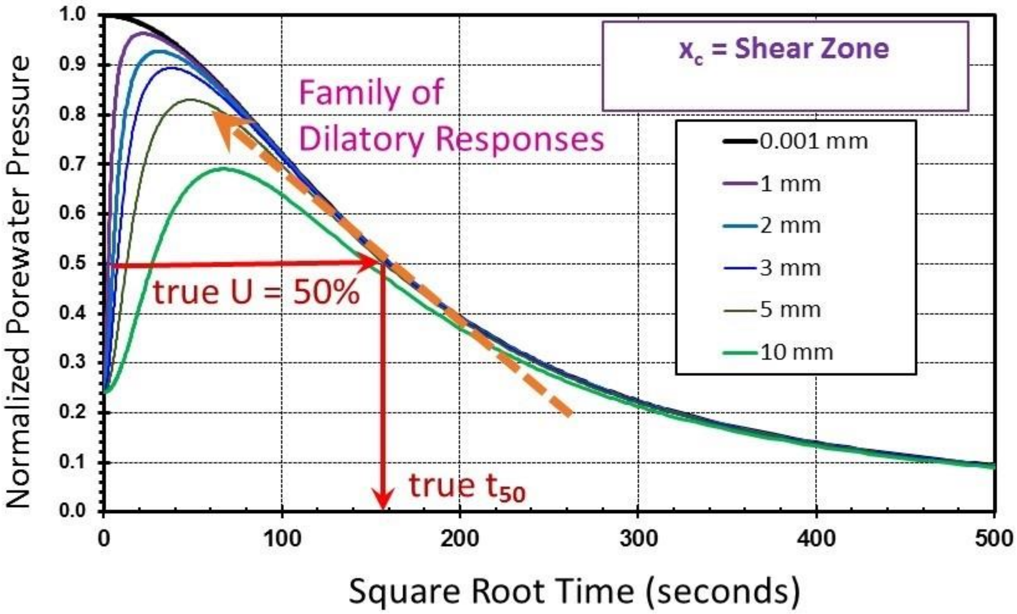

Figure 8.12: Family of theoretical dilatory dissipations for varying shear thickness zones

The procedure for adjusting the dilatory dissipation curve is to pick a point on the post-peak u_2 response and project the data back to a time t = 0 on the square root of time plot. The concept is depicted in ***Figure 8.13***.

Figure 8.14 shows an application of the adjusted dissipation curve procedure resulting in a t_{50} of 14.4 minutes. Using the simplified method of ***Equation 8.12*** with same chosen I_r = 32, the derived c_{vh} = 0.15 mm^2/s compares favorably with that using the more involved and rigorous

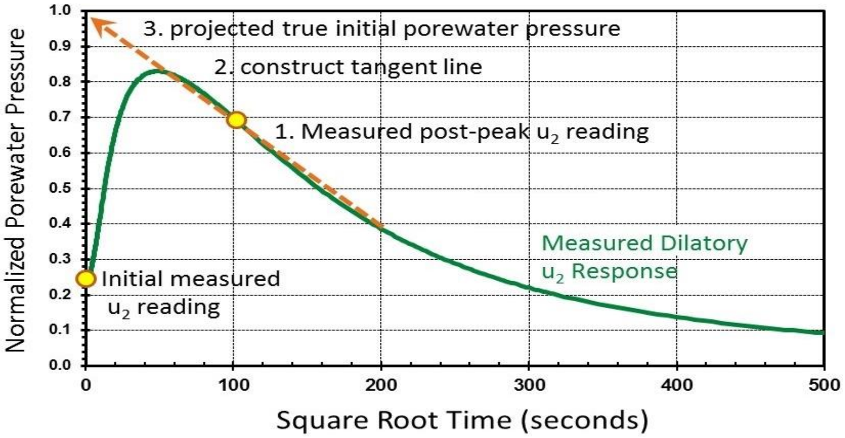

Figure 8.13: Recommended procedure for obtaining the "true" initial porewater pressure and characteristic t_{50} from normalized u_2 readings versus square root time plot

calculations given previously in Figure 8.8 where a value of c_{vh} = 0.10 mm^2/s was obtained. Laboratory reference values for the coefficient of consolidation of the hard Taranto clay are found in the range: 0.10 mm^2/s ≤ c_{vh} ≤ 0.25 mm^2/s (Bruzzi & Battaglio 1987; Burns & Mayne 1998a, 1998b).

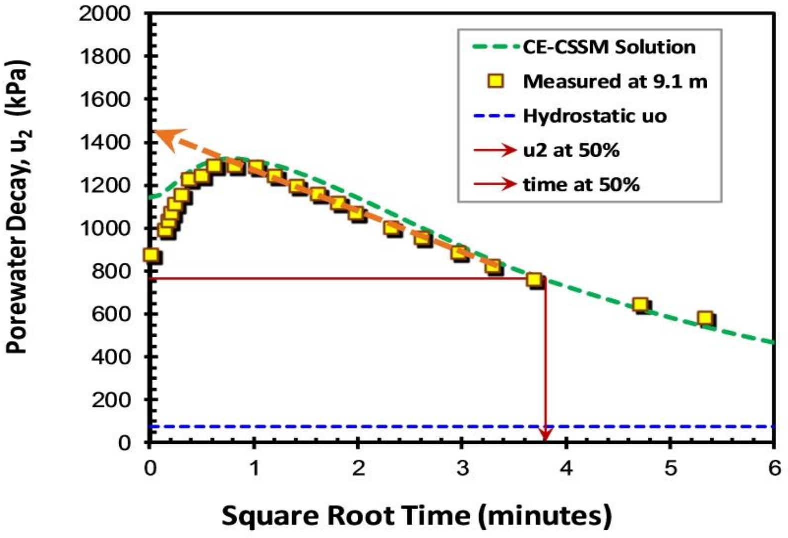

EQUIVALENT MONOTONIC SOLUTION

Note: u_2 and u_0 in kPa

Estimated True Initial u_2 Reading =	1450
Final Equilibrium Pore Pressure =	78
Take u at 50% as average of above	
u_2 Reading at U = 50% Consol =	764
Scaled sqrt t_{50} (min) =	3.8
Measured t_{50} (min) =	14.44
Measured t_{50} (sec) =	866.4

$$c_{vh} = \frac{T_{50}' \cdot a^2 \cdot I_R^{0.75}}{t_{50}}$$

Time Factor T_{50}' (monotonic) =	0.03
U = 50% degree of consolidation	
Rigidity Index, $I_R = G/s_u$ =	32
Probe radius, a (mm) =	17.85
Calculated c_{vh} (mm^2/s) =	0.148
Calculated c_{vh} (cm^2/min) =	0.089

Figure 8.14: Adjusted dilatory dissipation curve procedure applied to Taranto clay

8.3 Permeability

Soil permeability quantifies the flow rate of water in-situ under differential pore pressures. This is different than the coefficient of consolidation, which balances the soil-deformation against porewater pressure dissipation. Soil permeability (k) is also called hydraulic conductivity or the coefficient of permeability, and is in units of m/s. It is related to the more fundamental intrinsic permeability (K) or absolute permeability, which is given in units of m^2, by the relationship:

$$k = K(\gamma_f/\mu_f) \tag{8.13}$$

where γ_f = unit weight of the fluid and μ_f = viscosity of the fluid.

8.3.1 Soil Permeability Anisotropy

Adapting the approach by Leroueil et al. (1991) and Leroueil & Jamiolkowski (1991), a guideline to geological situations governing permeability anisotropy is given in ***Table 8.1***.

Table 8.1: Permeability anisotropy in natural soils (adapted after Leroueil et al. 1991)

Nature of the formation	**Ratio k_h/k_v**
Homogeneous clays of marine, alluvial, deltaic, and lacustrine origin	1 to 1.5
Sedimentary clays with discontinuous lenses and layers, well-developed macrofabric	2 to 3
Varved clays and silts with continuous permeable layers	1.5 to 5
Highly stratified soils with interbedded layers of clay, silt, sand, and/or gravel	2 to 10

For the majority of natural clays, the horizontal permeability is only around 10% to 20% higher than the vertical value (Mesri, Lo, and Feng 1994; Leroueil and Hight 2003). A summary of several special series of laboratory series of permeability tests on different natural soft clays is given in ***Figure 8.15*** whereby both standard vertical measurements of hydraulic conductivity (k_v) are compared with horizontal values (k_h) using radial permeameter devices. Generally, the ratio of k_h/k_v averages about 1.1 for intact clays of marine and water-borne origins.

For varved clays and highly stratified deposits, the ratio of horizontal to vertical permeabilities is higher and may range from 1.5 to 5 or more (Saxena, Hedberg, and Ladd 1978). Very rarely, k_h/k_v approaches 10 in the case of highly stratified deposits and formations.

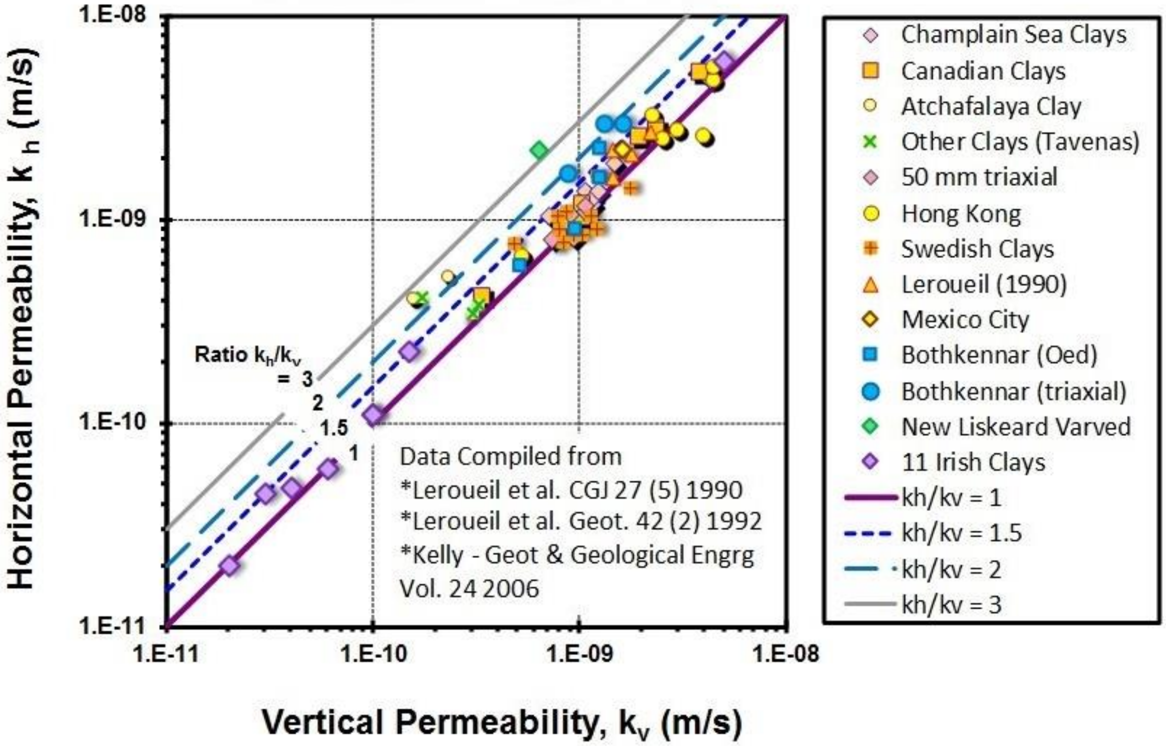

Figure 8.15: Comparing horizontal to vertical permeability at different sites

8.3.2 Soil Permeability from Dissipation Tests

A simple empirical method for estimating the coefficient of soil permeability from piezocone dissipation tests with 10 cm^2 cone probes was presented by Parez and Fauriel (1988), as shown in ***Figure 8.16***. The various wedge regions for several soil types were obtained from available data on normally consolidated deposits. Taking a line through the centers of these wedges gives an approximate trend:

$$k(cm/sec) \approx (251 \cdot t_{50})^{-1.25} \tag{8.14}$$

where the time t_{50} is specified in seconds.

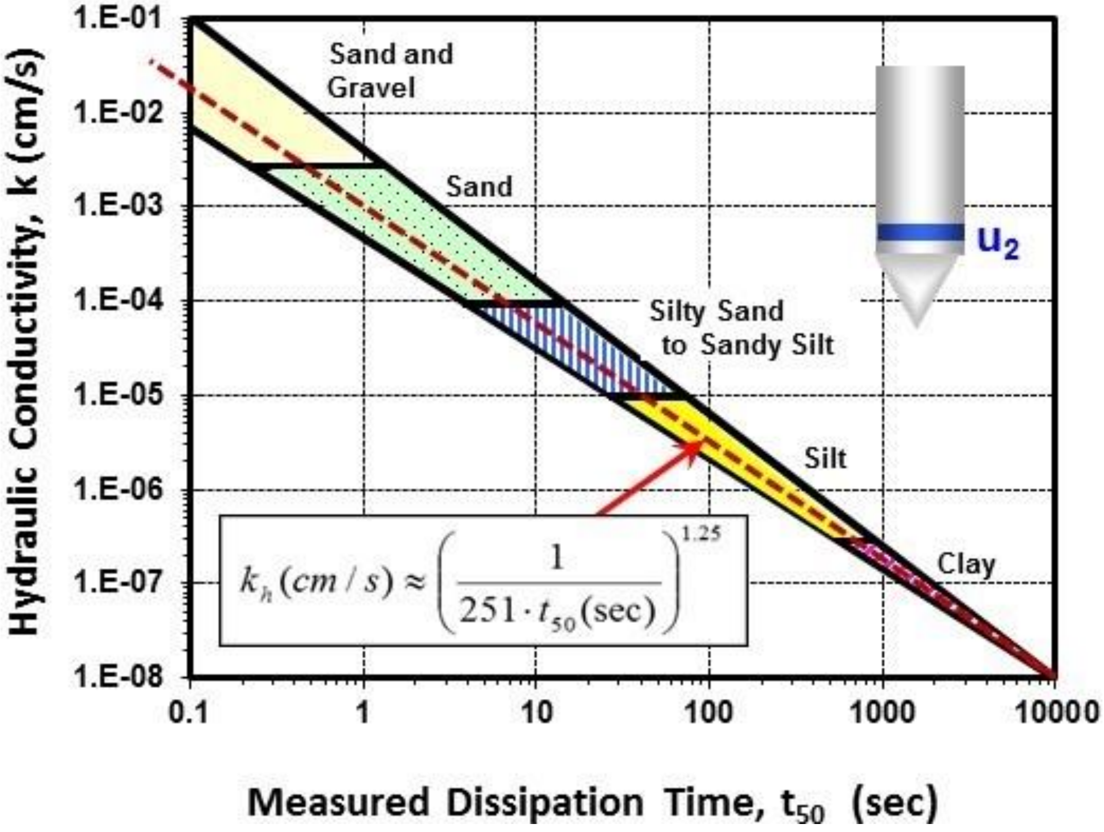

Figure 8.16: Empirical trend for hydraulic conductivity versus dissipation time t_{50} for 10-cm^2 penetrometers (after Parez and Fauriel 1988)

8.3.3 Permeability from Soil Behavior Type

Lunne et al. (1997) assigned estimated values and ranges of soil permeability for each of the 9 zones in the normalized soil behavioral charts (SBTn). Using these as a guide, Robertson and Cabal (2010) provided the following algorithms that relate hydraulic conductivity (k) in terms of the CPT material index (I_c) for soil zones 2 through 7:

$$k(m/s) = 10^{0.952-3.04 I_c}; 1.0 < I_c \leq 3.27 \tag{8.15}$$

$$k(m/s) = 10^{-4.52-1.37 I_c}; 3.27 < I_c \leq 4.0 \tag{8.16}$$

In lieu of two linear expressions, a continuous approximation can be fitted to the selected reference values by:

$$k\ (m/s) \approx (I_{cRW})^{-18} \tag{8.17}$$

as shown in ***Figure 8.17***

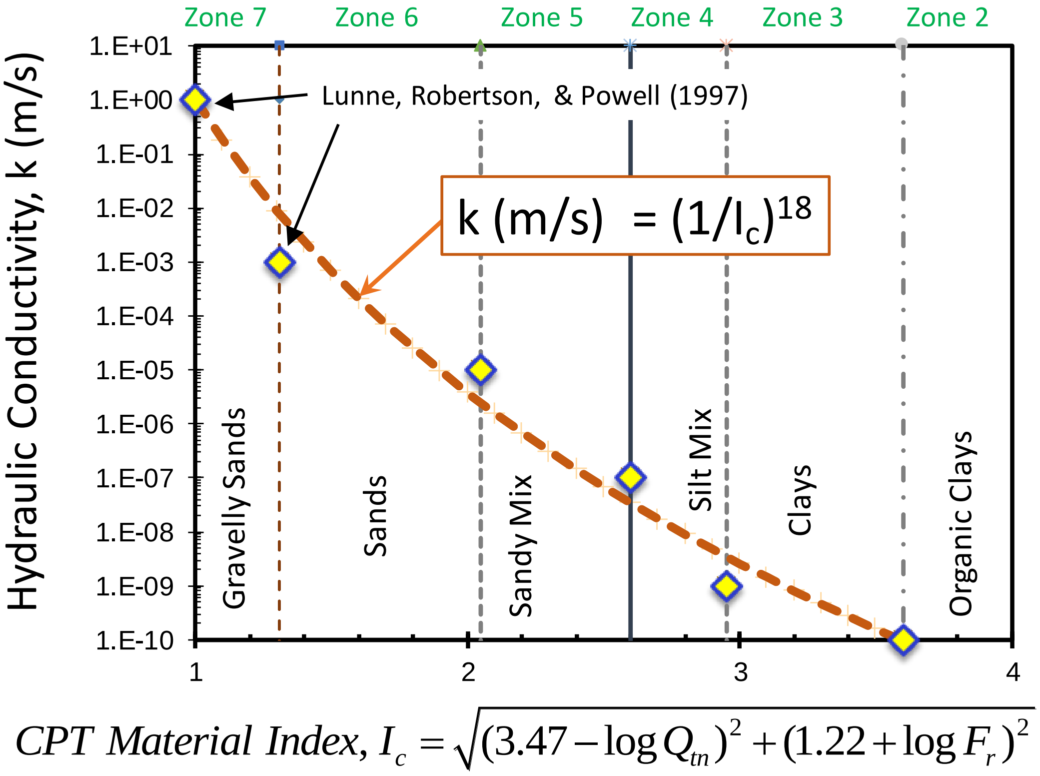

Figure 8.17: Hydraulic conductivity estimated from CPT material index (modified after Robertson and Cabal 2010)

8.4 Case Study: Bothkennar, UK

Using the two aforementioned approaches, results from CPTU soundings and dissipation tests were used to provide evaluations of soil permeability (k) at the Bothkennar soft clay research site in Scotland (Nash, Powell, and Lloyd 1992; Nash, Sills, and Davison 1992). Dissipation tests are reported by Jacobs and Coutts (1992) for both u_1 and u_2 piezocones. Where necessary, equivalent values of t_{50} were made for the u_2 position from u_1 data based on site-specific correlations. Several independent measurements of permeability were made by laboratory triaxial, oedometer, and flow tests, as well as by field methods (Leroueil et al. 1992).

Overall, reasonable agreement in seen for these measurements in comparison with the two simple CPTU methods discussed: (a) t_{50} value in the Parez & Fauriel (1988) trend; and (b) CPT material index I_c method, as seen in ***Figure 8.18***.

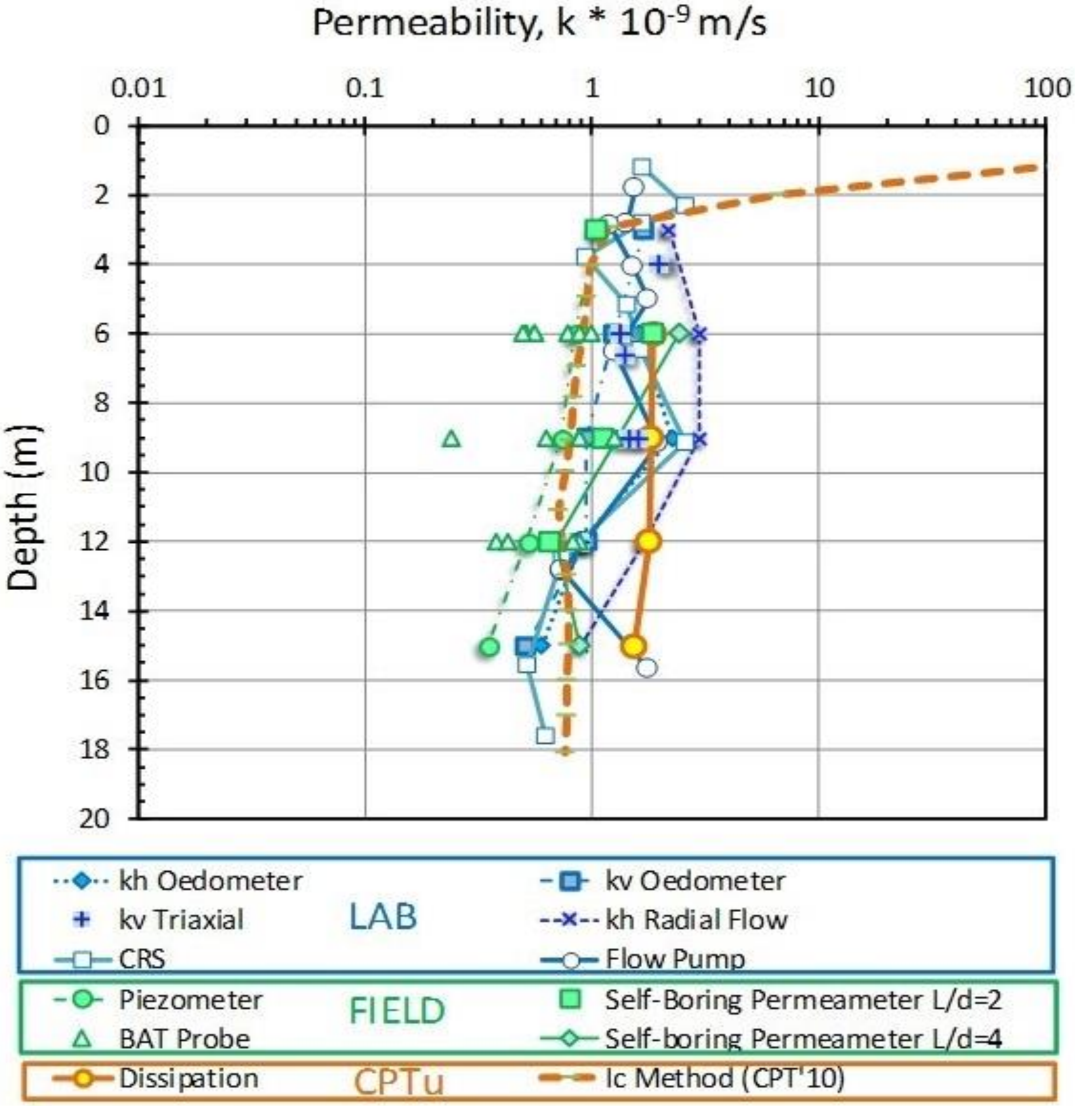

Figure 8.18: Comparison of laboratory and field measurements of hydraulic conductivity in soft clay at Bothkennar test site, Scotland

9 Liquefaction Evaluation by CPT

Liquefaction is the phenomenon that occurs when soils lose strength and behave as a liquid. This occurs when loading of the ground increases porewater pressures and reduces the effective stress state in the soil. This manifests in ground surface instabilities that cause the ejection of watery sands, subsidence, sand boils, settlement, tilting, bearing capacity failure, lateral spreading, cracking, and other events. ***Figure 9.1*** shows some examples of the destructive consequences following several recent earthquake events that occurred following soil liquefaction.

Haiti Earthquake – 12 Jan 2010

Christchurch, New Zealand - 2011

Chile – 27 Feb 2010

Nakaminato, Japan – 11 March 2011

Figure 9.1: Recent earthquake events exhibiting soil liquefaction and ground damage

Soil liquefaction most often occurs in loose sandy soils that have a high groundwater condition, although the process can also happen in silty and gravelly soils. Details concerning the background, understanding, and development of liquefaction behavior can be found in Idriss & Boulanger (2008).

There are two main categories of liquefaction: (a) Flow (or static) liquefaction; and (b) Cyclic liquefaction.

Flow liquefaction manifests as a rapid and brittle undrained loss of soil strength that occurs in sloping terrain, including earth embankments, mine tailings dams, hydraulic fills, and natural sandy to silty soil deposits. In these cases, the soil is already existing in an unstable state and a triggering mechanism (increased load or overburden, sudden groundwater change, blast event, etc.) results in a landslide, slope instability, or even a catastrophic flow failure, such as the recent Brumadinho tailings event in 2019 that resulted in 270 deaths and widespread environmental contamination in Brazil.

Cyclic liquefaction can occur during medium to large size earthquakes when the ground is subjected to shaking and levels of repeated loading that cause elevated porewater pressures in the soil which reduces the effective stress state. This can happen in flat horizontal ground as well as sloping terrain. Large earthquakes of moment magnitude $M_w \approx 7.5$ occurred in 2010 and 2012 in New Zealand that resulted in extensive liquefaction around Christchurch. Typical manifestations of liquefied soils are exhibited by sand boils, flowing sands, subsidence, lateral spread, and bearing capacity failures of buildings.

This chapter concerns the use of CPT for evaluating liquefaction potential in soils.

9.1 Flow Liquefaction

Static or flow liquefaction most often occurs in saturated contractive soils on sloping ground and may be triggered under static conditions such as a rise in the phreatic surface or water infiltration following a heavy rainfall. Flow liquefaction may also be triggered by transient earthquake loading.

Soils prone to flow liquefaction are characterized by their “contractive” soil behavior, whereby volumetric strains decrease during shear, in contrast to “dilative” soil response, whereby volumetric strains increase. Moreover, these soils tend to be brittle and exhibit a rapid loss of strength at low strain levels, resulting in rapid and progressive flow failures.

The identification of soil conditions susceptible to flow liquefaction can be made on the basis of conventional rotary drilling, high quality sampling, and careful laboratory testing, combined with in-situ testing and geophysical measurements; however, at great cost in terms of time and money (Robertson et al., 2000). This is especially true for sands, silty sands, and silts because undisturbed sampling methods (e.g., freezing, gel sampling) are quite difficult and expensive. As an alternative, the use of in-situ tests offers the expedient and economic assessment of flow liquefaction potential, particularly in mine tailings where screening is often used during all stages of dam construction.

Of practical use, the cone penetration test (CPT), especially piezocone testing (CPTU), offers three continuous recordings of soil response with depth: cone tip resistance (q_t), sleeve friction (f_s), and dynamic porewater pressure (u_2), thus well suited for the identification and screening of flow liquefaction problems. Additional data, including shear and compression wave velocities, can be obtained during seismic cone tests (SCPTu).

9.1.1 State Parameter

Current methods for the screening and evaluation of flow liquefaction potential of tailings, hydraulic fills, and natural loose soil deposits rely on an evaluation of the state parameter (ψ) defined as (Been & Jefferies 1985):

$$\psi = e_0 - e_{cs} \tag{9.1}$$

where e_0 = initial void ratio and e_{cs} = void ratio at critical state for a constant mean effective stress p' within the context of critical-state soil mechanics (CSSM), as presented in ***Figure 9.2.***

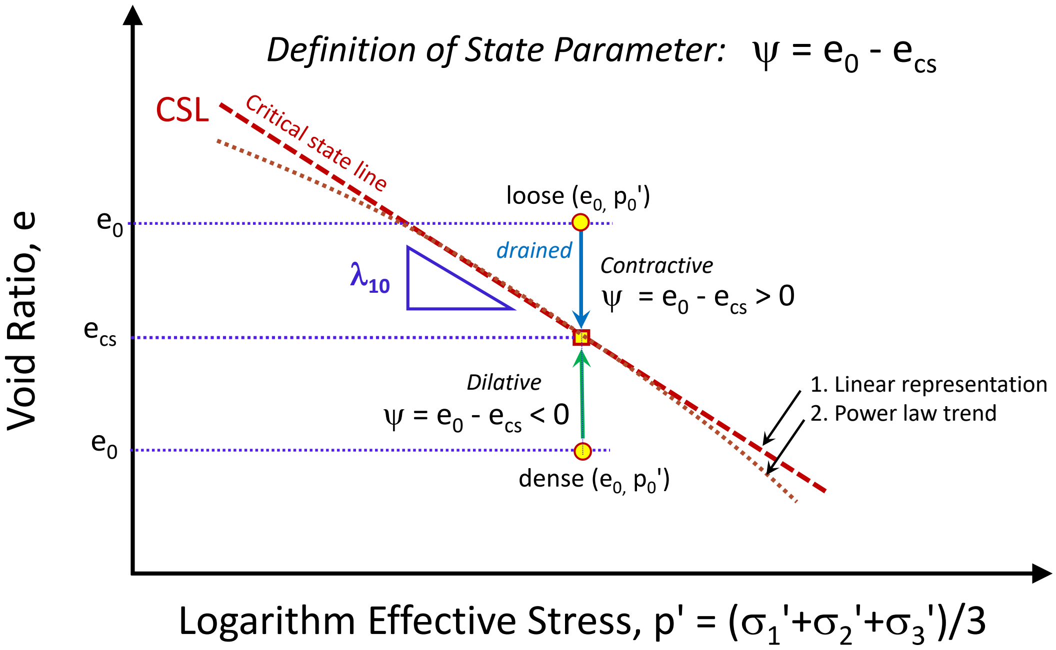

Figure 9.2: Representation of critical state parameter ψ in graph of void ratio versus logarithm of mean effective stress

The critical state line (CSL) is conventionally represented as a straight line in $e\text{-}\ln_e(p')$ plot by slope λ, or alternatively in a plot of void ratio (e) versus $\log_{10}(p')$ plot by slope λ_{10}, but also as a curved relationship in a power law format, as detailed by Reid et al (2020).

When the soil behavior shows a decrease in volume, such as loose sands and silts, the contractive response is indicative of possible instability and collapse, thus prone to flow liquefaction. In contrast, dense soils exhibit an increase in volume termed dilatant or dilative response and considered not susceptible to flow liquefaction. As such, a value of $\psi = 0$ signifies the CSSM threshold for the contractive-dilatant boundary.

9.1.2 CPT Parameters

The three readings (q_t, f_s, u_2) obtained by CPTU are utilized to evaluate soil stratigraphy, soil behavioral types, and a suite of geoparameters that are needed in engineering analyses and design. The measurements are often post-processed into net readings, such as net cone resistance ($q_{net} = q_t - \sigma_{vo}$), excess porewater pressure ($\Delta u = u_2 - u_0$), and effective cone resistance ($q_E = q_t - u_2$), and also utilized in terms of normalized and dimensionless parameters, including: $Q = q_{net}/\sigma_{vo}'$, $U = \Delta u/\sigma_{vo}'$, $B_q = \Delta u/q_{net}$, and $F = 100 \cdot f_s/q_{net}$ (%), where σ_{vo} = total overburden stress,

u_0 = in-situ equilibrium porewater pressure, and σ_{vo}' = effective vertical stress. Note that the two porewater pressure parameters are related via: $B_q = U/Q$. Additional details can be found in Lunne, Robertson, & Powell (1997).

An updated form of Q (also termed Q_t and Q_{t1}) is the stress-normalized cone tip resistance, $Q_{tn} = (q_{net}/\sigma_{atm})/(\sigma_{vo}'/\sigma_{atm})^n$ where the exponent "n" is a variable that ranges from about 0.5 in sands to 0.75 for silts to 1.0 in clays, and has been directly related to the CPT material index, I_c (Robertson 2009b).

In addition, the effective cone resistance can be normalized to $Q_E = (q_t-u_2)/\sigma_{vo}'$ which is equivalent to $Q_E = Q\cdot(1-B_q)+1$. This is used in the CPT soil classification system by Jefferies & Been (2015).

9.2 CPT Screening Methods for Flow Liquefaction

Herein, three methods for the screening of flow liquefaction potential by CPT are considered: (1) $\psi = -0.05$ criterion (Jefferies & Been 2015); (2) $Q_{tn,cs} = 70$ threshold, as described later in Section 2.2 (Robertson 2010a); and (3) yield stress ratio at critical-state, or $YSR_{csl} \approx 2.8$ (Mayne & Sharp 2019).

Additional post processing of CPT for flow liquefaction concerns are discussed by Olson & Stark (2002, 2003), and Monfared & Sadrekarimi (2013) but not covered here.

9.2.1 State Parameter Approach

Been et al. (1986; 1987a) established a framework for assessing ψ in sands that describes initial state, soil behavior, strength, and compressibility using laboratory testing and a number of intermediate geoparameters which were correlated to normalized CPT parameters (Q, B_q, F) from large scale chamber tests and laboratory triaxial results on reconstituted soil samples. Extensions to the method for silts and clays are described by Been et al. (2012b), Been (2016), and Jefferies & Been (2015).

In the stand-alone CPT approach, the slope of the CSL is found either from normalized sleeve friction (Plewes et al. 1992):

$$\lambda_{10} \approx 0.1\cdot F\ (\%) \tag{9.2}$$

or alternatively using their definition of CPT material index:

$$I_c{}^* = \sqrt{\{3-\log[Q\cdot(1-B_q)+1]\}^2+\{1.5+1.3\log(F)\}^2} \tag{9.3}$$

which is related to slope of the CSL by the expression (Reid 2015):

$$\lambda_{10} \approx 1/(34 - 10\cdot I_c{}^*) \tag{9.4}$$

The state parameter ψ is found from:

$$\Psi = -\frac{1}{m'}\cdot\ln\left[\frac{Q_p(1-B_q)+1}{k'}\right] \tag{9.5}$$

where $Q_p = (q_t - p_0)/p_0'$ = normalized cone resistance in terms of mean stress, $p_0' = ⅓ \cdot \sigma_{vo}' \cdot (1+2 \cdot K_0)$, with K_0 = lateral stress coefficient. The terms k' and m' are empirical fitting parameters found through the following trends:

$$m' = 11.9 - 13.3 \cdot \lambda_{10} \tag{9.6}$$

$$k' = M_c \cdot (3 + 0.85/\lambda_{10}) \tag{9.7}$$

where the friction parameter $M_c = 6 \cdot \sin\phi'/(3-\sin\phi')$ is found within the context of CSSM. For screening purposes, a value of $M_c \approx 1.20$ (or $\phi' = 30°$) is suggested.

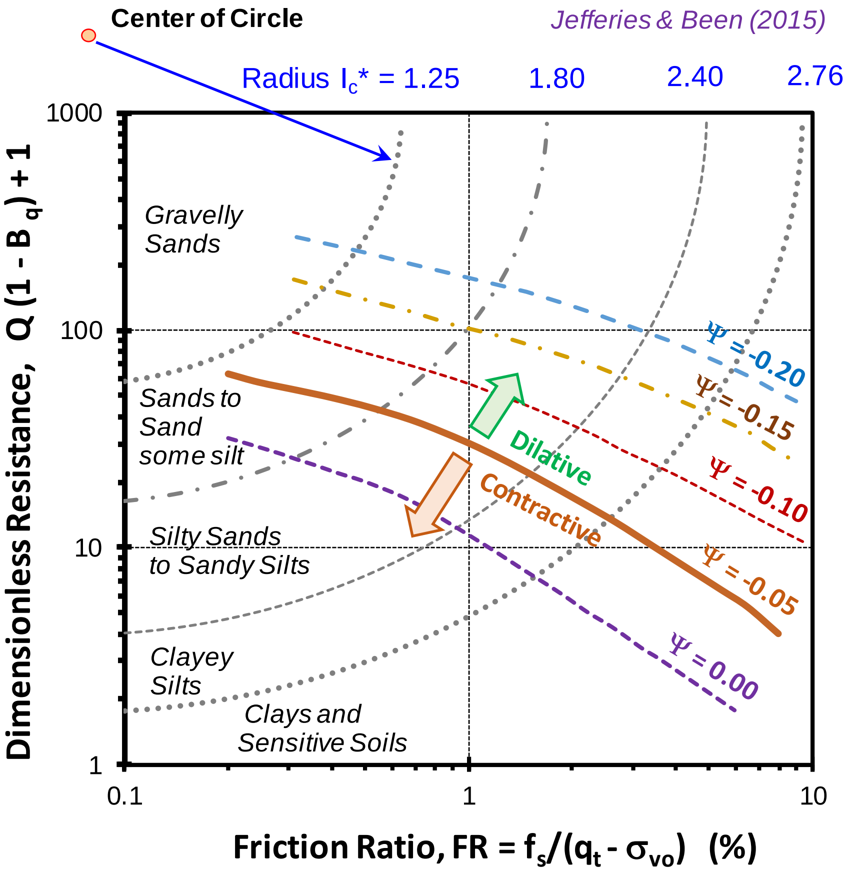

Figure 9.3: Screening for contractive-dilative soils and flow liquefaction using state parameter ψ approach by Jefferies & Been (2015)

In lieu of the theoretical critical state threshold $\psi = 0$, a practical value $\psi = -0.05$ was adopted, thus contractive soils prone to flow liquefaction are identified when $\psi > -0.05$. The general concept of screening for flow liquefaction via the state parameter approach is shown in ***Figure 9.3***.

9.2.2 Normalized Cone Resistance Approach

In this approach, the soil behavioral type is assessed by the SBT charts which use the Q-F diagrams of Robertson (1990, 1991) and Lunne et al. (1997). In an updated format detailed by Robertson (2009b), the Q is replaced by a modified cone tip resistance: $Q_{tn,}$ that was utilized in section 9.1.2. Specifically, the exponent "n" is found by iteration:

$$n = 0.381 \cdot I_{cRW} + 0.05 \cdot \sigma_{vo}'/\sigma_{atm} - 0.15 \leq 1.0 \qquad (9.8)$$

where a modified CPT material index (I_{cRW}) is given by:

$$I_{cRW} = \sqrt{(3.47 - \log Q_{tn})^2 + (1.22 + \log F)^2} \qquad (9.9)$$

Robertson (2010) defined regions within CPT soil behavior type charts to identify potential soil layers that may be susceptible to flow liquefaction and cyclic liquefaction, as well as define undrained versus drained response and contractive versus dilative behavior. Robertson (2010a,b) found that normalized cone resistance adjusted for fines content, designated ($Q_{tn,cs}$), trended over a range of state parameter from $0.0 < \psi < -0.20$, such that:

$$\psi = 0.56 - 0.33 \cdot \log_{10}(Q_{tn,cs}) \qquad (9.10)$$

where $Q_{tn,cs} = K_c \cdot Q_{tn}$ is the normalized equivalent cone resistance for clean sands. The adjustment factor is found from (Robertson & Wride 1998):

$$\text{For } I_c \leq 1.64: \quad K_c = 1 \qquad (9.11a)$$

$$\text{For } I_c > 1.64: \quad K_c = 5.581 \cdot I_c^3 - 0.403 \cdot I_c^4 - 21.63 \cdot I_c^2 + 33.75 \cdot I_c - 17.88 \qquad (9.11b)$$

For the case $\psi = -0.05$ at the contractive-dilative (CD) boundary, the associated value of $Q_{tn,cs} = 70$ (Robertson 2009b; Robertson 2010a, b), as shown in ***Figure 9.4***. Soils that exhibit a value of $Q_{tn,cs} < 70$ are considered contractive, and thus susceptible to flow liquefaction. Also, the contractive-dilative (CD) boundary line is part of the soil behavior type charts updated by Robertson (2016) and presented earlier as Figure 3.8.

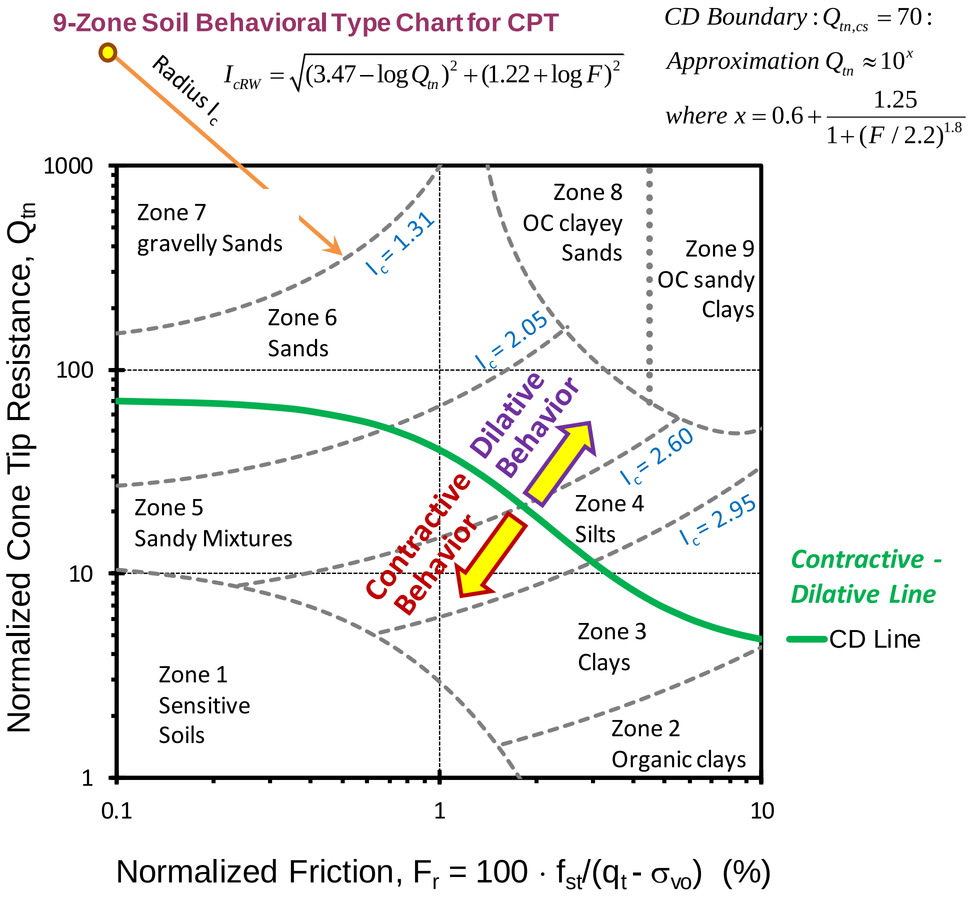

Figure 9.4: Screening for contractive-dilative soils and flow liquefaction using normalized cone resistance equivalence for clean sands by Robertson (2010a,b)

9.2.3 Yield Stress Ratio from CPT

The yield stress, σ_p' (or preconsolidation) of soils can be evaluated from CPT net resistance and material index, I_c (Mayne 2017; Agaiby & Mayne 2019):

$$\sigma_p' = 0.33(q_{net})^{m'} \cdot (\sigma_{atm}/100)^{1-m'} \qquad (9.12)$$

where m' is an exponent that depends upon soil type (Mayne et al. 2009), specifically: m' = 1.0 (intact inorganic clays), 0.9 (organic clays), 0.85 silts, 0.80 (silty sands to sandy silts), 0.72 (clean uncemented quartz-silica sands). The exponent has been related to the CPT material index, I_{cRW}, as shown in ***Figure 9.5***.

$$\sigma_p' = 0.33 \cdot (q_t - \sigma_{vo})^{m'} \cdot (\sigma_{atm}/100)^{1-m'}$$

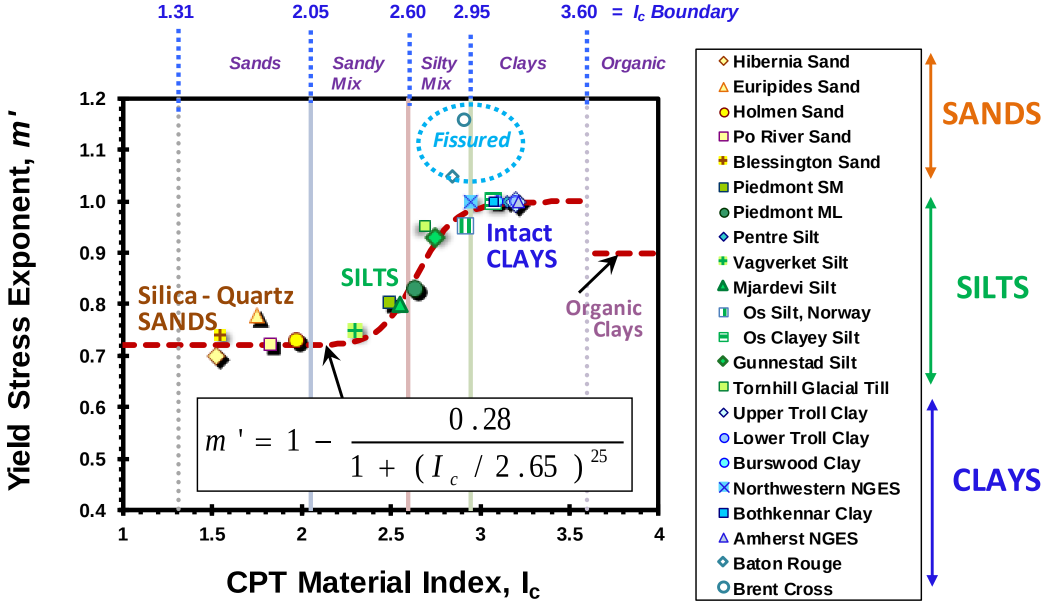

Figure 9.5: Exponent for evaluating yield stress in soils from CPT material index (after Mayne, Coop, Springman, Huang, & Zornberg 2009)

The normalized form is the yield stress ratio (YSR), or apparent overconsolidation ratio (AOCR):

$$\text{YSR} = \sigma_p'/\sigma_{vo}' \quad (9.13)$$

Derived in terms of the simple shear mode, ***Figure 9.6*** shows that the value of YSR at the critical state line can be found from (Mayne & Sharp 2019):

$$\text{YSR}_{csl} = (2/\cos\phi')^{1/\Lambda} \quad (9.14)$$

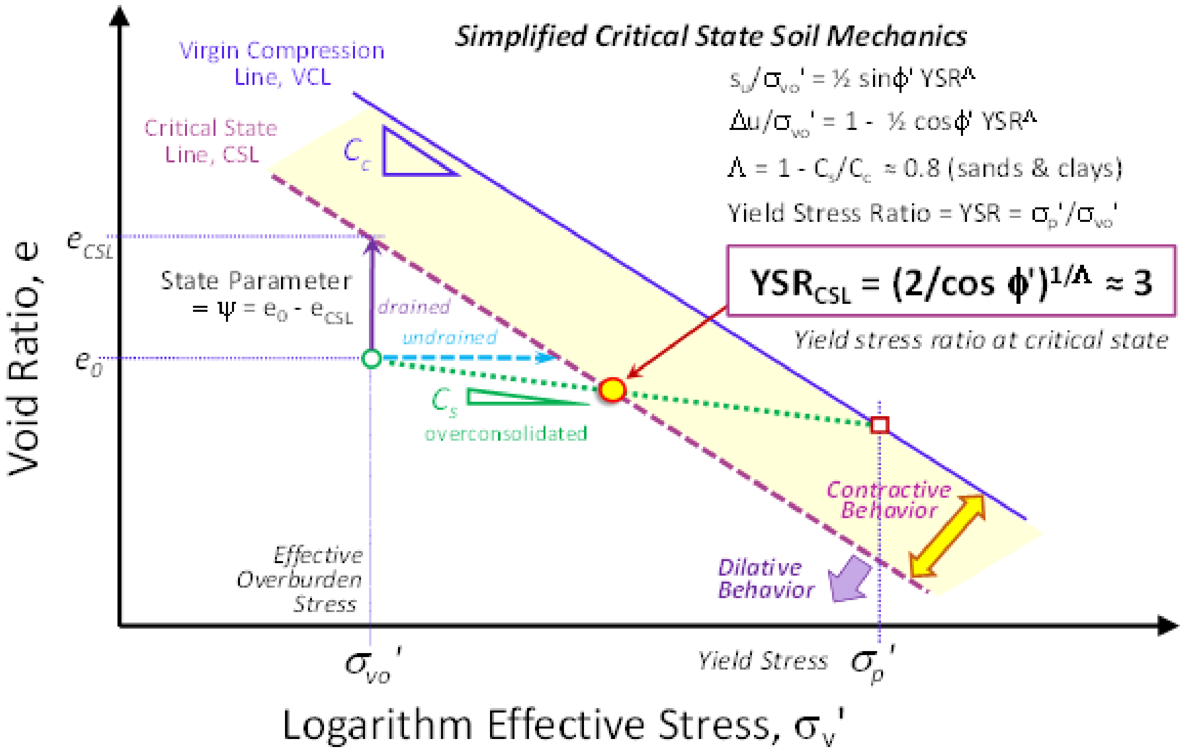

Figure 9.6: Screening for contractive-dilative threshold and flow liquefaction from YSR method using simplified critical state soil mechanics (after Mayne & Sharp 2019)

where $\Lambda = 0.8$ is a CSSM parameter related to the compression and swelling lines. For friction angles between $20° \leq \phi' \leq 40°$, the range gives: $2.6 < YSR_{CSL} < 3.3$.

Interestingly, Jefferies & Been (2006) discuss the value of OCR at critical state for triaxial compression mode, however their overconsolidation ratio is expressed in terms of mean effective stress, designated R_p. Specifically, R_p at the CSL has a value of 2 for Modified Cam Clay and 2.7 for the original Cam Clay constitutive soil model.

The evaluation of ϕ' for equation (9.15) is obtained from CPT by sorting drained behavior ($I_c \leq 2.6$) typically associated with sands, from undrained response ($I_c > 2.6$) that is characteristic of clayey soils. Thus, for the case of drained CPT response at a standard rate of push of 20 mm/s, the value $I_c \leq 2.6$:

$$\phi' = 17.6° + 11.0° \cdot \log_{10}(Q_{tn}) \tag{9.15}$$

Undrained penetration occurs when $I_c > 2.6$, therefore:

$$B_q > 0.05: \quad \phi' \approx 29.5° B_q^{0.121} \cdot [0.256 + 0.336 \cdot B_q + \log_{10}(Q)] \tag{9.16}$$

$$B_q \leq 0.05: \quad \phi' \approx 8.18° \cdot \ln_e (2.13 \cdot Q) \tag{9.17}$$

For overconsolidated soils, the Q is replaced with $Q' = Q/YSR^{\Lambda}$ (Ouyang & Mayne 2019).

9.3 Case Histories of Flow Liquefaction

The three CPT screening methods for flow liquefaction are applied to four case studies involving a natural loose sandy deposit and three tailings dam deposits. Two of the tailings were very loose and resulted in failures, while the third tailings consisted of dense compacted soils.

9.3.1 Jamuna Bridge, Bangladesh

The western slopes of the Jamuna Bridge site experienced over 30 submarine flow slides in very young natural sandy sediments. Details are provided by Yoshimini et al. (1999) who discuss the normally consolidated fine-medium sands which contained 15 to 30% mica content. Mean grain size (D_{50}) ranged from 0.1 to 0.2 mm and percent fines (PF) varied from 2 to 10%. ***Figure 9.7*** shows the mean profiles of q_t and f_s from 22 CPTs at the site with the corresponding material index (I_c) with depth.

Application of the aforementioned CPT screening procedures are presented in ***Figure 9.8***. The state parameter approach of Jefferies & Been (2015) hovers around the threshold value $\psi \approx -0.05$, thus indicating marginal flow liquefaction potential while the $Q_{tn\text{-}cs}$ method determines a rather consistent $Q_{tn\text{-}cs} \approx 50$ which is well below the threshold of 70 and therefore strongly contractive and prone to flow liquefaction. The YSR method indicates contractive soils below 3 m, in fact, the soils may have been forced to YSR < 1 indicating underconsolidation at depths greater than 16 m, therefore unstable and very susceptible to flow liquefaction.

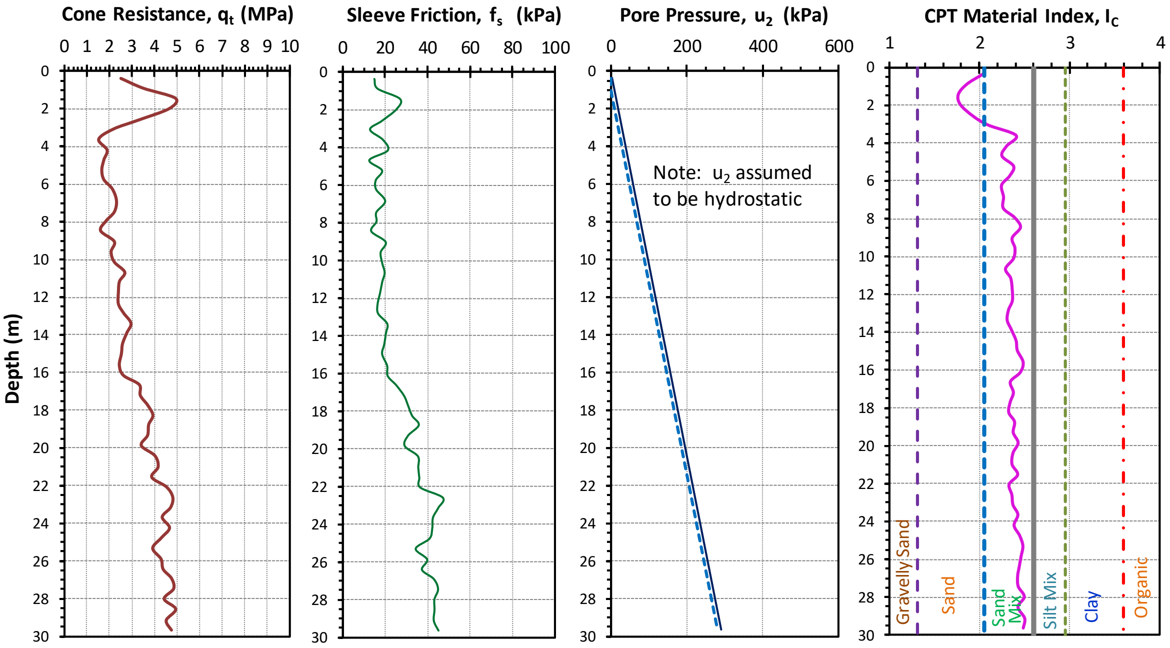

Figure 9.7: Mean CPT profiles for natural sands at Jamuna Bridge that experience flow liquefaction (data from Yoshimini et al. 1999)

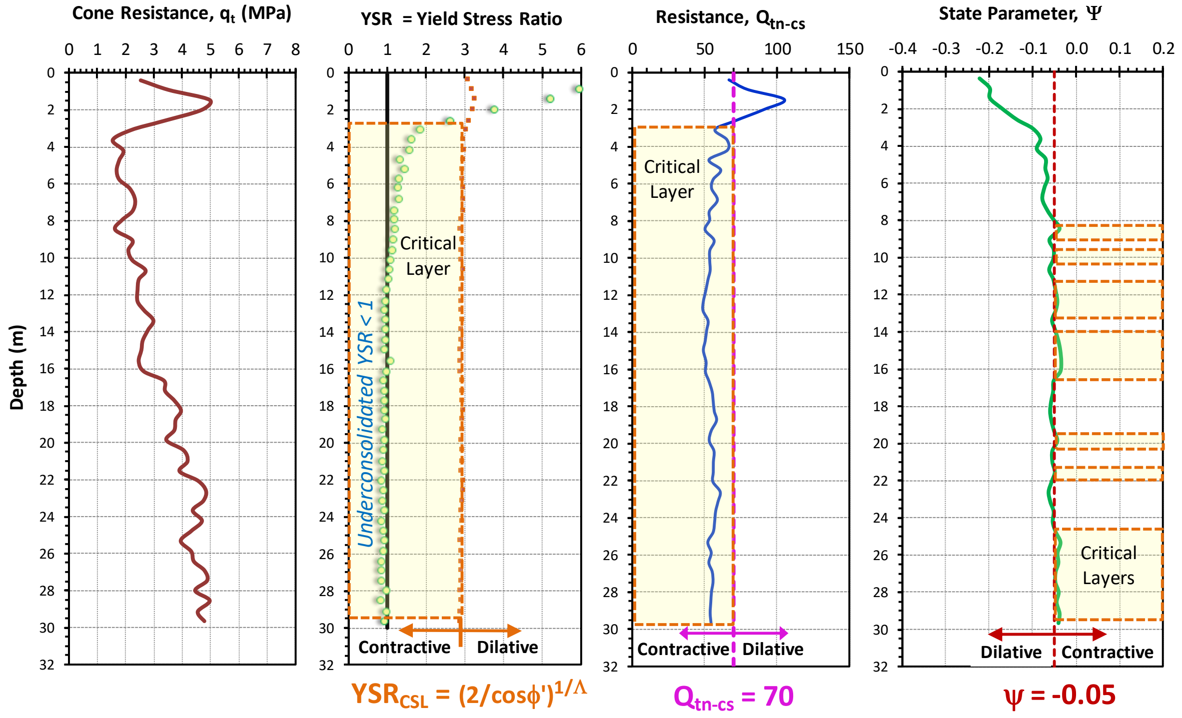

Figure 9.8: Application of three screening methods for flow liquefaction in natural loose sands at Jamuna Bridge, Bangladesh

9.3.2 Compacted Tailings, Western Canada

A compacted tailings facility in western Canada is used as an example for the quantification of primarily dilative soils (Mayne & Sharp 2019). Results from representative piezocone testing are shown in ***Figure 9.9*** with the profiles of q_t, f_s, u_2, and I_c with depth. In terms of the SBTn system, the index I_c indicates mainly the presence of sands (zone 6) and gravelly sands (zone 7), except for a limited zone of a sandy mixture (zone 5) at depths of between 10 to 11 m.

Post-processing the CPT data for the Western Canada tailings site is shown in ***Figure 9.10***. All three methods clearly categorize that the majority of the soil profile consists of dilative geomaterials, excepting the thin loose layer encountered at depths of 10 to 11 m which is clearly identified as contractive. This special case study shows the consistency of all three approaches in assessing contractive and dilative soil behavior.

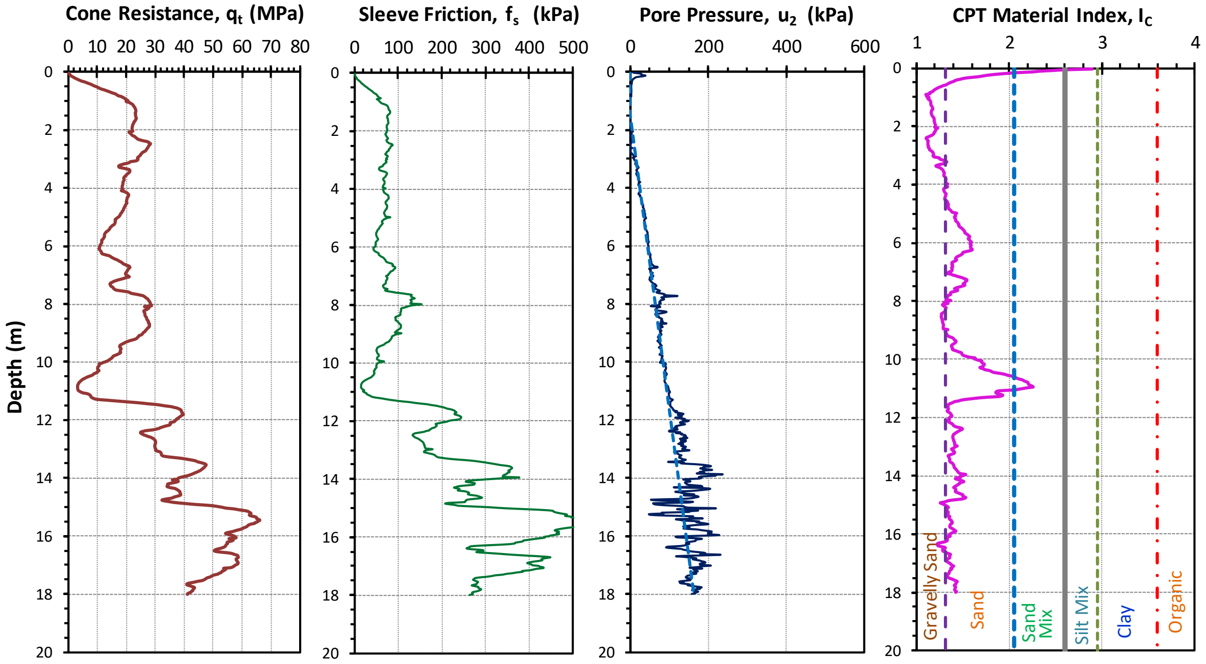

Figure 9.9: Representative CPT profile for compacted tailings sands in Western Canada (data from Mayne & Sharp 2019)

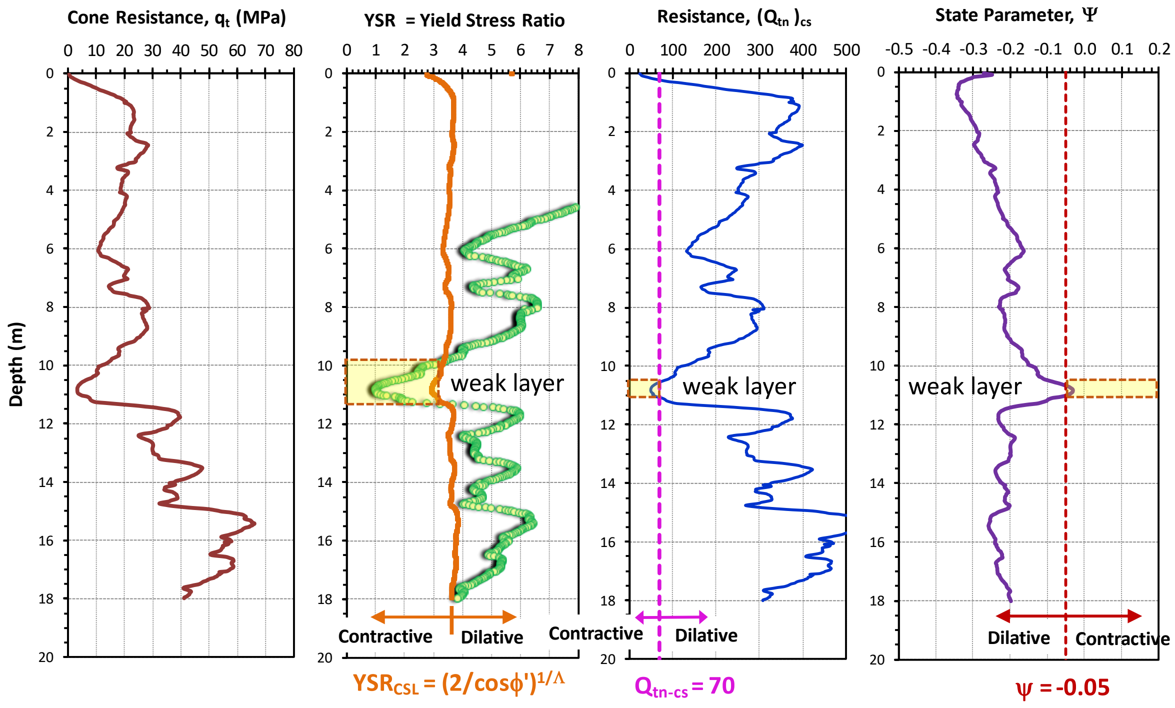

Figure 9.10: Application of three screening methods for contractive-dilative soil behavior and flow liquefaction in compacted sand tailings in Western Canada

9.3.3 Cadia Tailings Failure, Australia

A gold tailings facility in the New South Wales area of Australia failed on 09 March 2018 with the release of slurry. Luckily no fatalities or pollution occurred, however, the reconstruction efforts were projected to take approximately 2 years for the restoration of the impoundment facilities. Details concerning the mine operations, geotechnical data, analyses, and causes of the embankment failure are given by Jefferies et al. (2019).

Figure 9.11 shows a representative CPTU in the area of failure, with corresponding profiles of q_t, f_s, u_2, and I_c with depth. The results indicate the presence of very silty to clayey soil types within the upper 58 m of the sounding. Many sandy lenses or stringers are notable throughout most of the profile.

Application of all 3 post-processing approaches for Cadia are presented in ***Figure 9.12***. The J&B approach shows a consistently highly contractive soil profile with $\psi \approx +0.10$ and the Robertson (2010) method a rather constant profile $Q_{tn\text{-}cs} \approx 20$ with depth. Moreover, the CPT-evaluated YSR ≈ 1 throughout the depths also indicates the presence of highly contractive soils.

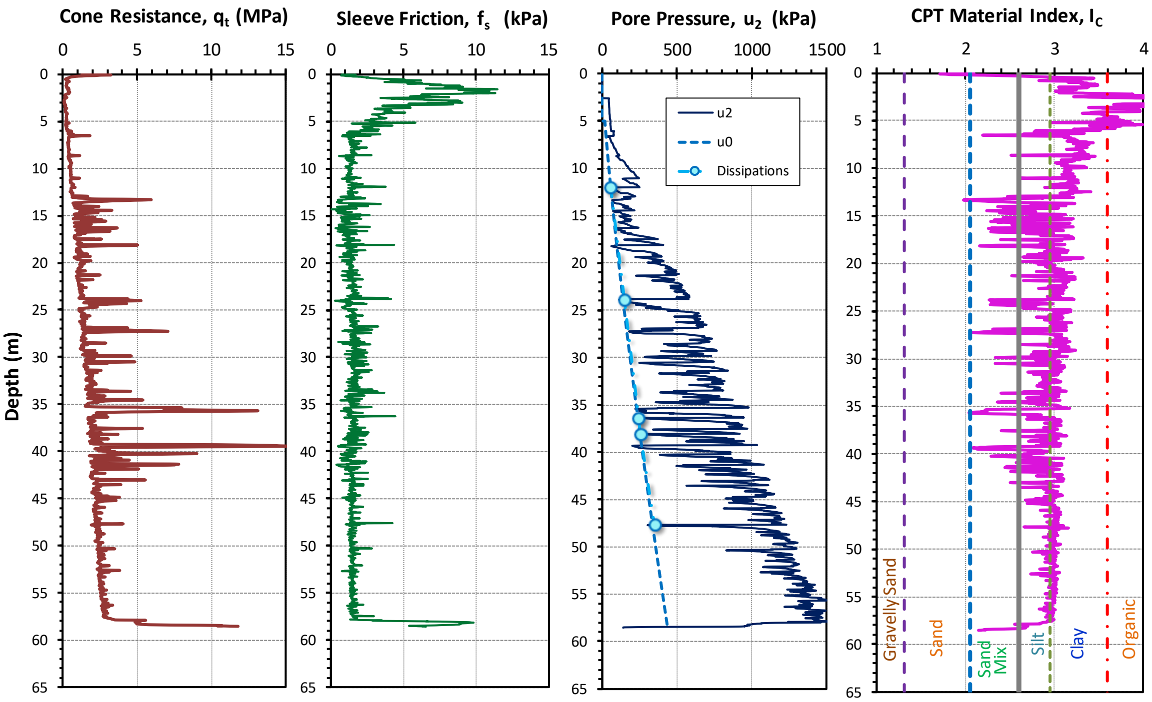

Figure 9.11: Representative CPT profile in gold tailings that experienced flow liquefaction at Cadia Valley, Australia

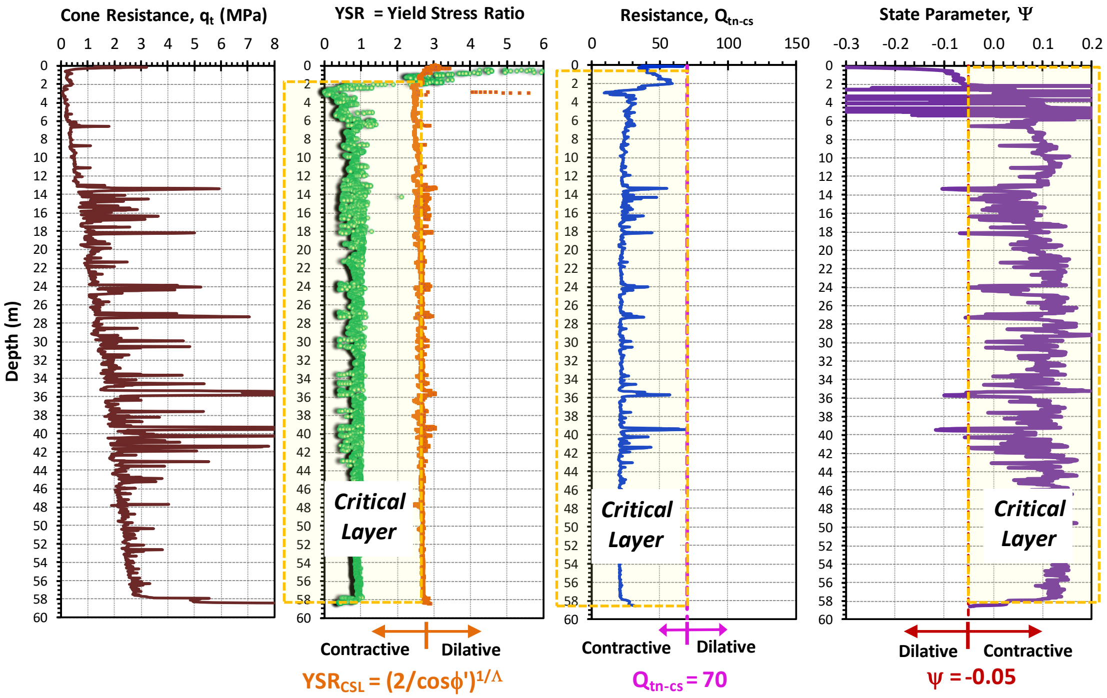

Figure 9.12: Application of three screening methods for flow liquefaction to tailings embankment failure at Cadia Valley, Australia

9.3.4 Fundão Tailings Failure, Brazil

On 05 November 2015, the spectacular failure of an iron ore tailings dam just southeast of Belo Horizonte, Brazil resulted in 19 deaths, extensive environmental damage, and widespread contamination (Reid 2019). The dam failure released 44 million m^3 of toxic mine tailings into the Doce River. Full details on the geotechnical aspects of the construction history of the tailings, CPT results, laboratory testing, stability analyses, and forensic studies are reported by Morgenstern et al. (2016).

Profiles of q_t, f_s, u_2, and I_{cRW} from CPTU sounding F02 are presented in ***Figure 9.13***. The three screening approaches for flow liquefaction are shown in ***Figure 9.14*** where the YSR and $Q_{tn,cs}$ methods clearly show the fragile condition of the tailings, yet the ψ approach barely indicates instability and likely collapse, mostly localized zones of contractive soils in the upper 16 m.

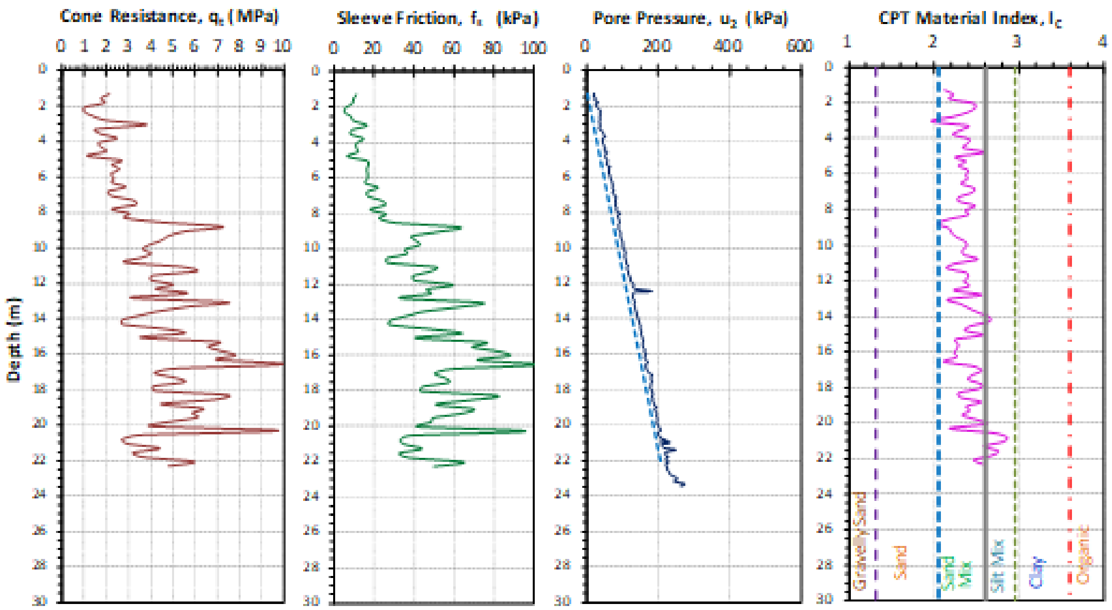

Figure 9.13: Representative CPT profile F02 in iron ore tailings that experienced catastrophic flow liquefaction failure at Fundão, Brazil

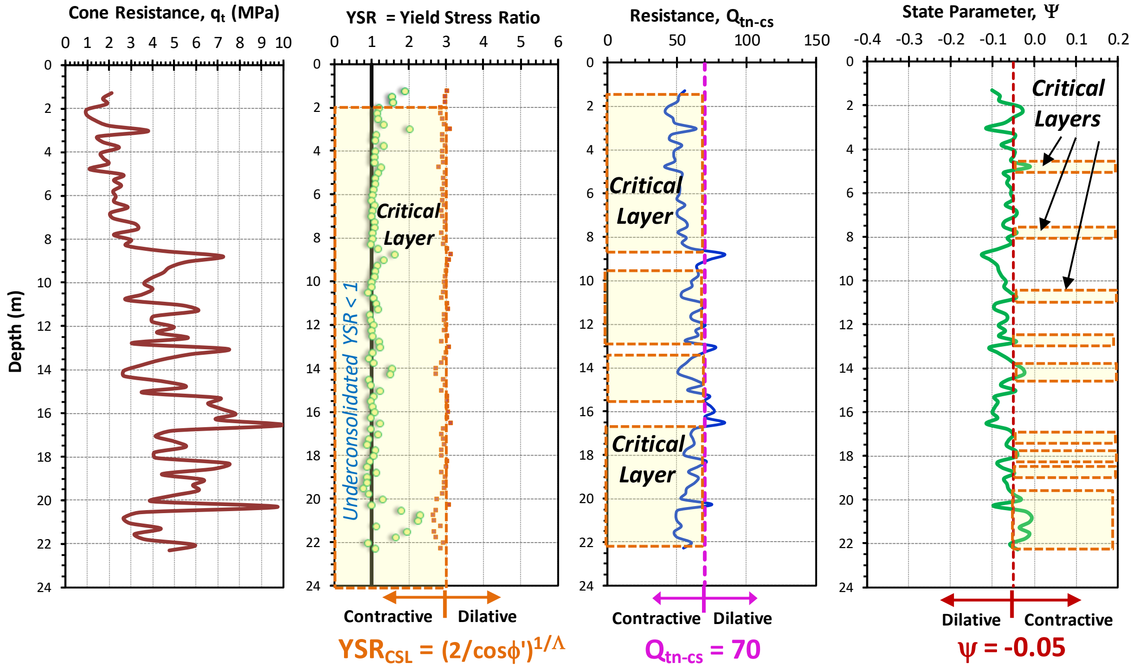

Figure 9.14: Application of three flow liquefaction screening methods from CPTU at Fundão tailings dam, Brazil

9.3.5 Addition of New Surcharge Loadings

The YSR method easily allows the assessment of future conditions and the contractive-dilative state of the tailings deposit due to the placement of new surcharge and fill. With the ψ approach and $Q_{tn\text{-}cs}$ method, this is not so straightforward.

The conceptual evaluation of an existing soil fill or tailings embankment is depicted in ***Figure 9.15*** showing the profile of yield stress and current effective overburden stress. As new fill or surcharge is added, the corresponding increase in σ_{vo}' results in a reduction in the YSR profile. For the case shown, the fill is initially dilative throughout the entire thickness of 30 m. However, as additional surcharge is added, the profile becomes contractive in the lower portions.

Additional discussion on this issue is given by Mayne et al. (2017) and Mayne & Sharp (2019, 2022). Moreover, Styler et al. (2018) provide several actual case studies involving sand fill at various times after surcharge placement and the associated CPT results at these various stages of loading.

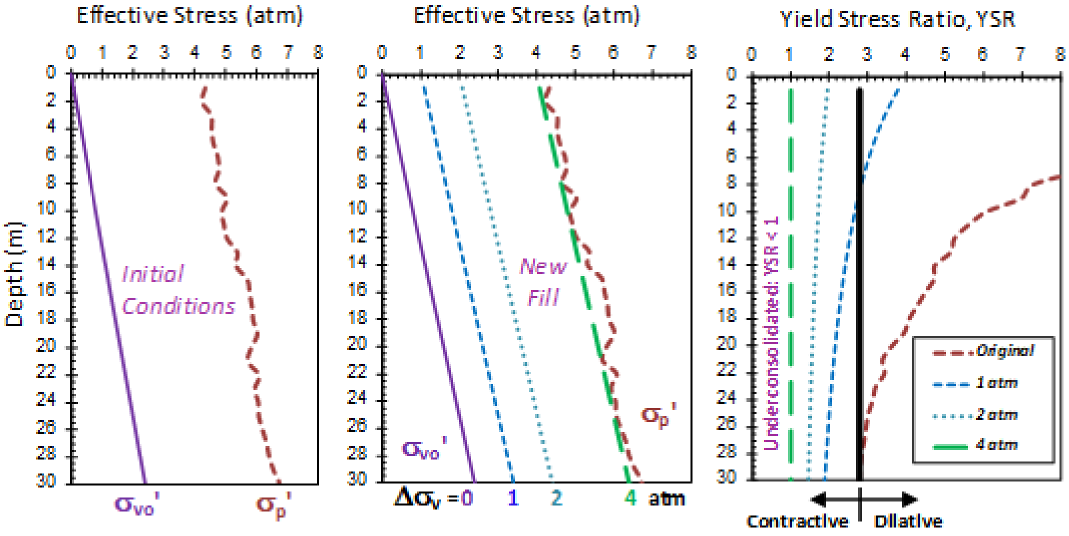

Figure 9.15: Conceptual changes in YSR due to new surcharge placement on existing tailings dam

The yield stress ratio approach is based on a simple nexus that links an analytical solution for clays based on spherical-cavity expansion theory and critical-state soil mechanics (SCE-CSSM) and statistical results originally obtained from CPT chamber tests on sands (Mayne 2017). Initial calibration of the SCE-CSSM solution for YSR was made for 206 natural clays that had been subjected to laboratory consolidation testing of undisturbed samples and field piezocone tests with data taken at corresponding elevations (Chen & Mayne 1996). Chamber tests from 26 different sands provided over 600+ CPT data points for statistical analyses (Mayne 2001).

Together these datasets for clay and sands were incorporated to identify a common link in the interpretation that allowed a simplified unified approach that relates yield stress to net cone resistance and soil type (Mayne, Coop, Springman, Huang, & Zornberg 2009). A final step provided a direct relationship between the soil behavior type to the CPT material index (I_c) that was calibrated using a variety of sands, silts, clays, and mixed soil types from 93 natural soil deposits (Agaiby & Mayne 2019).

Thus, the basis of the YSR approach is quite different from the ψ method of Jefferies & Been (2015) which was formulated from testing of reconstituted sands and tailings. The calibrated findings of the YSR approach are primarily obtained from natural soil deposits tested by in-situ CPT soundings to depths of 30 or 40 m.

Some additional limitations to the YSR approach can be stated. As the initial formulation of the YSR approach focused on clays, the critical state adopted the simple linear e-$\log_{10}(\sigma_v')$ form that is commonly associated with consolidation results. The extension of this assumption to sands and silty sands may in fact have limited application over certain stress ranges. Much discussion has arisen in the geotechnical literature over the utilization of a more complex and curved critical state line for coarse-grained soils, as suggested by Figure 9.2. For instance, the reader is directed to the works of Pestana & Whittle (1995), Li & Wang (1998), and Reid et al. (2020) for additional debate and details on this issue.

9.4 Cyclic Liquefaction Evaluation By CPT

9.4.1 Seismic Ground Motions

The evaluation of cyclic liquefaction potential is commonly performed using a simplified cyclic stress-based approach that compares the level of ground shaking against the available soil resistance. The level of ground shaking due to an earthquake is represented by the cyclic stress ratio, CSR. In terms of simple shear mode, the CSR is the ratio of the cyclic shear stress to effective stress. The magnitude of CSR can be obtained directly from numerical software programs (e.g., SHAKE, DEEPSOIL, etc.) or estimated from the following:

$$CSR_{7.5} = \frac{\tau_{ave}}{\sigma_{vo}'} = 0.65 \cdot \left(\frac{a_{\max}}{g_a}\right) \cdot \left(\frac{\sigma_{vo}}{\sigma_{vo}'}\right) \cdot r_d \cdot \frac{1}{MSF} \tag{9.18}$$

where a_{max} = PGA = peak (horizontal) ground acceleration, (a_{max}/g_a) is the normalized peak ground acceleration or PGA divided by the gravity acceleration constant (g_a = 9.8 m/s^2), σ_{vo} and σ_{vo}' are the total and effective vertical overburden stresses, respectively, r_d is a stress reduction coefficient, and MSF = magnitude scaling factor.

The $CSR_{7.5}$ represents the normalized shear stress (τ_{ave}/σ_{vo}') induced in the soil by the earthquake event (i.e, the seismic demand) and commonly referenced to a benchmark case with M_w = 7.5 having a 15 s duration. For sloping ground and high overburden stresses (i.e., z > 30 m), added inclusions may include a slope correction factor (K_α) and/or overburden correction factor (K_σ), as discussed by Idriss & Boulanger (2008).

The ability of the soil to resist the triggering of liquefaction is quantified in terms of a cyclic resistance ratio (CRR), as illustrated by ***Figure 9.16***. If the CSR exceeds the CRR, liquefaction can

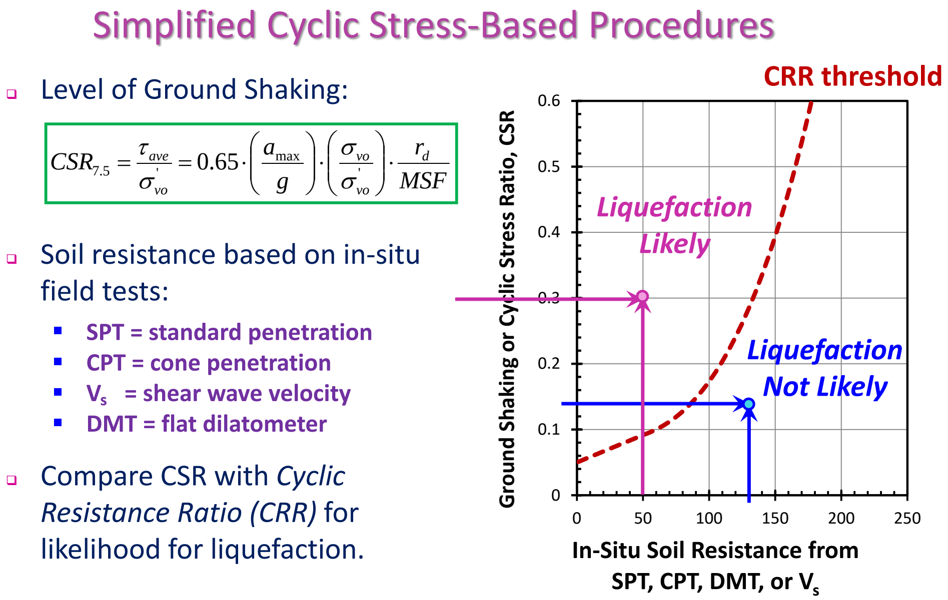

Simplified Cyclic Stress-Based Procedures

- Level of Ground Shaking:

$$CSR_{7.5} = \frac{\tau_{ave}}{\sigma'_{vo}} = 0.65\cdot\left(\frac{a_{\max}}{g}\right)\cdot\left(\frac{\sigma_{vo}}{\sigma'_{vo}}\right)\cdot\frac{r_d}{MSF}$$

- Soil resistance based on in-situ field tests:
  - **SPT = standard penetration**
  - **CPT = cone penetration**
  - **V_s = shear wave velocity**
  - **DMT = flat dilatometer**
- Compare CSR with *Cyclic Resistance Ratio (CRR)* for likelihood for liquefaction.

Figure 9.16: General concept of cyclic stress-based procedure for cyclic liquefaction

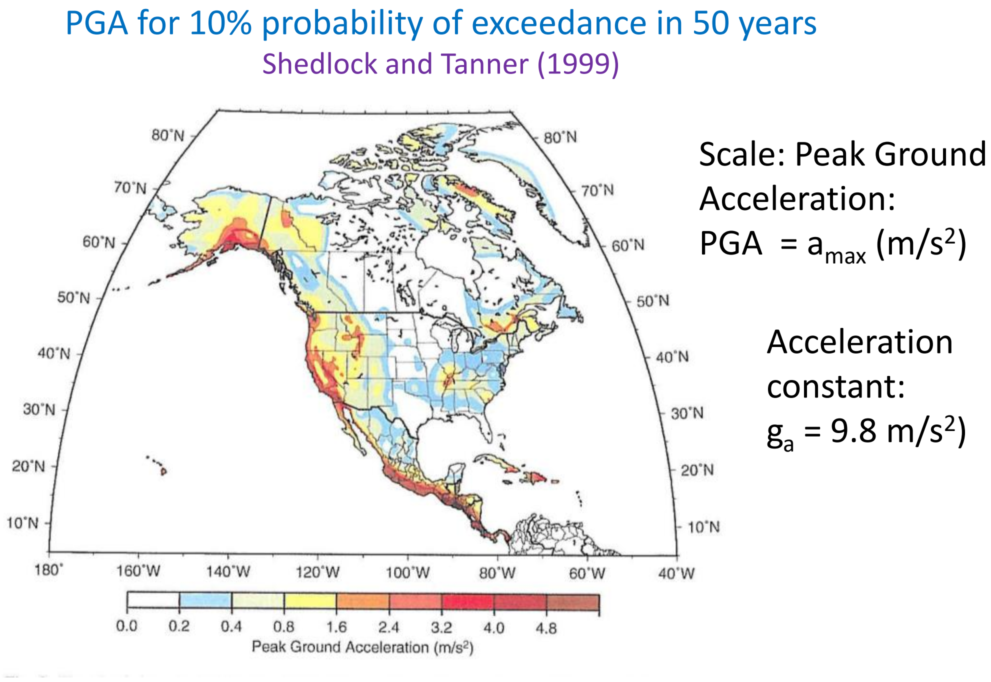

PGA for 10% probability of exceedance in 50 years

Shedlock and Tanner (1999)

Scale: Peak Ground Acceleration:
PGA = a_{max} (m/s^2)

Acceleration constant:
g_a = 9.8 m/s^2)

Figure 9.17: Seismic map for North and Central America (Shedlock & Tanner 1999)

be expected; otherwise, if CSR < CRR, liquefaction is not anticipated. The CRR has been correlated to a number of different in-situ tests including: (a) standard penetration test (SPT), (b) cone penetration tests (CPT), (c) flat dilatometer test (DMT), and (d) shear wave velocity (V_s) measurements. A summary of the standard approaches for SPT, CPT, and V_s are given in Youd et al. (2001).

For preliminary analyses, the PGA can be estimated from seismic maps such as those published by the United States Geological Survey (USGS) and Geological Survey of Canada (GSC). For example, Shedlock & Tanner (1999) present area maps showing the PGA for North and Central America, as shown in ***Figure 9.17***.

Procedures for determining the CSR and CRR from CPT depend upon the specific method adopted. For instance, ***Figure 9.18*** shows the CSR versus normalized cone resistance with associated CRR curves for four different approaches. The CRR curves are determined by either deterministic or probablistic analyses from data sets developed from prior earthquake events. In ***Figure 9.18***, a total of 140 case studies were compiled from site which had undergone a seismic event from a major earthquake. At 30 of these sites, no evidence of liquefaction was apparent (represented by open square dots). In contrast, at 110 site, major indications of liquefaction were reported, including such features as sand boils, ejecta, ground subsisdence, cracking and/or fissure, building tilting and/or settlement, ground movement, etc. These sites are represented by solid blue circles. The CRR is an attempt to demarcate the two categories of sites, separating "liquefied" sites from "non-liquefied" sites.

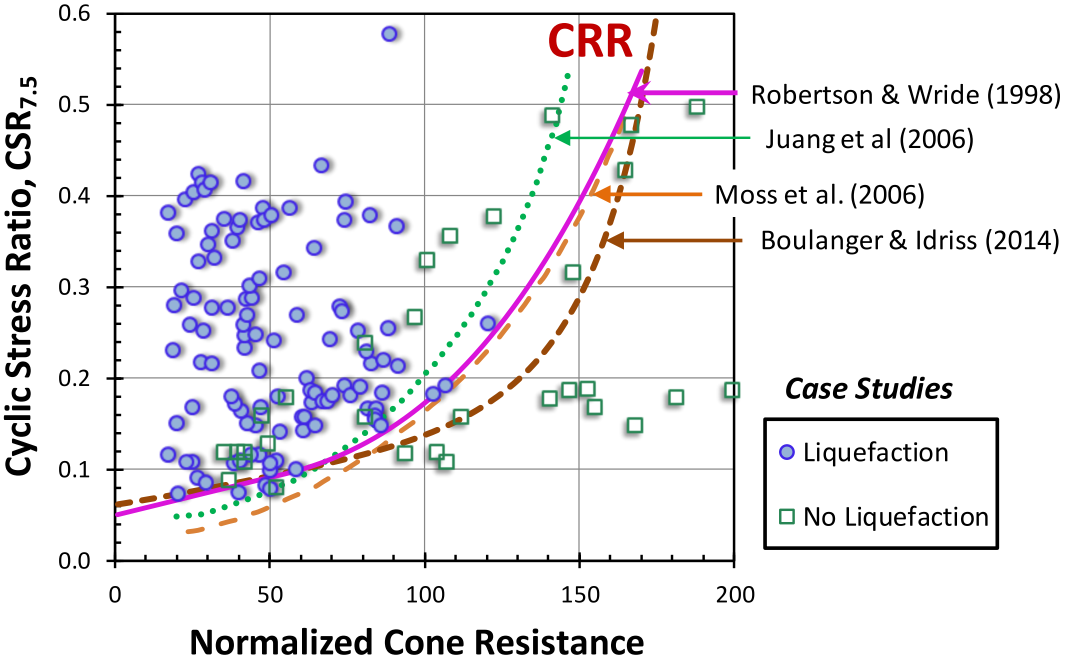

Figure 9.18: Cyclic stress ratio (CSR) versus normalized cone resistance showing cyclic resistance ratios (CRR) from 4 different methods. (updated from Robertson 2009c)

Herein two CPT methods are presented: (a) NCEER, or National Center for Earthquake Engineering Research (Youd et al. 2001; Robertson & Wride 1998); and (b) UCD, or Univ. California-Davis (Boulanger & Idriss 2014). The NCEER approach was developed from two workshops held by the National Science Foundation (NSF) with a final consensus given by 16 experts in the field. The UCD approach represents an updated assessment using additional new data from major earthquakes.

Of general note for both the NCEER and UCD methods, soils which exhibit a value of $I_c \leq 2.6$ are considered susceptible to liquefaction (sands and silty sands), whereas $I_c > 2.6$ implicates clays and clayey silts that are not technically liquefiable (Idriss & Boulanger 2008).

9.4.2 NCEER Approach

The NCEER approach for CPT cyclic liquefaction evaluation follows the method of Robertson and Wride (1998). For the calculation of CSR, the stress reduction coefficient (r_d) decreases from 1.0 at the ground surface to a value of 0.5 at 30 m and can be obtained as a function of depth (z, in meters) following the recommendations of Youd et al. (2001):

$$r_d = \frac{1 - 0.411\, z^{0.5} + 0.0405\, z + 0.00175\, z^{1.5}}{1 - 0.418\, z^{0.5} + 0.0573\, z - 0.00621\, z^{1.5} + 0.00121\, z^{2}} \qquad (9.19)$$

The profile for r_d is depicted in ***Figure 9.19***.

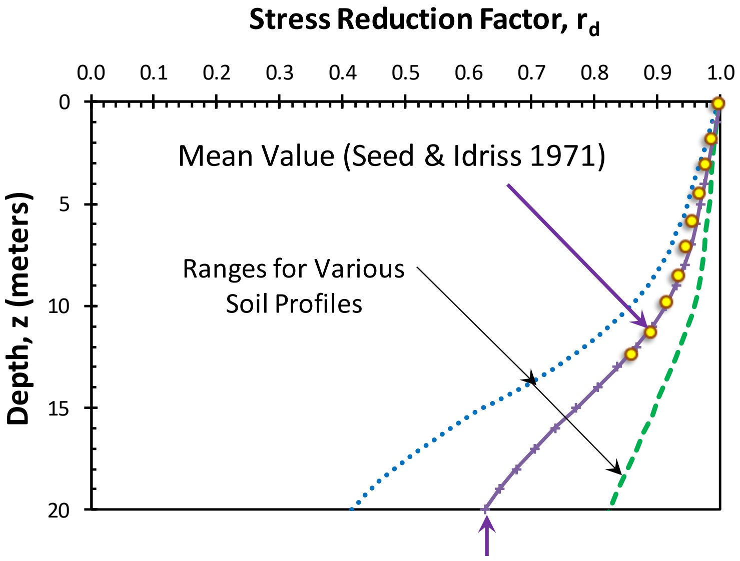

$$r_d = \frac{1 - 0.411\, z^{0.5} + 0.0405\, z + 0.00175\, z^{1.5}}{1 - 0.418\, z^{0.5} + 0.0573\, z - 0.00621\, z^{1.5} + 0.00121\, z^{2}}$$

Figure 9.19: Stress reduction factor (r_d) for NCEER approach (Youd et al. 2001)

For the NCEER approach, the magnitude scaling factor (MSF) depends upon the moment magnitude (M_w) of the earthquake. The MSR is presented in ***Figure 9.20*** and expressed:

$$MSF = \left(\frac{7.5}{M_w}\right)^{2.56} \tag{9.20}$$

in order to evaluate the level of ground shaking, or CSR given by equation (9.18).

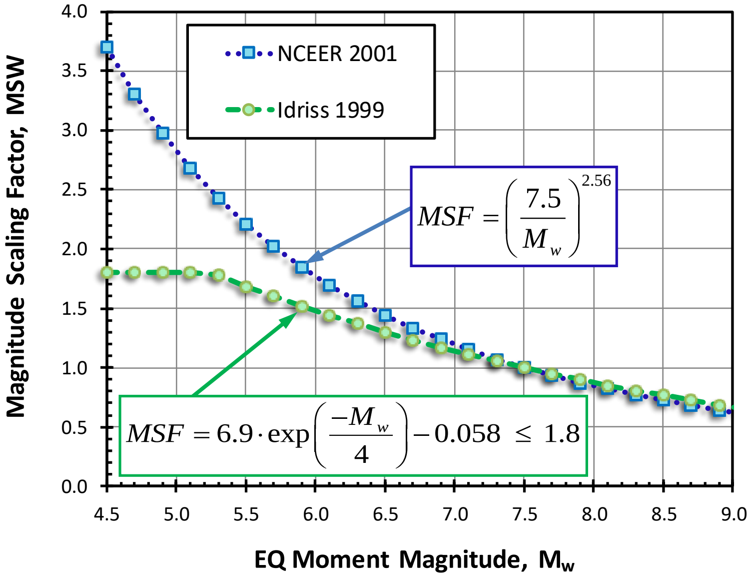

Figure 9.20: Magnitude scaling factors for NCEER methods

For each elevation in the CPT sounding, the CSR is compared with the level of ground resistance, represented by the cyclic resistance ratio (CRR) shown in ***Figure 9.21*** that is obtained from the following expressions:

For $(Q_{tn})_{cs} < 50$:

$$CRR_{7.5} = 0.833 \cdot \left[\frac{(Q_{tn})_{cs}}{1000}\right] + 0.05 \tag{9.21a}$$

For $50 \le (Q_{tn})_{cs} \le 160$:

$$CRR_{7.5} = 93 \cdot \left[\frac{(Q_{tn})_{cs}}{1000}\right]^3 + 0.08 \tag{9.21b}$$

where $Q_{tn,cs}$ = the equivalent clean sand stress-normalized cone resistance is detailed in Section 9.2.2. When the level of ground shaking exceeds the available in-situ soil resistance, that is: CSR > CRR, then liquefaction is likely. In fact, we can define the factor of safety (FS) against liquefaction as simply:

$$FS_{liq} = \frac{CRR_{7.5,\sigma v'=1\,atm}}{CSR_{7.5,\sigma v'=1\,atm}} \tag{9.22}$$

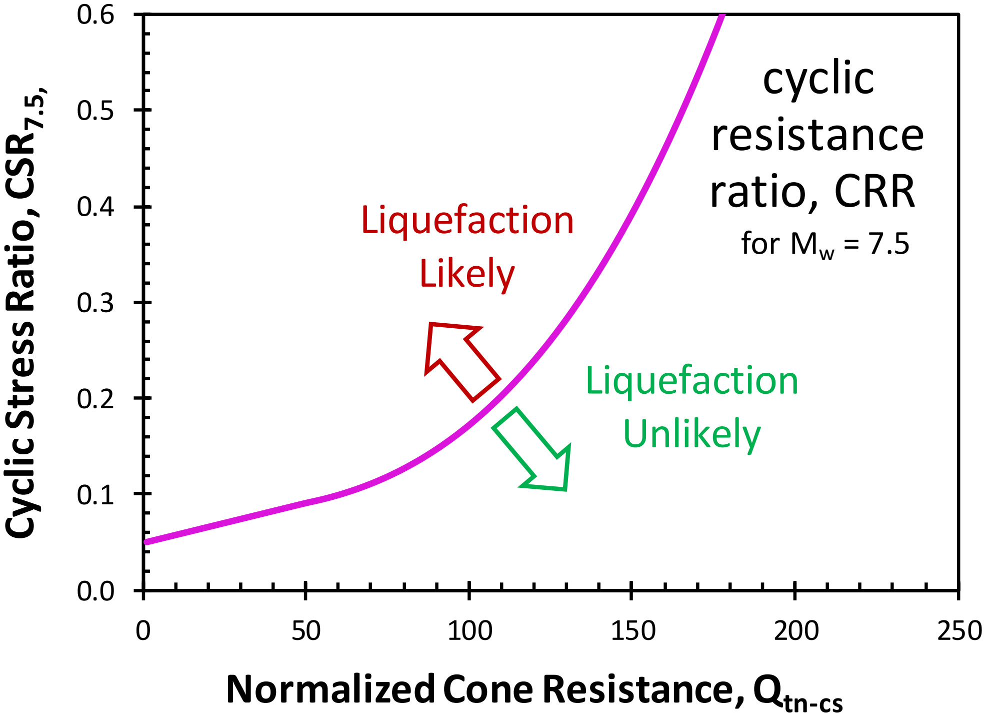

Figure 9.21: Cyclic stress ratio (CSR) versus normalized cone resistance $Q_{tn,cs}$ with cyclic resistance ratio (CRR) for evaluating cyclic liquefaction potential from CPT using NCEER method (Robertson & Wride, 1998; Youd et al. 2001)

Applying statistical evaluations to the dataset, CRR curves of different probabilities of occurrence have been developed from mapping functions (Ku et al. 2012). These have been approximately related to the calculated safety factor *FS* to estimate the liquefaction probability P_L from the NCEER approach that are shown in ***Figure 9.22*** and can be expressed (Ku et al. 2012):

$$P_L = \frac{1}{1+(FS/0.9)^6} \tag{9.23}$$

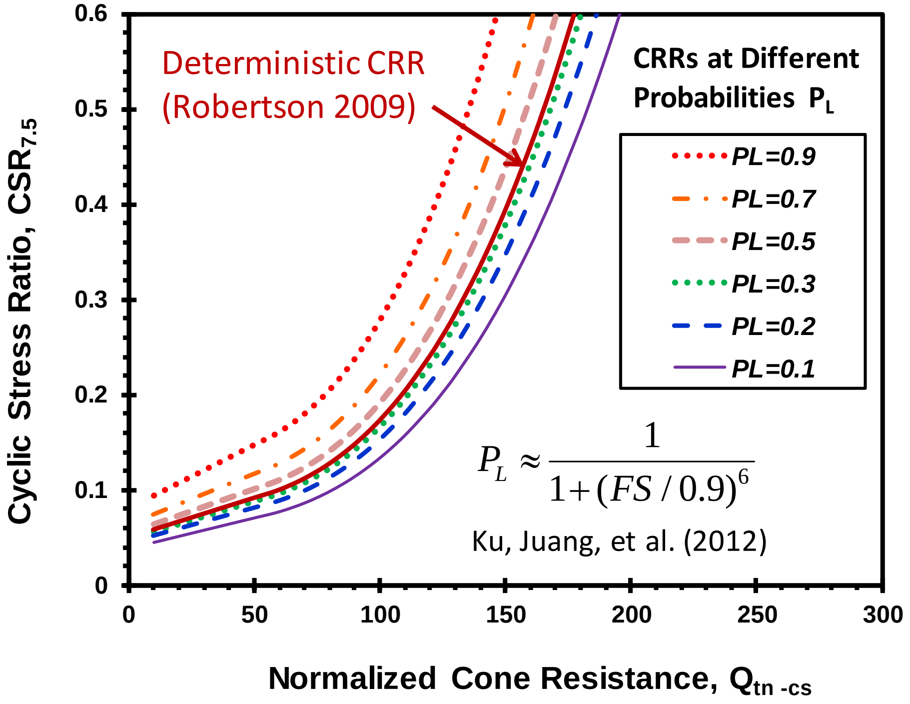

Figure 9.22: Probability CRRs for CPT from NCEER dataset

9.4.3 UCD Method for Cyclic Liquefaction from CPT

Since the NCEER consensus reports were developed over two decades ago, a good number of new case studies from large seismic events worldwide have provided additional data to allow updating of the various cyclic resistance ratios (CRRs), as well as the cyclic stress ratios (CSR), for each of the in-situ test methods. Full details on the updated CPT methods are given by Idriss & Boulanger (2008) and Boulanger & Idriss (2014).

The level of ground shaking by the earthquake is represented by the cyclic stress ratio (CSR) and is given by the following expression for flat horizontal ground:

$$CSR_{7.5,\,\sigma v'=1\,atm} = 0.65 \cdot \left(\frac{a_{\max}}{g}\right)\left(\frac{\sigma_{vo}}{\sigma_{vo}'}\right) \cdot r_d \cdot \frac{1}{MSF} \cdot \frac{1}{K_\sigma} \qquad (9.24)$$

where the first three terms have been detailed previously. For the Boulanger and Idriss (2014) approach, the stress reduction factor (r_d) is expressed as a function of depth (z) and magnitude (M), as presented in ***Figure 9.23***.

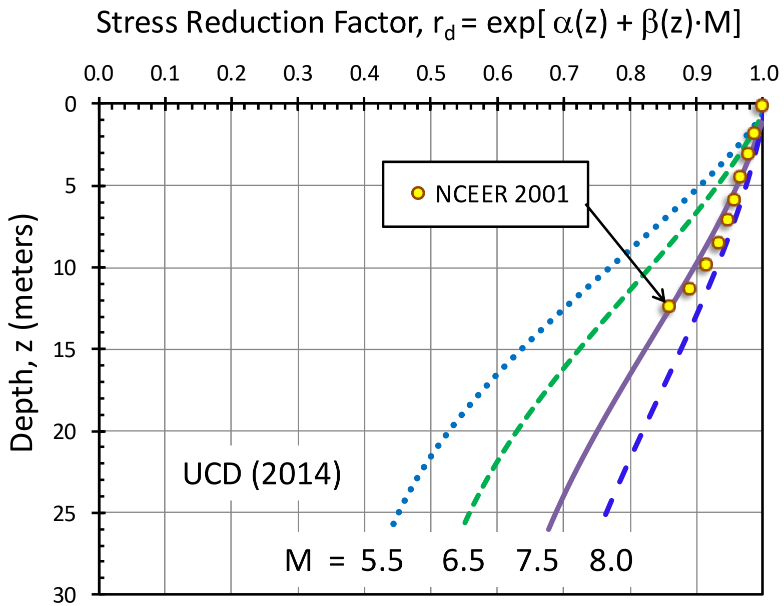

$\alpha(z) = -\,1.012 \; - 1.126 \cdot \sin\left[\,(z/11.73) + 5.133\right]$

$\beta(z) = +0.106 + 0.118 \cdot \sin\left[\,(z/11.28) + 5.142\right]$

Note: Depth z in meters and sine terms in radians

Figure 9.23: Stress reduction factor (r_d) for the updated UCD approach for cyclic liquefaction (after Boulanger & Idriss 2014)

Initially, the CPT material index (I_c) as defined by Robertson (2009a, 2009b, 2010) can be used to evaluate soil type and provide an estimate of the fines content of the sand, as discussed by Boulanger and Idriss (2014):

$$FC\ (\%) = 80\ (I_c + C_{FC}) - 137 \quad \text{where } 0\% \leq FC \leq 100\% \tag{9.25}$$

The term C_{FC} is a site-specific calibration factor where the CPT readings can be calibrated with soil samples from adjacent side-by-side borings: $-0.29 \leq C_{FC} \leq +0.29$. In the event no samples are available, an initial estimate of $C_{FC} \approx 0$ may be used for preliminary efforts. Note also that the driving of split-spoon samples during the SPT has been recognized to increase measured fines contents because of particle crushing, fracture, and cracking.

For the UCD method, the stress-normalized cone resistance for clean sands is evaluated as a function of effective overburden stress and relative density:

$$Q_{c1N} = C_{Ne} \cdot q_c/\sigma_{atm} \tag{9.26}$$

where the stress normalization factor is given by:

$$C_{Ne} = (\sigma_{atm}/\sigma_{vo}')^m \leq 1.7 \tag{9.27}$$

For general CPT interpretation in soils, the use of $q_{net} = q_t - \sigma_{vo}$ is essentially mandatory, where q_t = total cone tip resistance (Robertson, 1990; Lunne et al., 1997; Mayne, 2007). However, in clean sands, $q_t \approx q_c$ because induced penetration pore water pressures are low ($u_2 \approx u_0$). Also, since total overburden stress is small relative to cone tip resistance ($q_t >> \sigma_{vo}$) in clean sands at depths $z < 30$ m, essentially: $q_{net} \approx q_t \approx q_c$. Since liquefaction applies primarily to sands, the updated approach by Boulanger & Idriss (2014) has thus retained q_c in its formulations.

The exponent *m* varies with relative density (D_R) of the sand, such that:

$$m = 0.785 - 0.521 \cdot D_R \tag{9.28}$$

For this approach, the relative density of clean sands is given by:

$$D_R\ (\%) = 0.478\ (q_{c1N})^{0.264} - 1.063 \tag{9.29}$$

For clean to silty sands, the measured (or estimated) fines content is used to adjust the normalized cone resistance to that for an equivalent clean sand:

$$q_{c1N\text{-}cs} = q_{c1N} + \Delta q_{c1N} \tag{9.30}$$

where the fines content correction term is expressed:

$$\Delta q_{c1N} = \left(\frac{q_{c1N}}{14.6} + 11.9\right) \cdot \exp\left[1.63 - \left(\frac{9.7}{FC+2}\right) - \left(\frac{15.7}{FC+2}\right)^2\right] \tag{9.31}$$

Then this corrected and normalized CPT resistance is used to obtain the exponent *m*:

$$m = 1.338 - 0.249\ (q_{c1N\text{-}cs})^{0.264} \tag{9.32}$$

where it is restricted to the range: $0.264 \leq m \leq 0.782$.

The available strength of the ground to resist an earthquake is represented by the cyclic resistance ratio (CRR) for a $M_w = 7.5$ and effective overburden stress at $\sigma_v' = 1$ atm as shown in ***Figure 9.24***, which is evaluated from:

$$CRR_{7.5,\sigma v'=1\,atm} = \exp\left[\frac{q_{c1N-cs}}{113} + \left(\frac{q_{c1N-cs}}{1000}\right)^2 - \left(\frac{q_{c1N-cs}}{140}\right)^3 + \left(\frac{q_{c1N-cs}}{137}\right)^4 - 2.80\right] \tag{9.33}$$

The level of ground shaking represented by the cyclic stress ratio (CSR) given by equation (9.24) depends on the magnitude scaling factor (MSF) and overburden stress factor (K_σ), both of which are dependent on the normalized cone resistance in the UCD procedure. As such, the MSF is derived from the earthquake magnitude and normalized-corrected penetration resistance:

$$MSF = 1 + (MSF_{max} - 1) \cdot [\ 8.64 \cdot \exp(-M/4) - 1.325\ ] \tag{9.34}$$

where the maximum MSF value is imposed:

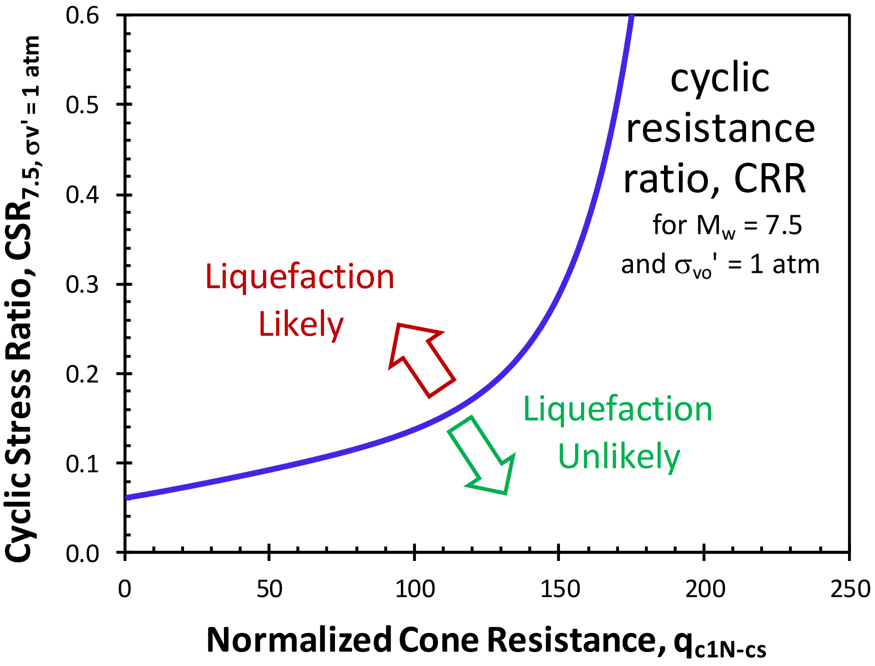

Figure 9.24: Cyclic stress ratio (CSR) versus normalized cone resistance q_{c1N-cs} with cyclic resistance ratio (CRR) for evaluating cyclic liquefaction potential from CPT using UDC procedure (Boulanger & Idriss 2014)

$$\mathrm{MSF}_{max} = 1.09 + [\,(q_{c1N\text{-}cs})/180\,]^3 \;\leq\; 2.2 \tag{9.35}$$

The overburden stress factor is also expressed as a function of normalized corrected penetration resistance and level of effective stress (Boulanger and Idriss 2014):

$$K_\sigma \;=\; 1 - C_\sigma \cdot \ln(\sigma_{vo}'/\sigma_{atm}) \;\leq\; 1.1 \tag{9.36}$$

where the parameter C_σ is determined from:

$$C_\sigma = 1/[\,37.3 - 8.27\cdot (q_{c1N\text{-}cs})^{0.264}\,] \;\leq\; 0.3 \tag{9.37}$$

Of additional note, in addition to the deterministic approach discussed herein, the UCD procedure also provides a family of curves of probability of liquefaction using the CPT.

9.4.4 Yield Stress Ratio for Screening of Cyclic Liquefaction

The aforementioned procedure for yield stress ratio at critical state (YSR_{csl}) for delineating contractive versus dilative soil behavior can also serve as a simple screening of ground susceptible to cyclic liquefaction. The concept here is that contractive soils are prone to liquefaction, whereas dilatant soils are not susceptible to liquefaction.

9.5 Case Studies Involving Cyclic Liquefaction

Three case studies will be presented to show a comparison of the simplified cyclic stress-based approach and YSR at critical state line. For the former, the NCEER method is utlilized.

9.5.1 Case Study: Felipito Bridges, Mexico

The Felipito case study involves the performance of two parallel bridges (one highway and one railroad), as presented by Turner et al. (2014, 2016). ***Figure 9.25*** shows the site location and a photo of both bridges that cross the Colorado River in the northern Baja California peninsula. The site was subjected to the 2010 M 7.2 El Mayor-Cucuapah earthquake which imparted a peak ground acceleration of PGA = 0.27 g, resulting in a partial collapse of the railroad bridge which was supported by driven steel pilings. The undamaged highway bridge was situated on drilled shaft foundations. Geotechnical investigations utilized the results of shear wave velocity profiles, SPT borings, and CPTu soundings, supplemented with limited laboratory testing.

A representative CPT-01 sounding was selected for evaluation, as presented in ***Figure 9.26***. Post-processing of the data included: (a) an evaluation of the effective stress and yield stress profiles (Figure 9.26d); and (b) cyclic liquefaction analyses that compare the level of ground shaking, i.e., the cyclic stress ratio (CSR) with the level of ground support, or cyclic resistance ratio (CRR), as shown in Figure 9.26e. The CSR was adjusted to a reference value for M_w = 7.5 using the NCEER analysis (Robertson & Wride 1998; Youd et al. 2001). This identified five sandy layers having a high likelihood of liquefaction where the CSR > CRR. The results can be further processed to provide a comparison of the normalized values, including: yield stress ratio (YSR = σ_p'/σ_{vo}') and factor of safety (FS = CRR/CSR), as presented in ***Figure 9.27***.

(a) (b)

Figure 9.25: Liquefaction case study of Felipito Bridges, Mexico: (a) EQ epicenter and site location; (b) highway and railroad bridges (Turner et al. 2014)

Notably, when the FS < 1, we have a strong likelihood of liquefaction. The five sand layers are found to be more or less corresponding to the same depths as those identified as contractive sands per the threshold YSR approach. Of additional note, a thin sixth sand layer at a depth of 16.2 m is also identified as contractive by the YSR approach whereas only marginally liquefiable via the NCEER analyses.

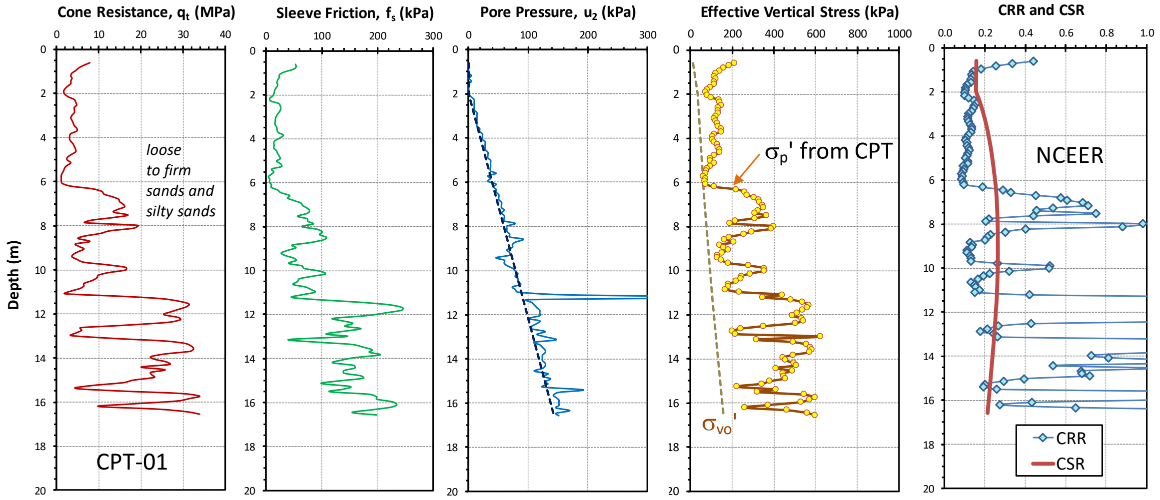

Figure 9.26: Results of CPT-01 at Felipito Bridges site: (a) cone resistance, q_t; (b) sleeve friction, f_s; (c) pore pressure, u_2; (d), effective stresses σ_{vo}' and σ_p' from CPT; (e) CRR and CSR from NCEER cyclic liquefaction analyses.

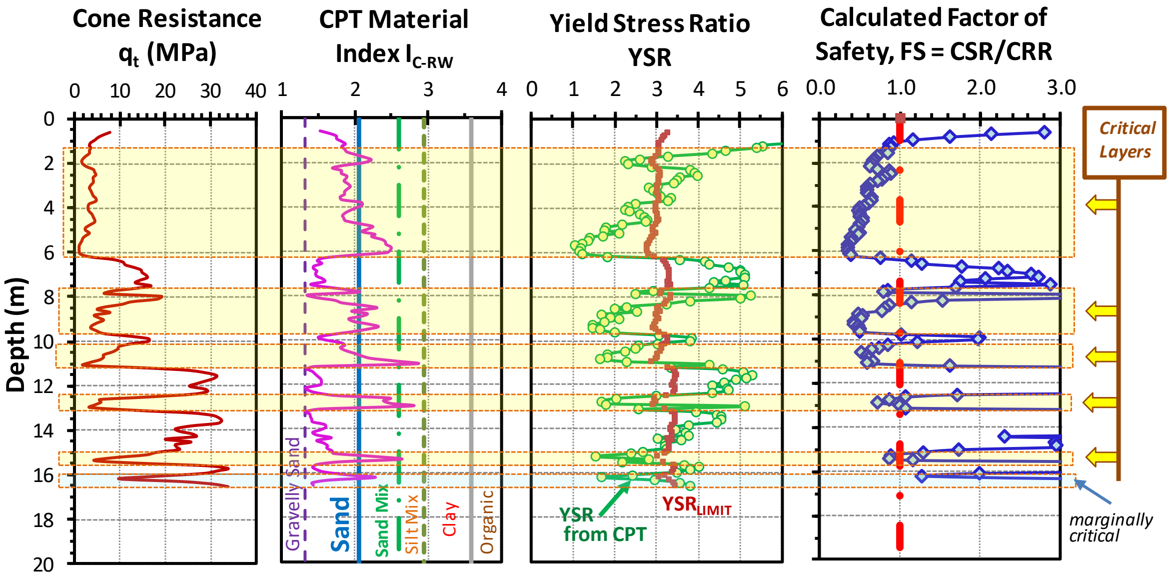

Figure 9.27: Post-processing of normalized liquefaction parameters at Felipito Bridges site: (a) cone resistance, q_t; (b) CPT material index, $I_{c\text{-}RW}$; (c) yield stress ratio, YSR; and (d) FS against liquefaction using NCEER procedure

9.5.2 Case Study: Wildlife Site, California

The 1987 Superstition Hills Earthquake ($M_w = 6.6$) resulted in liquefaction at the Wildlife research site in Imperial Valley of southern California. The Wildlife site has been instrumented with an array of ground motion sensors and porewater pressure piezometers for geotechnical research and has experienced 4 earthquakes in the past four decades. The University of Texas - Austin conducted liquefaction research activities at the facility (Cox 2006) and results from sounding CPT-47 Test C are presented in ***Figure 9.28***. The peak ground acceleration for the 1987 event is taken as PGA = 0.206 and the groundwater table is 1 m deep. It can be seen that there are four critical layers of liquefaction concern with FS < 1 in the right-hand portion of the figure. These same four layers coincide with the values of in-situ YSR from the CPT profile that fall below the YSR_{csl} threshold and indicate contractive soil behavior.

Also note the two layers at depths of 1.5 to 2.5 m and from 6.8 m to termination depth at 8 m which have $I_c > 2.6$, therefore not considered "liquefiable" in the technical definition (Idriss & Boulanger 2008).

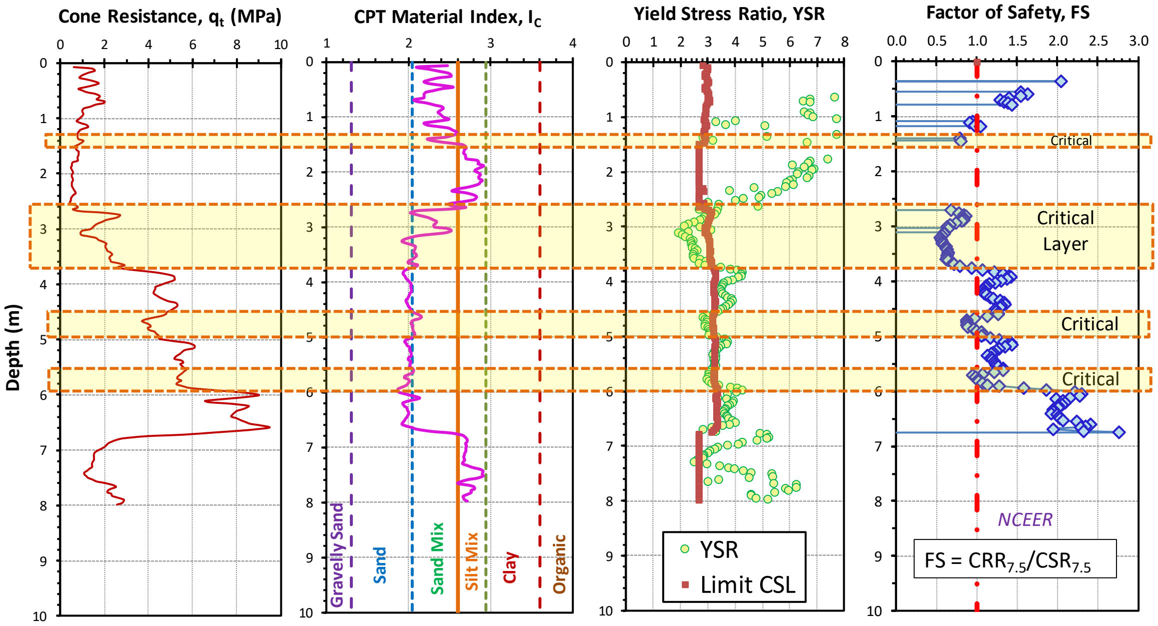

Figure 9.28: Profiles at Wildlife research site, CA: (a) cone resistance, (b) index I_c; (c) YSR and threshold; (d) Factor of Safety using NCEER method.

9.5.3 Case Study: Christchurch, New Zealand

A significant number of liquefaction sites became apparent following four main earthquake events in Christchurch, NZ during 2010 and 2011. One example case study is detailed by Green et al. (2014) for Site 11 at a park along the Kaiapoi River that experienced surficial liquefaction at the ground surface during both the Darfield ($M_w = 7.1$; PGA = 0.231 g) and Christchurch ($M_w = 6.2$; PGA = 0.181 g) earthquake events. ***Figure 9.29*** presents a representative CPT sounding (CPT-KAN-26) from the site. For the Darfield EQ, screening of the critical liquefied layers where the

CRR < CSR clearly matches the same layers identified when YSR < YSR_{csl}.

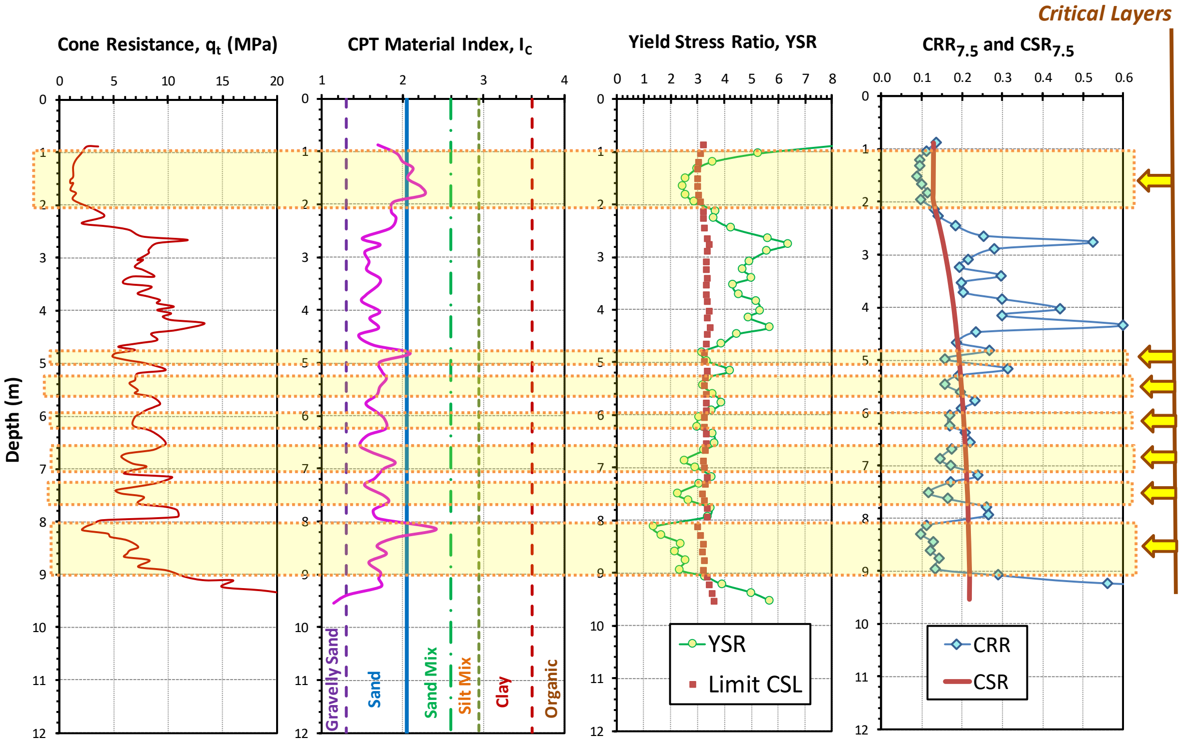

Figure 9.29: Profiles at North Kaiapoi, Christchurch, NZ: (a) cone resistance, (b) index I_c; (c) YSR and threshold; (d) CSR and CRR using NCEER method

9.6 Post-cyclic Undrained Strength Evaluation

Derivations for assessing the post-cyclic liquefied strength of sands from CPT results have been developed (Olson and Johnson, 2008; Robertson, 2010; Boulanger and Idriss, 2014; Sadrekarimi 2014). This parameter is also called the residual undrained shear strength or liquefied undrained strength and designated $s_{u(\text{liquefied})}$ or s_u(LIQ) or s_r, as well as other alternative nomenclature.

9.6.1 UIUC Method

Research by the geotechnical group at the University of Illinois-Urbana-Champaign (UIUC) compiled data from 33 flow liquefaction case studies worldwide (Olson & Stark 2002). Most of the data on the liquefied soils came from either standard penetration tests (SPT) or relative density evaluations, however, with only 11 case studies directly made by CPT. Therefore, they made some assumptions on converting SPT and D_R data to an equivalent normalized cone resistance (q_{c1}) based on fines content and/or grain size characteristics, where:

$$q_{c1} = \frac{1.8 \cdot q_c}{0.8 + (\sigma_{vo}' / \sigma_{atm})} \tag{9.38}$$

where qc is in units of MPa. From the geometry of the flow liquefaction case studies, Olson &

Stark (2002) backcalculated the undrained liquefied strength of the soils (s_uLIQ) and expressed this in terms of a dimensionless ratio: $s_u(LIQ)/\sigma_{vo}'$ that was correlated to the normalized q_{c1}. ***Figure 9.30*** presents the dataset trend that can be expressed:

$$\frac{s_u(LIQ)}{\sigma_{vo}'} = 0.03 + 0.0143 \cdot q_{c1} \pm 0.03 \;\; for \; q_{c1} \leq 6.5MPa \tag{9.39}$$

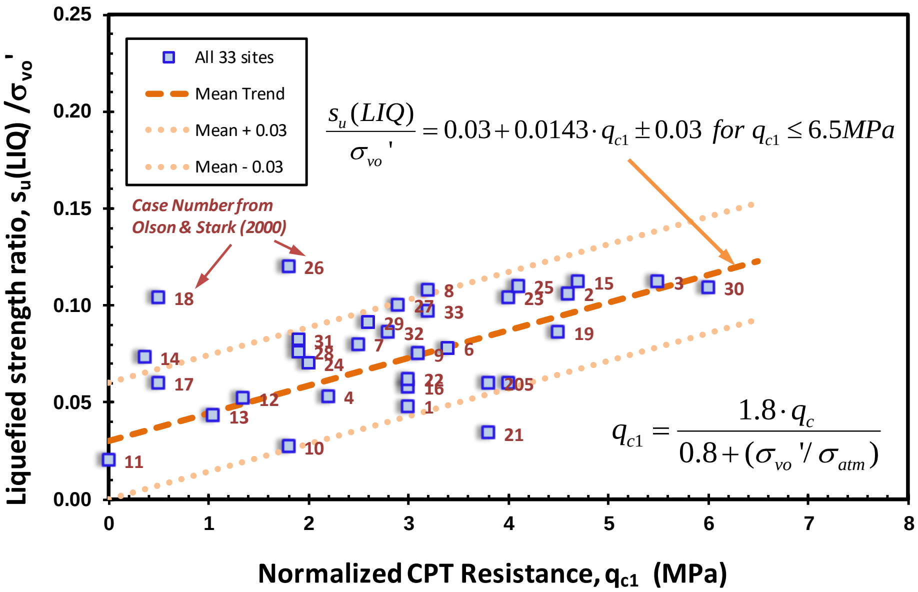

Figure 9.30: Relationship for liquefied strength from normalized cone resistance using UIUC method (adapted after Olson & Stark 2002)

9.6.2 UCD Approach

The University of California at Davis (UCD) method for cyclic liquefaction also provides a means to estimate the post-cyclic undrained (residual) strength. This strength is termed S_r by Idriss & Boulanger (2015) and expressed as an undrained strength ratio, S_r/σ_{vo}', or $s_u(LIQ)/\sigma_{vo}'$.

The UCD method uses a normalized cone resistance that is adjusted for fines content (FC) per a set of tabulated values (i.e., Table 3) provided by Idriss & Boulanger (2015) that is presented graphically here as ***Figure 9.31***. The normalized cone resistance corrected for FC for residual strength is:

$$q_{c1Ncs\text{-}Sr} = q_{c1N} + \Delta q_{c1Ncs\text{-}Sr} \tag{9.40}$$

where q_{c1N} is obtained from eqn (9.26) and the adjustment for FC is given by:

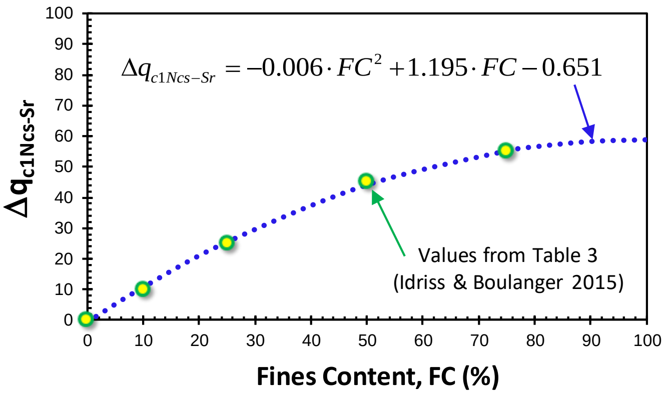

Figure 9.31: Relationship for fines content correction using UCD method

$$\Delta q_{c1Ncs-Sr} = -0.006 \cdot FC^2 + 1.195 \cdot FC - 0.651 \tag{9.41}$$

The evaluation of the residual undrained strength ratio is then given for two cases: (a) where void ratio redistribution is expected to be significant following liquefaction; (b) when the void ratio redistribution will be negligible. Both cases are shown in ***Figure 9.32*** with case studies listed by Idriss & Boulanger (2015). These can be represented by the following equations:

Case 1: $$\left(\frac{s_r}{\sigma_{vo}'}\right)_{CASE1} = \exp\left[\frac{q_{c1Ncs-Sr}}{24.5} - \left(\frac{q_{c1Ncs-Sr}}{61.7}\right)^2 + \left(\frac{q_{c1Ncs-Sr}}{106}\right)^3 - 4.42\right] \leq \tan\phi' \tag{9.42}$$

Case 2: $$\left(\frac{s_r}{\sigma_{vo}'}\right)_{CASE2} = \left(\frac{s_r}{\sigma_{vo}'}\right)_{CASE1} \cdot \left[1 + \exp\left(\frac{q_{c1Ncs-Sr}}{11.1} - 9.82\right)\right] \leq \tan\phi' \tag{9.43}$$

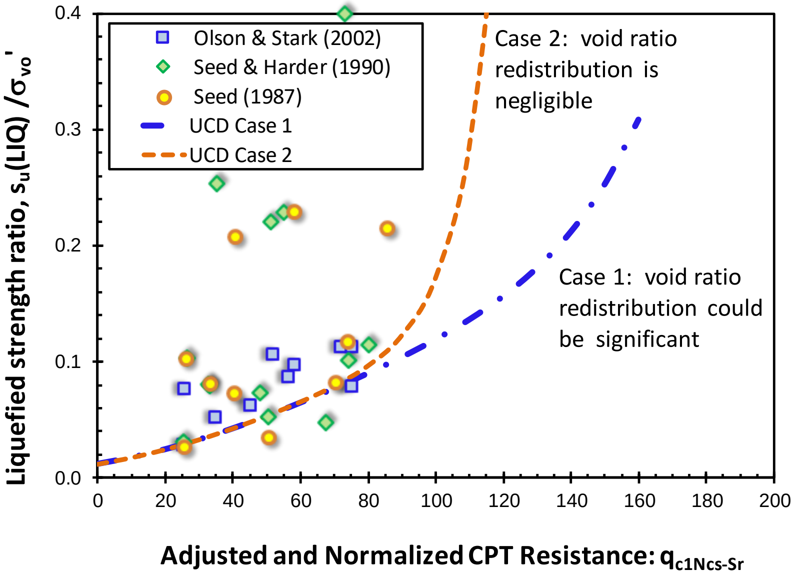

Figure 9.32: Liquefied strength from adjusted and normalized cone resistance using UCD method (adapted from Idriss & Boulanger 2015)

9.6.3 Robertson Method

Using an updated approach reported by Robertson (2021), ***Figure 9.33*** shows the relationship for normalized residual undrained strength to effective overburden ratio, $s_{u(liq)}/\sigma_{vo}'$, with normalized CPT cone tip resistance for an equivalent clean sand that can be expressed:

$$\frac{s_{u(liq)}}{\sigma_{vo}'} \approx 0.0007 \cdot \exp(0.084 \cdot Q_{tn,cs}) + \frac{0.3}{Q_{tn,cs}} \quad > 0.0178 \tag{9.44}$$

which applies to soils exhibiting $I_{cRW} < 3.0$. A recommendation is also given to the use of a minimum value $s_{u(liq)} = 1$ kPa for $\sigma_{vo}' < 50$ kPa (Robertson 2021).

For critical projects having severe consequences, the evaluation of the residual undrained strength should be accompanied by other independent means, including field vane tests, ball penetrometer, and/or laboratory strength testing on undisturbed samples.

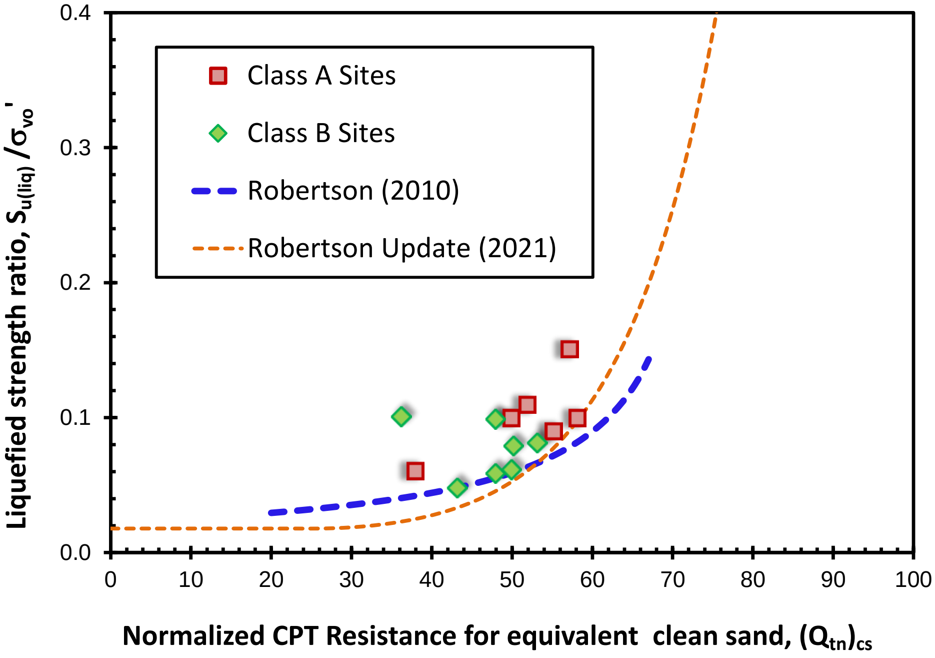

Figure 9.33: Recommended undrained strength ratio of liquefied sands from CPT normalized resistance (after Robertson, 2021).

9.7 Ground Deformations from Liquefaction

Liquefaction can cause subsidence and settlements in the ground due to volumetric and shear strains. The level of strains has been related to the relative density of sands and intensity of liquefaction. Four cases can be considered, as detailed by Zhang et al. (2004). ***Figure 9.34*** depicts simplified geometries of the ground conditions that are covered.

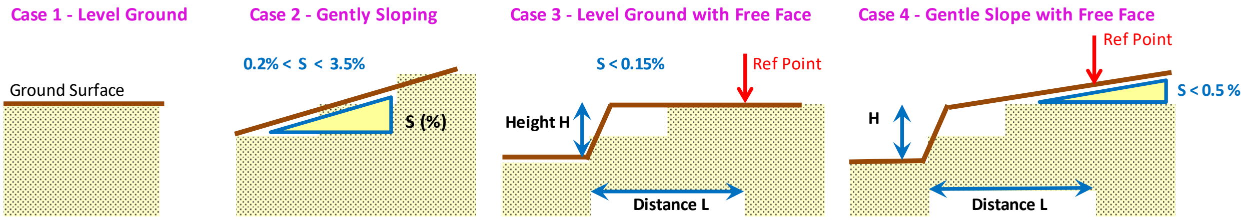

Figure 9.34: Four simplified cases for level and sloping ground during liquefaction

Vertical settlements for level ground conditions are calculated on the basis of volumetric strains, while lateral deformations are associated with sloped terrain.

9.7.1 Volumetric Strains

The volumetric strains are determined on the basis of the calculated factor of safety (FS) against liquefaction and the relative density (D_R) of the sands, as illustrated by ***Figure 9.35***. The seismic-induced permanent settlements (s_z) are calculated from the integration of ε_{vol} with depth:

$$s_z = \int_0^z \varepsilon_{vol}\, dz \qquad (9.45)$$

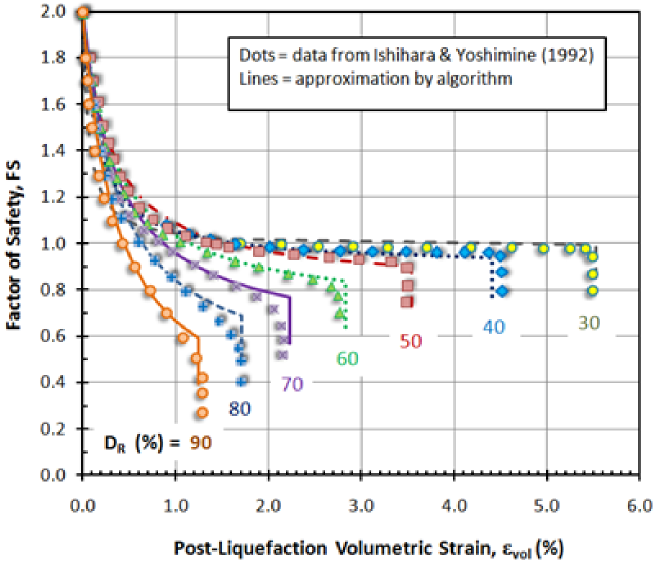

Figure 9.35: Relationship of volumetric strain (ε_{vol}) in terms of factor of safety against liquefaction (FS) and sand relative density (D_R).

Algorithms to represent the laboratory results obtained by Ishihara & Yoshimi (1992) on cyclically-loaded sand are given here. Determine the sand relative density from the expression:

$$D_R\ (\%) = 76 \cdot \log_{10}(Q_{tn\text{-}cs}) - 85 \leq 100\% \tag{9.46}$$

where normalized cone resistance for an equivalent clean sand is limited to $Q_{tn\text{-}cs} < 200$. For values above 200, set $D_R = 100\%$.

$$\text{Define: } m_x = 1.91962 - 0.0072 \cdot D_R \tag{9.47}$$

$$\text{for } D_R \leq 50\%\text{: Define: } b_x = 2 \cdot 10^{-6} \cdot (D_R)^{3.04} \tag{9.48a}$$

$$\text{For } D_R > 50\%\text{: Define } b_x = 0.0112 \cdot D_R - 9 \cdot 10^{-5} \cdot (D_R)^2 - 0.0769 \tag{9.48b}$$

$$\text{Determine the limiting volumetric strain: } \varepsilon_{vol\text{-}Limit} = 18.76 - 3.891 \cdot \ln_e(D_R) \tag{9.49}$$

Calculate limiting factor of safety (FS_{limit}):

$$FS_{limit} = 2 - 1/[m_x + b_x/\varepsilon_{vol\text{-}limit}] \tag{9.50}$$

Determine volumetric strains:

$$\text{If } FS \geq 2\text{, then: } \varepsilon_{vol} = 0 \tag{9.51a}$$

$$\text{If } FS < FS_{limit}\text{, then } \varepsilon_{vol} = \varepsilon_{vol\text{-}Limit} \tag{9.51b}$$

$$\text{If } FS_{limit} \leq FS < 2\text{, then: } \varepsilon_{vol} = b_x/[1/(2-FS) - m_x] \tag{9.51c}$$

The degree to which the approximate algorithms match with the laboratory data are reasonable, as evident from ***Figure 9.35***.

9.7.2 Case Study from Felipito Bridge, Mexico

At the prior cyclic liquefaction case study from the Felipito Bridges, Mexico site discussed in Section 9.5.1, vertical ground movements around the highway piers showed some 300 to 500 mm of settlement following liquefaction. ***Figure 9.36*** shows the relative movement near Bent 6 at the site.

Figure 9.36: Photo at Bent 6 of Felipito Highway Bridge showing 30 to 50 cm of vertical displacements following soil liquefaction (from Turner et al. 2014).

For the analysis of displacements following liquefaction, ***Figure 9.37*** presents the cone resistance data, relative density, volumetric strains, and cumulative vertical displacements at Felipito. Using sounding CPT-01, a displacement of 400 mm compares with the observed range of movements (300 to 500 mm).

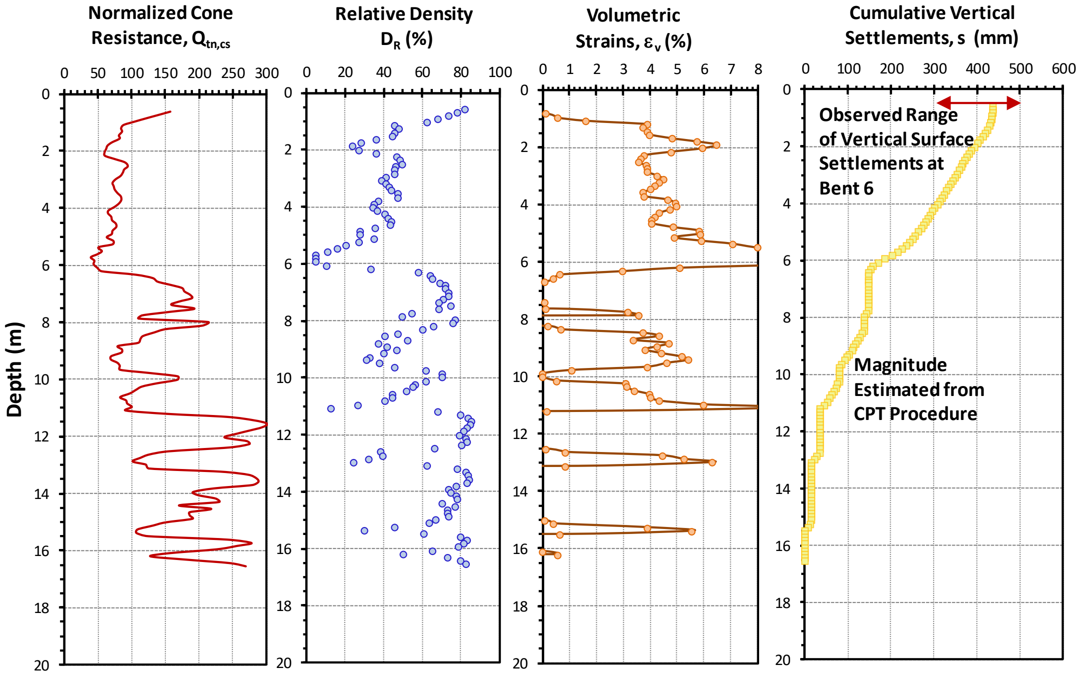

Figure 9.37: Profiles at Felipito Bridges site, Mexico: (a) normalized cone resistance; (b) D_R from CPT; (c) volumetric strains; and (d) cumulative vertical displacements with depth

9.7.3 Lateral Displacements

In sloping terrain and/or ground with a free-face condition, the occurrence of liquefaction can result in lateral spreading and horizontal movements downhill. The magnitudes of induced lateral displacements (LD) can be estimated from the maximum cyclic shear strains (γ_{max}) which are integrated with depth to obtain the lateral displacement index (LDI):

$$LDI = \int_0^z \gamma_{MAX} \, dz \qquad (9.52)$$

The level of cyclic shear strains was studied under laboratory controlled conditions by Ishihara & Yoshimine (1992) who related magnitude of γ_{max} to the factor of safety and sand relative density. In addition, a limiting value of cyclic shear strains was established from the work of Seed (1976, 1979) and Housner et al. (1985). The resulting methodology is presented graphically in Figure 9.35 (Zhang et al., 2004; Robertson 2004).

For gently sloping ground, depending upon the slope angle (0.2% < S < 3.5%), the calculated lateral displacements (LD) are obtained from:

$$LD/LDI = S + 0.2\ (\%) \qquad (9.53)$$

For free-face conditions (Fig. 9.34), the geometry of distance from the CPT sounding location to the face location (L) and the height of the free face (H) are used to obtain the amount of lateral displacements ($4 < L/H < 40$):

$$LD/LDI \;=\; 6\,(H/L)^{0.8} \tag{9.54}$$

The following algorithms are used to approximate the laboratory results of Figure 9.35.

Define the Limiting value of Factor of Safety (LFS):

$$LFS = 0.0002{*}(D_R)^2 - 0.0322{*}D_R + 1.768 \tag{9.55}$$

The limiting cyclic shear strain (LCSS):

$$LCSS = 144 - 3{\cdot}D_R + 0.0164{\cdot}(D_R)^2 \tag{9.56}$$

Calculate the Maximum Shear Strain (MSS):

$$\text{If } FS < LFS. \text{ then: } MSS = LCSS \tag{9.57a}$$

$$\text{If } 1 < FS < 2; \text{ then: } MSS = +3.55{\cdot}(FS) - 4.7 \tag{9.57b}$$

$$\text{If } FS \geq 2; \text{ then: } MSS = 0 \tag{9.57c}$$

$$\text{If } LFS \leq FS \leq 1; \text{ then: } MSS = LCSS - (LCSS - 3.5){\cdot}(FS - LFS)/(1-LFS) \tag{9.57d}$$

Reasonable agreement can be seen between the laboratory results and approximation algorithms in ***Figure 9.38***.

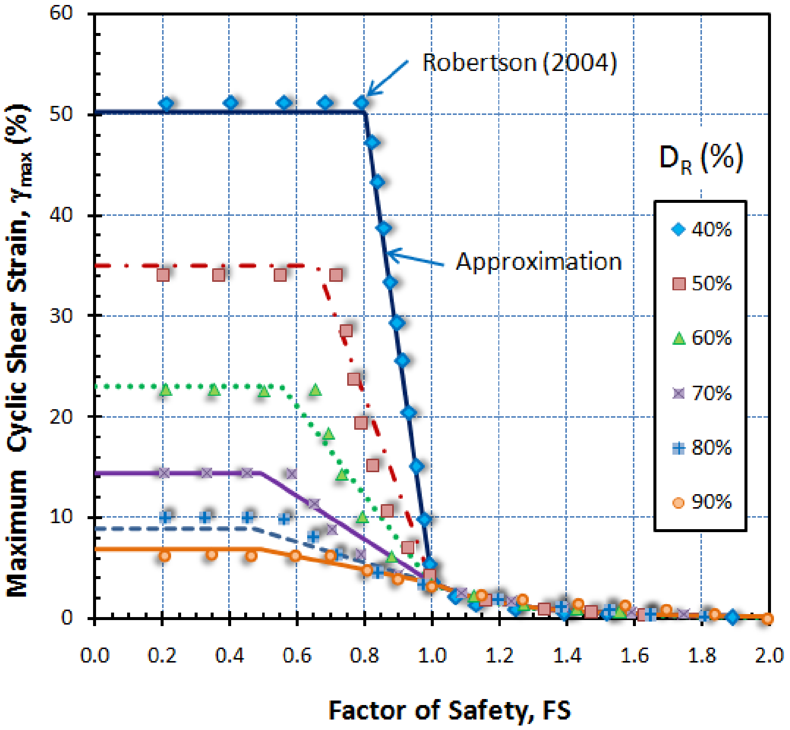

Figure 9.38. Relationship for Maximum Shear Strain (MSS = γ_{max}) in terms of sand relative density (D_R) and calculated factor of safety against liquefaction(FS).

9.8 Cyclic Resistance Using Shear Wave Velocity

With SCPTU, the opportunity exists to use the shear wave velocity (V_s) to represent the ground resistance available to withstand cyclic liquefaction. In fact, the NCEER procedures offer a parallel method using the same procedure for CSR as given by equation 9.18 (Youd et al. 2001). Three CRR values are provided that depend upon the fines content (FC) which are presented in ***Figure 9.39*** that can be expressed:

$$CRR = a_v \cdot \left(\frac{V_{s1}}{100}\right)^2 + b_v \cdot \left(\frac{1}{V_{s1}{*} - V_{s1}} - \frac{1}{V_{s1}{*}}\right) \tag{9.58}$$

where $a_v = 0.022$ and $b_v = 2.8$ are empirical fitting constants, $V_{s1} = V_s/(\sigma_{vo}'/\sigma_{atm})^{0.25}$ = normalized measured shear wave velocity, and $V_{s1}* = 200$, 210, and 220 m/s for values of FC = 35%, 20%, and 5%, respectively.

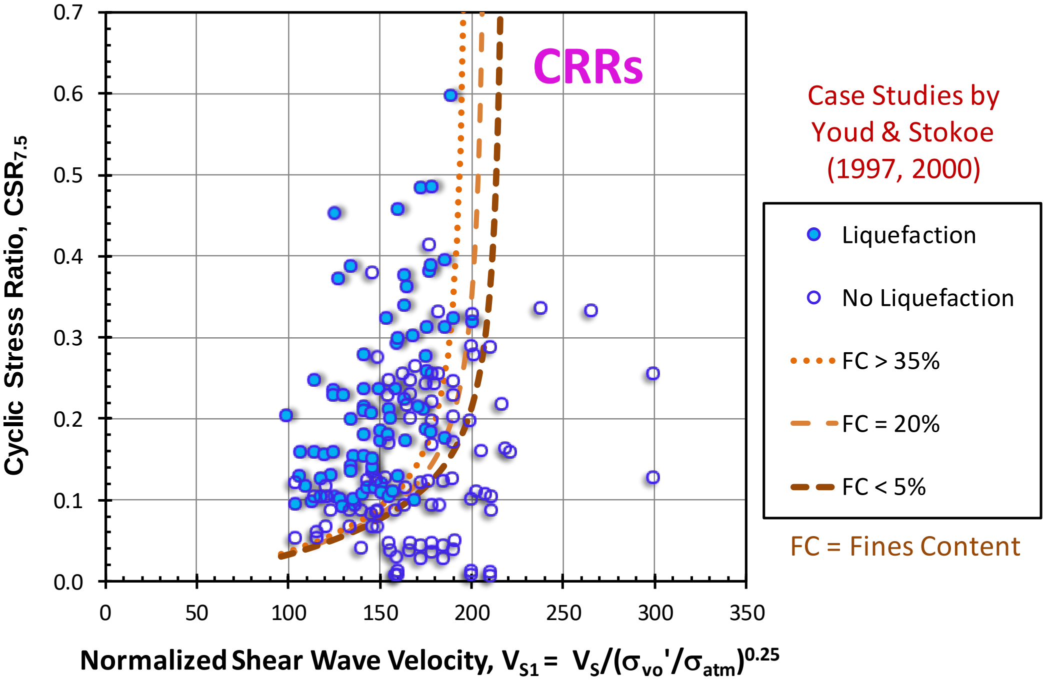

Figure 9.39: Deterministic CRS vs. V_{s1} liquefaction curves using NCEER method (after Youd et al. 2001)

The use of V_{s1} also affords a separate and independent assessment of liquefaction potential for comparison to the evaluation made by cone resistance, either using $Q_{tn,cs}$ from NCEER or $q_{c1N\text{-}cs}$ from UCD approach.

An updated database to the aforementioned was compiled by Kayen et al. (2013) who added 301 new liquefaction field case histories from China, Japan, Taiwan, Greece, and the USA to the NCEER case studies that formed a data set of 422 seismic records for statistical analyses. While the procedure for obtaining CSR differs because of a more complex r_d calculation and the use of a different definition for MSW, the overall results can be generally appreciated by the number of data presented in ***Figure 9.40***.

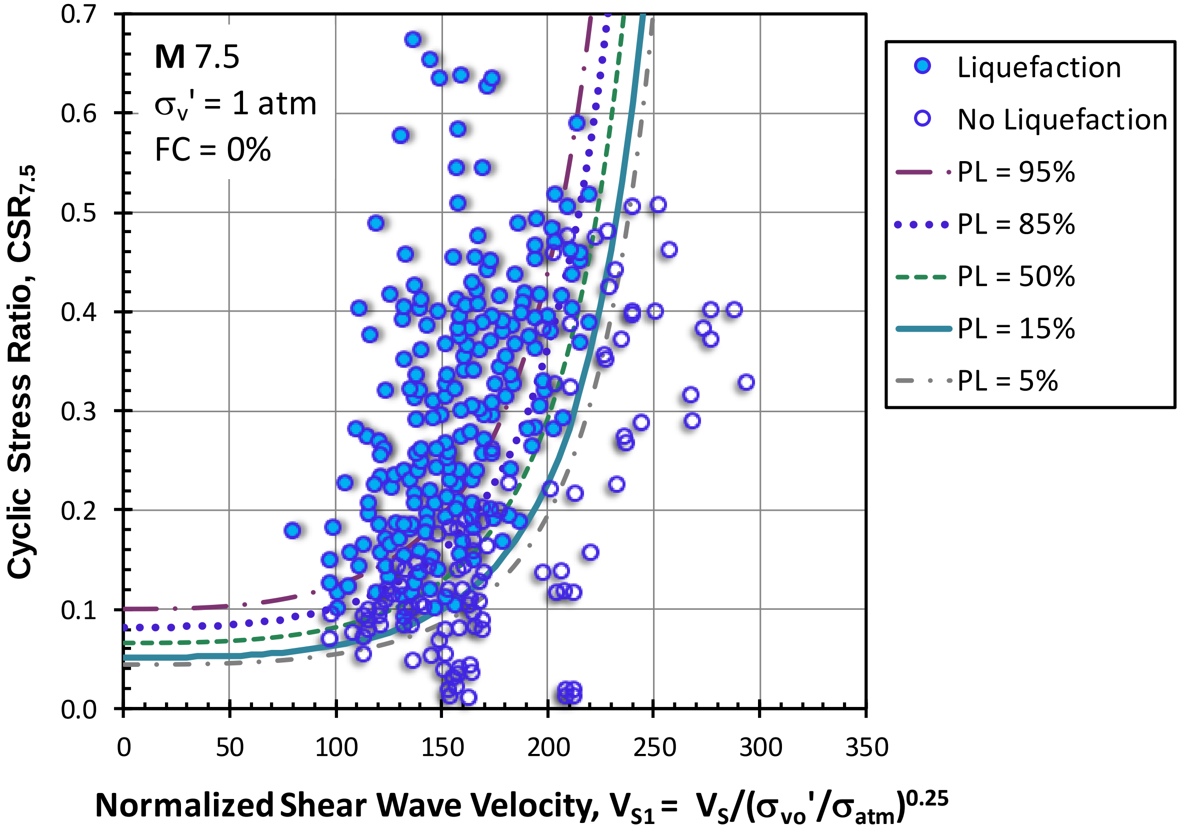

Figure 9.40: CSR with V_{s1} and family of CRR curves for different probabilities of liquefaction (P_L) from updated analyses by Kayen et al. (2013) using 422 seismic case studies

10 Advanced Penetration Testing

In addition to the cone penetrometer, piezocone, and seismic cone, specialized penetrometers have been developed to address specific needs, including: resistivity CPTU, vision cones, vibrocones, temperature cones, radio-isotope CPT, dielectric cones, as well as other sensors (Mayne 2007).

In this section, some details will be given on the following CPT probes in use: (a) resistivity or electrical conductivity CPTU; (b) gamma cones; and (c) full flow penetrometers.

Of additional note, the field program can include modified testing procedures to quantify special nuances of soil behavior including: (a) variable rate testing (and related twitch tests); (b) continuous-interval shear wave velocity measurements; and (c) measurements of compression wave velocities with depth; as well as other methods.

10.1 Resistivity Piezocone (RCPTU) or Conductivity Cone

Resistivity piezocone testing (RCPTU) finds use in geoenvironmental site investigations and coastal explorations. Resistivity (ρ_b) and its reciprocal, electrical conductivity ($\kappa = 1/\rho_b$), are a measure of the electrical characteristics of the ground and can be useful in assessing subsurface corrosion potential, soil contamination, and the interface between saltwater and fresh water (Campanella & Weemees, 1990; Pidlisecky et al. 2006). Resistivity profiles can also be interpreted to infer lithographic changes in soil layers and recently found to help identify sensitive and quick clays (Löfroth et al. 2013).

Resisitivity is measured in ohm-meters (Ω-m) and is a property of the medium (Campanella 2008). Both resistivity and electrical conductivity are direct current (DC) type measurements. Dielectric, or relative permittivity, is a similar type measurement but taken in terms of alternating current (AC).

Similar to surface resistivity surveys, the downhole measurement of resistivity employs paired sets of electrodes, usually in groups of four (either Wenner or Schlumberger arrays), but other configurations are also available. For resistivity piezocone testing (RCPTu), the electrodes can either be included as part of the penetrometer, or alternatively positioned axially in a trailing module behind the cone penetrometer. ***Figure 10.1*** shows several of the available configurations used in RCPTu.

A representative resistivity piezocone sounding from the Opelika national geotechnical experimentation site is presented in ***Figure 10.2***. The natural ground consists of residual fine sandy silts that were formed in place by the weathering and disintegration of schistose and gneissic bedrock of the Appalachian Piedmont geology. In general, the observed values of resistivity range between 100 and 400 ohm-m at this site.

- **Resistivity Cones**
- **Conductivity CPT**
- **Dielectric CPTu**

Configurations

- **2 electrode array**
- **4 electrode arrays**
- **Wenner or Schlumberger**

Figure 10.1: Selected resistivity penetrometers and electrical conductivity probes

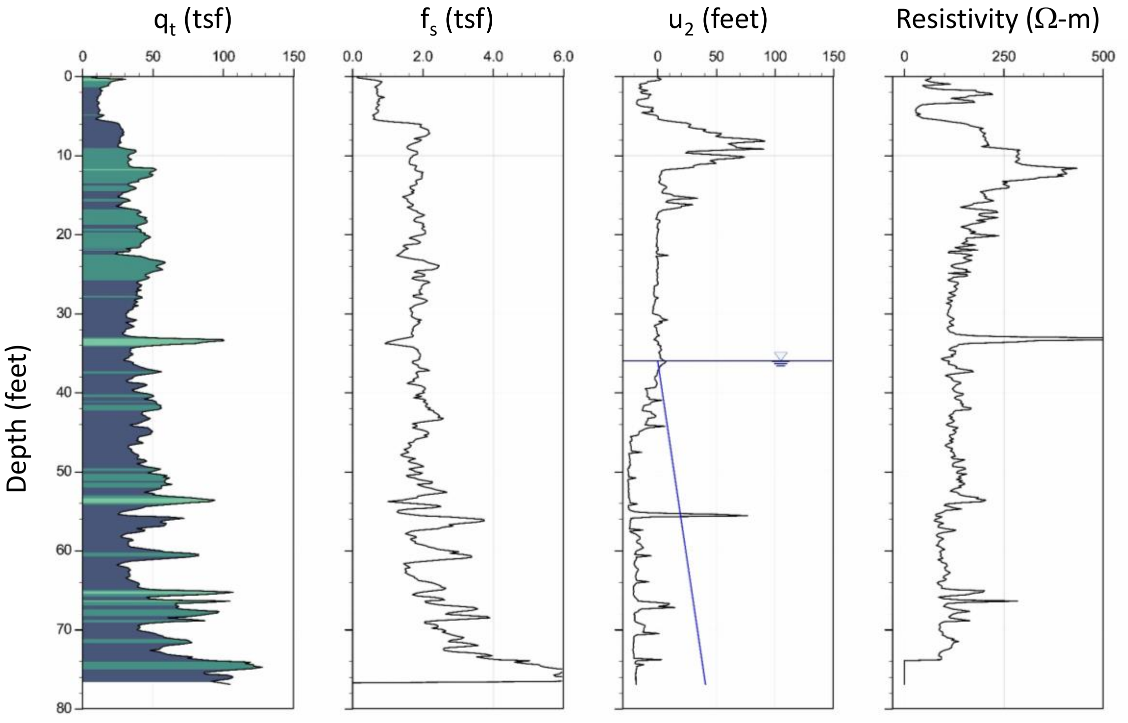

Figure 10.2: Illustrative example of RCPTU in residual sandy silt at Opelika, AL

Resistivity testing is performed in conjunction with piezocone penetration testing with the addition of a module to determine the electrical resistivity of the soil. The module contains electrodes which are in direct contact with the surrounding soil/water/air matrix during penetration. The module measures the voltage drop between the electrodes during penetration in order to calculate the resistance of the surrounding soil. This resistance primarily depends upon the electrical conductivity of the pore-fluid within the soil.

The use of a resistivity module for geoenvironmental applications is described by Campanella (2008) where he presents a table of typical bulk-resistivity measurements made in different geoenvironmental conditions. In metal mine tailings with oxidized sulphide leachate, the bulk resistivity was 0.01 to 20 Ω-m, without oxidized sulphide leachate the bulk resistivity increased to 20 to 100 Ω-m. Once calibrated to the electrical properties of a given soil and fluid, the resistivity measurements can be used to calculate the saturation of the soil.

Figure 10.3 shows an RCPTU profile collected in the Fraser River Delta. This profile includes both the resistivity and the inverse of the resistivity, the conductivity. The resistivity profile shows significant dispersion above the ground water table. This is likely due to heterogeneous degrees of saturation. This dispersion is eliminated below the ground water table. The upper sand layer has a higher resistivity than the lower fine-grained layer. The resistivity profile can be useful for identifying soil layers and may be indicative of soil saturation.

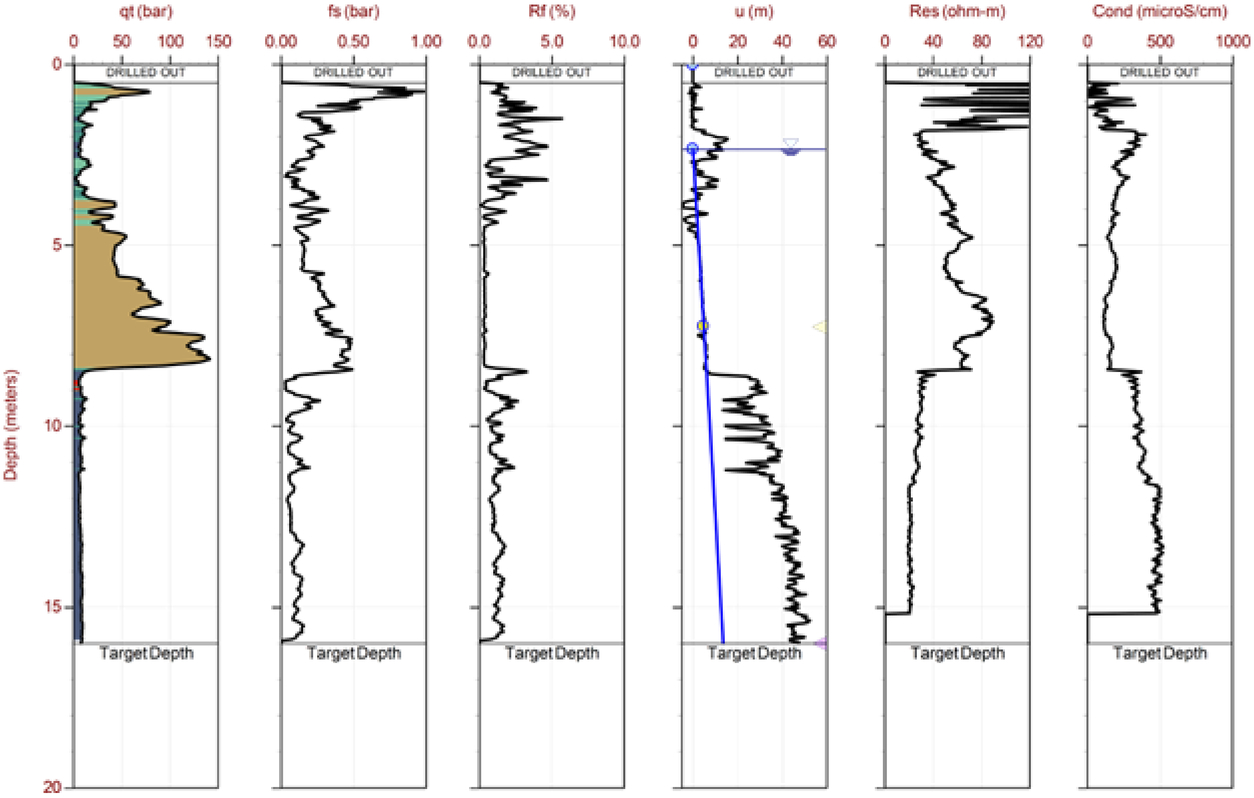

Figure 10.3: RCPTU profile in the Fraser River alluvial delta showing the relationship between resistivity and the ground water table and soil type

10.2 Passive Gamma Piezocone Testing (GCPTU)

Gamma Cone Penetration Testing (GCPTU) uses a passive-gamma module attached behind the cone probe. The module housing contains a scintillating crystal that glows when it is struck by gamma rays. The gamma-module uses a photo-multiplier-tube and associated internal electronics to monitor this scintillating crystal. The observed gamma-ray incidents are counted up and used to calculate the gamma counts-per-second (cps), which is reported in the GCPTU soundings. Quantitative application of gamma measurements requires repeatability between soundings and equipment.

There are three common Naturally Occurring Radioactive Minerals (NORMs). These are natural radioisotopes of Potassium (^{40}K), Thorium (^{232}Th), and Uranium (^{238}U). These three radioisotopes exist in nature due to exceptionally long half-life times of a similar magnitude to the age of the Earth. Potassium is in illite and feldspar minerals, Thorium is associated with heavy minerals, and Uranium is found in uranium salts and organic shale (Ellis and Singer 2007).

Gamma piezocone testing has proven particularly useful in Oil Sand Tailings (OST) deposits. The mineralogical constituents of bitumen ore remain in the tailings by-product and gamma profiling can identify different tailings units. The gamma measurements in these tailings are proportional to the total fines content (weight of fines / total weight) due to the potassium in the illite mineral. It is not proportional to the geotechnical fines content (weight of fines / weight of solids). The total fines content is proportional to the in-situ concentration of ^{40}K in OST.

The generated gamma rays from these natural sources will interact with matter. This interaction makes it possible to observe gamma rays in-situ. The propagating gamma rays can re-coil, lose energy, and change direction in a process known as Compton scattering. When the gamma ray energy drop below 100 keV, the ray can be extinguished by photoelectric absorption. Gamma rays with energies higher than 1022 keV and split into two rays of 511 keV in a process known as pair-production. (Berger 1961) presents table of energy absorption coefficients that averages these three matter interaction effects. For a typical density of tailings a generated gamma ray from ^{40}K may travel from 10 to 20 cm. This means that the GCPTU gamma profile responds to the same soil measured by the cone penetration test.

Gamma levels (counts/s) are not material properties and are significantly affected by the design of the probe. To provide a quantitative measure for ongoing assessment, careful and consistent manufacturing of the probe is required. Calibration procedures are also required to maintain assurance that each probe is performing uniformly and in a predictable way.

GCPTU profiles in oil sand tailings (OST) may include recycle water, fluid tailings, soil-like tailings, and natural ground. The typical measurements in these types of materials can be used to identify the tailings units and to estimate OST properties – such as solids content and fines content. ***Figure 10.4*** shows an example GCPTU profile through OST.

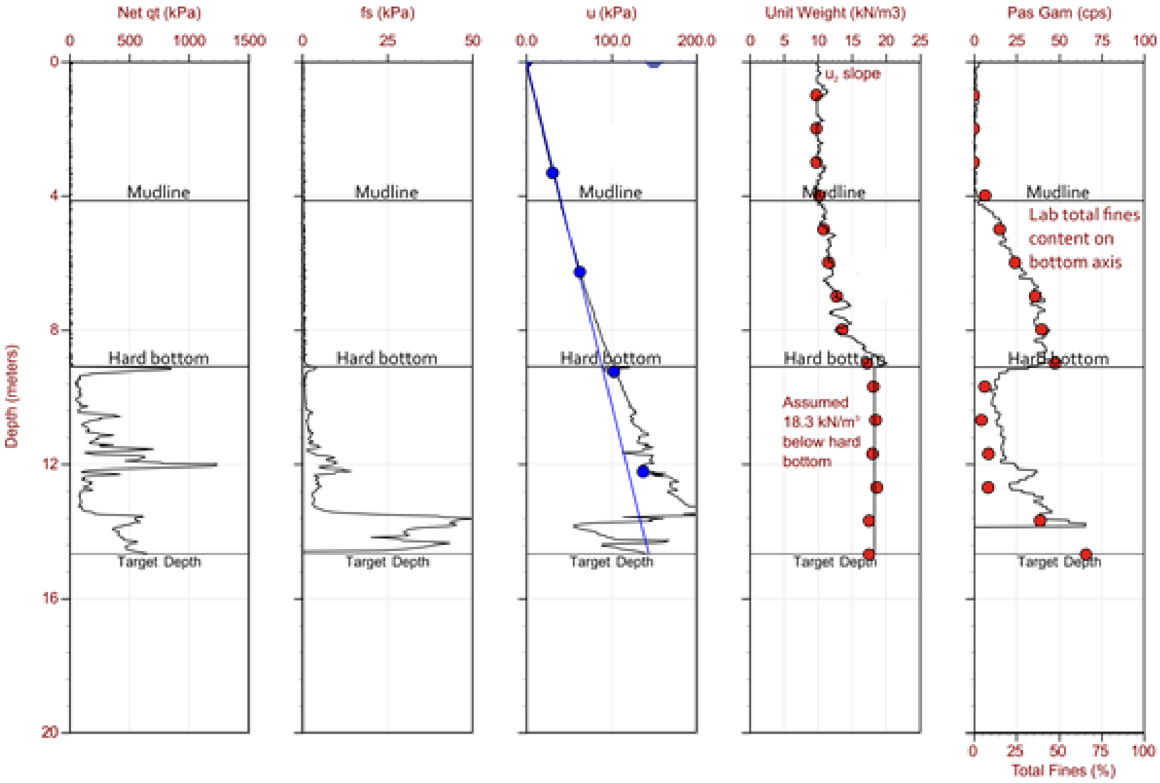

Figure 10.4: Representative GCPTU profile in oil sand tailings through recycle water, fluid tailings, and soil-like tailings

GCPTU measurements in OST recycle water produce an easily identifiable GCPTU profile. First, the corrected tip resistance, q_t, equals the pore pressure u_2. The friction sleeve, f_s, is nearly zero. The pore pressure channel, u_2, increases at approximately 9.8 kPa per meter (i.e., kN/m^3) in pure water and slightly higher in saline water.

Recycle water has negligible concentrations of natural radioisotopes. The observed passive gamma rates are nearly 0 cps. There can be an increase in gamma rates at the pond surface due to atmospheric radiation. Over a very short depth, the impact of atmospheric radiation is completely shielded by the recycle water.

Hitting the mudline typically has no discernable effect on q_t measurements. The friction sleeve, f_s, will still be nearly 0 kPa. The slope of u_2 will begin to deviate from 9.8 kN/m^3; but this change can be nearly imperceptible. Consequently, the standard cone probe results cannot be used to identify the mudline depth with any degree of confidence. However, below the mudline, the tailings contain a concentration of natural radioisotopes. Therefore, the mudline corresponds with a sharp increase in passive gamma rates. The GCPTU can be used to easily identify the mudline depth.

All gamma ray measurement devices have an efficiency factor that reduces the in-situ concentration of gamma rays to a measured gamma rate. This efficiency factor depends on the module shielding, module electronics, and scintillating crystal geometry and type. By sheer coincidence, the ConeTec passive gamma module has an efficiency factor that produces measured gamma rates approximately equal to the total fines content in fluid oil sand tailings. The mudline definition of 5% solids corresponds to a gamma rate of 5 cps.

The froth-treatment process concentrates minerals containing ^{232}Th and ^{238}U radioisotopes that naturally occur in the parent ore body. The passive gamma measurements in fluid froth treatment tailings are not proportional to the total fines content. In froth-treatment tailings we measure passive gamma rates that are an order of magnitude larger than conventional OST tailings. While this removes one application of the GCPTU site investigation tool, it adds another. The GCPTU profiles can be used to easily identify depth-ranges of froth-treatment affected tailings.

Other uses of GCPTU include: (a) fines detection in clays having radioactive emitting elements; and (b) hazardous waste detection in man-made deposits containing hazardous elements.

10.3 Continuous Interval SCPTU

Employing an autoseis generator, continuous-interval shear wave (CiV$_S$) measurements can be obtained such that the shear wave velocity readings become comparable and as frequent as the cone penetrometer values, on the order of several centimeters (McGillivray & Mayne 2008; Styler & Mayne 2013; Ku, et al. 2013a; 2013b). The continuous-interval seismic piezocone test (CiSCPTU) is the fastest method for collecting a full suite of data in soils.

The many recorded wavelets from geophone readings during CiV$_S$ taken in Norfolk, Virginia are shown as a summary plot in ***Figure 10.5***. The main arrivals of the shear waves can be seen as a "waterfall" evident in the profile to the final termination depth at 22 m. A visual examination clearly shows a change in soil layering at around 9 m depth. These wavelets can be post-

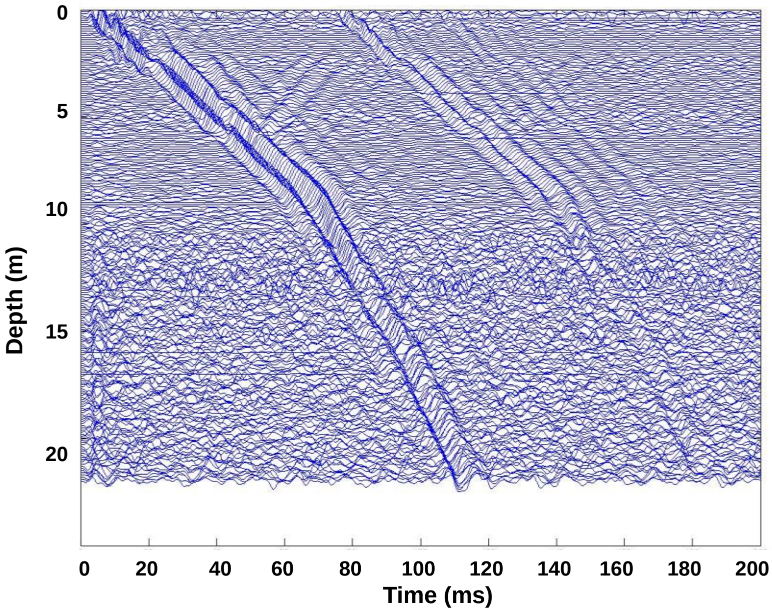

Figure 10.5: Wavelet recordings from continuous-interval V$_s$ measurements in Norfolk, VA

processed using a matching process with MatLab or other software to develop a near-continuous profile of V_s with depth (Ku et al. 2013b).

The full CiSCPTu sounding from Norfolk, Virginia is shown in ***Figure 10.6*** with profiles of four continuous readings with depth: cone tip resistance (q_t), sleeve friction (f_s), penetration porewater pressure (u_2), and shear wave velocity (V_s). Also shown are results from conventional downhole tests (DST) with paired left- and right-strikes to obtain V_s at one-meter intervals. This offers an economic, expedient, and efficient means to procure information on the geostratigraphy, soil engineering parameters, and geophysical data in a single sounding. It is noteworthy that both the continuous V_s and conventional DST results capture the significant step up in velocity at the Holocene–Yorktown interface at a 9m depth. Specifically, the upper Holocene sediments at this site show Vs values of around 130 to 160 m/s, whereas the lower Miocene deposits exhibit higher V_s between 240 to 340 m/s.

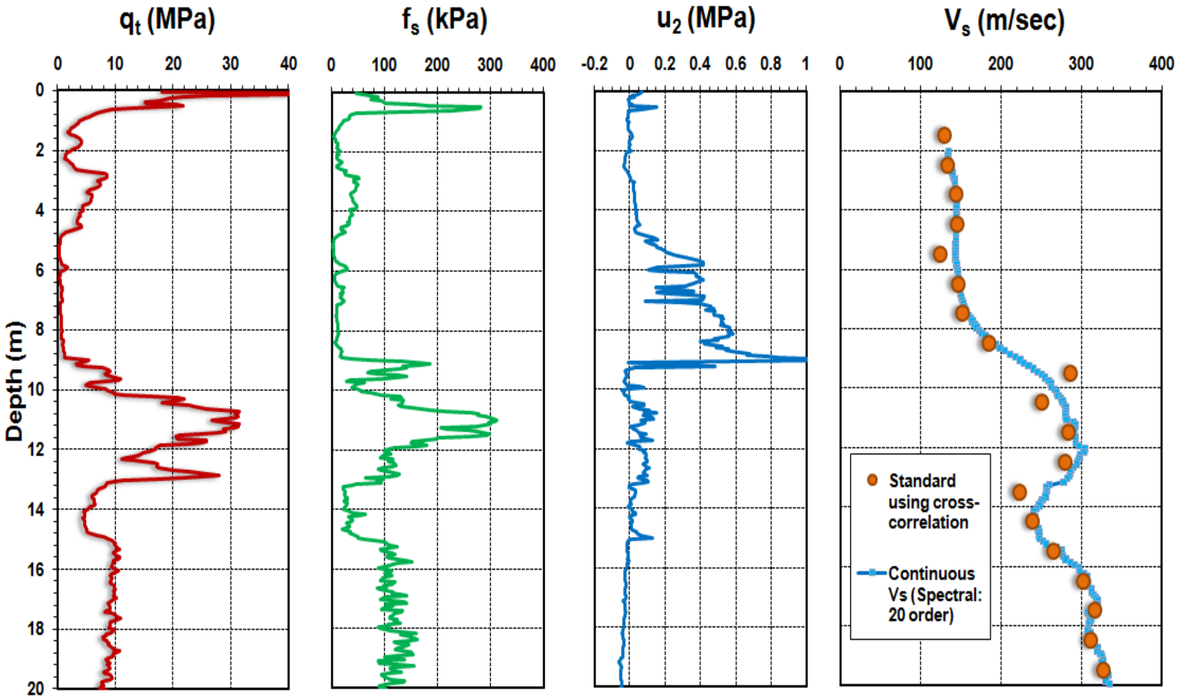

Figure 10.6: Results of CiSCPTu sounding at Norfolk, VA: (a) cone tip resistance, (b) sleeve friction, (c) porewater pressure, and (d) shear wave velocity (Ku et al. 2013b)

10.4 Compression Wave Measurements

There are two types of seismic body waves: shear (S-wave) and compression (P-wave). Compression wave velocities are obtained though down-hole seismic testing in boreholes or during seismic cone penetration tests. Compression wave investigations require different seismic sources, receivers, and data processing than shear wave investigations.

Compression wave velocities depend on the bulk modulus of the soil. The very small strain elastic bulk modulus of the soil is sensitive to full saturation. Compression wave velocity profiling is a site-investigation technique that can be used to identify fully saturated soil zones. Compression wave velocities can be combined with shear wave velocities to calculate the Poisson ratio (Section 7.5.2).

It is much more challenging to obtain compression wave velocities than shear wave velocities. It requires more effort and field experience in order to confirm that compression waves are in the observed traces. Downward propagating compression waves can lose significant fractions of their energy at impedance boundaries due to reflections, refraction, and the generation of shear waves at the boundary. These impedance boundaries are simply sharp changes in the V_P profile. Compression wave profiling requires the use of different seismic sources than the sources used to generate shear waves. It requires consideration for the offset of the seismic source on the ground surface. Data reduction is also complicated by interference from different seismic wave forms. Data reduction must also resolve high compression wave velocities, which magnifies any errors in the interpretation propagation times.

Compression waves can be generated by vertically striking a metal plate on the ground surface with a sledgehammer or by using geophysical MASW sources. These compression waves are observed in-situ using seismic sensors within the cone probe. Butcher et al. (2005) state that these sensors should be vertically orientated to permit the assessment of compression waves. Styler et al. (2016) examined both vertical and horizontal geophones for the compression wave characterization. ***Figure 10.7*** shows the recorded wave traces from the 9 m offset to a seismic testing depth of 40 m in Richmond, BC. The compression wave was observed with both the horizontal X geophone and vertical Z geophone. The Y-geophone, which was not aligned with the wave propagation direction, did not respond to the compression wave.

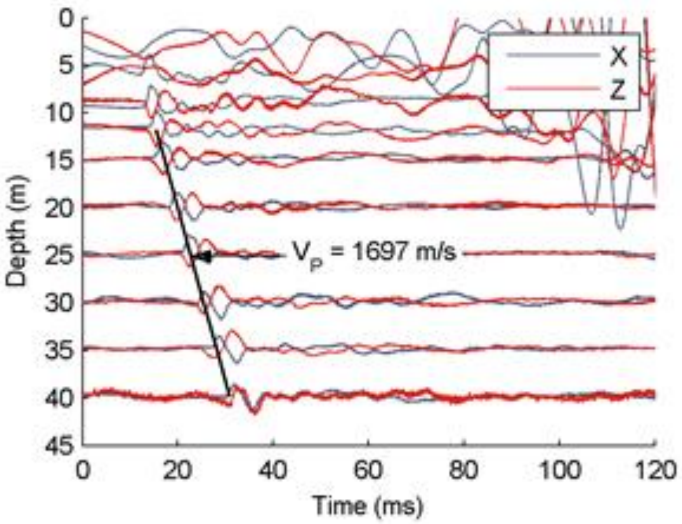

Figure 10.7: Compression wave response on X and Z orientated geophones from a source offset of 9 m at a site in Richmond, BC from Styler et al. (2016)

Laing (1985) observed a wave velocity of 6250 m/s using vertical orientated accelerometers. This was much faster than the anticipated 1400 to 1600 m/s compression wave velocity through fully saturated soil. She concluded that it was a wave traveling through the steel cone rods. Styler et al. (2016) also observed these rod-waves in a test at Kamloops, BC. This test was performed with a source offset of 1.8 m. These rod-waves are identified in ***Figure 10.8***.

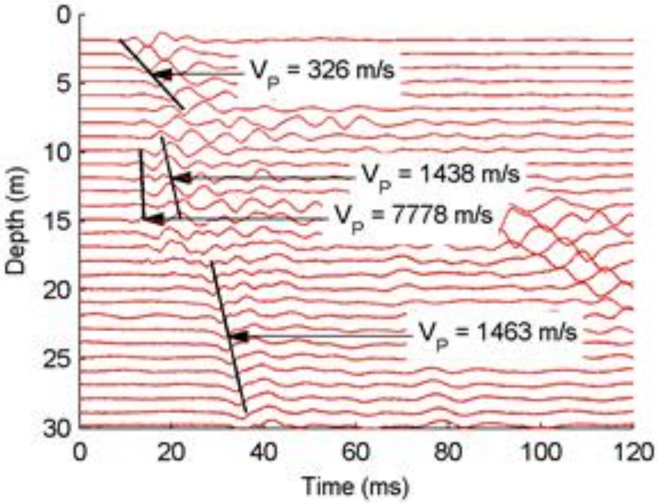

Figure 10.8: Compression wave response on a vertical geophone from a source offset of 1.8 m showing a wave through rods between 10 and 15 m from Styler et al. (2016)

Gillespie (1990) reported that compression waves have frequencies between 400 and 600 Hz, however, this is found not to be the case in many circumstances. Styler et al. (2016) report on a compression wave testing using X and Z accelerometers in Richmond, BC. These results are presented in ***Figure 10.9***, which shows an easily observed compression wave and the frequency contents of the compression waves were mostly less than 250 Hz.

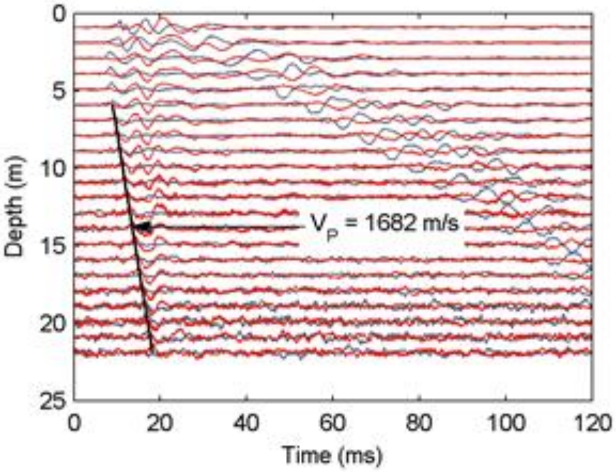

Figure 10.9: Compression wave response from horizontal and vertical accelerometers with a source offset of 3 m from Styler et al. (2016)

Compression wave profiling can be challenging, but it is not insurmountable. It requires more attention and effort in the field data collection. It requires careful examination of the measured traces in order to identify the compression waves from the shear waves, rod-waves, and any reflected or refracted waves in the traces. Compression waves can be obtained to significant depths. ***Figure 10.10*** presents a profile of compression waves observed to depths in excess of 80 m. Full saturation is clearly indicated at the break-point in the compression wave arrivals.

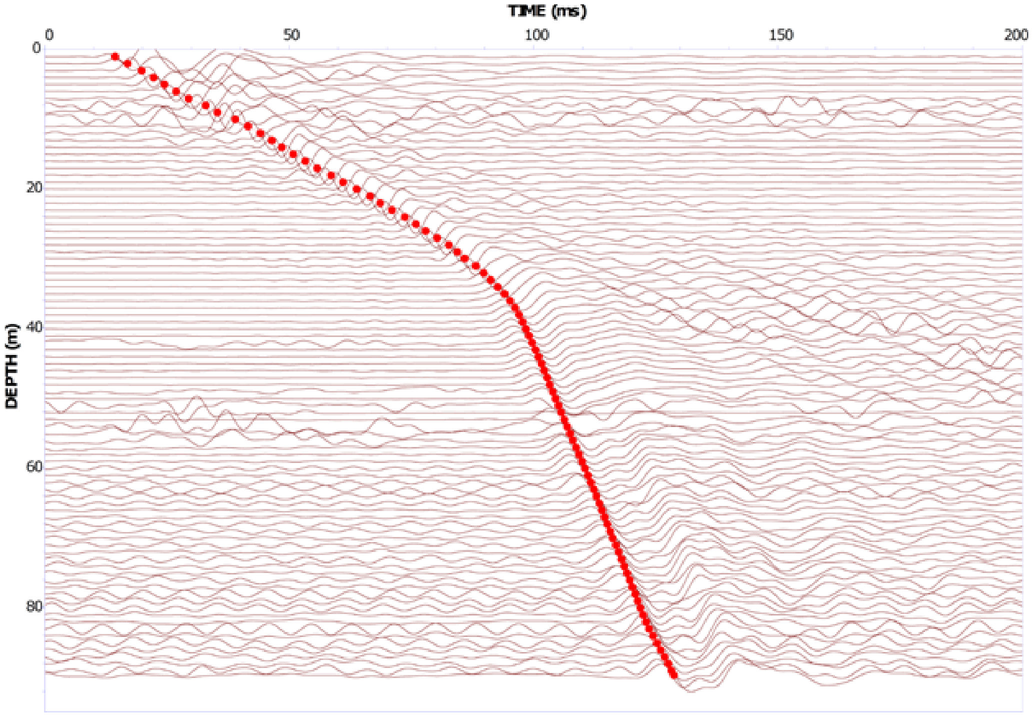

Figure 10.10: Compression waves observed to a depth in excess of 80 m (processed with a 0-200 Hz bandpass filter)

10.5 Full-Flow Penetrometers

A number of full-flow penetrometers were introduced to better profile strengths in very soft offshore sediments where $s_u < 10$ kPa (200 psf), including plate, T-bar, and ball-type (Randolph 2004), as well as hemi-ball and toroidal versions (Yan et al. 2011). The family of full-flow probes is depicted in ***Figure 10.11***. In essence, these devices are electronic cone penetrometers outfitted with much larger heads having a cross sectional area = 100 cm^2 (15.5 in^2) that replace the standard yet smaller 10-cm^2 (1.55 in^2) 60° angled conical tip. The probe head designs are also intended to be a special shape to facilitate soft soils to flow completely around it. In addition to use in very soft offshore clays, the T-bar and ball penetrometers have found applicability in soft mine tailings and slimes, as well as very soft natural onshore deposits.

For direct comparison, ***Figure 10.12*** shows the standard cone penetrometer, T-bar, plate, and ball penetrometers. An advantage of full-flow penetrometers includes a higher resolution of the load cell since the force is directed over a larger cross-sectional area and a minimization of the porewater pressure correction for unequal end areas.

Testing standards for the equipment and procedures for field operation of full-flow penetrometer probes are given by DeJong et al. (2010a).

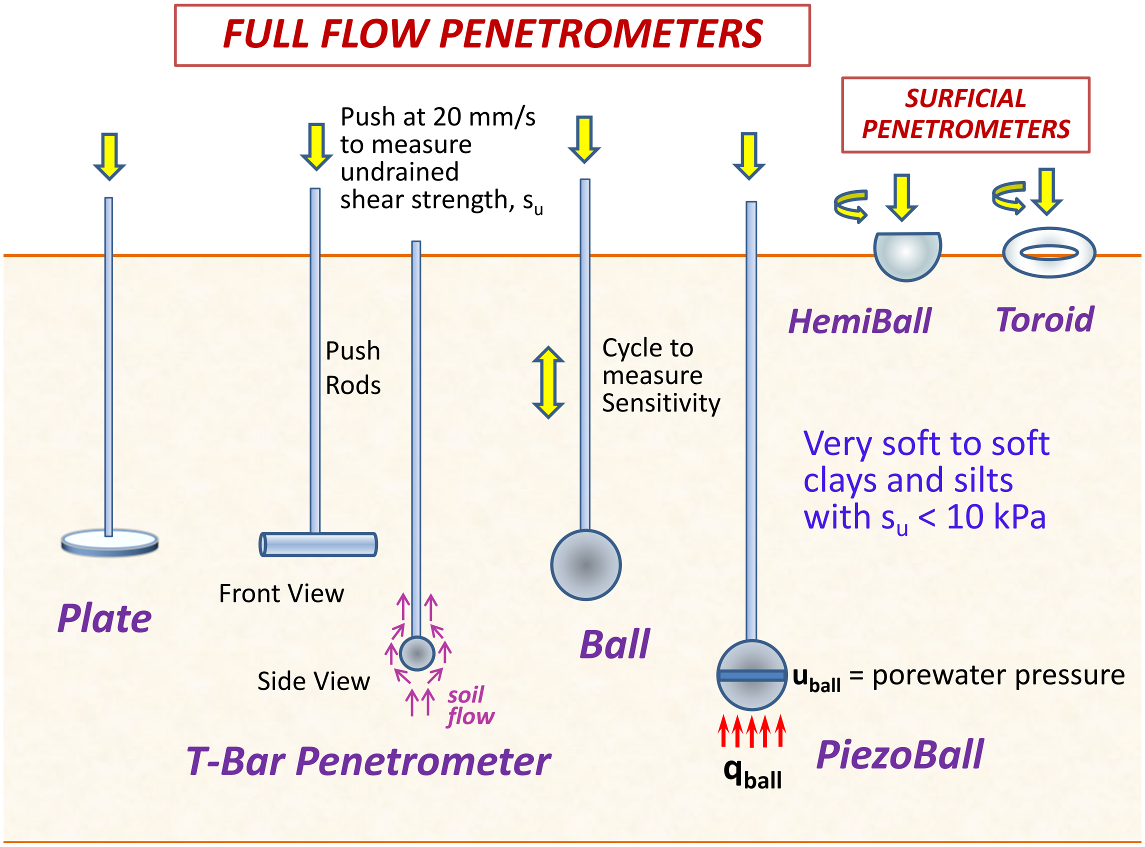

Figure 10.11: Family of full-flow penetrometers for very low strength soils

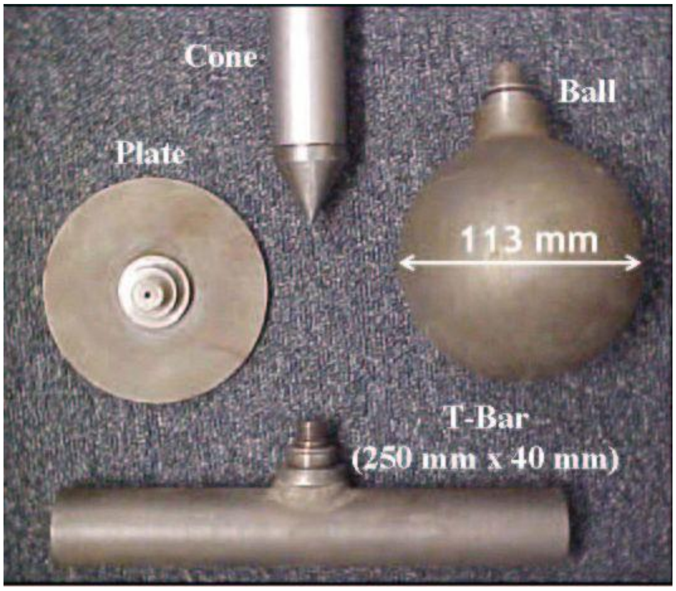

Figure 10.12: View of T-bar, plate, ball, and cone penetrometers (courtesy Jason DeJong)

10.5.1 T-Bar

Beyond profiling strengths in offshore sediments, the T-bar has found good use in characterizing the in-situ undrained shear strength of very soft soils, including natural sensitive clays, mine tailings, slurries, and slimes (DeJong et al. 2010b). The equation for estimating the peak undrained shear strength of soft clays from the measured resistance of a T-bar penetration test (TBT) takes the form:

$$s_u = q_{Tbar} / N_{Tbar} \qquad (10.1)$$

where the bearing factor N_{Tbar} depends on shearing mode. For instance, N_{Tbar} can take on a value of 10.5 for triaxial compression (s_{uc}), while a value of 12 is more suited to an averaged s_{uAVE} (average of triaxial compression, simple shear, and triaxial extension) have been recommended based on a comprehensive testing program (Low et al. 2010). Site specific calibration of the bearing factor for a particular geomaterial under study is certainly warranted (DeJong et al. 2010a).

With the CPTU in very soft, normally to lightly overconsolidated sediments, σ_{v0} can be a significant proportion of q_t. The measured porewater pressures can also be in a similar magnitude as q_t. These effects reduce the certainty in determining the proportion of the cone tip resistance due to the soil response. This increases the uncertainty in the estimated values of s_u and are considered the likely reason for the large scatter in many published N_{kt} values.

In an effort to reduce inaccuracies due to these large corrections and to continue to achieve a continuous profile of resistance, full-flow testing with a T-bar tip was first introduced in centrifuge testing (Stewart 1991) and then in the field (Stewart and Randolph 1994). Since its introduction, field testing has been carried out at well-characterized sites in Australia (Chung and Randolph 2004), Norway (Lunne et al. 2005), Ireland (Long and Gudjonsson 2004), and the USA (DeJong et al. 2004). Subsequently the use of the Ball penetrometer, a spherical ball mounted on the end of the push rods (Chung and Randolph 2004; DeJong et al. 2008) has become more common.

Figure 10.13 shows a comparison of the undrained shear strength profiles in soft clays at a site in North Charleston, SC using both the flat plate dilalometer test (DMT) and T-bar test. Beneath the crustal layer at depths below 2 m, the agreement in the evaluated profile of s_u is quite good between the two tests.

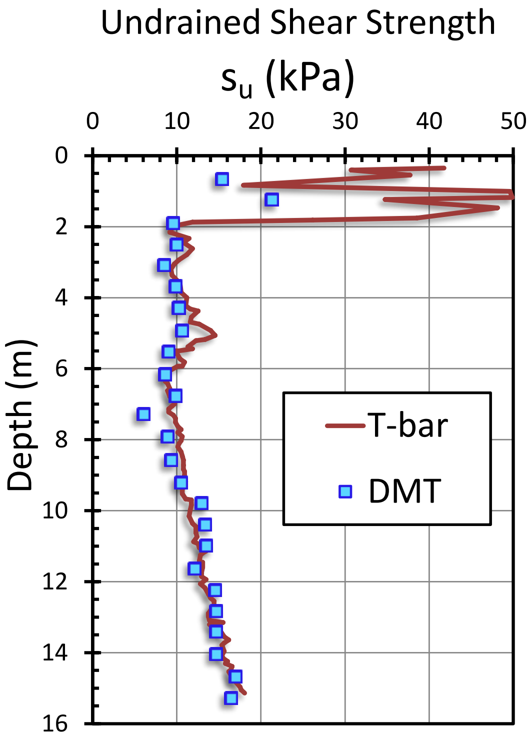

Figure 10.13: Comparison of T-bar and DMT strength profiling in soft soil in South Carolina (data from Cargill & Camp 2010)

In addition to measuring peak strengths, a cyclic phase of testing can be performed at selected depths to evaluate the remolded strength, thus determine the sensitivity (S_t) of soft clay soils.

While the standard rate of penetration for T-bar is identical to the CPT at 20 mm/s (0.8 in/s), variable rate testings can also be applied to investigate both strain rate behavior and drainage conditions (i.e., fully undrained, partially drained, and full drained).

10.5.2 Ball Penetrometer

As the T-bar is non-symmetric about one horizontal axis, recent preference has been drawn towards the fully symmetric Ball penetrometer which is also a type of full-flow probe for very soft soils. The basic principles are similar for both devices.

The determination of undrained shear strength from the ball penetration test (BPT) is similar to that for the T-bar, except that the bearing factor N_{ball} is used. For s_{uc}, a value of $N_{ball} = 9.5$ is characteristic of soft clays, while a value of 11 found for s_{uAVE} (Low et al. 2010). A comparison of the very good agreement between s_u profiles from ball and VST are shown in ***Figure 10.14*** for very soft soils in Northern Alberta.

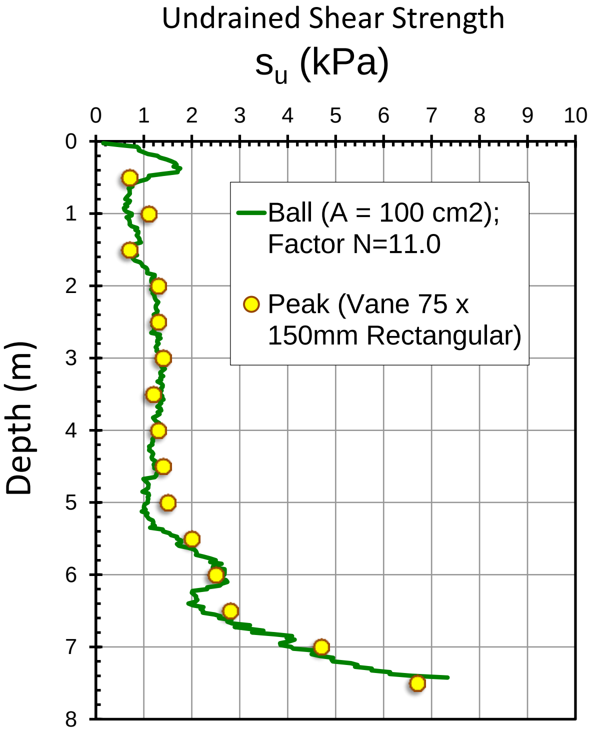

Figure 10.14: Comparison of T-bar and VST strength profiling in very soft soils

The ball penetrometer can also be subjected to cycles to determine the sensitivity of fine-grained soils, in a manner similar to T-bar testing (Yafrate et al. 2007). In research efforts, the ball penetrometer has been outfitted with a porewater pressure transducer that is connected to a filter element, located either at the frontal apex or various equatorial positions on the sphere, to provide additional information useful in site characterization of the soft ground (Peuchen et al. 2005; Long et al. 2014).

The ball penetration resistance is interpreted using empirical coefficients by relating the results to VST or laboratory undrained shear strengths. This is shown in Equation 10.2. Typical values for N_{ball} range from 9 to 12, a much tighter range than the CPT N_{kt} factors.

$$N_{ball} = \frac{q_{ball} - \sigma_{v0}}{(s_u)_{fv}} \tag{10.2}$$

The N_{kt} and N_{ball} factors have been observed to decrease with increasing vane sensitivity (DeJong et al. 2011). This suggests that the progressive failure mechanism that lowers the peak vane strength is also responsible for lowering the penetration resistance, otherwise these factors would increase.

The larger surface area of the ball engages a larger volume of in-situ soil to provide a penetration resistance. It will average out any minor lenses in the deposit. Boulanger and DeJong (2018) reviews thin layer identification with CPT and notes that the penetration resistance is strongly influenced by soils within 10 to 30 cone diameters from the tip. If that same ratio is applied to a 100 cm^2 ball (diameter 11.3 cm) then it is averaging the soil response within 1.1 to 3.4 m. Therefore, the BPT is ideal for obtaining average undrained strengths for thick layers, it cannot be used to characterize thin layers.

The ball penetrometer shown in ***Figure 10.15*** includes a friction sleeve. The friction measurements are in the shadow of the ball and are generally not used in any interpretations as the soil has been significantly affected from soil flowing around the ball. The pore pressure is also measured immediately behind the ball in order to calculate the systematic unequal end-area corrections. These pore pressure measurements should also not be used empirically with CPT based interpretations methods.

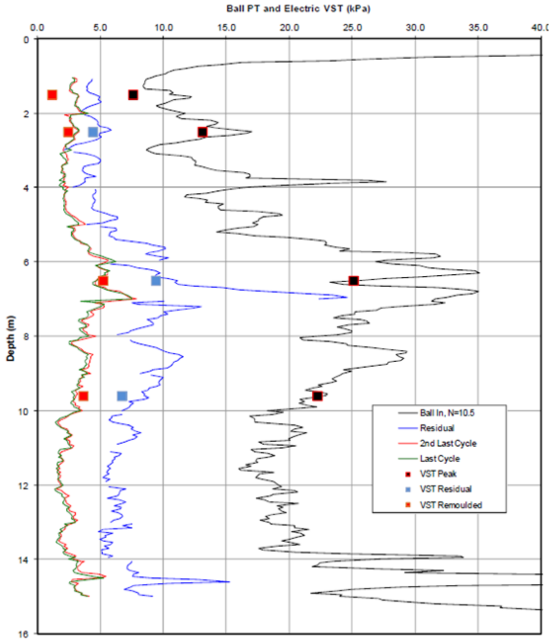

Figure 10.15: Profile comparing VST results against cyclic ball testing using $N_{ball} = 10.5$ *reported by Schaeffers and Weemees (2012)*

While the ball penetrometer has lost two measurements to infer soil properties, it gains a measurement through cyclic testing. Cyclic ball penetrometer testing can be performed to remold the in-situ soil. This enables a direct measurement of a remolded strength and a calculation of soil sensitivity. ***Figure 10.15*** shows an undrained vane strength profile calculated from a net ball penetration resistance. This includes results from ball penetration cycles and from remolded vane shear testing.

The BPT has a number of advantages as a site-investigation tool. These advantages include:

- Efficient profiling of peak undrained strength
- Efficient profiling of remolded undrained strength through cyclic testing
- Increased confidence in undrained strength results in soft soils due to a reduction in the relative magnitude of systematic corrections

The BPT is a specialized tool. It cannot be used as widely as the CPT.

The disadvantages of the BPT compared to the CPT are:

- Increased penetration resistance can reach shallow refusal
- Unable to punch through some stronger layers that may overlie weaker soils
- Only applicable to soft soils and requires prior knowledge of the site
- Loss of informative friction and pore water pressure measurements due to lack of empirical experience compared to the CPT
- Inability to characterize thin layers due to large zone of soil reaction

10.6 Variable Rate Penetration Testing

At the standard rate of 20 mm/s, CPTU conditions are considered to represent fully drained behavior in sands ($\Delta u = 0$), while in contrast, taken to be fully undrained response in clays ($\Delta V = 0$). In silts and mixed soil types, however, a partial drainage condition can predominate. As such, variable rate cone penetration testing (VRCPT) can be implemented to define regions of drained versus partially-drained versus undrained soil behavior, as outlined by Randolph (2004). The variable rate tests can also be performed with T-bar and/or ball or piezo-ball penetrometers.

In VRCPT, the entire sounding can be performed using a constant rate of penetration that is compared with the results from a sounding at the standard rate. ***Figure 10.16*** shows results from a series of VRCPTU conducted at different rates in Bassendean silt which has a mean grain size of around 70 microns (Suzuki 2015). Rates of CPTU were applied from 20, 2, 0.2, 0.02, and 0.002 mm/s. For soft soils, as the rate decreases from 20 mm/s, a general trend is to observe the q_t increase while the porewater pressure u_2 reading decreases.

Results of VRCPTU can be produced from field testing with standard size cone penetrometers, as well as scaled down tests using either 1-g chamber tests or centrifuge deposits and mini-penetrometers (d = 10 mm). Another variant is the "twitch test" whereby just a portion of the vertical field soil profile is chosen and rates of penetration are initially started at the standard rate of 20 mm/s and then stepped down to provide rate data over a limited depth interval (Randolph 2004). Some example results of twitch testing in soft Burswood clay are shown for both piezocone and T-bar, as shown by ***Figure 10.17***. The CPTU twitch tests were varied from 20 mm/s down to as low as 0.02 mm/s while the T-bar tests slowed to a final value of 0.01 mm/s.

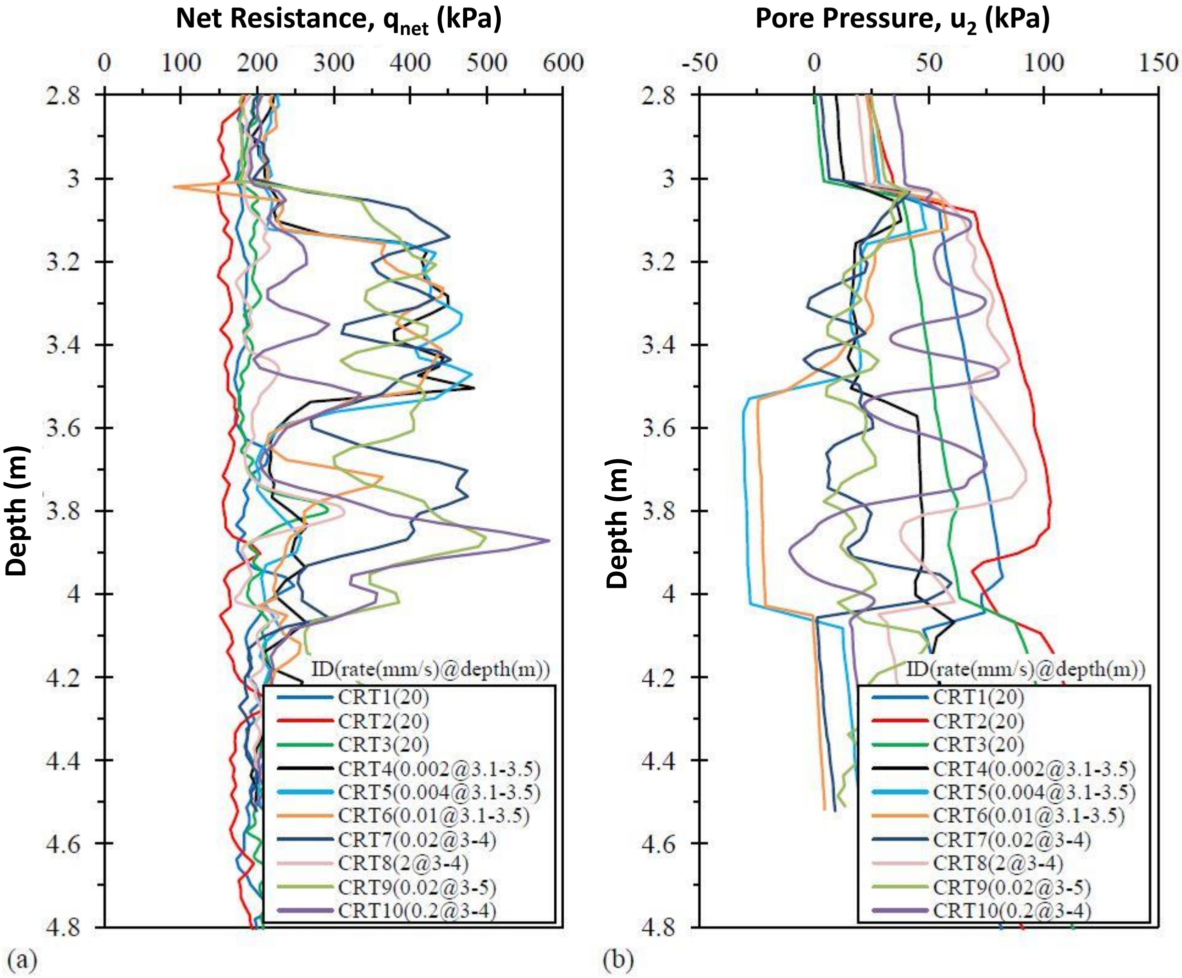

Figure 10.16: Results of VRCPTU in Bassendean silt at penetration rates ranging from 0.002 mm/s to 20 mm/s: (a) net cone resistance; (b) porewater pressure (Suzuki 2015)

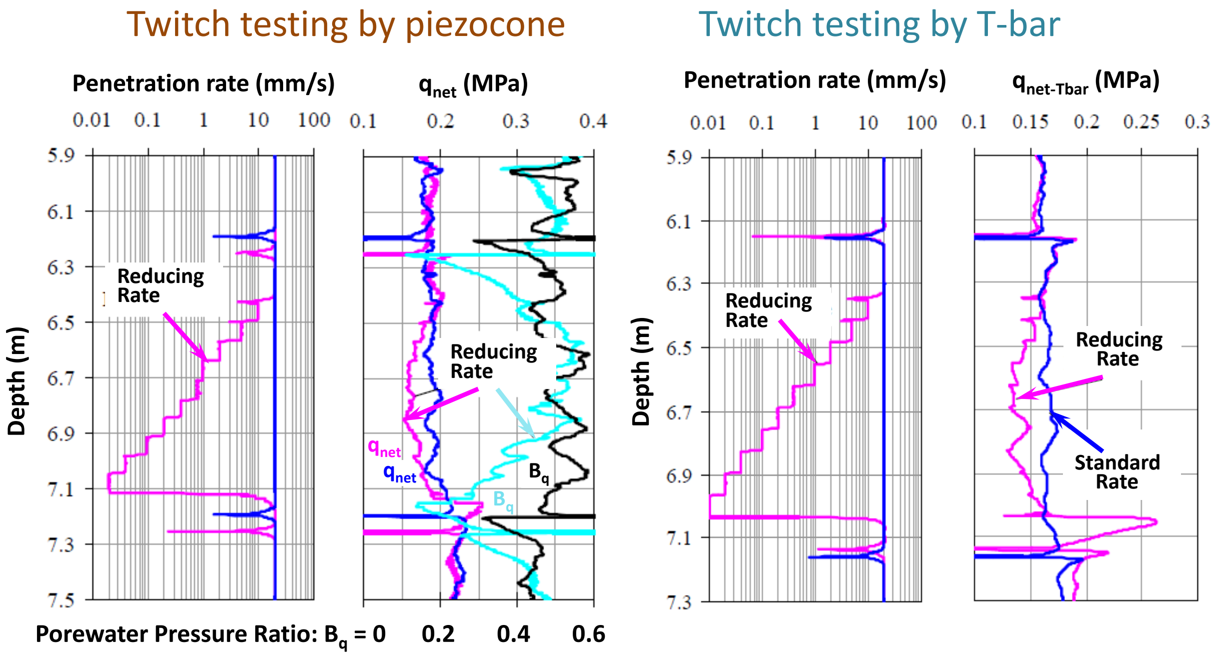

(a) (b) (c) (d)

Figure 10.17: Results from twitch type VRCPT in soft clay at Burswood, Australia: (a) CPTU rate; (b) CPTU reading of net cone resistance and B_q; (c) T-bar rate; and (d) T-bar q_{net} (from Randolph 2004)

Post-processing of variable rate and twitch testing can show the effect of drainage conditions on the measured CPT, T-bar, and/or ball penetration readings. For example, results from VRCPTU in kaolinitic deposits are shown in ***Figure 10.18*** using a normalized velocity (V') along the x-axis:

$$V' = v \cdot d / c_v \tag{10.3}$$

where v = actual penetration velocity, d = probe diameter, and c_v = coefficient of consolidation.

For this geomaterial, it can be seen that the ranges of undrained behavior are exhibited when V' > 30 while fully drained behavior ($B_q \approx 0$) is found when V' < 0.3. Consequently, partially drained response is noted to be intermediate and corresponding to: 0.3 < V' < 30. Similar ranges of V' are found for the drained-partially drained-undrained thresholds for other soils (DeJong et al. 2012). In fact, the following equations are used for these ranges (DeJong & Randolph 2012):

$$\frac{Q}{Q_{ref}} \approx 1 + \left(\frac{(Q_{drained} / Q_{ref}) - 1}{1 + (V / V_{50})^c} \right) \tag{10.4}$$

$$\frac{B_q}{B_{q-ref}} \approx 1 - \frac{1}{1 + (V / V_{50})^c} \tag{10.5}$$

where Q_{ref} = reference value of normalized Q (here taken as undrained value) and $B_{q\text{-}ref}$ is similar for the porewater pressure response. The exponent "c" and term V_{50} are empirical fitting parameters. For an example, the results for VRCPTU in kaolin shown in ***Figure 10.18*** were obtained with: c = 1.0, V_{50} = 6, Q/Q_{ref} = 2.2, and $B_{q\text{-}ref}$ = 0.55.

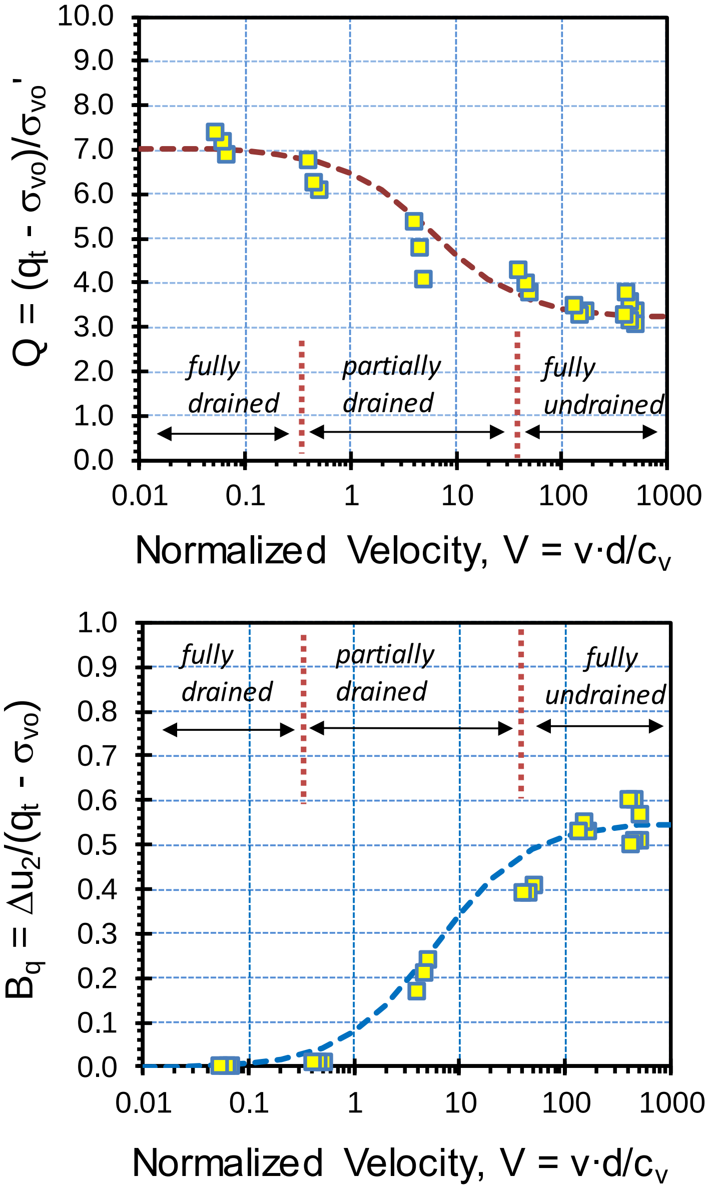

Figure 10.18: Summary results of VRCPTU in kaolin deposit (Schneider 2007)

A generalized approach to ascertain the drainage conditions in silts, mixed soil types, and tailings during CPTU was developed by DeJong et al. (2012). The penetration rate versus c_v for various normalized velocities are presented for undrained, partially-drained, and drained conditions in ***Figure 10.19***.

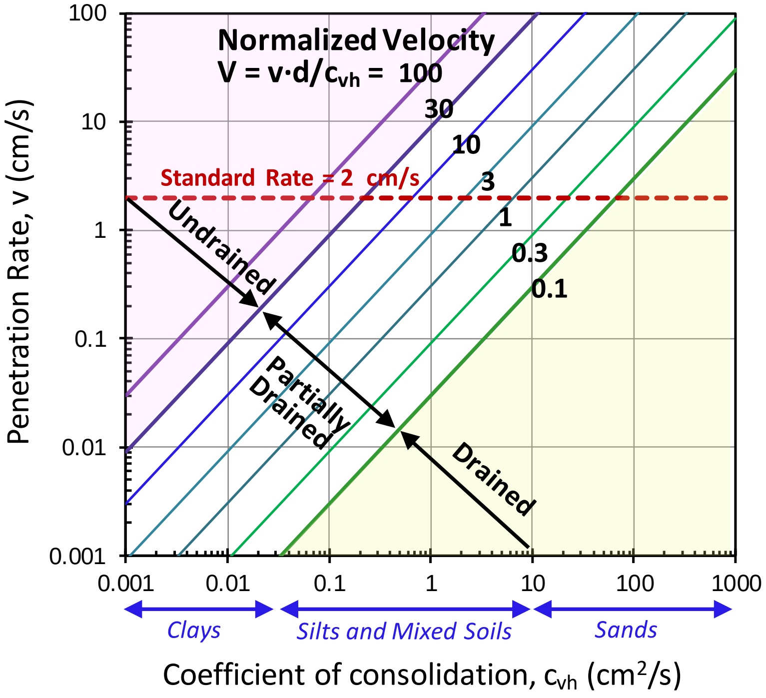

Figure 10.19: Chart for assessing drainage conditions during penetration in soils (modified after DeJong et al. 2012)

10.6.1 NTH Solution Applied to VRCPTU

Detailed earlier, the effective stress friction angle (ϕ') of normally-consolidated clays can be interpreted from CPTU data in terms of normalized parameters Q and B_q using the NTH solution. The effective stress friction angle is a fundamental soil property and independent of the stress path, therefore undrained and drained tests, as well as partially-drained stress paths will reach the same effective stress envelope.

It is therefore of interest to show Q and B_q data from VRCPTU on a variety of 20 different soils, including clays, silts, and mixed soil types, as presented in ***Figure 10.20***. Here, contours of ϕ' from the NTH solution are presented on the Q-B_q diagram. The VRCPTU data from the various soils follow the contours for individual values of ϕ', thereby helping to validate the NTH solution.

Of final note, VRCPTU has found use in helping to characterize mine tailings and slimes, primarily because they exhibit behavior of intermediate geomaterials (e.g., Dienstmann et al. 2018; DeJong & Green 2020).

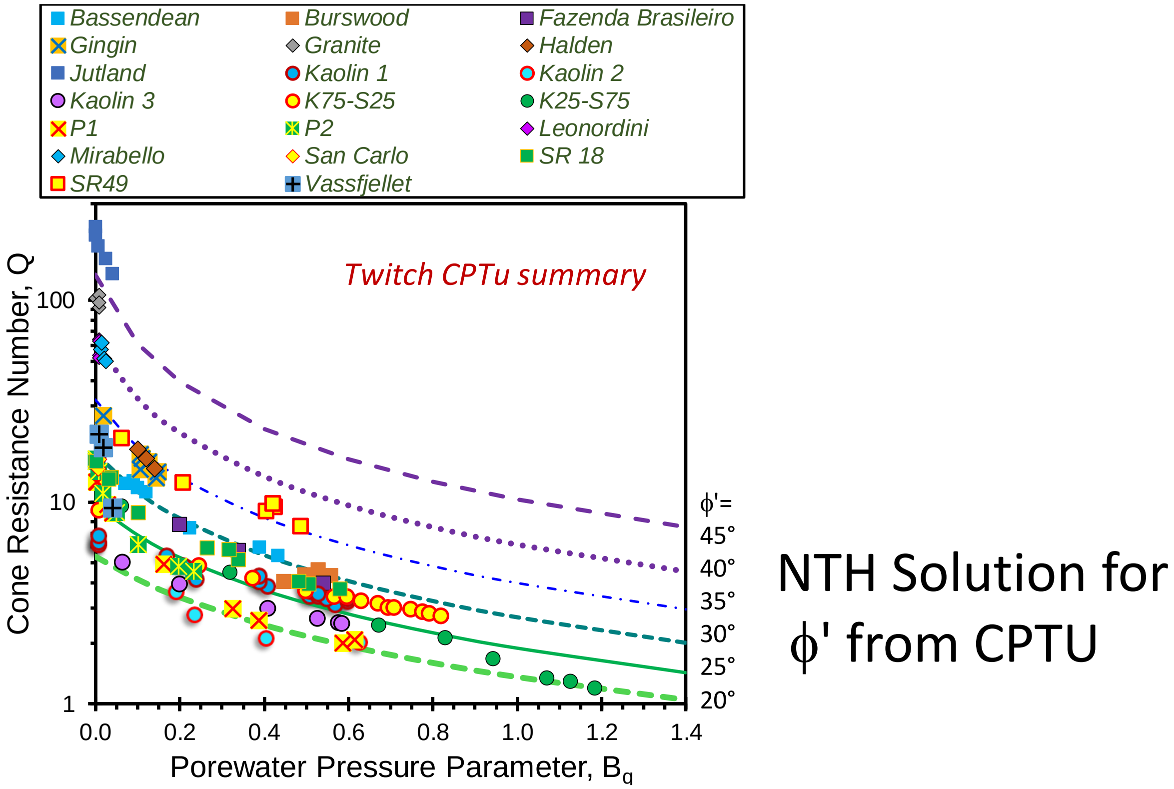

Figure 10.20: Data from 20 series of VRCPTU in mixed soil types, clays, and silts confirming NTH solution for ϕ' from Q and B_q (after Ouyang & Mayne 2020a)

10.7 Machine Learning and Big Data for CPTu Interpretation

Machine Learning (ML) is a subfield of Artificial Intelligence (AI) which deals with the development of algorithms that enable computers to perform a specific task, without the need of rule-based programming. ML models acquire information from existing data, allowing the computers to discover predictive rules applicable for future data.

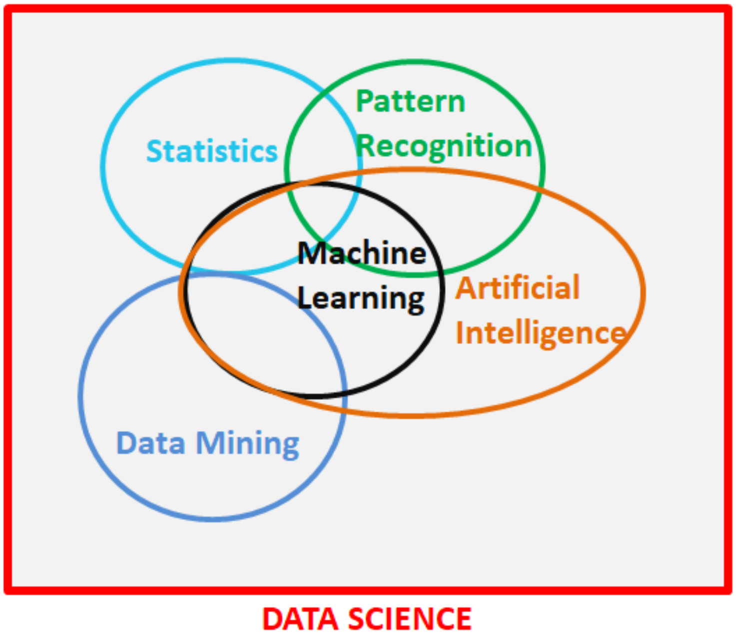

Figure 10.21: A Venn diagram of data science (source: https://towardsdatascience.com/clearly-explained-how-machine-learning-differs-from-statistical-modeling-967f2c5a9cfd).

ML has become widespread in almost all industries and disciplines to provide valuable data-driven insights for making more informed decisions. Geotechnical engineering is a discipline that frequently uses empirical relationships to estimate soil properties and thus can greatly benefit from ML. Data-driven approaches have gained substantial interest over traditional modelling because not only do they deal better with uncertainties and complexities in geotechnical engineering problems, they also do not require prior assumptions about the fundamental and physical relationships between parameters. ML algorithms can therefore lead to more robust predictive models compared to traditional modelling.

ML models are generally data-hungry and need large datasets to train and can continuously adapt as more data become available. In general, as more data are available, the more accurate and robust the prediction becomes. ML can be applied on high dimensional datasets with numerous input and output variables.

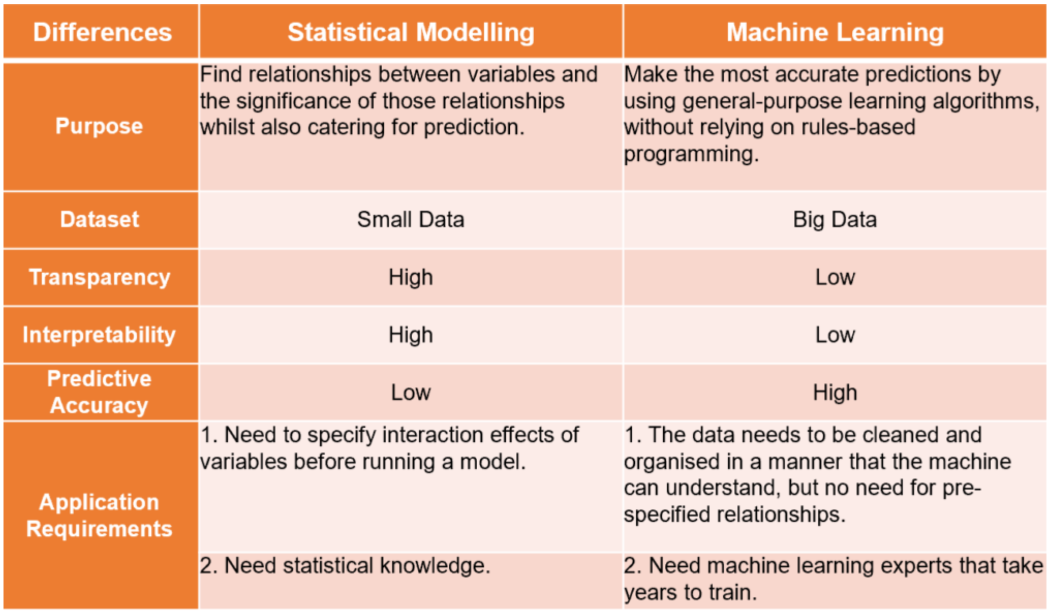

Differences	Statistical Modelling	Machine Learning
Purpose	Find relationships between variables and the significance of those relationships whilst also catering for prediction.	Make the most accurate predictions by using general-purpose learning algorithms, without relying on rules-based programming.
Dataset	Small Data	Big Data
Transparency	High	Low
Interpretability	High	Low
Predictive Accuracy	Low	High
Application Requirements	1. Need to specify interaction effects of variables before running a model.	1. The data needs to be cleaned and organised in a manner that the machine can understand, but no need for pre-specified relationships.
	2. Need statistical knowledge.	2. Need machine learning experts that take years to train.

Figure 10.22: Differences between statistical and ML modelling (source: https://turintech.ai/insights/machine-learning-vs-statistical-modelling-which-one-is-right-for-your-business-problem*).*

With increasing computational power, ML has gained substantial interest in the geotechnical engineering community and has gradually become an alternative solution for geotechnical problems. In recent years, several studies have investigated the use of ML for CPT data interpretations and soil classifications. Example applications of ML for CPT interpretations can be found in Erzin and Ecemis (2016), Reale et al. (2018), Wang et al. (2019), Zhang et al. (2021), Erharter et al. (2021), Rauter & Tschuchnigg (2021), and Entezari et al. (2020, 2021a, 2021b, 2022).

The availability of large in-situ testing databases, specifically CPTu databases, coupled with ML techniques provide an opportunity to develop site-specific models for better site characterization. ML is also a powerful tool for investigating refinements to existing empirical CPTu relationships. With more accurate in-situ predictions of soil properties, geotechnical analysis using the CPTu can be improved. While various amounts and types of drilling and sampling on certain projects may always be required, ML-based CPTu models can add more accurate meaning to in-situ test profiles while providing a rapid, cost-effective, repeatable alternative; potentially reducing the site investigation's overall schedule and cost.

10.7.1 Estimation of Solids and Fines of Tailings

Styler et al. (2018) developed empirical relationships, called Tailings Behaviour Type (TBT) models, to estimate tailings constituents from in-situ Gamma Cone Penetration Test (GCPTu) measurements. Entezari et al. (2020) developed a regional TBT model to estimate tailings solids and total fines from in-situ GCPTu using neural networks and a dataset comprised of paired GCPTu-laboratory results (n = 13,000) collected over a ten-year period from a mining area with predominately clay mineral and quartz sand tailings. The input variables used in neural networks included the undrained shear strength (S_u), the slope of the dynamic pore water pressure versus depth, the passive gamma response, as well as the latitude, longitude, and the mining property name where the data was collected. ***Figure 10.23*** shows the ternary diagram of the development dataset. The relationships between laboratory measured and TBT predicted solids and total fines content are shown in ***Figure 10.24.*** A performance evaluation showed that TBT models can predict the solids and fines content of the studied deposits within 4.0 and 4.9% error (by weight), respectively. An example tailings constituent profile estimated using the developed TBT models is shown in ***Figure 10.25***. The laboratory results are over-plotted to visually assess the performance of the TBT models.

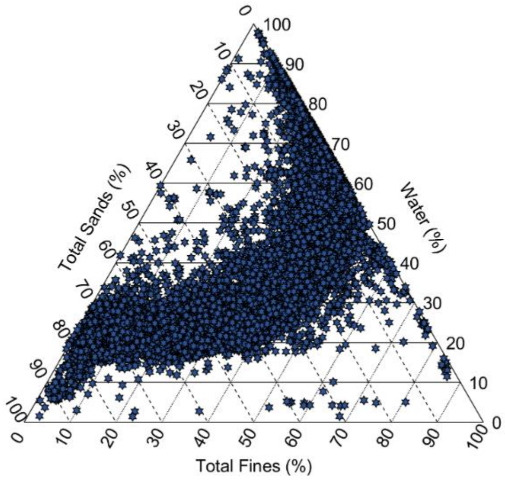

Figure 10.23: The ternary diagram of the development dataset (Entezari et al. 2020)

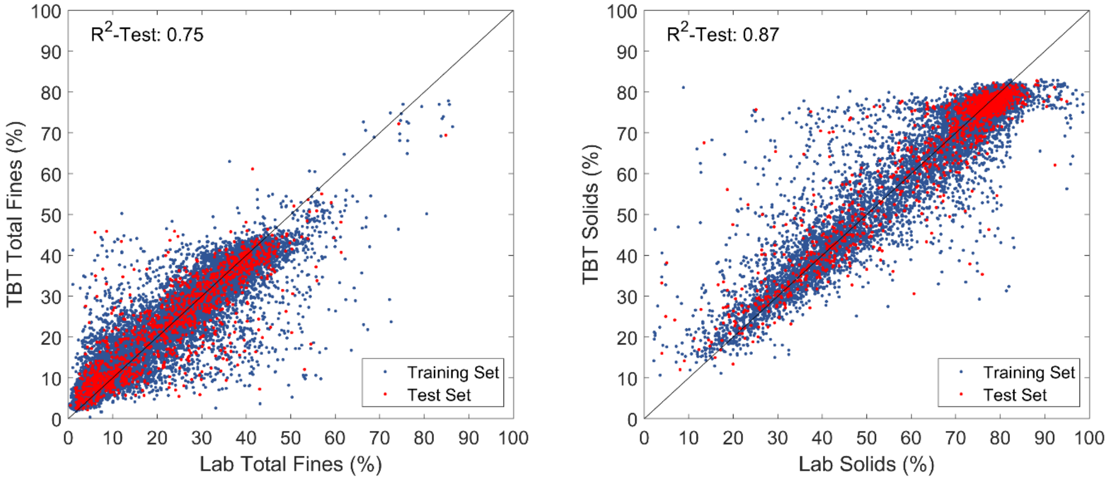

Figure 10.24: The relationship between laboratory measured and TBT predicted solids content (left) and total fines content (right) (Entezari et al. 2020)

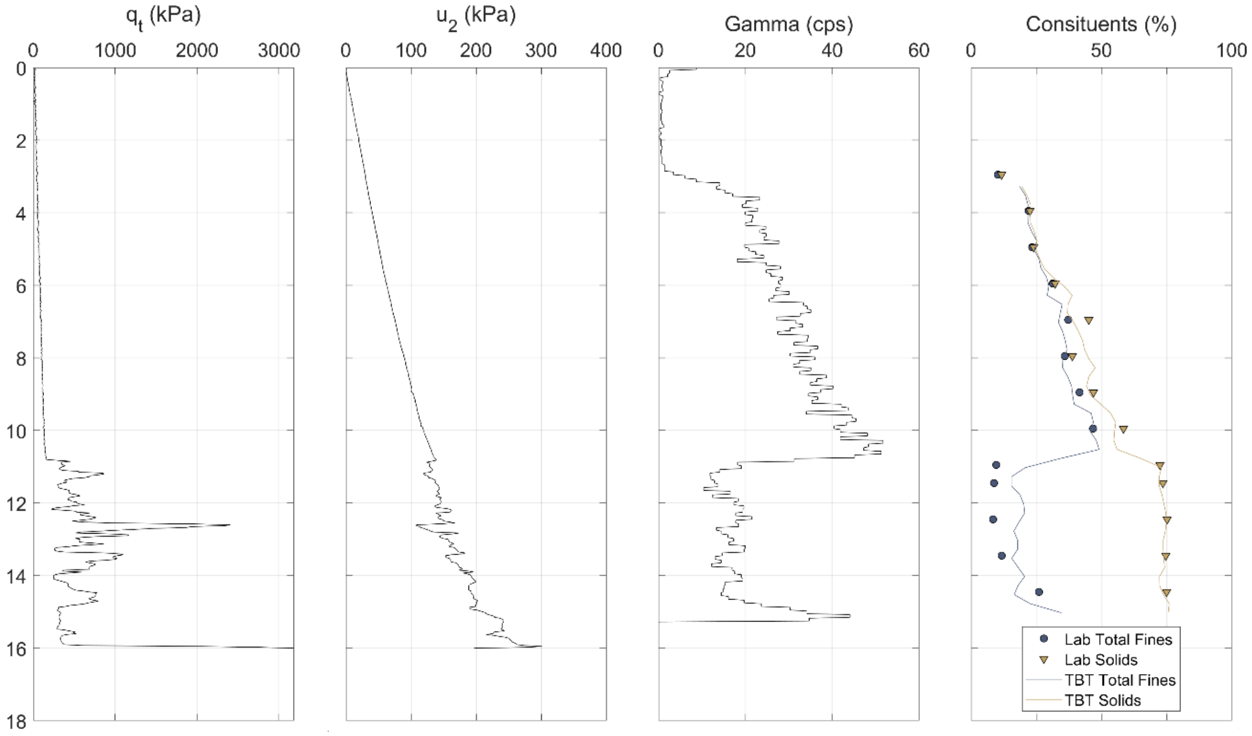

Figure 10.25: Example TBT profile in fluid and soil-like tailings (Entezari et al. 2020)

In another study, Entezari et al. (2021a) explored the potential of a support vector machine (SVM) algorithm to estimate geotechnical fines of sandy soil-like tailings from GCPTu. They trained various SVM models with different combinations of GCPTu parameters (***Table 10.1***) and showed that a model trained with q_t, f_s, u_2, friction ratio (R_f), and gamma can predict the geotechnical 75 µm fines content of the studied deposits with 7.8% error. The performance of the developed models was observed to be significantly better than the traditional I_c based approach (Robertson and Wride 1998) in estimating the geotechnical 75 µm fines content of loose sandy tailings (***Table 10.1***). The relationships between laboratory measured and estimated geotechnical 75 µm fines content from trained SVM model (SVM 1 in ***Table 10.1***) and I_c based method are shown in ***Figure 10.26***. An example profile of geotechnical 75 µm fines content estimated using the developed SVM model (SVM 1 in ***Table 10.1***) are shown in ***Figure 10.27***. The I_c estimated geotechnical fines and the laboratory measured geotechnical 75 µm fines are overplotted in order to compare them with the SVM results.

Table 10.1: The bias and error values for predicting fines content with various SVM models trained using different combinations of GCPTu data as input features (modified from Entezari et al. 2021a)

Model	**Input Features**	**Bias (%)**	**Error (%)**
SVM 1	q_t, f_s, u_2, R_f, gamma	-1.2	7.8
SVM 2	q_t, u_2, gamma	-0.9	8.0
SVM 3	q_t, f_s, u_2	-0.64	9.1
SVM 4	q_t, u_2	-0.52	9.1
SVM 5	q_t, f_s	2.0	14.0
I_c Method	q_t, f_s	-20	31.0

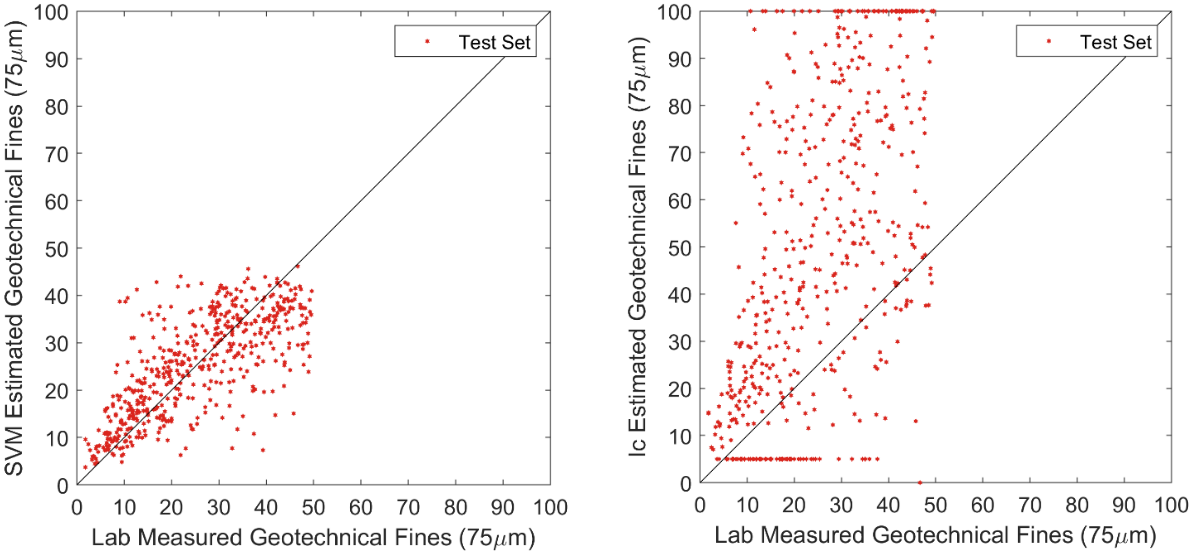

Figure 10.26: The relationship between laboratory measured and estimated geotechnical 75 µm fines content from trained SVM model (left) and Ic based method (right) on a test set (Entezari et al. 2021a)

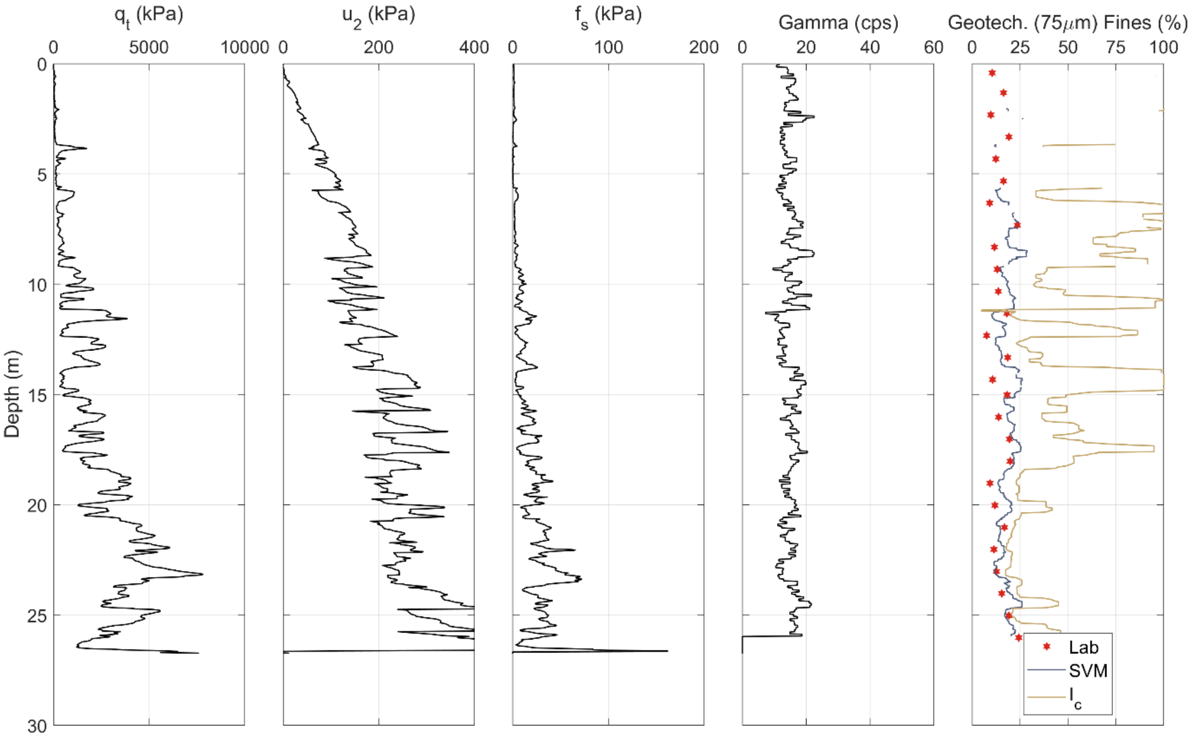

Figure 10.27: Example profile of geotechnical 75 µm fines content estimated using the SVM model and the I_c method. Laboratory results are overplotted for comparison (Entezari et al. 2021a)

10.7.2 Estimation of Soil Unit Weight

The potential of a ML approach for the estimation of soil unit weight from CPTu data was investigated by Entezari et al. (2021b). A compiled database (n = 1228) of paired CPTu readings and laboratory measured unit weights from different field test sites with a variety of soil types, geological environments, and stress histories was used to explore and develop a ML algorithm directly estimating unit weights from CPTu data. The random forest (RF) algorithm was employed to calibrate the CPTu readings to the soil unit weights. Various RF models were trained with different combinations of input features (***Table 10.2***). Results showed that a RF model trained with q_t, f_s, u_2, and z as input features (RF3 in ***Table 10.2***) could estimate unit weight with an error of ±0.93 kN/m^3. The relationships between measured and estimated unit weight using the developed RF model as well as those obtained from Robertson and Cabal (2010) and Mayne et al. (2010) methods are shown in ***Figure 10.28***. A comparison performed between the RF models and some of the existing relationships in literature (***Table 10.3***) showed that all the random forest models developed in this study outperform the existing CPT relationships to estimate unit weight.

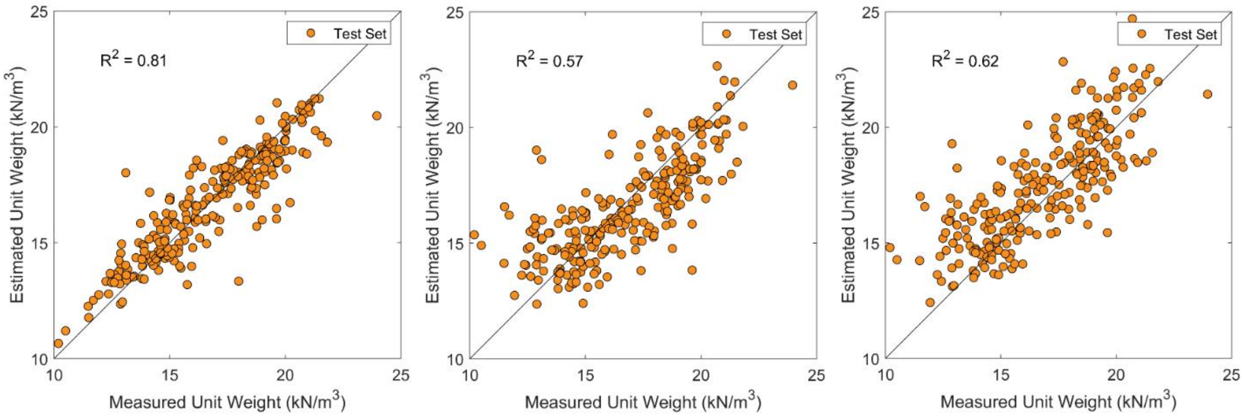

Figure 10.28: Relationship between laboratory measured and estimated unit weight from random forest (left), Robertson and Cabal (2010) method (middle) and Mayne et al. (2010) method on the test set (Entezari et al. 2021b)

Table 10.2: Performance of various random forest (RF) models trained using different combinations of input features (Entezari et al. 2021b)

Model	Input Features	R^2	Bias (kN/m^3)	Error (kN/m^3)
RF1	q_t, f_s, u_2, u_o, σ'_{vo}, z	0.86	-0.05	0.80
RF2	q_t, f_s, u_2, u_o, z	0.82	0	0.93
RF3	q_t, f_s, u_2, z	0.81	0.01	0.93
RF4	q_t, f_s, u_2	0.73	0.10	1.08
RF5	q_t, f_s, z	0.77	0.03	1.04
RF6	q_t, f_s	0.70	0.13	1.27

Table 10.3: Performance of some of the existing relationships to estimate unit weight (Entezari et al. 2021b)

Model	R^2	Bias (kN/m^3)	Error (kN/m^3)
Robertson & Cabal (2010)	0.57	0.39	1.57
Mayne et al. (2010)	0.62	-0.74	1.61
Mayne (2014)	0.53	0.69	1.62
Lengkeek (2018)	0.60	-0.18	1.59

10.7.3 Estimation of Shear Wave Velocity (V_S)

The use of ML to predict V_S from piezocone penetration test (CPTu) was explored by Entezari et al. (2022). A very large dataset of paired V_S-CPTu data (n = 104,500) compiled from SCPTu soundings completed in a wide variety of soil types with various stress histories and geological environments was used to develop ML models to directly estimate V_S from CPTu data. ***Table 10.4*** lists the summary statistics of the paired dataset. The dataset was tested with the random forest algorithm to develop the models. The models were trained using four input parameters including q_t, u_2, f_s, and z (depth). Furthermore, the impacts of soil microstructure and cementation on estimated V_S results were investigated and separate models were developed for the categories of uncemented and cemented soils. The plot of normalized tip resistance (Q_{tn}) versus small-strain rigidity index (I_G) to identify uncemented and cemented soils is shown in ***Figure 10.29***. Results showed that the all-soils model developed using RF algorithm can estimate V_S with ±49.5 m/s error (***Figure 10.30***). The model developed for uncemented soils showed a significant improvement and could predict V_S with ±28.2 m/s error (***Figure 10.31***). The model developed for cemented soils achieved an accuracy of ±54.1 m/s (***Figure 10.31***). All the developed ML models outperformed the existing relationships tested in this study. A summary of model performances is presented in ***Table 10.5***. An example profile of V_S estimated using the random forest models is shown in ***Figure 10.32***.

Table 10.4: Summary statistics of the V_S-CPTu dataset (Entezari et al. 2022)

	Min	**Max**	**Mean**
V_S (m/s)	9	1000	251
qt (kPa)	124.4	94,053	8396
fs (kPa)	1.01	1577	117.6
u2 (kPa)	-163.8	8713	245.6
z (m)	0.3	129.6	17.3
σ'vo (kPa)	0.1	2185	215.4

Total number of data pairs = 104,054

Table 10.5: Performance of different models (Entezari et al. 2022)

	Bias±Error (m/s)		
Model	All Soils	Uncemented	Cemented
RF-All Soils	-8.5 ± 49.5	-23.4 ± 34.8	27.2 ± 62.8
RF-Uncemented	NA	0.6 ± 28.2	NA
RF-Cemented	NA	NA	-12.3 ± 54.1
Mayne (2006)	12.0 ± 68.6	-7.2 ± 52.5	51.1 ± 82.8
Robertson (2009)	21.5 ± 64.3	-6.1 ± 50.3	69.2 ± 57.8

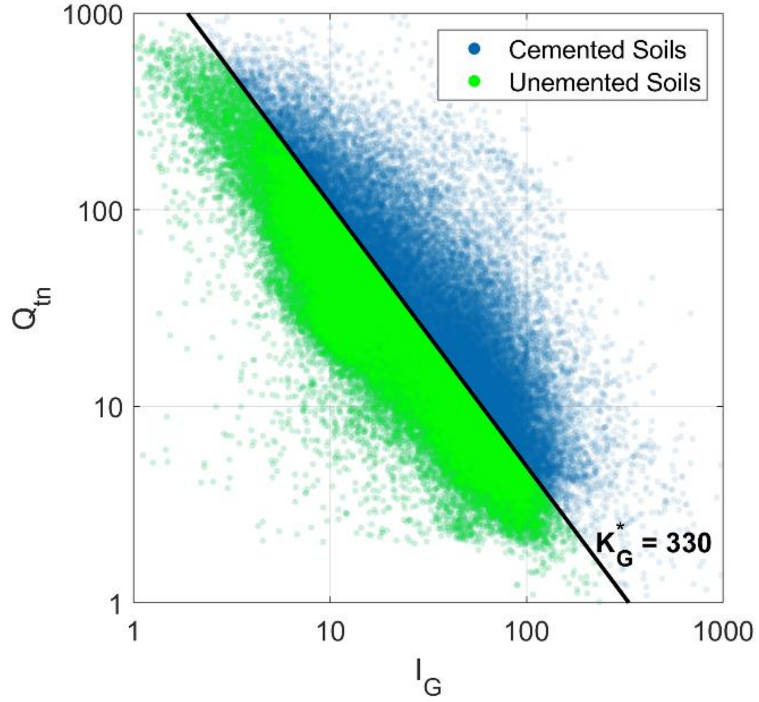

Figure 10.29: The dataset plotted in the Q_t-I_G chart (Entezari et al. 2022)

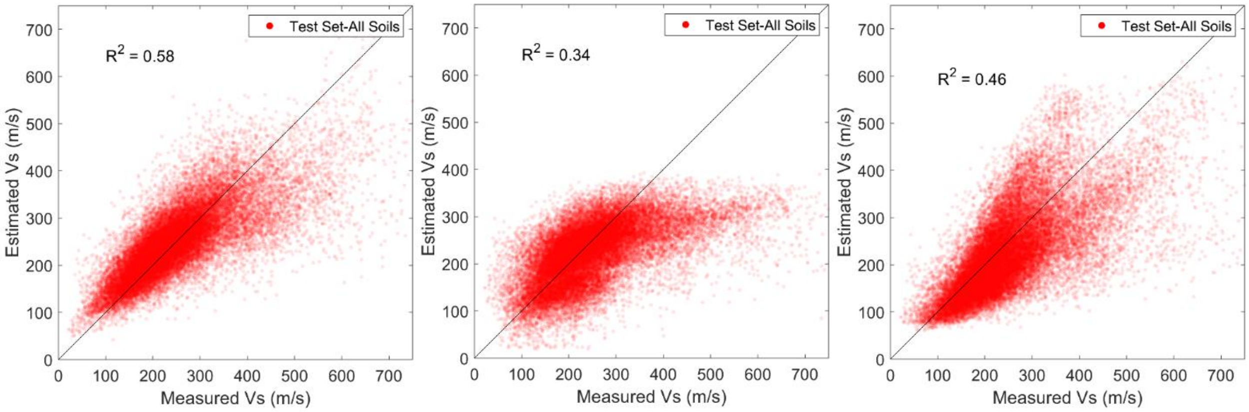

Figure 10.30: Relationship between measured and estimated V_S from random forest (left), Mayne (2006) method (middle) and Robertson (2009) method on the test set (Entezari et al. 2022)

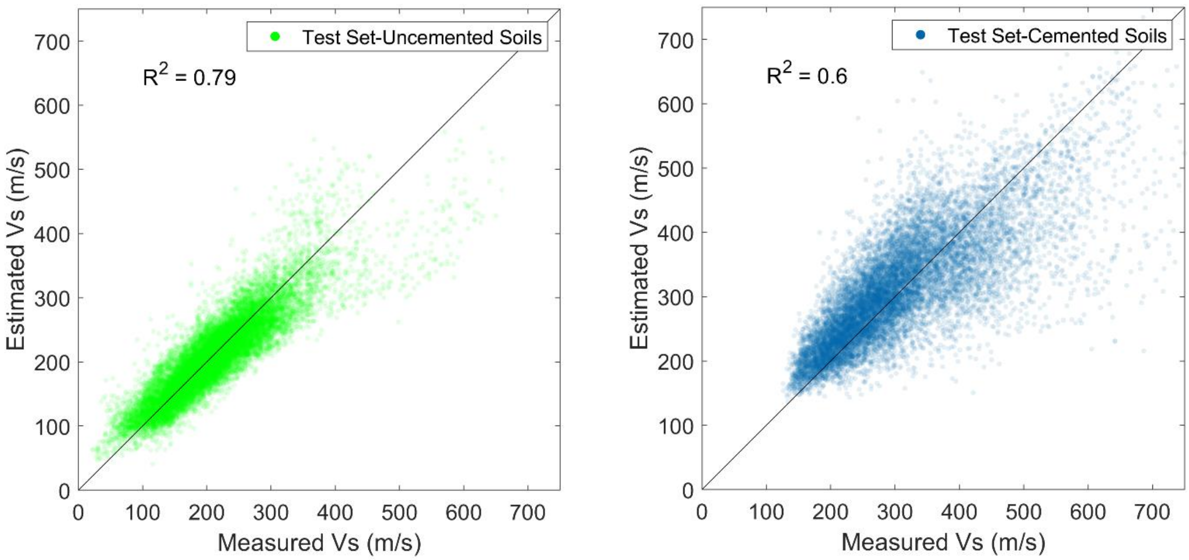

Figure 10.31: Relationships between measured and random forest estimated V_S of the uncemented (left) and cemented soils (right) on the test set when separate models were trained using uncemented and cemented soils in the training set (Entezari et al. 2022)

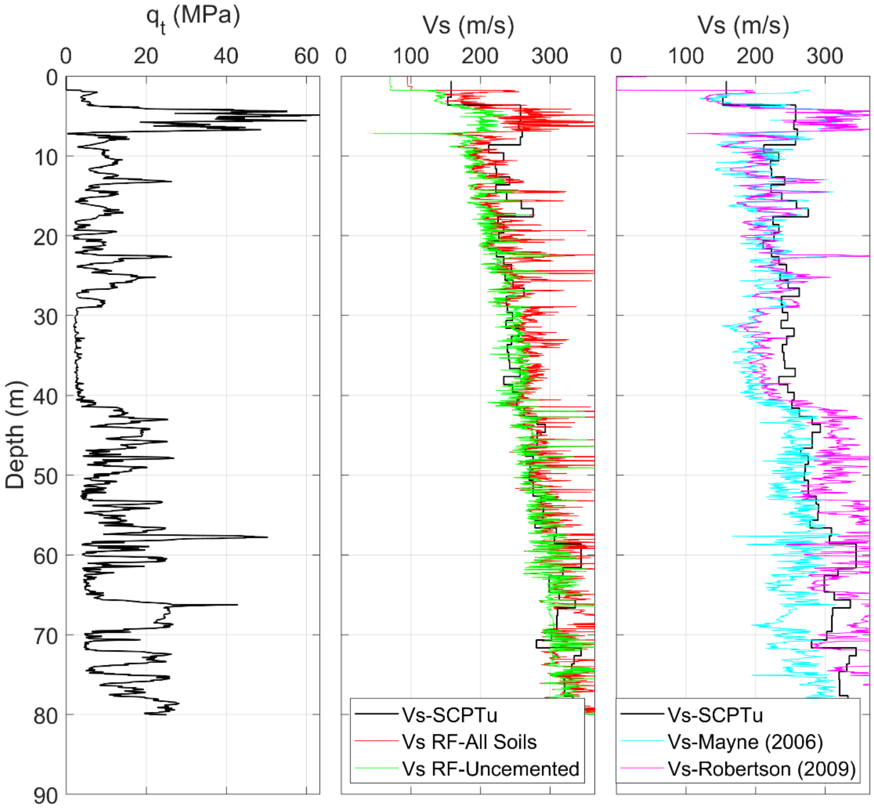

Figure 10.32: Example profile of Vs estimated from random forest models and existing relationships (Entezari et al. 2022)

11 References

Abdulhadi, N., Germaine, J.T. and Whittle, A.J. 2012. Stress-dependent behavior of saturated clay. *Canadian Geotechnical Journal* 49 (8): 907–916.

Adamczyk, J. 2012. Basic geotechnical properties of mining and processing waste - a state of the art analysis. *AGH Journal of Mining and Geoengineering* 36 (2): 31–41.

Agaiby, S.S. 2018. Advancements in the interpretation of seismic piezocone tests in clays and other geomaterials. *Ph.D. Dissertation*, School of Civil & Environmental Engineering, Georgia Institute of Technology, Atlanta, GA USA: 925 pages.

Agaiby, S.S. and Mayne, P.W. 2016. Use of shear wave velocity to estimate stress history and undrained shear strength of clays. *Proc. 5th Intl. Conf. on Geotechnical & Geophysical Site Characterization* (ISC-5, Gold Coast), Australian Geomechanics Society.

Agaiby, S., Mayne, P.W. and Woeller, D.J. 2016. Evaluation of undrained shear strength and stress history in intact clays using seismic piezocone tests. *Proceedings GeoVancouver 2016* (Proc. 69th Canadian Geotechnical Conference, Westin): www.cgs.ca

Agaiby, S.S. and Mayne, P.W. 2018a. Interpretation of piezocone penetration and dissipation tests in sensitive Leda Clay at Gloucester test site. *Canadian Geotechnical Journal*, 55(12): 1781-1794.

Agaiby, S.S. and Mayne, P.W. 2018b. Evaluating undrained rigidity index of clays from piezocone data. Proc. 4th Intl. Symposium on Cone Penetration Testing (CPT'18, Delft), CRC Press/Balkema: 65-72.

Agaiby, S.S. and Mayne, P.W. 2019. CPT evaluation of yield stress in soils. *Journal of Geotechnical & Geoenvironmental Engineering* 145(12): doi.org/10.1061/(ASCE) GT.1943-5606.0002164.

Agaiby, S.S. and Mayne, P.W. 2020. Indirect estimation of fines content using the modified CPT material index. *Proc. GeoCongress 2020: Modeling, Geomaterials, and Site Characterization*, (Minneapolis, GSP 317), ASCE, Reston, VA: 569-582.

Amoroso, S., Monaco, P., Lehane, B.M. and Marchetti, D. 2014. Examination of the potential of the seismic dilatometer (SDMT) to estimate in situ stiffness decay curves in various soil types. *Soils and Rocks* 37 (3): 177–194.

Andersen, K.H, and Schjetne, K. 2013. Database of friction angles of sand and consolidation characteristics of sand, silt, and clay. *Journal of Geotechnical and Geoenvironmental Engineering* 139 (7): 1140–1155.

Andrus, R.D, Mohanan, N.P., Piratheepan, P., Ellis, B.S. and Holzer, T.L. 2007. Predicting shear-wave velocity from cone penetration resistance. *Proceedings of the 4th International Conference on Earthquake Geotechnical Engineering, Thessaloniki, Greece*.

ASTM D2487. Standard Practice for Classification of Soils for Engineering Purposes (Unified Soil Classification System). *Soil and Rock*, Vol. 04.08, American Society for Testing & Materials, West Conshohocken, PA.

ASTM D2488. Standard Practice for Description and Identification of Soils (Visual-Manual Procedure). *Soil and Rock*, Vol. 04.08, American Society for Testing & Materials, West Conshohocken, PA.

ASTM D5778. Standard Test Method for Electronic Friction Cone and Piezocone Penetration Testing of Soils. *Soil and Rock*, Vol. 04.08, American Society for Testing & Materials, West Conshohocken, PA.

ASTM D7400. Standard Test Method for Downhole Seismic Testing. *Soil and Rock*, Vol. 04.09, American Society for Testing & Materials, West Conshohocken, PA.

Baldi, G., Bellotti, R., Ghionna, V., Jamiolkowski, M. and Pasqualini, E. 1981. Cone resistance in dry NC and OC Sands. *Cone Penetration Testing and Experience*, (Proceedings National Convention, St. Louis), ASCE, Reston, Virginia: 145-177.

Baldi, G., Bellotti, R., Ghionna,V., Jamiolkowski, M. and Lo Presti, D. 1989. Modulus of sands from CPTs and DMTs. *Proc. Intl. Conf. on Soil Mechanics & Foundation Engineering*, Vol. 1 (ICSMFE, Rio de Janeiro), Balkema, Rotterdam: 165–170. www.issmge.org

Barentsen, P. 1936. Short description of a field testing method with cone-shaped sounding apparatus. *Proceedings 1st International Conference on Soil Mechanics and Foundation Engineering*, Harvard University: 6–10. Download from: www.issmge.org

Been, K. and Jefferies, M.G. 1985. A state parameter for sands. *Geotechnique* 35(2): 99-112.

Been, K., Crooks, J.H.A., Becker, D.E. and Jefferies, M.G. 1986. The cone penetration test in sands: Part I: State parameter interpretation. *Geotechnique* 36(2): 239–249.

Been, K., Jefferies, M.G., Crooks, J.H.A. and Rothenburg, L. 1987a. The cone penetration test in sands: Part II, general inference of state. *Geotechnique* 37(3): 285–299.

Been, K., Lingnau, B.E., Crooks, J.H.A. and Leach, B. 1987b. Cone penetration test calibration for Erksak Sand. *Canadian Geotechnical Journal* 37 (4): 601–610.

Been, K., Crooks, J.H.A. and Jefferies, M.G. 1988. Interpretation of material state from the CPT in sands and clays. *Penetration Testing in the UK,* (Proceedings of the Geotechnology Conference, Birmingham), Thomas Telford, London: 215–218.

Been, K. 1989. Cone penetration test calibration for Erksak (Beaufort Sea) sand: Reply. *Canadian Geotechnical Journal* 26 (1): 177–182.

Been, K., and Jefferies, M.G. 1993. Towards systematic CPT interpretation. *Predictive Soil Mechanics,* (Proceedings of the Wroth Memorial Symposium, Oxford), Thomas Telford, London: 121-134.

Been, K., Obermeyer, J., Parks, J. and Quiñonez, Q. 2012a. Post-liquefaction undrained shear strength of sandy silt and silty sand tailings. *Proceedings Tailings and Mine Waste 2012*, Keystone, Colorado State University, Fort Collins, CO: 325-335.

Been, K., Romero, S., Obermeyer, J. & Hebeler, G. 2012b. Determining in-situ state of sand and silt tailings from the CPT. *Proc. 12th Tailings and Mine Wastes Conference*, Keystone, Colorado State University, Fort Collins, CO.

Been, K. 2016. Characterizing mine tailings for geotechnical design. *Geotechnical and Geophysical Site Characterization 5*, Vol. 1 (Proc. ISC-5, Gold Coast), Australian Geomechanics Society: 41–55. Also published in: *Australian Geomechanics Journal* 50 (4): 59–78.

Begemann, H.K.S. 1953. Improved method of determining resistance to adhesion by sounding through a loose sleeve placed behind the cone. *Proceedings of the 3rd International Conference on Soil Mechanics and Foundation Engineering* (ICSMFE), Switzerland: 16–27. www.issmge.org

Begemann, H.K.S. 1965. The friction jacket cone as an aid in determining the soil profile. *Proceedings of the 6th International Conference on Soil Mechanics and Foundation Engineering*, Vol. 1 (ICSMFE, Montreal): 17–20.

Berger, R.T. 1961. The X-or gamma-ray energy absorption or transfer coefficient: tabulations and discussion. *Radiation Research* 15 (1). Academic Press, Inc.: 1–29.

Bolton, M.D. 1986. The strength and dilatancy of sands. *Géotechnique* 36 (1): 65–78.

Boulanger, R.W. and Ziotopoulou, K. 2012. PM4Sand (Version 2): A sand plasticity model for earthquake engineering applications. *Report UCD/CGM-12/01*. Center for Geotechnical Modeling, University of California, Davis.

Boulanger, R.W. and Idriss, I.M. 2014. CPT and SPT based liquefaction triggering procedures. *Report UCD/CGM-14/01*. Center for Geotechnical Modeling, University of California, Davis.

Boulanger, R.W. and DeJong, J.T. 2018. Inverse filtering procedure to correct cone penetration data for thin-layer and transition effects. Proc. 4th Intl. Symposium on Cone Penetration Testing, (CPT'18, Delft), CRC/Taylor & Francis, London: 25-44.

Bozozuk, M. 1972. The Gloucester test fill. *PhD dissertation*, Department of Civil Engineering, Purdue University, West Lafayette, IN: 184 pp.

Briaud, J-L 2007. Spread footings in sand: load settlement curve approach. *Journal of Geotechnical and Geoenvironmental Engineering* 133 (8): 905–920.

Bruzzi, D, and Battaglio, M. 1987. Pore pressure measurements during cone penetration tests. I quaderni dell'ISMES, *Report No. 229*, Experimental Institute for Models and Structures, Milan, Italy.

Burland, J.B. 1989. Small is beautiful —the stiffness of soils at small strains. *Canadian Geotechnical Journal* 26 (4): 499–516.

Burns, S.E. and Mayne, P.W. 1998a. Monotonic and dilatory pore-pressure decay during piezocone tests in clay. *Canadian Geotechnical Journal* 35 (6): 1063–1073.

Burns, S.E. and Mayne, P.W. 1998b. Penetrometers for soil permeability and chemical detection. *Report CEEGEO-98-1*. Geosystems Engineering Group, Civil & Environmental Engineering, Georgia Tech Research Corporation, Georgia Institute of Technology, Atlanta, GA: 154 pages.

Burns, S.E. and Mayne, P.W. 2002. Analytical cavity expansion-critical state model for piezocone dissipation in fine-grained soils. *Soils and Foundations* 42 (2): 131–137.

Butcher, A.P., Campanella, R.G., Kaynia, A.M. and Massarsch, K.R. 2005. Seismic cone downhole procedure to measure shear wave velocity - a guideline. *Proceedings of the International Symposium on Geophysical Testing in Geotechnical Engineering ISSMGE TC10,* Osaka, Japan.

Cabal, K. and Robertson, P.K. 2014. Accuracy and repeatability of CPT sleeve friction measurements. *Proc. 3rd Intl. Symposium on Cone Penetration Testing* (CPT'14), Las Vegas: 271-278. Download from: www.usucger.org

Campanella, R.G., Gillespie, D. and Robertson, P.K. 1982. Pore pressure during cone penetration testing. *Proc. 2nd European Symposium on Penetration Testing*. Vol. 2, (ESOPT, Amsterdam), Balkema, Rotterdam: 507-512.

Campanella, R.G., Robertson, P.K. and Gillespie, D. 1986. Seismic cone penetration test. *Use of in Situ Tests in Geotechnical Engineering*, (GSP 6, Blacksburg), ASCE, Reston, VA: 116–130.

Campanella, R. G., and Weemees, I. 1990. Development and use of an electrical resistivity cone for groundwater contamination studies. *Canadian Geotechnical Journal* 27 (3): 557–567.

Campanella, R.G. 1994. Field methods for dynamic geotechnical testing. *Dynamic Geotechnical Testing II* (STP 1213), ASTM, West Conshohocken, PA: 3-23.

Campanella, R.G. 2008. Geoenvironmental site characterization (The James K. Mitchell Lecture). *Geomechanics and Geoengineering: An International Journal* 3 (3), Taylor & Francis: 155–165. Also in *Geotechnical & Geophysical Site Characterization 3* (Proc. ISC-3, Taipei): 3-16.

Cargill, P.E. and Camp, W.M. 2010. Strength evaluation of soft marine clay in Atlantic coastal plain using in-situ methods. *Proc. 2nd Intl. Symposium on Cone Penetration Testing*, Vol. 2 (CPT'10, Huntingdon Beach, CA), Omnipress. www.cpt10.com

Casagrande, A. 1936. The determination of the preconcolidation load and its practical influence. *Proceedings 1st International Conference on Soil Mechanics & Foundation Engineering*, Vol. 3 (ICSMGE, Harvard University, Cambridge, MA): 60–64

Chandler, R.J. 1988. The in-situ measurement of the undrained shear strength of clays using the field vane. *Vane Shear Strength Testing in Soils: Field and Laboratory Studies*. ASTM STP 1014, American Society for Testing & Materials, West Conshohocken, PA: 13-44.

Chen, B.S-Y., and Mayne, P.W. 1994. Profiling the overconsolidation ratio of clays by piezocone tests. *Report CEEGEO-94*. Civil & Environmental Engineering, Georgia Tech Research Corp, Atlanta GA: 280 p. Download: http://geosystems.ce.gatech.edu/Faculty/Mayne/papers/index.html

Chen, B.S-Y., and Mayne, P.W. 1996. Statistical relationships between piezocone measurements and stress history of clays. *Canadian Geotechnical Journal* 33 (3): 488–498.

Chin, C.T., Chen, J.R., Hu, I.C., Yao, D. and Chao, H.C. 2007. Engineering characteristics of Taipei clay. Characterization & Engineering Properties of Natural Soils, Vol. 3, (IS-Singapore), Taylor & Francis Group, London: 1755-1804.

Cho, G-C., Dodds, J. and Santamarina, J.C. 2006. Particle shape effects on packing density, stiffness, and strength: natural and crushed sands. *Journal of Geotechnical and Geoenvironmental Engineering* 132 (5): 591–602.

Chung, C.K., and Finno, R.J. 1992. Influence of depositional processes on the geotechnical parameters of Chicago glacial clays. *Engineering Geology* 32 (4). Elsevier: 225–242.

Chung, S.F., and Randolph, M.F. 2004. Penetration resistance in soft clay for different shaped penetrometers. *Proceedings of the 2nd International Conference on Geotechnical Site Investigation*, Vol. 2 (ISC-2, Porto), Millpress, Rotterdam: 671–677.

Cox, B.R. 2006. Development of a direct test method for dynamically assessing the liquefaction resistance of soils in-situ. *PhD dissertation*, Civil Engineering Dept., University of Texas, Austin: 541 pages.

Cruz, I.R., and Mayne, P.W. 2006. Interpretation of CPTUs carried out in lacustrine Mexico City soft clay. *Site and Geomaterial Characterization (Proc. GeoShanghai, GSP 149),* ASCE, Reston, VA: 24–31.

Cubrinovski, M. and Ishihara, K. 2002. Maximum and minimum void ratio characteristics of sands. *Soils and Foundations* 42 (6): 65–78.

Dahlberg, R. 1974. Penetration, pressuremeter, and screw plate tests in a preloaded natural sand deposit. *Proceedings of the European Symposium on Penetration Testing*, Vol. 2 (ESOPT): Stockholm: 68–87.

DeJong, J.T., Yafrate, N.J., DeGroot, D.J. and Jakubowski, J. 2004. Evaluation of the undrained shear strength profile in soft layered clay using full-flow probes. *Geotechnical and Geophysical Site Characterization*, Vol. 1 (ISC-2, Porto), Millpress, Rotterdam: 679-686.

DeGroot, D.J., Poirer, S.E. and Landon, M.M. 2005. Sample disturbance: soft clays. *Studia Geotechnica et Mechanica,* Vol. XXVII, No. 3-4: 91-105.

DeGroot, D.J., Landon, M.M. and Poirer S.E. 2019. Geology and engineering properties of sensitive Boston Blue Clay at Newbury, Massachusetts. *AIMS Geosciences* 5(3): 412-447.

DeJong, J.T., Yafrate, N.J. and Randolph, M.F. 2008. Use of pore pressure measurements in a ball full-flow penetrometer. *Proceedings of the 3rd International Conference on Geotechnical and Geophysical Site Characterization*, Vol. 2 (ISC-3, Taipei), Taylor & Francis Group, London.

DeJong, J.T., Yafrate, N.J., DeGroot, D.J., Low, H.E. and Randolph, M. 2010a. Recommended practice for full-flow penetrometer testing and analysis. ASTM *Geotechnical Testing J.* 33 (2): 137-149.

DeJong, J.T., Yafrate, N.J. and DeGroot, D.J. 2010b. Evaluation of undrained shear strength using full-flow penetrometers. *J. Geotechnical & Geoenvironmental Engrg.* 137 (1): 14-26.

DeJong, J.T., Yafrate, N.J. and DeGroot, D.J. 2011. Evaluation of undrained shear strength using full-flow penetrometers. *Journal of Geotechnical and Geoenvironmental Engineering* 137 (1): 14–26.

DeJong, J.T. and Randolph, M.F. 2012. Influence of partial consolidation during cone penetration on estimated soil behavior type and pore pressure dissipation measurements. *Journal of Geotechnical and Geoenvironmental Engineering* 138 (7): 777–788.

DeJong, J.T., Jaeger, R.A., Boulanger, R.W., Randolph, M.F. and Wahli, D.A.J. 2012. Variable penetration rate cone testing for characterization of intermediate soils. *Geotechnical & Geophysical Site Characterization 4*, Vol. 1 (Proc. ISC-4, Pernambuco), Taylor & Francis Group, London: 25-42.

DeJong, J.T. and Green, K.C. 2020. Variable penetration rate CPT for mine tailings characterization. *Proceedings, Tailings & Mine Wastes*, Colorado State University: 679-692.

Demers, D. and Leroueil, S. 2002. Evaluation of preconsolidation pressure and the overconsolidation ratio from piezocone tests of clay deposits in Quebec. *Canadian Geotechnical Journal* 39 (1): 174–192.

Diaz-Rodriguez, J.A., Leroueil, S. and Aleman, J.D. 1992. Yielding of Mexico City Clay and other natural clays. *Journal of Geotechnical Engineering* 118 (7): 981–995.

DiBuö, B., D'Ignazio, M., Selãnpaã, J., Länsivaara, T. and Mayne, P.W. 2019. Yield stress evaluation of Finnish clays based on analytical CPTu models. *Canadian Geotechnical Journal:* Vol. 57 (11): 1623 - 1638. https://doi.org/10.1139/cgj-2019-0427.

Dienstmann, G., Schnaid, F., Maghous, S. and DeJong, J. 2018. Piezocone penetration rate effects in transient gold tailings. *Journal of Geotechnical & Geoenvironmental Engineering* 144(2): 04017116.

Doherty, P., Kirwan, L, Gavin, K., Igoe, D., Tyrrell, S., Ward, D. and O'Kelly, B.C. 2012. Soil properties at the UCD geotechnical research site at Blessington." *Bridge and Concrete Research in Ireland 2012,* Dublin, Ireland, 6-7 September, 2012.

Donaghe, R.T. and Townsend, F.C. 1978. Effects of anisotropic versus isotropic consolidation in consolidated undrained triaxial compression tests of cohesive soils. ASTM *Geotechnical Testing Journal* 1 (4): 173-189.

Douglas, B. and Olson, R.S. 1981. Soil classification using electric cone penetrometer. *Cone Penetration Testing and Experience,* (Proc. ASCE National Convention, St. Louis), ASCE, Reston, VA: 209–227.

Edil, T.B. and Wang, X. 2000. Shear strength and K_0 of peats and organic soils. *Geotechnics of High Water Content Materials*, ASTM STP 1374, American Society for Testing & Materials, West Conshohocken, PA: 209-225.

Ellis, D.V. and Singer, J.M. 2007. *Well Logging for Earth Scientists*. Vol. 692. Springer Science, Dordrecht: 708 p.

Entezari, I., Boulter, T., McGregor, S., and Sharp, J. 2021. Machine learning to estimate fines content of tailings using gamma cone penetration testing, *Proc. Mine Waste and Tailings 2021*, Brisbane, Australia.

Entezari, I., McGowan, D., and Sharp, J. 2020. Tailings characterization using cone penetration testing and machine learning, *Proc. Tailings & Mine Wastes 2020*, University of British Columbia, Vancouver, 695-704.

Entezari, I., Sharp, J. and Mayne, P.W. 2021. Soil unit weight estimation using the cone penetration test and machine learning. *Proc. GeoNiagara: The 74th Canadian Geotechnical Conference:* www.cgs.ca

Entezari, I., Sharp, J., and Mayne, P.W. 2022. A data-driven approach to predict shear wave velocity from CPTu measurements, *Proc. 5th International Symposium on Cone Penetration Testing*, Bologna, Italy.

Erharter, G.H., Oberhollenzer, S., Fankhauser, A., Marte, R., and Marcher, T. 2021. Learning decision boundaries for cone penetration test classification, *Computer-Aided. Civil & Infratstructure Engrg.* 1: 1-15.

Erzin, Y. & Ecemis, N. 2016. The use of neural networks for the prediction of cone penetration resistance of silty sands. *Neural Comput. Appl.* 28: 727–736.

Esposito III, M.P. and Andrus, R.D. 2016. Peak shear strength and dilatancy of a Pleistocene Age sand. *Journal of Geotechnical and Geoenvironmental Engineering* 143 (1).

Fahey, M. and Carter, J.P. 1993. A finite element study of the pressuremeter test in sand using a nonlinear elastic plastic model. *Canadian Geotechnical Journal* 30 (2): 348–362.

Fahey, M. 1998. Deformation and in-situ stress measurement in geotechnical site characterization. *Geotechnical Site Characterization*, Vol. 1 (Proc. ISC-1, Atlanta), Balkema, Rotterdam: 49–68.

Fellenius, B.H., and Eslami, A. 2000. Soil profile interpreted from CPTU data. *Proceedings of Year 2000 Geotechnics Conference,* Southeast Asian Geotechnical Society, Asian Institute of Technology, Bangkok, Thailand, 1:163–171.

Fellenius, B.H., Harris, D.E. and Anderson, D.G. 2004. Static loading test on a 45 m long pipe pile in Sandpoint, Idaho." *Canadian Geotechnical Journal* 41 (4): 613–628.

Fellenius, B.H. 2020. *Basics of Foundation Design*, Electronic Edition, Sidney, BC: 529 pages. Download from: www.fellenius.net

Finno, R.J. and Chung, C-K. 1992. Stress-strain-strength responses of compressible Chicago glacial clays. *Journal of Geotechnical Engineering* 118 (10): 1607-1625.

Finno, R.J., Gassman, S.L. and Calvello, M. 2000. NGES at Northwestern University. *National Geotechnical Experimentation Sites*, Geotechnical Special Publication No. 93. American Society of Civil Engineers (ASCE), Reston, VA: 130–159.

Fioravante, V., Jamiolkowski, M., Ghionna, V.N. and Pedroni, S. 1998. Stiffness of carbonate Quiou sand. *Geotechnical Site Characterization,* Vol. 2 (Proc. ISC-1, Atlanta), Balkema, Rotterdam: 1039–1049.

Foott, R. and Ladd, C.C. 1981. Undrained settlement of plastic and organic clays. *Journal of the Geotechnical Engineering Division* 107 (8): 1079–1094.

Getchell, A. and Benoît, J. 2014. Geotechnical test embankment at Dover, New Hampshire. *Report NHDOT 11238-M* by Univ. of New Hampshire, Durham: 103 pages.

Ghafghazi, M. and Shuttle, D.A. 2008. Interpretation of sand state from cone penetration resistance. *Géotechnique* 58 (8): 623–634.

Gifford, D.G., Kraemer, S.R., Wheeler, J.R. and McKown, A.F. 1987. *Spread Footings for Highway Bridges*, FHWA Report RD-86/185, Federal Highway Administration, Dept. of Transportation, Washington, DC, 222 pages.

Gillespie, D.G. 1990. Evaluating shear wave velocity and pore pressure data from the seismic cone penetration test. *PhD thesis*, Dept. of Civil Engineering, University of British Columbia.

Gorman, C.T., Drnevich, V.P. and Hopkins, T.C. 1975. Measurement of in-situ shear strength. *In-Situ Measurement of Soil Properties*, Vol. II (Proc. NCSU, Raleigh), ASCE, Reston, VA: 139–140.

Green, R.A., Cubrinovski, M., Cox, B.R., Wood, C., Wotherspoon, L., Bradley, B. and Maurer, B.W. 2014. Select liquefaction case histories from the 2010-2011 Canterbury Earthquake sequence. *Earthquake Spectra* 30 (1): 131-153. DOI: 10.1193/030713EQS066M.

Greig, J.W. 1985. Estimating undrained shear strength of clay from cone penetration tests. *MASc thesis,* Dept. of Civil Engineering, Univ. British Columbia, Vancouver, BC: 187 pages.

Hallal, M.M., and Cox, B.R. 2019. Theoretical evaluation of the interval method commonly used for downhole seismic testing. *Proceedings of the ASCE Geo-Congress 2019: 8th International Conference on Case Histories in Geotechnical Engineering,* (GSP 311, Philadelphia), ASCE, Reston, VA: 376-386

Hamouche, K.K., Leroueil, S., Roy, M. and Lutenegger, A.J. 1995. In-situ evaluation of K_0 in eastern Canada clays." *Canadian Geotechnical Journal* 32 (4): 677–688.

Hegazy, Y.A. and Mayne, P.W. 1995. Statistical correlations between V_S and cone penetration data for different soil types. *Proceedings of the International Symposium on Cone Penetration Testing,* Vol. 2, (CPT'95, Linköping), Swedish Geotechnical Society: 173-178.

Hight, D.W., Paul, M.A., Barras, B.F., Powell, J.J.M., Nash, D.F.T., Smith, P.R., Jardine, R.J. and Edwards, D.H. 2003. The characterisation of the Bothkennar clay. *Characterisation & Engineering Properties of Natural Soils,* Vol. 1, Swets & Zeitlinger, Lisse, The Netherlands: 543–597.

Holtz, R.D., Kovacs, W.D. and Sheahan, T.C. 2011. *An Introduction to Geotechnical Engineering* (2nd Edition). Pearson Publishing, Upper Saddle River, NJ: 853 p.

Hong, S-J., Lee, M-J., Kim, T-J. and Lee, W-J. 2009. Evaluation of CPTU cone factors for Busan Clay using pore pressure ratio. *Journal of the Korean Geotechnical Society* 25 (1). Korean Geotechnical Society: 77–88.

Houlsby, G.T. and Teh, C.I. 1988. Analysis of the piezocone in clay. *Penetration Testing 1988,* (Proc. ISOPT-1, Orlando), Vol. 2, Balkema, Rotterdam: 777–783.

Houlsby, G.T. and Yu, H-S. 1990. Finite element analysis of the cone pressuremeter test. *Pressuremeters* (Proc. 3rd Intl. Symposium on Pressuremeters, Oxford), Thomas Telford, London: 221-230.

Housner, G.W. et al. (1985). *Liquefaction of Soils During Earthquakes*. Committee on Earthquake Engineering, Commission on Engineering & Technical Systems, National Research Council, National Academy Press, Washington, DC: 240 p.

Hryciw, R.D., Ghalib, A.M. and Raschke, S.A. 1998. In-situ soil characterization using vision cone penetrometer (VisCPT). *Geotechnical Site Characterization* (Proc. ISC-1, Atlanta), Vol. 2: Balkema, Rotterdam: 1081–1086.

Hryciw, R.D, and Shin, S. 2004. Thin layer and interface characterization by VisCPT. *Proceedings of the 2nd International Conference Site Characterization* (ISC-2, Porto), Vol, 1, Millpress, Rotterdam:701–706.

Hu, L., Wu, H., Zhang, L. and Zhang, P. 2017. Geotechnical properties of mine tailings. *Journal of Materials in Civil Engineering* 29 (2).

Idriss, I.M. and Boulanger, R.W. 2008. *Soil Liquefaction During Earthquakes*. Monogram MNO-12, Earthquake Engineering Research Institute, Oakland, CA: 266 pages. www.eeri.org

Idriss, I.M. and Boulanger, R.W. 2015. The 2nd Ishihara Lecture: SPT- and CPT-based relationships for the residual shear strength of liquefied soils. *Soil Dynamics and Earthquake Engineering* 68: 57–68.

Igoe, D. and Gavin, K. 2019. Characterization of the Blessington sand geotechnical test site. *AIMS Geosciences* 5 (2): 145-162. DOI: 10.3934/geosci.2019.2.145

Ishihara, K. 1984. Post-earthquake failure of a tailings dam due to liquefaction of pond deposit. *Proceedings, First International Conf. on Case Histories in Geotechnical Engineering*, University of Missouri–Rolla: 1129-1143.

Ishihara, K. and Yoshimine, M. 1992. Evaluation of settlements in sand deposits following liquefaction during earthquakes. *Soils & Foundations* 32(1): 173-188.

ISO 224760-1 (2012). Geotechnical investigation and testing. Field Testing. Part 1: Electrical cone and piezocone penetration test. Technical Committee ISO/TC 182 Geotechnics, International Organization for Standardization, New York. www.iso.org.

Jacobs, P.A. and Coutts, I.S. 1992. A comparison of electric piezocone tips at the Bothkennar test site. *Géotechnique* 42 (2): 369–375.

Jamiolkowski, M., Ladd, C.C., Germaine, J.T. and Lancellotta, R. 1985. 'New developments in field and laboratory testing of soils. *Proceedings of the 11th International Conference on Soil Mechanics and Foundation Engineering*, Vol. 1 (ICSMFE, San Francisco), Balkema, Rotterdam: 57–154.

Jamiolkowski, M. and Pepe, M.C. 2001. Vertical yield stress of Pisa Clay from piezocone tests. *Journal of Geotechnical and Geoenvironmental Engineering* 127 (10): 893–897.

Jamiolkowski, M., LoPresti, D.C.F., and Manassero, M. 2001. Evaluation of relative density and shear strength of sands from cone penetration test and flat dilatometer test. *Soil Behavior and Soft Ground Construction* (GSP 119), ASCE, Reston, VA: 201-238.

Jardine, R.J., Gens, A., Hight, D.W. and Coop, M.R. (2004). Developments in understanding soil behavior. *Advances in Geotechnical Engineering*, Vol. 1 (Proc. Skempton Conference), Institution of Civil Engineers, London: 103-140.

Jeeravipoolvarn, S., Scott, J.D. and Chalaturnk, R.J. 2009. 10-meter standpipe tests on oil sands tailings: long-term experimental results and prediction. *Canadian Geotechnical Journal* 46: 875–888.

Jefferies, M.G. and Davies, M.P. 1991. Soil classification by the cone penetration test: discussion. *Canadian Geotechnical Journal* 28 (1): 173–176.

Jefferies, M. and Been, K. 2006. *Soil Liquefaction: A Critical State Approach*. First Edition, CRC Press, London: 512 pages.

Jefferies, M. and Been, K. 2015. *Soil Liquefaction: A Critical State Approach*. Second Edition, CRC Press, London: 712 pages.

Jefferies, M., Morgenstern, N.R., Van Zyl, D., and Wates, J. (2019). *Report on NTSF Embankment Failure, Cadia Valley Operations for Ashurst*, Australia, Document Number H356804-00000-22A-230-0001: 119 pages. https://www.newcrest.com/

Jeyapalan, J.K. and Boehm, R. 1986. Procedures for predicting settlements in sands, *Settlement of Shallow Foundations on Cohesionless Soils: Design & Performance*, (GSP 5), ASCE, Reston, Virginia: 1-22.

Johns, D. and Murray, L. 2018. Characterisation of pore pressures in tailings dams and the implications for design. *Proceedings, Mine Waste Tailings Conference Proceedings*, Brisbane, Australia, July 23-24: 239–249.

Karlsrud, K., Lunne, T. and Brattlien, K. 1996. Improved CPTU interpretations based on block samples. *Publikasjon-Norges Geotekniske Institutt* 202. Norwegian Geotechnical Institute, Oslo: 195–201.

Karlsrud, K., Lunne, T., Kort, D.A. and Strandvik, S. 2005. CPTU correlations for clays. *Proceedings of the 16th International Conference on Soil Mechanics and Geotechnical Engineering*, Vol. 2 (ICSMGE, Osaka), Balkema, Rotterdam: 693-702.

Karlsrud, K. and Hernandez-Martinez, F.G. 2013. Strength and deformation properties of Norwegian clays from laboratory tests on high-quality block samples. *Canadian Geotechnical Journal* 50 (12): 1273–1293.

Kayen, R., Moss, R.E.S., Thompson, E.M., Seed, R.M., Cetin, K.O., Der Kiureghian, A., Tanaka, Y. and Tokimatsu, K. 2013. Shear-wave velocity–based probabilistic and deterministic assessment of seismic soil liquefaction potential. *Journal of Geotechnical and Geoenvironmental Engineering* 139 (3): 407–419.

Keaveny, J.M. and Mitchell, J.K. 1986. Strength of fine-grained soils using the piezocone. *Use of in Situ Tests in Geotechnical Engineering*, (GSP 6, Blacksburg), ASCE, Reston, VA: 668–685.

Koerner, R.M. 1970. Effect of particle characteristics on soil strength. *Journal of Soil Mechanics & Foundations Division* (ASCE), Vol 96 (SM 4): 1221-1234.

Konrad, J-M., and Law, K.T. 1987. Undrained shear strength from piezocone tests. *Canadian Geotechnical Journal* 24 (3): 392–405.

Koutsoftas, D.C. and Ladd, C.C. 1985. Design strengths for an offshore clay. *Journal of Geotechnical Engineering* 111 (3): 337–355.

Krage, C.P., Broussard, N.S. and DeJong, J.T. 2014. Estimating rigidity index (I_R) based on CPT measurements. *Proceedings of the 3rd International Symposium on Cone Penetration Testing,* (CPT'14, Las Vegas, Nevada): 727–735. Download from: www.usucger.org

Krage, C.P., DeJong, J.T., DeGroot, D.J., Dyer, A.M. and Lukas, W.G. 2015. Applicability of clay-based sample disturbance criteria to intermediate soils. *Proceedings 6th International Conference on Earthquake Geotechnical Engineering*, Christchurch, New Zealand. Paper ID 131.

Ku, C-S. and Juang, C.H. 2012. Liquefaction and cyclic softening potential of soils: a unified piezocone penetration testing-based approach. *Geotechnique* 62(5): 457-461.

Ku, T. and Mayne, P.W. 2013. Yield stress history evaluated from paired in-situ shear moduli of different modes. *Engineering Geology* 152 (1). Elsevier: 122–132.

Ku, T., Mayne, P.W, and Cargill, E. (2013a). Continuous-interval shear wave velocity profiling by auto-source and seismic piezocone tests. *Canadian Geotechnical Journal* 50 (1): 382-390.

Ku, T., Weemees, I., Cargill, E., Mayne, P.W. and Woeller, D. 2013b. Post-processing continuous shear wave signals taken during cone penetrometer testing. *Geotechnical Testing Journal* 36 (4). ASTM International: 543–552.

Ku, T. and Mayne, P.W. 2015. In-situ lateral stress coefficient (K_0) from shear wave velocity measurements in soils. *Journal of Geotechnical and Geoenvironmental Engineering* 141 (12). American Society of Civil Engineers: 10.1061/(ASCE) GT.1943-5606.0001354.

Kulhawy, F.H, and Mayne, P.W. 1990. *Manual on Estimating Soil Properties for Foundation Design*. EPRI Report EL-6800, Electric Power Research Inst., Palo Alto, CA; 306 pages.

Kulhawy, F.H, and Mayne, P.W. 1991. Relative density, SPT, and CPT interrelationships. *Calibration Chamber Testing*. Elsevier, New York: 197–211.

Ladd, C.C., Germaine, J.T., Baligh, M.M. & Lacasse, S.M. (1980). Evaluation of self-boring pressuremeter tests in Boston Blue clay. *Report FHWA-RD-80/052*, Mass. Inst. of Technology, Cambridge/MA submitted to Federal Highway Administration, Washington, DC: 239 p.

Ladd, C.C. 1991. Stability evaluation during staged construction. *Journal of Geotechnical Engineering* 117 (4): 540–615.

Ladd, C.C, and DeGroot, D.J. 2003. Recommended practice for soft ground site characterization. *Soil & Rock America* (SARA 2003: Proc. 12th Panamerican Conference on Soil Mechanics and Geotechnical Engineering), Vol. 1, Verlag GmbH Essen, Germany: 1–57.

Laing, N.L. 1985. Sources and receivers with the seismic cone test. *PhD thesis*, Dept. of Civil Engineering, University of British Columbia.

Landon, M.M., DeGroot, D.J. and Jakubowski, J. 2004. Comparison of shear wave velocity measured in situ and on block samples of a marine clay. *Proceedings of GeoQuebec: 57th Canadian Geotechnical Conference,* Canadian Geotechnical Society: 22–28.

Landon, M.M. 2007. Development of a non-destructive sample quality assessment method for soft clays. *PhD thesis*, Dept. of Civil Engineering, University of Massachusetts, Amherst.

Lengkeek, H.J., de Greef, J., and Joosten, S. 2018. CPT based unit weight estimation extended to soft organic soils and peat. *Cone Penetration Testing 2018*. (Proc. CPT'18, Delft University of Technology, The Netherlands), CRC Press: 389-394.

Larsson, R. and Mulabdić, M. 1991. Piezocone tests in clay. *SGI Report No. 42,* Swedish Geotechnical Institute, Linköping: www.swedgeo.se

Lee, J., Salgado, R. and Carraro, J.A.H. 2004. Stiffness degradation and shear strength of silty sands. *Canadian Geotechnical Journal* 41 (5): 831–843.

Lee, M.J., Hong, S.J., Kim, J.J. and Lee, W. 2010. Cone tip resistance of highly compressible Jeju beach sand. *GeoFlorida 2010: Advances in Analysis, Modeling & Design*, (GSP 199), ASCE, Reston, VA: 990–997.

Lehane, B, and Cosgrove, E. 2000. Applying triaxial compression stiffness data to settlement prediction of shallow foundations on cohesionless soil. *Geotechnical Engineering* 143 (4). Thomas Telford Ltd: 191–200.

Lehane, B.M. and Jardine, R.J. 2003. Effects of long-term pre-loading on the performance of a footing on clay. *Géotechnique* 53 (8). Thomas Telford Ltd: 689–695.

Lehane, B.M. 2011. Shallow foundation performance in a calcareous sand. *Proc. Frontiers in Offshore Geotechnics II* (ISFOG-Perth), Taylor & Francis Group, London: 427-432.

Leroueil, S. and Jamiolkowski, M. 1991. Exploration of soft soil and determination of design parameters, *Proceedings, GeoCoast'91*, Vol. 2, Yokohama; Port & Harbor Research Institute: 968-998.

Leroueil, S., Leart, P., Hight, D.W. and Powell, J.J.M. 1992. Hydraulic conductivity of a recent estuarine silty clay at Bothkennar. *Géotechnique* 42 (2). Thomas Telford Ltd: 275–288.

Leroueil, S., Bouclin, G., Tavenas, F., Bergeron, L. and La Rochelle, P. 1991. Permeability anisotropy of natural clays as a function of strain. *Canadian Geotechnical Journal* 27 (5): 568–579.

Leroueil, S. and Hight. D.W. 2003. Behavior and properties of natural soils and soft rocks. *Characterisation and Engineering Properties of Natural Soils,* Vol. 1, Swets & Zeitlinger, Lisse, The Netherlands: 29–254.

L'Heureux, J-S. and Long, M. 2017. Relationship between shear wave velocity and geotechnical parameters for Norwegian clays. Journal of Geotechnical & Geoenvironmental Engineering 143(6): 04017013.

L'Heureux, J-S., Lindgård, A., and Emdal, A. 2019. The Tiller-Flotten research site: Geotechnical characterization of a very sensitive clay deposit. *AIMS Geosciences* 5(4): 831-867. doi: 10.3934/geosci.2019.4.831

Li, X.S. and Wang, Y. 1998. Linear representation of steady-state line for sand. *Journal of Geotechnical & Geoenvironmental Engineering* 124 (12): 1215–1217.

Liao, T. and Mayne, P.W. 2006. Automated post-processing of shear wave signals. *Proceedings of the 8th US National Conference on Earthquake Engineering, San Francisco*: 460–471.

Locat, J., Tanaka, H., Tan, H.S., Dasari, G.R. and Lee, H. 2003. Natural soils: geotechnical behavior and geological knowledge. *Characterisation and Engineering Properties of Natural Soils* Vol. 1, Balkema, Rotterdam: 3–28.

Löfroth, H., Suer, P., Schälin, D., Dahlin, T. and Leroux, V. 2013. Mapping of quick clay using sounding methods and resistivity in the Göta River Valley. *Geotechnical & Geophysical Site Characterization 4*, Vol. 2 (Proc. ISC-4, Pernambuco), Taylor & Francis Group, London: 1001-1008.

Long, M. and Gudjonsson, G.T. 2004. T-Bar testing in Irish soils. *Proceedings of the 2nd International Conference on Geotechnical and Geophysical Site Characterization*, Vol. 2 (Proc. ISC-Porto), Millpress, Rotterdam: 719–726.

Long, M., Colreavy, C., Ward, D. and Quigley, P. (2014). Piezoball tests in soft Irish clays. *Proc. 3rd Intl. Symposium on Cone Penetration Testing* (CPT'14, Las Vegas): 467-475. www.usucger.org

Low, H.E. 2009. Performance of penetrometers in deepwater soft soft characterization. *PhD dissertation*, Dept. Civil & Mining Resources Engineering, Univ. Western Australia.

Low, H.E., Lunne, T., Andersen, K.H., Sjursen, M.A., Li, X. and Randolph, M.F. (2010). Estimation of intact and remoulded undrained shear strengths from penetration tests in soft clays. *Geotechnique* 60 (11): 843-859.

Lu, Q., Randolph, M.F., Hu, Y. and Bugarski, I.C. 2004. A numerical study of cone penetration in clay. *Géotechnique* 54 (4): 257–267.

Lunne, T., Christoffersen, H.P. and Tjelta, T.I. 1985. Engineering use of piezocone data in North Sea clays." *Proceedings of the 11th International Conference on Soil Mechanics & Foundation Engineering*, Vol. 2 (ICSMFE, San Francisco), Balkema, Rotterdam: 907–912.

Lunne, T., Robertson, P.K. and Powell, J.J.M. 1997. *Cone Penetration Testing in Geotechnical Practice*, EF-Spon/CRC Press, Blackie Academic & Professional, London: 418 p.

Lunne, T., Randolph, M.F., Chung, S.F., Andersen, K.H., and Sjursen, M. 2005. Comparison of cone and T-bar factors in two onshore and one offshore clay sediments. *Proceedings of the International Symposium on Frontiers in Offshore Geotechnics,* (ISFOG, Perth): 19–21.

Lunne, T., Berre, T., Andersen, K.H., Strandvik, S. and Sjursen, M. 2006. Effects of sample disturbance and consolidation procedures on measured shear strength of soft marine Norwegian clays. *Canadian Geotechnical Journal* 43 (7): 726–750.

Lunne, T. 2012. The CPT in offshore soil investigations-a historic perspective. *Geomechanics and Geoengineering* 7 (2), Taylor & Francis: 75–101.

Lunne, T., Knudsen, S., Blaker, Ø., Vestgården, T., Powell, J.J.M., Wallace, C.F., Krogh, L., Thomsen, N.V., Yetginer, G. and Ghanekar, R.K. 2019. Methods used to determine maximum and minimum dry unit weights of sand: Is there a need for a new standard ? Canadian Geotechnical Journal 56: 536-553. http://dx.doi.org/10.1139/cgj-2017-0738

Lupini, J.F., Skinner, A.E. and Vaughn, P.R. 1981. The drained residual strength of cohesive soils. *Geotechnique* 31(2): 181-213.

Mahmoodzadeh, H. and Randolph, M.F. 2014. Penetrometer testing: effect of partial consolidation on subsequent dissipation response. *Journal of Geotechnical and Geoenvironmental Engineering* 140 (6): 04014022

Maki, I.P., Boulanger, R.W., DeJong, J.T. and Jaeger, R.A. 2013. State-based overburden normalization of cone penetration resistance in clean sand. *Journal of Geotechnical and Geoenvironmental Engineering* 140 (2). doi.org/10.1061/(ASCE)GT.1943-5606.0001020

Marchetti, S., Monaco, P., Calabrese, M. and Totani, G. 2004. DMT-predicted versus measured settlements under a full-scale instrumented embankment at Treporti (Venice, Italy)."

Geotechnical and Geophysical Site Characterization, Vol. 2 (Proc. ISC-2, Porto), Millpress, Rotterdam: 1511–1518.

McGillivray, A.V. and Mayne, P.W. (2008). An automated seismic source for continuous shear wave profiling. *Geotechnical & Geophysical Site Characterization 2008*, (Proc. ISC-3, Taipei), Taylor & Francis Group, London: 1347-1352.

McQueen, W., Miller, B., Mayne, P.W. and Agaiby, S. 2016. Piezocone dissipation tests at the Canadian Test Site No. 1, Gloucester, Ontario. *Canadian Geotechnical Journal* 53(5): 884-888.

Mayne, P.W. 1980. Cam-Clay predictions of undrained shear strength. *Journal of the Geotechnical Engineering Division*, ASCE, Vol. 106 (GT11): 1219-1242.

Mayne, P.W. and Kulhawy, F.H. 1982. K_0-OCR relationships in soils. *Journal of Geotechnical Engineering* 106 (6): 851–872.

Mayne, P.W. and Stewart, H.E. 1988. Pore pressure response of K_0-consolidated clays. *Journal of Geotechnical Engineering* 114 (11): 1340-1346.

Mayne, P.W. 1988. Determining OCR in clays from laboratory strength. *Journal of Geotechnical Engineering* 114 (1): 76-92.

Mayne, P.W., Kulhawy, F.H., and Kay, J.N. 1990. Observations on the development of pore water pressures during piezocone penetration in clays", *Canadian Geotechnical Journal* 27 (4): 418-428.

Mayne, P.W. 1991. Determination of OCR in clays by piezocone tests using cavity expansion and critical state concepts. *Soils and Foundations* 31 (2): 65–76.

Mayne, P.W. and Harris, D.E. (1993). Axial load-displacement behavior of drilled shaft foundations in Piedmont residuum. *FHWA Reference No. 41-30-2175 Report* to ADSC/ASCE by School of Civil & Environmental Engineering, Georgia Institute of Technology, Atlanta, GA: 172 pages. Download: http://geosystems.ce.gatech.edu/Faculty/Mayne/papers/index.html

Mayne, P.W. and Rix, G.J. 1995. Correlations between shear wave velocity and cone tip resistance in natural clays. *Soils and Foundations* 35 (2): 107–110.

Mayne, P.W., Robertson, P.K., and Lunne, T. 1998. Clay stress history evaluated from seismic piezocone tests. *Geotechnical Site Characterization*, Vol. 2 (Proc. ISC-1, Atlanta), Balkema, Rotterdam: 1113-1118.

Mayne, P.W. 2001. Stress-strain-strength-flow parameters from enhanced in-situ tests. *Proceedings, International Conference on In-Situ Measurement of Soil Properties & Case Histories* (In-Situ 2001), Bali, Indonesia, 27-47. Download from: www.usucger.org

Mayne, P.W., Christopher, B.R., Berg, R., and DeJong, J.T. 2002. *Subsurface Investigations - Geotechnical Site Characterization*. Publication No. FHWA-NHI-01-031, National Highway

Institute, Federal Highway Administration (FHWA), Dept. of Transportation, Washington, D.C., 301 p. Download: geosystems.ce.gatech.edu/Faculty/Mayne/papers/index.html

Mayne, P.W. 2005. Keynote: Integrated Ground Behavior: In-Situ and Lab Tests. *Deformation Characteristics of Geomaterials*, (Proc. IS-Lyon 2003), Taylor & Francis Group, London: 154–176.

Mayne, P.W. and Pearce, R.A. 2005. Site characterization of Bootlegger Cove Formation clay for Port of Anchorage. *Frontiers in Offshore Geotechnics* (Proc. ISFOG, Perth), Taylor & Francis Group, London: 951-955.

Mayne, P.W. 2006. Undisturbed sand strength from seismic cone tests. *Geomechanics and Geoengineering: An International Journal* 1 (4). Taylor & Francis: 239–257.

Mayne, P.W. 2007a. *NCHRP Synthesis 368 on Cone Penetration Testing*. Transportation Research Board, National Academy Press, Washington, DC: 118 pages. PDF from: www.trb.org

Mayne, P.W. 2007b. In-situ test calibrations for evaluating soil parameters. *Characterisation and Engineering Properties of Natural Soils*, Vol. 3, Taylor & Francis Group, London: 1601–1652.

Mayne, P.W. 2008. Piezocone profiling of clays for maritime site investigations. *Geotechnics in Maritime Engineering*, Vol. 1 (Proceedings, 11th Baltic Sea Geotechnical Conference, Gdansk), Polish Committee on Geotechnics: 333-350.

Mayne, P.W. and McGillivray, A.V. 2008. Improved shear wave measurements using autoseis sources. *Deformational Characteristics of Geomaterials* (Proc. IS-Atlanta), Vol. 2, IOS Press, Amsterdam: 853–860.

Mayne, P.W., Coop, M.R., Springman, S., Huang, A-B., and Zornberg, J. 2009. State-of-the-Art Paper (SOA-1): Geomaterial Behavior and Testing. *Proc. 17th Intl. Conf. Soil Mechanics & Geotechnical Engineering*, Vol. 4 (ICSMGE, Alexandria, Egypt), Millpress/IOS Press Rotterdam: 2777-2872. Download: www.issmge.org

Mayne, P.W, Peuchen, J., and Bouwmeester, D. 2010. Unit weight evaluation from CPT. *Proceedings, 2nd Intl. Symposium on Cone Penetration Testing*, Vol. 2, (CPT'10, Huntington Beach, California): 169-176. Download from: www.usucger.org

Mayne, P.W, Peuchen, J., and Bouwmeester, D. 2011. Soil unit weight estimated from CPTu in offshore soils. *Frontiers in Offshore Geotechnics II* (Proc. ISFOG 2010, Perth), Taylor & Francis Group, London: 371-376.

Mayne, P.W. and Peuchen, J. 2012. Unit weight trends with cone resistance in soft to firm clays. *Geotechnical and Geophysical Site Characterization 4*, Vol. 1 (Proc. ISC-4, Pernambuco), CRC Press, London: 903-910.

Mayne, P.W., Uzielli, M. and Illingworth, F. 2012. Shallow footing response on sands using a direct method based on cone penetration tests. *Full Scale Testing and Foundation Design* (Proceedings GSP 227 honoring Bengt Fellenius), ASCE, Reston, Virginia: 664-679.

Mayne, P.W. 2014. Interpretation of geotechnical parameters from seismic piezocone tests. Proceedings, 3rd Intl. Symposium on Cone Penetration Testing, (CPT'14, Las Vegas): 47-73. PDF available at: www.usucger.org

Mayne, P.W. and Woeller, D.J. 2014. Generalized direct CPT method for evaluating footing deformation response and capacity on sands, silts, and clays. *Geo-Congress 2014: Geo-Characterization and Modeling for Sustainability*, (GSP 234, Atlanta), ASCE, Reston, Virginia: 1983-1997.

Mayne, P.W. and Woeller, D.J. 2015. Advances in seismic piezocone testing. *Geotechnical Engineering for Infrastructure & Development* (Proc. XVI ECSMGE, Edinburgh), Vol. 6, ICE Publishing, London: 3005-3009.

Mayne, P.W., Peuchen, J. and Baltoukas, D. 2015. Piezocone evaluation of undrained strength in soft to firm offshore clays. *Frontiers in Offshore Geotechnics III*, Vol. 2 (Proc. ISFOG, Oslo), Taylor & Francis Group, London: 1091-1096.

Mayne, P.W. 2016. Evaluating effective stress parameters and undrained shear strengths of soft-firm clays from CPTU and DMT. *Australian Geomechanics Journal* 51 (4): 27–55.

Mayne, P.W. 2017. Stress history of soils from cone penetration tests. 34th Manual Rocha Lecture, *Soils & Rocks*, Vol. 40 (3), Sept-Dec., Brazilian Society for Soil Mechanics, Saö Paulo: 203-218. http://www.soilsandrocks.com.br/

Mayne, P.W., Styler, M., Woeller, D.J. and Sharp, J. 2017. Identifying contractive soils by CPT material index for flow liquefaction concerns. Paper ID 827, *Proceedings GeoOttawa 2017: 70 Years of Canadian Geotechnics and Geoscience*, Canadian Geotechnical Society, Ottawa ON: www.cgs.ca

Mayne, P.W. and Dasenbrock, D. 2018. Direct CPT method for 130 footings on sands. *Innovations in Geotechnical Engineering,* (Proc. IFCEE, Orlando, GSP 299), ASCE, Reston, VA: 135-146.

Mayne, P.W., Greig, J. and Agaiby, S. 2018. Evaluating CPTU in sensitive Haney clay using a modified SCE-CSSM solution. *Proceedings 71st Canadian Geotechnical Conference: GeoEdmonton 2018*, Paper ID No. 279, Canadian Geotechnical Society: www.cgs.ca

Mayne, P.W. and Peuchen, J. 2018. Evaluation of CPTU Nkt cone factor for undrained strength of clays. *Proc. 4th Intl. Symposium on Cone Penetration Testing* (CPT'18, Tech. Univ. Delft), CRC Press/Balkema, : 423-430.

Mayne, P.W. and Styler, M. 2018. Soil Liquefaction Screening Using CPT Yield Stress Profiles. *Geotechnical Earthquake Engineering and Soil Dynamics V: Liquefaction Triggering, Consequences, and Mitigation* (GSP 290, Proc. GEESD-V, Austin), ASCE, Reston, VA: 605-616.

Mayne, P.W. and Agaiby, S.S. 2019. Profiling yield stress and identification of soft organic clays using piezocone tests. *Proc. 16th Pan Am Conference on Soil Mechanics & Geotechnical Engineering*, (Geotechnical Engineering in the XXI Century, SMIG Cancun), IOS Press, Rotterdam: 220-227. www.isssmge.org: doi: 10.3233/STAL190043

Mayne, P.W., Paniagua, P., L'Heureux, J-S., Lindgård, A., and Emdal, A. 2019. Analytical CPTu model for sensitive clay at Tiller-Flotten site, Norway. *Proc. XVII ECSMGE: Geotechnical Engineering Foundation of the Future*, Paper 0153, Reykjavik, Icelandic Geotechnical Society: www.issmge.org

Mayne, P.W. and Sharp, J. 2019. CPT approach to evaluating flow liquefaction using yield stress ratio. *Proceedings of Tailings and Mine Waste 2019*, Vancouver, Published by the Institute of Mining Engineering, University of British Columbia: 655-670. tailingsandminewaste.com

Mayne, P.W. 2020. The 26th Széchy Lecture: Use of in-situ geotechnical tests for foundation systems. *Proceedings of the Széchy Károly Emlékkonferencia*, published by the Hungarian Geotechnical Society, Budapest: 12-73.

Mayne, P.W., Agaiby, S.S., and Dasenbrock, D. 2020. Piezocone identification of organic clays and peats. *Proc. GeoCongress 2020: Modeling, Geomaterials, and Site Characterization*, (Minneapolis, GSP 317), ASCE, Reston, VA: 541-549.

Mayne, P.W. and Benoît, J. 2020. Analytical CPTU models applied to sensitive clay at Dover, New Hampshire. *Journal of Geotechnical & Geoenvironmental Engineering* 146(12) DOI: 10.1061/(ASCE) 12 GT.1943-5606.0002378

Mayne, P.W. and Sharp, J. 2022. Screening for flow liquefaction for tailings and natural soils by CPTU. *Proc. 20th Intl. Conf. on Soil Mechanics & Geotechnical Engineering* (ICSMGE, Sydney).

Mengé, P., Vinck, K., Van den Broeck, M., Van Impe, P.O. and Van Impe, W.F. 2016. Evaluation of relative density and liquefaction potential with cpt in reclaimed calcareous sand. *Proc. The 5th International Conference on Geotechnical and Geophysical Site Characterisation*, (ISC-5, Gold Coast), Australian Geomechanics Society: 1235–1240.

Mesri, G. 1989. A reevaluation of $s_{u(mob)}$ = $0.22\sigma'_p$ using laboratory shear tests. *Canadian Geotechnical Journal* 26 (1): 162–164.

Mesri, G., and Abdel-Ghaffar, M.E.M. 1993. Cohesion intercept in effective stress-stability analysis. J*ournal of Geotechnical Engineering*, 10.1061/(ASCE)0733-9410(1993)119:8(1229): 1229–1249.

Mesri, G., Lo, D.O.K. and Feng, T.W. 1994. Settlement of embankments on soft clays. *Vertical and Horizontal Deformations of Foundations and Embankments*, Vol. 1 (Proc. Settlement'94, College Station, TX: GSP 40), ASCE, Reston, VA: 8–56.

Młynarek, Z., Wierzbicki, J. and Tschuschke, W. 2005. CPT National Report: Poland. *Proceedings, Symposium on Cone Penetration Testing,* Swedish Geotechnical Society, Linköping: Vol. 3: 157–165. Download proceedings from: www.usucger.org

Mlynarek, Z., Wierzbicki, J. Gogolik, S. and Bogucki, M 2014. Shear strength and deformation parameters of peat and gyttja from CPTU, SDMT, and VT tests. *Proceedings, 5th Intl. Workshop on CPTU and DMT in soft clays and organic soils*, Poznan, Polish Committee on Geotechnics: 193-209.

Mohammad, L.N., Titi, H.H., Herath, A., et al. 2000. Investigation of the applicability of intrusion technology to estimate the resilient modulus of subgrade soil. *FHWA Rept. No. DTFH71-97-PTP-LA-14*. Louisiana Transportation Research Center, Baton Rouge.

Monfared, S.D. and Sadrekarimi, A. 2013. An overview of existing methods for estimating state parameter from cone penetration test results. *Proceedings GeoMontreal*, 66th Canadian Geot. Conf., Canadian Geotechnical Society, Ottawa: 7 pages.

Morioka, B.T. & Nicholson, P.G. 2000. Evaluation of liquefaction of calcareous sand, *Proc.10th Intl. Symposium on Offshore and Polar Engineering*, (ISOPE), Vol. II, Seattle: p. 494-500.

Morgenstern, N.R., Vick, S.G., Viotti, C.B. and Watts, B.D. 2016. *Fundão tailings dam review panel: Report in the immediate causes of the failure of the Fundão Dam*. Cleary Gottlieb Steen & Hamilton LLP, New York. http://fundaoinvestigation.com/

Nash, D.F.T., Powell, J.J.M. and Lloyd, I.M. 1992a. Initial investigations of the soft clay test site at Bothkennar." *Géotechnique* 42 (2): 163–181.

Nash, D.F.T., Sills, G.C. and Davison, L.R. 1992b. One-dimensional consolidation testing of soft clay from Bothkennar. *Géotechnique* 42 (2): 241–256.

Nutt, N.R.F. and Houlsby, G.T. 1991. Cone pressuremeter in carbonate (Dogs Bay) sand." *Calibration Chamber Testing*, (Proc. ISOCCT, Potsdam), Elsevier, New York: 265-276.

Olson, S.M., and Stark, T.D. 2002. Liquefied strength ratio from liquefaction flow failure case histories. *Canadian Geotechnical Journal* 39 (3): 629–647.

Olson, S.M., and Stark, T.D. 2003. Yield strength ratio and liquefaction analysis of slopes and embankments. *Journal of Geotechnical & Geoenvironmental Engineering*: 129(8): 727–737.

Olson, S.M. and Johnson, C.I. 2008. Analyzing liquefaction-induced lateral spreads using strength ratios. *Journal of Geotechnical and Geoenvironmental Engineering* 134 (8): 1035–1049.

Ouyang, Z. and Mayne, P.W. 2018. Effective friction angle of clays and silts from piezocone. *Canadian Geotechnical Journal*. 55(9): 1230–1247; doi.org/10.1139/cgj-2017-0451.

Ouyang, Z. and Mayne, P.W. 2019. Modified NTH method for assessing effective friction angle of normally consolidated and overconsolidated clays from piezocone tests. *Journal of Geotechnical & Geoenvironmental Engineering* 145(10), ASCE doi.org/10.1061/(ASCE) GT.1943-5606.0002112

Ouyang, Z. and Mayne, P.W. 2020a. Variable rate piezocone data evaluated using NTH limit plasticity solution. ASTM *Geotechnical Testing Journal* 44 (1): doi.org/10.1520/GTJ20190183

Ouyang, Z. and Mayne, P.W. 2020b. Effective stress friction angle of normally-consolidated and overconsolidated intact clays from piezocone tests. *Geotechnical Engineering Journal of the SEAGS and AGSSEA*, Vol. 51, No. 2: 1-6. ISSN 0046-5828

Pane, V., Brignoli, E., Manassero, M. and Soccodato, C. 1995. Cone penetration testing in Italy. *Proceedings, Symposium on Cone Penetration Testing,* Vol. 1 (CPT'95), Swedish Geotechnical Society, Linköping: 101-114. PDF available at: www.usucger.org

Papadopoulos, B.P. 1992. Settlements of shallow foundations on cohesionless soils. *Journal Geotechnical Engineering* 118 (3): 377-393.

Parez, L. and Fauriel, R. 1988. Le piézocône améliorations apportées à la reconnaissance des sols. *Revue Française de Géotechnique*, No. 44. EDP Sciences, Paris: 13–27.

Parkin, A.K. 1991. Chamber testing of piles in calcareous sand and silt. *Calibration Chamber Testing*, (Proc. ISOCCT, Potsdam), Elsevier, New York: 289–302.

Perret, D., Charrois, E. and Bolduc, M. 2016. Shear wave velocity estimation from piezocone test data for eastern Canada sands." *Proceedings, GeoVancouver: 69th Canadian Geotechnical Conference:* Canadian Geotechnical Society: www.cgs.ca

Pestana, J.M. and Whittle, A.J. 1995. Compression model for cohesionless soils. *Geotechnique* 45 (4): 611-631.

Peuchen, J., Adrichem, J., and Hefer, P. A. 2005. Practice notes on pushing penetrometers for offshore geotechnical investigation. *Frontiers in Offshore Geotechnics* (Proc. ISFOG-1, Perth), Taylor & Francis, London: 973–979.

Pidlisecky, A., Knight, R. and Haber, E. 2006. Cone-based electrical resistivity tomography. *Geophysics,* Vol. 71 (4): G157-G167.

Plewes, H.D., Davies, M.P., and Jefferies, M.G. 1992. CPT based screening procedure for evaluating liquefaction susceptibility. *Proc. 45th Canadian Geotechnical Conference (Toronto)*, Vol. 4, BiTech Publishers, Vancouver, BC: 1–9.

Plewes, H.D., Pillai, V., Morgan, M.R. and Kilpatrick, B.L. 1993. In-situ sampling, density measurements, and testing of foundation soils at Duncan Dam. *Proc. 46th Canadian Geotechnical Conference (Saskatoon)*, BiTech Publishers, Vancouver: 223–235.

Powell, J.J.M. and Quarterman, R.S.T. 1988. The interpretation of cone penetration tests in clays, with particular reference to rate effects. *Penetration Testing 198*8, Vol. 2 (Proc. ISOPT-1, Orlando), Balkema, Rotterdam: 903–909.

Powell, J.J.M. and Lunne, T. 2005a. Use of CPTU data in clays and fine grained soils. *Studia Geotechnica et Mechanica* 27 (Issues 3-4): 29–66.

Powell J.J.M. and Lunne T. 2005b, A comparison of different sized piezocones in UK clays, *Proc. Intl. Conf. Soil Mechanics & Geotech Engineering*, Vol. 2 (Proc. XVI ICSMGE, Osaka): 729-735.

Quille, M.E., and O'Kelly, B.C. 2010. Geotechnical properties of zinc/lead mine tailings from Tara Mines, Ireland." *Proceedings of the 2010 Geoshanghai International Conference: Geoenvironmental Engineering and Geotechnics: Progress in Modeling and Applications,* (GSP 204, Shanghai), ASCE, Reston, VA: 111–117.

Quiros, G.W. and Young, A. 1988. Comparison of field vane, CPT, and laboratory strength data at Santa Barbara channel site, *Vane Shear Strength Testing in Soils: Field and Laboratory Studies.* ASTM, STP 1014: 306–317.

Randolph, M.F. 2004. Characterisation of soft sediments for offshore applications. *Geotechnical & Geophysical Characterization*, Vol. 1 (Proc. ISC-2, Porto) Millpress, Rotterdam: 209–232.

Rauter, S. & Tschuchnigg, F. 2021. CPT data interpretation employing different machine learning techniques. *Geosci. J.* 11(7), 265.

Reale, C., Gavin, K., Librić, L., Jurić-Kaćunić, D. 2018. Automatic classification of fine-grained soils using CPT measurements and Artificial Neural Networks. *Adv. Eng. Inform.* 36: 207–215.

Reid, D. 2019. Additional analyses of the Fundão Tailings storage facility: In-situ state and triggering conditions. *Journal of Geotechnical & Geoenvironmental Engineering* 145(11): 04019088

Reid, D. 2015. Estimating slope of critical state line from cone penetration test—an update. *Canadian Geotechnical Journal* 52 (1): 46–57.

Reid, D., Fourie, A., Ayala, J.L, et al. 2020. Results of a critical state line testing round robin programme. *Geotechnique* 71(7): 616-630. https://doi.org/10.1680/ jgeot.19.P.373

Rix, G.J., Mayne, P.W., Bachus, R.C., et al. 2019. *NCHRP Manual on Subsurface Investigation*, Web Document 258, National Cooperative Highway Research Board, Transportation Research Board, Washington, DC: 373 pages. www.trb.org

Robertson, P.K. and Campanella, R.G. 1983. Interpretation of cone penetration tests. part i: sand.” *Canadian Geotechnical Journal* 20 (4): 718–733.

Robertson, P.K., Campanella, R.G., Gillespie, D. and Greig, J. 1986. Use of piezometer cone data. *Use of in Situ Tests in Geotechnical Engineering*, (GSP 6, Blacksburg), ASCE, Reston, VA: 1263–1280.

Robertson, P.K. 1990. Soil classification using the cone penetration test. *Canadian Geotechnical Journal* 27 (1): 151–158.

Robertson, P.K. 1991. Soil classification using the cone penetration test: reply. *Canadian Geotechnical Journal* 28 (1): 176–178.

Robertson, P.K. and Wride (Fear), C.E. 1998. Evaluating cyclic liquefaction potential using the cone penetration test. *Canadian Geotechnical Journal* 35 (3): 442–459.

Robertson, P.K., Wride, C.E., List, B.R., Atukorala, U., Biggar, K.W., Byrne, P.M. et al. 2000. The CANLEX project: Summary and conclusions. *Canadian Geotechnical Journal* 37(3): 563–591.

Robertson, P.K. 2004. Evaluating soil liquefaction and post-earthquake deformations using the CPT. *Geotechnical & Geophysical Site Characterization*, Vol. 1 (Proc. ISC-2, Porto), Millpress, Rotterdam: 233–249.

Robertson, P.K. 2009a. CPT-DMT correlations. *Journal of Geotechnical and Geoenvironmental Engineering* 135 (11): 1762–1771.

Robertson, P.K. 2009b. Interpretation of cone penetration tests—a unified approach. *Canadian Geotechnical Journal* 46 (11): 1337–1355.

Robertson, P.K. 2009c. Performance-based earthquake design using the CPT. *Proceedings, International. Conf. on Performance-Based Design in Earthquake Geotechnical Engineering* (IS-Tokyo), CRC Press, London: 21 pages.

Robertson, P.K. 2010a. Estimating in-situ state parameter and friction angle in sandy soils from CPT. *Proc. 2nd Intl. Symposium on Cone Penetration Testing* (CPT'10, Huntington Beach, CA), Vol. 2, Omnipress, Wisconsin: 471-478.

Robertson, P.K. 2010b. Evaluation of flow liquefaction and liquefied strength using the cone penetration test. *Journal of Geotechnical and Geoenvironmental Engineering* 136 (6): 842–853.

Robertson, P.K., and K.L Cabal. 2010. Estimating soil unit weight from CPT.” *Proceedings of the 2nd International Symposium on Cone Penetration Testing,* Vol. 2 (CPT’10, Huntingdon Beach, CA), Omnipress: 447–454.

Robertson, P.K., and K.L. Cabal. 2015. *Guide to Cone Penetration Testing for Geotechnical Engineering, 6th Edition*. Gregg Drilling, Signal Hill, CA: 140 p.

Robertson, P.K. 2016. Cone penetration test (CPT)-based soil behavior type (SBT) classification system—an update. *Canadian Geotechnical Journal* 53 (12): 1910–1927.

Robertson, P.K. 2021. Evaluation of flow liquefaction and liquefied strength using the CPT: an update. *Canadian Geotechnical Journal* 18 (6): https://doi.org/10.1139/cgj-2020-0657

Sadrekarimi, A. 2014. Effect of the mode of shear on static liquefaction analysis. *Journal of Geotechnical and Geoenvironmental Engineering* 140 (12): 04014069.

Salgado, R., Mitchell, J.K. and Jamiolkowski, M. 1998. Calibration chamber size effects on penetration resistance in sand. *Journal of Geotechnical and Geoenvironmental Engineering* 124 (9): 878–888.

Salgado, R., Bandini, P. and Karim, A. 2000. Shear strength and stiffness of silty sand. *Journal of Geotechnical and Geoenvironmental Engineering* 126 (5): 451–462.

Sandven, R. 1990. Strength and deformation properties of fine grained soils obtained from piezocone tests. *PhD thesis*, Institutt for Geoteknikk, Norwegian Inst. of Technology (NTH), Trondheim.

Saxena, S.K., Hedberg, J. and Ladd, C.C. 1978. Geotechnical properties of Hackensack Valley Varved Clays of New Jersey." *Geotechnical Testing Journal* 1 (3): 148–161.

Schaeffers, J. and Weemees, I. 2012. Comparison of in-situ shear strength measurement techniques of soft clays. *Vancouver Geotechnical Society Symposium*.

Schmertmann, J.H. 1970. Static cone to compute static settlement over sand. *Journal of the Soil Mechanics & Foundations Division* (ASCE), Vol. 90 (SM3): 1011-1043.

Schmertmann, J.H. 1978. *Guidelines for Cone Penetration Test: Performance and Design*. Rept. FHWA-TS-78-209, Federal Highway Administration, Washington, DC: 146 p.

Schmertmann, J.H. 1986. Dilatometer to compute foundation settlement. *Use of In-Situ Tests in Geotechnical Engineering* (GSP 6, Blacksburg), ASCE, Reston, VA: 303–321.

Schmidt, B. 1983. Discussion: "K_0-OCR relationships in soil", *Journal of the Geotechnical Engineering Division,* ASCE, Vol. 109 (GT2): 866-867.

Schnaid, F. 2005. Geocharacterisation and properties of natural soils by in situ tests. *Proceedings 16th International Conference on Soil Mechanics and Geotechnical Engineering*, Vol. 1 (ICSMGE, Osaka), IOS Press, Rotterdam: 3-46. PDF available from: www.issmge.org

Schnaid, F. 2009. *In Situ Testing in Geomechanics: The Main Tests*. CRC Press, Taylor & Francis. London: 320 p.

Schneider, J.A. 2007. Analysis of piezocone data for displacement pile design. *PhD dissertation*, School of Civil & Resource Engineering, Univ. of Western Australia, Perth.

Schneider, J.A., Randolph, M.F., Mayne, P.W. and Ramsey, N.R. 2008. Analysis of factors influencing soil classification using normalized piezocone tip resistance and pore pressure parameters. *Journal of Geotechnical and Geoenvironmental Engineering* 134 (11): 1569–1586.

Schneider, J.A. and Hotstream, J.N. 2010. *Cone Penetrometer Comparison Testing*. Report WHRP 0092-10-10, Wisconsin Highway Research Project prepared by Univ. of Wisconsin-Madison, Dept. of Civil & Environmental Engineering: 298 pages.

Schneider, J.A., Hotstream, J.N., Mayne, P.W. and Randolph, M.F. 2012. Comparing CPTU Q–F and Q–$\Delta u_2/\sigma'_{v0}$ soil classification charts. *Géotechnique Letters* 2 (4): 209–215.

Schofield, A.N. and Wroth, C.P. 1968. *Critical State Soil Mechanics*. McGraw-Hill, London: 310 p.

Seed, H.B. 1976. State of the art paper: Evaluation of soil liquefaction effects on level ground during earthquakes. *Liquefaction Problems in Geotechnical Engineering*, (Proc. ASCE National Convention, Philadelphia), Preprint 2752, American Society of Civil Engineers, Reston/VA: 1-104.

Seed, H.B. 1979. Soil liquefaction and cyclic mobility evaluation for level ground during earthquakes. *Journal of Geotechnical Engineering*, Vol. 105 (GT2): 201-256.

Seed, H.B. 1987. Design problems in soil liquefaction. *Journal of the Geotechnical Engineering Division* (ASCE) 113(8): 827–845.

Seed, R.B. and Harder, L.R. 1990. SPT-based analysis of cyclic pore pressure generation and undrained residual strength. *Proceedings, Seed Memorial Symposium*. Vancouver, BC: BiTech Publishers: 351–376.

Senneset, K., Sandven, R., Lunne, T., By, T. and Amundsen, T. 1988. Piezocone tests in silty soils. *Penetration Testing 1988, Vol. 2* (Proc. ISOPT-1, Orlando), Balkema, Rotterdam: 955–966.

Senneset, K., Sandven, R. and Janbu, N. 1989. Evaluation of soil parameters from piezocone tests. *Transportation Research Record* 1235, National Academy Press, Washington, DC: 24-37.

Shedlock, K.M. and Tanner, J.G. 1999. Seismic hazard map of the western hemisphere. *Annali Di Geofisica* Vol. 42(6): 1199-1214,

Sills, G. 1998. Development of structure in sedimenting soils. *Philosophical Transactions of the Royal Society*, London: 2515–2534.

Stark, T.D. and Eid, H.T. 1994. Drained residual strength of cohesive soils. *Journal of Geotechnical Engineering*, 10.1061/(ASCE)0733-9410(1994)120:5(856): 856–871.

Stark, T.D. and Eid, H.T. 1997. Slope stability analyses in stiff fissured clays. *Journal of Geotechnical & Geoenvironmental Engineering*, 10.1061/(ASCE)1090-0241(1997): 123:4(335): 335–343.

Stark, T.D. and Olson, S.M. 1995. Liquefaction resistance using CPT and field case histories. *Journal of Geotechnical Engineering* 121 (12): 856–869.

Stark, T.D., Lewis, J.R., Castro, G., Walberg, F.C. and Mathews, D.L. 2011. Liquefaction subsurface investigation for Milford Dam. *Canadian Geotechnical Journal* 48 (10): 1504–1519.

Stark, T.D., and Hussain, M. 2013. Empirical correlations: Drained shear strength for slope stability analyses. *Journal of Geotechnical & Geoenvironmental Engineering* 139(6): 853–862, 10.1061/(ASCE)GT.1943-5606.0000824.

Stewart, D.P. 1991. A new site investigation tool for the centrifuge. *Proceedings of the International Conference on Centrifuge*, Univ. CO-Boulder, Colorado, USA.

Stewart, D.P., and Randolph, M.F. 1994. T-bar penetration testing in soft clay. *Journal of Geotechnical Engineering* 120 (12): 2230–2235.

Stolte, A.C. and Cox, B.R. 2020. Towards consideration of epistemic uncertainty in shear wave velocity measurements obtained via seismic cone penetration testing. *Canadian Geotechnical Journal* 57: 48–60 (2020) dx.doi.org/10.1139/cgj-2018-0689

Stuedlein, A.W. 2008. Bearing capacity and displacement of spread footings on aggregate pier reinforced clay. *PhD Dissertation*, Dept. of Civil & Environmental Engineering, Univ. of Washington, Seattle: 585 pages.

Styler, M.A. and Mayne, P.W. 2013. Site investigation using continuous shear wave velocity measurements during cone penetration testing at Gloucester, Ontario. *Proceedings, GeoMontreal 2013, 66th Canadian Geotechnical Conference*, Paper 345.

Styler, M.A., Weemees, I., and Mayne, P.W. 2016. Experience and observations from 35 years of seismic cone penetration testing (SCPTu). *Proceedings GeoVancouver 2016* (Proc. 69th Canadian Geotechnical Conference), Canadian Geotechnical Society: www.cgs.ca

Styler, M.A., Mayne, P.W., McGowan, D. and Sharp, J.T. 2018a. Predicting changes in static liquefaction susceptibility using cone penetration tests. *Proceedings, The Mine Waste and Tailings Conference*, Session 10, Paper 41, Brisbane: tailings.ausimm.com

Styler, M.A., McGowan, D. and Sharp, J. 2018b. Characterizing soft soil sand tailings by gamma cone penetration testing. *Proceedings. IOSTC’18, Edmonton, AB.*

Styler, M.A., Greig, J. and Nguyen, M. 2019. Estimating drainage conditions during in-situ cone penetration. *Proceedings Geo-Congress 2019,* (GSP 311, Philadelphia), ASCE, Reston, Virginia.

Sully, J.P. and Eschesuria, H.J. 1988. In-situ density measurement with nuclear cone penetrometer. *Penetration Testing 1988*, Vol. 2 (Proc. *ISOPT-1,* Orlando), Balkema, Rotterdam: 1001–1006.

Sully, J.P. 1991. Measurement of in situ lateral stress during full-displacement penetration tests. *PhD thesis*, Dept of Civil Engineering, University of British Columbia, Vancouver, BC.

Sully, J.P., Robertson, P.K., Campanella, R.G. and Woeller, D.J. 1999. An approach to evaluation of field CPTU dissipation data in overconsolidated fine-grained soils. *Canadian Geotechnical Journal* 36 (2): 369–381.

Susila, E. and Hryciw, R.D. 2003. Large displacement FEM modelling of the cone penetration test (CPT) in normally consolidated sand. *International Journal for Numerical and Analytical Methods in Geomechanics* 27 (7): Wiley Online Library: 585–602.

Suzuki, Y. 2015. Investigation and interpretation of cone penetration rate effects. *PhD dissertation*, School of Civil, Environmental, and Mining Engineering, Univ. of Western Australia: 323 pages.

Tanaka, Y. and Sakagami, T. 1989. Piezocone testing in underconsolidated clay. *Canadian Geotechnical Journal* 26 (4): 563–567.

Tanaka, H. 2000. Sample quality of cohesive soils: lessons from three sites: Ariake, Bothkennar and Drammen. *Soils and Foundations* 40 (4): 57–74.

Tara, D.J. 2012. Pitt River Bridge 2007 static pile loading test. *Full-Scale Testing and Foundation Design: Honoring Bengt H. Fellenius*, (GSP 227), ASCE, Reston, VA: 289–306.

Tavenas, F. and Leroueil, S. 1987. State-of-the-art on laboratory and in situ stress-strain-time behavior of soft clays. *International Symposium on Geotechnical Engineering of Soft Soils*, 1–146.

Taylor, B.B., Lewis, J.F. and Ingersoll, R.W. 1993. Comparison of interpreted seismic profiles to geotechnical borehole data at Hibernia. *Proceedings of the 4th Canadian Conference on Marine Geotechnical Engineering*, St. John's, Newfoundland: 685–708.

Teh, C.I. and Houlsby, G.T. 1991. Analytical study of the cone penetration test in clay. *Géotechnique* 41 (1): 17–34.

Thompson, G.R. and Long, L.G. 1989. Hibernia geotechnical investigation and site characterization. *Canadian Geotechnical Journal* 26 (4): 653–678.

Torrez-Cruz, L.A. (2015). CPT-based soil type classification in a platinum tailings storage facility. From Fundamentals to Applications in Geotechnics, (Proc. 15th PCSMGE, Buenos Aires), IOS Press, Amsterdam: 406-413.

Tumay, M.T., Abu-Farsakh, M. and Zhang, Z. 2008. From theory to implementation of a CPT-based probabilistic and fuzzy soil classification. *From Research to Practice in Geotechnical Engineering*, GSP 180, ASCE, Reston, Virginia: 259–276.

Tümay, M.T., HatipKarasulu, Y., Młynarek, Z. and Wierzbicki, J. 2011. Effectiveness of CPT-based classification methods for identification of subsoil stratigraphy. *Proceedings of the 15th European Conference on Soil Mechanics & Geotechnical Engineering*, Athens: 91–98.

Turner, B., Brandenberg, S.J. and Stewart, J.P. 2014. Evaluation of collapse and non-collapse of parallel bridges affected by liquefaction and lateral spreading. *PEER Report 2014/10*, Pacific Earthquake Engineering Research Center, Univ. California, Los Angeles: 111 p.

Turner, B.J., Brandenberg, S.J. and Stewart, J.P. 2016. Case study of parallel bridges affected by liquefaction and lateral spreading. *Journal of Geotechnical & Geoenvironmental Engineering* 142(7): 05016001.

Uzielli, M., Mayne, P.W. and Cassidy, M.J. 2013. Probabilistic assessment of design strengths for sands from in-situ testing data. *Modern Geotechnical Design Codes of Practice, Advances in Soil Mechanics & Geotechnical Engineering*, Vol. 1, IOS-Millpress, Amsterdam: 214-227.

Uzielli, M. and Mayne, P.W. 2019. Probabilistic assignment of effective friction angle of sands and silty sands from CPT using quantile regression. *Georisk: Assessment & Management of Risk for Engineered Systems and Geohazards* 13(4): 272-275. DOI: 10.1080/17499518.2019.1663388

Vardanega, P.J., and M.D. Bolton. 2013. Stiffness of clays and silts: normalizing shear modulus and shear strain. *Journal of Geotechnical and Geoenvironmental Engineering* 139 (9): 1575–1589.

Yafrate, N.J. 2008. Use of full flow penetrometers in soft clay. PhD dissertation, Dept. Civil & Environmental Engineering, Univ. of California at Davis.

Velosa, C.L. Remmes, B. and Bik, M. 2013. Strength characterization of soft marine deposits off East Africa using the CPT stinger method. *Proceedings, Offshore Technology Conference*, Houston, TX. Intecsea.

Vucetic, M. and Dobry, R. 1991. Effect of soil plasticity on cyclic response. *Journal of Geotechnical Engineering* 117 (1): 89–107.

Wair, B.R., DeJong, J.T. and Shantz, T. 2012. *Guidelines for Estimation of Shear Wave Velocity Profiles*. PEER Report 2012/08, Pacific Earthquake Engineering Research Center, Univ. CA: 95 p.

Walton, W.H., and Butler, W. 2009. Root cause analysis of TVA Kingston dredge pond failure on December 22, 2008 Volume I–Summary report volume II–geological and field explorations. AECOM.

Wang, H., Wang, X., Wellmann, J.F., Liang, R.Y. 2019. A Bayesian unsupervised learning approach for identifying soil stratification using cone penetration data. *Can. Geotech. J.* 56: 1184–1205.

Wehr, W. 2005. Influence of the carbonate content of sand on vibrocompaction. *Proc. 6th International Conference on Ground Improvement Techniques*, Coimbra, Portugal.

Whittle, A.J., DeGroot, D.J., Ladd, C.C. and Seah, T-H. 1994. Model prediction of anisotropic behavior of Boston Blue Clay. *Journal of Geotechnical Engineering* 120 (1): 199-224.

Wroth, C.P. 1984. Interpretation of in situ soil tests. *Géotechnique* 34 (4): 449–489.

Wroth, C.P. and Houlsby, G.T. 1985. Soil mechanics-property characterization and analysis procedures." *Proceedings of the 11th International Conference Soil Mechanics & Foundation Engineering,* Vol. 1, (ICSMFE, San Francisco), Balkema, Rotterdam: 1–54. www.issmge.org

Yafrate, N.J., DeJong, J.T. and DeGroot, D.J. 2007. The influence of full-flow penetrometer area ratio on penetration resistance and undrained and remoulded shear strength. *Proc. 6th Intl. Offshore Site Investigation & Geotechnics Conference*, London; Society for Underwater Technology: 461-468.

Yan, Y., White, D.J. and Randolph, M.F. 2011. Penetration resistance and stiffness factors for hemispherical and toroidal penetrometers in uniform clay. ASCE *International Journal of Geomechanics* 11 (4): 263-275.

Yoshimine, M., Robertson, P.K. and Wride (Fear), C.E. 1999. Undrained shear strength of clean sands to trigger flow liquefaction. *Canadian Geotechnical Journal* 36(5): 891-906.

Youd, T.L. 1973. Factors controlling maximum and minimum densities of sands. *Evolution of Relative Density and Its Role in Geotechnical Projects Involving Cohesionless Soils*, ASTM STP 523, American Society for Testing & Materials, West Conshohocken, PA: 98-112.

Youd, T.L., Idriss, I.M., Andrus, R.D., Arango, I., Castro, G., Christian, J.T., Dobry, R. et al. 2001. Liquefaction resistance of soils: summary report from the 1996 NCEER and 1998 NCEER/NSF workshops on evaluation of liquefaction resistance of soils. *Journal of Geotechnical and Geoenvironmental Engineering* 127 (10): 817–833.

Yu, H.S. and Mitchell, J.K. 1998. Analysis of cone resistance: review of methods. *Journal of Geotechnical and Geoenvironmental Engineering* 124 (2): 140–149.

Zhang, G., Robertson, P.K. and Brachman, R.W.I. 2004. Estimating liquefaction-induced lateral displacements using the standard penetration test or cone penetration test. *Journal of Geotechnical & Geoenvironmental Engineering* 130(8): 861-871.

Zhang, W., Wu, C., Zhong, H., Li, Y., Wang, L. 2021. Prediction of undrained shear strength using extreme gradient boosting and random forest based on Bayesian optimization. *Geosci. Front.* 12: 469–477.

GLOBAL LEADERS IN SITE CHARACTERIZATION

CANADA

Vancouver, BC
Corporate Head Office
201 - 8327 Eastlake Drive
Burnaby, BC, V5A 4W2
+1-604-273-4311
+1-604-273-4066 (Fax)
conetecYVR@conetec.com

Operations
9545 Telegraph Trail
Surrey, BC, V4N 4G9
+1-604-888-2206
conetecYVR@conetec.com

Kelowna, BC
2848 Fenwick Road,
Kelowna, BC, V1X 5E4
+1-250-765-2210
conetecYVR@conetec.com

Calgary, AB
6235 B 86 Ave SE
Calgary, AB, T2C 2S4
+1-587-620-2205
conetecAB@conetec.com

Edmonton, AB
2820 Ellwood Drive SW
Edmonton, AB, T6X 0A9
+1-780-485-1095
conetecAB@conetec.com

Fort McMurray, AB
+1-604-273-4311
+1-780-880-0161
conetecAB@conetec.com

Toronto, ON
9033 Leslie St., Unit 15
Richmond Hill, ON, L4B 4K3
+1-905-886-2663
conetecON@conetec.com

Sudbury, ON
2601 Belisle Drive Unit 4
Val Caron, Sudbury, ON, P3N 1L1
+1-905-886-2663
conetecON@conetec.com

UNITED STATES

Anchorage, AK
+1-778-378-5095
conetecAK@conetec.com

Seattle, WA
1237 S Director St
Seattle, WA 98108
+1-253-397-4861
conetecWA@conetec.com

Portland, OR
3530 NW St Helens Road
Portland, OR 97210
+1-253-397-4861
conetecWA@conetec.com

San Francisco, CA
820 Aladdin Avenue
San Leandro, CA, 94577
+1-510-357-3677
conetecCA@conetec.com

Salt Lake City, UT
3750 W 500 South
Salt Lake City, UT, 84104
+1-801-973-3801
conetecSLC@conetec.com

West Berlin, NJ
436 Commerce Lane, Unit C
West Berlin, NJ, 08091
+1-856-767-8600
conetecNJ@conetec.com

Richmond, VA
606-S Roxbury Industrial Center
Charles City, VA, 23030
+1-804-966-5696
conetecVA@conetec.com

Houston, TX
3452 Bacor Road
Houston, TX 77084
+1-281-944-9013
conetecTX@conetec.com

Chicago, IL
1335 Louis Ave.
Elk Grove Village, IL 60007
+1-224-228-6286
conetecIL@conetec.com

MEXICO AND SOUTH AMERICA

Mexico City, Mexico
Av. Paseo de la Reforma 300, piso 13.
Col. Juárez 06600. MÉXICO, D.F.
+1-253-397-4861
conetecMX@conetec.com

Lima, Peru
Av. Producción Nacional 201,
Chorrillos - Lima, Perú
+51 (1) 719-2404
+51 991-888-209
conetecSA@conetec.com

Santiago, Chile
Apoquindo 3885, OF 1801, PS 18
Las Condes
Santiago, Chile
+56 (9) 9351 0696
conetecSA@conetec.com

South America
+56 (9) 9351 0696
conetecSA@conetec.com

SCAN HERE FOR OFFICE LOCATIONS

AUSTRALIA AND OCEANIA

Brisbane, Queensland
6 Chapman Place
Eagle Farm QLD 4009
+61 (0)4-0720-8389
conetecAU@conetec.com

Perth, Western Australia
113 Radium Street
Welshpool WA 6106
+61 (0)4-0720-8389
conetecAU@conetec.com

SOUTHERN AFRICA

Johannesburg, RSA
1 Park Rd, Richmond
Johannesburg 2092
South Africa
smcgregor@conetec.com

EUROPE

United Kingdom
Coldharbour Barn
Coldharbour Lane, Iden
East Sussex, TN31 7UT
+44 (0) 1797 280050
info@lankelma.co.uk

Scandinavia
Fleminggatan 2
60224 Norrkoping
Sweden
smcgregor@conetec.com

CONETEC MUD BAY DRILLING MIKISEW CONETEC LANKELMA

conetec.com | mudbaydrilling.com | lankelma.com